Technical Report

TR-10-49

Climate and climate-related issues for the safety assessment SR-Site

Svensk Kärnbränslehantering AB

December 2010

Svensk Kärnbränslehantering AB
Swedish Nuclear Fuel
and Waste Management Co

Box 250, SE-101 24 Stockholm
Phone +46 8 459 84 00

ISSN 1404-0344
SKB TR-10-49
ID 1263140
Updated 2013-02

Climate and climate-related issues for the safety assessment SR-Site

Svensk Kärnbränslehantering AB

December 2010

Keywords: Climate, Glacial, Ice sheet, Periglacial, Permafrost, Sea level, Global warming, Safety assessment, SR-Site.

Update notice

The original report, dated December 2010, was found to contain both factual and editorial errors which have been corrected in this updated version. The corrected factual errors are presented below.

Updated 2011-10

Location	Original text	Corrected text
Page 198, paragraph 2, line 1	…starts about 8 kyrs after present…	…starts about 7 kyrs after present…
Page 199, Figure 4-28, figure text line 5	...starts to grow around 8 kyrs…	...starts to grow around 7 kyrs…
Page 208, Table 4-5, line 7, column 2	7400 after present (AP) (9400 AD)	7000 after present (AP) (9000 AD)

Updated 2013-02

Location	Original text	Corrected text
Page 159, paragraph 6, line 5	/SKB 2010e Section 5.1.2/	/Lindborg 2010 Section 5.1.2/
Page 282, reference Jaquet et al. 2010	SKB TR-10-46	SKB R-10-46
Page 295, reference SKB 2006b	SKB TR-09-19	SKB TR-06-19
References	SKB, 2010d. Landscape Forsmark, SR-Site Biosphere. SKB TR-10-05, Svensk Kärnbränslehantering AB.	Lindborg T (ed), 2010. Landscape Forsmark – data, methodology and results for SR-Site. SKB TR-10-05, Svensk Kärnbränslehantering AB.

Preface

This document presents information on climate and climate-related issues relevant for long-term safety of a KBS-3 repository for spent nuclear fuel. It supports the safety assessment SR-Site.

The report was compiled by Assoc. Prof. Jens-Ove Näslund, SKB. A number of additional authors have contributed to various sections of the report as listed in Table 1-1.

The report was reviewed by Dr. Mike C. Thorne (Mike Thorne and Associates Limited), Prof. Peter Jansson (Stockholm university) and Dr. Lillemor Claesson Liljedahl (SKB).

Stockholm, December 2010

Jens-Ove Näslund
Person in charge of the SKB climate programme

Contents

1 Introduction

1.1 Purpose of the report

The purpose of this report is to document current scientific knowledge on climate and climate-related conditions, relevant to the long-term safety of a KBS-3 repository, to a level required for an adequate treatment in the safety assessment SR-Site. The report also presents a number of dedicated studies on climate and selected climate-related processes of relevance for the assessment of long term repository safety. Based on this information, the report presents a number of possible future climate developments for Forsmark, the site selected for building a repository for spent nuclear fuel in Sweden (Figure 1-1). The presented climate developments are used as basis for the selection and analysis of SR-Site safety assessment scenarios in the SR-Site main report /SKB 2011/. The present report is based on research conducted and published by SKB as well as on research reported in the general scientific literature.

1.2 Strategy for managing climate-related issues in safety assessments

1.2.1 Climate and climate-related changes

Climate-related changes such as the development of permafrost and ice sheets and variations in shore-level are the most important naturally occurring external factors affecting a repository for spent nuclear fuel in a time perspective up to hundreds of thousands of years. Most of the processes occurring in the biosphere and geosphere are likely to be affected by climate and climate-related changes in one way or another.

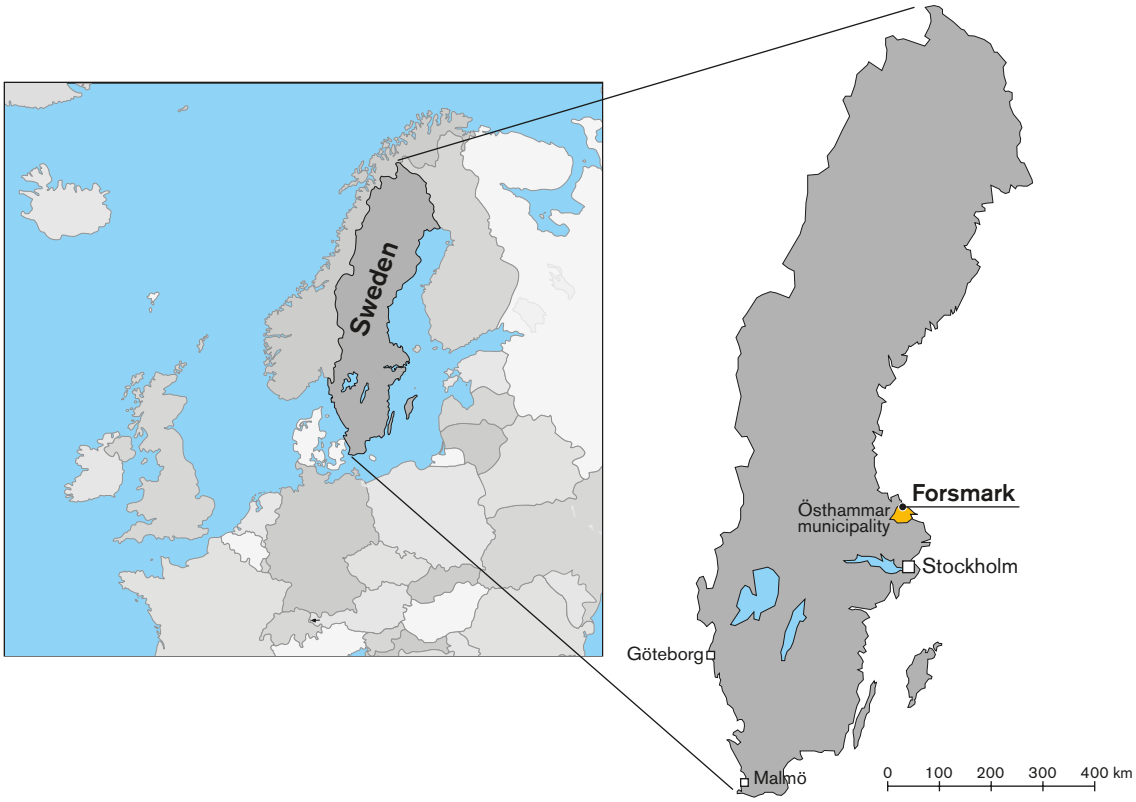

Figure 1-1. *Location map.*

Over the past 2.5 million years, Scandinavia has experienced several cycles of glaciation e.g. /Ehlers and Gibbard 2004/. Cold periods that include ice sheets gradually growing to maximum extents are known as *glacials*. Intervening periods with warm climate, when the ice sheets have extents similar to that at the present day, are called *interglacials*. A *glacial cycle* consists of a glacial and an interglacial. Within the glacial periods, warmer *interstadial* periods occur, as well as cool *stadial* periods. The shifting between glacials and interglacials is depicted for instance in the variation of the content of the heavy oxygen isotope, ^{18}O, in deep-sea sediments e.g. /Lisiecki and Raymo 2005/, which reflects both the temperature of the sea and the volume of water that has been bound in land-based ice sheets and glaciers globally, see Figure 1-2.

Figure 1-2 shows that over the last 700 kyrs, glacial-interglacial cycles of about 100 kyr duration have dominated global climate variation. The time frame of a Quaternary glacial-interglacial cycle, around 100 kyrs, is similar to the time it takes for the radioactivity in the spent fuel to decay to levels comparable to the activity in the natural uranium that was once used to manufacture the fuel /SKB 2011/. The time scale of a safety assessment for a final repository for spent nuclear fuel is one million years. The 100 kyr time scale, corresponding to a first future glacial cycle, forms a basis for the analysis of repository safety. For the remainder of the assessment period, this glacial cycle is assumed to be repeated. Alternative developments over the first 100 kyrs, including for instance periods of anthropogenic global warming, are also analysed. A time frame of 100 kyrs is also reasonable when determining the extremes of climate conditions the repository should be designed to withstand.

In very long time perspectives, several millions of years, geological processes like plate tectonic movements and uplift or downwarping, additional to crustal displacements due to glacial loading and unloading, will affect both the Earth climate system and the repository for spent nuclear fuel. However, the SR-Site safety assessment address timescales up to one million years /SKB 2011/, and therefore these geological processes are not included in the safety assessment.

1.2.2 Impact on repository performance and safety

Climate changes, permafrost development and the growth and decay of ice sheets will alter not only surface but also subsurface conditions. Freezing of groundwater, the presence of ice sheets, and changes in shore-level will change permeability, water turnover, groundwater pressure, groundwater flow and chemical composition. The ice load will alter rock stresses during different phases of a glaciation. This will, in turn, change bedrock permeability and as ice sheets melts away, a combination of large horizontal stresses and high pore water pressures may cause glacially induced faulting. In general, the integrated effects of the continuous evolution of climate-related conditions need to be considered, but

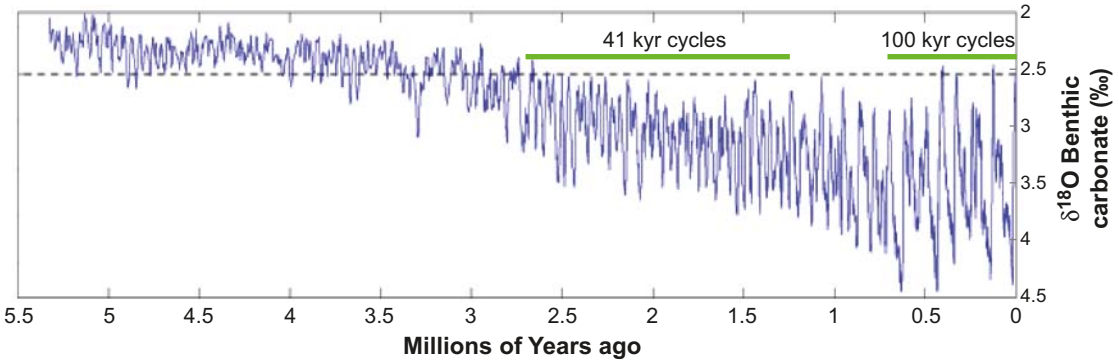

Figure 1-2. *Variations of $\delta^{18}O$ in deep-sea sediments over the last 5.5 million years /Lisiecki and Raymo 2005/. High $\delta^{18}O$ values indicate large global ice volume and low sea water temperature, i.e. colder climate conditions, whereas low $\delta^{18}O$ values indicate the opposite. The last 700 kyrs have been dominated by 100 kyr long glacial cycles. Modified from /Global Warming Art 2007, after Lisiecki and Raymo 2005/.*

there are also a number of more specific phenomena of importance for repository safety that require special attention. Based on the results of earlier and the present safety assessments, these include:

- The maximum hydrostatic pressure occurring at repository depth for glacial conditions.
- The maximum permafrost and ground freezing depth.
- The possible penetration of oxygen-rich groundwater to repository depth during glacial conditions.
- The possible penetration of dilute groundwaters to repository depth during glacial and temperate conditions, potentially causing erosion of buffer and backfill.
- The potential for glacially induced faulting.
- Factors affecting retardation in the geosphere, like high groundwater fluxes and mechanical influences on permeability.

1.2.3 Strategy for managing long-term evolution of climate-related processes

Definition of climate change and climate domains

There are various definitions of *climate change*. In the present report, climate change is defined according to the definition by the Intergovernmental Panel on Climate Change (IPCC), namely as "any change in climate over time whether due to natural variability or as a result of human activity" /IPCC 2001/. This differs from the definition used by United Nation's Framework Convention on Climate Change (UNFCCC) that defines climate change as "a change of climate that is attributed directly or indirectly to human activity that alters the composition of the global atmosphere, and that is in addition to natural climate variability over comparable time periods". Since climate may change due to both natural variability and to anthropogenic influences, the definition of climate change in SR-Site follows the one of IPCC.

From a safety assessment point of view, it is not possible to predict a single climate evolution in a 100 kyr time perspective with enough confidence for a safety assessment, although some attempts have been made to predict climate over this time scale, e.g. /Shaffer et al. 2009/. However, based on knowledge of climate variations in the past and on inferred future climate change, the extremes within which the climate of Sweden may vary can be estimated with reasonable confidence, also within this long time frame. Within these limits, characteristic climate-related conditions of importance for repository safety can be identified. The conceivable climate-related conditions can be represented as *climate-driven process domains* /Boulton et al. 2001a/ where such a domain is defined as "a climatically determined environment in which a set of characteristic processes of importance for repository safety appear". In the following parts of the report these climate-driven process domains are referred to as *climate domains.* The identified climate domains are denominated:

- The temperate climate domain.
- The periglacial climate domain.
- The glacial climate domain.

The purpose of identifying climate domains is to create a framework for the assessment of issues of importance for repository safety associated with particular climatically determined environments that may occur in Sweden. If a repository for spent nuclear fuel fulfils the safety requirements for plausible climate developments, including the transitions between climate domains, then the uncertainty regarding the climate domains more precise extent in time and space is of less importance.

The temperate climate domain is defined as regions without permafrost or presence of ice sheets. It is dominated by a temperate climate in a broad sense, with cold winters and either cold or warm summers. Precipitation may fall at any time of the year. The precipitation falls either as rain or snow. The temperate climate domain has the warmest climate of the three climate domains. Within the temperate climate domain, a site may also at times be submerged by the sea. Climates dominated by global warming are also included in the temperate climate domain.

The term periglacial is today used for a range of cold but non-glacial processes. In the periglacial environment, permafrost is a central, but not defining, element /French 2007/. However, for the present work, the *periglacial climate domain* is defined strictly as regions that contain permafrost.

Furthermore, the periglacial climate domain is a cold region but without the presence of an ice sheet. In this climate domain, permafrost occurs either in sporadic (less than 50% spatial coverage), discontinuous (between 50 and 90% coverage), or continuous form (more than 90% coverage). Although true for most of the time, regions belonging to the periglacial climate domain are not necessarily the same as regions with a climate that supports permafrost growth. For example, at the end of a period with periglacial climate domain the climate may be relatively warm, not building or even supporting the presence of permafrost. Instead, permafrost may be diminishing. However, as long as permafrost is present, the region is defined as belonging to the periglacial climate domain, regardless of the prevailing temperature at the ground surface. This way of defining the climate domain is used because the presence of the permafrost is more important for the safety function of the repository than the actual temperature at the ground surface. In general, the periglacial climate domain has a climate colder than the temperate climate domain and warmer than the glacial climate domain. Precipitation may fall either as snow or rain. Within the periglacial climate domain, a site may also at times be submerged by the sea.

The glacial climate domain is defined as regions that are covered by glaciers or ice sheets. Within the glacial climate domain, the glacier or ice sheet may in some cases be underlain by sub-glacial permafrost. In line with the definition of the periglacial climate domain, areas belonging to the glacial climate domain may not necessarily at all times have a climate that supports the presence of ice sheets. However, in general, the glacial climate domain has the coldest climate of the three climate domains. Precipitation normally falls as snow in this climate domain.

As previously mentioned, it is currently not possible to make confident long-term predictions of future climate, particularly taking into account the potential long-term significance of inferred current human-induced perturbations of the natural climate system. It is, however, likely that all three climate domains will appear repeatedly during the one million year assessment period, i.e. any reasonable evolution will have to address them, and transitions between them.

Reference glacial cycle, climate cases and safety assessment scenarios

The climate domains are first used to describe a *reference glacial cycle* for the coming 120 kyrs (Section 4.5), comprising a repetition of conditions reconstructed for the last glacial cycle (Section 4.4). The *reference glacial cycle* is not to be seen as a prediction of a future climate development at Forsmark, but as *one example* of a conceivable future evolution that covers climate-related conditions and sequences that could be expected in a 100 kyr time perspective. Furthermore, using a *reference glacial cycle* based on the last glacial cycle does not mean that glacial- and permafrost processes are regarded as more probable than processes related to warm climates for e.g. the coming 100 kyrs. The *reference glacial cycle* is supplemented by a number of additional climate cases that describe alternative possible future developments of climate and climate-related processes at Forsmark (Figure 1-3). The selection and description of these climate cases are based on i) knowledge on past changes in climate and environmental parameters, ii) anticipated future climate change affected by anthropogenic action, and iii) knowledge as to which processes are of importance for repository safety. A large part of the information used to select the climate cases has been obtained from previous safety assessments. In SR-Site, six future climate cases are described, including the *reference glacial cycle*, see Figure 1-3 and Section 4.5 and Chapter 5. For a summary of how the climate and climate-related processes develop in the six climate cases, see Section 5.6. For a description of the rationale of using a reference glacial cycle based on a reconstruction of conditions for the last glacial cycle, see Section 4.1.

The six climate cases are in turn used as the basis for the construction of safety assessment scenarios /SKB 2011/. In the safety assessment, the *reference glacial cycle* is used to construct a *main scenario*, aiming at describing a reasonable evolution of the repository system given the timing and lengths of periods with different climate domains as derived from the *reference glacial cycle*. There are two variants of the main scenario, i) a *base case,* comprising the reconstruction of climate and climate-related processes as described in the *reference glacial cycle*, i.e. the repetition of reconstructed last glacial cycle conditions, and ii) a *global warming variant,* defined from the *global warming case*, see Figure 1-3. The base case serves as one example of the evolution of climate, climate-related processes and the repository for a glacial cycle dominated by natural climate change, i.e. a development not affected by anthropogenically cased global warming. The base case is complemented by the global warming variant (Figure 1-3), where the inferred current human influence on climate is taken into account.

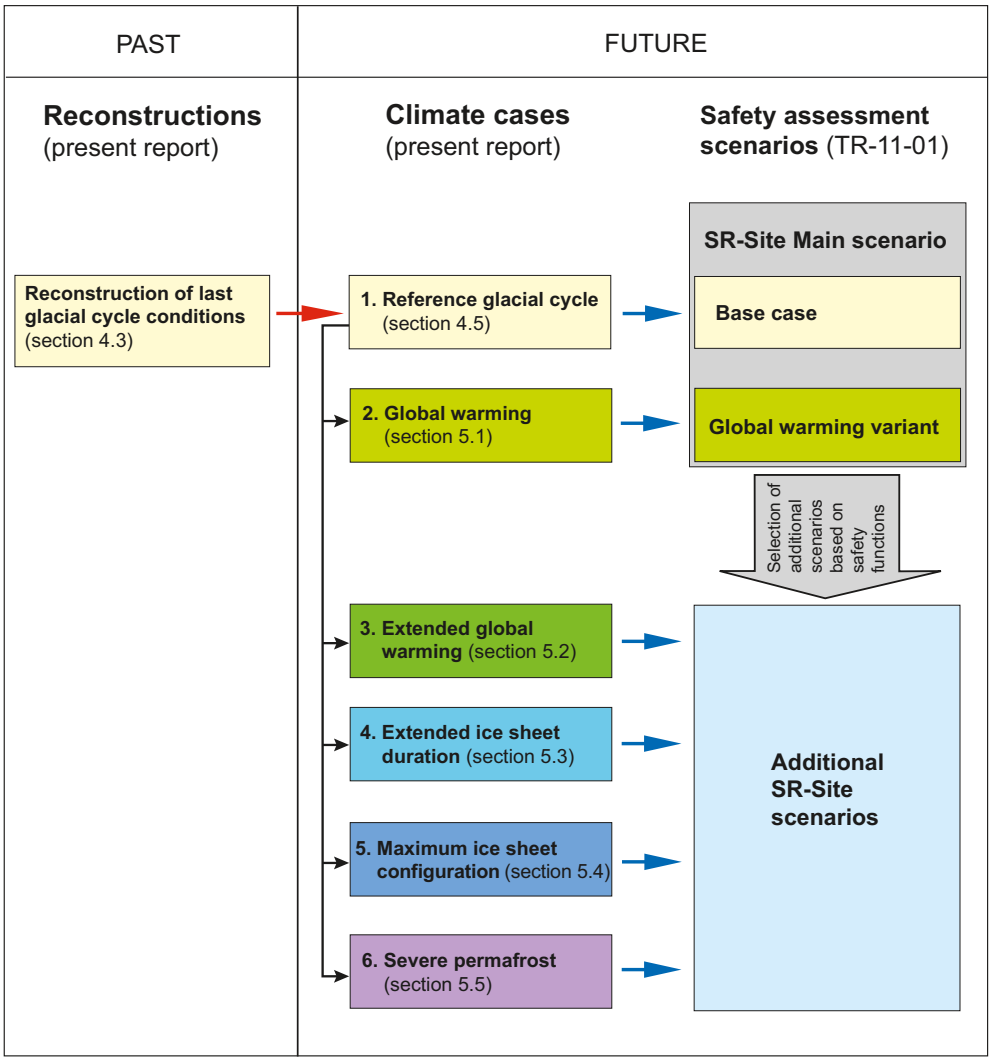

Figure 1-3. *Relationship between the reconstruction of last glacial cycle conditions, the reference glacial cycle, the additional climate cases, and the corresponding SR-Site safety assessment scenarios. The red arrow indicates the choice of repeating the reconstructed last glacial cycle conditions for a future reference glacial cycle. The black arrows indicate modifications made to the reference glacial cycle in order to construct additional future climate cases to obtain a comprehensive coverage of possible climate developments of relevance for long-term safety. Blue arrows show which climate cases have been used for the analysis of which safety assessment scenario. The figure also shows in which sections the climate cases are described in the present report. For information on the SR-Site safety assessment scenario selection (grey arrow) see the text and /SKB 2011/.*

Following the safety assessment analysis of the main scenario, a number of *additional scenarios* of importance for repository safety are selected (Figure 1-3). The scenario selection is based on the evolution in the main scenario and on an understanding of repository safety, see /SKB 2011/. The latter is expressed through a number of safety functions and safety function indicators, used to make a structured selection of additional scenarios. Detailed information about the safety function indicators and how the scenario selections are made is found in /SKB 2011/. Following the scenario selection, the additional scenarios are analyzed using the information from the associated climate cases (Figure 1-3). The additional scenarios essentially address relevant situations not covered by the main scenario.

For example, for the glacial climate domain the maximum possible ice sheet thickness is one parameter of interest for the analysis of hydrostatic pressure at repository depth. In the *base case of the main scenario*, the development of ice sheet thickness comes from a reconstruction of the Fennoscandian ice sheet during the last glacial cycle (Section 3.1.4), whereas in an *additional scenario* the effect of ice sheet thicknesses greater than those during the last glacial cycle are analysed using information from

the *maximum ice sheet configuration case* (Section 5.4), see Figure 1-3. In this way, the main scenario describes a plausible evolution of ice sheet thickness, and the additional scenario describes relevant variations of this evolution.

It is important to include the climate domains and sequences that have the greatest impact on repository safety. It is also important to include sequences yielding the peak risk during the assessment period. Based on results of earlier analyses, the highest risks (i.e. relating to radiogenic exposure to humans) are likely to occur during periods of temperate climate. Typical situations are i) a terrestrial system that has accumulated radionuclide releases over a long time, possibly at early stages in sea or lake sediments that subsequently is exposed and used for agriculture, and ii) a well intruding into the host rock and used for domestic purposes. In addition, periods of periglacial climate domain needs to be considered, where permafrost conditions change transport efficiency, exposure pathways and accumulation processes, and also constrains the land-use and use of well water.

1.3 Structure of the report

1.3.1 Overall report structure and authors

Following the introduction chapter, the present report includes three main chapters:

- An overview description of the climate system (Chapter 2).
- Identification and discussion of climate and climate-related issues, including reconstructions of the identified variables for the last glacial cycle (Chapter 3).
- A description of climate and climate-related conditions for the safety assessment reference glacial cycle (Chapter 4).
- A description of climate and climate-related conditions for the complementary climate cases (Chapter 5).

Chapter 2 includes an overview of present knowledge of the Earth's climate system and the climate conditions that can be expected to occur in Sweden on a 100 kyr time perspective. Based on this, climate-related issues relevant for the long-term safety of a KBS-3 repository are identified. These are documented in Chapter 3 to a level required for an adequate treatment in the safety assessment. Subsequently, in Chapter 4, an evolution for a 120 kyr year period is presented, including discussions of identified climate-related issues of importance for repository safety.

In Chapter 2 "The climate system" the intention is not to give a complete picture of the Earth climate system but rather a summary sufficient for identification of climate-related conditions and processes with a possible impact on repository performance. The interactions between these processes of importance for repository performance and other parts of the climate system set the limits for the documentation of the climate system in this report.

In Chapter 3 there are five sections that, in detail, describe the climate-related phenomena within the climate domains that may affect repository safety functions. These sections deal with the general characteristics of ice sheets, glacial hydrology, shore-level displacement, permafrost, and surface denudation, and for most of these parameters dedicated reconstructions of the development during the last glacial cycle are presented.

In Chapter 4 the complete reconstruction of last glacial cycle conditions is presented, together with the resulting *reference glacial cycle* over a future 120 kyr period. The latter thus includes the identified climate-related issues of importance for repository safety. Chapter 4 also includes a section with examples of last glacial cycle climates, since the range and variability during the last glacial cycle could be expected also for future glacial cycles.

In Chapter 5 the additional climate cases are described, complementing the *reference glacial cycle* described in Chapter 4. For instance, cases of global warming are included here (including detailed information for the Forsmark site), as well as other possible future climate developments.

In this context, a short comment on time scales should be made. Since Chapter 3 and Sections 4.1 to 4.4 mainly deals with reconstructions of climate-related conditions for the last glacial cycle the time scales used here runs from 120 kyrs before present (BP) up to present day. In Section 4.5 and

onwards, on the other hand, the reconstructions from the previous parts are used to construct cases of future developments of climate-related conditions. Therefore, the time scale used in Section 4.5 and onwards in the report runs from present day to 120 kyrs into the future.

In addition, the present report also includes three appendices. Appendix 1 and 2 describe data sets on temperature and ice sheet profiles respectively, data that subsequently have been used within other SR-Site activities. Appendix 1 gives a detailed account of the air- and ground temperature data sets that have been produced for SR-Site, and have been used for e.g. ice sheet (Section 3.1.4) and permafrost modelling /Hartikainen et al. 2010/. The appendix presents the original data, how the data have been modified within SR-Site, and a discussion about data uncertainty. Appendix 2 describes in detail the 2D ice sheet profiles that are used for modelling of groundwater flow under glacial conditions /Vidstrand et al. 2010/ and for THM studies /Lönnqvist and Hökmark 2010/. The temperature and ice sheet profile data sets are also presented in the /SKB 2010a/. Appendix 3 contains studies on a hypothetical situation where freezing at repository depth and bentonite buffer erosion are combined, complementing the information in the buffer freezing scenario in the SR-Site **Main report**.

As further described in the SR-Site **Main report** and in /SKB 2010b/ the content of the present report has been audited by comparison with national FEP databases from other assessment projects as compiled by NEA (Nuclear Energy Agency), see the SR-Site **FEP-report**. The models used for the construction of the *reference glacial cycle* and some of the complementary climate cases are documented in the SR-Site **Model summary report** /SKB 2010f/, while the data produced by the models are presented in the SR-Site **Data report** /SKB 2010a/. Results from the present climate report are used in the SR-Site **Main report** /SKB 2011/ and in reports supporting the main report.

The present report follows as far as possible the SR-Site template for documentation of processes regarded as internal to the repository system. However, the term processes is typically not used in this report, instead the term *issue* has been used. Each issue includes a set of processes together resulting in the behaviour of a system or feature. For instance, “ice sheet dynamics” is the result of several climatological, hydrological, and mechanical processes. But as the ice sheet can be seen as one entity in its interaction with the bed, these processes are jointly accounted for under the heading “ice sheet dynamics”. Given the content of the report, and the aim of following the template for SR-Site process reports, there is some necessary repetition of text between some of the chapters and sections.

A list of abbreviations is found at the end of the report.

The experts involved in describing the basic information about the climate system and climate-related issues are listed in Table 1-1. In addition, the sections “Handling in the safety assessment SR-Site” and “Handling of uncertainties in SR-Site” have been produced by Jens-Ove Näslund, SKB, in collaboration with the expert that assembled the information on the issue in question. All experts contributing to the present report are included in the SR-Site expert database. The sections The climate system, Climate variability and change, Climate in Sweden and Isostatic adjustment and shore-level displacement were originally written for the SR-Can safety assessment /SKB 2006a/ by the authors listed in Table 1-1, and have been adapted for the present report by Jens-Ove Näslund, SKB.

1.3.2 Structure for description of climate-related issues

In discussing each of the various climate-related issues, the following standardised structure has been adopted.

Overview/general description

Under this heading, a general description of the current knowledge regarding the climate-related issue is given.

Controlling conditions and factors

The external and internal conditions and factors that control each “issue” are discussed. *External* refers to systems that are not part of the described system/feature and that the described system/feature interacts with. For example, for “ice sheet dynamics”, the atmosphere and the bed are external factors and relevant aspects of them are described. *Internal* refers to conditions and factors governing system/feature

Table 1-1. Contributors to individual chapters and sections in the present report.

Chapter	Section(s)	Subsection(s)	Author(s)
1. Introduction	1.1–1.6	All	Jens-Ove Näslund, SKB
2. The climate system	2.1 Components of the climate system	All, except 2.1.3	Jörgen Bogren and Torbjörn Gustavsson, Klimator AB, Gothenburg University
		2.1.3	Jörgen Bogren and Torbjörn Gustavsson, Klimator AB, Gothenburg University
			Jens-Ove Näslund, SKB
	2.2 Climate forcing	2.2.1, 2.2.3	Jörgen Bogren and Torbjörn Gustavsson, Klimator AB, Gothenburg University
		2.2.2, 2.2.4	Jens-Ove Näslund, SKB
	2.3 Climate dynamics	All, except 2.3.4	Jörgen Bogren and Torbjörn Gustavsson, Klimator AB, Gothenburg University
		2.3.4	Moberg et al. 2006, Stockholm university
			Jens-Ove Näslund, SKB
	2.4 Climate in Sweden and Forsmark	2.4.1	Hans Alexandersson, Swedish Meteorological and Hydrological Inst. (SMHI)
		2.4.2	Jens-Ove Näslund, SKB
3. Climate and climate-related issues	3.1 Ice sheet dynamics	All	Jens-Ove Näslund, SKB
3.	3.2 Ice sheet hydrology	All, except 3.2.4, 3.2.6, 3.2.8	Peter Jansson, Stockholm university
		3.2.4	Peter Jansson, Stockholm university
			Jens-Ove Näslund, SKB
		3.2.6, 3.2.8	Jens-Ove Näslund, SKB
3.	3.3 Isostatic adjustment and shore-level changes	3.3.1, 3.3.7	Jens-Ove Näslund, SKB
			Pippa Whitehouse, University of Durham
		3.3.2, 3.3.4, 3.3.5	Pippa Whitehouse, University of Durham
		3.3.3, 3.3.6, 3.3.8	Jens-Ove Näslund, SKB
	3.4 Permafrost	3.4.1, 3.4.4, 3.4.5, 3.4.7	Juha Hartikainen, Aalto University School of Science and Technology
			Jens-Ove Näslund, SKB
		3.4.2, 3.4.3	Juha Hartikainen, Aalto University School of Science and Technology
		3.4.6, 3.4.8	Jens-Ove Näslund, SKB
	3.5 Surface denudation	3.5.1–3.5.4,	Mats Olvmo, Gothenburg university
			Jens-Ove Näslund, SKB
		3.5.5–3.5.8	Jens-Ove Näslund, SKB
4. Climate and climate-related conditions for the SR-Site safety assessment	4.1 Rationale and general approach	All	Jens-Ove Näslund, SKB
	4.2 Weichselian glacial history	4.2.1	Jens-Ove Näslund, SKB
			Hanna Lokrantz, Bergab*
			Gustav Sohlenius, SGU*
		4.2.2	Jens-Ove Näslund, SKB
	4.3 Examples of Weichselian climates	All, except 4.3.2 section on Early MIS 3, 4.3.2 section on Middle MIS 3	Jens-Ove Näslund, SKB
		4.3.2 Early MIS 3	Karin Helmens, Stockholm University**
			Jens-Ove Näslund, SKB
		4.3.2 section on Middle MIS 3 and 4.3.3. section on Late Weichselian	Jens-Ove Näslund, SKB
			Erik Kjellström, Rossby Centre, Swedish Meteorological and Hydrological Inst. (SMHI)***
			Jenny Brandefelt, KTH***
			Gustav Strandberg, Rossby Centre, Swedish Meteorological and Hydrological Inst. (SMHI)***

Chapter	Section(s)	Subsection(s)	Author(s)
	4.4 Reconstructed last glacial cycle conditions at Forsmark	All	Jens-Ove Näslund, SKB
	4.5 Reference glacial cycle	All	Jens-Ove Näslund, SKB
5. Additional climate cases for the safety assessment SR-Site	5.1 Global warming case	All, except 5.1.7	Jens-Ove Näslund, SKB
		5.1.7	Jens-Ove Näslund, SKB
			Erik Kjellström, Rossby Centre, Swedish Meteorological and Hydrological Inst. (SMHI)***
			Jenny Brandefelt, KTH Royal Institute of Technology***
			Gustav Strandberg, Rossby Centre, Swedish Meteorological and Hydrological Inst. (SMHI)***
	5.2 Extended global warming case	All, except 5.2.3 section on Sea-level rise up to year 2100	Jens-Ove Näslund, SKB
		5.2.3 section on Sea-level rise up to year 2100	Jens-Ove Näslund, SKB
			Lars Brydsten, Umeå University****
			Anders Engqvist, KTH Royal Institute of Technology****
			Tobias Lindborg, SKB****
	5.3 Extended ice sheet duration case	All	Jens-Ove Näslund, SKB
	5.4 Maximum ice sheet configuration case	All	Jens-Ove Näslund, SKB
	5.5 Severe permafrost case	All, except 5.5.3	Jens-Ove Näslund, SKB
		5.5.3	Juha Hartikainen, Aalto University School of Science and Technology*****
			Jens-Ove Näslund, SKB
	5.6 Summary of climate cases for the SR-Site safety assessment		Jens-Ove Näslund, SKB
Appendix 1 – Air temperature data	All	All	Jens-Ove Näslund, SKB
Appendix 2 – Ice sheet profiles	All	All	Jens-Ove Näslund, SKB
Appendix 3 – Combination of buffer erosion and freezing		A3.1	Jens-Ove Näslund, SKB
		A3.2	Juha Hartikainen, Aalto University School of Science and Technology******
		A3.3	Martin Birgersson, ClayTech
		A3.4	Jens-Ove Näslund, SKB

Authors with asterisks have not directly contributed written parts to the report. Instead texts have been adapted by Jens-Ove Näslund from the following supporting reports:

* /Lokrantz and Sohlenius 2006/.
** /Helmens 2009a/.
*** /Kjellström et al. 2009b/.
**** /Brydsten et al. 2009/.
***** /Hartikainen et al. 2010/.
****** /SKB 2006a, Section 4.4.1/.

behaviour and that are generally included in models of the system/feature, e.g. for "ice sheet dynamics" the creep process of ice. The external and internal conditions and factors are those that relate to the described behaviour of the system/feature, e.g. for "ice sheet dynamics" air temperature, geothermal heat flow and ice properties.

A table summarising the influence of the climate-related issue on the geological barrier of the repository is presented. The table includes the geosphere variables influenced by the system/feature and the variables associated with the system/feature that are required to be known to quantify the interaction between the system/feature and the repository system, e.g. for "ice sheet dynamics" basal temperature and melt-rate. In this context, the repository system includes both the geosphere and the engineered barriers.

Natural analogues/observations in nature

Under this heading observations in nature and, when applicable, present-day natural analogues regarding the process are summarised.

Model studies

In this section model studies of the process are summarised. This documentation focuses on process understanding and for instance includes sensitivity analyses. The handling of external and internal controlling conditions and factors are described, e.g. if spatially and temporally varying internal conditions considered.

Time perspective

The time scales on which the system/feature operates and changes are documented.

Handling in the safety assessment SR-Site

The handling of the documented interactions with the repository is discussed. As a result of the information under this subheading, a mapping of the climate-related issues to method of treatment and, in relevant cases, applicable models are produced. The mapping is characterised on various time scales.

Handling of uncertainties in SR-Site

Given the adopted handling in the safety assessment SR-Site as described above, the treatment of different types of uncertainties associated with the issue, within that general framework, is summarised under the following headings.

Uncertainties in mechanistic understanding: The uncertainties in the general understanding of the issue are discussed based on the available documentation and with the aim of answering the question: Are the basic scientific mechanisms governing the issue understood to a level necessary for the suggested handling? Alternative models may sometimes be used to illustrate this type of uncertainty.

Model simplification uncertainties: In most cases, the quantitative representation of a process contain simplifications, for instance in a numerical model. These may result in a significant source of uncertainty in the description of the system evolution. Alternative models or alternative approaches to simplification for a particular conceptual model may sometimes be used to illustrate this type of uncertainty.

Input data and data uncertainties: The input data necessary to quantify the process for the suggested handling are documented. The treatment of important input and output data and associated data uncertainties are described in detail in /SKB 2010a/, to which reference is made as appropriate.

Adequacy of references

For the description of each climate-related issue, the qualification of key references are described.

1.4 Publications supporting the SR-Site Climate report

1.4.1 Publications produced for SR-Site

Within the SKB climate programme, about 15 supporting reports and publications have been produced to support the SR-Site Climate report. Many of the topics that have been studied are by necessity linked to each other and in some cases therefore partly overlapping. Studies on climate, palaeoclimate and Weichselian glacial history were conducted by /Helmens 2009a, Houmark-Nielsen 2009, Kjellström et al. 2009b (including erratum Feb 2010), Wohlfarth 2009/. A special issue of Boreas /Wohlfarth and Näslund 2010/, with papers on conditions in Scandinavia during a long period prior to the Last Glacial Maximum of the last glacial cycle, was published as a result of a workshop on this topic arranged by SKB in 2007 /Näslund et al. 2008/. Permafrost development was studied by /Hartikainen et al. 2010/ while glacial hydrology was studied by /Jansson and Näslund 2009/. Surface denudation (i.e. weathering and erosion) was investigated by /Olvmo 2010/, while bore hole temperatures, geothermal heat and palaeoclimate was studied by /Sundberg et al. 2009/. Various aspects of glacial isostatic adjustment have been studied, such as sea-level change and shore-level displacement /Whitehouse 2009/ and crustal stresses under glacial conditions /Lund et al. 2009, Lund and Näslund 2009/. In addition, /Brydsten et al. 2009/ studied extreme sea-levels at Forsmark up until year 2100.

The climate studies performed for SR-Site have resulted in a number of scientific publications, or contribution to such publications, published in *peer-reviewed* journals, see /Whitehouse et al. 2006, Helmens et al. 2007a, Engels et al. 2008a, 2008b, Bos et al. 2009, Brandefelt and Otto-Bliesner 2009, Clark et al. 2009, Helmens et al. 2009b, Väliranta et al. 2009, Engels et al. 2010, Helmens and Engels 2010, Kjellström et al. 2010a, Ampel et al. 2010, Wohlfarth 2010, Strandberg et al. 2010, Brandefelt et al. 2011, Van Meerbeeck et al. *submitted/*.

Furthermore, the following conference abstracts have been presented from the SR-Site climate studies /Engels et al. 2006, Bos et al. 2007, Brandefelt and Strandberg 2007, Helmens et al. 2007b, Helmens et al. 2007c, Kaislahti-Tillman et al. 2007, Väliranta and Helmens 2007, Engels et al. 2008c, 2008d, Helmens et al. 2008, Kjellström et al. 2008, Strandberg et al. 2008, Väliranta et al. 2008, Helmens 2009b, Helmens et al. 2009a, Kjellström et al. 2009a, Strandberg et al. 2009a, b, Brandefelt et al. 2010, Helmens et al. *submitted*, Shala et al. *submitted*/.

In addition to the above SR-Site studies, a large number of papers from the general scientific literature have been used as input to the present SR-Site Climate report.

1.4.2 Publications produced for SR-Can, in parts or in whole used for the SR-Site Climate report

In addition to the reports and publications produced for SR-Site described above, some of the publications produced for the SR-Can safety assessment have in parts or in whole been used also for SR-Site. This includes parts of the SR-Can Climate report /SKB 2006a/, and studies on climate /Hohl 2005, Moberg et al. 2006/, Weichselian glacial history /Lokrantz and Sohlenius 2006/, glacial hydrology /Jansson et al. 2007/, glacial erosion /Påsse 2004/, and shore-level displacement /Påsse 2001/.

1.5 Interactions between the climate programme and other SR-Site programmes

Data and information from the climate programme has been used within many other parts of the SR-Site safety assessment. The main flow of data within the climate programme and to other SR-Site activities are summarised in Figure 1-4 and below.

Data on air temperature have been used to simulate the development of ice sheets (Section 3.1.4) and permafrost, see Section 3.4.4, 5.5.3 and /Hartikainen et al. 2010/ and for evaluation of thermal gradients and geothermal heat flow /Sundberg et al. 2009/. Data on changing ice sheet configurations over time have in turn been used for studies of variations in stress in the Earth crust /Lund et al. 2009/, which are used for assessing the potential for and consequences of glacially induced faulting /SKB 2010c/. Ice sheet data are also needed for simulations of groundwater flow under glacial conditions /Vidstrand et al. 2010/. Data from permafrost simulations have been used to make appropriate

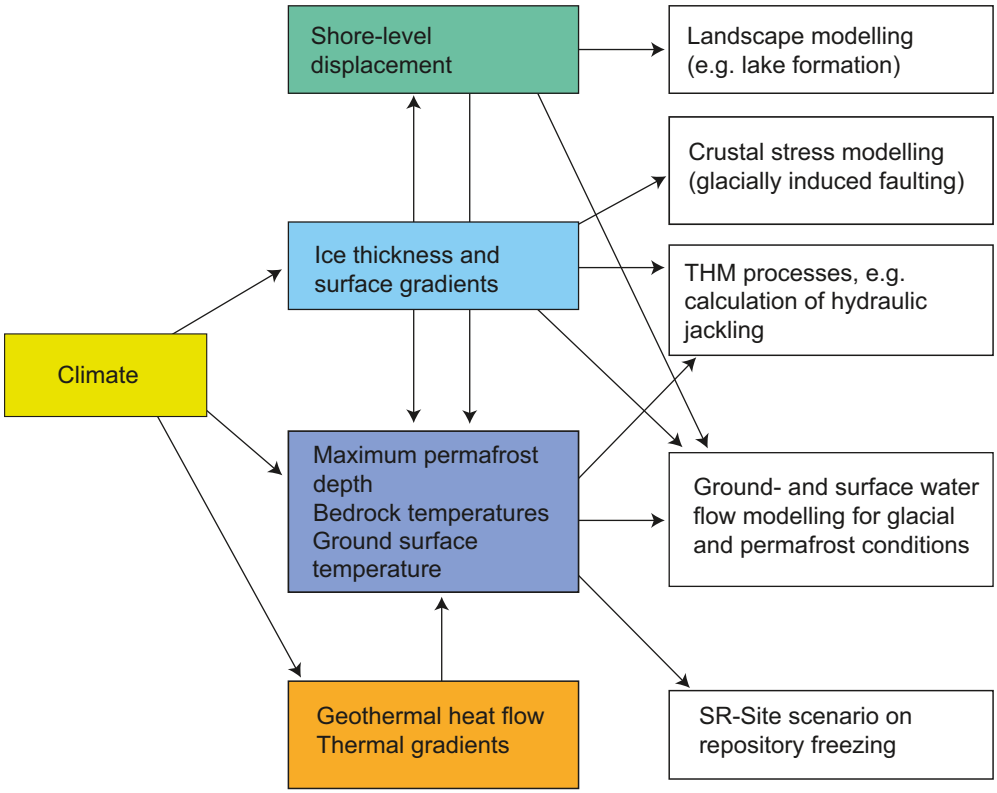

Figure 1-4. *Main flow of climate- and climate-related data in SR-Site. Coloured boxes show data within the climate programme. White boxes show other SR-Site activities, using data from the climate programme. THM processes=Thermo-hydro-mechanical processes.*

selections of conditions when studying groundwater flow under permafrost conditions /Vidstrand et al. 2010/ as well as for studies of surface hydrology under a colder climate /Bosson et al. 2010, SKB 2010d/. Data on shore-level change have been used for a description of the past and future evolution of the landscape as influenced by e.g. the isostatic recovery from the last glacial cycle /Söderbäck 2008, SKB 2010d, e/, for instance in order to model future lake formation. Shore-level data are also used for studying groundwater flow in potential future situations when the isostatic uplift has progressed further. Data on permafrost and glacial development have also been used for investigating THM processes /Lönnqvist and Hökmark 2010/ and for assessing the potential for freezing of various parts of the repository /SKB 2011/. Climate data were also included in the site selection process /SKB 2010e/.

1.6 Summary of main changes made since the SR-Can Climate report

Below is a summary of main changes in the SR-Site Climate report compared to the SR-Can Climate report /SKB 2006a/. In addition to these major changes, all chapters and sections of the report have been updated.

- Complementary and up to date studies on Weichselian glacial history are included, used for the motivation and description of the reconstruction of the last glacial cycle and the SR-Site *reference glacial cycle*.
- In order to better describe possible future climate variability and to exemplify climates with the different climate domains, dedicated climate model simulations have been performed for selected periods during the last glacial cycle and for a future climate dominated by global warming.
- Detailed site-specific permafrost simulations have been performed in 2D, with an improved permafrost model, complementary to the 1D permafrost simulation performed for SR-Can.

- Complementary information on shore-level displacement from 3D GIA simulations is included.
- Uncertainties in the palaeotemperature curves used for e.g. ice sheet- and permafrost simulations are better described.
- A major update in the description of ice sheet hydrology have been made in accordance with recent literature.
- Knowledge and descriptions of possible future climate changes have been updated according to recent literature.
- The number of possible future climate evolutions for further analysis in the safety assessment has been increased from four to six.
- A dedicated description of transitions between climate domains have been included.
- Detailed information and evaluation of the temperature proxy data used for simulations of ice sheets and permafrost have been included (Appendix 1).
- Detailed information on ice sheet profiles used in geohydrological studies have been included (Appendix 2).
- In SR-Can, the process of surface denudation (i.e. surface erosion and weathering) was reported in the Geosphere process report /SKB 2006b/. In SR-Site, this process has been moved to the Climate report (Section 3.5). In addition, this section now includes a study on denudation for a region centred at Forsmark.
- In SR-Site, crustal stress studies for analysis of glacially induced faulting are not included in the Climate report as was done in SR-Can. Instead, these studies are reported in /SKB 2010c/.
- A new complementary study on the effect of freezing of water in bentonite buffer clay cavities have been included.
- Because the SR-Site safety assessment only concerns the Forsmark site, the present report describes climate and climate-related issues only for the Forsmark site. The SR-Can Climate report described both the Forsmark and the Laxemar site.

2 The climate system

Weather and climate has great impact on Earth's life and environment. The always changing weather is determined by the fluctuating state of the atmosphere surrounding us, and characterised and described by weather elements such as air temperature, air pressure, humidity, clouds, precipitation, visibility and wind. The predictability of weather is limited. The reason for this is that the atmospheric characteristics and processes determining the weather can only be predicted over periods from a few hours up to about two weeks.

The climate is by definition a summary of weather conditions during a certain period of time within a certain area. Climate is usually described as mean values of the weather parameters and their variability over a specific time-span and covering a distinct area. The climate varies between different places due to factors such as latitude, altitude, distance to the ocean and vegetation. The climate also varies over time on different time scales from decadal, through centennial, and millennial to several thousands and millions of years. The complex range of climatic variability is a result of external forcing acting on the Earth's climate system as well as of internal factors acting within the system. The climate system includes five major components: the atmosphere, the hydrosphere, the cryosphere, the land surface and the biosphere (Figure 2-1). Within the climate system, there are many physical, chemical, and biological processes that interact on a wide range of temporal and spatial scales both within and between the components.

The general descriptions of the climate system in Chapter 2 is based on information from /Ahrens 1994, Bogren et al. 1998, Burroughs 2001, Ruddiman 2001, Weart 2003/. More specific information is based also on other references as mentioned in the text.

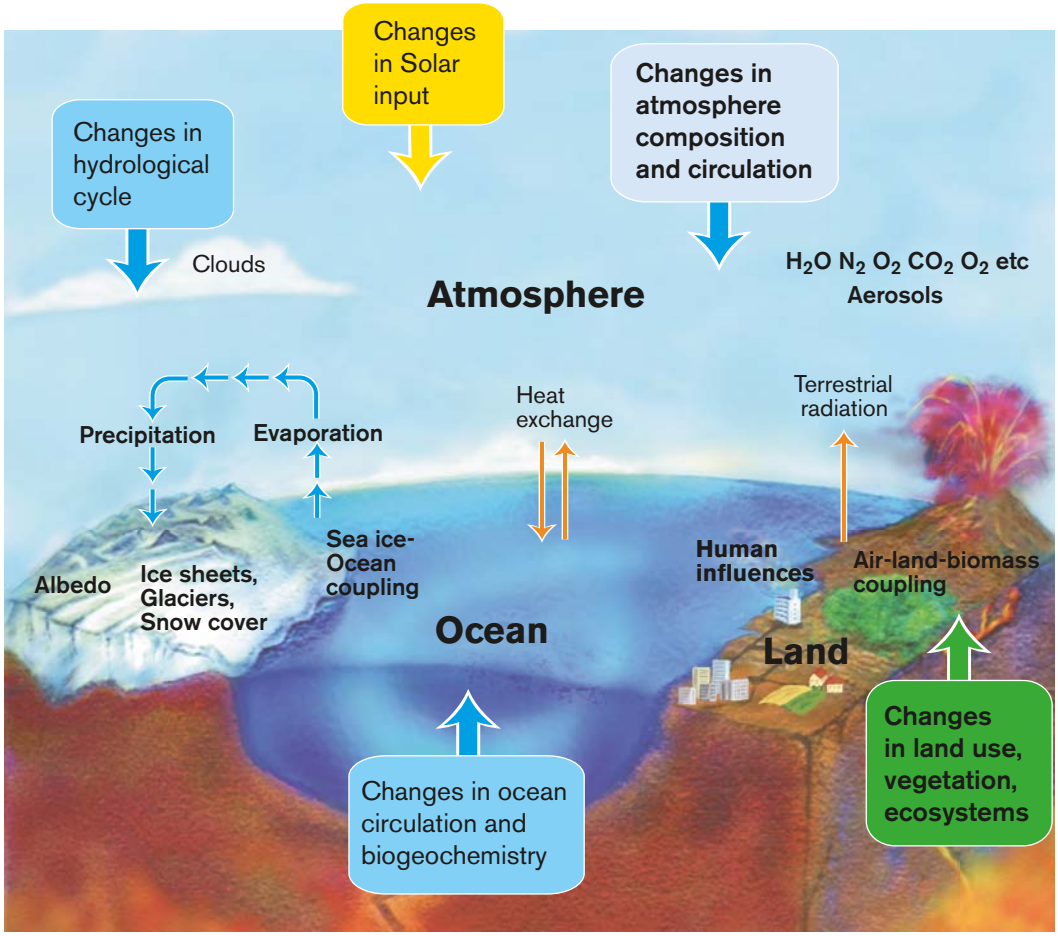

Figure 2-1. *Schematic view of the components of the global climate system, their processes, interactions and some aspects that may change (boxes). Modified from /NSF 2000/.*

2.1 Components of the climate system

The aim of this section is to give a brief overview of the main components of the climate system, in order to set the context for readers not familiar with climatology, ice sheets, permafrost etc, and also to set the rest of the report content in a wider framework.

2.1.1 The atmosphere

Overview/general characteristics

The atmosphere is the mixture of gases that surrounds the Earth, being held there by gravity. About half of its mass is to be found in the lowest 5–6 km and more than 99% of the mass is within 40 km of the surface of the Earth. This can be compared with the radius of the Earth which is about 6,400 km. The atmosphere is generally considered to be c. 1,000 km thick. However, it has no distinct outer border but a successive decrease of density as it merges into the inter-planetary medium. The origin of the atmosphere is gases that were released from the interior of the Earth by, for example, volcanic eruptions. The atmosphere has undergone major changes during the evolution of the Earth due to several factors, in which changes of solar radiation and biological activities have played important roles. Oxygen was not added to the atmosphere until produced by living organisms through photosynthesis, an event that began in the late Archaean, ~2.7 billion years ago.

The atmosphere can be divided into four major layers: the *troposphere*, the *stratosphere*, the *mesosphere* and the *thermosphere* (Figure 2-2). This division is based upon the temperature structure of the atmosphere. In the lowest layer, the troposphere, all processes that we know as weather take place. The troposphere contains almost all of the water vapour and clouds, and approximately 75% of the total atmospheric mass. The troposphere is characterised by a more or less uniform decrease in temperature with height, averaging 0.65°C per 100 m. Generally, it has an increasing wind speed with height except close to the ground surface where topography affects the wind. The upper part of the troposphere is limited by the tropopause, which is very important since it prevents convective, vertical air movement. The distance from the Earth surface to the tropopause varies according to latitude and season ranging from 16–17 km at the poles to 8–9 km at the equator.

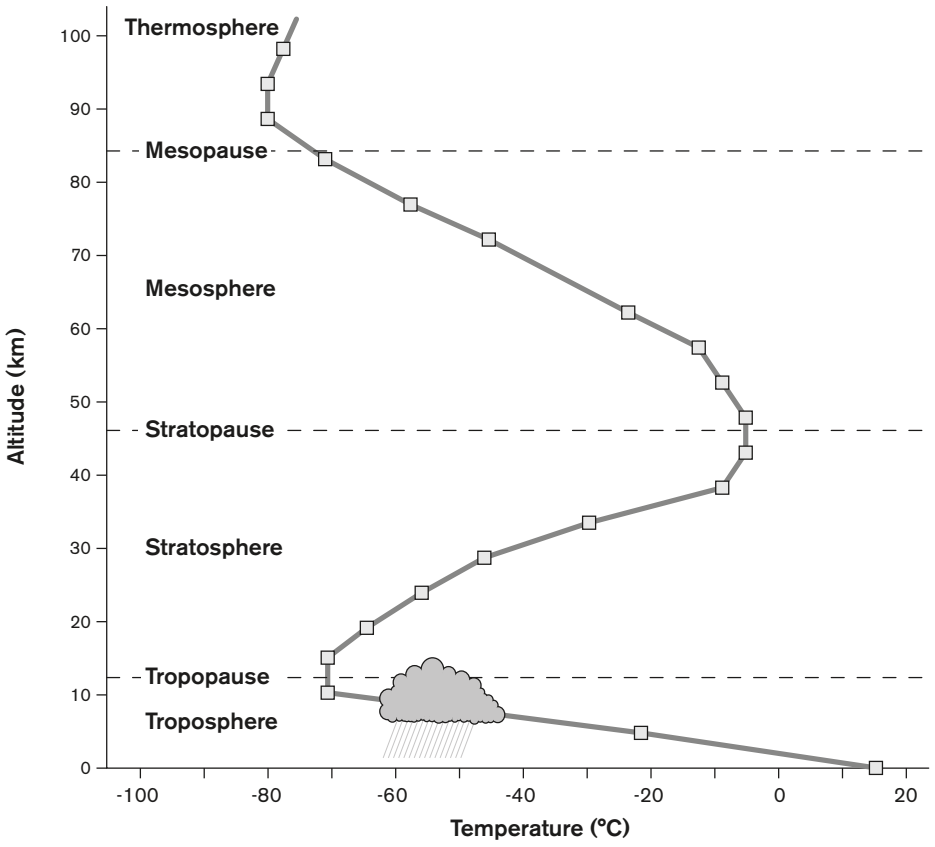

Figure 2-2. *Vertical structure of the atmosphere.*

Composition

The natural atmosphere can be divided into three types of constituents: permanent gases, variable gases, and non-gaseous constituents. Of the permanent gases, the main components are nitrogen (N_2), 78.1% volume mixing ratio, oxygen (O_2), 20.9% volume mixing ratio and argon (Ar) 0.93% volume mixing ratio. These gases are mostly passive in meteorological processes, they have only limited interactions with the incoming solar radiation and they do not interact with the infrared radiation emitted by the Earth. However, oxygen is highly active chemically; it can combine with other substances and also form ozone (O_3).

The variable gases on the other hand, such as carbon dioxide, methane, nitrous oxide and also ozone, absorb and emit infrared radiation. They are the most important components in terms of meteorological processes. These gases are also called greenhouse gases, and they are sparsely occurring with a total volume mixing ratio in dry air of less than 0.1% by volume. However, these gases play an essential role in the energy budget of the Earth/atmosphere system (Figure 2-3). The atmosphere also contains the greenhouse gas water vapour with a volume mixing ratio that is highly variable having a typical value of about 1%. These greenhouse gases absorb the infrared radiation emitted by the Earth. Thus they tend to raise the temperature close to the Earth's surface. The greenhouse gases water vapour, carbon dioxide, and ozone also absorb solar short-wave radiation. Water vapour is the strongest greenhouse gas and has a fundamental effect on climate as it exhibits strong spatial and temporal variations in concentration.

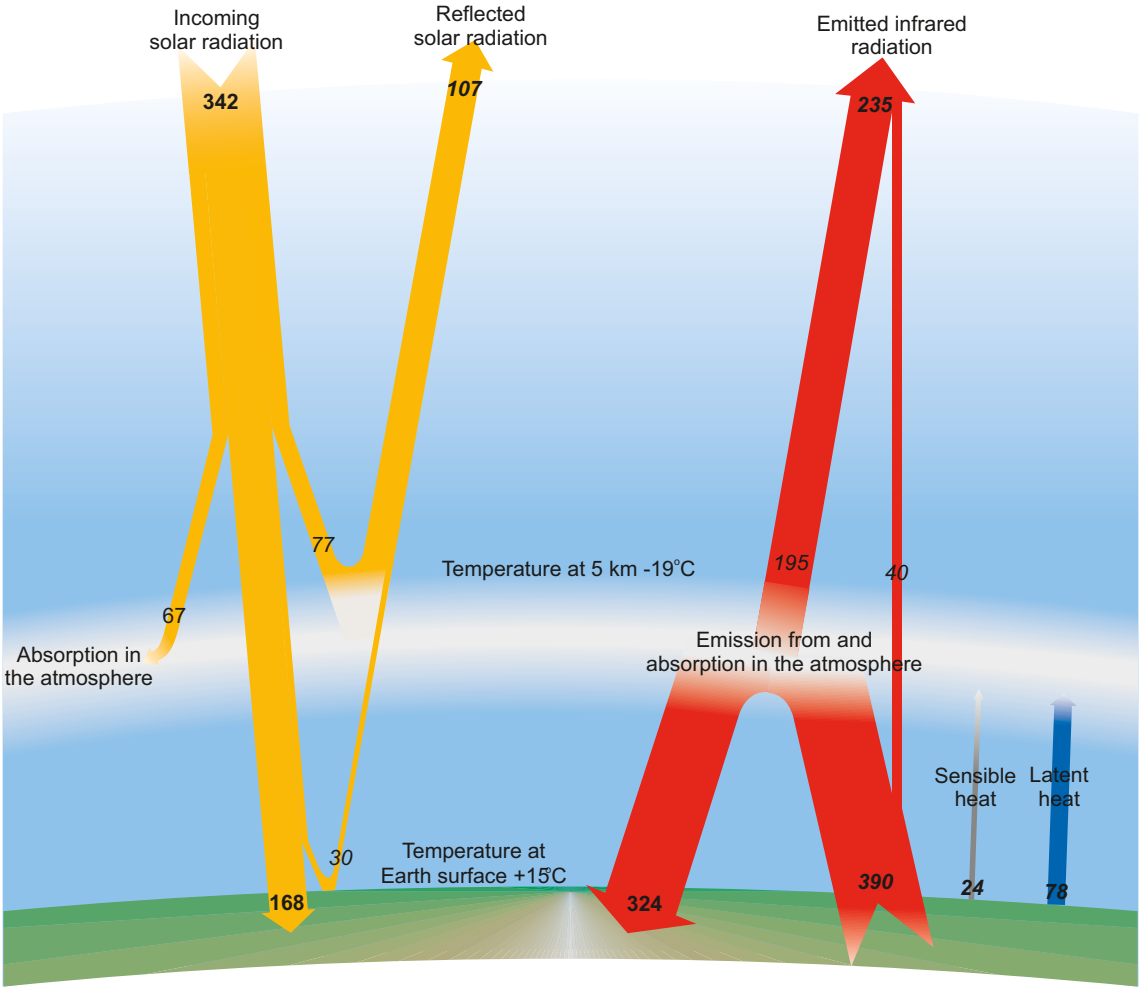

Figure 2-3. *Earth's radiation and energy balance. Units are expressed in* Wm^{-2}.

In the atmosphere, there are also non-gaseous constituents including dust, smoke and salt particles often referred to as aerosols (solid and liquid particles). These are present in different concentrations from a few million particles per cubic metre of air and they can affect the transmission of radiation through the atmosphere. The effect depends on particle characteristics such as shape, size and colour, and also on the particle distribution and their altitude above the surface. Sulphate aerosols are of great importance in the atmosphere, since they directly affect cloud formation, and also on the size of the cloud droplets formed, which in turn has an influence on cloud albedo. The content of aerosols in the atmosphere is altered by such things as volcanic eruptions and human activities. Although most climate-related effects of particles arise below the tropopause, volcanic eruptions can eject particles into the stratosphere.

Dynamics – atmospheric circulation

The atmosphere is in continuous motion. The underlying cause of the atmospheric circulation is the pressure differences caused by the unequal distribution of solar radiation over the Earth's surface and the unequal heating of land and ocean areas. Averaged over the entire Earth, incoming solar radiation equals outgoing radiation. This energy balance is not maintained for each latitude, since the tropics experience a net radiative gain in energy whereas the Polar Regions suffer a net loss. These inequities are balanced when heat is transported from equatorial regions pole-ward.

The thermal energy in the atmosphere is transferred in different ways; by convection, conduction, latent heat transfer, advection and radiation. *Convection* means that the heated atmosphere is physically transported from one location to another in, for example, rising thermals. By *conduction,* heat energy is transferred through the medium by molecular impact, whereas the medium itself does not move. *Latent heat transfer* means that the heat energy absorbed by the melting or evaporation of water in one location may be released elsewhere in the atmosphere when the water vapour subsequently condenses or the water freezes. Heat energy may be transferred horizontally by *advection* when the winds cause the mass movement of the atmosphere. Finally, energy is transferred in the atmosphere through the emission and absorption of *radiation*, moving through the space at the velocity of light.

The motion of the atmosphere is determined by two types of forces; driving forces and steering forces resulting in the pattern of winds. The driving forces exist regardless of whether or not the air is moving. Vertically, gravity is acting downwards whereas the vertical pressure gradient, with lower pressures at higher altitude, tend to force air upwards. Gravity and the vertical pressure gradient are generally close to being in balance. Horizontal pressure gradients forcing air movement are also present, and are both spatially and temporally variable on a range of scales. The steering forces are related to the motion of the air. The Coriolis effect, due to the rotation of the Earth, deflects the air from its initial motion generated by the driving forces. Frictional forces depend on the degree of roughness of the surface the air moves over and act to reduce the wind speed resulting from the prevailing pressure gradient and to produce a component of flow across the isobars. Around curved isobars, the centripetal acceleration produces a force that deflects the inward motion.

The general circulation of the atmosphere is seen in Figure 2-4. The circulation of the troposphere conforms to a pattern that is characterised by low pressure areas in the tropics where warm air rises. The rising air spreads towards the poles in the upper troposphere and eventually descends in the middle latitudes. This forms part of the so-called Hadley cells. The sinking air leads to the development of large areas dominated by subtropical high pressures. These high-pressure cells are stable and occur over oceans and continents. From these high-pressure areas the trade winds have their origin. Over the poles the coldest air masses, with dense relatively stable air, are found. The cold and dense polar air drifts towards the middle latitudes where, in contact with the warmer air, it gives rise to cyclonic activity. The interaction of cold and warm air masses in the middle latitudes is largely influenced by a belt of high-speed winds at high altitude in the upper troposphere.

The semi-stationary *polar front* (Figure 2-4) is where cold polar air masses and warm tropical air masses meet. When these air masses move, large horizontal undulations, Rossby waves, form in the polar front. Due to the temperature gradients and moving air masses, the polar front generates mid-latitude low-pressure cyclone systems. Further north, where the polar air mass meets the even colder arctic air mass, a similar *arctic front* is formed, which may be as strong as the polar front.

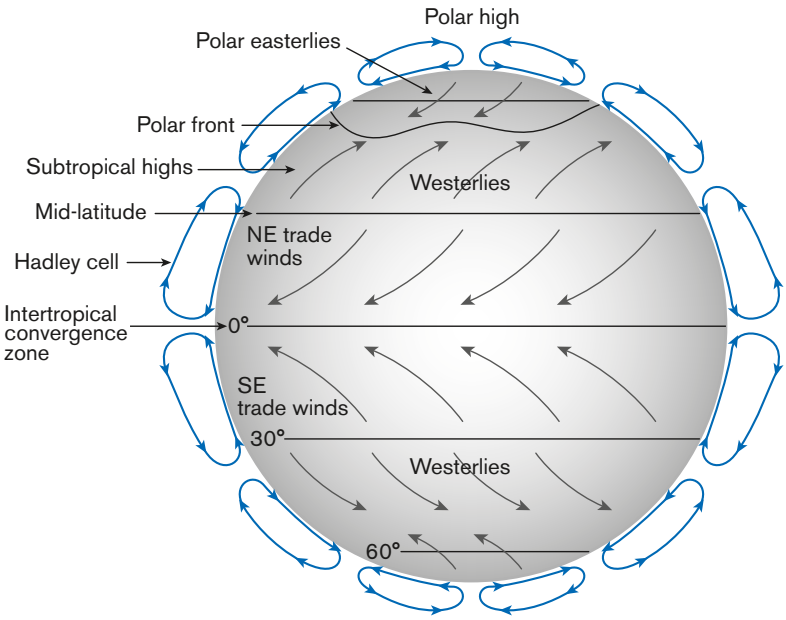

Figure 2-4. *The general circulation of the atmosphere, shown as a three-cell circulation model. The atmosphere is the most unstable and rapidly changing part of the climate system.*

Semi-permanent centres of either high or low air pressure, associated with the polar front, characterise particular geographical areas. For instance, during the winter season, the Icelandic Low is located from near Iceland and stretches into the Barents Sea. It is associated with frequent cyclone activity, bringing precipitation in over Fennoscandia. In spring, when the arctic pressure gradients decrease, the Icelandic Low and other similar centres of low pressure weaken. In line with this, the so-called Siberian High, a prominent high pressure cell located over Eurasia in winter, is also weakened and replaced by a low pressure system during summer. In summer, pressure gradients are typically weaker than during winter, with less cyclonic activity as result. These semi-permanent centres of high or low pressure, and their seasonal variation, affect the entire weather pattern in the higher latitudes of the Northern Hemisphere, and in turn also the hydrosphere and cryosphere in these regions.

2.1.2 The hydrosphere

General structure

The hydrosphere comprises all liquid water that can be found on Earth. It includes groundwater, surface water in fresh-water lakes and watercourses and saline water in the oceans. Approximately 70% of the Earth's surface is covered by oceans, which make the oceans a very important part of the hydrosphere, and they play a major role within the climate system. The oceans have a large capacity for storing and transporting heat energy, and also serve as storehouses for carbon dioxide. Due to the large thermal inertia of the oceans, they play the role of a dampener of temperature changes.

One important aspect of the ocean is that it stores a much larger quantity of energy than the atmosphere. This is because of both its larger heat capacity and its much greater density. The vertical structure of the ocean can be divided into two layers, which differ in the scale of their interaction with the overlying atmosphere. The lower layer comprises the cold deep-water sphere, making up 80% of the ocean volume. The upper layer, which has closest contact with the atmosphere, is the seasonal boundary layer, a mixed water layer extending down only about 100 m in the tropics but several kilometres in Polar Regions. The seasonal boundary layer alone stores approximately 30 times as much heat as the atmosphere.

Dynamics – ocean circulation

The hydrosphere, like the atmosphere, is always in motion. The ocean temperature and salinity affect its motion. Cold water is dense and tends to sink. Sea salt is left in the water during the formation of sea ice in the Polar Regions, resulting in an increased salinity of the ocean. This cold and saline water is particularly dense and therefore tends to sink. This takes place in certain regions, such as in the North Atlantic, and is a driving force for the thermohaline circulation (Figure 2-5).

The transfer of heat between the surface layer and deeper layers of the ocean takes place through different mechanisms: i) diffusion or turbulent mixing which transfers heat from warmer layers to cold layers, ii) convection which happens when surface waters become cold and denser than the water below and thereby switch places often resulting in transferring of heat upwards, and iii) advection which is a large-scale flow transferring water from one place to another.

Advection of heat in the oceans often occurs in the form of currents that move the warm waters in the tropics toward the poles, and colder water from the Polar Regions toward the tropics. These currents exist on the surface and at great depths of up to about 4 km. The currents are driven by the winds, by thermoclines and by the rotation of the Earth. In contrast to the atmospheric circulation and winds, the ocean circulation and currents are more stable and reacts much more slowly to changes in external forcing than the atmosphere. In the Polar Regions, cold water sinks and spreads throughout the oceans, causing the deep ocean to be cold. In mid latitudes, this is balanced by the upwelling of relatively warm water. Horizontal variations in the density of the water play an important role in driving this large-scale overturning, and in this context evaporation of water from the ocean surface is of importance, since it increases the salinity and density of the remaining surface water.

There are linkages between anomalies in sea-surface temperatures and atmospheric long-wave circulation patterns. Shifts in sea-surface temperature anomaly patterns may therefore alter the prevailing circulation and climate. The atmosphere-ocean system involves a two-way interaction. Atmospheric impacts on the ocean are relatively short-term, whereas the oceans' effect on the atmosphere is relatively long-term because of the great thermal stability of the ocean.

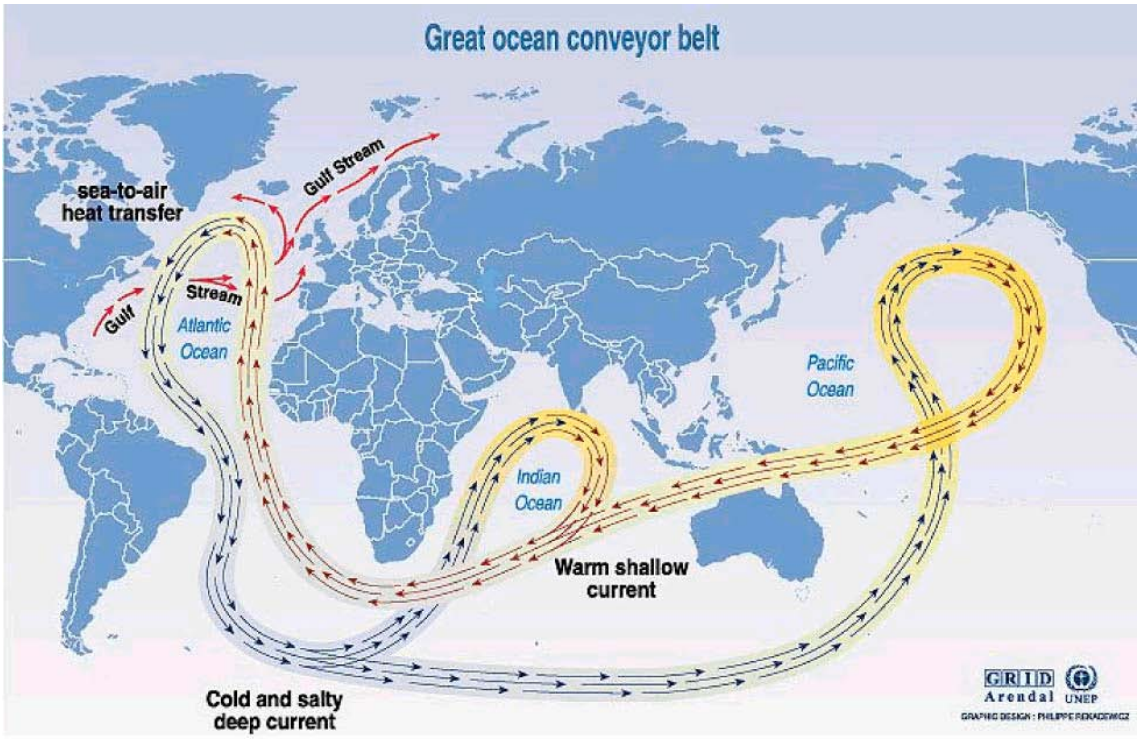

Figure 2-5. *The thermohaline circulation. From /Broecker 1991/.*

An important component of the system that is thought to be involved in abrupt climate change is the ocean circulation (Figure 2-5). Here, the key aspect is the thermohaline circulation in the North Atlantic, though other aspects of the circulation, such as wind-driven components, may also be of importance.

The global thermohaline circulation consists of cooling-induced deep convection; brine rejection and sinking at high latitudes; upwelling at lower latitudes; and the horizontal currents feeding the vertical flows. In the North Atlantic, where much of the deep sinking occurs, the thermohaline circulation is responsible for the unusually strong northward heat transport. The climate in Scandinavia is in this way to a large extent affected by the presence of the North Atlantic Drift, a northern part of the Gulf Stream. The heat transfer by this ocean current gives a significantly warmer climate in Fennoscandia than if this current was to be absent or reduced.

2.1.3 The cryosphere

The cryosphere comprises all the ice on Earth, that is, snow, sea ice, glaciers, ice sheets and the ice in frozen ground. Areas that are snow or ice covered throughout the year include for example Antarctica, Greenland, parts of the Arctic Ocean, and the high mountain ranges throughout the world. Snow and ice are important for the climate system since they have a high albedo, or reflectivity. Some parts of Antarctica reflect as much as 90% of the incoming solar radiation, compared with a global average of about 30%. Without the presence of snow and ice, the global albedo would be considerably lower and mean global temperatures would be higher.

Exchange of water between the cryosphere and the atmosphere is considerably less than between hydrosphere and atmosphere. Ice has low conductivity and large thermal inertia. Both sea ice and ice sheets also affect the oceans and ocean circulation. The large amount of freshwater stored in the ice sheets, and variations in ice sheet volumes, play a major role when it comes to salinity distribution and eustatic and isostatic processes that cause sea-level changes (see further Section 3.3). Through changes in ocean water salinity, variations in fresh water discharge from the cryosphere affect the ocean thermohaline circulation.

Snow

Seasonal snow cover is the largest component of the cryosphere by area, covering up to 33% of the Earth's total land surface. About 98% of the total seasonal snow cover is located in the Northern Hemisphere. Snow cover is an important climate variable because of its influence on energy and moisture budgets. The variations in snow cover between summer and winter accounts for the large differences in surface albedo, both on an annual basis and also between years. Snow may reflect as much as 90% of the incoming solar energy, whereas a snow-free surface such as soil or vegetation may reflect only 10 to 20%. Surface temperature is highly dependent on the presence or absence of snow cover, and temperature trends have been linked to changes in snow cover. In addition to the albedo effect, snow cover represents a significant heat sink during the melt period of the seasonal cycle due to a relatively high latent melting heat. As a result, the seasonal snow cover provides a major source of thermal inertia within the total climate system, as it takes in and releases large amounts of energy with little or no fluctuation in temperature.

Sea ice

Sea ice is formed by the direct freezing of the water on which it floats. If the water is saline, the salt is left in the sea water during the freezing process, making it more saline and dense, whereas sea ice consists of freshwater.

During the period 1979–2010, sea ice in the Arctic Ocean had an average maximum extent of 15 million km^2 in winter, while the average minimum extent were 7 million km^2 during summer /Fetterer et al. 2002/. The corresponding numbers for the Southern Ocean around Antarctica, during the period 1978–2007, was 18 and 3 million km^2. From the numbers it is seen that the seasonal variation is considerably larger in the Antarctic.

Sea ice is important because it regulates exchanges of heat, moisture, and salinity in the polar oceans. It insulates the relatively warm ocean water from the cold polar atmosphere except where cracks, or leads, in the ice allow exchange of heat and water vapour from the ocean to the atmosphere. The number of leads determines where and how much heat and water are lost to the atmosphere, which may affect local cloud cover and precipitation. Sea ice thickness, its spatial extent, and the fraction of open water within the ice pack can vary rapidly.

Sea ice acts to decouple the atmosphere and oceans, reducing the transfer of moisture and momentum, and in this way stabilises the energy transfers within the atmosphere. The formation of sea ice in polar regions can influence global thermohaline circulation patterns in the oceans, which greatly influence the global climate system.

Glaciers and ice sheets

Today two large ice sheets exist on the Earth, one in Greenland and one in Antarctica. The Antarctic ice sheet consists of the East Antarctic Ice Sheet (EAIS) and the West Antarctic Ice Sheet (WAIS). In all continents except Australia, ice in the form of mountain glaciers, or ice caps can be found at high altitudes. During the Last Glacial Maximum (LGM) period, around 20 kyrs BP, ice sheets covered about one third of the total land area of the Earth (nearly 47 million km^2), compared with the present situation with ice sheets and glaciers covering about 10% (15 million km^2) of the land surface.

A glacier, ice cap or ice sheet gains mass by accumulation of snow, which is gradually transformed to ice. Mass-loss, or ablation, is mainly accomplished by melting at the surface or base, with subsequent runoff or evaporation of the melt water. Some melt water may refreeze within the snow instead of being lost and some snow may sublimate or be blown off the surface. Ice may also be removed by discharge into floating ice shelves, from which it is lost by calving of icebergs and basal melting. Net accumulation occurs at higher altitude, net ablation at lower altitude; to compensate for net accumulation and ablation, ice flows from higher areas to lower by internal deformation and basal sliding (see further Section 3.1).

The Greenland and Antarctic ice sheet response to Global warming is discussed in Section 5.1. The two most important conditions for ice surface melting involve exposure to radiation and heat exchange with the air in contact with the ice. Radiation involves short-wave solar radiation as well as long wave radiation from water vapour and carbon dioxide in the atmosphere. The efficiency of solar radiation in melting is, to a large extent, influenced by the albedo of the glacier surface. If the surface is covered with fresh snow the albedo is typically 0.6 to 0.9 and most solar radiation is reflected. If the surface consists of glacier ice on the other hand, the albedo is 0.2 or 0.4 and melting due to the solar radiation is much more efficient.

Heat exchange with the air at the glacier surface takes place mainly in two ways: by conduction of heat from the air to the ice and by condensation of water vapour on the ice surface which results in the release of latent heat. Condensation of 1g water vapour on the surface releases enough heat to melt c. 7 g of ice. Conduction and condensation are both enhanced dramatically when windy conditions cause air turbulence close to the glacier surface.

Ice sheets have a large inertia, their response time to a change in external forcing, i.e. a climatic change, is in the range of 100 years to 10 kyrs whereas glaciers respond much faster, typically in the range of 10 to 100 years.

Finally, changes in the basal characteristics of ice sheets can lead to changes in ice sheet dynamics. In turn, this can release freshwater to the oceans, affecting ocean circulation patterns. Freshwater releases from ice-related processes can be catastrophic, e.g. the breaking of an ice dam leading to the rapid draining of the associated lake. It is believed that the draining of an ice-dammed lake in North America (Lake Agassiz) was at least partly involved in the initiation of the Younger Dryas cold climate event during the last deglaciation.

Permafrost

Permafrost affects climate since it has an impact on vegetation and a role in the storage and release of carbon. Much of the Northern Hemisphere frozen ground is overlain by evergreen boreal forest.

These boreal forests comprise both a source and a sink of carbon. The Arctic contains nearly one-third of the Earth's stored soil carbon. If the high northern latitudes experience a significant temperature increase, the regional soils would begin to release carbon and methane into the atmosphere. This could lead to even higher temperatures, fuelling the cycle of carbon release and temperature rise. The presence of permafrost also has an effect on groundwater flow and composition, both in periglacial regions and under ice sheets. For example, it may stop groundwater recharge from the surface by forming an impermeable upper layer, or it may result in freeze-out of salts in front of an advancing permafrost freeze front (see further Sections 3.4 and 4.5.3).

2.1.4 The land surface

The appearance of the land surface is critical when it comes to transfer of energy received from the sun to the atmosphere. Depending on the vegetation, the porosity and saturation of the soil and its thermal properties the amount of energy that is transferred to the atmosphere can vary. The energy can be returned as long-wave radiation, which will heat the atmosphere, or it can be used for evaporation of water. Soil moisture has a strong influence on the surface temperature since energy is required for its evaporation.

Vegetation and topography determines the roughness of the land surface affecting turbulence and the surface winds. Particles and dust from the surface are suspended into the atmosphere by the winds and affect the radiation balance in the atmosphere. Physical and chemical processes affect certain characteristics of the soil, such as moisture availability and water run-off, and the fluxes of greenhouse gases and aerosols into the atmosphere.

The presence of mountain ranges also influence global climate. North-south orientated mountain ranges in particular have the ability to influence global atmospheric circulation patterns. In turn, climate also affects mountain ranges, since climate governs important denudation processes, for example fluvial or glacial erosion. These processes cause down-wearing of mountain ranges. Orogenic processes and continental drift, forming mountain ranges, are processes acting over time scales of millions of years.

2.1.5 The biosphere

The different ecosystems existing on Earth have significant impact on the composition of the atmosphere when it comes to uptake and release of greenhouse gases. Photosynthesis by both terrestrial plants and marine biota can store significant amounts of carbon from carbon dioxide, playing a central role in the carbon cycle. Another important natural carbon sink is the oceans, where absorption of carbon dioxide via physicochemical and biological processes takes place. Ecosystem characteristics are also of importance to the budgets of many other greenhouse gases, for example methane and nitrous oxide. The exchange and storage of the trace gases are to a great extent influenced by the biosphere which in turn is sensitive to climate.

2.2 Climate forcing

Climate is changing naturally on time scales of a few tens to more than 100 kyrs. These changes are due to i) insolation changes caused by variations in the Earth orbit, ii) processes related to tectonism, such as volcanism, and iii) alterations of the radiation emitted by the sun. In addition to the change and variability of these natural external modifiers of the global climate system, natural internal variability is a characteristic of the system as well. The latter has often a more regional than global character. In addition to the natural forcing, there is also an anthropogenic forcing of the climate, one example being the burning of fossil fuels that increases the concentration of greenhouse gases in the atmosphere.

2.2.1 Earth-orbital variations

According to the Milankovitch theory variations in the Earth's orbit around the sun has been a main forcing factor of the Pleistocene glacial/interglacial cycles (Figure 2-6 and 1-2). Glaciations in the past were principally a function of variations in the Earth's orbital parameters, and the resulting redistribution of solar radiation reaching the Earth. A key to explaining how the variation in orbital parameters

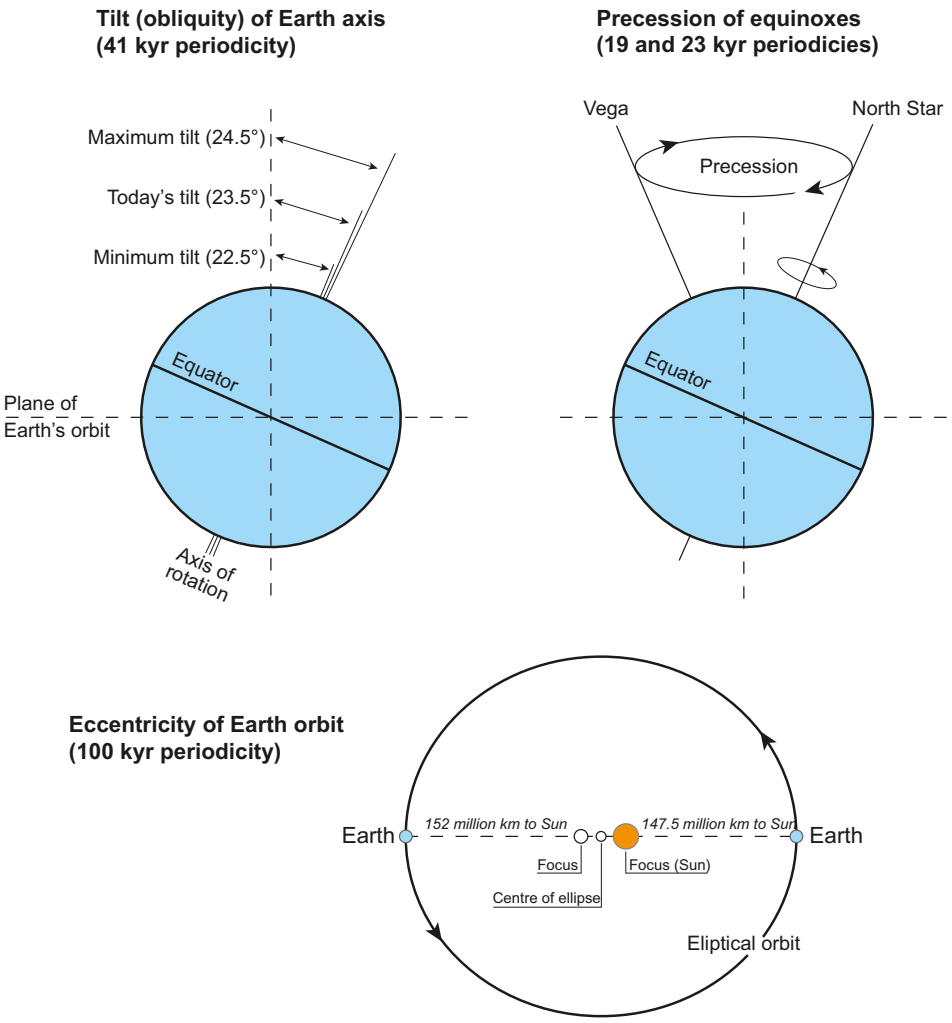

Figure 2-6. *Earth's orbital parameters affecting the seasonal distribution (obliquity and precession) and amount of solar radiation reaching the Earth (eccentricity). Modified from /Tarbuck and Lutgens 1999/.*

can trigger ice ages is the amount of solar radiation received at Northern high latitudes during the summer. This is critical to the growth and decay of ice sheets. When summer insolation is strong, more radiation is absorbed at Earth's surface at high latitudes resulting in a warmer climate. In contrast, when insolation is weak, less radiation is received at Earth's surface at high latitudes, and the reduction in radiation cools the regional climate.

Latitudinal and seasonal variations in incident solar radiation due to the precession of the equinoxes (19- and 23 kyr periodicies) and variations in the tilt (obliquity) of the Earth's axis (41-kyr periodicity) (Figure 2-6), together with important internal feed-back mechanisms in the atmosphere-ocean system, are sufficient to drive the significant climatic changes observed on these time scales. By comparison, the 100-kyr eccentricity periodicity is the weakest of the orbital effects. However, it is these weaker eccentricity variations that have dominated the pattern of glacial-interglacial cycles over the last 700 kyrs /cf. Hays et al. 1976, Imbrie et al. 1992/. Prior to this time, i.e. before the middle Pliocene transition, the obliquity played a larger role in regulating the glacial cycles /cf. Raymo and Nisancioglu 2003, Naish et al. 2009/. After the middle Pliocene transition, ice sheet volumes are larger and deep sea water temperatures are cooler /Clark et al. 2006/. The mechanisms by which the climate switches between different dominating orbital periodicities, and why the very weak 100-kyr eccentricity periodicity at present is manifested as significant climate changes with growth and decay of major ice sheets on both hemispheres, are however still not understood e.g. /Paillard 2001, Tziperman and Gildor 2003, Rial 2004, Clark et al. 2006, Hönisch et al. 2009/. Nevertheless, it is clear that the Milankovitch theory alone is not sufficient to explain climate variability for the past millions of years; it needs to be accompanied by major, highly non-linear, internal changes within the climate system involving the oceans, the atmosphere and continental ice sheets.

2.2.2 Alteration of solar radiation

The sun is the most powerful source of energy that affects the climate system. The energy output of the sun varies over time, being correlated with sunspot activity or magnetic storms. During periods of maximum sunspot activity, the sun emits more energy than during periods with minimum sunspot activity. Solar variation affects the radiation balance of the Earth, but to what degree this impacts global climate is not yet understood. Fluctuations in solar output may account for climate variations over time scales of decades and centuries, and in the long-term on time scales up to billions of years.

2.2.3 Tectonic processes

Tectonic processes, acting over millions of years, alter the configuration of continents and oceans on Earth and also the composition of the atmosphere by intermittent volcanic eruptions. The configuration of the continents influences the path of the ocean currents and thus has an impact on heat transport from low to high latitudes in the oceans as well as in the global wind system. Orogenic uplift results in mountain ranges, which may contribute to increasing the land surface area permanently covered by snow. Also, if there is a change in the characteristics of land and water surfaces, or in the relative distribution of land and sea, this can affect the radiation balance and, in consequence, the climate.

Volcanism, although driven by the slow movement of the tectonic plates, occurs irregularly on much shorter timescales. Volcanic eruptions replenish the carbon dioxide in the atmosphere, removed by the biosphere, and also emit considerable quantities of dust and aerosols. Volcanic activity can therefore affect the energy budget and regulation of the global climate system.

Volcanic eruptions can have an immediate and profound impact on climate when fine particles such as dust and ash together with gases are ejected into the stratosphere. Whereas volcanic modification of the lower atmosphere is removed within days by the effects of rainfall and gravity, stratospheric modification may remain for several years, gradually spreading to cover much of the globe. The amounts of aerosols ejected by volcanic eruption into the atmosphere may vary on widely different time-scales, causing natural variations in the radiative forcing. The variations can be either negative or positive, but the climate system must react to restore the balance. Generally, a positive radiative forcing tends to warm the surface and a negative radiative forcing tends to cool it.

2.2.4 Anthropogenic forcing

Anthropogenic forcing is a result of human activities that have an impact on the climate. Three different processes are considered to have the largest effects. The first is the release of greenhouse gases, mainly arising from burning of fossil fuel, which absorb and re-emit the longwave radiation from Earth, increasing the temperature of the atmosphere. Secondly, increased amounts of aerosols in the atmosphere may act to either increase or decrease the temperature of the atmosphere. Thirdly, by changing the surface characteristics of the Earth, the albedo is affected which in turn alters the radiation balance.

Climate scenarios based on global and regional climate models indicate for the 21st century a substantial rise in air temperatures, a considerable change in hydrological conditions and a rise in global sea-level due to increased greenhouse gas levels e.g. /IPCC 2007/, see further Section 5.1 and 5.2. The long-term effects of carbon dioxide emissions have been studied by e.g. /Archer and Ganopolski 2005, Montenegro et al. 2007, Archer and Brovkin 2008/, showing that a significant amount of anthropogenic carbon dioxide could remain in the atmosphere for a thousand years and longer, and that ultimate recovery occurs on time scales of tens to hundreds of thousands of years, see further Section 5.1 and 5.2.

2.3 Climate dynamics

Many of the processes and interactions within the climate system are non-linear, meaning that there is no simple proportional relation between cause and effect. A complex, non-linear system may display a chaotic behaviour. The behaviour of the system is critically dependent on small changes of initial conditions. This does not necessarily mean that the behaviour of non-linear chaotic systems is unpredictable. The development of the daily weather is a useful example. The development of weather

systems creating the daily weather is governed by this non-linear chaotic dynamics. This does not exclude successful weather prediction, but the predictability of the weather becomes limited to a period of approximately two weeks. The climate system is also to a high degree nonlinear, but statistical characteristics of various climates may still be described and analysed by climate models.

Climate at the global, regional and local scales is forced or influenced by a wide range of factors. These factors and their characteristic timescales are illustrated in Figure 2-7.

On a short timescale, the climate system is affected by a variety of internal feedbacks, items 6, 9, 10, 11 and 12 in Figure 2-7, counting the oceans to be an integral part of the global climate system. It is these short-term feedbacks that contribute to the natural variability of climate on annual and decadal timescales, in the context of which longer-term trends have to be detected and evaluated. Aperiodic events, such as volcanic activity, can also perturb the climate on these timescales, with individual volcanic eruptions typically affecting climate for a few years at most, though prolonged periods of enhanced volcanism may have more profound effects.

On short timescales, the orbital characteristics of the Earth do not change substantially, so the main factor forcing an overall trend in climate characteristics is the evolution of the atmosphere, notably the changes in carbon dioxide and other greenhouse gas concentrations and in atmospheric aerosol concentrations. On both short and medium timescales, internal feedbacks are known to substantially modify the effects of this external forcing.

On multi-millennial timescales, variations in orbital characteristics interact with changes in greenhouse-gas concentrations to force alterations in climate. The effects of the Milankovitch orbital variations have been recognized for many decades. However, more recently, variations in atmospheric greenhouse gas concentrations have been shown to be an important forcing factor together with orbital variations, e.g. /Cheng et al. 2009, Yin and Berger 2010/.

Imposed upon this natural variability are the changes in greenhouse gas concentrations that arise from human activities, primarily the burning of fossil fuels. Between 1850 and 1950, the concentration of atmospheric carbon dioxide rose from a pre-industrial value of 280 ppmv to 310 ppmv, and by 2005 the concentration was 379 ppmv /IPCC 2007/. Future increases in greenhouse gas concentrations are estimated for a large range of emissions scenarios, and form the basis for model simulations of future climate change /IPCC 2007/.

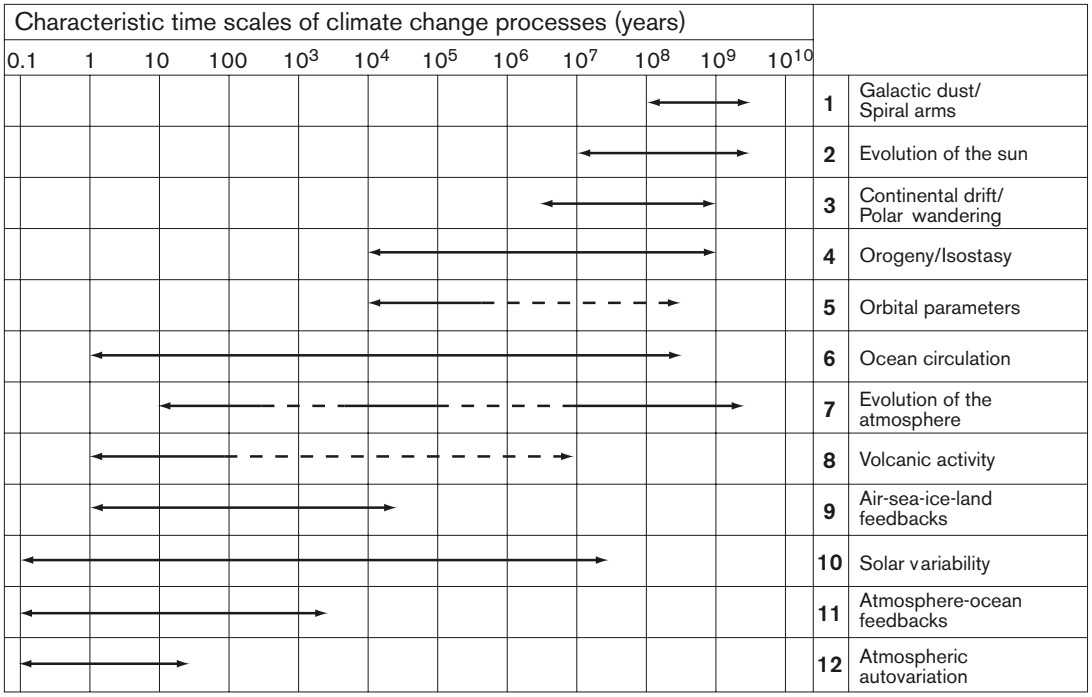

Figure 2-7. *Characteristic timescales of climate change processes. From /Goodess et al. 1992/.*

2.3.1 Energy budget and radiation balance

The Earth can be considered as a physical system with an energy budget that includes all gains of incoming energy and all losses of outgoing energy. The total flux of power entering the Earth's atmosphere is dominated by solar radiation (99.985%). A small amount is received from geothermal energy (0.0135%), which is produced by stored heat produced by radioactive decay leaking out of the Earth's interior, and tidal energy (0.002%) produced by the interaction of the Earth's mass with the gravitational fields of other bodies such as the moon. The outgoing energy from the Earth is determined by the albedo which on average amounts to 0.3. This means that 30% of the incident solar energy is reflected back into space, whereas 70% is absorbed by the Earth and reradiated as infrared radiation. Of the 30% reflected energy, 6% is reflected from the atmosphere, 20% from the clouds, and 4% is reflected from land, water and ice. The absorbed energy is eventually re-radiated mainly by the clouds and atmosphere (64%) and by the ground (6%). The radiation budget represents the balance between incoming energy from the Sun and outgoing thermal (longwave) and reflected (shortwave) energy from the Earth (Figure 2-3).

The various factors that influence the radiation balance can be divided into internal and external mechanisms. Internal factors are all mechanisms affecting the atmospheric composition (volcanism, biological activity, land use change, human activities). The main external factor is solar radiation. External and internal factors are closely interconnected. Increased solar radiation for example results in higher average temperatures and higher water vapour content of the atmosphere. Water vapour is a heat-trapping gas that absorbs infrared radiation emitted by the Earth surface. This absorption can lead to either higher temperatures through radiation forcing or lower temperatures as a result of increased cloud formation which in turn increases the albedo.

2.3.2 The hydrological cycle

The hydrological cycle involves the evaporation and precipitation of water, transport of water vapour by the atmosphere, runoff from the continents to the oceans, and the net transfer of water by ocean currents. Evaporation and precipitation account for approximately 80% of the required non-radiative energy transfer from the Earth's surface to the atmosphere.

The exchange of water vapour and heat between the atmosphere and oceans has a profound impact on climate. The atmosphere and the ocean are strongly coupled to each other and the exchange between these systems is an important way of feeding energy into the weather systems as well as the oceans. Precipitation, condensation, and cloud formation in the atmosphere is part of the hydrological cycle, which also affects the seas and oceans. Through precipitation and run off the salinity and thus the thermohaline circulation of the oceans can be affected.

2.3.3 The carbon cycle

Carbon dioxide is another important component that is exchanged between atmosphere and ocean maintaining a balance. The solubility of carbon dioxide in water is temperature dependent and in cold water in the polar regions carbon dioxide is dissolved and sinks into the deep ocean. Near the equator, the carbon dioxide is outgassed when the cold water upwells and warms. If there are large quantities of sea ice present, the exchange between atmosphere and ocean is hindered.

Looking at Late Pleistocene glacial/interglacial timescales (with glacial cycles of around 100 kyrs), there is a strong linkage between temperature changes (in atmosphere and oceans) and the amount of carbon dioxide in oceans and atmosphere. This interaction between temperature and carbon dioxide is on these time scales an important process that, together with e.g. orbital changes in insolation, governs the shifts between glacials and interglacials.

2.3.4 Feedback mechanisms and climate change

Feedback mechanisms refer to processes whereby an initial change or response to an external forcing either reinforces the initial change (positive feedback) or weakens it (negative feedback). Some of the processes involved in climate system feedback-mechanisms are briefly presented in Figure 2-1, and further discussed below.

Temperature – water vapour and cloudiness

As previously mentioned, the most important greenhouse gas is water vapour. It has a concentration in the atmosphere that is strongly correlated to temperature and varies in concentration from 0.2% in very dry air to more than 3% in humid air. The dependence of concentration on temperature results in a positive feedback. A warming of the atmosphere allows the air to hold more water vapour resulting in an increased absorption of heat. This enhanced greenhouse effect increases the warming, resulting in even more water vapour in the air. A positive feedback loop is started amplifying the initial warming. If a cooling is initiated, the feedback will result in additional cooling. However there are complications when dealing with water vapour since the atmospheric content of water vapour affects the amount of clouds. Although clouds can have either positive and negative feedback effects, depending on their type, overall an increase in cloudiness is considered to be a negative feedback, so that changes in cloud cover characteristics compensate for more than half of the positive feedback from water vapour and albedo changes.

Temperature – carbon dioxide

Carbon dioxide is a greenhouse gas affecting the temperature and climate of the Earth. Climate model studies suggest that the global mean warming from a doubling of the amount of carbon dioxide in the atmosphere is likely to lie in the range 2°C to 4.5°C, with a most likely value of about 3°C /IPCC 2007/. An increase of greenhouse gases alters the global temperature both by increasing the amount of heat absorbed in a cloud-free atmosphere and by trigging feedback mechanisms, both positive and negative. One such positive feedback mechanism is the increased potential for holding more water vapour in the atmosphere when temperature increases. Other feedbacks relate to changes in the distribution of vegetation and polar ice sheets.

Temperature – albedo

When a cooling climate increases the extent of snow and ice, the albedo of the new snow covered surface is increased. The high albedo causes further cooling and a positive feedback enhances the progress of cooling. Conversely, the same feedback process amplifies climate warming.

Vegetation – albedo and precipitation

During cooling of the climate in high latitude areas, the spruce forest is replaced by tundra, increasing the reflectivity of the land during the winter season. This causes an enhanced cooling as a positive feedback. If the climate becomes warmer, the tundra is replaced by forest and the feedback results in more absorbed solar radiation and a warmer climate.

If climate becomes wetter at high latitudes, the area of forests might increase. More vegetation results in an increase of water vapour transfer back to the atmosphere. As a positive feedback, rainfall can locally increase. A change towards drier climate will work the opposite way.

Other feedback mechanisms

Increases in atmospheric turbidity (aerosol abundance) will affect the atmospheric energy budget by increasing the scattering of incoming solar radiation. Atmospheric turbidity has been shown to be higher during glacial episodes than in interglacials, with a consequent reduction in direct radiation reaching the Earth's surface. Such a situation will enhance the cooling associated with glacial periods.

Climate variability and change

As previously mentioned, climate is changing naturally on time scales of some tens to more than 100 kyrs, due to e.g. solar variability, volcanic eruptions, and insolation changes caused by variations in the Earth's orbit. Recent climate changes, however, are also affected by increased atmospheric concentrations of greenhouse gases. According to /IPCC 2007/, the recent rise in greenhouse gases is mainly due to human activities. Climate scenarios based on global and regional climate models indicate for the 21st century a substantial rise in air temperatures, a considerable change in hydrological conditions, and a rise in global sea-level due to increased greenhouse gas concentrations in the atmosphere /IPCC 2007/. The impact of such changes is expected to exhibit distinct and important geographical differences.

The future climate will be shaped by both anthropogenic and natural forcing, as well as by unforced internal variability. The scenarios for the anthropogenic climate forcing rely on assumptions about future human activities as a result of societal choices, including future population changes and economic development. These scenarios for future anthropogenic climate forcing have been used to force climate models, in order to develop scenarios for the future climate changes towards the end of the current century e.g. /IPCC 2007, Kjellström et al. 2009b/. Inferences on the internal climate variability can be made both from past data and by means of climate modelling. Scenarios for the future *natural* climate forcing are, however, difficult to construct as the relevant mechanisms are not fully understood in a predictive sense. We can, nevertheless, estimate the possible magnitude of future natural change, based on inference drawn from natural climate changes in the past e.g. /Moberg et al. 2006, Kjellström et al. 2009b/.

For recent ideas on how anthropogenic forcing may modify climate today and in the future, see /IPCC 2007/ and references therein. For further descriptions of future cases of global warming, see Section 5.1 and 5.2, including specific climate modelling results relevant to the Forsmark region presented and discussed in Section 5.1.7.

2.4 Climate in Sweden and Forsmark

2.4.1 Climate in Sweden

The following description of the present climate in Sweden is from /Ministry of the Environment 2001/. Sweden is located in the northerly west wind belt, an area where the prevailing winds come from the south and west. The North Atlantic Drift and the numerous areas of low pressure produce a climate with winters that are 20–30°C warmer than at corresponding latitudes in Siberia and Canada. The precipitation brought by the frequent low pressures gives fairly plentiful rain and snow, although there is some rain shadow effect east of the Norwegian mountains.

According to the most frequently cited climate classification system (Köppen), Sweden has a temperate, moist climate with year-round precipitation. Along the coasts of southern Sweden, the climate is warm-temperate, with a natural cover of deciduous forest. The climate in the rest of the country is cool temperate, the predominate vegetation being coniferous forest. Tundra conditions prevail in the mountains. The battle between areas of warm and cold air along the polar front, and Sweden's location between the Atlantic in the west and the largest continental mass on Earth to the east, results in dramatic changes in the weather, particularly in winter. Often, a change in wind direction will suffice for icy Siberian conditions to be replaced by mild air from the Atlantic.

Summer temperatures are largely governed by altitude, and to a lesser extent by latitude. Thus the mean temperature in July is 15–16°C along the entire coast. The mean temperature in summer drops by 0.6°C with every 100 m of altitude. Even though there is little difference in temperature between southern and northern Sweden in high summer, summer itself (defined as the time of the year when the mean diurnal temperature is above 10°C) is much longer in the south than in the north. For example, in southernmost Sweden, summer lasts for five months, compared with three in the northernmost region. The turn of the seasons in spring and autumn, when the mean daily temperature is between 0 and 10°C, is also much shorter in the north. So in Lapland in northernmost Sweden, winter lasts for just over half the year, whereas the coast of Skåne, in the far south, only has winter for a few weeks. The vegetation growing season, defined as the part of the year when the mean diurnal temperature is over 5°C, varies considerably over the country. It lasts for between 210 and 220 days in southernmost Sweden (western and southern Skåne and the coast of Halland), but is only half as long in the far north.

Local conditions such as topography and proximity to the sea or large lakes influence the climate locally. The mean temperature in January can be extremely low in valleys with open terrain in inland areas of northern Sweden (−15 to −17°C). Elsewhere in northern Sweden the January mean temperature is generally between −9 and −14°C, except along the coast in the south of the region where, as in much of the central inland region, the mean January temperature is −5 to −8°C. In the southern and eastern part of central Sweden, the mean temperature is −3 to −5°C in January, while it is −1 to −2°C in southern coastal areas owing to the ameliorating effect of the nearby open sea. The temperature can vary a great deal, from approximately −50 to almost +40°C. The lowest recorded temperature is −53°C, recorded at two locations in northern Sweden. Elsewhere in Sweden the coldest recorded temperatures are −30 to −40°C, except along some parts of the southern coast, where it has never fallen below

−25 to −30°C. The highest recorded temperatures display much less geographical variation than the lowest; in southern and central Sweden and along the northern coast, the records are between 34 and 36°C. Very occasionally, temperatures also rise above 30°C in other parts of the country. Over much of Sweden annual precipitation is between 600 and 800 mm. Annual precipitation in the mountains, most exposed to westerly winds in northern Sweden (western Lapland and Jämtland), is between 1,500 and 2,000 mm. On the western slopes of the southern uplands, maximum annual precipitation is 1,300 mm. The Abisko area in northernmost Sweden has least precipitation, approximately 450 mm per year. This area lies in the rain shadow of the mountains to the west.

In more or less the entire country, precipitation is heaviest during July–November. Most precipitation falls along fronts as areas of low pressure move across the country. But several weeks may sometimes go by in spring and early summer without any rain. Most of Sweden usually has a snow cover in winter. In the mountains of Lapland, the ground has a snow cover for an average of 225–250 days a year. Most of the rest of northern Sweden is covered in snow for more than 150 days a year. In central Sweden and upland areas of the south, there is a snow cover on average between 100 and 150 days each winter. In the rest of southern Sweden, there is a snow cover for between 50 and 100 days, except along the west coast and the far south, where snow lies for less than 50 days each winter. The maximum snow depth averages more than 60 cm throughout almost all of northern Sweden; the mountains generally have more than a metre of snow. Air pressure distribution over the European continent causes winds from south and west to predominate. However, winds from other directions are fairly common because of the numerous areas of low pressure arriving from the west, and the circulation of winds around them. Occasionally, lows reaching Sweden develop into storms so intense that winds reach hurricane force along the coast and above the tree line. For a more detailed account of the present climate in Sweden, see /Raab and Vedin 1995/.

An overview of climate proxy data and what they can tell us about climate in Sweden during the last millennium, or in some cases even longer back in time is presented in /Moberg et al. 2006/. That report also provides more detailed climate information from Swedish instrumental data for the last 260 years. A tentative evolution of climate in Sweden for the last millennium, as simulated by a climate model, is also provided. Taken together, these three basic types of information are used to illustrate possible Swedish climate variations during the last millennium. /Moberg et al. 2006/ provides a benchmark for the likely range within which our regional climate has varied naturally during the last millennium.

2.4.2 Climate at Forsmark

The climate in the Forsmark region has typical values for the climate on the Swedish east coast (Table 2-1), with a mean annual air temperature of +5°C and an annual mean precipitation of 559 mm. Over the last few years (2004–2006), a time series of meteorological observations made specifically at the Forsmark site showed that the annual mean air temperature for this short period was +7°C and the annual mean precipitation 546 mm /Löfgren 2010/. The differences compared with the climatological data from SMHI (Table 2-1) are probably due to a combination of the following factors i) the short observational period at the Forsmark site, ii) local spatial variations in climate, iii) climate change over time.

The study by /Kjellström et al. 2009b/ exemplifies climates in Sweden and in the Forsmark area by modelling possible future and past climate situations within a 100 kyr time perspective, see Sections 4.3.2, 4.3.3 and 5.1.7. For cases of periglacial conditions (colder and drier), as well as for future conditions dominated by global warming (warmer, wetter), the outputs from the regional climate model simulation are used to illustrate how air temperature, precipitation, runoff and evaporation in the Forsmark region may be under such climate conditions. In addition to the modelling studies, the climate of Fennoscandia has also been studied by analyses of geological climate archives, e.g. /Helmens 2009a/. Descriptions of these studies are given in Section 4.2.

Table 2-1. Climate data for the Forsmark region (mean values for the period 1960–1990) /SMHI 2001/. The precipitation was measured at Östhammar whereas the air temperature was measured at Risinge.

Site	Mean annual precipitation (mm/yr)	Mean annual air temperature (°C)	Mean summer temperature, JJA (°C)	Mean winter temperature, DJF (°C)
Forsmark	576	+5.0	+14.9	−4.3

3 Climate and climate-related issues

3.1 Ice sheet dynamics

3.1.1 Overview/general description

Glaciers and ice sheets may form in climate regions where, in places, the winter snow precipitation is not completely melted away during summer. A glacier is an ice mass that has been formed by successive local accumulation of snow, with ice movement due to ice deforming under its own weight. An *ice sheet* is defined as a glacier that spreads out in all directions from a central dome, i.e. a large glacier (> 50,000 km^2 in area) that is not confined by the underlying topography. In reality, the flow pattern of ice sheets is not radial from a single dome. Instead, ice often flows out from a number of elongated *ice divides*, with the ice divides constituting the highest parts of the ice sheet.

Generally, ice flow velocities are moderate to slow within an ice sheet, with ice moving a few tens of metres per year. However, certain well-defined parts of ice sheets, so called *ice streams*, exhibit significantly faster ice flow. Ice streams are typically some tens of kilometres wide and several hundreds of kilometres long. Ice velocities within present-day ice streams are several hundred metres per year, in some cases exceeding 1,000 m a^{-1} /cf. Joughin et al. 2004/. Since surrounding ice typically moves considerably slower, high velocity gradients across the ice stream margins produce distinct *shear zones* with heavy crevassing. Because of the high ice flux in ice streams, these features may drain large portions of ice sheets. Ice streams are often characterised by specific basal thermal and hydrological conditions, differing from those of the surrounding ice sheet.

The margin of an ice sheet may be either on land or in water. If the ice margin is positioned in the sea or in a lake, it is common that the outer part of the ice sheet is floating on the water, constituting an *ice shelf*. The boundary between the floating and grounded ice is the ice sheet *grounding-line*.

If the basal thermal and topographical conditions are favourable, sub-glacial melt water may accumulate in topographic lows beneath the ice, forming *sub-glacial lakes*. These are common features under the present Antarctic ice sheet, whereas none have so far been found beneath the Greenland ice sheet.

Mass balance

The growth and decay of ice sheets are determined by the *mass balance* of the ice mass. The mass balance constitutes the result of the mass gain, or *accumulation*, and the mass loss, or *ablation*, typically averaged one year. The mass gain of an ice sheet is completely dominated by the process of snow accumulation. Most of the snow falls and accumulates during winter seasons, but snow may also accumulate during summer. For ice sheet ablation on the other hand, a number of processes may be involved, the two most significant being surface melting of snow and ice (if the summer climate is warm enough) and calving of ice bergs from ice shelves (when the margin is at the sea). In addition, mass may also be lost from the ice sheet by melting of basal ice, and locally on the surface by sublimation of ice and snow. When a certain part of an ice sheet exhibits more accumulation than ablation during one year, that part is said to belong to the *accumulation area* of the ice sheet. This is in contrast to the *ablation area*, where there is a net loss of mass during one year. Central parts of ice sheets typically constitute accumulation areas, whereas in case of surface melting, lower parts of ice sheets constitute ablation areas (Figure 3-1). The line between the accumulation- and ablation areas is called the *equilibrium line*.

If the total ice sheet accumulation is greater than the total ablation during one year, the mass balance is said to be positive, whereas the opposite case produces a negative mass balance. If accumulation and ablation are equal, the mass balance is zero.

A positive mass balance over a number of years makes an ice sheet grow, whereas a negative mass balances reduces its size. However, changes in the size of ice sheets are very slow processes acting over hundreds and thousands of years. The *response time* of an ice sheet is the time it takes for a steady-state ice sheet to come to a new steady-state condition after a climate change. Since climate is constantly changing, ice sheets are never in true steady-state, but are constantly adjusting their size and shape to the prevailing climate.

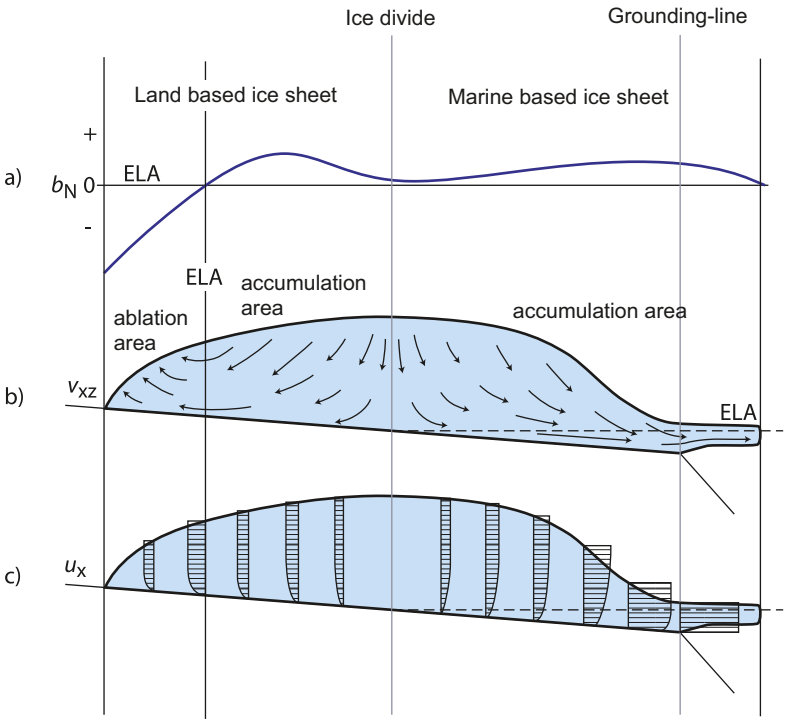

Figure 3-1. *Schematic ice sheet cross section. Panel a) shows the surface net balance distribution (b_N), panel b) shows ice velocity trajectories (v_{xz}) as well as distribution of accumulation- and ablation areas, and panel c) shows the horisontal velocity component (u_x). ELA denotes equilibrium line altitude. Modified from /Holmlund and Jansson 2003, after Denton and Hughes 1981/.*

Ice temperature. The temperature of the ice is of fundamental importance for the behaviour and characteristics of glaciers and ice sheets. Among other things, it has a strong effect on the movement, dynamics and hydrology of the ice. Two types of glacier ice can be defined based on temperature; 1) *Temperate ice* (or *warm ice*) with the ice temperature at the pressure melting point, and 2) *Polar ice* (or *cold ice*) with the ice temperature below the pressure melting point. Cold ice is harder than temperate ice, and also impermeable to water unless crevasses are present.

Glaciers and ice sheets are often classified according to their thermal characteristics. In the simple case, a glacier where all ice has a temperature at the pressure melting point throughout the year is called a *temperate glacier* or *temperate ice sheet,* whereas a glacier in which all the ice is below the pressure melting point throughout the year is called a *polar glacier* or *polar ice sheet*. However, an ice sheet or glacier need not consist exclusively of temperate or polar ice. In many cases, it can contain both ice types, and in such a case it is called *polythermal*.

Of particular interest is the temperature of the ice at the ice sheet bed, i.e. the basal thermal condition. An ice sheet can be *cold-based* or *warm-based*. A cold-based ice sheet has cold basal ice, and it is frozen to its bed. There is no free water at the bed, and no sliding of basal ice over the substrate is taking place. A warm-based ice sheet is at the pressure melting point at the bed. Free water is, in this case, present at the ice/bed interface, and the ice may slide over the substrate. This has important consequences both for ice kinematics and landform development. A polar ice sheet may be either cold-based or warm-based. In the case of a warm-based polar ice sheet, it is typically only the lower-most part of the ice that is at the pressure melting point, whereas most of the ice sheet consists of polar ice. One part of a polar ice sheet may thus be cold-based at the same time as other parts are warm-based. This is the present case for the Greenland and Antarctic ice sheets. Warm-based and cold-based ice sheets are also called *wet-bed ice sheets* and *dry-bed ice sheets*.

Glaciers and ice sheets experience melting of basal ice where the basal ice temperature is at the pressure melting point. Heat for this melting can be added from geothermal heat flux and from frictional heating by internal deformation of basal ice. The thermodynamic situation at the base of an ice sheet is determined by the thermal properties of ice. Energy can be transferred by diffusion

along a temperature gradient in ice as in all materials. However, the solidus of the ice-water vapour phase space has a negative slope, which means that the melting or freezing temperature is depressed with increasing pressure by 0.09 K/Pa. As a general statement, freezing of liquid water occurs when temperature and pressure satisfy the generalised Clapeyron equation e.g. /O'Neill and Miller 1985/:

$$\frac{p_w}{\rho_w} - \frac{p_i}{\rho_i} = \frac{L}{273.15} T + \frac{P_o}{\rho_w} \qquad \text{Equation 3-1}$$

where p_w = water pressure, ρ_w = water density, p_i = ice pressure, ρ_i = ice density, L = ice density coefficient of latent heat of fusion, T = temperature in degrees centigrade, and P_0 = osmotic pressure. Equation 3-1 couples the effect of temperature and pressure. It is a general thermodynamic relationship not specific for the case of ice sheets and glaciers. However, the phase change of the ice-water system is not only controlled by temperature and pressure. Two other factors may also be of importance; 1) the presence of solutes in water, and 2) surface tension arising from interface curvature. Just as in the case with an increasing pressure, an increase in solutes in liquid water also depresses the melting/freezing point. This effect is referred to as the osmotic pressure e.g. /Padilla and Villeneuve 1992/, and it is included in Equation 3-1. If liquid water is present at the base of an ice sheet, and it contains solutes, this will together with the pressure modify the ice melting point. The second factor constitutes an ice/water interfacial effect. The finer grains that a sediment has, the higher the curvature of the ice-water interface becomes, which in turn lowers the melting point /Hohmann 1997/. For example, in clays, liquid water has been observed at temperatures down to −10°C /O'Neill and Miller 1985/.

If the effect of phase curvature is taken into consideration the Clapeyron equation may be modified to /Raymond and Harrison 1975/:

$$T = -\frac{273.15}{L}\left(\frac{1}{\rho_i} - \frac{1}{\rho_w}\right) p_w - \frac{273.15\sigma_{iw}}{L\rho_i r_p} - \frac{273.15}{\rho_w L} P_o \qquad \text{Equation 3-2}$$

where σ_{iw} = ice-water surface energy, and r_p = characteristic particle radius. Equation 3-2 is the fundamental equation for the ice-water phase transition given by /Hooke 2004/. In this equation, the first of the three terms describes the effect of pressure on the ice-water phase transition, the second term describes the effect of interfacial pressure, and the third term the effect of osmotic pressure. Equation 3-2 thus gives the complete treatment of the ice-water phase transition. Commonly only the first term is used for calculations of the pressure melting point beneath glaciers and ice sheets, often rewritten in glaciological literature to give a simplified expression for calculating the pressure melting point /cf. Remy and Minster 1993/:

$$T = -\frac{h}{1503} \qquad \text{Equation 3-3}$$

where T = pressure melting point temperature (°C), and h = ice thickness (m). The effect of the lowering of the pressure melting point described above is, in the case of an ice sheet, that the melting point is lowered by c. 2 K beneath 3 km of ice. This is very important, since the basal conditions change drastically if the bed of an ice sheet becomes melted or frozen. This affects ice sheet flow by turning on and off basal sliding, governs if glacial erosion can take place or not, and of course has a profound impact on basal hydrology.

To demonstrate the effect of ice sheet surface conditions on the temperature distribution within polar ice sheets, we start with a simplified case of a steady-state ice sheet with no ice flow, corresponding to an artificial situation at an ice divide (no horizontal flow) without any precipitation (no vertical flow). Figure 3-2a shows the vertical temperature profile through such an ice mass given a surface temperature of −20°C and a specified geothermal heat flux at the base. The resulting temperature profile is a straight line from the surface temperature down towards the bed. In this case the vertical temperature profile reaches the pressure melting point temperature near the bed, resulting in a warm-based polar ice sheet.

Next we consider the same case but with snow accumulation at the ice sheet surface, which means we are introducing a vertically downward directed ice movement. Generally, this lowers the temperatures within the ice sheet as seen in (Figure 3-2b). Due to the vertical velocity and cold surface climate, cold ice is advected downward, while the geothermal heat warms this descending ice.

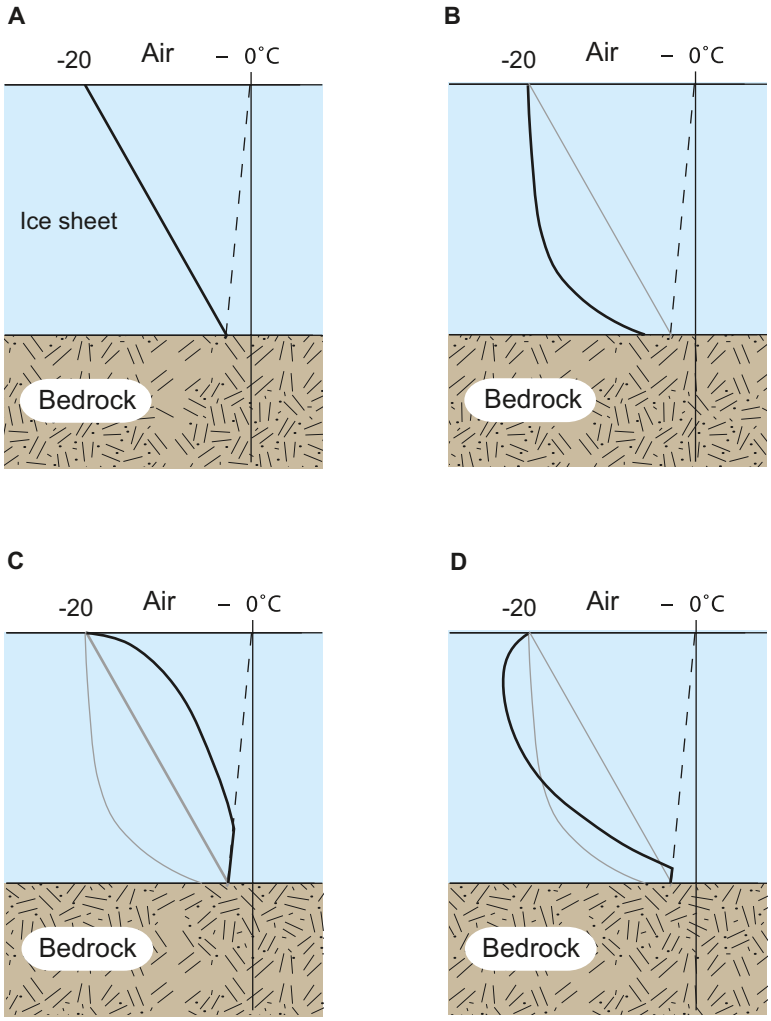

Figure 3-2. *Vertical temperature profiles through a 2000 m thick theoretical polar ice sheet. The dashed line denotes the pressure melting point temperature. a) No ice flow (dead-ice body), b) Vertical ice flow only – accumulation area (reflecting only a surface accumulation rate), and c) Vertical ice flow only – ablation area, d) Horizontal and vertical ice flow – accumulation area. Grey lines show the cases from the previous plates. Modified from /Holmlund and Jansson 2003, after Sharp 1960/.*

The upper part of the ice sheet develops an almost isothermal zone, whereas the ice warms quickly near the bed. In this example the ice sheet below this accumulation area has become cold-based. Higher precipitation rates at the surface, i.e. higher vertical velocities, result in an increased thickness of the isothermal zone and also decrease the basal temperature. Furthermore, lower air temperatures at the ice sheet surface also decrease the ice column temperatures, and vice versa.

If we instead consider an ablation area, with net mass loss at the surface, the vertical ice movement will be directed upwards. In this case, the upward vertical velocity produces a generally warmer ice column, in this example resulting in temperate conditions at the bed (Figure 3-2c).

The last case to consider is a more realistic situation, when we also have horizontal ice movement. Figure 3-2d shows a typical situation within the accumulation area of an ice sheet, but not located directly on an ice divide. The horizontal velocity component is advecting cold ice into the site, ice that was formed in higher, colder parts of the ice sheet. Compared with the situation in Figure 3-2b, the minimum temperature is now found at some depth below the surface, since the ice at the surface, formed locally at the site, is warmer (Figure 3-2d). This positive temperature gradient near the surface has been observed in several deep drill holes, see for example the Mirny, Century 13, and Byrd 9 drill hole temperatures in (Figure 3-3). Furthermore, due to the horizontal ice movement, ice in the lower part of the ice sheet is warmed by internal friction, as this is where most of the internal deformation of the ice is taking place. In this example, the ice sheet has again become warm-based.

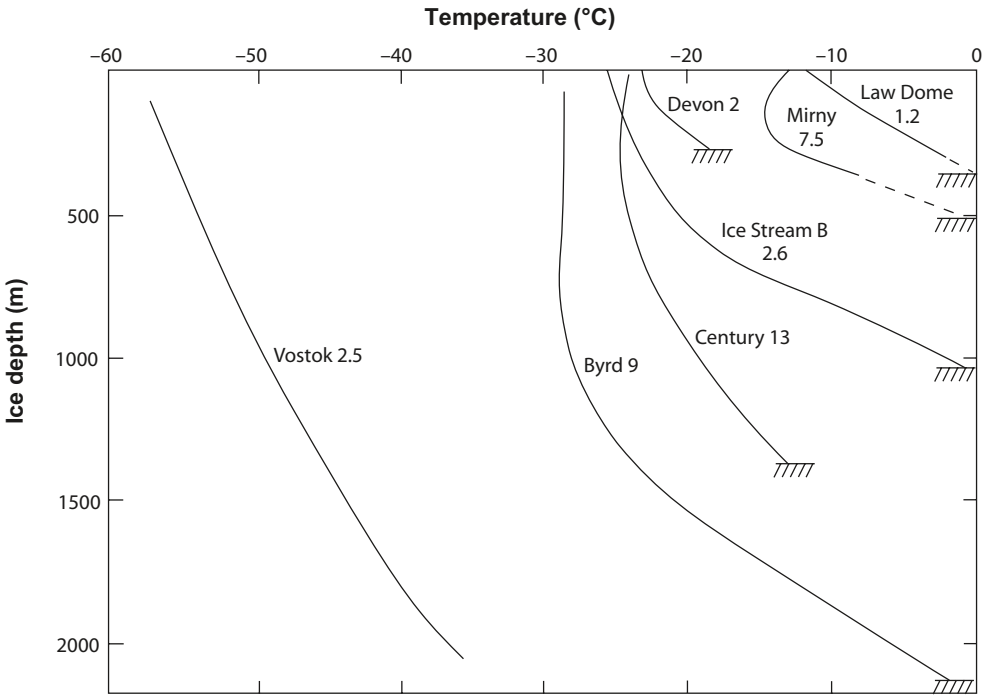

Figure 3-3. *Borehole temperature data from the Greenland and Antarctic ice sheet. From Modified from /Holmlund and Jansson 2003, after Paterson 1994/.*

Including these processes, the resulting englacial and subglacial temperatures along a flow line are as shown in Figure 3-4. Typical polar ice sheet accumulation rates and air temperatures are assumed. The lowest englacial temperatures are found in the highest central parts of the ice sheet, and the highest ice temperatures are found near the front. Basal melting is taking place in the interior part of the ice sheet and close to the margin, with a zone of basal frozen conditions in between. A narrow zone of basal frozen conditions at the margin may also occur due to decreasing vertical velocity.

In nature, the topography of the landscape beneath the ice sheet is also of great importance for the basal temperature distribution. Topographic lows are more prone to experience basal melting conditions that topographic heights. This is both due to the fact that the pressure melting point is lowered more in depressions (due to the greater ice thickness and higher basal pressures) than over surrounding higher terrain, and due to the lower insulating capacity of thinner ice over topographic highs. The result is, for example, that a floor of a large valley in general is more likely to have experienced longer periods of basal melting than surrounding elevated areas e.g. /Näslund 1997/.

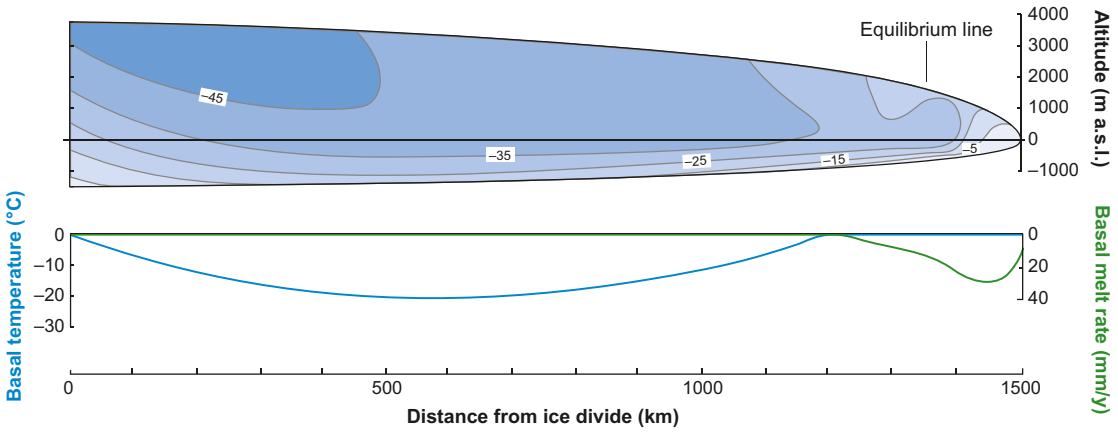

Figure 3-4. *Example of modelled ice sheet temperature distribution along a flow line. Ice temperatures are in °C. Basal melt rates are high near the terminus because of the strain heating effect from rapid ice flow in the region around the equilibrium line. Modified from /Hooke 1977/.*

An additional important process affecting ice temperature takes place if the air temperate allows surface melting during spring periods, for example at low elevations of an ice sheet in a warming deglaciation climate, or during times of early ice sheet formation. After the winter period with cold temperatures, the temperature in the upper snow/firn pack of the ice sheet is well below the freezing point. As surface melting starts, meltwater percolates down in to the snow pack and re-freezes at some depth. During the re-freezing process, latent heat is released (334 kJ/kg, corresponding to the latent heat of fusion for ice) which warms the surrounding snow. As the process continues the entire snow pack can be transformed to temperate conditions during a few weeks. This is a very efficient process, and the result is that temperate ice instead of cold ice is formed at the location. This may have been an important process during build-up phases of Fennoscandian ice sheets, having an important effect on the thermal characteristics of early ice sheets /Näslund 1998/.

Ice movement and thermodynamic feed-back. The stresses induced by the mass of overlaying ice induce deformation or strain in the ice. The resulting ice movement, often referred to as *internal deformation*, is present in all glaciers (being one of the main criteria for the term *glacier*). The shear stress at the base of an ice sheet is calculated from:

$$\sigma = \rho\, gh \sin\alpha \qquad \text{Equation 3-4}$$

where σ is the shear stress, g is the acceleration of gravity, h is the ice thickness, and α is the ice sheet surface slope. The most common flow law of ice describing the strain rate of ice under pressure is Glen's flow law /Glen 1955/:

$$\dot{\varepsilon} = \left(\frac{\sigma}{B} \right)^n \qquad \text{Equation 3-5}$$

where $\dot{\varepsilon}$ is the strain rate, σ is the shear stress, B is a viscosity parameter that increases as the ice gets more difficult to deform, a parameter depending on among other things ice temperature and crystal fabric, and n is an empirically determined constant (~3) that depends on the specific creep process that is operating. The main effect of Glen's flow law is that moderate increases in stress (ice thickness) result in a substantial increase in strain rate. For example, a doubling of the amount of stress results in 2^3, that is 8, times higher deformation rate (Figure 3-5).

In ice sheets the horizontal ice velocity increases from the ice divides, where it is zero toward the margin. The steeper surface slope at the margin induces larger driving stresses which makes the ice deformation rate high. For an ice sheet with an ablation area, i.e. an ice sheet ending on land (Figure 3-1) the maximum horizontal velocity is at the equilibrium line, whereas in the case of a marine ice sheet margin, the maximum velocity is at the ice sheet grounding-line (Figure 3-5).

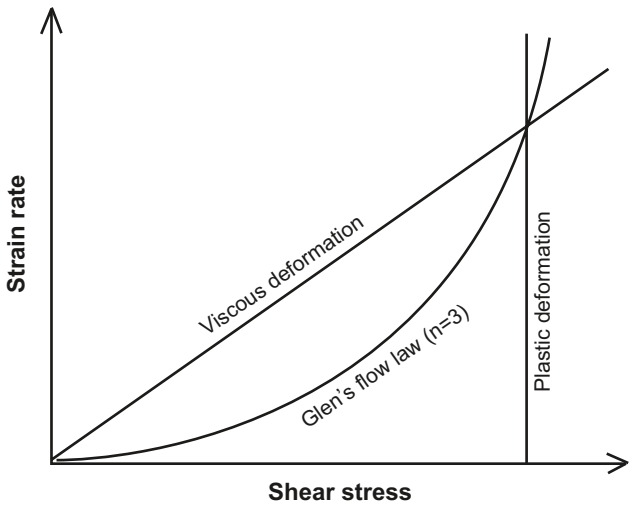

Figure 3-5. *Deformation rate versus shear stress for various flow laws, including Glen's flow law for ice. Modified from /Holmlund and Jansson 2003/.*

The stress that acts on the uppermost layer of a glacier does not produce a creep or plastic deformation. Instead the uppermost part of the ice, about 30–100 m thick depending on ice temperature, is brittle, often resulting in typical fractures, or *crevasses*. Most of the internal deformation takes place near the bed where stresses are highest. The overlaying ice moves along more or less as a uniform block on top of the deforming ice. This is indicated as the internal deformation portion of the ice velocity in Figure 3-6.

There is also another process that may contribute to glacier movement. If the ice sheet is wet-based, the ice may slide over the substrate, and the substrate itself may deform, especially if the water pressure at the bed is high. The surface ice velocity is, in this case, the sum of the component from internal deformation and the component from basal sliding and deformation (Figure 3-6). For all practical purposes, one can assume that *basal sliding* does not occur if the bed is frozen. Therefore, not all glaciers, or all parts of an ice sheet, have the sliding ice flow component. However, where it is present, it may be of great importance, for example in ice streams, which are typically warm-based. Here, the observed surface flow may be completely dominated by basal sliding /Engelhardt and Kamb 1998/. High basal water pressures are favourable for intense basal sliding /Engelhardt et al. 1990/, as well as smooth bed topographies and deformable, water-saturated tills e.g. /Kamb 2001, Iverson et al. 1995/.

Within glaciers and ice sheets there are important thermodynamic feedback mechanisms, in the following exemplified by a discussion on ice streams. As seen above, the viscosity of the ice is affected by the ice temperature, with higher ice temperatures giving more easily deformable ice. At the same time, the internal deformation itself produces frictional heat, with higher velocities producing more heat. This gives a positive feedback mechanism; high internal deformation rates increase the temperature of the ice, which in turn makes the ice even easier to deform.

On the other hand, looking at the basal thermal conditions of ice streams, there may be additional thermodynamic processes acting. A fast-flowing warm-based ice stream may drain a lot of ice from the ice sheet. Over time this will reduce the thickness of the ice, also over the ice stream itself. The thinner ice insulates less well from cold surface temperatures, which leads to less melting at the bed, and eventually also to a shift from warm-based to cold-based conditions. This reduces the velocity of the ice stream considerably and the ice flux deformational heating reduces accordingly. The ice stream now drains much less ice than before, which in time results in increased ice thicknesses /Payne 1995/. The larger ice thickness warms the bed, which again may become wet-based and basal sliding may start again. This process suggests that ice streams may have an inherited built-in unstable behaviour. It has been suggested as one explanation for the cyclic Dansgaard-Oeschger events recorded in glacial marine sediment cf. /Andrews and Barber 2002/.

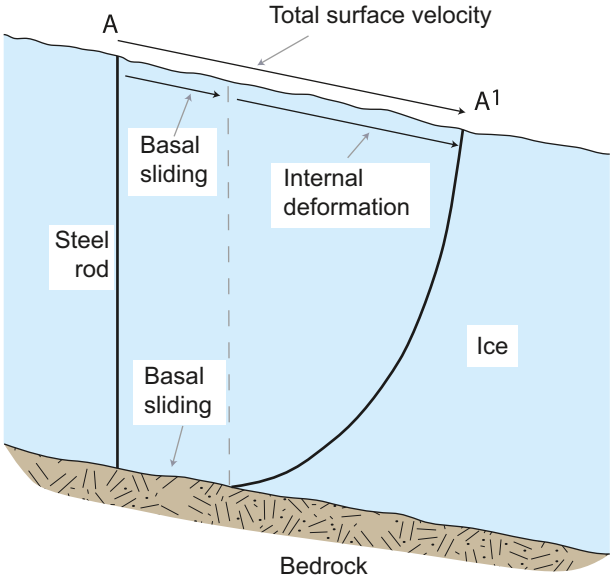

Figure 3-6. *Internal deformation and basal sliding demonstrated by the deforming of a steel rod from time A to A¹. Modified from /Holmlund and Jansson 2003, after Sharp 1960/.*

In addition, the dynamics of an ice sheet, and in particular its ice streams, and the ice sheet response to changes in climate, are to a large degree governed by the prevailing subglacial hydrology. This field of knowledge is in rapid advance, see further Section 3.2. One process that traditionally has not been incorporated in large-scale ice sheet models is the coupling of longitudinal stresses within the ice e.g. /Pattyn 2003/, that is downstream and upstream push- and pull effects, a process of importance for proper modelling of ice streams and grounding line features. Several recent ice sheet models have implemented this process.

3.1.2 Controlling conditions and factors

The upper boundary of the ice sheet system is the ice sheet surface, whereas the lower boundary is the ice sheet bed, i.e. the interface between basal ice and substrate. In accordance with ice sheet fluctuations the lateral extent of these boundaries changes over time.

Upper boundary condition – Climate. The boundary condition at the ice sheet surface is the prevailing climate, i.e. air temperature and precipitation, including its variation over time. The air temperature at the ice sheet surface is determined mainly by the latitude, altitude and climate changes. The latitude at a site is fixed, but the altitude varies with the local thickness variations of the ice sheet and associated isostatic responses. The typical air temperature pattern over an ice sheet is with the lowest temperatures in the ice sheet interior, and higher surface temperatures closer to the margin. If temperatures are greater than 0°C during summer, surface melting takes place on the lower parts of the ice sheet surface. This melting typically amounts to several m of ice per year, with large variations according to the prevailing temperature regime. Surface melt rates are lower closer to the equilibrium line. In general, during cold stages of ice sheet growth, the amount of surface melt water production is small compared with the amounts of water produced during ice sheet deglaciation under warmer climate conditions.

Most precipitation that falls on ice sheets falls as snow. During relatively warm climates at low ice sheet elevations, precipitation may occur as rain. Snow accumulation and surface ablation are not distributed evenly over the ice sheet surface. The precipitation pattern reflects ice surface elevation and degree of continentality, often giving a pattern of high accumulation rates close to the ice sheet margin with diminishing values towards the interior. On mid-latitude ice sheets, like the former Fennoscandian ice sheet, the precipitation pattern is strongly affected by the prevailing west-wind belt and associated low-pressure tracks. This results in an orographic effect which gives most precipitation on the western side of large Fennoscandian ice sheets. Typical coastal accumulation rates of the Antarctic ice sheet are 0.3–0.6 m a^{-1} (water equivalents), whereas the interior parts gets less than 0.1 m a^{-1} in precipitation /Giovinetto and Zwally 2000/, i.e. here polar desert conditions prevail. On an ice sheet surface, regional and local variations of great magnitude in the amount of snow accumulation often occur, mainly due to wind re-distribution of snow in regions close to the ice sheet margin (Figure 3-7).

To initiate ice sheet growth in a non-glaciated region, local climate need to change. That can either occur due to global climate change, towards lower local summer temperatures or higher winter precipitation rates, or, over long time scales, by tectonic uplift, or a combination of climate and tectonics. Generally, ice sheet formation in Fennoscandia involves small alpine glaciers in the Scandinavian mountain range that grow into a mountain-centred ice sheet, and then grow to a full-scale ice sheet /Andersen and Mangerud 1989, Lundqvist 1992, Kleman et al. 1997/. Increasing evidence suggests very dynamic ice sheet and climate behaviour during the last glacial cycle, with ice sheet growth phases interspersed by extended periods with restricted ice coverage, see also Section 4.2.

Lower boundary condition – Ice sheet bed. The lower boundary condition of the ice sheet system is the ice sheet bed. The substrate typically either consist of bedrock, in Fennoscandia normally crystalline rocks, or bedrock covered by till. There are two important parameters to consider here; 1) the topography of the landscape, and 2) the amount of geothermal heat flow.

The topography of the bed is of importance for the basal boundary conditions of ice sheets, as discussed above. Above all, an ice sheet bed with strong relief produces basal thermal conditions with stronger lateral temperature gradients than an ice sheet bed with smooth topography. The first case also implies larger spatial variations in basal melt water production.

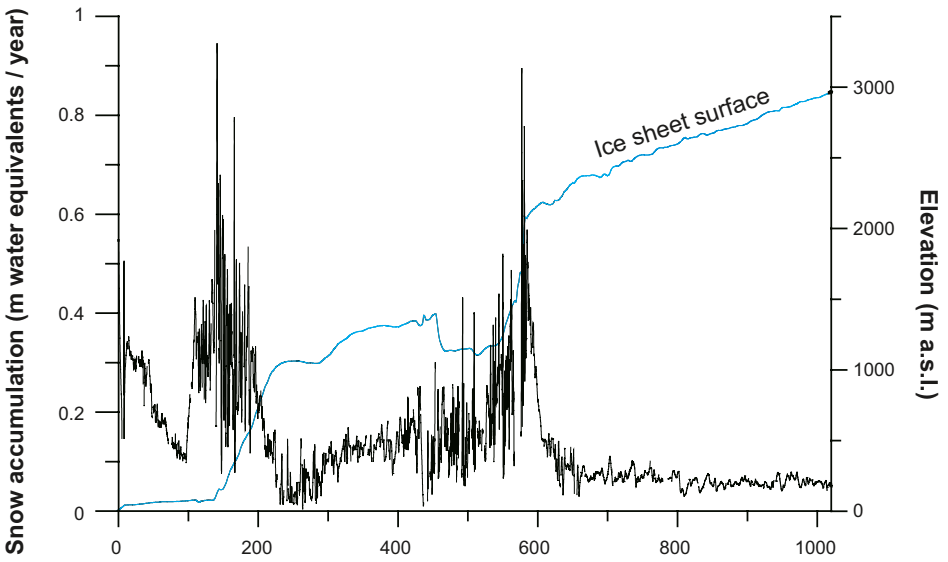

Figure 3-7. *Accumulation rates and ice surface elevations along a profile in over the East Antarctic ice sheet. The accumulation is high in the coastal area and low in the interior. Due to wind redistribution of snow, exceptionally high values with strong variations are found in areas of nunataks and steep surface slope. From /Richardson 2004/.*

The geothermal heat flux is also of great importance for the basal condition of ice sheets e.g. /Waddington 1987/, affecting basal ice temperatures, hydrology, ice dynamics, and the erosional capacity of the ice. Typically, for a 3 km thick ice sheet at steady-state, a 20% error in geothermal heat flux generates a 6 K error in calculations of basal ice temperatures. This has direct implications on, for example, numerical ice sheet modelling. If the geothermal heat flow is not realistic in the model setup, ice sheet models will not produce useful data on basal melting and other characteristics. Numerical ice sheet modelling studies have also shown that basal ice temperatures are sensitive to relatively small changes in geothermal heat flow e.g. /Greve and Hutter 1995, Siegert and Dowdeswell 1996/.

For the modelling study presented in Section 3.1.4, /Näslund et al. 2005/ calculated a distributed, high-resolution geothermal heat flow data set for an approximate core area of the Fennoscandian ice sheet, and embedded this within lower-resolution data published for surrounding regions. In the following, a brief overview of the geothermal heat flux calculation is given.

The geothermal heat flow, or surface heat flow density (HFD), in cratonic areas consists of two components: (1) heat produced within the mantle and core of the Earth and (2) heat produced within the crust. The contribution from the Earth's interior (so-called Moho- or reduced heat flow) arises from the cooling of the Earth and formation of a solid core, and from radiogenic heat production, e.g. /Pollack et al. 1993/. The crustal component consists of radiogenic heat production where heat is produced by the natural radioactive decay of primarily ^{238}U, ^{232}Th, and ^{40}K /Furlong and Chapman 1987/. The Moho heat flow has a smooth spatial variation, possibly depending on mantle convection cell distribution /Beardsmore and Cull 2001/, whereas the spatial variation in concentration of radioactively decaying nuclides in the lithosphere generates a heat flow with large spatial variations. The surface HFD can be estimated by a heat flow-heat production (Q-A) relationship of the form

$$Q = q_0 + DA_0 \qquad \text{Equation 3-6}$$

/Birch et al. 1968, Lachenbruch 1968, Beardsmore and Cull 2001/ where Q is the surface heat flow density (or geothermal heat flow), q_0 is the Moho heat flow, D represents the vertical distribution of heat-producing radionuclides in the lithosphere and A_0 is the radiogenic heat production from near-surface rocks.

The regional HFD pattern does not correlate with gravity variations /Balling 1984/, magnetic anomalies /Riddihough 1972/, or crustal thickness /Čermák et al. 1993/. However, within the Baltic shield, as well as in other areas with similar geological settings, there is close correlation between HFD and

regional geological units, with higher heat flow from acid (commonly granitic) areas and lower heat flow values from basic areas e.g. /Landström et al. 1979, Malmqvist et al. 1983/.

The calculation of HFD values for Sweden and Finland were based on detailed data sets from numerous γ-emission measurements from bedrock and till. In Sweden, airborne surveys of γ-emissions have been carried out by the Geological Survey of Sweden (SGU), sampling data at 70 m intervals along flight lines with 17 km separation. In order to avoid shielding effects from vegetation and lakes, only data from exposed bedrock and till surfaces were used in the calculations. The Finnish data set is based on radiometric γ-emission measurements of 1,054 till samples providing full spatial coverage of the country /Kukkonen 1989/.

The calculation of HFD is performed in several steps. First, the concentrations of ^{238}U, ^{232}Th, and ^{40}K are calculated from the γ-emission measurements, using information from detailed reference measurements over calibration plates with well known isotopic concentrations. Near-surface heat production was then calculated from the concentrations of radionuclides. In addition, the Moho heat flow contribution needs to be considered. The distributed Moho heat flow by /Artemieva and Mooney 2001/ was added to the near-surface heat production data set. Finally, the HFD data set was re-sampled to a grid with 5 km resolution. To provide HFD coverage for the entire model domain, data for surrounding areas were added from the much coarser observed global HFD data set provided by /Pollack et al. 1991/. The resulting geothermal heat flow distribution is shown in Figure 3-8.

Within the LGM ice margin, the new data set shows that the geothermal heat flow varies by a factor of as much as 2.8 (geothermal heat flow values ranging between 30 and 83 mW/m^2), with an average of 49 mW/m^2. This average value is 17% higher than 42 mW/m^2, the typical uniform value used in ice sheet modelling studies of Fennoscandia. Using this new distributed data set on geothermal heat flow, instead of a traditional uniform value of 42 mW/m^2, yields a factor of 1.4 larger total basal melt water production for the last glacial cycle /Näslund et al. 2005/. Furthermore, using the new data set

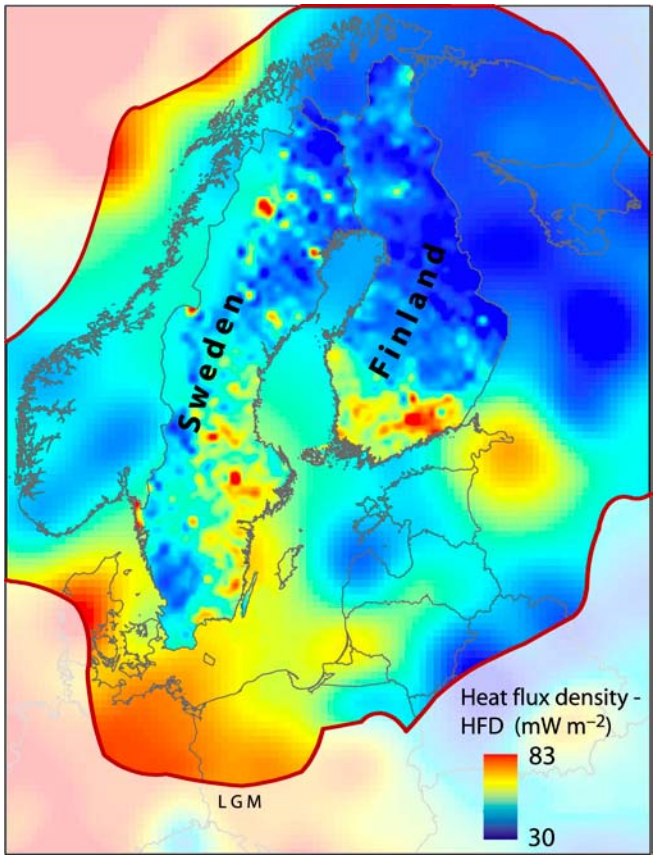

Figure 3-8. *Geothermal heat flow distribution over Fennoscandia. From /Näslund et al. 2005/.*

in high-resolution modelling, results in increased spatial thermal gradients at the bed. This enhances and introduces new local and regional effects on basal ice temperatures and melt rates. The results show that regional to local variations in geothermal heat flow need to be considered for proper identification and treatment of thermal and hydraulic bed conditions under the Fennoscandian and other similar ice sheets /Näslund et al. 2005/.

Ice properties. The exponent n in Glen's flow law (Equation 3-5) is dependent on the active creep process. Numerous field experiments and laboratory tests of glacier ice suggest that n should be ~3. The typical creep process taken into account is a simple power-law creep, where the creep rate is proportional to the stress raised to some power greater than 1, for example:

$$\dot{\varepsilon} \propto \sigma^3 \qquad \text{Equation 3-7}$$

On the other hand, with certain temperature, stress, and grain-size combinations, diffusional creep instead of power-law creep could take place in ice sheets /Duval et al. 1983/, which would lower the value of n to less than 3. Other recent studies suggest that n should be between 1 and 2 for deformation at low stresses, low temperatures, and low cumulative strains /Alley 1992, Montagnat and Duval 2000/. However, some of these conditions are likely to be important only down to depths of a few hundred metres in the coldest parts of ice sheets.

The viscosity constant B in Glen's flow law is dependent on a large number of parameters. Therefore, various modifications of Glen's flow law have been developed taking into account temperature, hydrostatic pressure, and crystal orientation. The last case is the most difficult, and it is done by introducing an anisotropy enhancement factor. The *c*-axes of the ice crystals are, to a large degree, uniformly distributed in the upper part of the ice sheet, i.e. the ice is basically isotropic. When the ice over time is affected by the weight of the accumulating overlying ice mass, it is vertically compressed and longitudinally stretched, which results in a conical distribution of c-axes orientations. Subsequently, when the ice is affected by the simple shear close to the ice sheet bed, the *c*-axes are typically re-oriented to a preferred single orientation. Development of *c*-axis fabrics has been obtained by re-crystallisation and ice grain rotation. Since it is known from ice core studies that the crystal orientation in ice sheets is not isotropic at depth, a non-isotropic flow law of ice improve, for example, ice sheet modelling, e.g. /Placidi et al. 2010/.

The ice sheet dynamics described above may affect a number of geosphere variables of importance for a deep geological repository (Table 3-1).

3.1.3 Natural analogues/observations in nature

Palaeo-ice sheets

The mid-latitudes of the Northern Hemisphere have experienced repeated continental-scale glaciations during the Late Cenozoic. As previously mentioned, these periods are referred to as *glaciations* and the warm periods between the glacials are called *interglacials*. The present interglacial is called the Holocene, and in north-western Europe, the last glaciation is named the Weichselian.

Palaeo-ice sheets have left geological traces in previously glaciated terrain in Fennoscandia, North America and Siberia, as well as abundant glacio-marine traces in adjacent ocean basins. Studies of North Atlantic marine sediments have shown that the first traces of eroding glaciers in Greenland and Fennoscandia date back to between 12 and 6.6 Myr BP /Jansen and Sjøholm 1991, Fronval and Jansen 1996/, with larger ice sheets present in Fennoscandia from around 2.75 Myr BP. During the last ~700 kyrs, glaciation cycles have been about 100 kyrs long cf. /EPICA community members 2004, Lisiecki and Raymo 2005/, preceded by a period of shorter (41 kyrs) glacial cycles e.g. /Raymo et al. 1998, McIntyre et al. 2001/, see Section 2.2.2.

Geological information on till stratigraphy, interstadial deposits, glacial landforms in loose sediments and in bedrock have for a long time been used for making reconstructions of the Weichselian glacial history. A summary of that work is provided in /Lokrantz and Sohlenius 2006/. Section 4.2 describes several recent studies that have been used for the reconstruction of the Weichselian glacial history for the SR-Site safety assessment and of climate conditions during this glacial cycle.

Table 3-1. A summary of how geosphere variables are influenced by ice sheet dynamics.

Geosphere variable	Climate issue variable	Summary of influence
Ground temperature	Basal ice temperature	During periods of cold-based ice coverage, low basal ice temperatures contribute to the formation of permafrost. During periods of warm-based ice coverage, basal ice temperatures at the pressure melting point contribute to permafrost degradation.
Groundwater flow	Basal thermal condition Basal melt rate Supply of surface melt water	If the ice sheet is cold-based no free water is available and there will be no groundwater recharge from basal melt water. If the ice sheet is warm-based, basal melting occurs at the ice/bed interface and groundwater recharge takes place. In addition, meltwater from the ice sheet surface will, in both cases, be transported to the bed in frontal-near areas of the ice sheet (see further Section 3.2). Groundwater recharge and flow will be determined by the presence of the ice sheet.
Groundwater pressure	Basal thermal condition Ice sheet thickness Basal melt rate Supply of surface melt water	If the ice sheet is warm-based, the water pressure at the ice/bed interface may reach as much as the ice sheet overburden pressure, and in certain cases more. The groundwater pressure also depends on the melt water supply and the flow properties of the en- and sub-glacial hydrological systems (see further Section 3.2). The groundwater pressure is also affected by the ice load compression of the bedrock pores and fractures.
Rock stresses	Basal condition Englacial ice temperatures Ice sheet thickness	Rock stresses will be influenced by the ice load and the hydrostatic pressure. Independently of basal conditions there will be an increase in vertical stresses corresponding to the ice thickness. The horizontal stresses will also increase. If the ice sheet is warm-based the prevailing water pressures at the ice/bed interface will also alter rock stresses. The alteration of rock stresses also depends on the duration of the ice load and the slope of the ice sheet surface. The slope of the ice sheet surface near the front is in turn highly dependent on englacial ice temperatures and basal thermal conditions.
Groundwater composition	Glacial melt water composition	The glacial melt water is oxygen rich. The combination of abundant melt water supply and high water pressures may cause injection of glacial melt water to larger depths than for non-glacial conditions. Also, the consumption of oxygen close to the surface may be limited due to the lack of organic matter and microbiological activity.

Various types of glacial landforms may also be used to infer information on basal thermal conditions of palaeo-ice sheets e.g. /Lagerbäck 1988a, Kleman et al. 1997, Kleman and Hättestrand 1999, Kleman and Glasser 2007/.

Present ice sheets

At present there are two ice sheets on Earth, the Antarctic (14 Mkm^2) and Greenland (1.7 Mkm^2) ice sheets. Large portions of these quasi-stable ice sheets are more than 3 km thick. In both cases, the ice sheet load has depressed the bed so that large portions are situated below sea-level. Offshore marine sediments have shown traces of waxing and waning Antarctic ice sheets of continental proportions back to 40–36 Myrs /Haq et al. 1987, Hambrey et al. 1992/, and Antarctic alpine glaciers may trace back to the Oligocene /Näslund 2001/. The present configuration of the Antarctic ice sheet is thought to have been relatively stable for the last 15–11 Myrs /cf. Shackleton and Kennett 1975, Marchant et al. 1993/.

The spatial patterns of basal thermal characteristics of the Antarctic and Greenland ice sheets are complex due to ice sheet dynamics, bed topography, and geothermal heat flux variability. For both ice sheets, parts of the bed are cold-based whereas other parts are warm-based, as seen from modelling studies (Figure 3-9), radar soundings and drill hole data. Ice sheet modelling has also, together with geological field observations and remote sensing studies, showed that ice streams are prominent features of the Antarctic ice sheet, penetrating far into the ice sheet interior (Figure 3-10). This has also been shown by remote sensing Interferometric Synthetic Aperture Radar (InSAR) studies /Joughin and Tulaczyk 2002/. The outer coastal-near parts of these ice streams are typically wet-based, whereas their upstream parts, high in the catchment areas, often are cold-based.

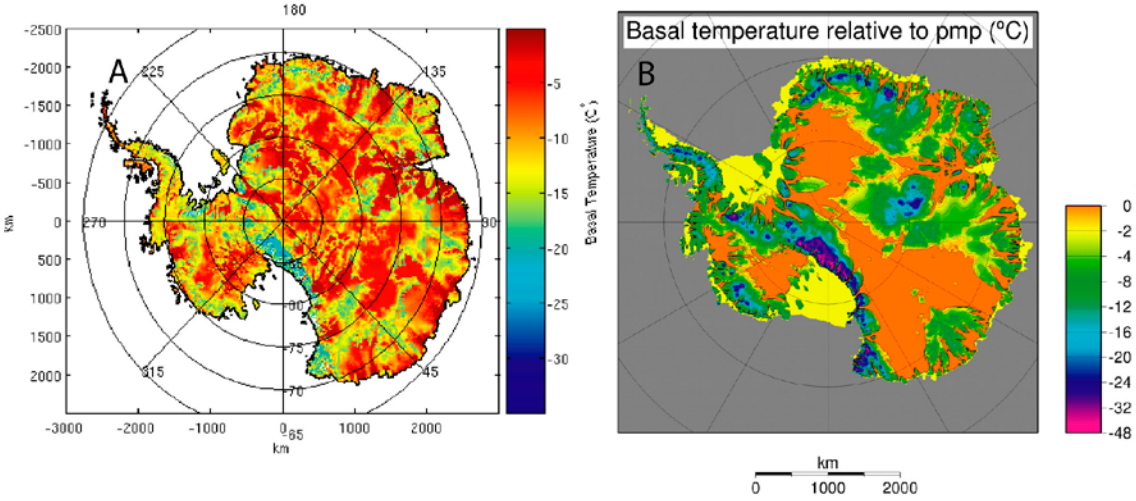

Figure 3-9. *Two examples of modelled present-day Antarctic ice sheet basal temperatures. Temperatures are expressed relative to the pressure melting point (pmp). Figure a) is from /Johnson 2004/ and b) from /Huybrechts 2006/.*

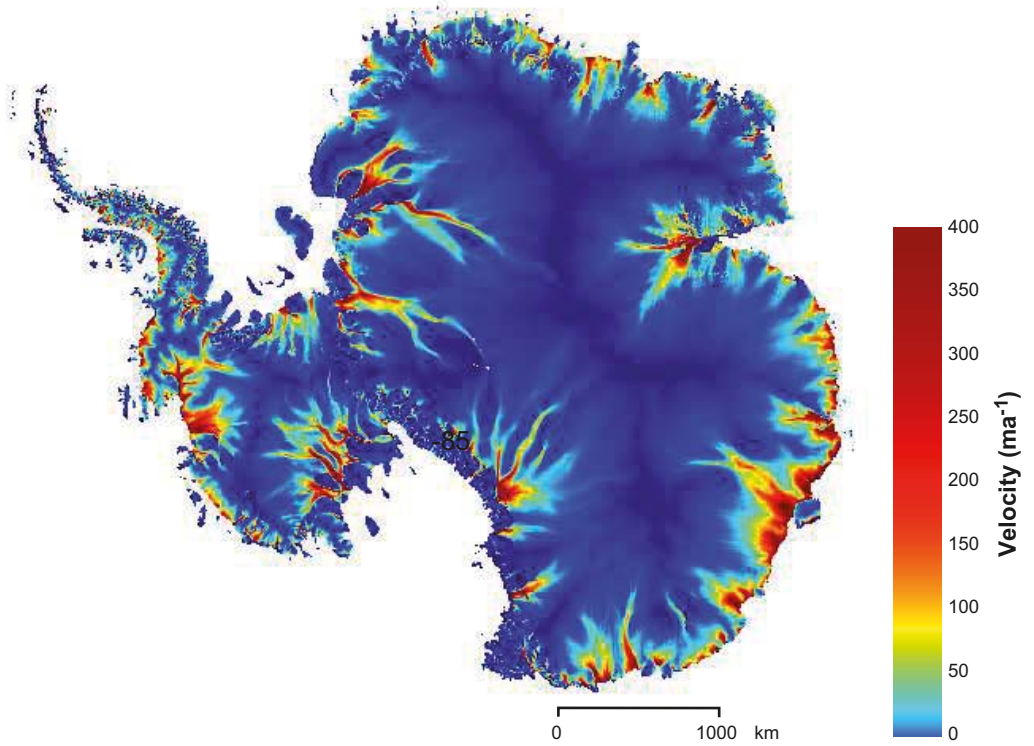

Figure 3-10. *Modelled Antarctic ice surface velocities. Fast-flowing ice streams (red/yellow/green colour) reach far into the ice sheet interior. From /Johnson 2004/ with numerical methods described in /Staiger et al. 2005/.*

During the main Pleistocene glacial periods, the Greenland and Antarctic ice sheets had a larger extent than at present. The major limiting factor on their maximum lateral extent is the bed topography; the Antarctic and Greenland ice sheet margins are both today located close to the coast line. The continental crust does not extend out very far from the present-day coast lines, and at the continental margin the water depth quickly becomes deeper. When the ice sheets grow larger the grounding-line migrates outward, resulting in a larger area for the grounded part of the ice sheet. The grounding line cannot advance past the continental margin due to the larger water depths outside. The continental margin thus constitutes a definite constraint on the maximum spatial size of Antarctic and Greenland ice sheets

during Late Cenozoic ice sheet fluctuations. The situation was similar for part of the Fennoscandian ice sheet. From a bed topography point of view there were no constraints for ice sheet growth from the Scandinavian mountain range towards east (the Baltic depression is not deep enough in this context), but, towards the west, Fennoscandian ice sheets, including the last Weichselian ice sheet, could not and did not extend farther west than the offshore continental margin /Svendsen and Mangerud 1987, Zweck and Huybrechts 2003/.

Although the sizes of the Antarctic and Greenland ice sheets were greater during the Late Pleistocene glacials, the maximum thicknesses need not have been larger. On the contrary, because of atmospheric moisture starvation during the colder climates, the interior parts of the ice sheets probably were thinner during the coldest parts of the glacial cycles e.g. /Huybrechts 1990/. In contrast, at the ice sheet margins the ice sheet thickness varies considerably during a glacial cycle. Areas where the ice thickness is zero during a warm interglacial period (i.e. at the exact margin) may experience an increase in ice thickness of several hundred metres, up to one kilometre, during a glacial maximum ice configuration /Näslund et al. 2000/. In turn, this means that the temporal changes in basal conditions of the ice sheets, for example changes in basal ice temperatures from the present interglacial pattern, were highly complex. For example, due to the changed ice configuration affecting ice sheet dynamics, some parts of the Antarctic ice sheet were warmer at the LGM ice configuration than at present, whereas at the same time, other parts were colder (Figure 3-11) cf. /Näslund et al. 2000/.

Recently, the coupling between the dynamic behaviour of the Greenland ice sheet and ice sheet hydrological processes have been inferred from a number of studies, see Section 3.2 and 5.1.

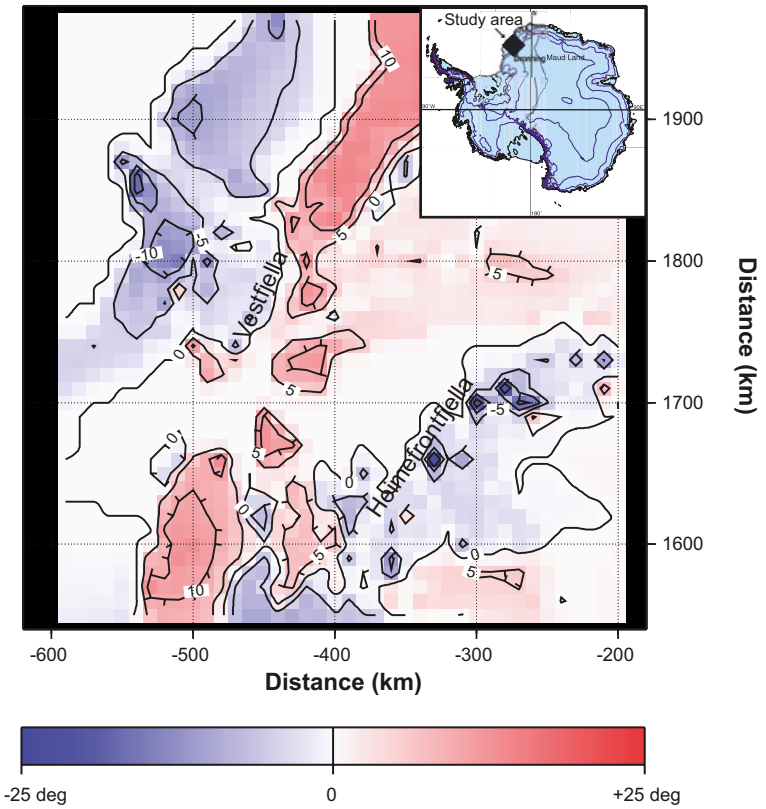

Figure 3-11. *Modelled difference in basal temperature between the present-day ice configuration and a maximum Pleistocene ice sheet configuration for part of the Antarctic ice sheet. For this single change in ice configuration, ice sheet thermodynamics induce complex changes in basal thermal pattern; some parts of the ice sheet become warmer at the bed the same time as other parts become colder. From /Näslund et al. 2000/.*

3.1.4 Model studies

Ice sheet modelling

Thermo-mechanical ice sheet modelling is a well established and useful tool for studying a large array of ice sheet-specific and ice sheet-related issues. Although ice sheet models have limitations, see e.g. /SCAR 2007/, they can be used to study characteristics and behaviour of present ice sheets, palaeo-ice sheets, and in some cases also inferred future ice sheets. As computer capacity has increased, more sophisticated models have been able to be run at higher spatial resolutions, which in turn has made it meaningful to compare detailed model output with various types of geological information, both for model verification and testing of glacial-geological hypotheses e.g. /Pattyn et al. 1989, Van Tatenhove and Huybrechts 1996, Näslund et al. 2003/.

Reconstructions of palaeo-ice sheet configurations, including ice thicknesses, may be done by two main groups of models. One group is thermo-mechanical ice sheet models that are based on ice physics and thermo-mechanical interactions e.g. /Huybrechts 1986, Boulton and Clarke 1990, Fastook 1994, Ritz et al. 1996, Payne and Dongelmans 1997, Marshall and Clarke 1997/. The second group of models are isostatic rebound models that are used to invert observations of crustal rebound and shoreline locations to estimate palaeo-ice thicknesses e.g. /Lambeck et al. 1998, Peltier 2004 /.

For the present study, UMISM (University of Maine Ice Sheet Model) /Fastook and Chapman 1989, Fastook 1990, 1994, Fastook and Prentice 1994, Johnson 1994/ was selected for the simulation of last glacial cycle ice sheet configurations. The UMISM code was selected since a large number of simulations of the last glacial cycle Fennoscandian ice sheet have been done with this model over the years e.g. /Fastook and Holmlund 1994, Holmlund and Fastook 1995, Näslund et al. 2003/. The UMISM was part of the European Ice Sheet Modeling Initiative (EISMINT) model intercomparison experiment and yielded output in agreement with many other physically-based ice sheet models /Huybrechts et al. 1996, Payne et al. 2000/, which further motivates the choice of model.

The resulting reconstruction of last glacial cycle ice sheet configurations for the Forsmark site, e.g. Figure 4-18, shows large similarities with corresponding data for a North American last glacial cycle scenario modelled using the Peltier model /Garisto et al. 2010/. This indicates that the selection of type of model is not critical for the general appearance of the ice sheets reconstructed for the last glacial cycle. In detail, however, the development of ice configurations over time in e.g. these two studies are expected to differ for several of reasons, including that the studies deal with two different geographical areas and indeed two different ice sheets (the Weichselian ice sheet over Eurasia and the Laurentide ice sheet over North America). For instance, the last glacial cycle Laurentide ice sheet is known to have been considerably larger and thicker than the Weichselian ice sheet.

The ice sheet system constitutes three main sub-systems: mass-balance, ice movement, and ice temperature. For these sub-systems the selected ice sheet model solves differential equations describing conservation of mass, momentum, and energy respectively. In addition, the ice sheet model needs to contain a description of climate. A mass balance parameterisation for the spatial pattern of air temperature and precipitation is used in UMISM. The model includes a mathematical description of precipitation based on a number of other parameters; distance from the pole, saturation vapour pressure (function of altitude and lapse-rate), and surface slope. This is an empirical relationship developed from the Antarctic ice sheet /Fastook and Prentice 1994/. Over a certain model domain, with a topography described by a Digital Elevation Model (DEM), this climate description gives a spatial pattern of air temperatures at ground level and a pattern of precipitation.

The UMISM also includes a simplified isostatic description for the behaviour of deforming bedrock due to the weight of the modelled ice sheet configuration. This is not a full self-gravitational spherical Earth model as used in the Glacial Isostatic Adjustment (GIA) modelling in Section 3.3. Instead, it is a hydrostatically supported elastic plate model, considered adequate for the purpose of placing the ice sheet surface at an appropriate altitude, and hence at an appropriate air temperature, for the mass balance calculations. Furthermore the UMISM also includes a subglacial hydrology model /Johnson 1994/ that is able to transport basal meltwater under the ice sheet according to prevailing pressure potentials governed by ice sheet thickness and basal topography.

A palaeo-temperature record was employed to run the ice sheet model (Figure 3-12). For the reconstruction of the Weichselian ice sheet, see below, the temperature proxy record for the last

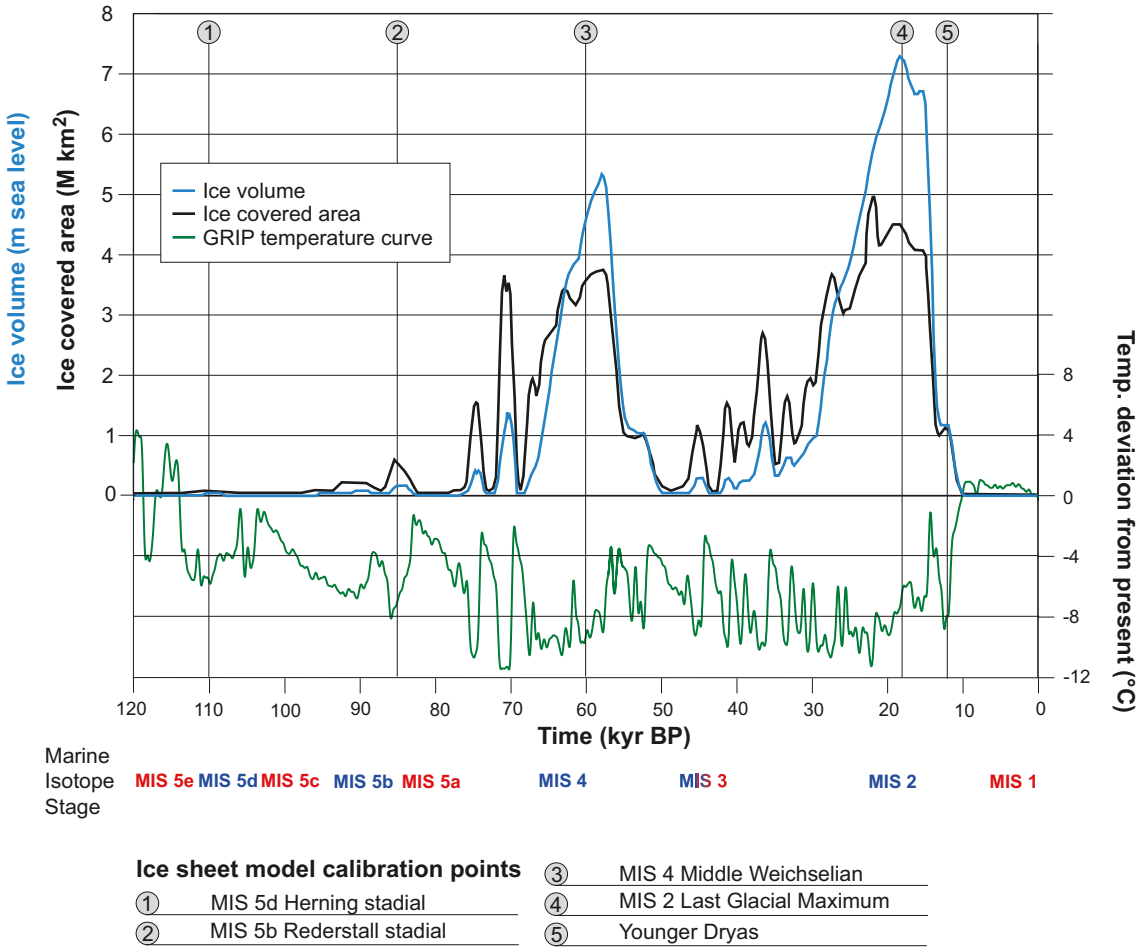

Figure 3-12. *GRIP proxy temperature curve and reconstructed ice covered area and ice volume for the reconstruction of the Weichselian ice sheet. Times of model calibration are shown, as well as Marine Isotope Stages (MIS) (warm stages in red and cold stages in blue).*

120 kyrs from the Greenland GRIP ice core has been used /Dansgaard et al. 1993/. The temperature file that was used contains 50 year averages of the original time series. For a detailed description of this temperature data set, including its use in the ice sheet modelling and its estimated uncertainties, see Appendix 1 and /SKB 2010a/.

In the modelling process, the variations in the temperature proxy curve are used to change the climate pattern (temperature and precipitation) over the model domain, initiating ice sheet growth in Fennoscandia. Once glaciers/ice sheets are formed, the modelled thermo-dynamic ice sheet system starts to evolve over time. In this way, the ice sheet model simulates the behaviour of the ice sheet as it responds to the external forcing such as changing climate or sea-level, as well as internal dynamics, such as ice stream variations caused by internal temperature oscillations at the bed.

The following are input parameters to the ice sheet model in the simulations of the Weichselian ice sheet:

1. The thermodynamic properties of the ice, including flow laws, sliding laws, feedback mechanisms etc.
2. Upper boundary conditions:
   Climate description (annual air temperature, and precipitation rates) from the mass balance parameterisation.

3. Lower boundary conditions:
   A. A DEM over Fennoscandia with a moderately high spatial resolution. For the reconstruction of the Weichselian ice sheet a grid size of 50 km was used. DEM data were taken from the ETOPO2 data base[1], depicting both continental topography and bathymetry;
   B. Geothermal heat flux at the bed.
4. Sea-level changes during the last 120 kyrs.
5. Proxy curve of palaeo-air temperatures during the past 120 kyrs (GRIP data).

The modelling starts 120 kyrs before present, and the model was run at a five year time step forward in time up to time zero (present). For each time step, output data are calculated for each grid cell and grid node, such as:

1. Ice thickness.
2. Englacial and basal ice temperatures.
3. Ice velocity.
4. Direction of ice movement.
5. Isostatic depression of crust.
6. Amount of basal melting or freeze-on of water.

Model setup. A model domain was selected to cover the maximum extent of the Weichselian ice sheet over Fennoscandia, with a spatial DEM resolution of 50 km. The thermomechanical coupling between ice movement and ice temperature was enabled, as well as a function by which the amount of basal sliding is coupled to the amount of basal meltwater present at the ice sheet bed. The *n* parameter in Glen's flow law (Section 3.1.2) was set to 3, whereas the values for the viscosity parameter *B* differs depending on ice temperature. Exemplified calculated values of *B* are seen in Figure 3-13. In the final model run, the model was run with a five year time step and data was saved from the model simulation at a 100 year interval.

The traditional way of specifying the basal thermal boundary condition in ice sheet modelling is to apply a single, uniform value of geothermal heat flow for the entire model domain. The magnitude of this geothermal heat flow value has often been set according to the general geological setting for the area to be studied. Thermodynamic modelling of Fennoscandian ice sheets has, for instance, used a single geothermal heat flow value typical for the Pre-Cambrian shield, the most common reported value being 42 mW/m^2 e.g. /Boulton and Payne 1992, Huybrechts and T'siobbel 1995, Payne and Baldwin 1999/. Others have used higher values, around 50–55 mW/m^2 e.g. /Hindmarsh et al. 1989, Forsström et al. 2003/.

For the model reconstruction of the Weichselian ice sheet, the geothermal data set of /Näslund et al. 2005/ was used as basal boundary condition. A so-called higher-order model, taking into account longitudinal push-and-pull effects within the ice sheet was used for specific studies of ice flow behaviour in relation to geothermal heat-flow anomalies in Sweden, see /Näslund et al. 2005/.

Model calibration. In studies in which ice sheet modelling aims at simulating palaeo-ice sheets, one needs to calibrate the behaviour of the model against known information on ice sheet extents. The reason for this is that we do not have full knowledge on a number of the processes and boundary conditions involved, for example on climate back in time, or ice sheet basal processes. In the present reconstruction of the Weichselian ice sheet, the UMISM model was calibrated by making adjustments of the proxy air temperature curve (Figure 3-12). Over the years, a large number of such simulations of the Fennoscandian ice sheet have been done with the UMISM model using this climate curve, which has given extensive experience of how to perform the model calibration. As mentioned above, the forcing in temperature for the ice sheet model is based on the GRIP ice core /Dansgaard et al. 1993/, see also Appendix 1. In the ice sheet calibration process, the entire temperature curve was shifted and amplified (Figure 3-14) so as to obtain calibrated ice sheet configurations that fitted

[1] ETOPO2, 2001. Global Digital Elevation Model (ETOPO2) representing gridded (2 minute by 2 minute) elevation and bathymetry for the world. Data were derived from the National Geophysical Data Center (NGDC) ETOPO2 Global 2' Elevations data set from September 2001.

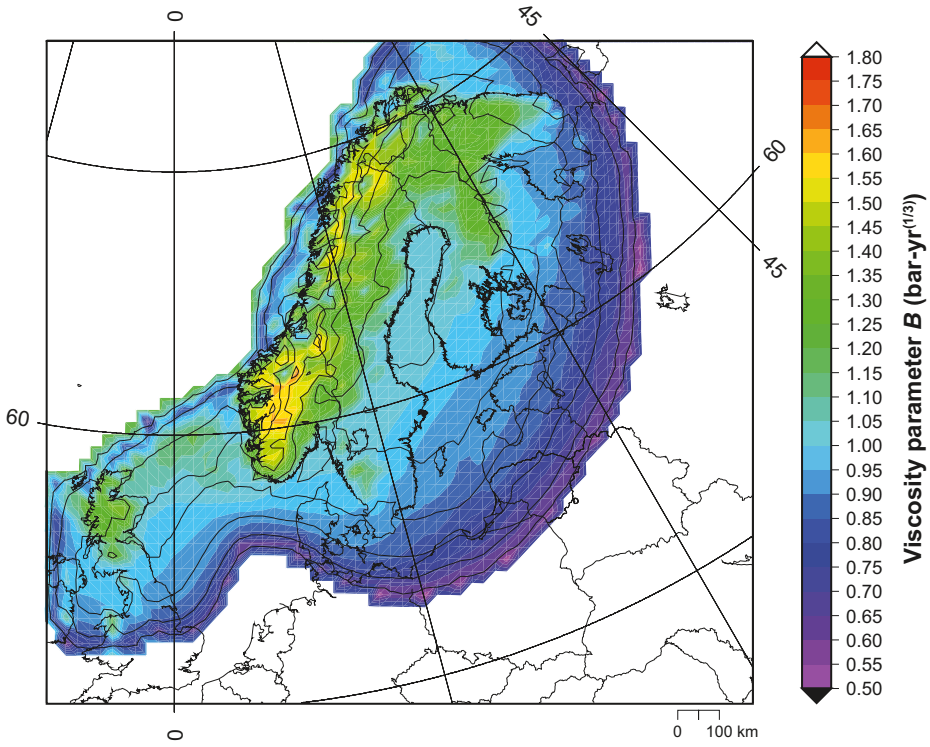

Figure 3-13. *Calculated flow-law viscosity parameter B at 18.5 kyrs BP (at around Last Glacial Maximum), shown as vertically integrated values along the ice column. Colder and harder ice is seen in the central parts of the ice sheet and over the Scandinavian mountain range (larger B values), while warmer and softer ice is seen closer to the ice margin (smaller B values). The white line shows the modelled ice sheet margin and the black lines shows ice thickness contours with a 500 m interval.*

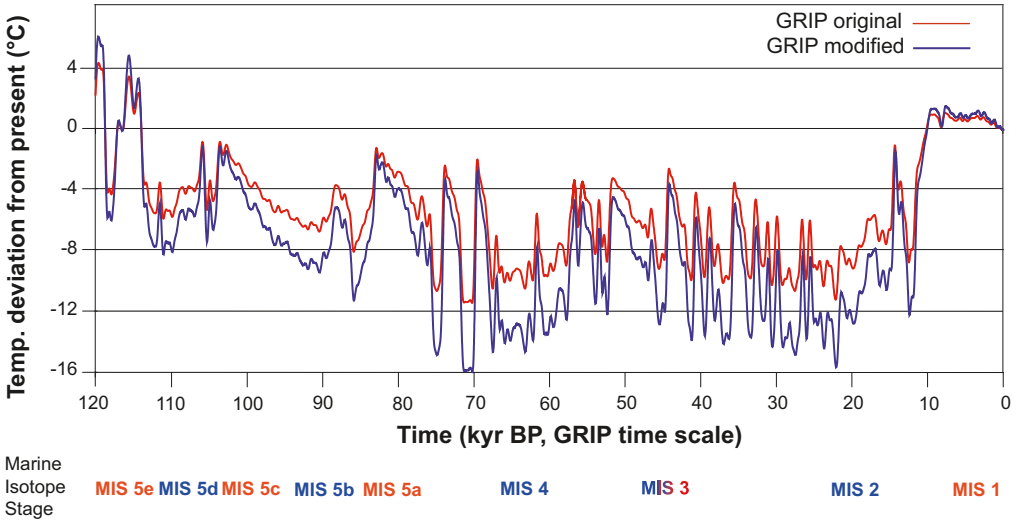

Figure 3-14. *Proxy palaeo-air temperature curves from the calibration process of the UMISM ice sheet model. The final calibrated curve that was used (blue) has larger amplitude that the original data (red), i.e. cold periods were even colder in the calibrated curve. In the calibration process, it was chosen to always change the entire curve in the same way. The temperature curve is discussed in detail in Appendix 1.*

as well as possible with geological observations on dated marginal positions. Model calibration was made for ice margins as described in /Lokrantz and Sohlenius 2006/ for MIS 5d (~110 kyrs BP), MIS 5b (~85 kyrs BP), MIS 4 (~60 kyrs BP), MIS 2 (~18 kyrs BP), and for the Younger Dryas (~12 kyrs BP) (Figure 3-12). Keeping all other input data constant in the calibration process, the modified temperature curve after model calibration results in Late and Middle Weichselian ice sheet configurations in good agreement with dated ice-marginal positions and Early Weichselian configurations in reasonably good agreement with geological interpretations. The characteristics and applicability of the GRIP temperature curve for the present study is further described and discussed in Appendix 1.

The resulting calibrated reconstruction of the Weichselian ice sheet is seen in Figures 3-12 and 3-15. Ice extends over the model domain during the cold stadials during Marine Isotope Stages (MIS) 5d, 5b, 4, and 2. During warmer interstadials, such as MIS 3, the ice cover is more restricted. As expected, there is a clear trend of more and more pronounced ice coverage during the stadials through the glacial cycle, with the LGM peak occurring at around 18 kyrs BP.

Different types of output data have been extracted and post-processed from the reconstruction of the Weichselian ice sheet, for example 1) basal and surface melt rates for groundwater modelling /Jaquet and Siegel 2006/, 2) Basal and subaerial temperatures for permafrost modelling (Section 3.4 and Appendix 1), 3) ice thickness variations for modelling of global isostatic adjustment (Section 3.3) and crustal stresses /Lund et al. 2009/, and 4) 2D ice sheet profiles for modelling of groundwater flow under glacial conditions /Vidstrand et al. 2010/, see also Appendix 2.

For more information on the ice sheet model, see /SKB 2010f/ and for further descriptions of model simplifications and uncertainties, see Section 3.1.7.

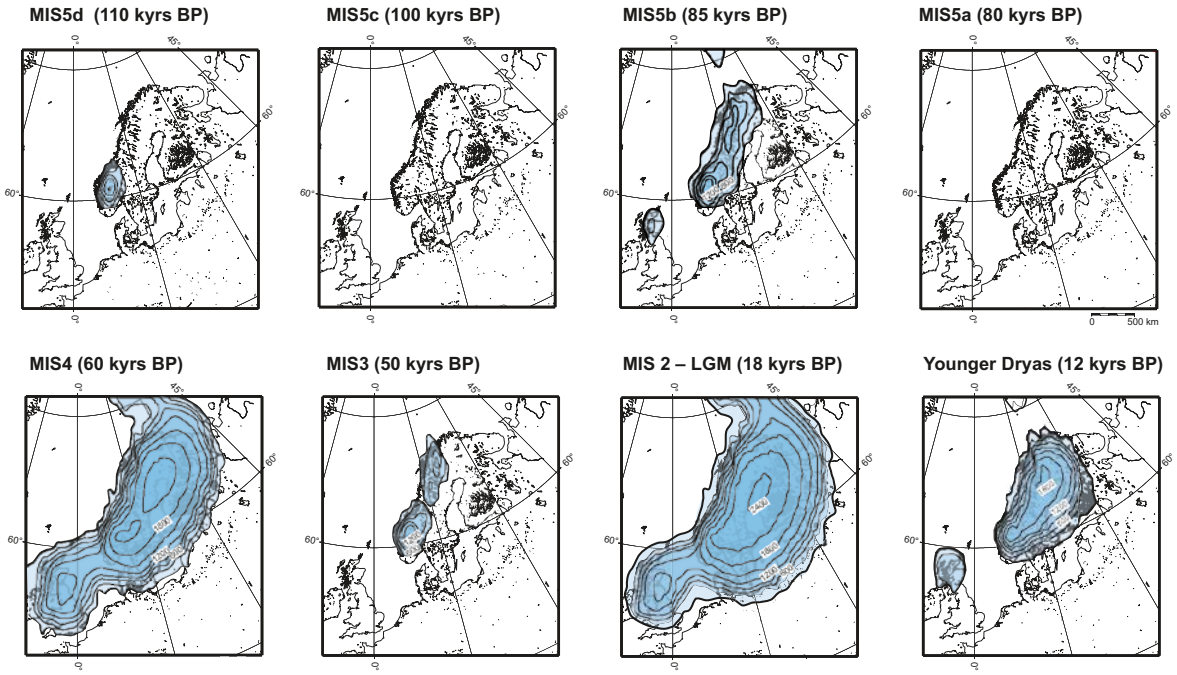

Figure 3-15. *Selected maps of ice sheet surface topography for the reconstructed Weichselian ice sheet. The ice sheet grows to its full LGM configuration in progressive phases of increasing maximum extent, with intervening periods of more restricted ice coverage. Contour lines show ice surface elevation with a 300 m contour interval. All maps show present day shoreline position.*

3.1.5 Time perspective

It is generally agreed that ice sheets take longer to grow than to decay. However, our knowledge of the final deglaciation phase is much better than of inception phases, reflecting the fact that there are more geological traces from the last deglaciation than from early stages. Since ablation by surface melting is a more efficient process than snow accumulation, this suggests that the time for ice sheet decay should be faster than the growth time /Paterson 1994/. In reality, this is also accentuated due to efficient ice shelf calving processes for marine parts of ice sheets, for example calving of the Fennoscandian ice sheet in the Gulf of Bothnia. In line with the present modelling results of the Weichselian ice sheet (Figures 3-12 and 3-15) it is generally concluded that ice sheets may build up in a series of glacial build-up periods, peaking in a glacial maximum close to the end of the glacial. The Fennoscandian ice sheet seems to have exhibited such dynamic behaviour during the last glacial cycle, Section 4.2. This has also been inferred from studies of so called Heinrich events cf. /Heinrich 1988/ recorded in North Atlantic marine sediments, suggesting that even large ice sheet systems are dynamic features, responding relatively quickly to rapid changes in climatic forcing.

During the last 700 kyrs, glacial cycles have typically had a duration of about 100 kyrs, with inter-glacials lasting around 10 to 20 kyrs e.g. /McIntyre et al. 2001, Tzedakis et al. 2009/. As noted above and discussed in Section 4.2, the last glacial cycle was also characterised by a number of cold growth phases and intervening warmer periods with less ice, although from the geological record we still do not know how to date or correlate all observed interstadial localities /Lokrantz and Sohlenius 2006/. A typical cold Weichselian stadial had duration of some thousands of years, see e.g. Figure 3-12 and Section 4.3.4. The deglaciation of the Weichselian ice sheet from the LGM ice margin to the last ice remnants in the Scandinavian mountain range took about 8 kyrs, including a number of temporal halts in the retreat, the most pronounced one occurring during the Younger Dryas (about 13–11.5 kyrs BP).

3.1.6 Handling in the safety assessment SR-Site

The evolution of ice sheets is investigated by means of numerical modelling. The base case of the main scenario in SR-Site is constructed from a *reference glacial cycle* based on an ice sheet model reconstruction of the Weichselian glaciation. The thermo-dynamic ice sheet model used is capable of simulating realistic ice sheets which are typically not in balance with the climate. Derived ice temperatures, together with density variations with depth, control ice viscosity and ice flow. The thermodynamic calculation accounts for vertical diffusion, vertical advection and heating caused by internal shear. The climate input, forcing ice sheet evolution, is the mean annual air temperature at sea-level, and its variation over time. The mass balance is determined from an empirical relationship based on a simple parameterisation of the ice sheet's effect on local climate /Fastook and Prentice 1994/. Distributed temperatures over the model domain are determined from height above sea-level and distance from the pole.

The model simulation of the Weichselian ice sheet over Fennoscandia was controlled by the proxy temperature curve from the GRIP ice core, obtained from central Greenland e.g. /Dansgaard et al. 1993/, see also Appendix A, a typical method used in ice sheet modelling of the Weichselian glacial cycle. The geothermal heat flow and its spatial variation has been shown to be of importance for obtaining realistic modelled basal ice temperatures and basal melt rates /Waddington 1987, Näslund et al. 2005/. Basal temperatures and basal water conditions are in turn important for the overall ice flow and ice dynamics. A detailed dataset of geothermal heat flux values, based on national measurements of gamma emissions in Sweden and Finland has been compiled /Näslund et al. 2005/, and has for the first time been used as input to an ice sheet model. This eliminates previous large uncertainties in geothermal heat flow, and associated uncertainties in modelled basal conditions of the ice sheet.

The ice sheet model was calibrated so that modelled ice sheet configurations were in agreement with dated geological information on ice-marginal positions (Section 3.1.4). For this purpose, geological information on the Weichselian glaciation history of Scandinavia was compiled by /Lokrantz and Sohlenius 2006/. For further information on the ice sheet modelling, see the preceding parts of Section 3.1.

3.1.7 Handling of uncertainties in SR-Site

Uncertainties in mechanistic understanding

Model simplification uncertainty. The most important simplifications made in the ice sheet modelling in the model reconstruction of the Weichselian ice sheet are the following.

The temperature proxy climate curve driving the model is the GRIP Greenland temperature curve. First of all this curve describes the climatic conditions at Greenland, but in the absence of similar palaeoclimate data from Fennoscandia, or other closer areas, these are the best data available. With the applied modelling approach, the Greenland proxy data generate Fennoscandian ice sheets that are in fair agreement with geological information on LGM and Younger Dryas ice margin positions, even *without* model calibration, which is a justification that this approach is valid. There are also uncertainties introduced by the conversion from oxygen isotope values in the ice core to Greenland palaeo-air temperatures /Johnsen et al. 1995/, see also Appendix 1. The temperature proxy climate curve is probably the biggest assumption made in the modelling experiments, and therefore this parameter has been selected for adjustment in model calibration.

In the model, the amount of basal sliding is coupled to the thickness of the basal water layer of the ice sheet. This is a simplification, but still a reasonable way of handling the difficult topic of basal sliding and the coupling between glacier hydrology and ice sheet dynamics. One thing that is excluded in the model is the possible presence of subglacial deformable sediments, for example in the Baltic depression, which may enhance ice velocities, especially in ice streams. The exclusion of the effects of such sediments could, in some cases, lead to some overestimation of ice thickness.

In the UMISM model, as in many other ice sheet models, the so-called shallow ice approximation is used. This means that the horizontal velocity is only dependant on the local driving stress. Horizontal and longitudinal englacial stresses are neglect, i.e. there are no push-and-pull effects within the ice sheet, as in nature. This is an appropriate assumption for the major part of the ice sheet, with the exception of frontal near parts and ice divides. In contrast, the model has not been used in such a way that this has been a shortcoming.

In the UMISM model, horizontal advection of heat was not included in the thermodynamic treatment of the ice. The result is that the model may overestimate basal ice temperatures to some extent. This is likely to be of importance only in fast-flowing situations like ice streams.

The hydrostatically supported elastic plate model included in the UMISM model is a simplification, but sufficient for adjusting bed- and ice sheet surface elevations to obtain a reasonably good surface mass balance.

The UMISM model does not include an ice shelf model. Instead, ice shelves are simulated by adjusting a marine calving rate directly at the dynamic grounding line.

The spatial resolution of model domain is approximately 50·50 km. This resolution may, in some cases, be too coarse to correctly depict smaller features in for example geothermal heat flow pattern.

Input data and data uncertainty

The temperature proxy climate curve. See section on Model simplification and uncertainty above, Section 3.1.4, and Appendix 1.

Digital elevation data. The accuracy of the ETOPO2 DEM is good enough for the 50·50 km and 10·10 km resolution ice sheet model simulations made.

Geothermal heat flux. The high-resolution data set on spatially varying geothermal heat flux is of high quality in the context of ice sheet modelling. In the new data set, high resolution geothermal data are available only for Sweden and Finland, not for the entire area covered by the Weichselian ice sheet. However, this does not affect modelled basal conditions in Sweden, since basically all parts of Sweden are located down-stream from areas with high-resolution data. There are assumptions made in the calculation of the data set that could be refined to improve the data set in the future, for example using a varying lithospheric thickness in the calculation of surface heat flow. Also, denser data on γ-emission measurements from bedrock are available for parts of Sweden, which may be used for future versions of the data set. All in all, this new type of ice sheet model input has improved ice sheet modelling significantly from all previous reconstructions of palaeo-ice sheets by numerical modelling.

Sea-level. The sea-level curve used as input is derived from numerical ice sheet modelling of all Northern Hemisphere ice sheets. The present volume of the Antarctic ice sheet was held constant. The maximum lowering of sea-level in this data set is 100 m, somewhat less than the ~120–135 m of global sea-level lowering at the LGM deduced from coral-reef data /Yokoyama et al. 2000/. However, this is of minor importance since the position of the grounding-line in the western Atlantic part of the ice sheet is determined by the bed topography (i.e. continental shelf location), and the eastern part is advancing and retreating over the Baltic Sea which does not have contact with the Atlantic during such low global sea-levels.

3.1.8 Adequacy of references

The SR-Can Climate report /SKB 2006a/, from which some of the studies are used, has undergone QA system handling including a factual review process. Other references used for the handling of ice sheet dynamical processes are either peer-reviewed papers from the scientific literature or from a text book /Paterson 1994/.

3.2 Ice sheet hydrology

This part of the report summarises the knowledge on water flow in and beneath glaciers and ice sheets. Many concepts in hydrology and hydraulics are applicable to water flow in glaciers. However, the unique situation of having the liquid phase flowing in conduits of the solid phase of the same material is not encountered elsewhere. This situation means that the heat exchange between the phases and the resulting phase changes also have to be accounted for in the analysis. The fact that the solidus in the pressure-temperature dependent phase diagram of water has a negative slope provides further complications. It means that ice can melt or freeze from both temperature and pressure variations.

3.2.1 Overview/general description

The hydrology of glaciers has been reviewed by several authors /Weertman 1972, Lang 1987, Röthlisberger and Lang 1987, Hooke 1989, Hubbard and Nienow 1997, Fountain and Walder 1998, Schneider 2000, Boulton et al. 2001b, Jansson et al. 2003, Hock and Jansson 2005, Hock et al. 2005/. However, most reviews concern specific topics and do not provide an overview. Therefore, /Jansson et al. 2007/ provides an overview of the theoretical knowledge on water flow in and beneath glaciers and ice sheets, and how these theories are applied in models to simulate the hydrology of ice sheets. The study provides both a broad overview and an in-depth understanding of glacier hydrology to be applied to ice sheets. In order to describe in detail the current understanding of water flow in conjunction with deforming ice and to provide understanding for the development of ideas and models, emphasis has in /Jansson et al. 2007/ been put on the mathematical treatments, which are reproduced in detail. Qualitative results corroborating theory or, perhaps more often, questioning the simplifications made in theory, are also given. The overarching problem with our knowledge of glacier hydrology is the gap between the local theories of processes and the general flow of water in glaciers and ice sheets. Water is often channelized in non-stationary conduits through the ice, features which due to their minute size relative to the size of glaciers and ice sheets are difficult to incorporate in spatially larger models. New work is emerging which attempts to bridge the gap between the ice sheet spatial-scale modelling and the details of our process understanding, see /Jansson et al. 2007/.

The general hydrological processes, summarized by e.g. /Jansson et al. 2007/ are similar under both glaciers and ice sheets since the driving forces are the same, differing only in magnitude and spatial scale. /Bell 2008/ has reviewed the role of water beneath the ice sheets on their stability and hence their mass balance since the dynamics influences fluxes of ice into the oceans. Indications also emerge that temperate basal conditions favouring sliding in the presence of water may be important for the observed waxing and waning of past ice sheets /Bintanja and van de Wal 2008/. /Bamber et al. 2007/ have summarized the developments in our view of ice sheets going from slow behemoths responding on time perspectives of millennia or longer to dynamically active features, capable of reactions on the order of years to decades.

The traditional view of the glacier hydrological system is similar to a combination of a groundwater system and a limestone karst system of shafts and tunnels, and consists of supra-, en- and sub-glacial system components. Figure 3-16 shows the situation on a typical glacier in summer.

The surface can be divided into two parts, a lower part where the surface consists of solid ice, referred to as the ablation area since a net loss of mass occurs in this area, and where water will run off by mostly channelised surface flow and an upper part, referred to as the accumulation area because a net mass gain occurs, where the surface consists of permeable snow or firn, snow that has survived at least one year of melting. The snow and firn pack is porous and allows water to percolate into the glacier and accumulate at depth as firn water bodies, equivalent to groundwater bodies whereas ice effectively is impermeable.

On an ice sheet, the snow-covered area can be further subdivided into zones depending on their thermal conditions, see Figure 3-16. At the centre of ice sheets, an example of which is modern Greenland, the snowpack is cold and no surface melting occurs during any part of the year. This is the *dry snow zone*. At some point at lower elevation, surface melting can occur because of warmer conditions caused by the atmospheric temperature lapse rate. Hence there is a zone where percolation occurs increasingly wetting the upper part of the snow pack at lower altitude since the potential for melt increases at lower altitude. This zone is called the *percolation zone*. At some

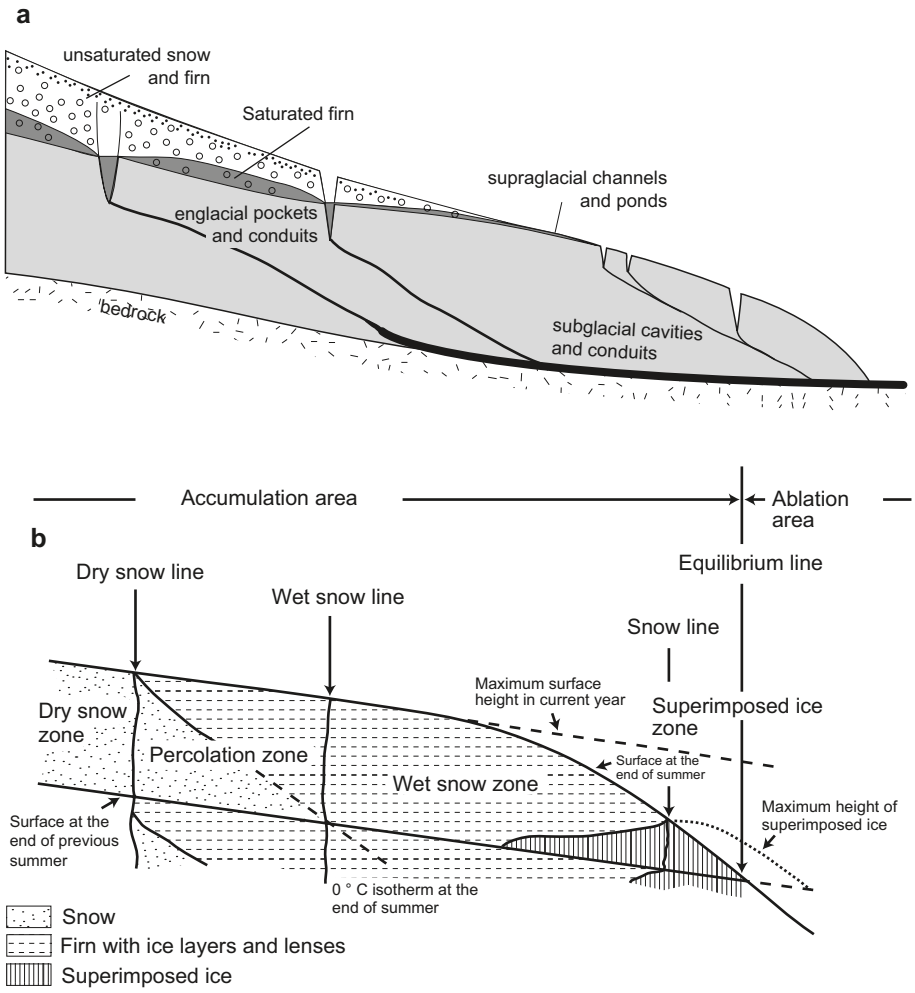

Figure 3-16. *a) The hydrological system of a glacier consist of supra-, en- and subglacial subsystems and interacts with the substrate hydrological systems. Modified from /Holmlund and Jansson 2003, after Röthlisberger and Lang 1987/. b) The glacier surface can be divided into different facies starting with the dry snow zone through the percolation zone to the wet snow zone. Modified from /Benson 1961, Müller 1962, Paterson 1994/.*

elevation the melting is strong enough to completely warm the snow pack. The zone of completely temperate snow is called the *wet snow zone*. These zones describe the conditions met during parts of the season. During winter most of the ice sheet will be covered by dry snow and development of the different zones initiate as air temperature rises during spring and summer. This also means that the different zones start to develop at lower altitude and move upglacier as the season progresses to reach their uppermost position at the end of the melt season or when the annual temperature cycle has reached maximum temperature. This also indicates that the surface flow system will develop throughout the entire melt season with accompanying effects on runoff and water input to an en- and subglacial drainage system.

Water is also generated at the base of ice sheets where the basal temperature is at the pressure melting point. The amount of energy available for melting is given by the geothermal heat flux and the deformational energy, so called *strain-heating*, in the ice produced by ice flow. The geothermal heat flux varies spatially according to the geologic structure of the Earth's crust /Näslund et al. 2005/ but does not vary significantly in time over the time periods under consideration for a geologic repository for spent nuclear fuel. The energy available from strain heating varies both spatially and temporally with the waxing and waning of the ice sheet as well as with the induction and demise of faster flow features in the ice sheet. There is, therefore, a strong feedback between ice deformation, heat production, and water production available for enhanced sliding beneath temperate-based parts of an ice sheet. The cold-temperate boundary is also affected by the strain heating, which may enlarge the areas subjected to basal melting. Typical basal melt rates may vary from a few to up to 10 mm/year, although even higher melt rates can probably occur under special circumstances where ice flow is very rapid or geothermal heat fluxes are abnormally high e.g. /Hooke 2004, p 34/. Such circumstances do not, however, occur on an ice sheet-wide scale.

Water generated at the surface from melt and liquid precipitation can enter the en- and subglacial system through crevasses and vertical shafts, *moulins*. If the ice is temperate, it may also be slightly permeable. Water that enters the glacier will flow through an englacial system for some time. Commonly water reaches the bed within a couple of ice thicknesses in distance but englacial drainage can occur over longer distances. Most often this is associated with over-deepened basins.

The area over which surface water can penetrate the ice sheet and reach the bed is not well known. Remote sensing of e.g. the Greenland ice sheet indicates that surface melting occurs up to very high altitudes but also that the melting zone varies substantially from year to year. Such conditions were surely present on the Weichselian ice sheet, especially during its retreat phase. Hence, water is in ample supply. Mechanisms whereby connections from the surface to the bed may be established through ice below the pressure melting point have been debated.

However, /Alley et al. 2005b/ have shown theoretically that water-filled crevasses may penetrate even cold ice and thus constitute a mechanism for establishing hydraulic connection between surface and bed, even on a thick largely cold ice sheet. Although no observations have been made of such crevasse-based linkages, observations of surface drainage patterns on the Greenland ice sheet indicate the presence of an intricate pattern of surface drainage and moulins connecting to the base even tens of kilometres from the terminus. The width of the zone in which water may reach the bed remains elusive but is likely to range between tens and several tens of kilometres. It is likely that the zones on the waning Weichselian ice sheet were at least similar in extent. Since the waning ice sheet probably exhibited surface profiles lower in elevation than, say, the modern quasi-steady state Greenland ice sheet, ablation zones were likely larger simply because larger areas of the Weichselian ice sheet were at lower elevation.

Once water enters the bed it can be transported in either fast or slow flow systems. The fast systems are able to transmit large quantities of water at low pressure. They can be thought of as tunnel systems. The slow systems transmit smaller quantities of water while maintaining higher pressure and holding larger volumes of water. One example of such a system is the so-called linked cavity system /Kamb 1987/. Figure 3-17 shows an example of how a slow system may be configured. The fast systems are self-organising and tend to occur at a spacing that is determined by flow volumes, although the mechanisms are not completely understood. The slow systems are dependent on smaller-scale roughness features. Detailed descriptions of the subglacial hydrological systems are given in /Jansson et al. 2007/.

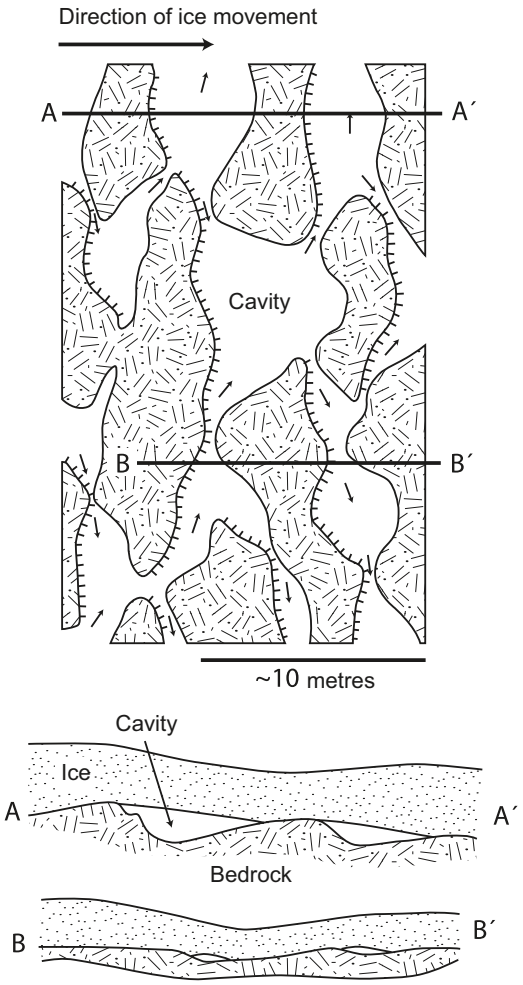

Figure 3-17. *Linked cavity system, an example of a subglacial slow flow system. Modified from /Holmlund and Jansson 2003, after Kamb 1987/.*

Because of the seasonal variations in water input from the surface (basal contributions do not vary on a seasonal basis), the en- and subglacial drainage pathways transmitting such water also experience seasonal variations see also /Jansson and Näslund 2009/. Conduits in ice adapt to transient hydraulic conditions by creep closure if water pressure is lower than hydrostatic ice pressure in the ice surrounding the conduit. If water fluxes increase, pressure builds to force more water through the conduits. This causes an increase in the viscous dissipation of heat and results in melting of the conduit walls and hence an increase in flow capacity of the system. The enlargement by melting may be faster than the creep closure depending on the transient hydraulic conditions. Hence, glacier conduit systems respond quickly to increases in water fluxes by enlarging the conduits. When water fluxes decrease, pressures in the system may drop drastically until creep closure has equilibrated to the water flux to maintain a balance between closure and conduit wall melting.

Seasonal, as well as shorter term, variations in water influx will affect the basal water pressures e.g. /Jansson and Näslund 2009/, although it is unlikely that diurnal variations in water pressure will significantly affect the pressure variations in an underlying groundwater aquifer because of their high frequency and the need for diffusion of such variations in a porous medium.

A detailed account of the supra-, en-, and subglacial hydrological system is given in /Jansson et al. 2007/.

Groundwater composition is indirectly influenced by ice sheet hydrology since it is the hydrological conditions at the ice/bed interface that control the recharge of glacial melt water into the bed which in turn will affect the composition of the groundwater.

3.2.2 Controlling conditions and factors

Climate – melt water supply

The coupling between the climate system and the hydrological system of glaciers and ice sheets is through the energy exchange between the atmosphere and the glacier surface. Energy arriving at the ice surface will be expended by first warming the surface to the melting point (if below melting to start with) and second to melt snow and ice at the surface. The energy balance at the glacier surface is given by

$$M+\Delta G = R+H - L_vE+L_fP' \qquad \text{Equation 3-8}$$

e.g. /Paterson 1994; all terms are in W m^{-2}/ where M is the heat used to melt snow and ice; this term represents a gain in heat and is negative if melt water refreezes in the snow pack; ΔG is the rate of gain of heat in a vertical column from the surface to the depth at which vertical heat transfer is negligible; H is the rate of heat transfer from the air to the surface by turbulence (H is negative if the air is cooler than the surface); L_v is the specific latent heat of vaporisation ($2.8 \cdot 10^6$ J kg^{-1}); E is the rate of evaporation from the surface (E is negative if condensation occurs); L_f is the specific latent heat of fusion for ice ($3.34 \cdot 10^5$ J kg^{-1}); and P' is the precipitation rate of rain (negligible if the surface is melting but significant for warming up the snow pack from refreezing under cold conditions). R is the net radiation, defined as $R = Q(1-\alpha)+I_i-I_o$, where Q is the rate of incoming solar direct and scattered radiation at the surface; α is the ratio between reflected and incident solar radiation, *albedo*; I_i is the rate of incoming long-wave radiation at the surface; and I_o is the rate of emission of long-wave radiation by the surface.

The surface melting can be calculated by applying Equation 3-8 to measured data from meteorological stations on glaciers and ice sheets. However, for estimating conditions on palaeo-ice sheets simpler solutions must be applied since all parameters in Equation 3-8 cannot be easily estimated. This has led to the development of statistical approaches to melt estimation. The most successful and most widely used is the *degree-day method* approach e.g. /Hock 2005/.

The degree-day method is based on the notion that melting is a function of the time the air is at a positive temperature. Hence degree-day methods use the integrated time of positive temperature as a proxy for the heat exchange and hence melting through empirical correlation between measured melting and integrated time of positive temperature. In its simplest form the sum is of positive degree-days, hence the name of the method, defined by $S = \Sigma_i \alpha_i T_i$ where T_i is the mean daily temperature and $\alpha_i = 1$ if $T_i \geq 0$°C and $\alpha_i = 0$ if $T_i < 0$°C. The melting is associated to the degree-day sum by a degree-day factor, λ, as $M = \lambda T$. /Hock 2005/ has summarised degree-day factors which show significant variation depending on local conditions. The degree-day approach has also been refined by /Hock 1998/ to yield a temporally varying sub-daily variation by introducing the potential direct solar radiation as a modulating factor γ_t to the empirical relationship, $M_t = \gamma_t \lambda T$, where subscript t denoted conditions at a specific time t.

Melt water is also generated englacially, and at the base of glaciers and ice sheets. The deformation that occurs as ice is flowing generates heat that can melt minute amounts of water. Water production through strain heating requires the ice to be temperate and varies proportionally to the deformation rate. There is a positive feedback between strain heating and melting in that strain heating also warms colder ice to the pressure melting point and thereby allows the ice to melt; water increases velocity which in turn increases the strains. The amounts produced by strain heating are relatively small. Estimates are difficult to make since they depend on the deformation rates which vary spatially. Based on the typical flow regime of an ice sheet, strain heating is negligible near the ice divide and is likely to increase towards the margins of the ice sheet.

Water is also generated subglacially through energy supplied by geothermal heat. The resulting melt rates will be directly proportional to the geothermal heat gradient in the bed rock. As with internal heating, geothermal heat may also first warm basal ice to its melting point resulting in subsequent melting. /Näslund et al. 2005/ have shown the importance of geothermal heat on the basal temperature and water production beneath the past Weichselian ice sheet.

The ice sheet hydrology described above may affect a number of geosphere variables of importance for a deep geological repository (Table 3-2).

Table 3-2. Summary of how geosphere variables are influenced by ice sheet hydrology.

Geosphere variable	Climate issue variable	Summary of influence
Groundwater flow	Sub-glacial hydrological system	Groundwater recharge and flow will be determined by the temperature regime, melt water production and thickness of the ice sheet (see Section 3.1). It is the configuration of the basal hydrological system that ultimately determines the distribution of melt water and thus groundwater recharge and distribution of water pressures at the ice/bed interface determining the gradients for groundwater flow.
Groundwater pressure	Sub-glacial hydrological system Melt water supply	The groundwater pressure depends on the pressure of the water at the ice/bed interface, the ice sheet thickness and the ice load compressing the subsurface (see Section 3.1). The pressure of the water at the ice bed interface is determined by the supply of melt water and the conductivity and distribution of conductive features in the sub-glacial system.

3.2.3 Natural analogues/observations in nature

Our knowledge on the hydrology of glaciers and ice sheets is largely based on observations from valley glaciers. However, there is no reason to believe that other processes would be present in association with an ice sheet, although the magnitude of the processes will be scaled proportionally to the differences between valley glacier scale (1–100 km^2) and ice sheet scale (1,000–10,000 km^2 and larger) /Jansson et al. 2007, Jansson and Näslund 2009/. Given today's climatological situation in Greenland, allowing for both ice sheet surface melting and cold, high polar surface conditions in the ice sheet interior, the best present analogue situation for a future Fennoscandian ice sheet is the Greenland ice sheet. Most of the descriptions of ice sheet observations in nature below therefore are from the Greenland ice sheet.

Indirect observations of the ice sheet hydrological system

There are some studies that implicitly involve a subglacial drainage system and processes therein. Observations of large, and from a glaciological perspective, abrupt changes in ice dynamics without corresponding changes in for example driving stress imply changes in the basal boundary condition. Ongoing thinning of sectors of ice sheets e.g. /Wingham et al. 2009/ may occur from changes in mass balance or from changes in ice dynamics. /Joughin et al. 1996/ observed a three-fold increase in velocity over a seven week period, of the Ryder Glacier, north Greenland, after which the velocities decreased to the original values. Drainage of supraglacial lakes into the ice sheet could have been responsible for this event.

/Zwally et al. 2002/ used GPS measurements at the equilibrium line near Jakobshavn to show that the ice sheet undergoes large annual variations in surface speed. They attributed these variations to the seasonal variations in water influx to a basal water system through moulins and crevasses, since velocity variations were clearly correlated to seasonal melt rates variations. /Price et al. 2008/ used modelling to show that variations in ice velocity, such as observed by /Zwally et al. 2002/, need not be forced locally but can also be the result from longitudinal coupling effects from movement further downstream.

/Moon and Joughin 2007/ used satellite interferometry to investigate the spatial variability in ice front position of 203 Greenland outlet glaciers. Their results indicate that the behaviour is closely linked to climate variability, thus implying that dynamic responses are forced by climate and not sustainable unforced processes. /van de Wal et al. 2008/ recorded large velocity variation along a transect of the Russell Glacier, a land-terminating outlet glacier in east Greenland. They show annual velocity variations varying by up to a factor of four. The increase in velocity occurs within days of measured melt rate increase. /Shepherd et al. 2009/ used a combination of satellite imagery and continuous dGPS measurements to show how the Russell Glacier catchment of the West Greenland ice sheet undergoes both temporal and spatial seasonal velocity variations as well as diurnal speedup and uplift events.

/Joughin et al. 2004/ observed changes in the flow speed of the Jakobshavn Isbrae where velocity was seen to decrease in the period 1985–1992 and then accelerate between 1992–2000 with additional acceleration up to 2003. Their study clearly indicates that the ice stream response can be complex and include both periods of deceleration and acceleration. /Holland et al. 2008/ proposed a different cause for the speed-up of Jakobshavns Isbrae. A sudden increase in subsurface ocean temperature occurred in 1997 along the entire west coast of Greenland. Such warm water could have accelerated the basal melting of the ice stream at the grounding line and hence caused it to become unstable. Whereas this process will be able to affect outlets reaching the sea, it does not help to explain the general increase in velocity observed around the perimeter of the Greenland ice sheet /Rignot and Kanagaratnam 2006, Joughin et al. 2008/. /Joughin et al. 2008/ showed that the land-terminating parts of the Greenland ice sheet underwent seasonal velocity changes. /Howat et al. 2007/ showed that two of Greenland's major outlets, the Helheim and Kangerdlugssuaq, underwent a rapid increase in flow in 2004 with a subsequent decrease in 2006 to near the pre-2004 levels. They argue that this response is due to re-equilibrium of the terminus after a calving event.

There is thus ample evidence that ice sheet dynamics change on time periods from diurnal and up to perhaps millennia. The variations observed on diurnal to annual scales are in perfect harmony with theory and observations on valley glaciers where the coupling to variability in the hydraulic system is evident. Ice sheets seem to have larger time-scale variability than typically observed on valley glaciers. This longer period variability is due to processes that occur on scales that cannot be found on valley glaciers and thus cannot produce similar features on the smaller glaciers.

Observations of ice sheet surface melt

The surface hydrology of the Greenland ice sheet has been studied by /Thomsen et al. 1989/ in relation to a proglacial river near Illulissat/Jakobshavn for hydroelectric power production planning. The study showed that the surface of the ice sheet was punctured by numerous moulins, each draining a well-defined area of the ice surface (Figure 3-18). Satellite-based imagery indicates that the surface of the eastern flank of the ice sheet is covered by perennial supraglacial lakes interconnected by streams (Figure 3-19). These lakes may experience episodic catastrophic drainage e.g. /Das et al. 2008, Shepherd et al. 2009/.

Satellite-based radar imagery also provides a good overview of the facies distribution on the Greenland Ice Sheet. Figure 3-20 shows the conditions from the centre of the ice sheet to the margin. The ablation area at this section of the ice sheet is approximately 100–150 km wide and the percolation and wet snow zones combined are 300–400 km wide. Unfortunately, it is impossible to conclude how much of the combined percolation and wet snow zone contributes to runoff. However, it is reasonable to think that half that width may contribute. Furthermore, in /ACIA 2005/ it was shown that the different zones vary substantially in location from year to year. The lack of long-time series of data makes it impossible to draw any conclusions as to what might be a typical situation.

Water generated at the glacier surface, and thus available for input to the glacier hydrological system, comes from a combination of melting of ice and snow and from rain. Direct measurements of melt have occurred within the framework of local projects over time. /van de Wal 1996/ and /Six et al. 2001/ have summarized some of the data originating from transects. Their data shows a potential four-year cycle in melt with no clear trend.

The Gravity Recovery and Climate Experiment (GRACE) has provided means for establishing mass change signals for regions such as the Greenland ice sheet where mass change due to climate change occurs. /Chen et al. 2006, Luthcke et al. 2006, Ramillien et al. 2006, Velicogna and Wahr 2006/ used GRACE data to evaluate mass losses from the Greenland ice sheet. Their results provide a strong independent indication that mass loss from the southern part of the Greenland ice sheet has increased substantially, thus verifying more local studies from /Rignot et al. 1997, Howat et al. 2005, Rignot and Kanagaratnam 2006, Luckman et al. 2006/. Much of the mass losses observed are from dynamic responses at outlet glaciers. It is unclear if this acceleration is due to increased surface melt, and associated basal lubrication, or if there are other critical triggering factors. It seems unlikely, however, that simultaneous response over larger lengths of the Greenland ice sheet margin should be caused by local triggering factors. /Wouters et al. 2008/ expand on the previous GRACE investigators' results and provide a refined and extended data record showing continued mass loss from the ice sheet including

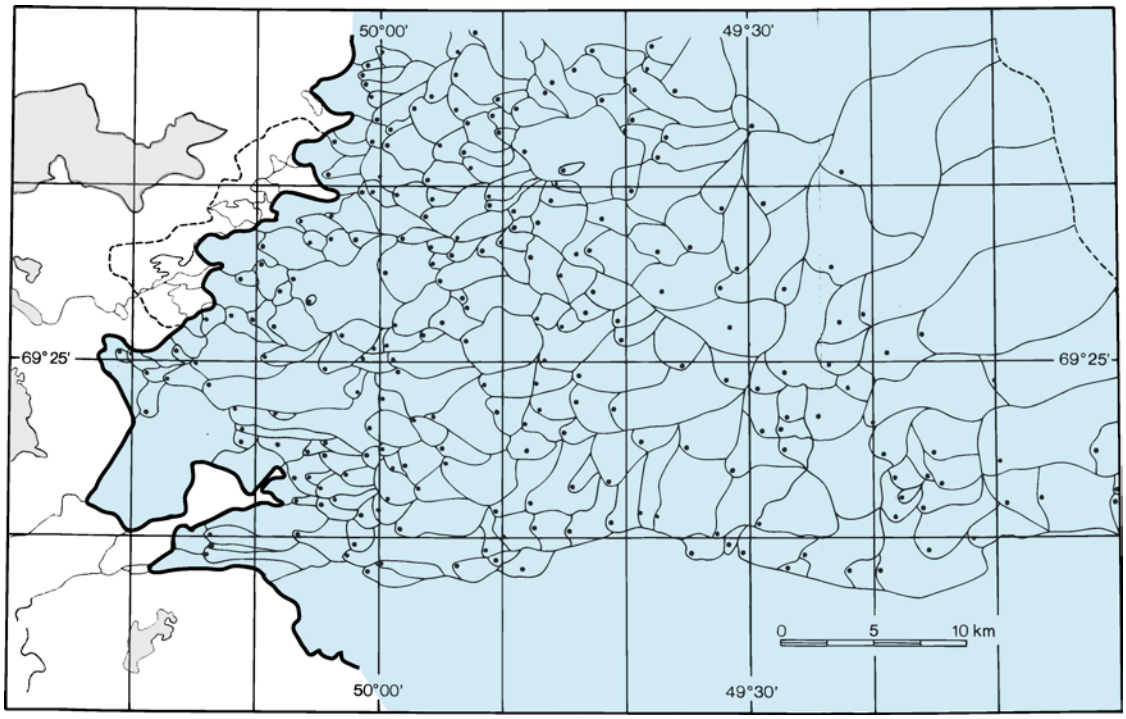

Figure 3-18. *Surface drainage basins on the ablation area of the Greenland Ice Sheet near Illulisat/ Jakobshavn area. Filled circles mark the location of moulins in each surface drainage basin. Modified from /Thomsen et al. 1989/.*

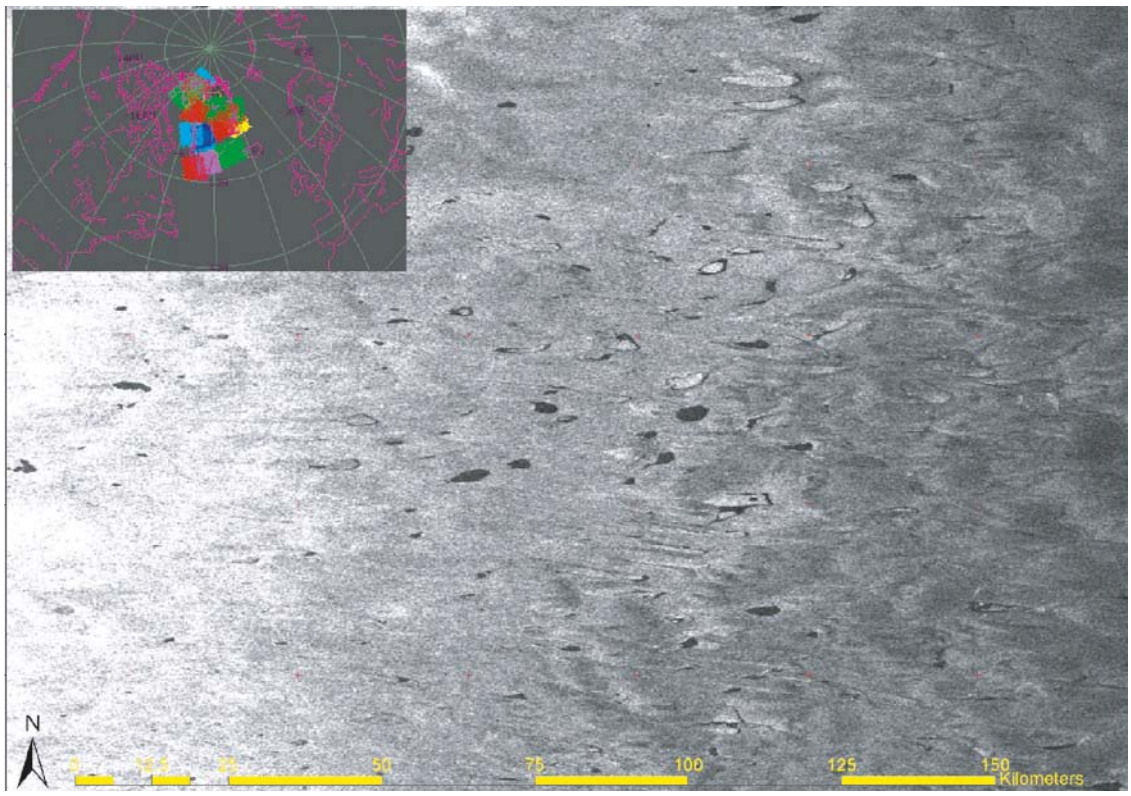

Figure 3-19. *Radarsat-1 ScanSAR image of the ablation zone of the Greenland Ice Sheet near Kangerlussuaq, East Greenland. The background grey scale indicates surface conditions from bare ice (white) through superimposed ice (medium grey) to wet snow (dark grey). The black areas are lakes that absorb the radar waves completely. Some lakes near the right centre have complete or partial lake ice cover, in some cases indicated by a central floe surrounded by a black rim of open water.*

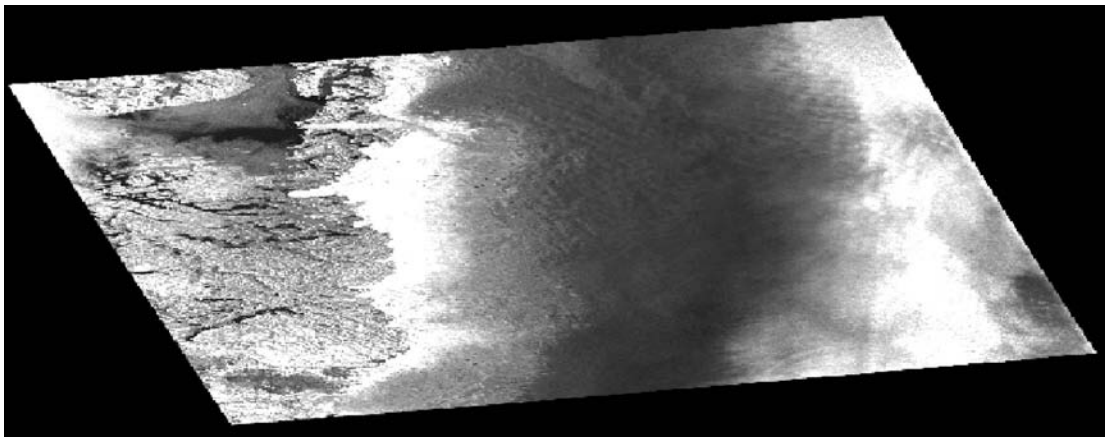

Figure 3-20. *Radarsat-1 ScanSAR image over east Greenland. The dark area at the centre of the image (between approximately –48° W and –44° W) comprises the percolation and wet snow zones that are bounded by the white dry snow zone to the right and the bare ice of the ablation zone to the left. The speckled grey zone to the extreme left in the image is bare ground outside of the ice sheet. A part of Disco Island is visible in the upper left corner of the image.*

large losses from the upper parts of the ice sheet, which was not observed in earlier studies. /Hanna et al. 2008/ verify the results from /Velicogna and Wahr 2006/ and find that the increase in melt on the ice sheet is coupled an increase in regional Northern Hemisphere air temperatures.

Through measurements of passive microwave emissions, /Steffen et al. 2004, Figure 6.18, p 205 in ACIA 2005/ show how the Greenland ice sheet experiences large spatially variable melt conditions. /Bougamont et al. 2005/ have reproduced Steffen et al.'s observations by applying a surface mass balance model to the Greenland ice sheet and forcing the model with ERA-40 re-analysis data (data from an analysis of meteorological observations from 1957 to 2002 produced by the European Centre for Medium-Range Weather Forecasts together with other institutions). Their work indicates surface melt can readily be obtained from large scale re-analysis data given model tuning through surface meteorology data from the ice sheet. /Bhattacharya et al. 2009/ use the melt-area time series covering the period 1979–2008 to show that the melt-area abruptly increased in 1995. This change can be related to a sign-reversal in the North Atlantic Oscillation. The change is also manifested in higher measured temperatures around the ice sheet.

One issue in discussing ice sheet hydrology is estimating the potential melt rates under a retreat scenario for the past ice sheets. /Ridley et al. 2005/ performed numerical modelling experiments with the Greenland ice sheet under warming scenarios. When subjecting the ice sheet to a $4 \cdot CO_2$ scenario for 3,000 years the ice sheet almost completely disappeared. One lesson from this experiment is that when more ground is exposed around the perimeter of the ice sheet, feedbacks from local summer circulation produced from warm ground around the ice sheet can augment the melting.

The Greenland ice sheet surface mass balance is obviously variable and directly coupled to the forcing climate variability. The water produced by melting also seems to affect the dynamics, not only on diurnal and annual time scales but also affecting longer-term trends in mass loss of peripheral parts, probably by influencing the dynamics of the Greenland ice sheet.

Observations of shorter-term variations of subglacial water pressure have been carried out on many glaciers, among them Storglaciären. Figure 3-21 shows a typical water pressure record from Storglaciären, northern Sweden. The hydrological system in this part of the glacier has been inferred to be a distributed tunnel (fast) system. The data shows how water pressures vary very rapidly in response to environmental factors influencing water input, air temperature governing glacier melt, and liquid precipitation causing rapid runoff events on the glacier surface. Such fast systems are characterised by rapid flow and pressures that fluctuate rapidly due to the inability of the system to maintain high pressures. For more details on this types of observations and their interpretation, see /Jansson and Näslund 2009/.

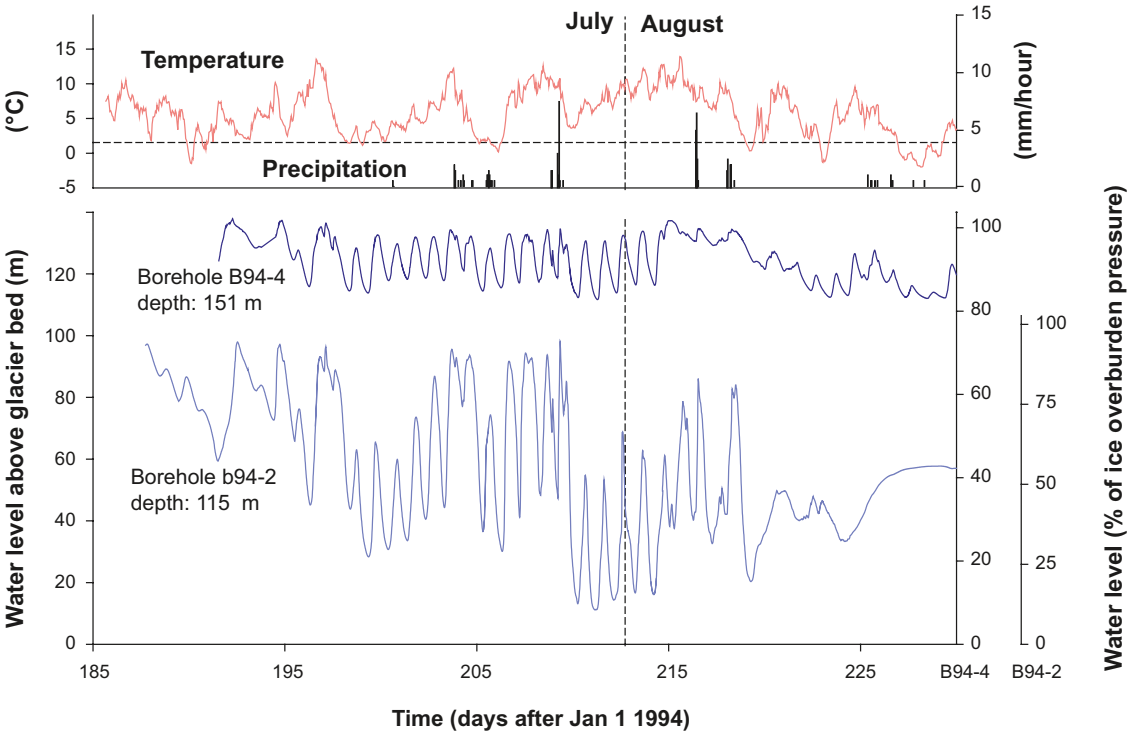

Figure 3-21. *Water pressure record from Storglaciären showing large diurnal variations in water pressure from near zero to near overburden pressure. Longer-term changes in the pattern of the water pressure fluctuations can also be seen. From /Jansson and Näslund 2009/.*

Observations of transfer of water from the ice sheet surface to the bed

Theories of how water can create pathways from the surface of a glacier or ice sheet, through cold ice, to the bed have been presented by e.g. /Weertman 1973, van der Veen 1998a, b, 2007, Alley et al. 2005b/. The idea is that water filled crevasses may propagate downwards through the ice. The crucial point for both Weertman's and Alley et al.'s work is the continuous recharge of water to the crevasse to keep it over-pressurized. Having crevasses form across supra-glacial streams or in surface melt ponds is thus an excellent environment for the process to be active. In the ablation area of glaciers, water is generally abounding and it is not hard to meet these criteria anywhere. /Fountain et al. 2005a, b/ also observed englacial water filled crevasses at varying depths in Storglaciären, where they appear to be an intrinsic part of the drainage system. This study changed the notion that englaclal crevasses could not exist under typical conditions found in glaciers.

Observations of surface lake drainage events on Greenland revitalized the theories by /Weertman 1973, Alley et al. 2005b, van der Veen 2007/. /Das et al. 2008/ observed the complete drainage of a 5.6 km^2 supra-glacial lake in ~1.5 hours into an opening crevasse on the Greenland ice sheet. They also observed significant changes in the velocity of the ice sheet as well as local uplift during the event. From this /Das et al. 2008/ infer that water reached the bed through 980 m of ice. Although the actual drainage pathways were not investigated or mapped, water seems at least to have gained access to the bed near the input point. This work shows compelling indications that the process described by /Weertman 1973/ and /Alley et al. 2005b/ is realistic. /Krawczynski et al. 2009/ used a model to calculate the volume of water required to propagate crevasses through the Greenland ice sheet. They found that small lakes of 250–800 m in diameter are sufficient to drive crevasses through 1–1.5 km of ice. Hence the conditions for propagating crevasses through the Greenland ice sheet are commonly met.

/Catania et al. 2008/ used common offset radar images to detect drainage pathways between the surface and the bed of the Greenland ice sheet in the vicinity of Jakobshavn. They found that detected connections are more abundant in the ablation zone than near or above the equilibrium line. Furthermore, the drainage features coincide with inferred regions of longitudinal extension, indicating that crevasse formation may play a decisive role for the location of moulins also on the ice sheet. In a subsequent, ground penetrating radar-based study /Catania and Neumann 2009/ identified that the drainage

connections between surface and bed seemed to be associated with areas of significant basal melting. Their conclusion was thus that the drainage features were persistent. This also implies that the drainage system to some extent is persistent in space.

The transfer of water from the surface of an ice sheet such as in Greenland, through its cold interior mass of ice, is thus possible. The mechanisms outlined by /Weertman 1973, Alley et al. 2005b, van der Veen 2007/ allows for propagation of water filled surface crevasses to the bed as long as the steady sufficient supply of water is maintained. Since melt water occurs in abundance in the ablation area and wet snow zone during the melt season, conditions are favourable over large areas of the Greenland Ice Sheet marginal zone.

In the case of the Greenland Ice Sheet, the thermal structure is such that the ice column is cold but may reach melting temperatures at the bed where conditions are favourable. Internal melting from ice deformational heat is thus not expected in the Greenland ice sheet. Deformational heat will, however, affect the temperature gradient near the base and affect the amount of basal melting possible beneath the ice sheet.

Observations of water generation at the ice sheet bed

Some observations of basal melt regimes beneath ice sheets have been presented. /Dahl-Jensen et al. 2003/ used NorthGRIP data and an ice flow model to calculate geothermal heat flow along a flow line obtaining variations between 50 and 200 mW/m^2. This yields basal melt rates of between 7.5 mm/year at the drill site and 11 mm/year further upstream from the NorthGRIP site. /Fahnestock et al. 2001/ used age-depth relationships from internal layering obtained from airborne radar surveys to calculate basal melt rates in northern Greenland. In one region, melt rates reach and exceed 100 mm/year, indicating geothermal heat fluxes of up to 970 mW/m^2. Such high geothermal heat fluxes indicate the presence of a unusual geological setting not found in the marginal areas of the Greenland ice mass. /Oswald and Gogineni 2008/ used radar echo intensity to map the occurrence of subglacial water beneath the northern part of the Greenland ice sheet. They concluded that significant portions of the bed may be melting. Basal conditions at ice core drilling sites verify their results e.g. /Fahnestock et al. 2001, Dahl-Jensen et al. 2003/. Oswald and Gogineni's data show that approximately 17% of the total flight line lengths indicated melting conditions.

Basal melt contributes significant volumes of water to the basal drainage system. In areas of surface influx of water to the bed during summer, the basally generated volumes are over-printed by the surface influxes. During winter, the entire basal drainage system experiences the basal melt derived fluxes. Basal melt is thus important in that it maintains subglacial flow throughout the year and in all areas where the ice sheet base is at the pressure melting point.

Subglacial lakes beneath ice sheets have been known to exist since the discovery of Lake Vostok, East Antarctica /Kapitsa et al. 1996/. Such lakes may be of substantial size; the largest lake, Lake Vostok, is 280 km long, 50–60 km wide and more than 1,000 m deep. Numerous large lakes have since been identified to exist beneath the Antarctic ice sheet /Siegert et al. 1996, Siegert 2005, Siegert et al. 2005/ by e.g. satellite-based remote sensing methods. Because the ice sheet is locally floating in the water of the lakes, the basal shear stress is locally zero which produce a near horizontal ice surface over the lake.

No subglacial lakes have so far been identified beneath the Greenland ice sheet. It is not known if subglacial lakes may have existed beneath the former Fennoscandian ice sheets.

Subglacial drainage

It is possible that unstable hydraulic situations can be caused by periodic build-up and release of subglacial lakes. /Alley et al. 2006/ suggested a mechanism for producing periodic outburst floods and accompanying dynamic events. The mechanism involves growth of ice shelves onto proglacial sills where they freeze on producing a seal. Water is thus trapped in deeper parts upstream of the sill, which with a growing ice sheet can become over-pressurized. If the basal temperature decreases on the sill, the over-pressurized water may escape causing an outburst flood. They suggest this process may have been involved with the so-called *Heinrich events* e.g. /Hemming 2004/ seen in marine sediment cores in the north Atlantic and for creation of subglacial lakes such as Lake Vostok. /Evatt et al. 2006/ developed a numerical model to investigate the potential for subglacial lakes. They find that lakes should fill and

drain periodically, basically as a function of the filling rate. The calculations allowed Evatt et al. to predict possible locations for subglacial lakes beneath the former Laurentide ice sheet in North America. Their locations agree with the positions of the palaeo-subglacial lakes proposed by /Munro-Stasiuk 2003/ and /Christoffersen et al. 2008/, however, the larger predicted lakes have not yet been identified.

Subglacial drainage beneath former ice sheets have been known to exist largely in view of the vast systems of eskers left by the ice sheet. For instance, /Clark and Walder 1994/ discussed the distribution of eskers in terms of a subglacial geology framework. They conclude that a vast system of subglacial tunnels or canals should exist beneath an ice sheet.

In Antarctica, e.g. /Denton and Sugden 2005, Lewis et al. 2006/ discuss observable melt water generated geomorphological features originating from larger extents of the ice sheet. /Sawagaki and Hirakawa 1997/ observed traces of meltwater in coastal areas of Antarctica. There are indications that large quantities of water drained through the Laurentide ice sheet during its waning phase e.g. /Barber et al. 1999, Clarke et al. 2003/. Some of the observations from Antarctica have been heavily discussed, but the evidence is mounting that major drainage events may occur. Hence, large scale, low frequency drainage phenomena are possible in ice sheets. In the case of the Fennoscandian ice sheet al. identified large-scale drainage phenomena are associated with subaerial lakes dammed by ice at the margin and not subglacial phenomena.

For further detailed information on the present knowledge on ice sheet hydrology see /Jansson et al. 2007 and Jansson 2010/.

3.2.4 Model studies

In a study made for SKB /Boulton et al. 2001b/ developed a theory of sub-glacial drainage beneath ice sheets based on flow in sub-glacial tunnels (R-channels), which are supposed to be the main agents of large-scale longitudinal melt water discharge (see Figure 3-22). The widespread glacial melt water is supplied to the tunnels as groundwater flow. The drawdown of the piezometric pressure by the tunnels provides the mechanism for predominantly transverse groundwater flow towards the tunnels.

The tunnels are developed from water-filled cavities formed at the ice/bed surface. The groundwater head elevation rises as a result of increased water supply to the bed or if the ice sheet advances over a low-conductive bed. Hence, in the theory of /Boulton et al. 2001b/, tunnel spacing is a function of the relation between bed transmissivity and melt water input.

In the summer season the high discharge by surface melting is expected to create short-lived water-filled voids between the large tunnels (Figure 3-23). Many of these voids will form locally beneath the bases of water conducting moulins and crevasses. In the winter seasons such drainage routes will be closed by internal ice flow. /Boulton et al. 2001b/ argued that the relatively long winters and short summers representative of the climate around large ice sheets will inhibit the development of well-integrated summer drainage patterns, except very close to the ice sheet margin.

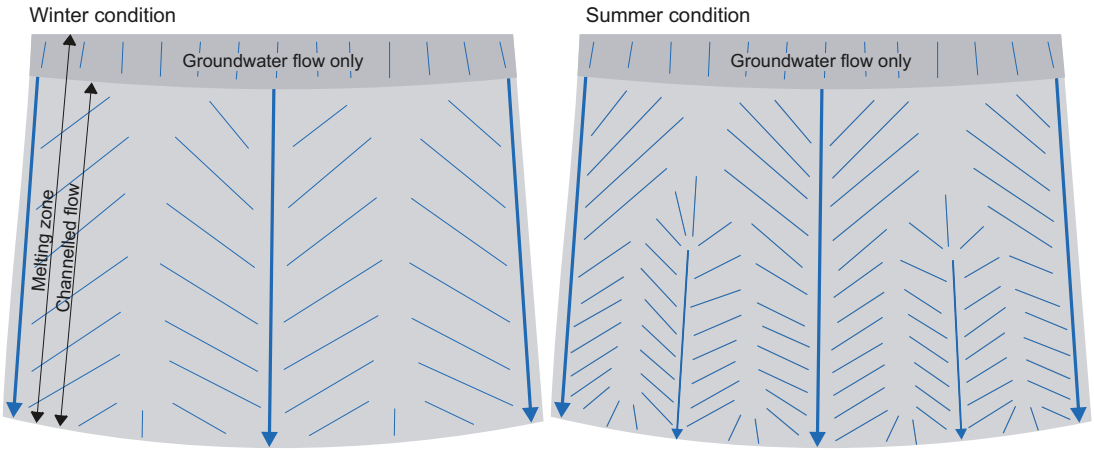

Figure 3-22. *Postulated patterns of groundwater flow in relation to the distribution of subglacial tunnels. From /Boulton et al. 2001b/.*

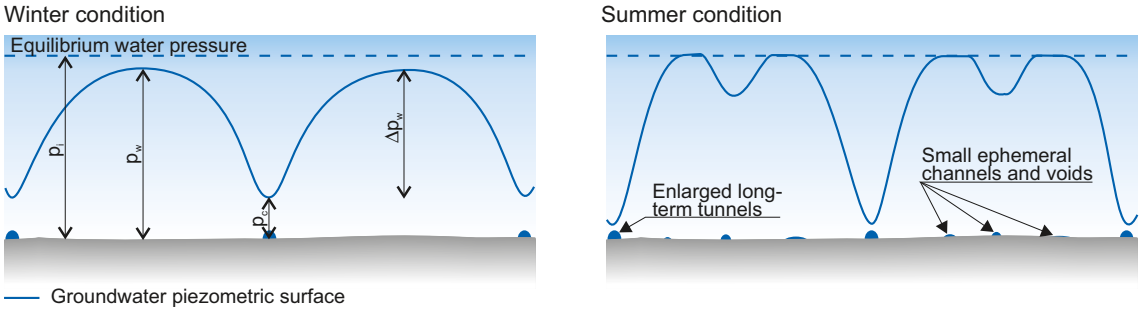

Figure 3-23. *Left: Transverse cross-section of a glacier showing the postulated relationships between groundwater surface and sub-glacial tunnels during the winter period. Right: The situation during the summer period of high discharge. Interfluve zones of high pressure, where effective pressures tend to zero, will tend to create short-lived water filled voids. From /Boulton et al. 2001b/.*

Ice sheet hydrology can be modelled in one of two main ways. Commonly the flow is represented by simple routing routines that follow the basic ideas laid down by /Shreve 1972/ where the discrete flow routing of water is not described, but where the water pressure potential is used to predict the direction of flow. This type of modelling probably correctly handles the flow paths of water but not the quantitities of water involved. Only three models exist in which the entire hydrological system or parts of it are modelled using a physically based model. In these models, the paths and quantities of water flowing in the system are handled. The choice of model depends on the purpose of the analysis in question, what geometric scale is to be studied, and available data. Two models describe the complete hydrology of a glacier /Arnold and Sharp 2002, Flowers and Clarke 2002a, b/.

The present state of physically-based models is still crude, in that these models have been tailored to specific glaciers or glacier types and are not necessarily easily and generally transferable. Melt water production and the supra-glacial system are handled comparatively well; it is probably also the simplest part to model since the entire system is easily observable. The en- and sub-glacial systems are more complicated, characterised by large variability in possible drainage system configurations. Much uncertainty yet remains as to the exact geometry of drainage systems and how these systems can co-exist or switch from one state to another, thus limiting the applicability of physically based modelling.

Modelling the physics of glacier hydrology is complex, since it involves the liquid phase, namely water, moving through the solid phase, namely ice, at the melting temperature. Furthermore, ice is deformable under relatively low stresses, which allows channels and conduits in glaciers to change size and shape much more rapidly than channels eroded in rock or sediment. The glacier system is thus transient on all time scales and over all spatial scales.

The first physically based models in glaciology were made to reproduce simple observable phenomena in glacier hydrology. /Röthlisberger 1972/ and /Shreve 1972/ presented simple numerical models (Röthlisberger: conduit flow; Shreve: water pressure potential flow) for water flow in glaciers. The assumptions made were that the rate of melt enlargement is balanced by creep closure (Röthlisberger) and that water pressure is in balance with ice pressure /Shreve 1972/. /Nye 1976/ and /Spring and Hutter 1981/ presented a physically based theory of unsteady flow through intraglacial channels. /Hooke 1984/ investigated the effects of non-steady conditions, in particular open channel flow, on the Röthlisberger system. This was elaborated by /Kohler 1995/ who investigated the ratio of open-to-filled channel flow in a subglacial system. Most models have assumed circular cross-section pipe flow and semi-circular tunnels. However, discrepancies between measurements and model calculations led /Hooke et al. 1990/ to propose low broad tunnels in place of semicircular ones in order to be able to apply Glen's flow law of ice deformation with reasonable viscosity parameter values. Conduit flow was found not to reproduce water pressure and fluxes observed during the surge of Variegated Glacier, Alaska. This prompted /Kamb 1987/ to propose the linked cavity system which combined large cross-section with small flow velocities. /Walder and Fowler 1994/ extended Röthlisberger's model to include 'canals' cut into deformable till.

A first approach to producing a complete physically based model for a glacier was reported in /Arnold et al. 1998/, henceforth referred to as the Arnold model. This model has three components. A surface-energy sub-model calculates distributed glacier surface melt water production. A routing sub-model takes rain- and melt-water and either delivers the total water flux to *a priori* prescribed moulins, where it enters the glacier interior or supraglacially to the ice margin. The third and final component is a subglacial sub-model that involves a conduit system. The englacial drainage is treated as part of the subglacial conduit system and simulated analogous to a sewage pipe system. Subglacial conduits are fed by a network of "drains", which represent moulins where water can enter or overflow from the system. Subglacial conduits can enlarge and contract in response to changes in the rates of wall melting and creep closure associated with changes in water inputs. In addition, the configuration of the system can change between a distributed system and a channelised system represented by different predefined numbers and geometries of conduits. "Distributed" links were changed to "channelised" flow paths as the modelled snowline passed in the up-glacier direction over each moulin. From this perspective the subglacial model is rigid, since switching between systems does not permit smooth transitions with the bed being partially drained by each system. The model was applied to Haut Glacier d'Arolla, Switzerland, and performed well in comparison with proglacial stream discharge, but limitations are indicated by discrepancies between model outputs and field observations of subglacial water pressure and water velocities, although the substantial features of these records could be reproduced.

/Flowers and Clarke 2002a, b/, henceforth referred to as the Flowers model, developed a different approach to a complete physically based model. The model comprises coupled surface runoff, englacial, subglacial, and groundwater systems. Each of the four components is represented as a two-dimensional, vertically integrated layer that communicates with its neighbours through water exchange. Melt is computed by a distributed temperature index model. Englacial hydrology is represented by describing a variety of bulk storage elements and allowing water transport between them in a system of cracks. Hence, the englacial system is treated as fracture-connected crevasses and pipes. The Flowers model was built to represent conditions at Trapridge Glacier, Canada, which is underlain by thick porous sediments. Their subglacial model, therefore, comprises flow through macroporous glacier sediments at the ice-bed interface and subsurface aquifers of buried sediment layers not directly exposed to the base of the glacier. Hence there are no explicit tunnels as in the Arnold model. The model reproduced well diurnal cycles of subglacial water pressure as measured in boreholes.

A crevasse-like englacial network, as adopted in the Flowers model, has been observed on Storglaciären, Sweden /Fountain et al. 2005a, b/, countering previous notions of englacial water flow through few melt-enlarged conduits. If permeable subglacial sediments are present, groundwater flow may be a significant part of the system, as in the Flowers model, or flow may occur in channels eroded into the subglacial sediments. On harder beds or beds of less permeable sediments such as tills, water flow may occur in conduit systems melted into the ice or in linked cavity systems. Hence, a general physically-based model would have to accommodate all these possibilities and even couple different types of systems beneath different parts of a glacier. Such a model would be inherently complex.

Another issue that is not satisfactorily addressed in existing models is the time-transgressive development of subglacial systems. In the Flowers model, this is not necessary since flow through porous sediments does not involve significant time-dependent changes, except possible changes such as development of piping or siltation of the porous media from fines produced through sediment deformation. In the case of the Arnold model, it is widely reported e.g. /Nienow et al. 1998/ that the subglacial drainage system changes both in sizes of conduits and in complexity of the network of channels through the course of a season. The subglacial system is very dynamic and it seems as if a complete and accurate model description of this system may be distant. However, most changes in such a system occur in response to rapid changes, both increases and decreases in water inputs, so a first-order approximation may be to switch between a series of systems prompted by key events in the forcing.

Hence the state of glacier hydrological modelling adequately reproduces the large-scale features, such as the regional direction of flow. Finer details, such as the position of individual conduits and the behaviour of the conduits and the water pressure within them are not completely resolved.

3.2.5 Time perspective

The time perspective of glacier hydrology can be divided in two main categories, times scales under which the ice sheet undergoes significant changes in volume and extent and where the associated hydrological conditions change with the ice sheet; and time scales under which the ice sheet can be considered constant in volume and extent and where the variability of the acting processes dominates.

Seen under the perspective of an entire glaciation, the hydrological system varies spatially with the size of the ice sheet. This means that different parts of the bed are either temperate or cold and can be associated with hydrological systems of different overall structure and parameterisation. The distribution of cold and temperate basal conditions changes in time and also in location with the waxing and waning ice sheet. From this perspective, a possible repository site will experience changing conditions of active hydrology under thawed bed conditions or cold frozen bed conditions. The location of large tunnel systems also varies on this time scale. This is because, with changing ice sheet configuration, the basal hydraulic conditions vary so that shifts in location of drainage pathways occur. How much time a specific location is subjected to either kind of condition is determined by the large-scale fluctuations of the ice volume and extent.

The processes in the hydrological system of an ice sheet exhibit variations ranging from diurnal (in the case of temperature-dependent melt variations) or possibly shorter duration (in the case of rainfall-induced variations) to seasonal variations that depend on temperature variations on an annual basis. Since all variations in temperature-induced melting and liquid precipitation yield variations in input to the hydrological system, they also yield variations in subglacial water pressure with oscillations on similar time scales. This means that the base of an ice sheet will exhibit variations on a diurnal and subdaily scale superimposed on longer-term variations coupled to weekly variations due to changing air masses of different temperature and lastly variations due to seasonal temperature fluctuations.

3.2.6 Handling in the safety assessment SR-Site

Information from natural analogues and model studies, Section 3.2.3 and 3.2.4 has been used for giving a description of the evolution of hydrological conditions and groundwater for glacial periods in the *reference glacial cycle* (Section 4.5.5), and also for setting up boundary conditions and discussing results of groundwater flow modelling for glacial conditions.

3.2.7 Handling of uncertainties in SR-Site

Uncertainties in mechanistic understanding

Although the theories and empirical studies of glacier hydrology are of appropriate quality to reproduce observed phenomena at individual glaciers or sites on glaciers, there are no generally applicable theories for the spatial and temporal variations in hydrology and hydraulic conditions. Perhaps more importantly, the coupling between discrete drainage pathways and the continuum mechanics of ice sheet models is not, thereby preventing integrated modelling. The main obstacle to enhancing our understanding of the dynamics of glacier hydrology is the transient nature of the system and difficulties in observing its structure and behaviour. The division between subglacially derived and surface-derived water emanating from, say, the Greenland ice sheet is also unknown. Almost exclusively, process studies have been made on valley glaciers. However, there is no reason to believe that other processes would be present in association with an ice sheet, although the magnitude of the processes will be scaled proportionally to the differences between valley glacier scale and ice sheet scale /Jansson et al. 2007, Jansson and Näslund 2009/.

3.2.8 Adequacy of references

The SKB reports produced for the handling of glacial hydrology /Jansson et al. 2007, Jansson and Näslund 2009/ have undergone the SR-Site QA system handling, including a documented factual review procedure. Also the SR-Can Climate report /SKB 2006a/, from which some of the studies are used, has undergone QA system handling including a factual review process. Other references used for the handling of the permafrost and freezing processes are either peer-reviewed papers from the scientific literature or from a text book /Paterson 1994/.

3.3 Isostatic adjustment and shore-level changes

In addition to the descriptions in the present section, a detailed in-depth description of the physics of glacial isostatic adjustment (GIA), how it affects sea-level, and the methods which are employed to study and understand these processes are presented in /Whitehouse 2009/.

The major part of Section 3.3.1 is adapted from /SKB 2006a, Section 3.3/ written by P. Whitehouse, whereas some parts are adapted from /Lund and Näslund 2009/. Section 3.3.2 is adapted from /SKB 2006a/. Section 3.3.3 is from /Lund and Näslund 2009/, and Section 3.3.4 is adapted from /SKB 2006a/ and /Whitehouse 2009/.

3.3.1 Overview/general description

The redistribution of mass associated with the growth and decay of continental ice sheets gives rise to major glacial loading and unloading effects over time scales of several tens of thousands of years. The response of Earth's crust, mantle and gravitational field is referred to as Glacial Isostatic Adjustment (GIA). For instance, during the decay of a major ice sheet, the unloading of mass results in a post-glacial rebound of the crust, which continues well after the disappearance of the ice. This process is well known from previously glaciated regions such as Canada and the United States, Fennoscandia, the British Isles and Siberia e.g. /Ekman 1991/; areas where this process is still active today, some 10–15 kyrs after the last deglaciation. In previously glaciated terrain without strong tectonism, glacial isostatic adjustment is the most significant geodynamic process governing vertical deformation of the crust, e.g. /Peltier 1994/.

During the Last Glacial Maximum (LGM), around 20 kyrs ago, the Laurentide ice sheet of Canada and the United States, and the Fennoscandian ice sheet had maximum thicknesses of around 2.5–3 km. When these large ice masses slowly formed, their weight resulted in a slow downwarping of Earth's crust. One important factor that governed both this process and the following glacial unloading is the physical properties of Earth's crust and mantle. In the downwarping process, mantle material has to be displaced and flow laterally in order to make room for the flexing crust. At times of ice sheet decay, mantle flow is reversed and the crust rebounds. Since the mantle viscosity is high, the downwarping and subsequent rebound are slow processes. Furthermore, it has been shown that a deglaciation of large Northern Hemisphere ice sheets results in deformation of the Earth's entire surface, producing a series of upwarps and downwarps away from the areas of the former ice sheets (Figure 3-24). However, the deformation is largest in the regions that were glaciated.

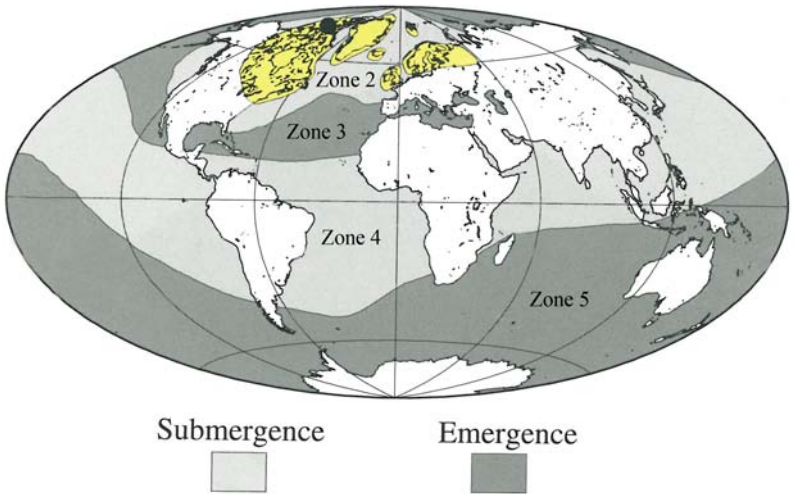

Figure 3-24. *Calculated deformation resulting from an instantaneous unloading of Northern Hemisphere last glacial cycle ice sheets at 16 kyrs BP. The results show five sea-level zones with similar sea-level histories within each zone. Sea-level zone 1 is marked in yellow. The entire Earth is affected by the unloading through a series of elevated and subsided regions away from the areas of the former ice sheets. Modified from /Clark et al. 1978/.*

The glacial isostatic adjustment process manifests itself not only in the slow rebound regions of past ice sheets. Current melting of glaciers produces additional GIA effects. As an example, Iceland is currently undergoing rapid glacial rebound due to a mass loss of Vatnajökull and other smaller ice caps e.g. /Árnadóttir et al. 2009/. Since the viscosity of the mantle is inferred to be three orders of magnitude lower beneath Iceland /Árnadóttir et al. 2009/, than below for example Fennoscandia, uplift rates on Iceland are on the order of 20 mm/year, in spite of the much smaller volume of ice loss.

Outside the ice sheet margin, an uplifted forebulge, or peripheral bulge, is formed e.g. /Mörner 1977, Fjeldskaar 1994, Lambeck 1995/. The forebulge is caused by flexure and a lateral displacement of mantle material extending outside the ice margin, and it may stretch for several hundreds of kilometres beyond a major ice sheet. The uplift of the forebulge is considerably smaller than the downwarping of the crust beneath the central parts of the ice sheet; on the order of tens of metres. During and after deglaciation, the area of the forebulge experiences land subsidence, exemplified by the ongoing lowering of the Netherlands, southern England and the east coast of the United States. It is worth noting that land subsidence in these regions is also a result of ongoing marine sediment loading. The location of maximum forebulge uplift migrates toward the formerly glaciated region as the ice sheet withdraws. In addition to the formation of the forebulge, the elasticity of the lithosphere may result in a downwarping of the crust, not only under the ice sheet, but also to some extent outside the ice margin. This produces a flexural depression between the ice margin and the forebulge, a depression where lakes may form from glacial meltwater.

At present, the crust beneath the Antarctic and Greenland ice sheets is depressed in a similar way as previously occurred under the Laurentide, Fennoscandian and Siberian ice sheets. In Greenland and Antarctica, the crust would also be subject to significant glacial rebound if these areas were to be deglaciated in the future.

The geoid is the equipotential surface of the Earth's gravitational field which best fits the undisturbed surface of the oceans. Shoreline migration is the result of changes in the height of the geoid relative to the solid surface of the Earth. Sea-level is defined to be zero on land and positive in the oceans, where it corresponds to the depth of the ocean. The surface of the ocean corresponds to the geoid surface (see Figure 3-25). Relative sea-level is the vertical height difference between the geoid at an arbitrary time and the present height of the geoid, where the height of the geoid is measured relative to the height of the solid surface (see Figure 3-25). Relative sea-level is defined to be zero at the present day. It is positive during *transgression*, when the intersection of the geoid with the solid surface is higher than present, and negative during *regression*, when the intersection of the geoid with the solid surface is lower than present. The shape of the geoid is governed by the gravitational field of the Earth and varies over time. Over time scales of 100 years to 100 kyrs, changes in relative sea-level throughout Fennoscandia are dominated by the process of glacial isostatic adjustment.

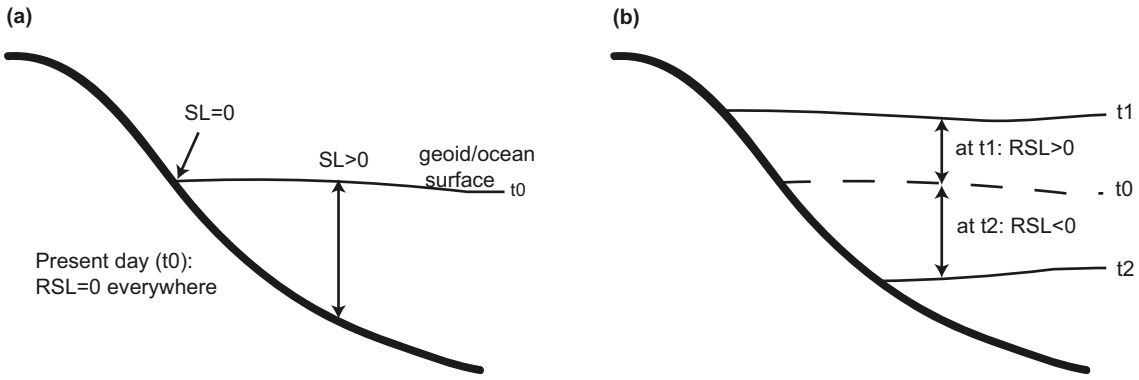

Figure 3-25. *(a) At time t0 sea-level (SL) is zero where the depth of the sea is zero, and positive where the depth of the sea is positive. Sea-level is defined to be zero on land. (b) At time t1 and t2 relative sea-level (RSL) is higher and lower respectively, as a result of the processes described in the text. Note that the change in relative sea-level is not uniform over the oceans, due to changes in the shape of the geoid.*

Relative sea-level changes associated with GIA are a result of the coupled phenomena *isostasy* and *eustasy*. Isostasy is the response of the solid Earth to loading or unloading by ice or water, and/or unloading and loading due to denudation and sedimentation, whereas eustasy refers to changes in global sea-level arising from a change in ocean water volume following a mass exchange between continental ice masses and the oceans.

Global relative sea-level changes exhibit complex spatial and temporal patterns, and are strongly dependent upon the location relative to major ice sheets. Relative sea-level change at locations far from ice sheets (hereafter referred to as far-field locations) is dominated by the eustatic signal; during deglaciation monotonic sea-level rise causes land inundation and the shift of shorelines inland. At locations close to ice sheets (hereafter referred to as near-field locations) the isostatic signal dominates; rebound of the solid surface from the time of deglaciation onwards causes land emergence and the migration of shorelines oceanwards. These are two end-member cases, and, in general, sea-level change, and hence shoreline migration, is governed by a complex interplay of isostatic and eustatic processes, operating on different time scales.

GIA-induced sea-level changes depend on the following factors (see Figure 3-26):

- The location and thickness of ice sheets.
- The depth and extent of the oceans.
- The structure and properties of the solid Earth and its response to surface loading.

Changes in surface loading arise due to the exchange of mass between ice sheets and ocean basins throughout a glacial cycle. The presence of ice-dammed lakes and the redistribution of sediments also contribute to changes in surface loading, although, in Fennoscandia, the short-lived nature of ice-dammed lakes, and their shallow depth, means that this perturbation to the pattern of surface loading probably has a negligible effect when considering the solid Earth response. The denudation of bedrock and redistribution of associated sediments persists over a much longer time scale, on the order of millions of years. On a regional scale, over a single glacial cycle, the effect of sediment redistribution upon solid Earth deformation is negligible in relation to the ice load, but over several glacial cycles, or locally, it may be of significance.

The Earth consists of the crust, the upper and lower mantle, and the outer and inner core. The lithosphere comprises the crust and part of the upper mantle. The average thickness of the lithosphere is c. 100 km, although this value varies between less than 30 km for oceanic lithosphere and up to more than 200 km for continental lithosphere /Watts 2001/. Lithospheric thicknesses in Fennoscandia range between ~60 km in the north-west and ~200 km in the south-east /Watts 2001/. The lithosphere is less dense than the mantle below and responds approximately elastically to forces applied at the

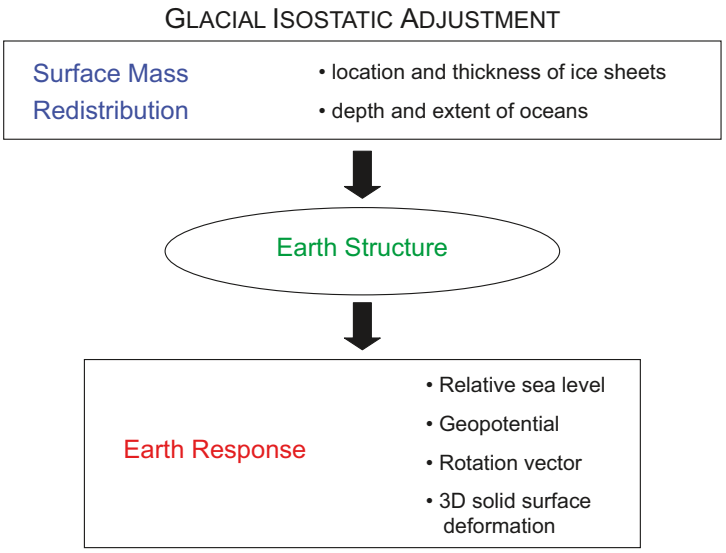

Figure 3-26. *The theory of Glacial Isostatic Adjustment (GIA): inputs and outputs of the system.*

surface. The deformation of this layer is short-lived once the load is removed. The mantle responds viscoelastically to forces applied over a time scale of ~100 kyrs. The recovery of this layer to a state of isostatic equilibrium following loading takes several orders of magnitude longer than the recovery of the lithosphere. The rheological properties of the lithosphere and upper and lower mantle determine the precise magnitude and duration of solid Earth deformation during a glacial cycle, and are discussed further in Sections 3.3.2 and 3.3.4. The outer and inner cores are not affected by GIA processes.

GIA-induced sea-level changes arise as a result of the gravitationally-consistent redistribution of water between ice sheets and ocean basins, and thus the evolution of surface loading. Any redistribution of surface mass alters the shape of the geoid, which in turn defines the position of the surface of the oceans.

The height of the geoid, or mean ocean surface, is dependent upon *direct* and *indirect* geoid perturbations /Milne et al. 2002/, as well as changes in ocean water volume and capacity of ocean basins. *Direct* effects refer to the deflection of the geoid due to the direct attraction of surface mass loads, such as ice sheets. *Indirect* effects refer to geoid perturbations arising due to the surface load-induced deformation. The volume of the oceans will vary as water is transferred to and from the ice sheets. Also changes in ocean capacity and bathymetry arise as a result of crustal and geoidal perturbations in response to ice and ocean loading. The ice-loading solid surface response includes the depression and rebound of the solid surface in the location of ice sheets, and the raising and lowering of glacial forebulges in areas surrounding the ice sheets. The ocean-loading response is similar to the ice-loading response. However, at continental margins ocean loading induces a levering of the continental lithosphere and a subsidence of offshore regions, this is referred to as *continental levering* /Clark et al. 1978/ (see Figure 3-27). The combination of ice and ocean loading leads to a decrease in the volumetric capacity of the ocean basins during glaciation, and an increase during deglaciation due to the growth and decay of offshore peripheral bulges, resulting in a globally uniform rise or fall in sea-level, respectively. The ongoing fall in sea-level following the last deglaciation due to the migration of water from equatorial regions to subsiding peripheral bulge regions has been termed *equatorial ocean syphoning* /Mitrovica and Peltier 1991, Mitrovica and Milne 2002/.

Changes in relative sea-level result in shoreline migration. A rise in relative sea-level and the consequent inland migration of the shore may be due to solid Earth subsidence, an increase in the height of the geoid/ocean surface as a result of ice sheet melting, or a combination of these processes. Similarly, a fall in relative sea-level and the consequent migration of the shore towards the ocean may be due to isostatic rebound, a fall in the height of the geoid/ocean surface due to ice sheet build up, or a combination of these processes. In the vicinity of the Fennoscandian ice sheet, the effects of isostatic deformation and

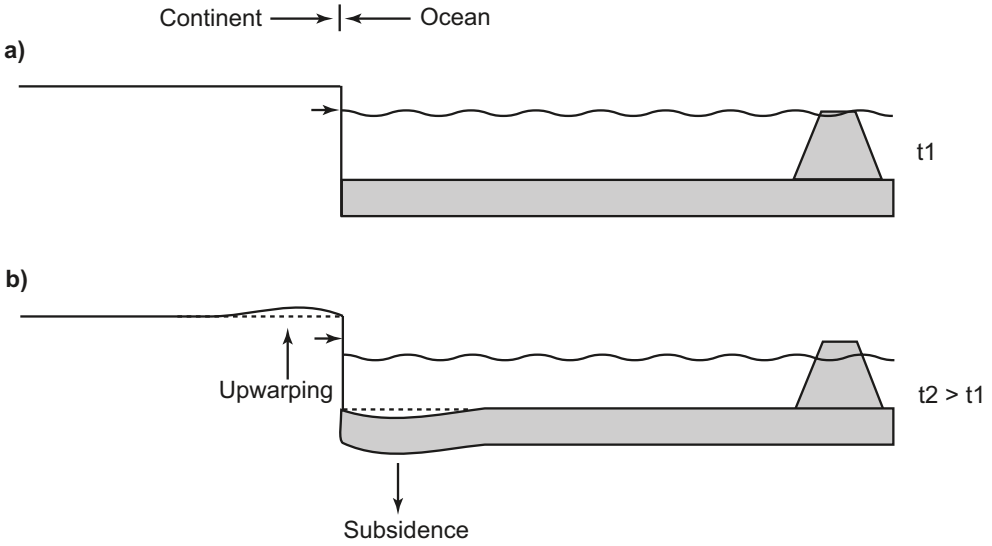

Figure 3-27. *Continental levering: the migration of water into offshore regions following deglaciation results in offshore subsidence and onshore upwarping. Ocean floor subsidence results in sea-level fall at far-field sites.*

changes to the height of the geoid/ocean surface occur simultaneously, and may have opposite effects on the position of the shoreline. Further, the surface of the Baltic Sea does not solely depend on the height of the geoid/ocean surface, but also on the elevation of its sills relative to the Atlantic sea-level, and ice thicknesses at locations with potential connections to the sea; these may cause it to become isolated from the global ocean.

Indirectly, groundwater flow and composition are influenced by shoreline migration. If the site is not subject to permafrost, and it is not covered by an ice sheet, the sea, or a lake, then the groundwater surface follows a subdued version of the topography. Groundwater flow will be driven by topography, assuming precipitation exceeds evaporation. If the site is submerged the situation will be almost stagnant and groundwater flow will be driven by density only /SKB 2010c/. Groundwater composition is affected, since relative sea-level affects the salinity of the Baltic Sea. Relative sea-level and the extent of the ice sheet determine whether there is a connection between the Baltic Sea and the ocean. This together with the runoff to the Baltic basin, determines the salinity in the sea/lake water.

3.3.2 Controlling conditions and factors

Loading

The main factors governing the evolution of relative sea-level, and hence shoreline migration, throughout Fennoscandia are the loading history – both with regard to ice and ocean water – and the rheological parameters governing the response of the solid Earth to such a load.

Near-field relative sea-levels are very sensitive to variations in the evolution of the near-field ice sheet, /Lambeck et al. 1998, Davis et al. 1999, Tamisiea et al. 2001, Milne et al. 2002, Kaufman and Lambeck 2002, Tamisiea et al. 2003/. There remain uncertainties in the details of ice loading during the last glacial cycle, especially with regard to estimates of ice thickness within Fennoscandia.

The details of far-field ice sheets are irrelevant for the prediction of relative sea-level change in Fennoscandia /Peltier 1998, Mitrovica et al. 2001b, Tamisiea et al. 2003, Bassett et al. 2005/; mass changes in the far field mainly provide an influence on global eustatic sea-level change. However, the overall characteristics of far-field ice sheets may also generate a long wavelength isostatic response in Fennoscandia. This response is likely to be dominated by the signal from a massive North American (Laurentide) ice complex. Due to the position of Fennoscandia on the Laurentide forebulge during the LGM /Mitrovica et al. 1994/, the presence of the Laurentide ice sheet is predicted to have generated 25–30 m of solid Earth uplift in central Fennoscandia at this time (see Section 3.3.4). The magnitude of this signal does not vary greatly across Fennoscandia (unlike the relative sea-level signal due to local ice loading), and is not dependent upon the local geometry of the Laurentide ice sheet; only its volume.

During the last deglaciation an ice-dammed lake prevailed within the Baltic depression when non ice-covered sills were above sea-level and all other potential connections between the Baltic Sea and the North Sea were dammed by the ice sheet ice e.g. /Björck 1995, Lambeck 1999/. The surface of the ice-dammed lake was constrained by the height of the ice sheet above sea-level and the surrounding topography, i.e. the sill levels, and there is evidence to suggest that immediately prior to the draining of the so called Baltic Ice Lake its surface was 25 m above the contemporary relative sea-level /Björck 1995/. Due to the relatively small volume of water released to the oceans as the ice lake drained the resulting perturbation of global sea-levels was insignificant /Lambeck 1999/. The shallow depth and the short duration of the ice lake mean that its impact on isostasy was negligible in comparison with the ice load.

Another process that may impact the loading is erosion and sediment transfer. Erosion and transport of sediment took place beneath warm-based parts of the ice sheet during previous glacial cycles, and this mass redistribution affects isostatic loading and topography. However, the average total depth of glacial erosion over all Late Pleistocene glacial cycles in lowland Precambrian parts of Fennoscandia is on the order of a few tens of metres, see Section 3.5. Therefore, on the time scale of one glacial cycle, the average unloading/loading effect of this process may be neglected. However, any local reshaping of the land will affect the evolution of the shoreline, and this needs to be taken into account.

Rheological parameters and topography

In order to determine the Earth's response to surface loading its internal rheological and density structure must be specified. The characteristic time scale for loading during a glacial cycle will excite both elastic and viscous responses, therefore a viscoelastic (Maxwell) rheology is adopted. Such a system behaves elastically on a short time scale and viscously on a long time scale when placed under stress.

Parameters describing the rheological properties of the Earth's lithosphere and upper and lower mantle define its response to loading during a glacial cycle. The average density and elastic structure of the Earth are taken from /Dziewonski and Anderson 1981/. The lithosphere is generally regarded as elastic for the purposes of GIA studies; this has been shown to be a good approximation throughout the development of the subject /McConnell 1968/.

The upper mantle lies below the lithosphere, extending to a depth of 660 km, and then the lower mantle extends to 2,900 km below the Earth's surface. The viscosity of the upper and lower mantle have been constrained to lie in the ranges $1 \cdot 10^{20}$–$2.6 \cdot 10^{21}$ Pa s and $2 \cdot 10^{21}$–$1 \cdot 10^{23}$ Pa s, respectively, as determined from previous GIA studies /Davis and Mitrovica 1996, Mitrovica and Forte 1997, Simons and Hager 1997, Lambeck et al. 1998, Davis et al. 1999, Milne et al. 2001, 2002, 2004, Mitrovica and Forte 2004/. Lateral variations in radial viscosity structure may be derived from seismic shear-velocity models by converting velocities to temperatures, and then using temperature to estimate viscosity.

Present-day topography is used to constrain palaeotopography. When calculating palaeotopography, see Section 3.5, we assume that all changes to the shape of the land arise from the differential GIA response across the region; however topography is also affected by tectonic, erosional and depositional processes.

The isostatic adjustment and shoreline migration described above may affect a number of geosphere variables of importance for a deep geological repository (Table 3-3).

3.3.3 Natural analogues/observations in nature

The GIA process may be observed by studying relative sea-level markers, both from the geological record and from tide gauge data, GPS observations of the 3D deformation of the solid surface, the time-variation of the gravity field as observed by satellites and land-based gravity surveys, and changes in the orientation of the Earth's rotation vector and length of day.

Geological and tide gauge data complement each other. Tide gauge data consist of monthly or annual observations of mean sea-level relative to a local solid Earth marker at coastal sites throughout the world. The data may be accessed through e.g. the "Permanent Service for Mean Sea-level" at www.pol.ac.uk/psmsl. In the Baltic region, such sea-level observations have been conducted systematically for more than a century. When measuring isostatic uplift rates with this method, it is necessary to correct the result in order to exclude the effect from eustatic variations. In non-coastal areas, present post-glacial rebound rates have been estimated by repeated geodetic levelling, tied to locations of sea-level observation. The results from these measurements show that the present uplift rate displays a concentric uplift pattern over Fennoscandia, with a maximum rate of slightly more than 9 mm/yr in the northernmost part of the Baltic Sea, see Figure 3-28.

The geological data, including palaeoshoreline positions, lake isolation and tilting information, cover a longer time period than the tide gauge data, but the tide gauge data are more accurate, both in terms of their vertical resolution and the dating of the information. In this context, shorelines or other geomorphological features that formed at the highest post-glacial sea-level, in front of the retreating ice sheet margin, provide the oldest estimate of former relative sea-level positions. However, the total amount of post-glacial uplift at a site is typically larger than can be inferred from, for example, raised beaches. A significant portion of the uplift takes place as the ice sheet starts to decay, *prior to the actual deglaciation* of a typical site situated at some distance from the maximum ice margin. The total maximum amount of glacial rebound that has occurred due to the decay of the Fennoscandian ice sheet is around 800 m, e.g. /Mörner 1979/ (Figure 3-28). This may be compared to the largest value on rebound as inferred from the highest marine limit, which is situated at ~280 m a.s.l. in the Swedish coastal region of the Gulf of Bothnia. Another related method to study glacial rebound is to analyze the amount and direction of tilt of palaeoshorelines of glacial lakes that formed behind the retreating ice margin. A selection of geological relative

Table 3-3. A summary of how geosphere variables are influenced by isostatic adjustment and shoreline migration.

Geosphere variable	Climate issue variable	Summary of influence
Rock stresses	Isostatic depression/rebound	The deformation of the Earth's crust will lead to altered rock stresses.
Groundwater pressure	Relative sea-level	If the site is not covered by the sea or a lake the groundwater pressures will be determined by topography and groundwater recharge. If the site is submerged the groundwater pressure will be determined by depth of the sea/lake.

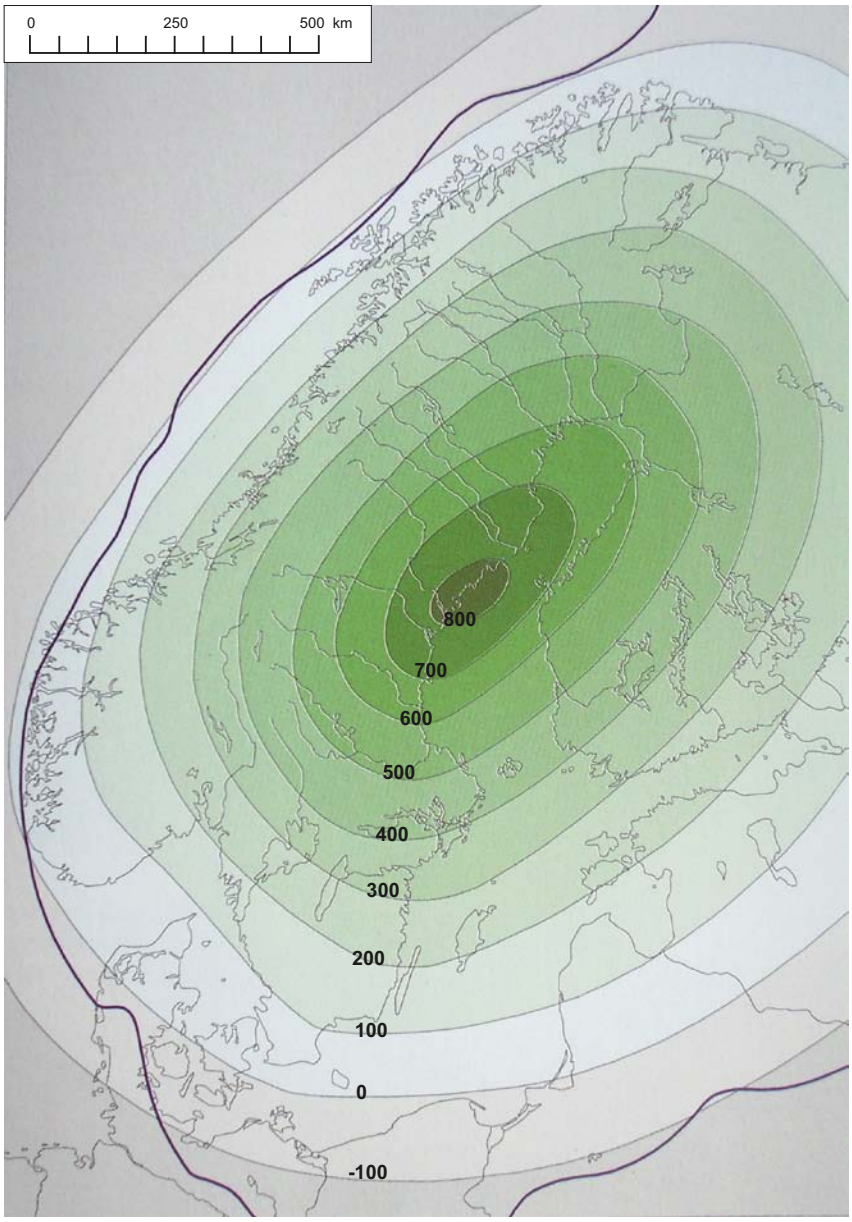

Figure 3-28. *Total amount of glacial rebound (metres) that has taken place due to the decay of the Fennoscandian ice sheet. The bold line shows the approximate maximum extent of the last Fennoscandian ice sheet. Note that the total amount of rebound is more than twice as large as the amount of rebound that may be inferred from raised beaches formed at the highest post-glacial sea-level (see the text). After /Fredén 2002/.*

sea-level data for Fennoscandia can be found in e.g. /Lambeck et al. 1998, Påsse 2001, Eronen et al. 2001, Kaufmann and Lambeck 2002, Whitehouse 2007[2]/, and references therein, but at present a complete compilation of such data does not exist.

Care must be exercised when interpreting palaeoshoreline data from the Baltic Sea; it is important to determine whether the data relate to sea-level or a lake level. An overriding problem with geological data in Fennoscandia is the lack of relative sea-level data prior to the LGM. Most of the evidence of shorelines prior to this time has been destroyed by the ice sheet. This makes it difficult to test relative sea-level predictions from before 20 kyr before present. Furthermore, the fact that shorelines can only form in ice-free locations provides an important temporal constraint for the testing of shoreline migration predictions against undated shoreline data.

As previously mentioned, observations of relative sea-level are required in both the near and far field. Far-field data provide constraints on eustatic sea-level change and hence the volume of ice contained in far-field ice sheets. Near-field data exhibit a more complex dependence upon the local distribution of ice and the Earth model.

One way of making direct observations of ongoing post-glacial crustal deformation is to use high quality data from networks of continuously operating permanent GPS receivers. GPS data provide satellite-measured observations of changes in baseline distances which yield present-day rates of vertical and horizontal motion at a series of discrete positions. GPS data from the BIFROST project /Johansson et al. 2002/ provide excellent spatial coverage of present-day solid Earth deformation throughout Fennoscandia to a high degree of accuracy. Typically, the GPS stations used in the BIFROST project were established within national land survey programmes with an initial aim of providing reference coordinates for other GPS measurements. The detailed analyses of data from such permanent GPS stations have provided new insight into the processes of post-glacial rebound or GIA in Fennoscandia and Canada, cf. /Scherneck et al. 2001, Henton et al. 2006/. The results provide information on both the rate of the vertical uplift component, as well as on the associated smaller horizontal component of crustal motion, e.g. /Johansson et al. 2002/ (Figure 3-29). The rates are averaged over the period of data collection, which is generally on the order of 10 years at the present, to yield estimates accurate to within ~0.1 mm/yr in the horizontal direction, and a few tens of a mm/yr in the vertical direction.

Uplift determined by these GPS observations show the same concentric uplift patterns as those derived from sea-level and levelling measurements. The fastest rebound occurs approximately in the areas where the Laurentide and Fennoscandian ice sheets had their greatest thicknesses. The maximum vertical uplift rate measured in this way in the area of the former Laurentide ice sheet is ~13 mm/yr /Henton et al. 2006/, while the corresponding value for Fennoscandia is ~11 mm/yr (Figure 3-29). The largest horizontal displacements are generally found in the area of the ice margins of the maximum extent of the ice sheet. The difference between the maximum vertical uplift rates as observed from sea-level/levelling measurements and from the analysis of GPS data is to a large extent covered by the uncertainty errors of the measurements, mainly in the sea-level measurements.

Since the GPS network yields an estimate for the full 3D deformation field, and the horizontal and vertical components of this field have different sensitivities to the ice history and Earth model, this opens up the possibility of constraining model parameters more accurately when these data are combined with sea-level observations. Combining the GPS data with sea-level data is particularly important when one considers that the GPS data are limited by their relatively short time span, and can only yield information about present-day deformation rates. Also, sea-level data are limited by their poor spatial coverage; a factor that is addressed by the distribution of GPS observations throughout the interior of Fennoscandia.

Another, indirect, way of studying ongoing post-glacial rebound is by absolute gravity measurements, e.g. /Lambert et al. 2001, Mäkinen et al. 2005/, a method that may be used to estimate also the remaining uplift in areas where the process is not complete.

[2] Whitehouse P, 2007. A relative sea-level data base for Fennoscandia. Durham university, February 2007. Excel data base stored at SKB, SKBdoc 1265613.

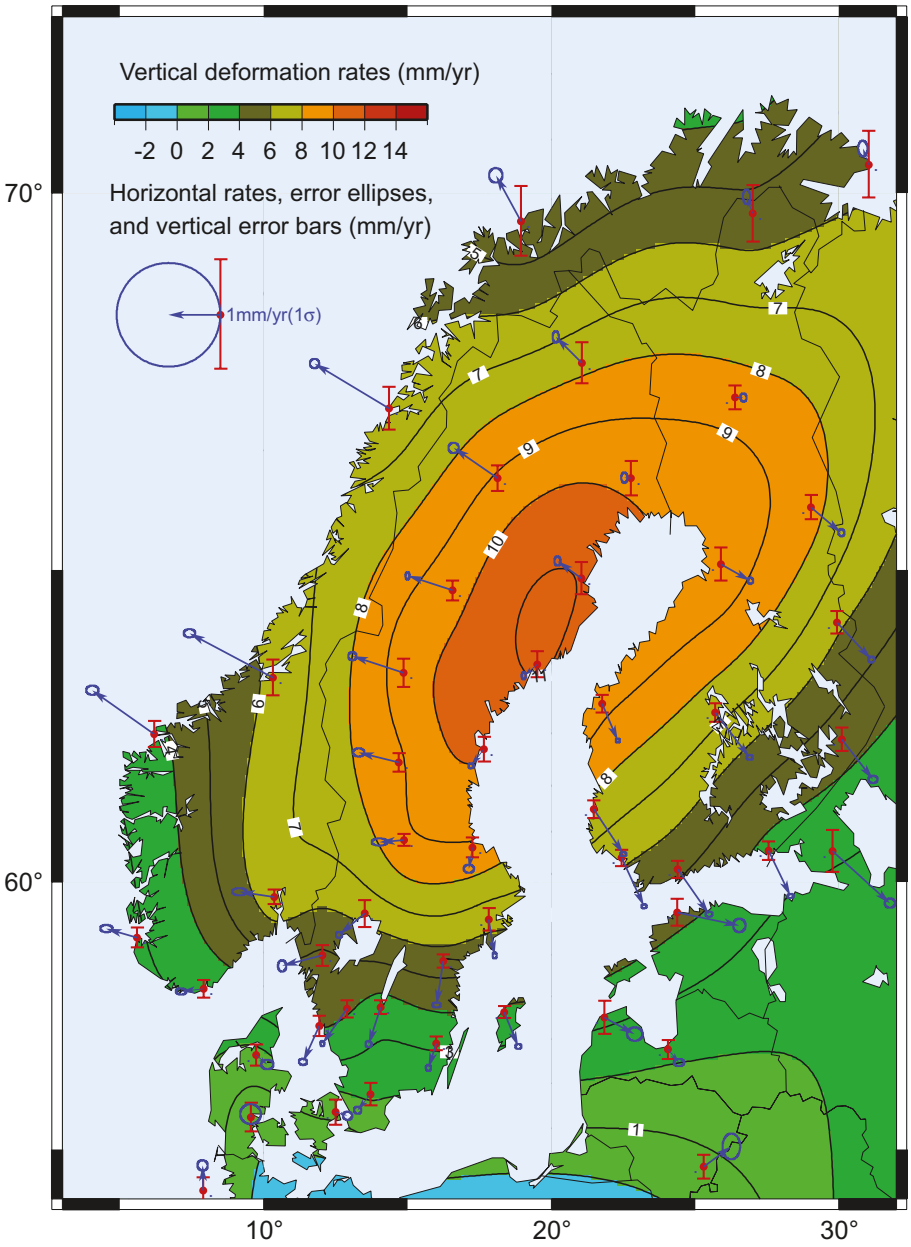

Figure 3-29. *Present-day crustal deformation over Fennoscandia as observed by continuous GPS measurements within the BIFROST project, e.g. /Scherneck et al. 2001/. The rebound displays a concentric pattern with a maximum rebound rate of ~11 mm/yr located approximately in the area of the former maximum ice sheet thickness. In the post-glacial upwarping process, a horizontal component of crustal deformation is also present (blue arrows), directed outward from the area of maximum depression. Modified from /Lidberg 2007/.*

3.3.4 Model studies

The GIA model

For a comprehensive and detailed review of present day GIA models, see /Whitehouse 2009, Chapter 4/. That chapter includes descriptions of different GIA approaches used by various research groups and relative accuracy of these methods. Recent improvements of the GIA theory are described, as well as current shortcomings of the models. The various data sets used to calibrate and verify the accuracy of the modelling are also briefly discussed. A shorter description of GIA models are given here, followed by the GIA simulations performed for the safety assessment.

The majority of GIA models solve the sea-level equation, which was originally developed by /Farrell and Clark 1976/, and describes the gravitationally-consistent redistribution of water from ice sheets

to ocean basins, and thus the evolution of the distribution of water between oceans and land-based ice sheets. Any redistribution of surface mass alters the shape of the geoid, which in turn defines the redistribution of water in the ocean basins; therefore an iterative procedure is required to solve the sea-level equation.

There have been many attempts to construct a dynamical model to explain the observed processes of GIA. Following /Farrell and Clark 1976/, early studies neglected the time dependence of ocean shorelines /Wu and Peltier 1983, Nakada and Lambeck 1989, Tushingham and Peltier 1991/, and the ice loading was simply applied as a series of 'finite elements' /Clark et al. 1978, Peltier et al. 1978, Wu and Peltier 1983/. In 1991, /Mitrovica and Peltier 1991/ derived a pseudospectral approach to solving the sea-level equation, and this method has been widely used throughout the field ever since. Models which take into account the time-varying nature of shorelines began to be developed in the early 1990s /Lambeck and Nakada 1990, Johnston 1993, Peltier 1994, 1998, Milne 1998, Milne et al. 1999, Peltier and Drummond 2002, Kendall et al. 2005/, and the effects of Earth-rotation have also subsequently been considered /Han and Wahr 1989, Bills and James 1996, Milne and Mitrovica 1998, Peltier 1998, Mitrovica et al. 2001a, Mitrovica et al. 2005/. Initial investigations into the effect of lateral variations in Earth structure are also in the process of being developed /Kaufmann et al. 2000, Wu et al. 2005, Latychev et al. 2005b, Paulson et al. 2005, Whitehouse et al. 2006/.

The GIA model used in this study was developed by Milne /Milne 1998, Milne and Mitrovica 1998, Milne et al. 1999/. Three refinements to the original sea-level equation presented by /Farrell and Clark 1976/ have been developed by /Mitrovica and Milne 2003/. Firstly, time-dependent shoreline positions are taken into account when calculating the ocean-loading function. Shorelines can change position by several hundreds of kilometres in flat terrains, and this must be accounted for in applying the ocean load. Secondly, the water influx into regions vacated by retreating, marine-based ice is carefully accounted for in the distribution of the load /Milne et al. 1999/. And thirdly, changes to the rotational state of the Earth as a result of both surface and internal mass redistributions are considered. The model used to generate predictions of relative sea-level change in this study is based on a new general theoretical foundation that includes all these advances.

The sea-level equation

The sea-level equation takes account of changes to the height of the geoid and the Earth's solid surface. Local factors, such as changes to the tidal regime, the consolidation of sediments, and tectonic processes, are neglected in this study.

$$\Delta\xi_{rsl}(\tau,\varphi) = \Delta\xi_{eus}(\tau)+\Delta\xi_{isos}(\tau,\varphi)+\Delta\xi_{local}(\tau,\varphi) \qquad \text{Equation 3-9}$$

In the above expression the left-hand side refers to changes in relative sea-level at time τ and location φ. The first term on the right-hand side is the time-dependent eustatic signal, the second term varies in space and time, and relates to the isostatic effects of glacial rebound, including both ice and water load contributions, and the third term refers to local factors, as described above. In order to solve Equation 3-9 in a gravitationally self-consistent manner, a pseudospectral algorithm /Mitrovica and Peltier 1991, Milne and Mitrovica 1998/ is employed. Green's functions are constructed to determine the GIA-induced perturbations to the geopotential and solid surfaces due to loading. The resulting temporal convolutions are evaluated by describing the GIA loading history as a series of discrete Heaviside increments. The spatial convolutions are performed by transforming the problem to the spectral domain and employing the pseudospectral algorithm /Mitrovica and Peltier 1991, Milne and Mitrovica 1998/.

The method by which relative sea-level is calculated at a certain position, at a certain time, may be broken down into a series of simplified steps. At the start of the model run, loading is applied to an Earth model that is assumed to be in isostatic equilibrium. Once an ice load is applied at each time step the resulting deformation of the solid Earth and the perturbation to the geoid are calculated. The new shape of the geoid determines the redistribution of water in the oceans and the new extent of the oceans. However, this redistribution of water in turn affects the shape of the geoid and the deformation of the solid Earth in oceanic regions, therefore an iterative procedure is used to ensure the correct treatment of perturbations to the solid and geoid surfaces; recalculations of the perturbation to the geoid and the redistribution of water are carried out until there are no further changes, at which point loading for the next time step is applied. Loading is applied via forward time stepping.

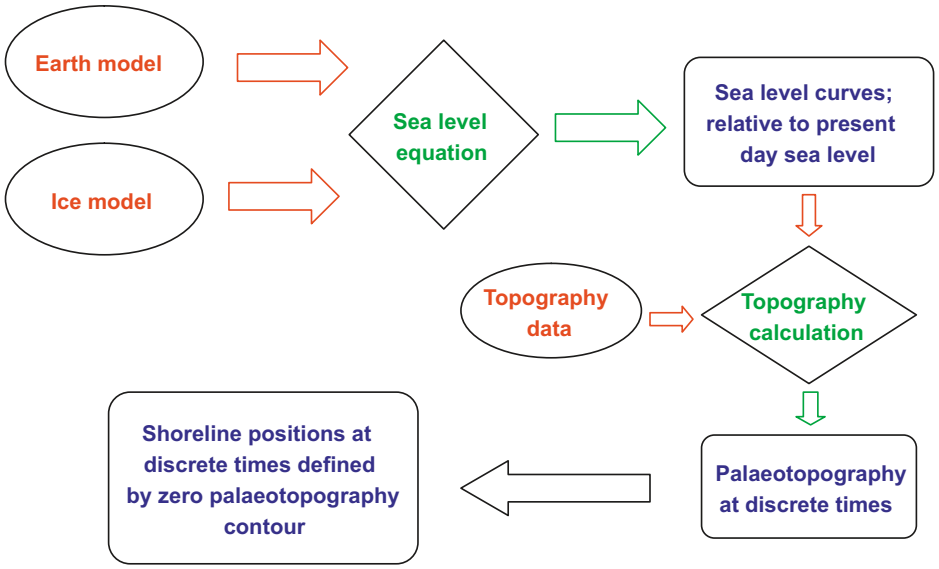

Figure 3-30. *Flow chart outlining the inputs (in red), calculations (in green) and outputs (in blue) required to calculate palaeoshoreline positions due to GIA processes.*

The final output of the GIA model consists of a series of global relative sea-level predictions for all time steps used in the model. In the method used here, relative sea-level is defined to be zero at the present day, and heights are given relative to this 'zero level' at all times in the past and future. Corrections are applied using present-day topography to determine the height of any point above or below sea-level at any given time. Assuming that the underlying topography is unaltered by erosion and sedimentation the evolution of palaeotopography is calculated via the following equation:

$$T(\varphi,\tau_p) = T(\varphi,\tau_0) - \xi_{rsl}(\varphi,\tau_p) \qquad \text{Equation 3-10}$$

where T is topography, defined to be the height of the solid surface above sea-level at time τ, and ξ_{rsl} is relative sea-level at time τ. τ_p refers to a time in the past, τ_0 refers to the present day, and φ is the location on the surface of the Earth. Shoreline positions at time τ_p are determined by the zero palaeotopography contour at that time.

Ice loading

The global ice loading model used in this study is modified from the ICE3G deglaciation history /Tushingham and Peltier 1991/, and has been calibrated using far-field relative sea-level data /Radtke et al. 1988, Fairbanks 1989, Bard et al. 1990, 1996, Chappell and Polach 1991, Chappell et al. 1996, Hanebuth et al. 2000, Yokoyama et al. 2000/. A eustatic curve has been used to tune the mass of ice contained within far-field ice sheets. The near-field ice loading for Fennoscandia is the one described in Section 3.1.4 and has been derived using a thermodynamic ice sheet model employing a proxy data palaeotemperatures curve. From this model, the extent and thickness of the Fennoscandian ice sheet at a series of discrete times from 116 kyr BP to the present day has been derived and used.

Ice loading history within Fennoscandia is the principal factor governing relative sea-level change in Fennoscandia. The loading history presented in Section 3.1.4 is perturbed to investigate the sensitivity of sea-level change to differences in ice thickness, the timing of deglaciation, the pattern of ice build-up, and the time scale over which loading is considered (Table 3-4). The extent of ice at each time step since the LGM has not been perturbed because the geometry of the ice sheets during this period are relatively well constrained by geological data. Details of the ice build-up prior to the LGM is less well constrained because geological evidence subsequently has been destroyed. However, for consistency, the ice extents for this period are also not altered. An Earth model consisting of a 96 km-thick elastic lithosphere, an upper mantle of viscosity $0.5 \cdot 10^{21}$ Pa s, and a lower mantle of viscosity $1 \cdot 10^{22}$ Pa s is used to investigate the response to the different loading models.

Table 3-4. Summary of ice loading models used in this study. In all cases the ICE3G global ice model is used to constrain the distribution and thickness of ice outside Fennoscandia.

Model	Description of loading model	Model run time
1	Weichselian glacial cycle as described in Section 3.1.4	116 kyr
2	Two Weichselian glacial cycles run after each other to give a double glacial cycle	232 kyr
3	Weichselian glacial cycle, loading only applied from 40 kyr BP	40 kyr
4	Weichselian glacial cycle with 90% ice thickness in Fennoscandia	116 kyr
5	Weichselian glacial cycle with 80% ice thickness in Fennoscandia	116 kyr
6	Weichselian glacial cycle with the timing of deglaciation advanced by 500 years	116 kyr
7	Weichselian glacial cycle modified with ice thickness allowed to increase linearly between 60 kyr BP and 20 kyr BP	116 kyr
8	Four relaxation models, as described in the isostatic memory section	Varies
9	Weichselian glacial cycle with all ice removed from Fennoscandia for the duration of the model run, as described in the section on far-field ice sheets	116 kyr

In Figure 3-31a the same Fennoscandian surface loading is used, but the model run is initiated at different times. Due to the assumption that the Earth is initially in isostatic equilibrium there will be some discrepancy between relative sea-level predictions at early times in a model started at 116 kyr BP and one that has already been running for 100 kyr because the Earth's response is dependent upon loading history as well as the instantaneous load (see the section on Isostatic Memory). Because the Earth has undergone a series of glacial cycles, a loading model that accounts for loading and unloading of the Earth during the previous cycle will give more realistic predictions for relative sea-level during the cycle of interest. However, the negligible difference between relative sea-level predictions from the single cycle, double cycle and 40 kyr models (models 1, 2, and 3 in Table 3-4), for times between 25 kyr BP and the present day, imply that no long-term error is introduced when a model with a later start time is used. It is important that the shortest possible time steps are used to ensure that the full loading history is captured; failure to do so will miss short time scale fluctuations in ice distribution, leading to a decrease in the accuracy of the relative sea-level predictions.

The effect of altering the thickness of ice in the loading model is illustrated in Figure 3-31b. There is little difference in the shape and magnitude of predicted relative sea-level curves for the 80%, 90% and 100% loading models during the minor glaciation between ~65 kyr BP and ~50 kyr BP (models 5, 4 and 1 in Table 3-4), but comparing results from the 80% and 100% models at the LGM yields differences of ~100 m at Forsmark. The larger the range of ice thicknesses used, the greater the range of relative sea-level predictions, as illustrated by the range of curves for Forsmark.

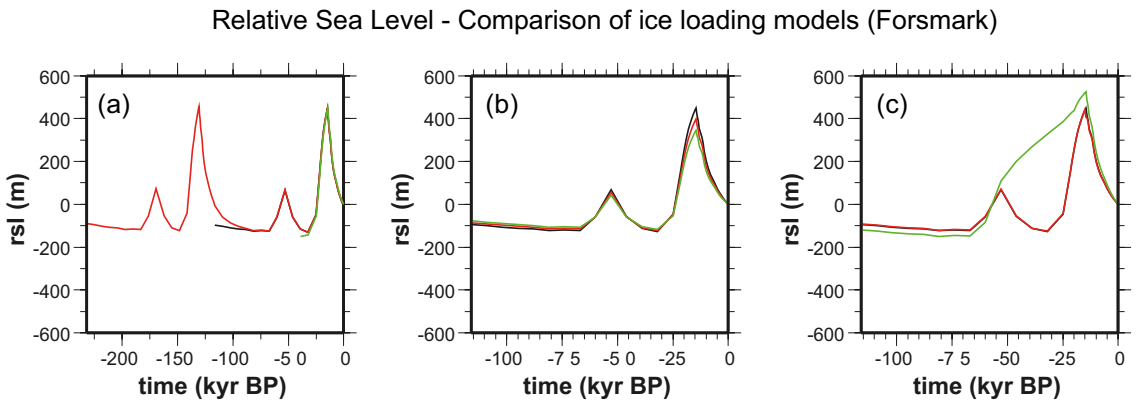

Figure 3-31. *Predicted relative sea-level curves for Forsmark. See Table 3-4 for details of the ice loading models. An Earth model with a thin lithosphere and low upper mantle viscosity has been used in all cases (Model A, Table 3-5). a) black: model 1, red: model 2, green: model 3. b) black: model 1, red: model 4, green: model 5. c) black: model 1, red: model 6, green: model 7.*

The timing of maximum relative sea-level is the same for all loading models except that where the timing of deglaciation is brought forwards by 500 years (model 6 in Table 3-4). In this case, maximum relative sea-level also occurs 500 years earlier. Apart from this time shift, which decays to zero by the present day, there is otherwise no difference between predictions for this model, and the Weichselian glacial cycle. The magnitude of the maximum relative sea-level is identical to that predicted by the single cycle, double cycle and 40 kyr loading models (models 1, 2 and 3 in Table 3-4).

In model 7 (Table 3-4), ice thickness is allowed to increase linearly between 60 kyr BP and 20 kyr BP. This model has been developed to test the postulation that there was a continuous ice sheet presence in Fennoscandia during this period /Lundqvist 1992/, see also Section 4.2 and 4.4. The pattern of continuous, linear ice sheet growth is purely an assumption of this model sensitivity test; the maximum ice thickness of the Weichselian glacial cycle is never exceeded, but the cumulative effect of loading the Earth for a longer period result in a greater amount of isostatic depression throughout Fennoscandia, and a greater relative sea-level maximum (Figure 3-31c). Therefore the GIA signal is not only a function of the thickness and timing of ice loading at a given time, but also the evolution of the loading.

The rate of change of relative sea-level throughout the glacial cycle is similar for all the loading models except the model where the pattern of ice sheet growth has been markedly altered prior to the LGM (model 7 in Table 3-4, Figure 3-31c). However, predictions of present-day uplift rates for the various models do highlight small differences between the models (see Figure 3-32). Uplift rates for the single cycle, double cycle, 40 kyr loading model and the model where the timing of deglaciation is shifted by a small amount are virtually identical. Much lower rates are predicted for the case where only 90% or 80% of the ice thickness is used, although the lateral extent over which rebound occurs is similar to the standard loading models. The final model, where the pattern of ice sheet growth has been altered, yields much greater present-day uplift rates, reflecting the fact that the solid Earth has to rebound from a position of greater isostatic depression at the LGM. In this final case, the area over which rebound is still taking place is greater than that predicted by the other loading models.

Comparisons between predictions from the GIA model, using the ice loading from the Weichselian glacial cycle as outlined in Section 3.1.4 (model 1 in Table 3-4), and observations of relative sea-level and present-day uplift rates in Fennoscandia show that the modelling overpredicts the GIA response (see Figures 3-33 and 3-34). There may be several reasons for this; either the ice load has been too large in the ice load history, as tested above with load models 4 and 5 reducing the Weichselian glacial cycle ice sheet thickness to 90% and 80% respectively, or the misfit could be a result of assuming a laterally homogeneous (1D) Earth structure, discussed in the section *A GIA case study with a Fennoscandian 3D Earth structure* below, or a combination of the two.

Unlike the geological evidence relating to the spatial extent of the Weichselian ice sheet, very few constraints upon the ice sheet thickness exist, and one explanation for the misfit could be that ice thicknesses in the loading model are too large. As pointed out by /Denton and Hughes 1981/, early ice sheet modelling studies of steady-state ice sheets, including their own, produced ice thicknesses that were greater than one would expect from ice sheets during a natural glacial cycle. This has since been confirmed by GIA modelling, showing that those thick ice sheet profiles result in a poor fit to relative sea-level observations. Subsequent dynamical approaches to ice modelling outlined in Section 3.1, including the model used in the present study, produce considerably thinner ice sheets, for example at the LGM. These models yield a closer fit to relative sea-level observations when used as an input to GIA models, but in the present study there is still a misfit to explain. Some of this difference may be explained by the fact that there are still gaps in our knowledge of basal processes related to, for example, sliding and sediment deformation under ice sheets. Another explanation could be that the assumption of a uniform Earth structure results in a too large GIA response, see below.

Earth rheology

The second main factor governing sea-level change, following the load history, is the Earth model. A three-layer, 1D radial structure is used in these experiments. A discussion of the reasonable joint parameter range for the rheological properties of the lithosphere and mantle can be found in Section 3.3.2. The details of the models used in this investigation are outlined below in Table 3-5.

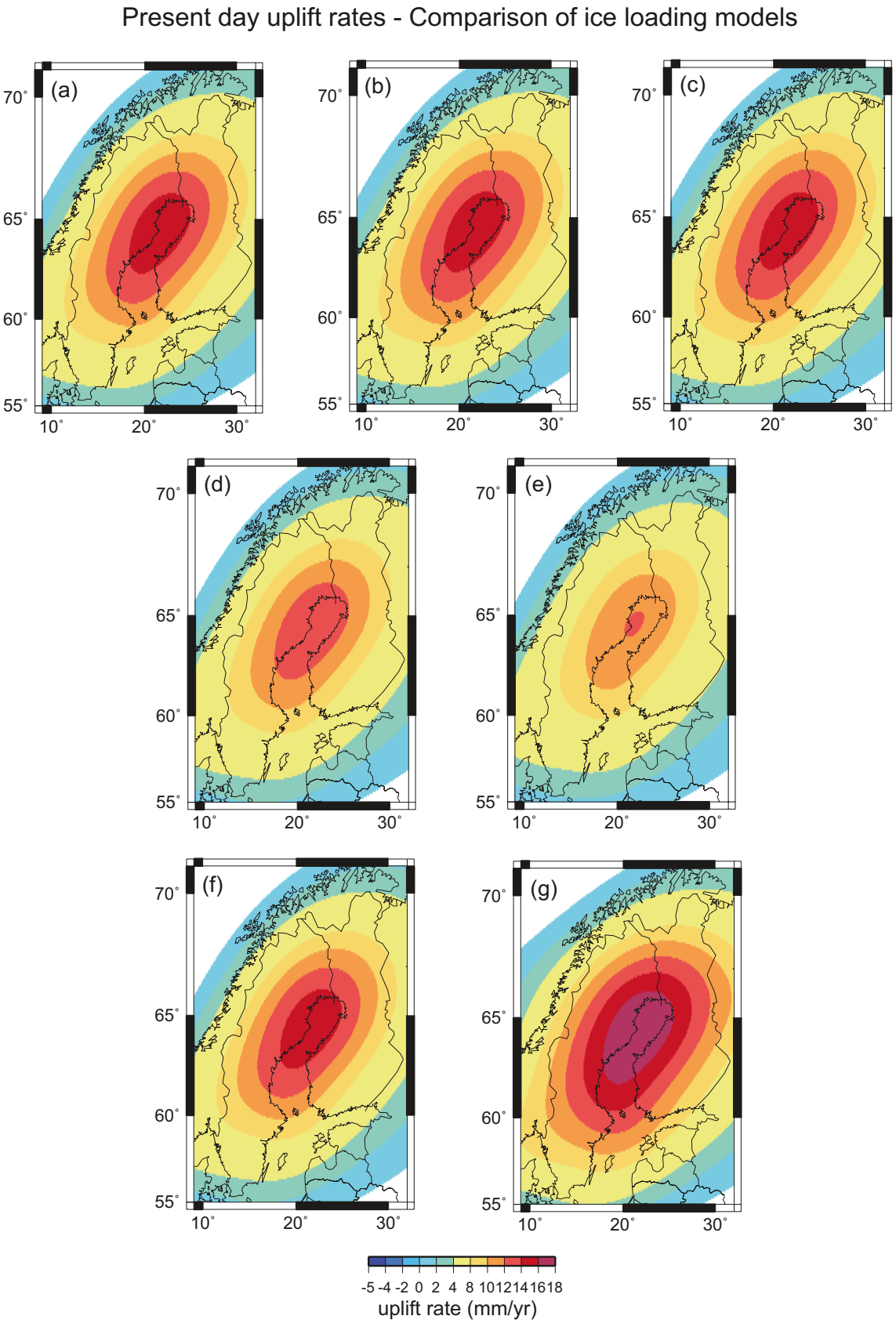

Figure 3-32. *Predicted present-day uplift rates throughout Fennoscandia for the various ice-loading models. See Table 3-4 for details of the loading models. An Earth model with a thin lithosphere and a low upper mantle viscosity has been used in all cases (Model A, Table 3-5). a) Loading model 1. b) Loading model 2. c) Loading model 3. d) Loading model 4. e) Loading model 5. f) Loading model 6. g) Loading model 7.*

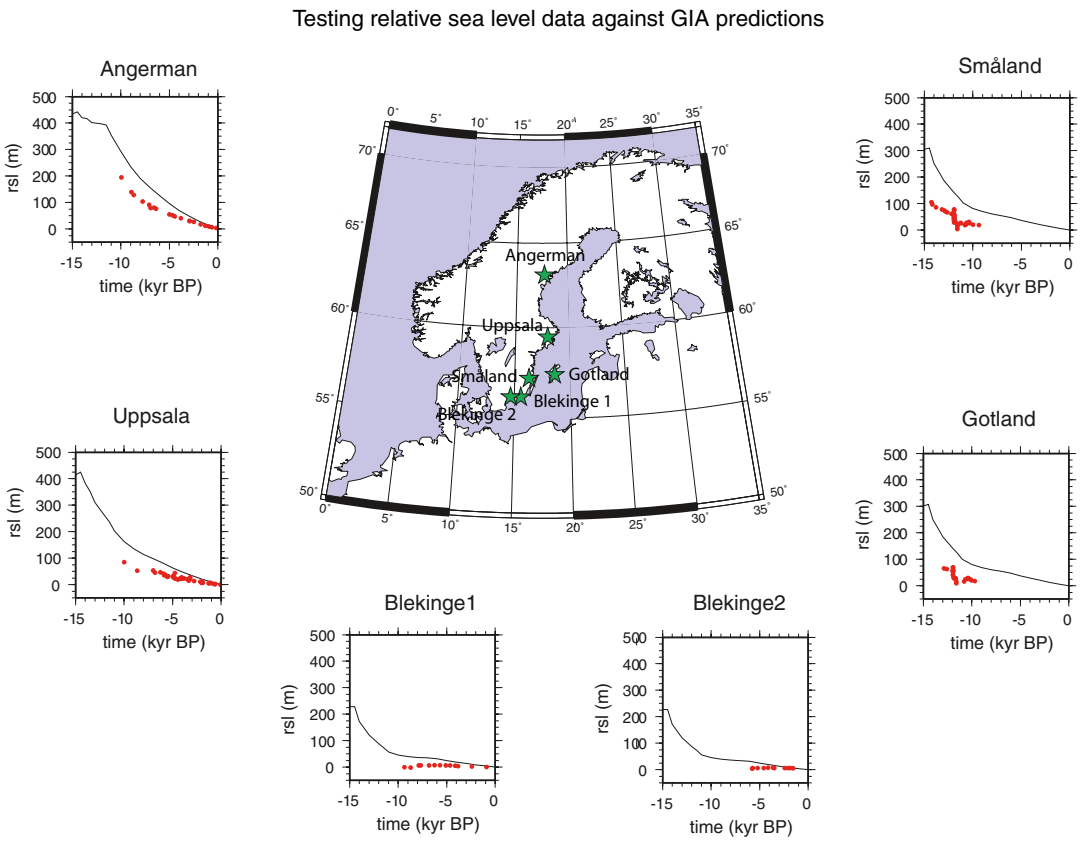

Figure 3-33. *Comparison between predicted relative sea-level (black line) and observations from relative sea-level markers (red points) at six sites in Fennoscandia (green stars) for the last 15 kyr. Data compiled from /Lambeck et al. 1998/.*

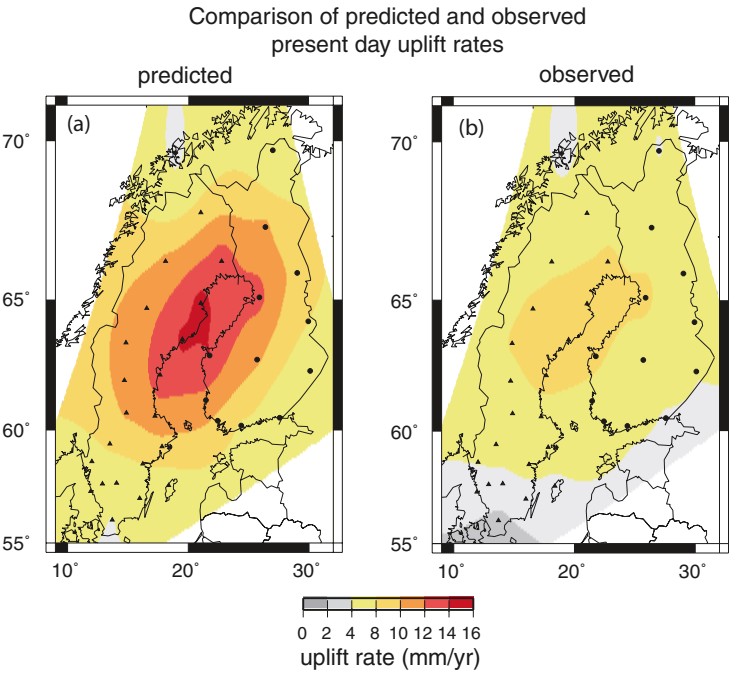

Figure 3-34. *Comparison of predicted and observed present-day uplift rates. a) Predicted present-day uplift rates interpolated at GPS sites (black dots and triangles). Data generated using the Weichselian glacial cycle loading model (model 1 in Table 3-4) and an Earth model consisting of a 96 km-thick elastic lithosphere, an upper mantle of viscosity $0.5 \cdot 10^{21}$ Pa s, and a lower mantle of viscosity $1 \cdot 10^{22}$ Pa s (model A in Table 3-5). b) Observed present-day uplift rates interpolated at GPS sites. Data from the BIFROST project /Johansson et al. 2002/.*

Table 3-5. A summary of the five Earth models considered in this study.

Model	Model description	Lithospheric thickness (km)	Upper mantle viscosity (Pa s)	Lower mantle viscosity (Pa s)
A	Thin lithosphere	96	$0.5 \cdot 10^{21}$	$1 \cdot 10^{22}$
B	Thin lithosphere, strong lower mantle	96	$0.5 \cdot 10^{21}$	$4 \cdot 10^{22}$
C	Thick lithosphere	120	$0.5 \cdot 10^{21}$	$1 \cdot 10^{22}$
D	Thick lithosphere, strong lower mantle	120	$0.5 \cdot 10^{21}$	$3 \cdot 10^{22}$
E	Thick lithosphere, strong upper mantle	120	$0.8 \cdot 10^{21}$	$1 \cdot 10^{22}$

For all of the loading models considered here, for the majority of the glacial cycle, there is less than ~20 m difference in predicted relative sea-level across all five Earth models (see Figure 3-35). However during the deglaciation of the Fennoscandian ice sheet, at around 14.5 kyr BP, the difference in predictions for the five Earth models increases to ~100 m for Forsmark. At any one time, differences in geoid height at any fixed point will be negligible if the same loading model is used; any differences in the relative sea-level are therefore due to variations in the solid Earth response to loading.

The divergence in the predictions is short-lived, implying that the phenomenon is related to the elastic properties of the lithosphere. In general, an Earth model with a thinner lithosphere will undergo the greatest isostatic deformation, resulting in the greatest relative sea-level prediction. From the results, it also seems that a model with a weaker lower mantle (e.g. models A and C) will undergo greater deformation than one with a stronger, or higher viscosity, lower mantle, while the model with the strongest upper mantle viscosity (model E), exhibits the smallest amount of solid Earth deformation.

Since the differences in relative sea-level predictions are short-lived, and very few relative sea-level data are available from this period, it is not possible to test these predictions against data in order to constrain the Earth parameters. Instead, present-day uplift rates must be used.

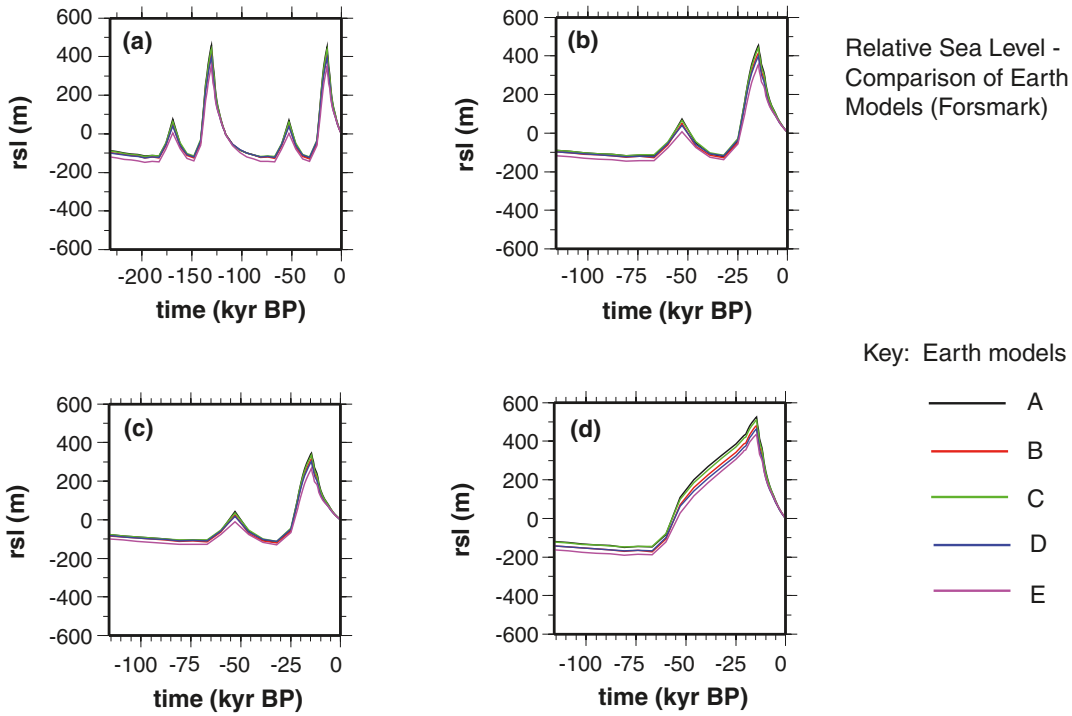

Figure 3-35. *Comparison of Earth models. Predicted relative sea-level curves for Forsmark for all five Earth models under consideration. See Table 3-4 for details of the loading models. a): Double Weichselian glacial cycle – loading model 2. b): Single Weichselian glacial cycle – loading model 1. c): Single Weichselian glacial cycle modified with 80% ice thickness in Fennoscandia – loading model 5. d): Single Weichselian glacial cycle modified with a constant, linear increase in ice thickness in Fennoscandia between 60 kyr BP and 20 kyr BP – loading model 7.*

Earth models with a thinner lithosphere (models A and B in Table 3-5) are predicted to experience greater present-day uplift rates, although the extent over which rebound takes place will be slightly smaller than for models with a thicker lithosphere (see Figure 3-36 and 3-37). Earth models with a weaker lower mantle (models A and C in Table 3-5) tend to experience greater present-day uplift rates, over a larger area, than models with the same lithospheric thickness but greater lower mantle viscosity (models B and D respectively in Table 3-5). The existence of a stronger upper mantle (model E in Table 3-5) also increases the predicted rate of uplift.

In reality, the Earth is not laterally homogeneous as assumed in these simulations, and variations in lithospheric thickness and mantle viscosity will perturb the GIA signal. /Paulson et al. 2005/ estimated that for realistic variations in mantle viscosity, present-day uplift rates may be altered by up to 10%. The effect of including a 3D Earth structure for Fennoscandia has been investigated by /Whitehouse 2009, Section 4.5.4/, part of which is presented in the section *A GIA case study with a Fennoscandian 3D Earth structure* below.

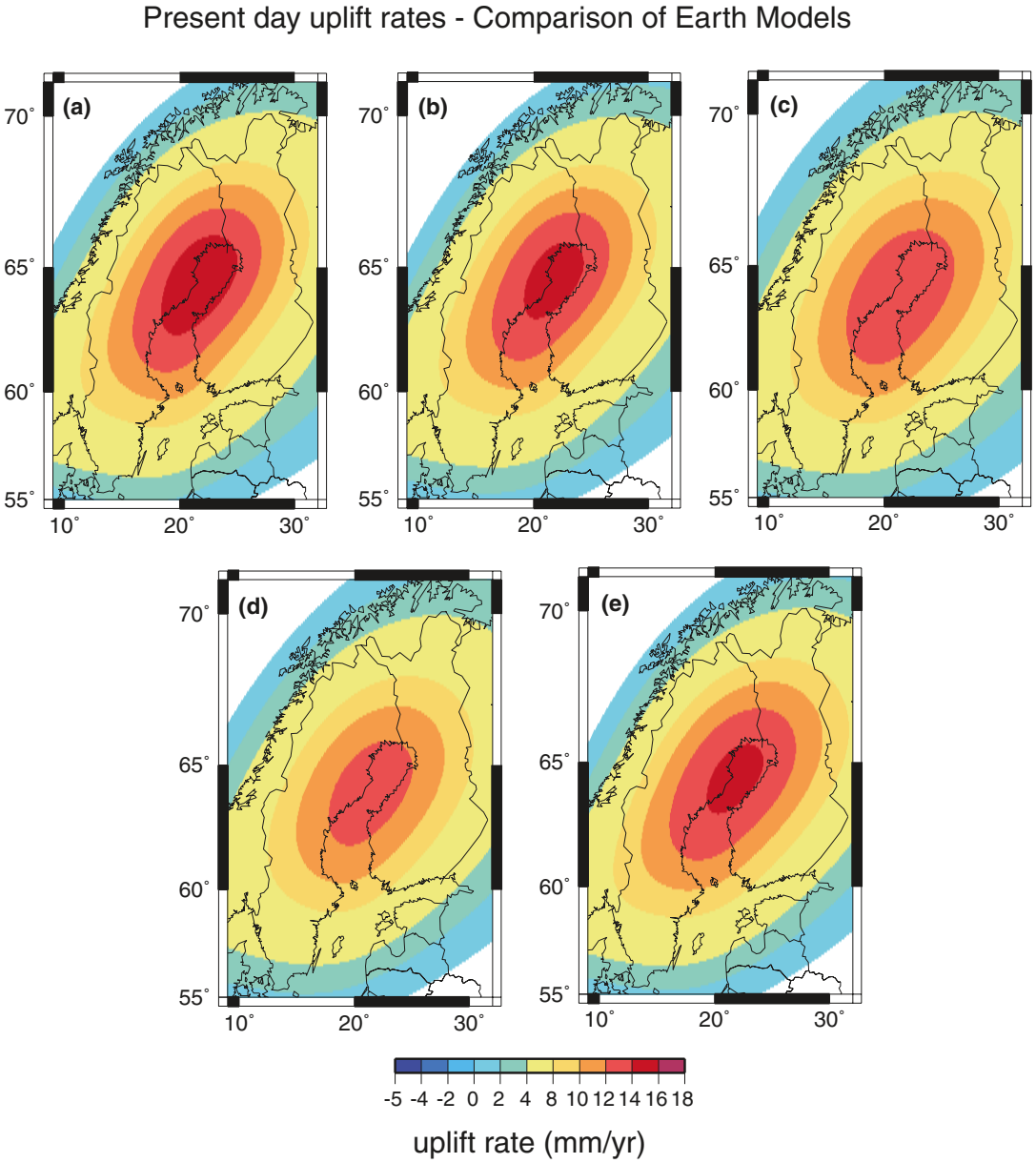

Figure 3-36. *Comparison of Earth models. Predicted present-day uplift rates throughout Fennoscandia for the five Earth models under consideration. The loading model is defined to be a single Weichselian glacial cycle (Model 1) in all cases. a) Earth model A. b) Earth model B. c) Earth model C. d) Earth model D. e) Earth model E.*

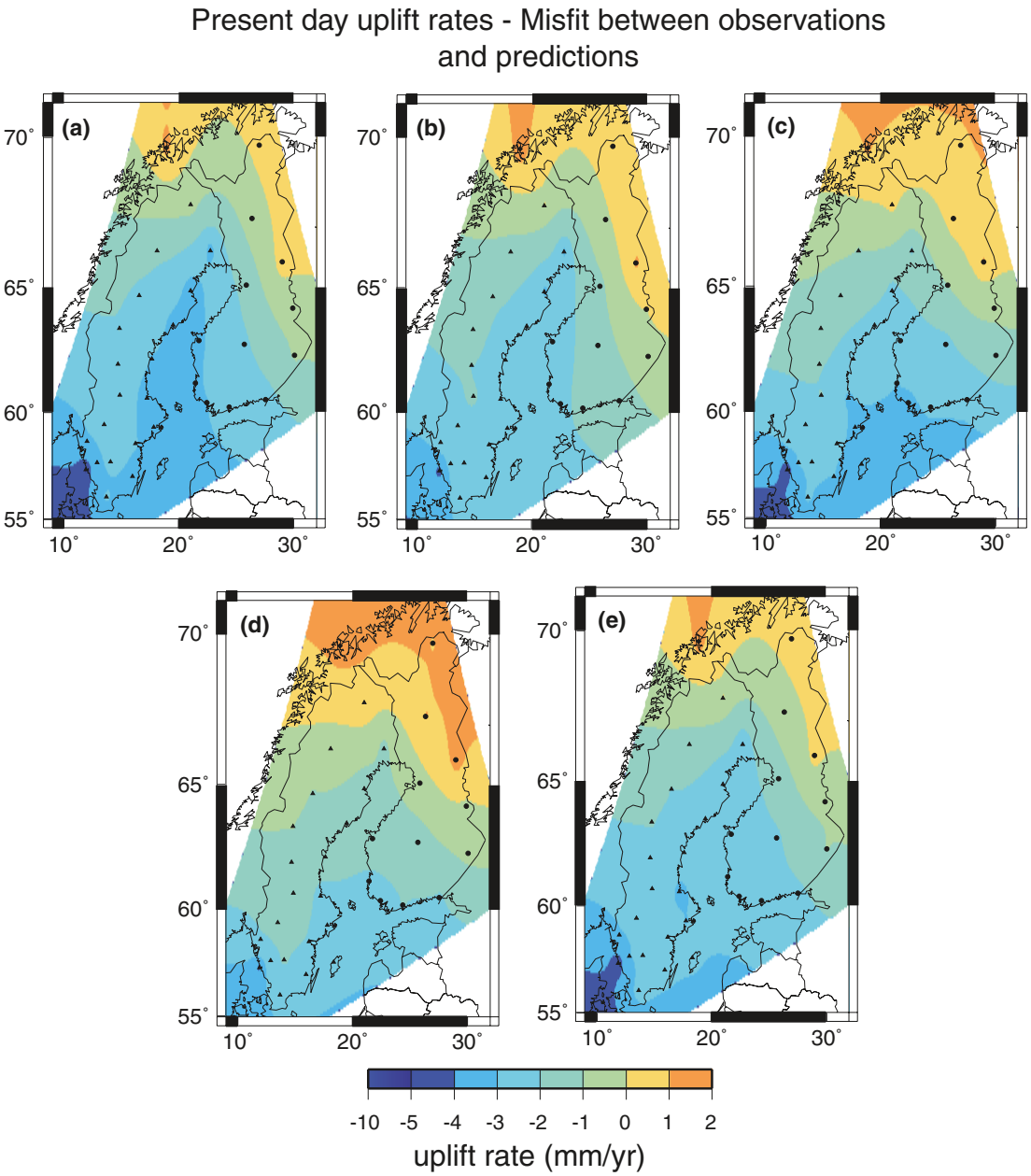

Figure 3-37. *Residual present-day uplift rates throughout Fennoscandia for the five Earth models under consideration. The predictions of Figure 3-36 are interpolated at the BIFROST GPS sites and then subtracted from the observed signal (see Figure 3-38). Loading and Earth models as in Figure 3-36.*

Isostatic memory

The time scale over which the GIA model is run has implications for the accuracy of relative sea-level predictions due to the viscous memory of the Earth model. The Earth is assumed to be in isostatic equilibrium at the start of a model run. In reality, the Earth is unlikely to reach such a state if the advance and decay of ice sheets continues with the same periodicity as seen in the past (Figure 1-2). Therefore, the model must be run for a long enough period that sufficient loading history is considered, and the initial condition of isostatic equilibrium does not affect predictions during the period of interest.

In order to investigate the recovery of the viscoelastic Earth model following unloading four loading models were defined.

- The ‘standard’ model: Weichselian glacial cycle loading is applied for a single glacial cycle.
- The ‘double’ model: Weichselian glacial cycle loading is applied over two consecutive glacial cycles.
- The ‘40 kyr’ model: Weichselian glacial cycle loading applied only from 40 kyr BP.
- The ‘80%’ model: Weichselian glacial cycle loading modified with only 80% ice thickness in Fennoscandia is applied for a single glacial cycle.

In all four cases, the loading models were run using three different Earth models (A, C and D in Table 3-5 above), and following the final loading time step at 0 kyr BP the relative sea-level calculations were allowed to run for another 60 kyr into the future without any further change to the distribution of surface loads, thus enabling the system to return to equilibrium.

The vertical solid Earth response was calculated at six sites for each model run. These sites were chosen to lie roughly 250 km apart along a profile running approximately south from the present-day centre of isostatic uplift (see Figure 3-38) in order to investigate the solid Earth response at a range of distances from the previous centre of ice loading, and for a range of loading histories.

Deformation at each of the six sites is defined to be zero at the start of the model run. During the experiment, solid Earth deformation at each site is measured relative to the initial position, with negative values indicating a decrease in elevation due to isostatic subsidence. The timing and magnitude of maximum depression is recorded in each case, and when the deflection of the site returns to less than 1% of the maximum deflection, equilibrium is assumed. The isostatic signal at sites 1, 4 and 6 are shown in Figure 3-39, whereas Table 3-6 summarises the results of the model runs.

For a given site and Earth model, there is little variation in the recovery time for the four different loading models. The shortest loading model is initiated only ~25 kyr before the timing of maximum deformation, and the difference in solid Earth deformation between this model and the double-cycle loading model is negligible from the timing of maximum deformation onwards (see Figure 3-39). Therefore the isostatic response of the Earth models is not dependent upon loading prior to ~25 kyr before the timing of maximum deformation, and a loading model need only contain information from ~25 kyr prior to the period of interest to ensure no distortion of the results due to initial conditions.

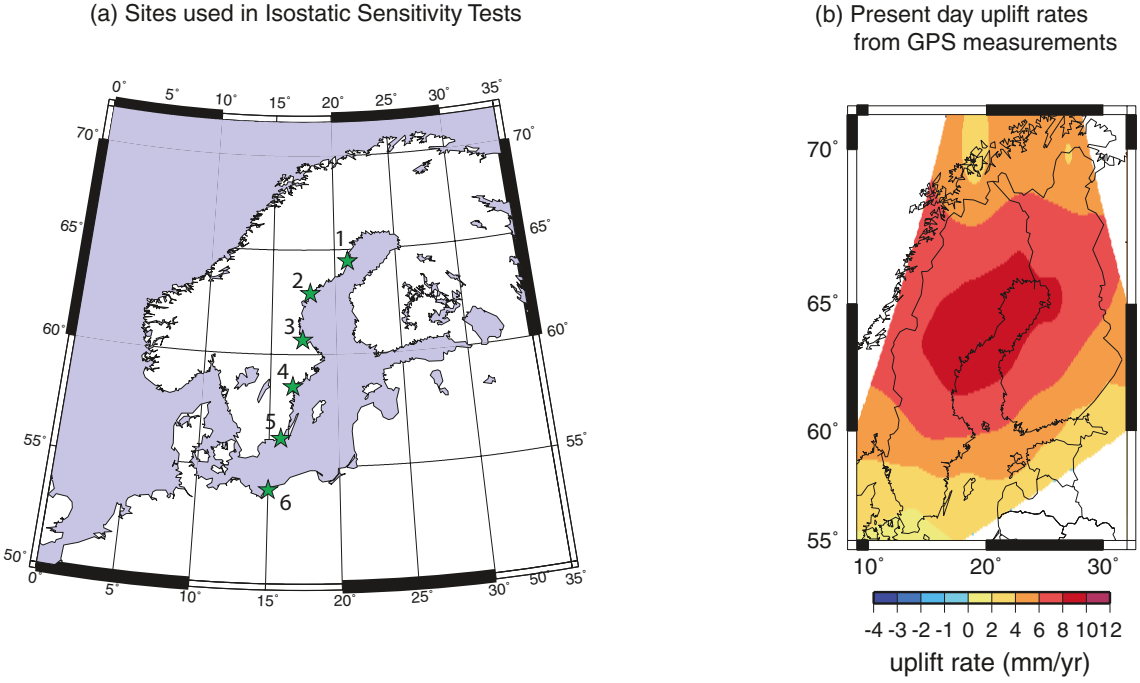

Figure 3-38. *a) Map showing the location of the six sites (green stars) where the isostatic response is calculated and b) the present-day pattern of uplift in Fennoscandia from BIFROST GPS rates /Johansson et al. 2002/.*

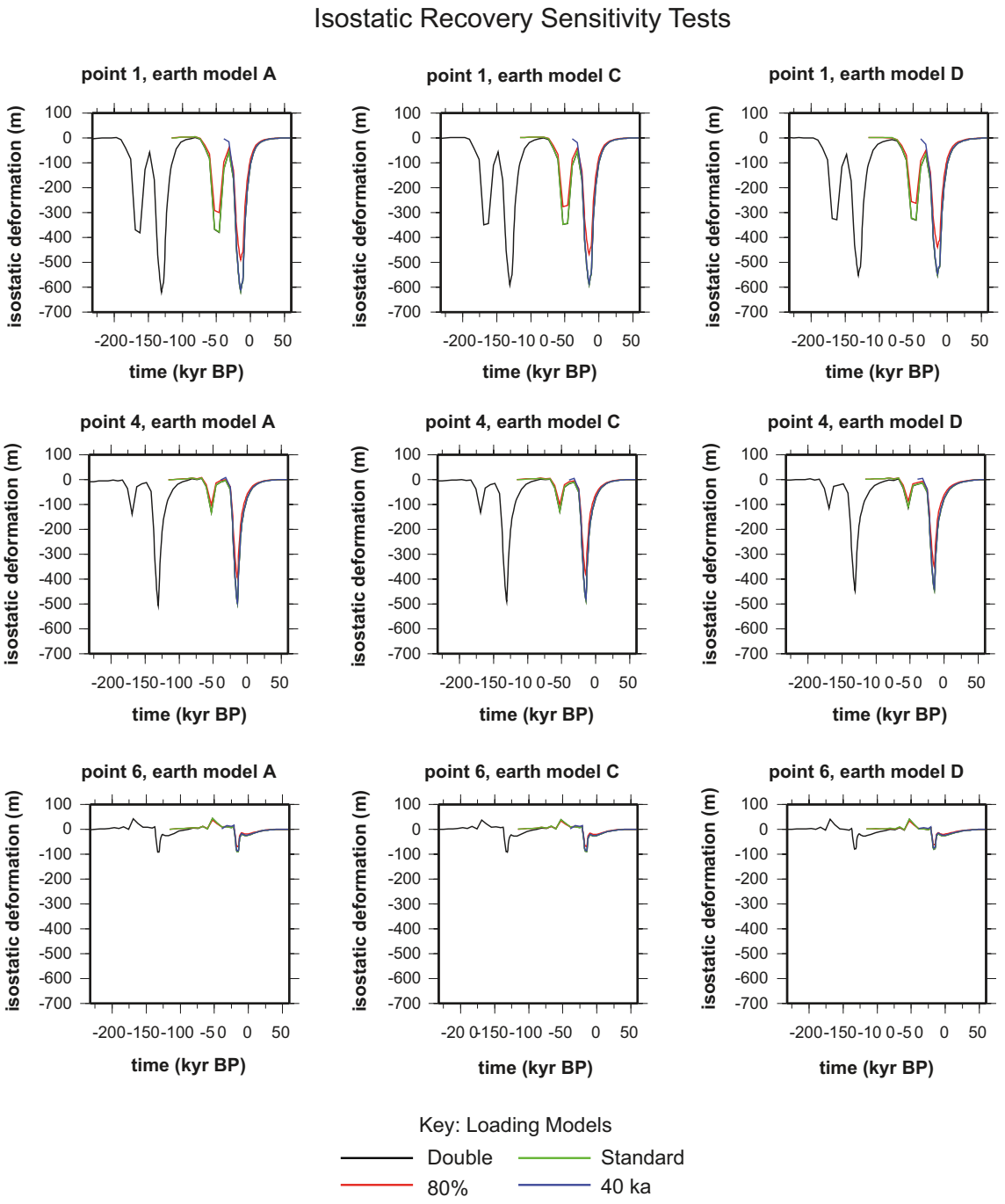

Figure 3-39. *Isostatic recovery sensitivity tests. Solid Earth deformation at sites 1, 4 and 6 (see Figure 3-38) for the four loading models and three Earth models described in the isostatic recovery sensitivity tests.*

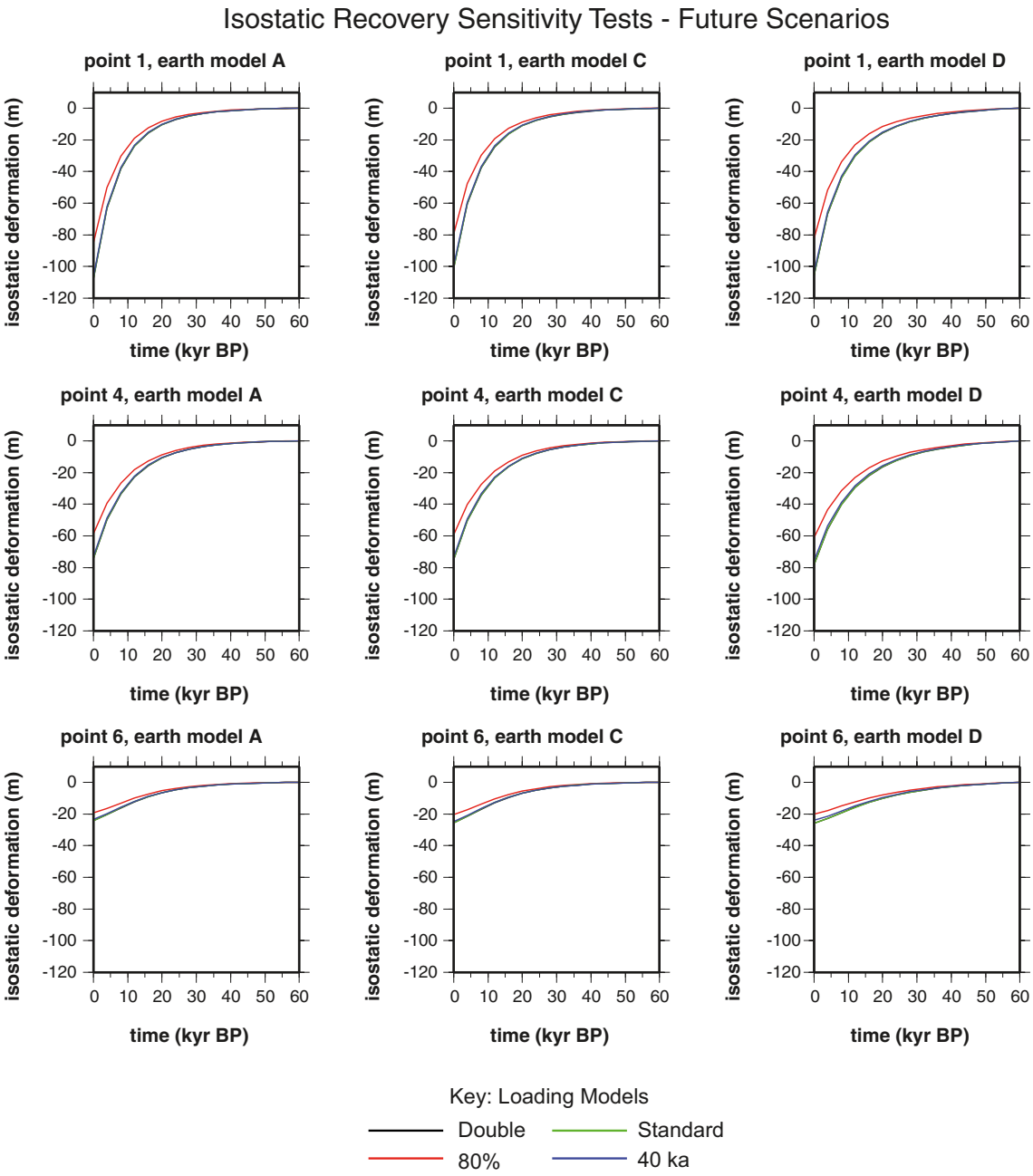

Figure 3-40. *Isostatic recovery sensitivity tests. Predictions of deformation between the present day and 60 kyr in the future. Deformation at the present day may be regarded as the remaining deformation before equilibrium is attained. Other details as for Figure 3-39.*

Table 3-6. Results of the isostatic recovery sensitivity tests. Each triplet of numbers, '(a/b) c', describe the time of maximum depression in kyr BP (a), the time of return to equilibrium in kyr after present (b), and the time it takes to return to equilibrium in kyr (c = b–a).

Earth model	Loading model	Point 1	Point 2	Point 3	Point 4	Point 5	Point 6
A	40 kyr	(–14.5/28) 42.5	(–14.5/28) 42.5	(–14.5/28) 42.5	(–14.5/32) 46.5	(–14.5/36) 50.5	(–15/44) 59
C	40 kyr	(–14.5/28) 42.5	(–14.5/28) 42.5	(–14.5/28) 42.5	(–14.5/32) 46.5	(–14.5/36) 50.5	(–15/44) 59
D	40 kyr	(–14.5/36) 50.5	(–14.5/36) 50.5	(–14.5/36) 50.5	(–14.5/40) 54.5	(–15/44) 59	(–17/56) 73
A	Standard	(–14.5/28) 42.5	(–14.5/28) 42.5	(–14.5/28) 42.5	(–14.5/32) 46.5	(–14.5/36) 50.5	(–15/44) 59
C	Standard	(–14.5/28) 42.5	(–14.5/28) 42.5	(–14.5/32) 46.5	(–14.5/32) 46.5	(–14.5/36) 50.5	(–15/44) 59
D	Standard	(–14.5/36) 50.5	(–14.5/36) 50.5	(–14.5/36) 50.5	(–14.5/40) 54.5	(–15/44) 59	(–17/52) 69
A	80%	(–14.5/28) 42.5	(–14.5/28) 42.5	(–14.5/28) 42.5	(–14.5/32) 46.5	(–14.5/36) 50.5	(–15/44) 59
C	80%	(–14.5/28) 42.5	(–14.5/28) 42.5	(–14.5/32) 46.5	(–14.5/32) 46.5	(–14.5/36) 50.5	(–15/44) 59
D	80%	(–14.5/36) 50.5	(–14.5/36) 50.5	(–14.5/36) 50.5	(–14.5/40) 54.5	(–15/44) 59	(–17/56) 73
A	Double	(–14.5/28) 42.5	(–14.5/28) 42.5	(–14.5/28) 42.5	(–14.5/32) 46.5	(–14.5/36) 50.5	(–15/44) 59
C	Double	(–14.5/28) 42.5	(–14.5/32) 46.5	(–14.5/32) 46.5	(–14.5/32) 46.5	(–14.5/36) 50.5	(–15/44) 59
D	Double	(–14.5/36) 50.5	(–14.5/36) 50.5	(–14.5/36) 50.5	(–14.5/40) 54.5	(–15/44) 59	(–17/56) 73

Following unloading, the time to reach equilibrium varies between ~40 kyr and ~75 kyr. This range, and the observation that regions of maximum deformation recover more rapidly, may partly be attributed to the non-linear nature of solid Earth rebound. However, the distribution of relaxation times is principally an artefact of the method by which rebound is calculated: The rebound criterion states that deflection must return to within 1% of the maximum deflection. Therefore regions of greatest deformation seem to recover more rapidly as they only need return to a larger absolute deflection. The positive isostatic deformation at point 6 (Figure 3-39) indicates that this site was uplifted as part of a glacial forebulge prior to being loaded. For all sites, the time for recovery was found to be similar for Earth models A and C, but the model with the stiffer lower mantle (Earth model D) took consistently longer to reach maximum deformation and recover to equilibrium.

The '80%' model was included in this study because it gives the closest fit to present-day uplift rates using the 1D GIA model. However, despite attaining a smaller maximum amount of deformation, the long-term rate of recovery for this loading model is not substantially different from that for models with 100% ice thickness. Therefore, the rate of isostatic recovery is not strongly dependent upon the magnitude of the load, but rather the timing of loading.

Importance of far-field ice sheets

Variations in the far-field Laurentide and Antarctic ice sheets perturb the shape and height of the global geoid signal, and generate an isostatic solid Earth response. Due to the distance of Fennoscandia from these ice sheets, the geoid signal will effectively be detected as a near-uniform rise or fall in the height of the geoid/ocean surface, dependent upon the surface mass change associated with these far-field ice sheets and distance from these surface masses. The solid surface signal due to far-field ice sheets will only be detectable in Fennoscandia if this region is located upon the forebulge of the deformation, as was the case during the maximum extent of the Laurentide ice sheet during the LGM /Mitrovica et al. 1994/.

The magnitude of the solid Earth signal due to far-field ice sheet loading was calculated using a standard global ice loading model for a single glacial cycle /Tushingham and Peltier 1991/ with the ice removed from Fennoscandia during the last glacial cycle. Estimates of horizontal and vertical deformation at the proposed site of Forsmark are shown in Figure 3-41.

The positive sign of the predicted vertical deformation due to far-field ice loading at Forsmark (Figure 3-41a) indicates that the site was situated on the deformational forebulge of the Laurentide ice sheet, as predicted by /Mitrovica et al. 1994/. However, the calculated signal may overpredict reality, due to the neglect of any lateral structure in the Earth model, see section *A GIA case study with a Fennoscandian 3D Earth structure* below. The negative sign of the horizontal deformation indicates motion in an easterly direction. The non-zero magnitude of predicted deformation at the present day simply implies that the system has not yet returned to equilibrium following the removal of the far-field ice load.

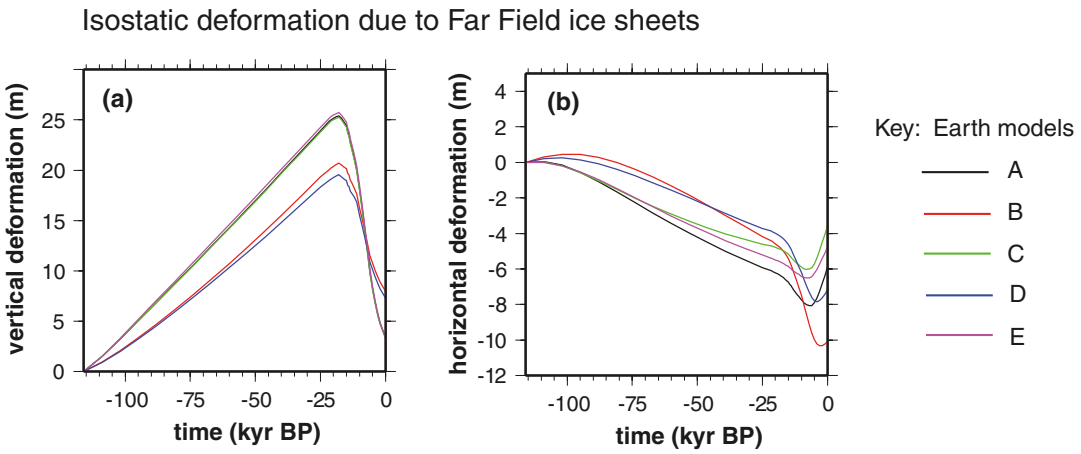

Figure 3-41. *Solid surface deformation at Forsmark due to far-field ice loading. See Table 3-5 for a description of the Earth models used. a) vertical deformation, b) horizontal deformation.*

The vertical deformation peaked at 18kyr BP, coincident with the maximum extent of the Laurentide ice sheet. The steady increase in the signal over time is a result of the gradual growth of the Laurentide ice sheet throughout the last glacial cycle. The magnitude of this deformation reached ~25 m for Earth models with a smaller lower mantle viscosity of $1{\cdot}10^{22}$ Pa s (models A, C and E), and only ~20 m for Earth models with a stronger lower mantle (models B and D). The strong lower mantle models demonstrate a slower, smaller response to loading, and a slower rate of recovery following unloading.

This separation in the style of deformation according to lower mantle viscosity is also seen in the smaller horizontal signal (Figure 3-41b). When a stronger lower mantle is assumed, the magnitude of deformation is smaller during the majority of the glacial cycle, except during deglaciation, when the recovery of the solid Earth is delayed by ~10 kyr for these models. The reason for this is unclear, but should provide a useful constraint upon lower mantle viscosities when testing predictions against data. In general, horizontal deformation peaks later than vertical deformation; at ~14.5 kyr BP for models with a weaker lower mantle, and ~4 kyr BP for models with a stronger lower mantle. A greater magnitude of horizontal deformation is predicted for models with a thinner lithospheric thickness of 96 km (as opposed to 120 km), but the absolute magnitude of the difference is small, and this phenomenon is not apparent in the vertical signal.

The magnitude of the far-field signal is small in comparison with predictions of near-field isostatic deformation (less than 10% of the total signal) during the Weichselian glaciation, but must not be neglected.

A GIA case study with a Fennoscandian 3D Earth structure

Note that in this 3D Earth structure case study, adapted from /Whitehouse 2009/, the overall aim is to investigate the sensitivity of GIA predictions to lateral Earth structure. To this end a comparison is made between dedicated 1D and 3D GIA simulation where the Earth structure has been specifically adjusted in order to give a relevant comparison between the two models. In turn, this means that the Earth structures have not been selected to give a best fit of e.g. uplift rates and shore-level displacement against observed data. Also note that the 1D-3D comparison study described here uses another ice sheet load history than the Weichselian glacial cycle used in the 1D simulations described in previous parts of Section 3.3.4.

State-of-the-art GIA models that account for 3D Earth structure use a range of geophysical observables to infer lateral variations in lithospheric thickness and mantle viscosity. Rayleigh wave dispersion data have been used to indicate variations in the thickness of the seismic lithosphere in Fennoscandia /Calcagnile 1982/, while coherence studies have been used in the same region to study gradients of flexural rigidity and elastic thickness /Poudjom Djomani et al. 1999, Watts 2001, Pérez-Gussinyé et al. 2004/. Fennoscandian lithospheric thickness variations, derived from elastic thickness estimates, are shown in Figure 3-42.

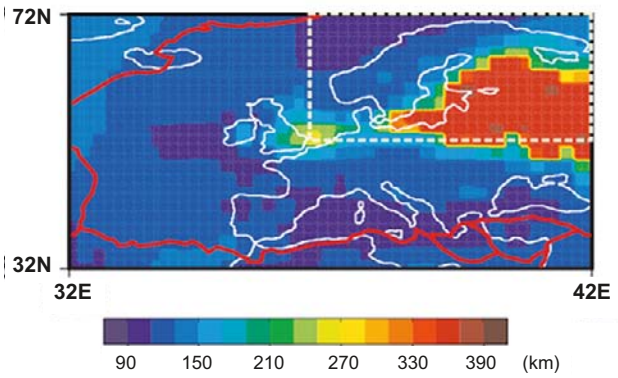

Figure 3-42. *Lithospheric thickness derived from the elastic thickness model of /Watts 2001/ and /Pérez-Gussinyé et al. 2004/. This is part of a global model where the thicknesses have been scaled to ensure a global mean lithospheric thickness of 120 km. The red lines define plate boundaries. The dashed area is used to define a Fennoscandian regional mode studied in /Whitehouse 2009/ (see text).*

A first-order observation from GIA studies that include 3D Earth structure is that lateral variations in mantle viscosity affect the magnitude, but not the pattern, of GIA-related *uplift* rates, however they affect both the magnitude and direction of *tangential* velocity rates /Kaufmann and Wu 1998, Kaufmann et al. 2000, Kaufmann and Wu 2002, Latychev et al. 2005b, Whitehouse et al. 2006/. A case study into the effect of including realistic Earth structure in Fennoscandian GIA models is presented here.

The sea-level theory presented in /Mitrovica and Milne 2003/ is implemented using the 3D finite volume model of /Latychev et al. 2005a/ to solve the sea-level equation on a spherical, rotating Earth. Even though this study focuses upon Fennoscandia, global calculations are carried out to ensure the correct redistribution of meltwater throughout the oceans.To give a global ice-loading history for the whole of the last glacial cycle that is tuned to fit global ice volumes as determined using far-field sea-level data /Bassett et al. 2005/, the ICE-3G global ice model of /Tushingham and Peltier 1991/ is used for all ice sheets except in Fennoscandia where the ice model of /Lambeck et al. 1998/ is used, see Figure 3-43.

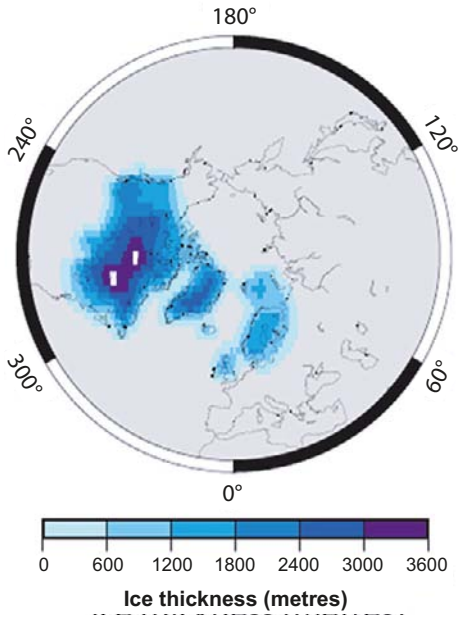

Figure 3-43. *Ice thicknesses in the Northern Hemisphere at the LGM (20 kyrs BP). From the model of /Tushingham and Peltier 1991, Lambeck et al. 1998/.*

Calculations are initially carried out using a 1D Earth model with a lithospheric thickness of 120 km, an upper mantle viscosity of $5 \cdot 10^{20}$ Pa s, and a lower mantle viscosity of $5 \cdot 10^{21}$ Pa s. The calculations are then repeated using an Earth model that includes lateral variations in lithospheric thickness and mantle viscosity, and attempts to account for the presence of plate boundaries. The 3D Earth model was derived using estimates of elastic thickness as a proxy for lithospheric thickness, and seismic velocity anomalies as a proxy for mantle viscosity. Plate boundary zones are defined to be 200 km-wide bands of low ($2 \cdot 10^{20}$ Pa s) viscosity within the lithosphere. Portions of this model are shown in Figure 3-42.

A scaling method is used to ensure that the 1D and 3D Earth models have the same depth-averaged mean structure; thus permitting a meaningful comparison of the results. For the lithosphere, this means that the elastic thicknesses of the 3D model were multiplied by a uniform constant to ensure that the global mean lithospheric thickness is still 120 km. This results in the use of lithospheric thicknesses of more than 300 km for the Fennoscandian shield: these values are larger than independent estimates e.g. /Calcagnile 1982/, but it should be noted that this study was carried out to explore the sensitivity of GIA calculations to variations in lateral Earth structure, and does not seek to accurately replicate global 3D Earth structure.

For the mantle, the logarithm of the lateral viscosity perturbations at each depth (the calculations are carried out upon a finite volume grid) are multiplied by a uniform constant to ensure the mean for that depth is the same as in the 1D model. For further details of the construction of the Earth model see /Whitehouse et al. 2006/.

Figure 3-44 shows the predicted present-day uplift and horizontal deformation rates for Fennoscandia generated using the 1D Earth model. Uplift is centred upon the region of maximum ice-loading, and horizontal deformation exhibits a radial pattern of motion away from the centre of uplift.

Figure 3-45 shows the misfit in present-day vertical and horizontal deformation rates between the 1D and 3D models. Note that the maximum differences of ~3 mm/yr for uplift rates and ~1 mm/yr for horizontal rates are greater than the current limit of observational uncertainty (e.g. from GPS measurements), implying that any inferences of Earth structure obtained from the inversion of geodetic data will be biased if a 1D profile is assumed.

In Figure 3-45 the 1D model predictions are subtracted from the 3D model predictions, therefore the blue region surrounded by the orange band in Figure 3-45a indicates that the 1D model predicts higher maximum uplift rates and lower minimum subsidence rates (more negative) than the 3D model. The differences are predominantly related to the magnitude of the predictions, and not the pattern, indicating that the introduction of lateral Earth structure has little effect upon the geometry of predicted uplift rates. However, in Figure 3-45b the change in the direction of the arrows indicates that both the magnitude and the pattern of horizontal deformation are perturbed with the introduction of realistic lateral Earth structure.

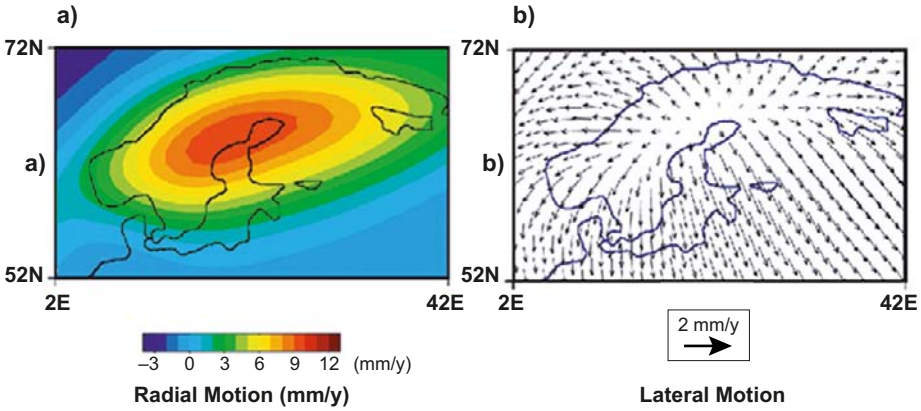

Figure 3-44. *Predicted present-day uplift rates (a) and tangential rates (b) generated using the best-fitting 1D Earth model for Fennoscandia and the ice model discussed in the text. Tangential rates are given relative to a point on the north coast of the Gulf of Bothnia.*

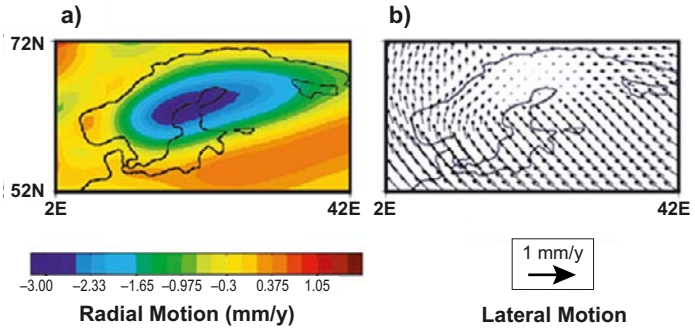

Figure 3-45. *Misfit between (a) uplift rates and (b) tangential rates generated using a 3D Earth model and a 1D Earth model. 1D rates are subtracted from 3D rates.*

The question of whether it will be possible to constrain 3D Earth structure via GIA modelling remains open. The large number of degrees of freedom means that it is unlikely to be possible to carry out a unique inversion of 3D viscosity structure using GIA observables. /Wu et al. 2005/ claim that 3D Earth structure can be resolved using relative sea-level data from the centre of present-day rebound. However, this is disputed in other studies e.g. /Spada et al. 2006, Whitehouse et al. 2006/, due to the similarity of the effect of lateral structure at different depths upon GIA observables. We investigate this aspect of GIA modelling below.

Figure 3-46 again shows the difference (3D minus 1D) between predicted vertical (left) and horizontal (right) deformation rates. A different aspect of the 3D model is varied in each row. In the first row (Figure 4-46a) lithospheric thickness variations are permitted in the 3D calculations, but upper and lower mantle viscosities are held at the uniform values of the 1D model. In the second row (Figure 3-46b) a band of low viscosity is defined within the lithosphere along plate boundaries to replicate the weak stress-coupling across these regions. Other parameters are fixed at the 1D values. In the third row (Figure 3-46c) upper mantle viscosities are allowed to vary laterally whereas the lower mantle viscosity and lithospheric thickness are held fixed, while in the fourth row (Figure 3-46d) lower mantle viscosities are allowed to vary while the upper mantle viscosity and lithospheric thickness are fixed. In the first, third and fourth cases, weak plate boundary zones are not included.

The similarity of Figures 3-46a and 3-46c, both in the magnitude of uplift differences and the direction of the horizontal misfit arrows, indicates that lateral Earth structure at different depths can produce similar velocity perturbations in Fennoscandia. Therefore it is unlikely that observations of present-day deformation rates will be able to uniquely infer the underlying Earth structure, or indeed identify the depth of any lateral heterogeneity.

The pattern in Figure 3-46d does not replicate the distribution of LGM ice-loading as in the previous cases, indicating a lesser dependence upon local ice-loading at lower mantle depths. Due to the transmission of stress, the lower mantle in Fennoscandia will play a part in supporting ice-loading in North America as well as Fennoscandia, and the pattern of horizontal perturbations, directed towards North America, reflects this.

The introduction of weak plate boundary zones induces a significant perturbation in horizontal deformation rates, but not vertical rates (Figure 3-46b). The reason for this is that the band of low viscosity decouples the transfer of stress across the plate boundary; the direction of the misfit arrows again reflects the non-negligible effect of North American ice sheet loading upon surface deformation in Europe. Uplift rates have a strong local dependence upon loading; hence there is no perturbation to these rates when plate boundaries are introduced.

The effect of introducing lateral Earth structure at different depths has an approximately linear cumulative effect upon present-day deformation rates. This may be deduced by observing that within the region of uplift the sum of the perturbations in Figure 3-46 approximately equals the cumulative effect (Figure 3-45a).

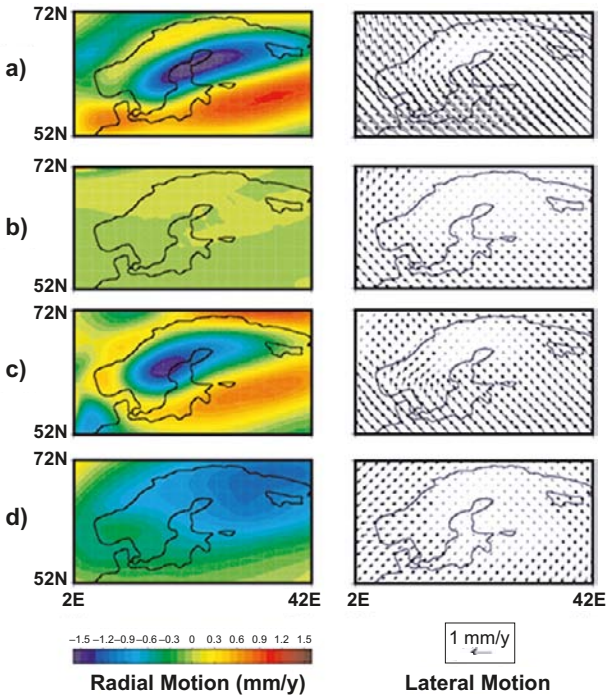

Figure 3-46. *(a) Misfit due to lateral variations in lithospheric thickness. (b) Misfit due to the inclusion of weak plate boundary zones. (c) Misfit due to lateral variations in upper mantle viscosity. (d) Misfit due to lateral variations in lower mantle viscosity. Left column: difference in uplift rates. Right column: difference in horizontal rates. All plots show 3D predictions minus 1D predictions.*

Predictions of relative sea-level history for the last 10 kyrs are also compared for the 1D and 3D models. Figure 3-47a shows the perturbation to relative sea-level predictions at 10 kyrs BP due to the inclusion of lateral Earth structure (3D prediction minus 1D prediction). There is again a strong correlation between the pattern of ice loading and the region of maximum perturbations, and there is also a large positive misfit to the east of Fennoscandia in the region of maximum lithospheric thickness (Figure 3-42). Once again the magnitude of perturbations due to the introduction of lateral Earth structure is greater than the observational uncertainty of relative sea-level data, which can be up to 10m. Therefore, the results show that inverting relative sea-level data to yield inferences of Earth parameters or ice loading history will lead to biased results if lateral structure is neglected.

Along the Norwegian west coast there is very little difference in predictions of relative sea-level by the two models at 10 kyrs BP. In the top left plot of Figure 3-48 the relative sea-level history for a coastal site with good relative sea-level data (Bjugn: shown by the left-hand star in the bottom plot of Figure 3-48) is plotted for the whole of the Holocene. The black curve is the prediction from the 1D model and the red curve is the prediction from the 3D model. The similarity of the curves is characteristic for sites along the length of this coastline, indicating that introducing lateral Earth structure into the GIA model makes little difference to Holocene relative sea-level predictions for this region. Relative sea-level data from the Norwegian west coast may therefore form a data set that is insensitive to the 3D Earth structure of this region, and hence may be used to tune GIA model inputs such as 1D Earth structure and ice load history. In this case, the poor fit to the data may be rectified by altering either the ice history or the depth-averaged viscosity profile of the Earth model.

The geographical region over which such data would be able to constrain input parameters is limited; it would be useful to also use relative sea-level data from within the Gulf of Bothnia to tune the GIA model. The predicted relative sea-level history for Ångermanälven is shown in the top right plot of Figure 3-48. Ångermanälven is the site of an extensive Holocene relative sea-level data set. It is situated on the east coast of Sweden (right-hand star in the bottom plot of Figure 3-48), in the centre of the region of maximum misfit for both uplift rates and 10 kyrs BP relative sea-level. The large difference between the two curves during the last 10 kyrs indicates that using such data to tune GIA model inputs will lead to biased inferences of Earth structure and ice history.

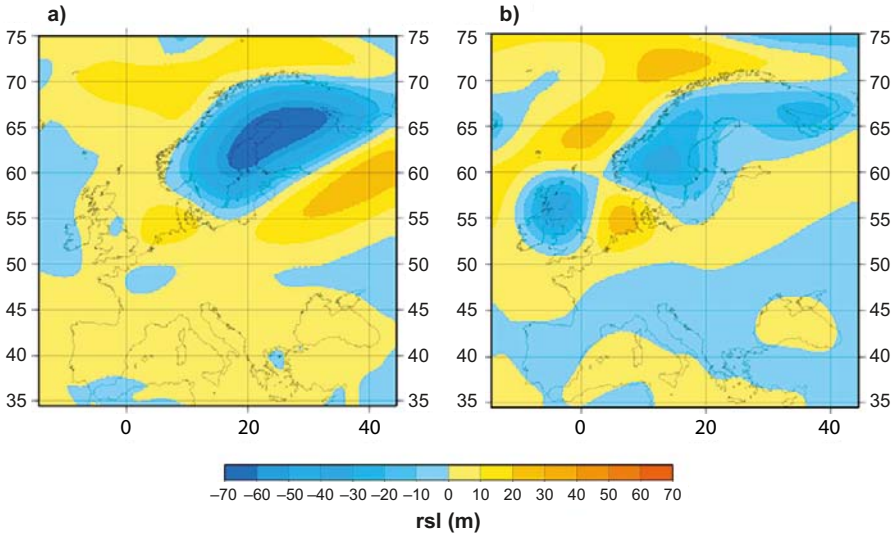

Figure 3-47. *Difference in relative sea-level predictions at 10 kyrs BP. (a) 3D model minus 1D model. (b) 3D model minus 'regional' 1D model (see text).*

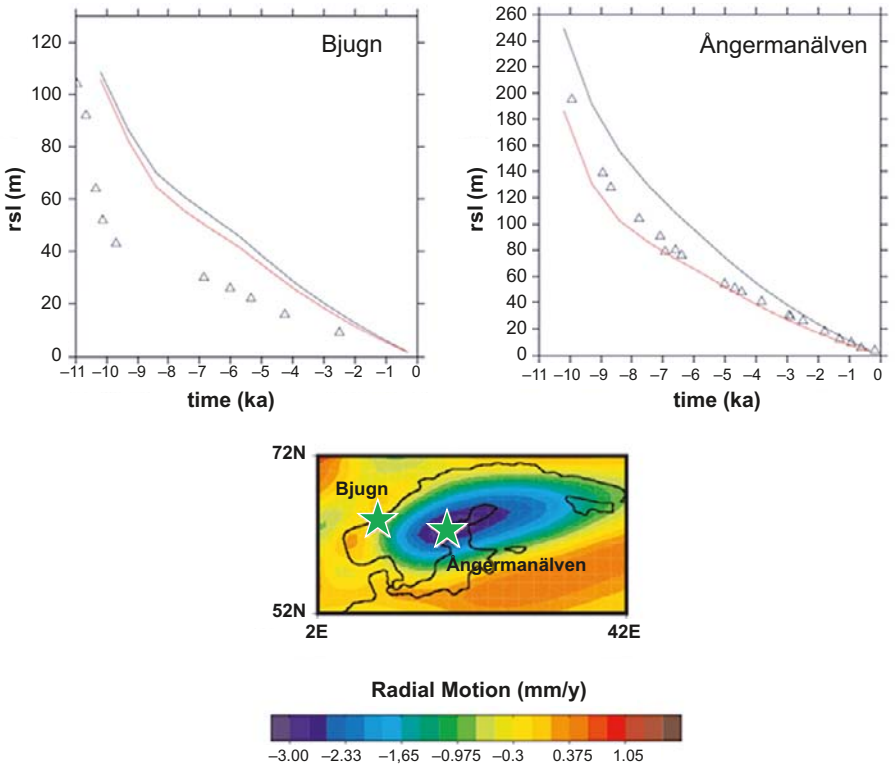

Figure 3-48. *Top left: Predicted relative sea-level history at Bjugn for the last 10 kyrs. Black line: 1D model. Red line: 3D model. Top right: Predicted relative sea-level history at Ångermanälven for the last 10 kyrs. Line colours are as for Bjugn. Relative sea-level data are shown as triangles; see /Lambeck et al. 1998/ for references. Bottom plot: Location map for Bjugn and Ångermanälven overlaid upon the misfit in uplift rates (as for Figure 3-45a).*

The difference in relative sea-level predictions for the 1D and 3D models is also plotted for Oskarshamn and Forsmark in Figure 3-49. To exemplify the magnitude of the error introduced by using a 1D Earth model instead of a 3D Earth model to predict relative sea-level, as done in the GIA studies, the difference at 10 kyrs BP is ~60 m at Forsmark (Figure 3-49).

The difference between 1D and 3D GIA simulations presented in this case study implies that ignoring lateral Earth structure and using a 1D Earth model in Fennoscandia leads to an over prediction of present-day uplift rates and the total amount relative sea-level change during deglaciation. This, in turn, conclusively shows that a significant part of the misfit between the 1D GIA model results and GPS observations arises from the 1D Earth structure assumption. In addition, the misfit could also include a component of having too large ice thickness in the Weichselian ice sheet reconstruction. In line with this, one general interpretation of the results from the case study is that using a 1D model will lead to inferred LGM ice thicknesses that are too small. A second general interpretation is that the use of a 1D model will lead to overestimates of mantle viscosity or lithospheric thickness in an attempt to fit the observational GPS and relative sea-level data.

It is computationally demanding to solve the sea-level equation using a full 3D model; therefore there is ongoing work to determine to what extent we can continue to improve our understanding of GIA using flat Earth models or a suite of spherically-symmetric 1D models. /Paulson et al. 2005/ suggest that GIA observables within formerly-loaded regions are only sensitive to the local viscosity structure, and a global model that adopts the relevant local viscosity structure should be sufficient to model GIA in that region. The situation becomes more complex away from the centre of the former ice sheets because GIA in these regions seems to be dependent upon both the local viscosity structure and that beneath the ice sheets, which may be different, thus a model that allows for lateral variations in viscosity is required.

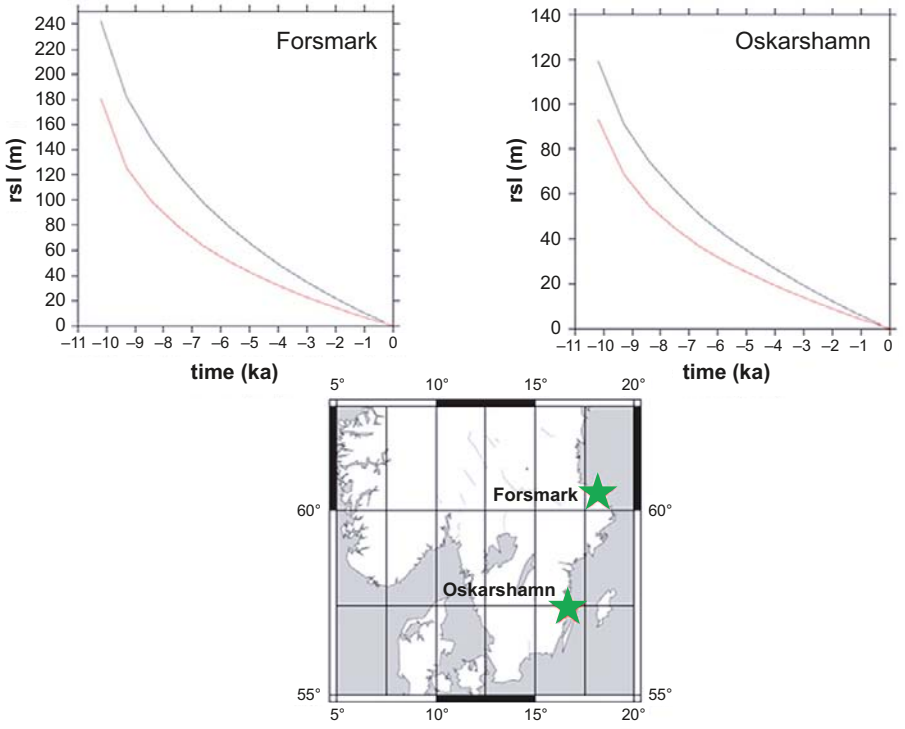

Figure 3-49. *Predicted relative sea-level curves for Forsmark and Oskarshamn calculated using 1D (black line) and 3D (red line) Earth models. Note that both the 1D and 3D GIA simulations used for this plot use another ice load history than the 1D GIA simulations in the previous parts of Section 3.3.4. The results should only be used to exemplify the error introduced by using 1D instead of 3D GIA modelling. At Forsmark, the difference at 10 kyrs BP is ~60 m.*

3.3.5 Time perspective

Shoreline migration is an ongoing process. It is strongly coupled to the global distribution of water between the oceans and land-based ice sheets, and the isostatic response of the Earth to loading during a glacial cycle. This isostatic deformation is a slow process in relation to the rate at which ice sheets grow and decay during such a cycle.

As ice sheets grow, water is removed from the oceans and global eustatic sea-level falls. During the build-up to the last glaciation, eustatic sea-level fell at a mean rate of ~1.3 mm/yr between 120 kyr BP and 20 kyr BP /Fleming et al. 1998, Yokoyama et al. 2000, Clark and Mix 2002, Milne et al. 2002, Peltier 2002, Mitrovica 2003/, although there were many departures from this rate during the build-up period, due to higher frequency climatic oscillations /Imbrie et al. 1984, Lambeck et al. 2002, Waelbroeck et al. 2002, Siddall et al. 2003/. During deglaciation, the initial rate of eustatic sea-level rise between ~21 kyr BP and 17 kyr BP was only ~6 mm/yr, followed by an average rate of ~10 mm/yr for the next 10 kyr /Fleming et al. 1998/. Perturbations from this rate occurred during meltwater pulses at ~14.5 kyr BP and ~11 kyr BP. These are attributed to rapid melting events, during which rates of eustatic sea-level rise reached ~15 mm/yr /Fairbanks 1989, Bard et al. 1990, 1996, Clark et al. 1996, Fleming et al. 1998, Lambeck and Chappell 2001, Lambeck et al. 2002, Peltier 2005, Bassett et al. 2005/. Rates of eustatic sea-level change fell to negligible values following the end of deglaciation around 5 kyr BP. However, meltwater is not distributed uniformly throughout the oceans due to the alteration to the shape of the geoid following the redistribution of surface masses. Sea-level can actually fall at sites within ~20° of a melting ice sheet /Farrell and Clark 1976/, therefore the rate of eustatic sea-level change is a poor indicator of local rates of sea-level change, especially for a local melt source.

The local rate of relative sea-level change incorporates both local changes in sea-level and the isostatic deformation of the solid Earth. The balance between rates of isostatic deformation and local sea-level change determine whether a site has advancing or retreating shorelines.

During the final build-up of the Fennoscandian ice sheet from ~32 kyr BP, isostatic rates of solid Earth subsidence due to surface loading by ice are estimated to have reached values of 40 mm/yr (see Section 3.3.4). During future glacial cycles, modelling predictions imply that maximum rates will be attained immediately prior to the time of greatest ice thickness. In general, the time of maximum ice thickness is predicted to precede the time of maximum solid Earth deformation, with the latter being delayed by up to ~3 kyr. During the period between maximum ice thickness and maximum deformation, the rate of solid Earth subsidence will decrease to zero.

There is usually a delay between the time of maximum deformation and the time at which a location becomes ice-free. Again, modelling predictions imply that as an ice sheet thins, rates of isostatic rebound will be low; < 20 mm/yr for this reconstruction of the Weichselian. Maximum rebound rates occur immediately following the final removal of an ice sheet, with uplift rates reaching ~75 mm/yr in this model at sites which had the greatest ice cover. The rate of rebound then decays exponentially with time; maximum rates at the centre of present-day uplift in Fennoscandia are ~10 mm/yr, and these are expected to decay to negligible values within the next 30 kyr (see Section 3.3.4).

During a glacial cycle, immediately following the removal of ice, local uplift rates are far greater than the rate of local sea-level changes, consequently a situation of regression dominates, and shorelines migrate oceanwards. The rate of shoreline migration depends upon the local gradient of topography. A typical Swedish Baltic Sea shoreline with a gradient of 2 m of elevation per 1km would experience 35 m/yr of oceanward shoreline migration for an uplift rate of 70 mm/yr, or 5 m/yr of oceanward shoreline migration for an uplift rate of 10 mm/yr (the present maximum in the Baltic region), assuming negligible changes in local sea-level.

A combination of decreasing rates of isostatic rebound and sea-level rise due to far-field melting slows the rate of regression with time, with a switch to transgression taking place if rates of local sea-level rise exceed the rate of local isostatic rebound. This situation is likely to arise during a global meltwater pulse at sites with low rebound rates, but will not be maintained because melting takes place on a shorter time scale than isostatic rebound. Rebound will once again become the dominant factor governing shoreline migration as sea-level changes become negligible. During the current interglacial period decaying uplift rates persist. These, along with processes related to ocean syphoning (see Section 3.3.1), act to maintain a situation of gradual oceanward shoreline migration throughout the majority of the Baltic region for the first few 10 kyr of an interglacial so long as the higher interglacial temperatures do not give rise to a longer-term melting event, such as the destabilization, and subsequent melting, of the Greenland Ice Sheet.

3.3.6 Handling in the safety assessment SR-Site

Isostatic evolution and shoreline displacement have been investigated by means of numerical modelling. In this context, the main question for the safety assessment is whether the Forsmark site is submerged or not. The salinity in the lake/sea covering the site is also of interest. A 1D GIA model has been used to simulate shoreline migration. The evolution of the shoreline has been calculated for a glacial-interglacial cycle using a loading function based on the Weichselian ice sheet simulation described in Section 3.1.4. The GIA model used for generating the Weichselian glacial cycle is that developed by Milne /Mitrovica and Milne 2003/. The *global* ice-loading function used in the study is modified from the ICE3G deglaciation history /Tushingham and Peltier 1991/, and has been calibrated using far-field relative sea-level data. A eustatic curve has been used to tune the mass of ice contained within far-field ice sheets. The Earth model is based on Maxwell rheology with a 1D radial three-layer structure. The lithosphere is represented by a 96 km thick layer with a very high viscosity and thus behaves as an elastic medium over GIA time scales, the density and elastic structure are from the preliminary reference Earth model (PREM) which has been determined to a high degree of accuracy by seismic methods /Dziewonski and Anderson 1981/.

At the start of a GIA model run, the Earth is assumed to be in isostatic equilibrium. In reality, the Earth is unlikely to reach such a state if glaciations occur with similar periodicity as in the past. To correct for this, the GIA modelling has been initiated by a glacial loading history yielding shorelines comparable to those reported by /Funder et al. 2002/ at the peak of marine inundation in the Early Eemian about 130 kyrs before present.

Complementary 3D GIA simulations have been made in order to quantify the error introduced by using a laterally homogeneous Earth model. The results show that the 1D modelling simulations probably over-predict the isostatic response to the ice sheet load as well as present day uplift rates.

For the analysis of the biosphere and hydrological evolution the shoreline evolutions during the first thousands of years of the initial period with temperate climate domain is extrapolated from shoreline data /Påsse 2001/, see Section 4.5.2. For further, detailed information on the GIA modelling, see the preceding parts of Section 3.3.

3.3.7 Handling of uncertainties in SR-Site

Uncertainties in mechanistic understanding

The processes involved in GIA, and their effect upon shoreline migration, are very well understood. There are no major uncertainties in our understanding of the mechanistic processes that cause shoreline migration.

Model simplification uncertainty

- Discussions of the uncertainty in the calculated shoreline are based on the sensitivity analysis and case study presented above.

  The assumption of a 1D Earth model is a simplification of the situation in Fennoscandia. A comparison between 1D and 3D GIA simulations /Whitehouse 2009/ shows that the assumption of a laterally homogeneous (1D) Earth structure over Fennoscandia probably results in an over-prediction of the isostatic response to ice sheet load and present-day uplift rates. As an example, the 1D-3D GIA model comparison shows that the 1D simulation potentially overestimates the relative sea-level change over the last 10 kyrs by up to 60 m at Forsmark.

- The time discretisation of the basic loading model is fairly coarse (every 7 kyr) between 116 kyr BP and 21 kyr BP, reflecting the lack of constraints upon ice history and sea-level prior to the LGM. If long time steps are used the loading function may be under- or over-estimated, leading to inaccuracies in relative sea-level, and hence shoreline migration, predictions for this period. A higher time resolution has been investigated, and discrepancies in relative sea-level predictions may be up to 50 m between a model that uses a time step of 7 kyr and one that uses a time step of 1 kyr, during periods of rapid change in ice sheet geometry. However, using a coarse time scale during the early stages of a model run has a negligible effect upon predictions of relative sea-level change during the latter stages of a model run. A high resolution time scale has been used for ice loading since the LGM, i.e. for the period when ice history is known reasonably accurately.

- At the beginning of a model run, the Earth is assumed to be in a state of isostatic equilibrium, with no deformation remaining from a previous glacial cycle or any other process that upsets the isostatic balance of the system. In reality, as the Earth enters each glacial cycle it will be pre-stressed, with deformation ongoing as a result of the previous loading event. GIA-induced deformation decays over a few tens of thousands of years, and after this period there will be a negligible difference between predictions from a model that started from equilibrium and one that was pre-stressed. However, in order to reproduce the relative sea-level evolution for the Weichselian as closely as possible the model was run twice in succession, with the second run taken to represent the Weichselian development. Nevertheless, a degree of inaccuracy remains at early times in the model since deformation will depend upon the details of the Saalian deglaciation, about which very little is known.

Input data and data uncertainty

As demonstrated by the similarity of the shoreline predictions for a range of rheological parameters in Section 3.3.4, uncertainties in the lithospheric thickness and mantle viscosity parameters are currently significant. The values of such parameters will be more tightly constrained following detailed analysis of the results of the GIA modelling in comparison with relative sea-level and GPS data.

3.3.8 Adequacy of references

The SKB report produced for the handling of isostatic adjustment and shore-level changes /Whitehouse 2009/ has undergone the SR-Site QA system handling, including a documented factual review procedure. Also the SR-Can Climate report /SKB 2006a/, from which some of the studies are used, has undergone QA system handling including a factual review process. Other references used for the handling of ice sheet dynamical processes are peer-reviewed papers from the scientific literature.

3.4 Permafrost

3.4.1 Overview/general description

Permafrost is defined as ground which remains at or below 0°C isotherm for at least two consecutive years /French 2007/. This definition is based exclusively on temperature, and disregards the texture, degree of compactation, water content, and lithologic character of the material. As a result, the term *permafrost* does not always equate to *perennially frozen ground*, since depending on pressure and composition of groundwater and on adsorptive and capillary properties of ground matter, water in ground may freeze at temperatures below 0°C. Therefore, permafrost encompasses the perennially frozen ground and a surrounding so-called *cryopeg*, i.e. a ground layer in which water remains unfrozen at sub-zero temperatures.

Permafrost and perennially frozen ground originate from the ground surface depending on a complex heat exchange process across the atmosphere/ground boundary layers and on an almost time-invariant geothermal heat flow from the Earth's interior. The heat exchange between the atmosphere and the Earth's surface is governed by solar radiation, longwave terrestrial and atmospheric radiations, sensible and terrestrial heat fluxes, and evaporation and condensation /Lockwood 1979, Washburn 1979, Lunardini 1981, Williams and Smith 1989, Smith and Riseborough 1996, Yershov 1998/.

Freezing of water within permafrost is based on the thermodynamics of interdependent thermal, hydraulic, mechanical, and chemical processes in the ground. In addition, freezing of water influences the thermal, hydraulic, mechanical, and chemical behaviour of the ground. Thermal properties change from those of unfrozen ground to those of frozen ground, affecting the heat transfer process. Ice formation in pores of the ground confines groundwater flow through the almost impermeable frozen ground, therefore altering the overall groundwater circulation. Ice formation can also cause deformation of the ground and changes in the mechanical stress state. Frost weathering and degradation of the ground surface and patterned ground are additional consequences of cyclic freezing and thawing processes. Moreover, exclusion of salts in the freezing of saline groundwater can lead to increased salinity concentrations in the unfrozen cryopeg.

Issues associated with permafrost development in the geosphere are comprehensively explained in /Washburn 1979, Williams and Smith 1989, Yershov 1998, French 2007/ and reviewed in e.g. /Gascoyne 2000, Ahonen 2001, Vidstrand 2003/. Experimental investigations of thermal-, hydrochemical- and mechanical impacts of freezing on bedrock properties have been reported by e.g. /Mackay 1997, Ruskeeniemi et al. 2002, Ruskeeniemi et al. 2004/, whereas model studies dealing with permafrost development in ground under climate change can be found in e.g. /Lunardini 1995, Kukkonen and Šafanda 2001/. More recently, some model studies on thermo-hydro-mechanical impacts of freezing processes on bedrock properties with implications for interactions between glaciers and permafrost in a time frame of a glaciation cycle (~100,000 years) have been conducted, e.g. /Bauder et al. 2003, Hartikainen 2004, SKB 2006a, Person et al. 2007, Lemieux et al. 2008a, b, c/. The effects of freezing of the geosphere on groundwater flow have been studied by e.g. /Vidstrand et al. 2010/.

3.4.2 Controlling conditions and factors

Climate and surface conditions

The principal factors controlling the heat exchange between the atmosphere and the Earth's surface are climate, topography, vegetation and snow covers, soil characteristics and water bodies. These factors are mutually dependent and can vary considerably in time and location. The main climatic parameters are insolation, air temperature, wind, and precipitation. Insolation is a driving force governing the heat exchange between the atmosphere and the Earth's surface and affecting the other climatic parameters. Air temperature, which is commonly applied to map permafrost distribution, controls the longwave atmospheric radiation, the turbulent heat exchange, and evaporation and condensation. Wind, in turn, mainly influences the sensible heat exchange, but also latent heat production and loss. Precipitation together with evaporation and condensation determine groundwater recharge, affecting the groundwater content and flow and hence the terrestrial heat flux.

Topography has a significant impact on climate conditions. Generally, air temperature decreases as altitude increases being affected by radiation, convection and condensation. The average air temperature decrease is approximately 0.65°C for every 100 metres increase in height /Danielson et al. 2003/. In addition, inversions are common in hilly terrain causing low-slope low-lying areas to experience significantly lower temperatures than higher lying and steeper-slope areas. Furthermore, the slope angle and azimuth affect the flux of shortwave radiation, and where topographical differences are large a more patchy distribution of permafrost is expected.

Vegetation and snow covers are sensitive to climatic conditions and topography. The characteristic parameters of the surface cover are surface albedo, emissivity, and roughness controlling the incoming shortwave radiation, the longwave terrestrial radiation and the turbulent heat exchange, respectively, as well as the thermal properties and the thickness of the surface cover affecting terrestrial heat transfer. In general, the vegetation and snow cover moderate the ground temperature and thus the aggradation of permafrost. Vegetation is an insulating cover limiting cooling in winter and warming in summer, hence reducing the annual fluctuation of ground temperature. Vegetation is also important for the creation of snow cover, which protects the ground from heat loss in winter. However, the high albedo of snow can lead to a snow surface temperature almost 2°C lower than the mean winter air temperature /Yershov 1998/. As a rule, for a majority of the surface covers, permafrost can build from the ground surface if the annual mean air temperature is lower than a value ranging between –9 and –1°C /Washburn 1979, Williams and Smith 1989, Yershov 1998, French 2007/. An exception occurs with peat layers, which can insulate the ground from warming in summer more effectively than from cooling in winter, with the resulting effect that permafrost can exist where the mean annual air temperature is above 0°C /Williams and Smith 1989/.

Properties and thickness of the soil cover affect the terrestrial heat flow. Of importance are the porosity and water content of the soil, influencing the annual fluctuation of ground temperature and the thickness of the active layer, i.e. the seasonally thawing ground layer. The soil cover also acts as an insulating cover, since the thermal conductivity of the soil cover is lower than that of the underlying bedrock.

Water bodies, i.e. sea, lakes, and watercourses, influence permafrost creation and distribution considerably since they have high specific heat content. A talik, i.e. an unfrozen layer, can exist beneath water bodies that do not freeze to their bottom in winter. Depending on the characteristics of the climatic zone, the critical depth of a water body to remain unfrozen in winter is approximately 0.2 to 1.6 metres /Yershov 1998/.

Sea water extensively reduces the development of costal permafrost. On the other hand, when the shore-level of a highly saline sea is rising, submerged permafrost and perennially frozen deposits can survive for a long time beneath a cold seabed /Washburn 1979, Yershov 1998/.

The hydrological conditions on the ground surface affect the freezing of groundwater. Especially under glaciated conditions, a warm-based overlying ice sheet increases the subglacial groundwater pressure, in which case the freezing point may decrease to such a degree that the subglacial ground is kept unfrozen. A similar, but minor, effect may occur when cold ground is submerged and submarine freezing is reduced by the pressure of the sea water. Furthermore, groundwater flow, whether carrying fresh glacial meltwater or saline seawater, can influence the freezing process by altering the chemical groundwater composition.

Table 3-7 summarises how geosphere variables are influenced by permafrost development.

Subsurface and repository

The ground temperature that defines the presence of permafrost and primarily governs the freezing of water in ground is principally controlled by the ground thermal energy balance in terms of heat transfer, geothermal heat production, the specific heat content and the amount heat generated by phase change processes of water. Heat transfer within the ground can occur through conduction, convection and radiation /Sundberg 1988/. In general, only conduction is regarded as important to permafrost evolution, since radiation is of importance only in unsaturated high-porosity ground at high temperatures, and convection is of importance only when groundwater and gas fluxes are large.

Heat conduction depends on the ground temperature gradient, ambient temperature conditions, and the thermal properties of the ground matter. Thermal conductivity, describing the ability of material to transport thermal energy, and heat capacity characterising the capability of material to store heat,

Table 3-7. Influence of permafrost development on geosphere variables.

Geosphere variable	Climate issue variable	Summary of influence
Temperature	Permafrost depth	Permafrost is by definition a thermal condition hence having no influence on temperature.
Groundwater flow	Frozen/unfrozen fraction of groundwater	Freezing occurs at temperatures below the freezing point /SKB 2010c/. Groundwater transformed from liquid to solid phase can be regarded as immobile. Filling fractures and pores, ice also affects the groundwater flow through permeability, which decreases with a reduction in the unfrozen fraction of groundwater.
Groundwater pressure	Frozen/unfrozen fraction of groundwater	The volume increase in the phase change of water from liquid to solid state causes an increase in the pressure of water which remains liquid. Moreover, freezing of water in porous ground matter can lead to cryosuction and depression of groundwater pressure in the unfrozen ground.
Groundwater composition	Frozen/unfrozen fraction of groundwater	When saline water is transformed from liquid to solid phase, the solutes are typically not incorporated in the crystal lattice of ice but transferred in the liquid phase. Therefore the salinity in the unfrozen fraction increases.
Rock stresses	Frozen fraction of groundwater	Deformations due to ice formation will lead to changes in rock stresses. The effect of the changes is strongest nearest to the surface where in situ stresses are lowest.
Fracture geometry	Frozen fraction of groundwater	Freezing can have some influence on the fracture geometry at shallow depths due to frost cracking. Close to the ground surface frost wedges can form to the depth of some metre. Otherwise, there can be widening of fractures due to freezing but the effect may be reversible as thawing takes place.

depend on a number of variables such as mineralogy, porosity and groundwater content. Having typically three to four times higher conductivity than other common rock forming minerals, quartz is the most important mineral for determining thermal characteristics in native rock materials.

When the porosity is less than 1%, freezing of water has a minor effect on heat transfer in water-saturated ground. The degree of saturation has relevance to the thermal properties of ground due to the very low thermal conductivity and heat capacity of air, e.g. the thermal conductivity of 1%-porosity granite can decrease by over 10% with decreasing saturation /Clauser and Huenges 1995/. In rock, heat capacity is not very dependent on ambient temperature and pressure conditions, whereas thermal conductivity is a rather variable function of both temperature and pressure. The thermal conductivity of granite decreases with increasing temperature by approximately 5 to 20% per 100°C and increases with increasing pressure by about 1 to 2.5% per 100 MPa /Seipold 1995/. The pressure dependence of thermal conductivity is increased when rocks are unsaturated /Sundberg 1988, Clauser and Huenges 1995/. Moreover, /Allen et al. 1988/ reported a strong correlation between lithology and permafrost depth, which could be directly explained by differences in thermal conductivity.

In addition to the thermal properties above, the hydrogeochemical and mechanical properties of the ground important for freezing of groundwater are permeability, porosity, adsorptive capacity of ground matter, chemical composition of groundwater and deformation properties of the ground.

Also, in the context of assessing the long-term safety of repositories for spent nuclear fuel, the spent nuclear fuel will generate heat with an exponentially decreasing rate for a considerable amount of time. This heat will warm up the surrounding bedrock /SKB 2010c/ and may thus act to reduce the thickness of permafrost above and near the repository (Section 3.4.4).

3.4.3 Natural analogues/observations in nature

At present, approximately 25% of the total continental land area of the Earth is occupied by permafrost. Permafrost distribution may be characterised into: i) continuous (more than 90% spatial coverage), ii) discontinuous (between 90 and 50% coverage), iii) sporadic (less than 50% coverage), and iv) subglacial forms. About one fifth of this permafrost is estimated to be subglacial in Antarctica and Greenland. Permafrost is abundant in Alaska, the northern parts of Canada and Russia, and in parts of China /French 2007/. Along the coast of southern and south-western Greenland both continuous and discontinuous permafrost can be found /Mai and Thomsen 1993/. The Northern Hemisphere distribution of permafrost is seen in Figure 3-50.

The deepest known permafrost occurs in the central part of Siberia in Russia, where thicknesses of up to 1,500 m have been reported /Fotiev 1997/. The extensive region of continuous permafrost in central Siberia corresponds to areas that are believed not to have been covered by Quaternary ice sheets and that experienced cold subaerial climate conditions during the last glacial cycle and onwards. In coastal areas, submarine permafrost may also exist, such as in northern Siberia where the permafrost formed during ice free periods of the last glacial cycle in regions subsequently covered by the Arctic Ocean. Furthermore, permafrost is frequently observed in mountainous terrain. For example, in the area of Tarfala in the Kebnekaise massif in northern Sweden, discontinuous permafrost has been reported to be 100 to 350 m thick at an altitude above 1,500 m a.s.l. /King 1984, Isaksen et al. 2001/.

SKB, together with co-funding parties from Finland (Geological Survey of Finland and Posiva), Great Britain (UK Nirex Ltd) and Canada (Ontario Power Generation and University of Waterloo), has carried out a research project on permafrost at the Lupin gold mine in northern Canada /Ruskeeniemi et al. 2002, 2004/. In this area, the depth of the permafrost extends to ~500−600 m. The main objective of the project was to provide data describing the subsurface conditions in a permafrost area with crystalline bedrock. Permafrost depth, temperatures, groundwater composition and hydraulic properties have been measured. The mean annual air temperature at this site is −11°C and the annual mean precipitation is low; ~270 mm /Ruskeeniemi et al. 2002/. Based on a seismic refraction survey, the depth of the active layer has been interpreted to be ~1.5 m, varying between 1.2 and 1.8 m. The present permafrost depth is believed to have been developed over the last 5,000 years. In the Lupin area, all shallow lakes freeze down to the bottom during winter. Lakes deeper than 2–3 m are expected to have unfrozen bottoms all year. The latter lakes may have the potential to support closed taliks. The large Lake Contwoyto, located about 1,300 m from the mine at surface, provides the most significant talik structure that may extend through the deep permafrost. However, direct observations beneath this lake are lacking.

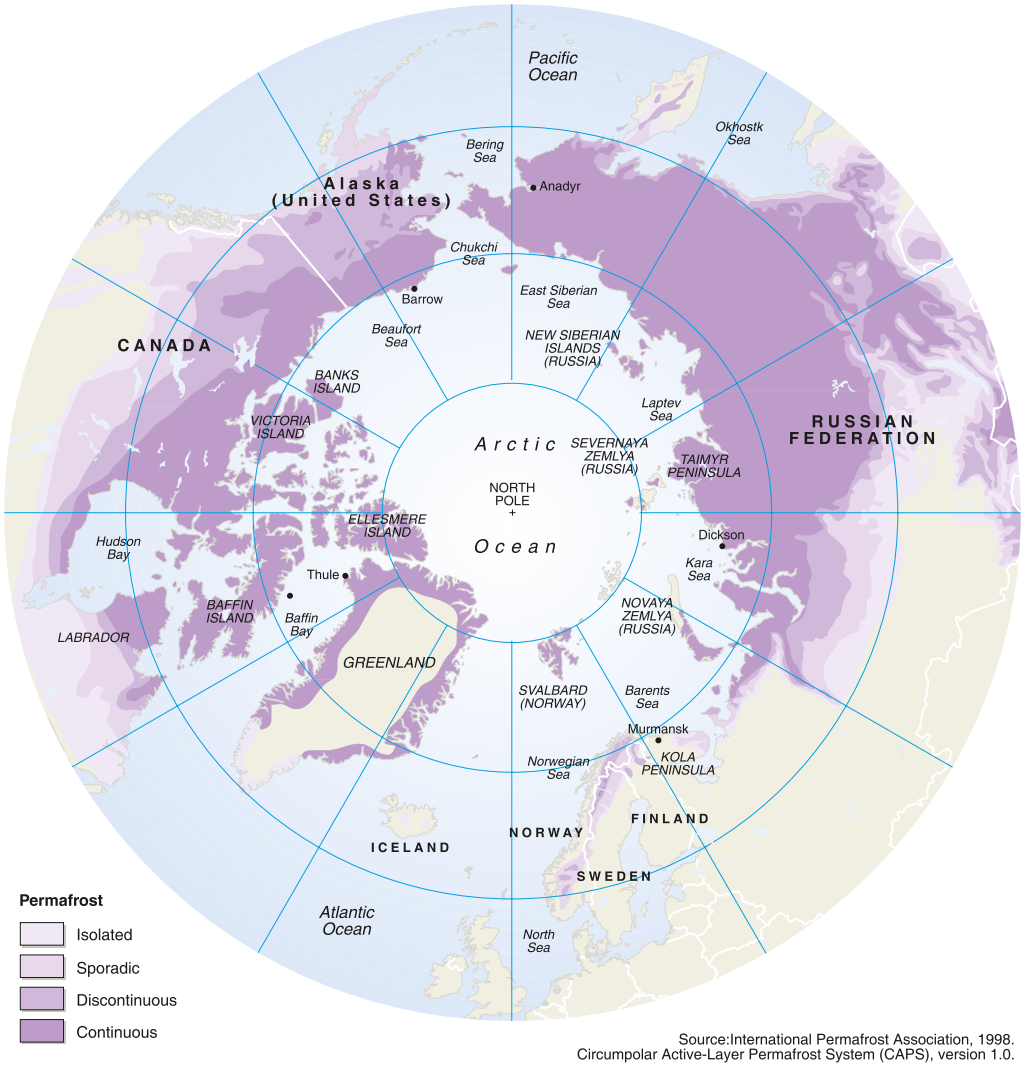

Figure 3-50. *Permafrost distribution in the Northern Hemisphere. From /UNEP/GRID-Arendal 2005/.*

In order to investigate the distribution of permafrost and locate salinity differences in the deep groundwaters, a number of electromagnetic soundings were conducted in the Lupin mine area. Furthermore, drillings were made from the deeper parts of the mine through the base of the permafrost, in order to sample groundwaters and to study the distribution of open fractures and hydraulic conditions. The main result of the electromagnetic sounding surveys was the identification of anomalies forming a subhorizontal layer at depths between 400 and 700 m. /Paananen and Ruskeeniemi 2003/ made the interpretation that this conducting layer represents saline or brackish water at the base of the permafrost. According to the temperature measurements made in the mine, the base of the permafrost occurs at a depth of 540 m. The drillings revealed the existence of a ~100 m thick unsaturated or dewatered zone below the permafrost. An alternative interpretation of the subhorizontal conductor at ~650 m depth could be that it represents the groundwater table /Ruskeeniemi et al. 2004/. The dry zone below the permafrost could either be a natural result of very limited recharge through the permafrost or an effect of mine drainage. No pressurised water or gas flow was observed in the boreholes. The available data from water sampling do not provide any evidence of highly saline water below the permafrost /Ruskeeniemi et al. 2004/.

3.4.4 Model studies

Two climate cases have been studied by permafrost modelling; i) the *Reconstructed last glacial cycle* and ii) the *severe permafrost case*, see Figure 1-3. In addition, a broad range of sensitivity tests have been made, covering the range of uncertainties associated with various parameters of importance for permafrost development. The simulations of the *Reconstructed last glacial cycle* are described in this section, whereas the simulations of the *severe permafrost case* are described in Section 5.5.

The simulations of permafrost for the reconstruction of the last glacial cycle have been done with two types of models, a 1D permafrost model and a 2D permafrost model improved from the 1D model. The 1D modelling was performed for the SR-Can safety assessment /SKB 2006a, Section 3.4/, but some of the results are used also for the SR-Site safety assessment. The 1D simulations were conducted specifically for the repository location. The 2D modelling /Hartikainen et al. 2010/ was conducted for the SR-Site safety assessment, and covers a 15 km long and 10 km deep vertical cross-section crossing most of the Forsmark site. Both simulations use site-specific input data from the Forsmark site investigation programme. Details on the input data used for the 1D and 2D permafrost simulations are found in /SKB 2006a, Section 3.4/ and /Hartikainen et al. 2010/ respectively.

The purpose of the modelling studies is to analyse the main factors of importance for the development of permafrost and perennially frozen ground at Forsmark. The permafrost models include mathematical expressions for freezing and thawing of saline groundwater-saturated bedrock. The bedrock is considered as an elastic porous medium and the groundwater as an ideal solution of water and ionic solvents. The models are based on the principles of continuum mechanics, macroscopic thermodynamics and the theory of mixtures being capable of describing heat transfer, freezing of saline water, groundwater flow and deformations of bedrock. In the 2D version of the model, the freeze-out and transport of solutes is included /Hartikainen et al. 2010/. The models are described further in /Hartikainen 2004, SKB 2006a, Hartikainen et al. 2010/.

To capture the most important factors and parameters affecting the development of permafrost, sensitivity analyses have been performed considering the following issues:

- Surface conditions.
- Subsurface conditions.
- Presence of the repository.

Surface temperatures, together with the influence of surface covers such as snow, vegetation and water bodies, have been included as factors of importance in the surface conditions. The investigated bedrock conditions are thermal properties of the bedrock and the geothermal heat flow. The sensitivity simulations carried out with the 2D permafrost model /Hartikainen et al. 2010/ are presented in the present report. Similar sensitivity experiments were carried out also with the 1D model /SKB 2006a, Section 3.4/. However, since the sensitivity experiments conducted with the 2D model /Hartikainen et al. 2010/ cover a broader range of cases than the sensitivity cases studied with the 1D model /SKB 2006a/, only some selected sensitivity tests from the 1D experiments are included in the present report. The heat generated by the spent fuel has been included in most simulations, and is also analysed in a dedicated 2D sensitivity simulation. In this context it should be noted that the repository depth was changed between SR-Can (for which the 1D simulations were made) where it was 400 m and SR-Site (for which the 2D simulations were made) where it is 450 m. Despite of this the resulting permafrost and freezing depths are very similar between the two studies, as demonstrated later on.

In the following, the 1D permafrost simulations for the location of the repository are described first, followed by the 2D simulations across the Forsmark site.

1D reconstruction of last glacial cycle permafrost conditions at the repository location

The 1D modelling experiments described below, conducted for the repository location, are from /SKB 2006a, Section 3.4/.

The 1D calculations were carried out in two steps; i) by using constant surface temperatures, and ii) using surface temperatures from the reconstruction of last glacial cycle conditions. The first task was to investigate the ground surface temperatures required to reach different permafrost depths. A set of constant mean annual ground surface temperatures were assumed and applied to a 1D subsurface model based on present-day reference data for Forsmark (Table 3-8, Figure 3-51). Note that since the 1D permafrost experiments were conducted, these input data have been updated for the Forsmark site. Updated input data on bedrock and groundwater properties were used for the 2D modelling studies /Hartikainen et al. 2010/, described in the second half of the present section.

The intention with the constant surface temperature simulations was to find steady state permafrost depths. The modelling, however, showed that no steady state could be reached in a time frame of two glaciation cycles. The results from this modelling effort for the time period of 120,000 years

are shown in Figure 3-52. The modelling indicates that reaching a permafrost depth of 450 m at Forsmark, without a heat contribution from spent fuel, requires a mean annual surface temperature of −8°C for around 120 kyrs. With the heat contribution from the fuel, surface temperatures need to be lower than −8°C. The thickness of the cryopeg varies from some metres to over 70 m (Figure 3-52). The results for permafrost development rates (aggradation rates) are shown in Figure 3-53.

In the 1D modelling of surface conditions, the objective was to define a correlation between air and surface temperatures in consideration of the insulating effects of surface covers. The so-called *n*-factor concept /Lunardini 1978/ yields an empirical relationship between the mean annual surface temperature $\overline{T}_s$ and the mean annual air temperature $\overline{T}_a$ as

$$\overline{T}_s = f\left(\overline{T}_a, A_a; n_{fr}, n_{th}\right) \qquad \text{Equation 3-11}$$

where A_a is the amplitude of annual air temperature variations, which can be defined as the half of the temperature difference between the monthly mean summer maximum and monthly mean winter

Table 3-8. Site-specific reference physical properties and conditions of rock mass and groundwater at Forsmark used for the 1D permafrost modelling /SKB 2006a/, mainly from site description model Forsmark 1.2 /SKB 2005a/. Note that since the 1D permafrost experiments were conducted, these data have been updated. Updated input data on bedrock and groundwater properties were used for the 2D modelling studies /Hartikainen et al. 2010/, described in the second half of the present section.

Rock mass							
Thermal properties							
Parameter	**Unit**	**Reference**	**Min**	**Max**	**Temperature dependency**		
Thermal conductivity	W/(m·K)	3.6	3.2	4.0	11.0% decrease/100°C increase		
Heat capacity	MJ/(m³·K)	2.3	2.1	2.5	27.5% increase/100°C increase		
Thermal diffusivity	mm²/s	1.57	1.28	1.9	38.6% decrease/100°C increase		
Interior Earth conditions by depth							
		0 m			**10,000 m**		
Parameter	**Unit**	**Reference**	**Min**	**Max**	**Reference**	**Min**	**Max**
Geothermal heat flow	mW/m²	59.0	48.0	65.0	43.2	41.7	46.0
Radiogenic heat prod.	µW/m³	2.5	1.0	3.0	0.92	0.37	1.1
Reference temperature conditions by depth							
Parameter	**Unit**	**400 m**	**500 m**	**600 m**			
Temperature	°C	10.6	11.7	12.8			
Temperature gradient	°C/km		11.0				
Reference hydro-mechanical properties by depth							
Parameter	**Unit**	**100 m**	**200 m**	**300 m**	**≥ 400 m**		
Bulk density	kg/m³	2,700	2,700	2,700	2,700		
Young's modulus	GPa	74	74	74	74		
Poisson's ratio	–	0.26	0.26	0.26	0.26		
Kinematic porosity	–	0.00001	0.00001	0.00001	0.00001		
Total porosity	–	0.0001	0.0001	0.0001	0.0001		
Permeability	m²	$1.0\cdot10^{-13}$	$1.0\cdot10^{-15}$	$1.0\cdot10^{-17}$	$1.0\cdot10^{-18}$		
Groundwater							
Reference salinity concentrations by depth							
Ionic solvent	**Unit**	**10 m**	**100 m**	**300 m**	**500 m**	**≥ 1,000 m**	
Na^+	g/m³	65	500	2,000	2,000	2,000	
Ca^{2+}	g/m³	60	250	1,200	1,000	3,500	
Cl^-	g/m³	15	1,300	5,500	5,500	10,000	
SO_4^{2-}	g/m³	20	170	500	400	50	

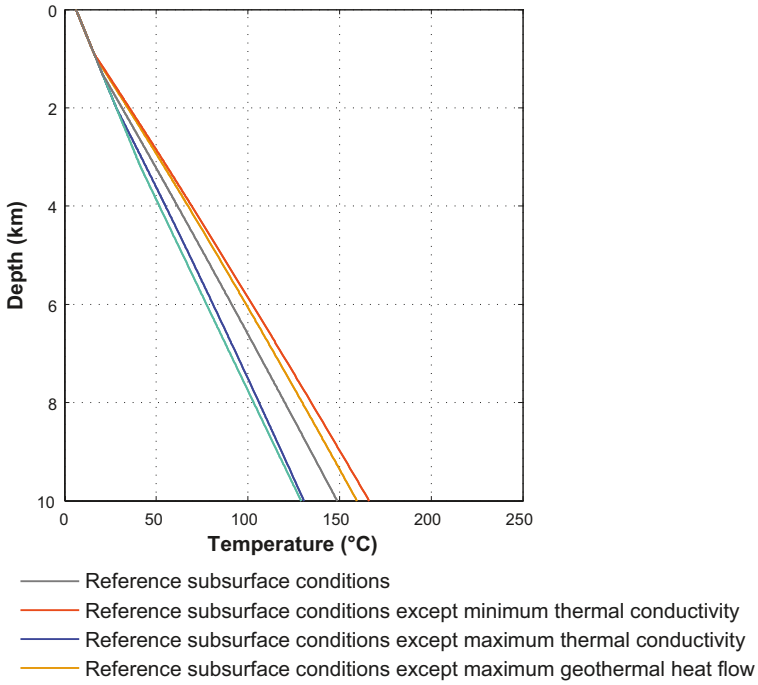

Figure 3-51. *Modelled present-day bedrock temperatures at the Forsmark repository location using the site-specific reference subsurface conditions in Table 3-8.*

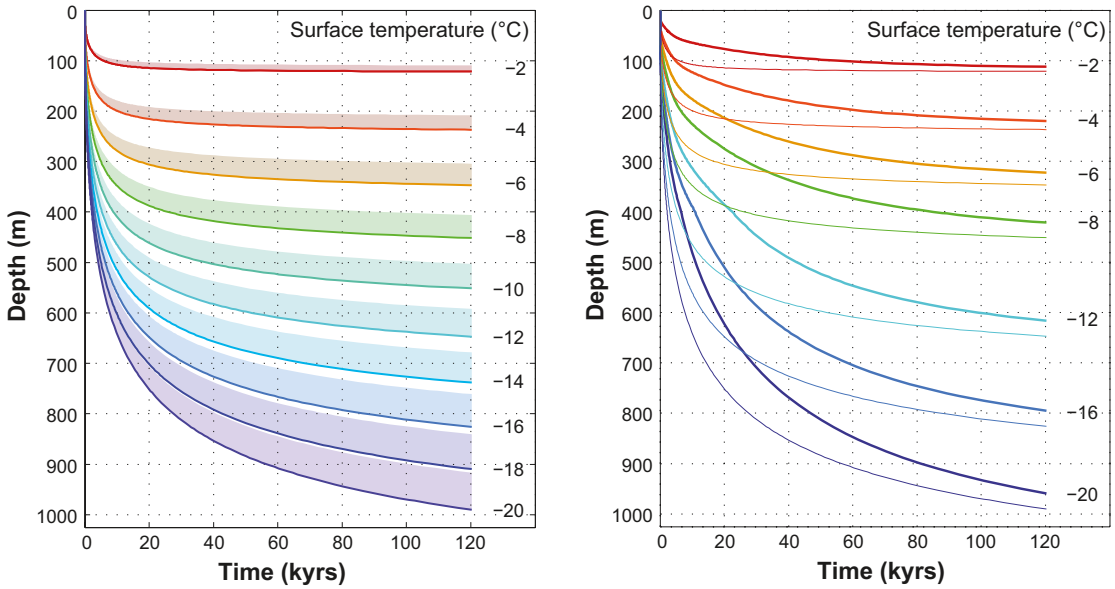

Figure 3-52. *Left: Evolution of permafrost depth (thick lines) and related cryopegs (shadowed areas) for constant ground surface temperatures of –2, –4, …, –20°C at the Forsmark repository location when reference subsurface properties are assigned. Right: Evolution of permafrost depth for different constant ground surface temperatures with and without the heat contribution from the repository (6,000 canisters). Bold lines show calculations with heat from the repository, whereas thin lines show calculations with no repository heat contribution.*

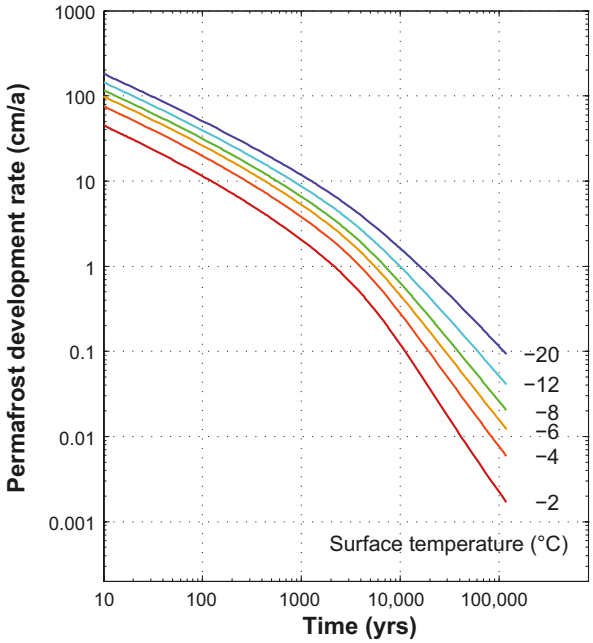

Figure 3-53. *Evolution of permafrost development rate for constant ground surface temperatures of –2, –4, –6, –8, –12 and –20°C at Forsmark when site-specific subsurface properties are assigned.*

minimum. n_{fr} and n_{th} are so-called freezing and thawing *n*-factors. These factors are ratios between the surface and air freezing indexes, i.e. annual time integrals of associated temperatures below the freezing point, and the surface and air thawing indexes, i.e. annual time integrals of associated temperatures above the freezing point, respectively. Depending on the type of surface cover, freezing *n*-factors can vary between 0.1 and 1 whereas thawing *n*-factors can have values in the range from 0.3 to 1.5 /Lunardini 1978, Shur and Slavin-Borovskiy 1993, Taylor 1995, 2001, Klene et al. 2001, Karunaratne and Burn 2004/. Figure 3-54 shows the relation of the mean annual air temperature to the mean annual ground surface temperature at Forsmark obtained for a reference surface cover when vegetation and snow are considered and for a bare surface when no vegetation and snow exist. The relationship is based on the assumption that ground surface and air temperature is constant over the whole glacial cycle, when the surface is not covered by ice-sheet or submerged.

Since the factors of major importance to the subsurface conditions are the bedrock thermal properties and the conditions affecting the geothermal heat flow, the development of permafrost was in /SKB 2006a/ investigated for extreme thermal diffusivities and geothermal heat flows as shown in Tables 3-8. These results are not repeated here, since similar sets of sensitivity tests were made with updated information on the geothermal properties at Forsmark with the 2D permafrost model /Hartikainen et al. 2010/, see further down in this section.

After the sensitivity analysis using constant surface temperatures, permafrost development was modelled for time-varying site-specific surface conditions. For this purpose, the ice sheet model in Section 3.1.4 was used to extract estimates of site-specific time series of ground-level annual air temperatures and basal ice sheet temperatures, as well as information on site-specific ice thickness variations. A description of these reconstructed temperatures for the last glacial cycle, including a discussion and estimates of their uncertainties, is found in Appendix 1. The GIA modelling described in Section 3.3.4 was used to produce input data on shore-level displacement.

The 1D permafrost model was used to reconstruct the permafrost conditions at the repository location for the reconstruction of the last glacial cycle. It was also used for studying a case with extreme surface conditions favouring permafrost growth /SKB 2006a/. The latter case is equivalent to the *severe permafrost case* analyzed with the 2D model (reported in /Hartikainen et al. 2010/ and later in Section 5.5.3), and is therefore not included in the present report. For the reconstruction of permafrost for the last glacial cycle, the air temperature curve seen in Figure 3-55 was applied. When the site is covered by the reconstructed the Weichselian ice sheet, surface temperatures equal the basal temperatures from the ice sheet model. When the site is submerged, as seen in the reconstruction of Weichselian shore-level variations, the surface temperature is set to +4°C.

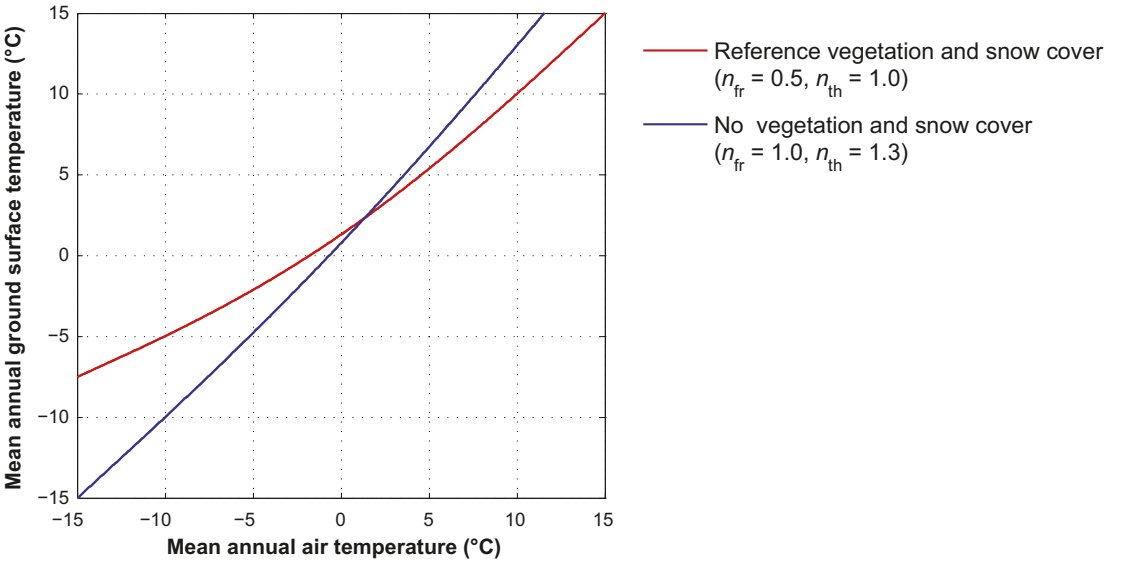

Figure 3-54. *Relationship between the mean annual air temperature and the mean annual ground surface temperature at Forsmark considering reference vegetation and snow cover, and no vegetation and snow cover.*

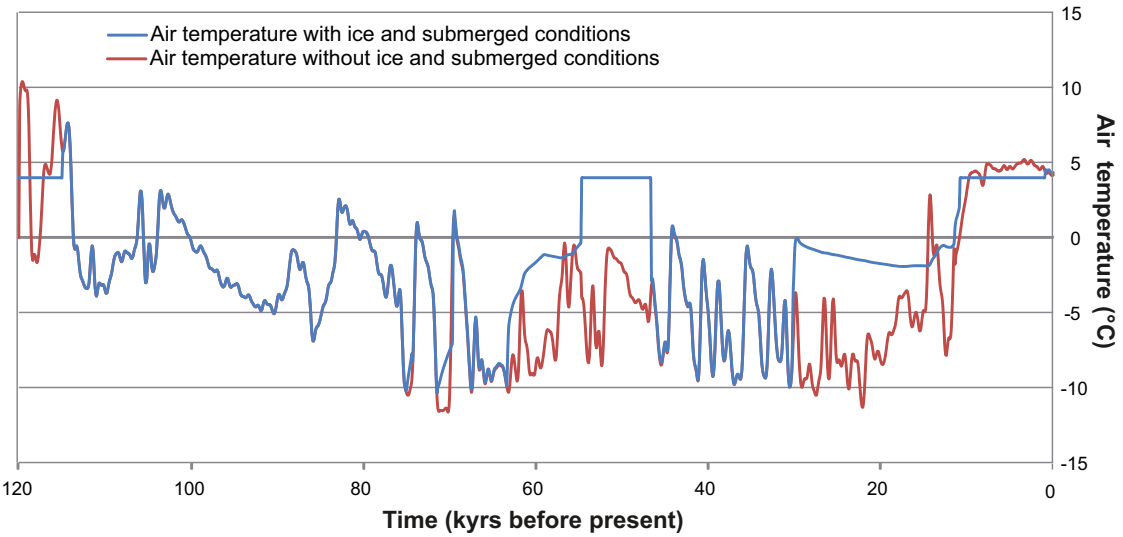

Figure 3-55. *Reconstructed air temperature curve for the Forsmark region for the past 120 kyrs, including estimated submerged periods of the Eemian, Mid-Weichselian and Holocene interglacials (blue line), see Appendix 1. The temperature scale shows absolute temperatures. The red line shows reconstructed last glacial cycle air temperatures without a presence of an ice sheet and submerged periods. The blue line includes periods of ice sheet coverage, i.e. it shows simulated basal ice temperatures for glaciated periods, air temperatures for ice-free periods, and also a temperature of +4°C for submerged periods. The curves have been used as input to the SR-Site 1D and 2D permafrost simulations /SKB 2006a, Hartikainen et al. 2010/. A submerged period during the Eemian was not included in the 1D permafrost simulations. The uncertainties of the temperature curves are discussed in Appendix 1, and the implications for modelled permafrost depths in the part of Section 3.4.4 describing the sensitivity studies made with the 2D permafrost model.*

The results of the development of permafrost, perennially frozen subsurface and cryopeg for reference surface conditions (Table 3-8) with vegetation and snow cover, and considering heat from the spent fuel are shown in Figure 3-56. The uncertainty in the modelled permafrost and freezing depths are analysed and discussed in the 2D permafrost modelling section below. The associated rates of permafrost aggradation and degradation are shown in Figure 3-57. The rather thick cryopeg layers during glaciations are due to large water pressures created by warm-based ice sheets keeping the subglacial bed unfrozen down to a temperature about –2°C.

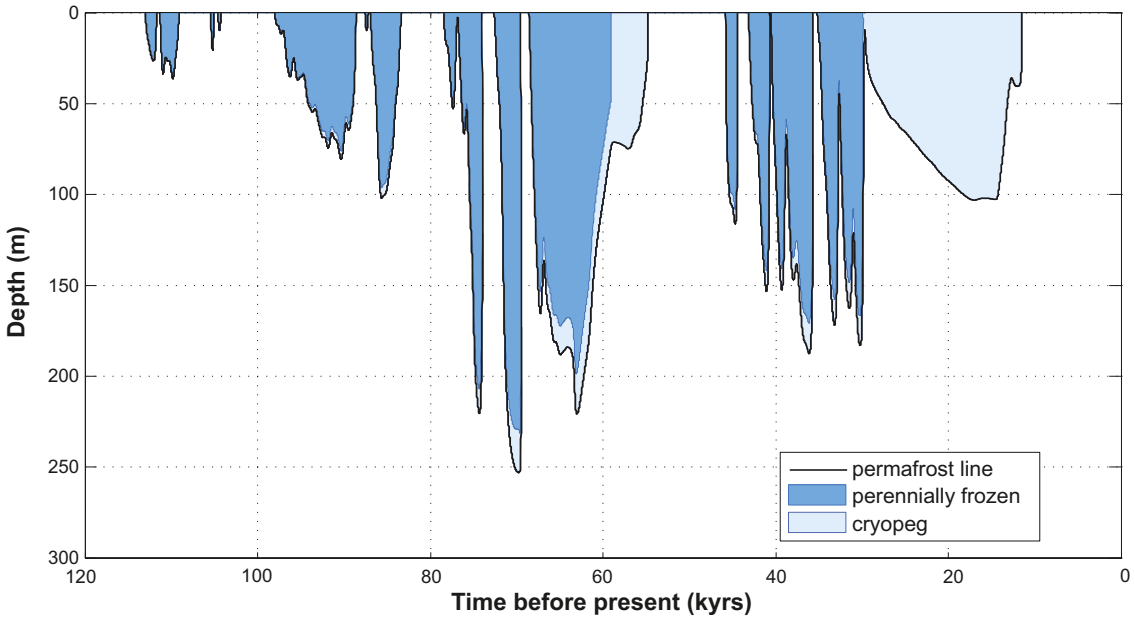

Figure 3-56. *Evolution of permafrost, perennially frozen subsurface and cryopeg at the repository location in Forsmark considering reference surface conditions, reference subsurface properties and heat from the spent fuel, see also /SKB 2006a/. The uncertainty in the modelled permafrost and freezing depths are analysed and discussed in the 2D permafrost modelling section below.*

The results show that surface conditions can be seen as the driving force for the development of permafrost, with the subsurface conditions and the heat from the spent fuel acting as either reducing or enhancing factors. The results indicate that permafrost (0°C isotherm) can develop to near repository depth under the reference surface conditions when the insulating effects of vegetation and snow cover are excluded.

Large water bodies will affect permafrost depth and will be associated with the presence of taliks. A talik can exist beneath a water body when the water bottom temperature remains above the freezing point. Based on field tests on temperature measurements in lakes e.g. /Yershov 1998, Burn 2002/, it was determined that a two metres deep water body maintains its bottom temperature above 0°C and that a water body deeper than 8 m has a bottom temperature around +4°C. The size of the water body required to retain a talik was investigated by permafrost modelling. To this end, permafrost development was simulated in the vicinity of circular lakes with constant positive lake bottom temperatures and constant negative lake bottom level bedrock temperatures. The results shown in Figure 3-58 (left panel) indicate that an open talik, completely penetrating the permafrost, can survive beneath a circular shallow lake, if its radius is greater than the thickness of surrounding undisturbed permafrost thickness. Furthermore, the results in Figure 3-58 (right panel) demonstrate that a radius greater than 0.6 times the thickness of surrounding undisturbed permafrost is big enough for a deep circular lake to maintain an open talik. The results apply for different lake bottom level bedrock temperatures.

For further sensitivity experiments conducted with the 1D permafrost model, see /SKB 2006a/.

In summary, the 1D permafrost study shows that the surface conditions are the driving force for the development of permafrost at Forsmark, while the subsurface conditions and the heat from the spent fuel acted as either reducing or enhancing factors. Permafrost can aggregate from some cm to some dm in a year whereas its degradation can take place several times faster, especially when the surface temperature is increased above 0°C and permafrost degrades simultaneously from the bottom upwards and from the top downwards. The results further show that the maximum permafrost depth in the reconstruction of last glacial cycle conditions occurs at 70 kyrs BP, prior to the first main ice sheet advance over the site. The permafrost depth is ~250 m at the repository location at this time. However, the uncertainty of surface and subsurface conditions also needs to be taken into account, something that was done in /SKB 2006a/. In the present report, this is done in the following 2D permafrost study.

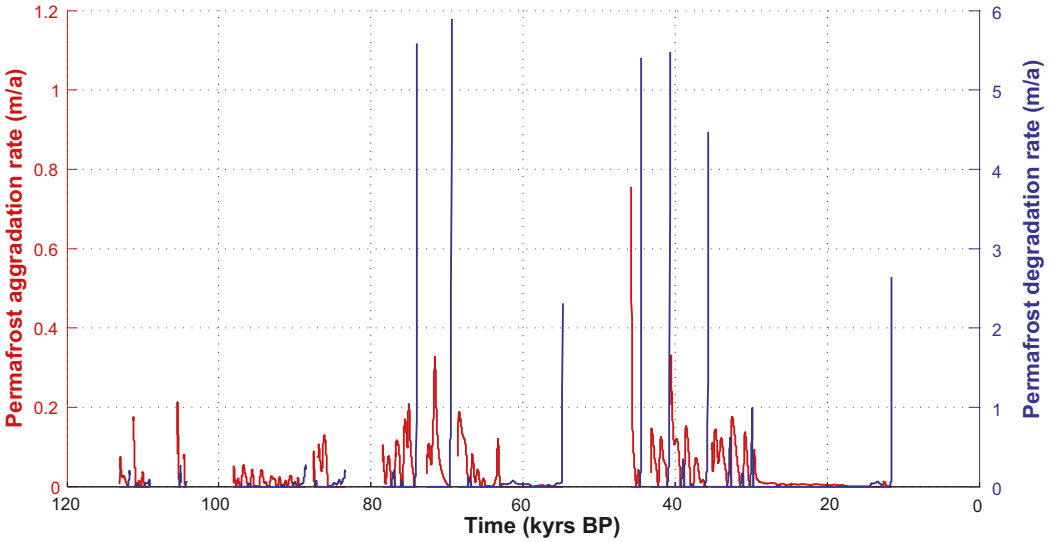

Figure 3-57. *Evolution of permafrost aggradation and degradation rates at the repository location in Forsmark considering reference surface conditions with vegetation and snow cover, reference subsurface properties and heat from the spent fuel, see /SKB 2006a/.*

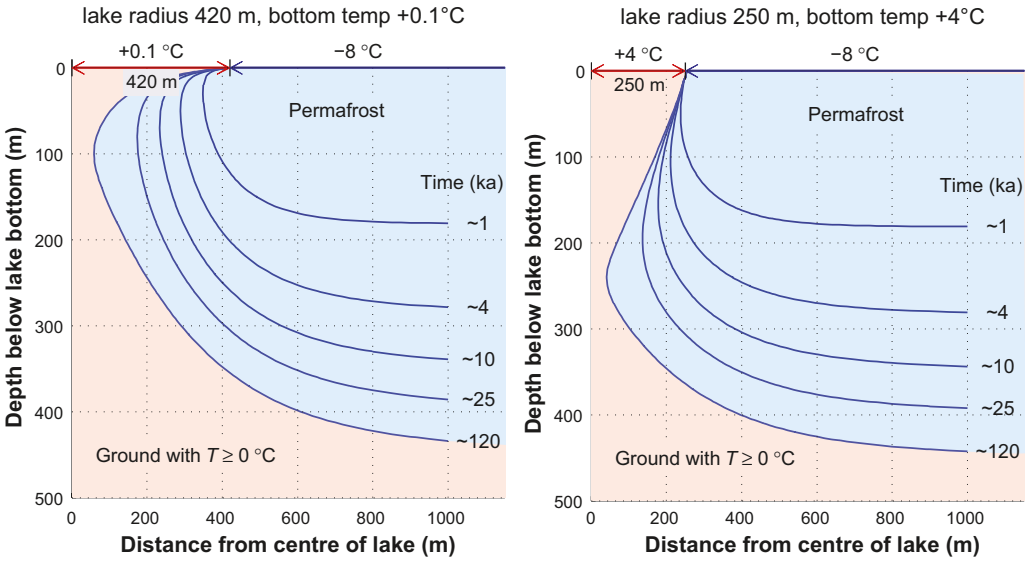

Figure 3-58. *Evolution of permafrost in the vicinity of a circular lake (red colour) at Forsmark. Left panel: the lake radius is 420 m and the constant lake bottom temperature +0.1°C. Right panel: the lake radius is 250 m and the constant lake bottom temperature +4°C. In both cases, a constant bedrock temperature of –8°C prevail at the lake bottom level.*

2D reconstruction of last glacial cycle permafrost conditions at the Forsmark site

The 2D permafrost study is a continuation and complement to the 1D study performed for SR-Can /SKB 2006a, Section 3.4 and 4.4.1/. The overall aim is to exemplify how permafrost and frozen ground develops over the Forsmark site (and not only at the repository location) during cold but ice-free periglacial phases of glacial cycles, and to further demonstrate the effects of uncertainties associated with processes and phenomena of importance for permafrost development. To this end, the 2D study provides a numerical estimation of the development of permafrost and perennially frozen ground along a profile covering a major portion of the Forsmark site and crossing the repository location (Figure 3-59), using site-specific surface and subsurface conditions. The objective is to investigate effects of multidimensional features of surface and subsurface conditions on the occurrence, development and distribution of permafrost and perennially frozen ground. Special emphasis is put on the modelling of surface conditions, including climate (temperature and humidity), soil, vegetation, water

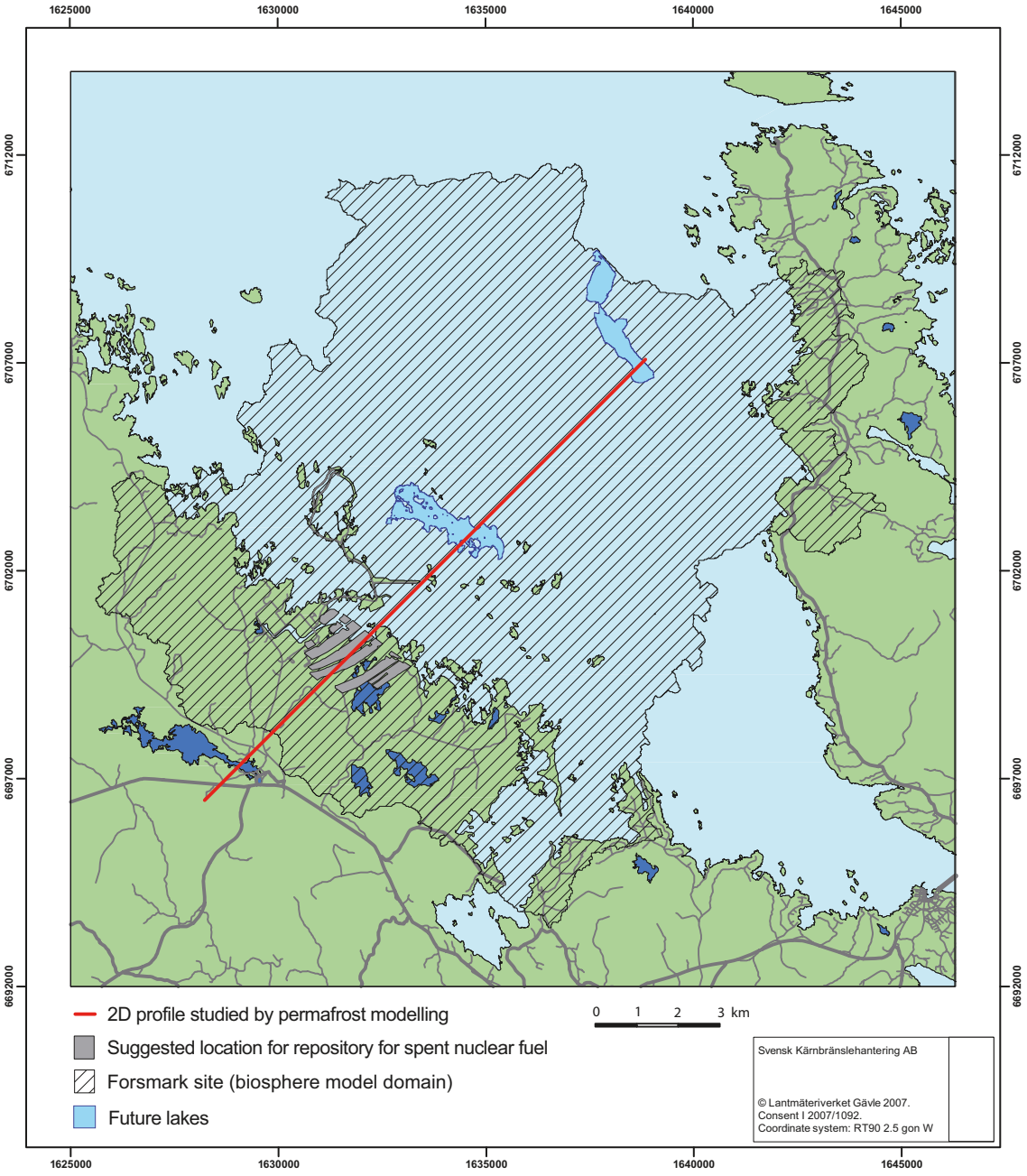

Figure 3-59. *The ~15 km long profile analysed in the 2D permafrost modelling study (red line), repository location (grey), and the Forsmark site (stippled) as defined and analysed in the SR-Site biosphere programme, e.g. /SKB 2010d, e/.*

bodies and topography, lateral variations in bedrock and surface physical properties and heat generation from the spent fuel. In addition, groundwater flow and salt transport processes are considered (in 2D); processes that were neglected in the 1D SR-Can study.

The mathematical model for freezing and thawing of the subsurface, based on the approach described in /Hartikainen and Mikkola 2006/, has been used in /Hartikainen and Mikkola 2004, Hartikainen 2006, SKB 2006a/. The model is capable of describing heat and mass transfer in a porous medium with freezing of groundwater depending on groundwater pressure and salt concentration and freezing-induced groundwater flow. In the present 2D study, by using the theory of mixtures and basic principles of continuum mechanics and thermodynamics, the mathematical model is reformulated in terms of Gibbs free energy functions by taking into account the effects of temperature, pressure and salinity concentration on the properties of groundwater and ice in a more accurate way. The reformulated

thermo-hydro-chemically coupled model consists of balance laws of mass, momentum and energy, and the constitutive laws of state and diffusion. A new feature of the model is the capability of describing the exclusion of salt during freezing and the density dependent groundwater flow in unfrozen and partially frozen ground. In addition, the effects of pressure and salinity concentration on the freezing temperature of groundwater are considered more accurately. A more detailed description of the 2D permafrost model used for the reconstruction of last glacial cycle permafrost conditions is found in /Hartikainen et al. 2010/.

The same climate development as used for the 1D permafrost simulations was used, complemented with more comprehensive sensitivity studies on e.g. air temperature uncertainties. However, the 2D reconstruction of last glacial cycle permafrost conditions do not consider the entire last glacial cycle, but instead only the ice-free period from 115 to 70 kyrs BP, i.e. the period prior to the first phase of ice sheet coverage in the reconstruction of the Weichselian ice sheet (see Section 3.1.4). This is motivated by the fact that this period ends with the deepest permafrost reconstructed at the site for the entire last glacial cycle, see /SKB 2006a/ and description of this 1D permafrost study above. However, for the *severe permafrost case* (Section 5.5), 2D permafrost simulations are carried out for the full glacial cycle, from 115 kyrs BP to present. Initial conditions are assumed to correspond to the present-day conditions (i.e. bedrock temperature, groundwater, salinity and pressure). Heat generated by the spent fuel in the repository is included in the simulations at 112 kyrs BP (see also Section 3.4.7).

Based on the results of the permafrost simulations in /SKB 2006a, Section 3.4 and 4.4.1/, the present analysis focuses on the following issues:

Subsurface conditions:

- Spatial variation of bedrock and soil thermal and hydraulic properties.
- Site-specific geothermal heat flow.
- Convectional heat transfer due to 2D groundwater flow.
- Heat generation from the repository for spent fuel.
- Salinity exclusion due to freezing and salt transport.

Surface conditions:

- Air temperature and its variation over time.
- Topographical features including slope and relief.
- Water bodies (sea and lakes), including the effect of isostatic uplift.
- Vegetation and snow cover as related to climate and topographical conditions.

The profile is located along the, very low, regional topographic gradient. In the direction of the profile, it covers a major part of the Forsmark site as defined by the biosphere model domain (Figure 3-59). For further description of the selection of the profile location, see /Hartikainen et al. 2010 Appendix A/.

Subsurface properties and conditions

The model domain encompasses an approximately 15 km long and 10 km deep vertical section consisting of six soil layers, 23 rock domains and 31 deformation zones as shown in Figures 3-59 and 3-60. Figure 3-61 illustrates the thermally different rock mass domains, the deformation zones of the upper 2.1 km of the model domain, as well as the present day Baltic Sea-level. The soil layers are shown in Figure 3-62. The thermal and hydraulic properties of soil domains are found in /Hartikainen et al. 2010, Table 2-1/, whereas Table 2-2 and Table 2-3 in the same publication give the thermal and hydraulic properties of the rock mass domains. Hydraulic properties of the deformation zones are presented in /Hartikainen et al. 2010 Appendix D/. The thermal properties of deformation zones are assumed identical to those of the corresponding rock mass domain. The bedrock below the depth of 2.1 km is assumed to have the same thermal and hydraulic properties as the rock domain in which the repository is located. The material properties of the bedrock are described in detail in /Hartikainen et al. 2010, Appendices D and E/. For the treatment of e.g. unfrozen groundwater content, also see /Hartikainen et al. 2010/. The numerical simulations were carried out using an unstructured finite element mesh of linear triangle elements. The mean grid spacing varied from less than 10 m close to the ground surface to about 300 m at the bottom of the model domain. The maximum time step for the adaptive time-integration scheme was limited to 100 years.

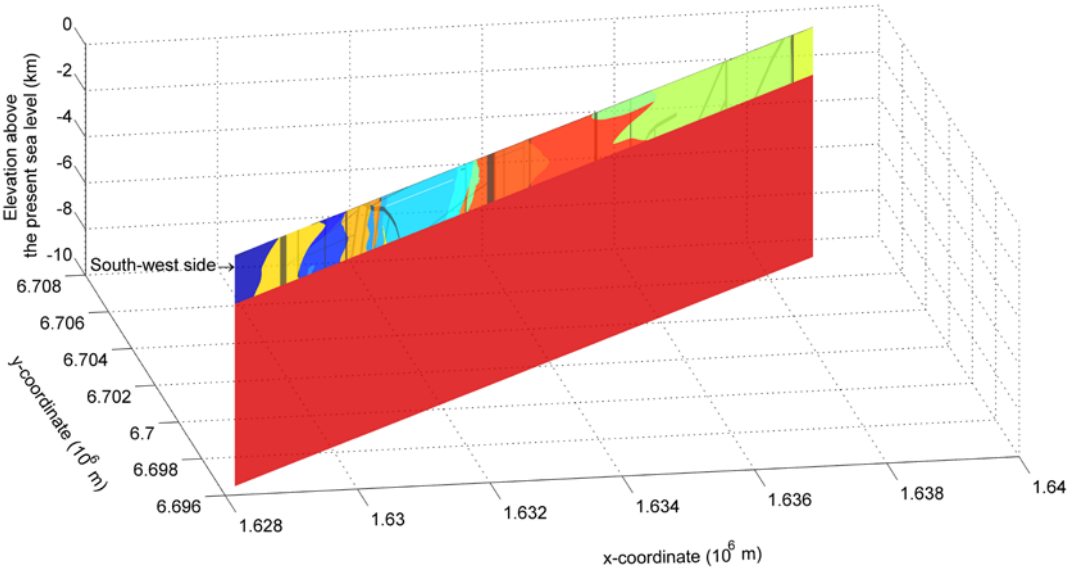

Figure 3-60. *The model domain used in the 2D permafrost simulations. Colours from blue to red signify the 23 rock domains considered, and grey the 31 deformation zones. Physical and thermal characteristics for the rock domains and deformations zones were obtained from the site investigation programme at Forsmark, see /Hartikainen et al. 2010/. The six soil layers described in /Hartikainen 2010 Appendix B/ and Figure 3-62, are too thin to be seen in this figure. The x-axis is directed eastward and y-axis northward. The RT-90 coordinates of the south-west side are x = 1,628,228 m, y = 6,696,472 m.*

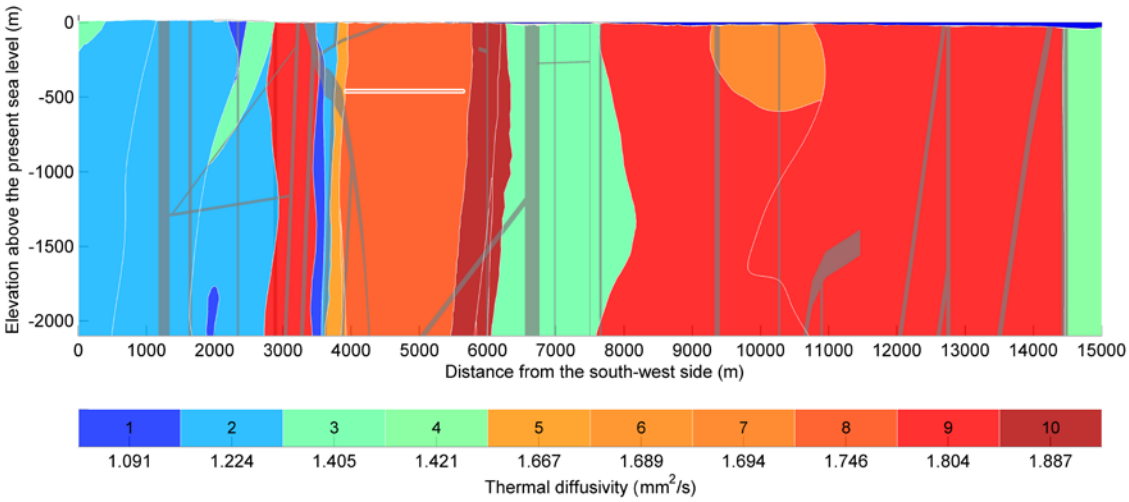

Figure 3-61. *The upper 2.1 km of the 2D model domain. Colours from blue to red signify rock domains with different thermal diffusivity. Numbers from 1 to 10 indicate the rock domains of Table 2-2 in /Hartikainen et al. 2010/. The location of deformation zones is illustrated in grey and the repository in white, at a depth of 450 m starting at a distance of about 4,000 m along the profile. The thin blue layer on the top surface represents the present day Baltic Sea-level. Further description and references for these data are found in /Hartikainen 2010 Appendix C/.*

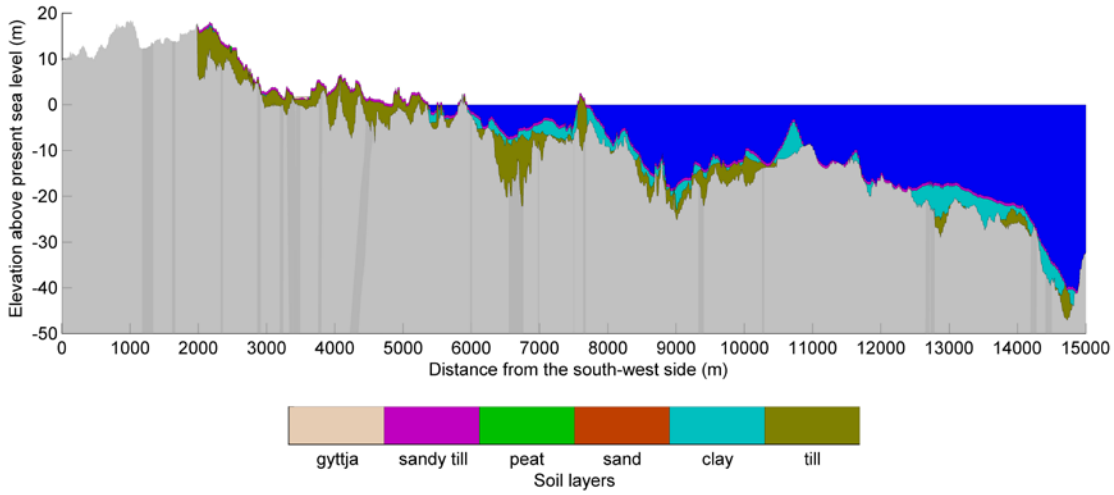

Figure 3-62. *The soil layers of the 2D model domain. Grey colour represents bedrock and blue the present day Baltic Sea. The gyttja, peat and sand layers are too thin to be seen in this figure. In addition, because the first 2,000 m of the model domain is outside the area of detailed site investigations, no information about the soil cover is used here. Further description and references for these data are found in /Hartikainen et al. 2010 Appendix B/. Note that the vertical axis has a scale which gives a strong vertical exaggeration of topography.*

The geothermal heat flow is an important subsurface parameter for permafrost modelling. The geothermal heat flow, crustal radiogenic heat production and ground temperature depth to ~1 km are based on /Sundberg et al. 2009/, see also /Hartikainen et al. 2010, Appendices B–F/. For a description of how these parameters are modelled for depths from ~1 km to 10 km, see /Hartikainen et al. 2010/. Figure 3-63 shows the initial ground temperature calculated for mean thermal properties.

The initial salinity concentration of groundwater for depths to ~1.5 km is described in /Hartikainen et al. 2010 Appendix F/, and for depths from ~1.5 km to 10 km it is obtained as a stationary solution using present concentration values on the surface and at the depth of 1.5 km. Figure 3-64 shows the initial salinity distribution in the model domain.

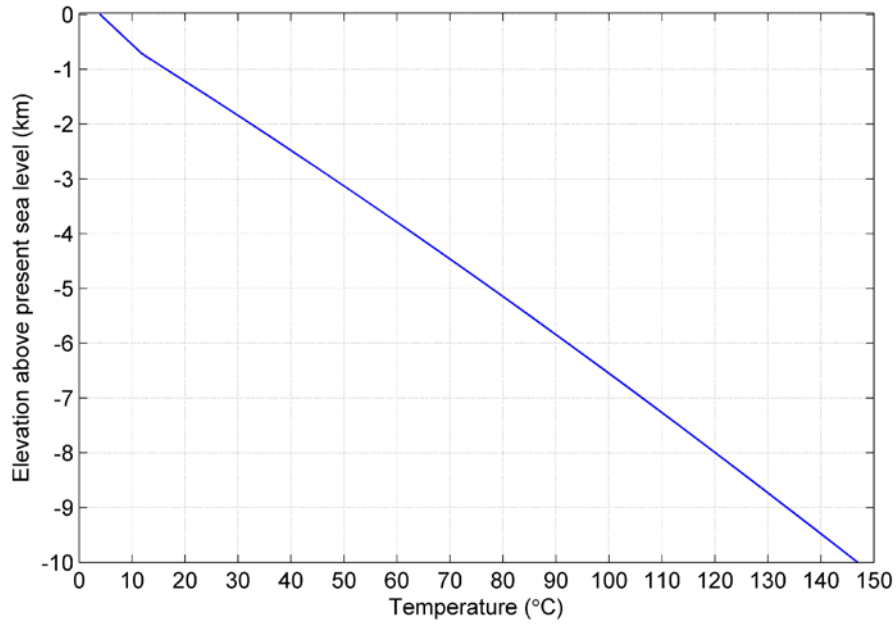

Figure 3-63. *Distribution of initial ground temperature for mean thermal properties used in the 2D permafrost modelling. For a description of these properties, see /Hartikainen et al. 2010, Table 2-2/.*

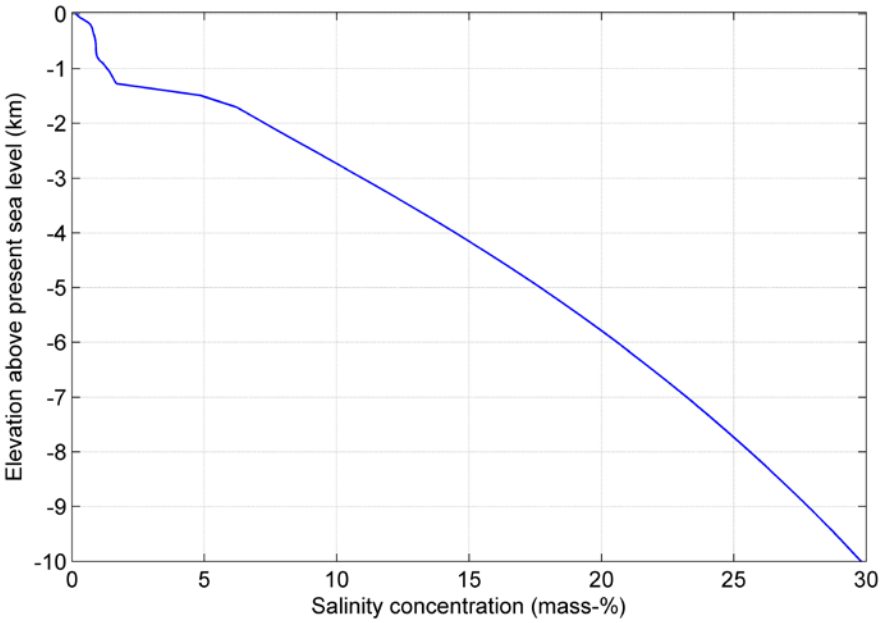

Figure 3-64. *Distribution of initial salinity concentration of groundwater /Hartikainen et al. 2010/.*

The present day groundwater pressure is determined as hydrostatic pressure based on the initial conditions of ground temperature and groundwater salinity concentration as well as the hydrostatic pressure at the bed of the Baltic Sea. The results for initial groundwater pressure are shown in Figure 3-65.

For a description of the localisation of the repository along the profile and the treatment of heat produced by the spent nuclear fuel, see /Hartikainen et al. 2010/.

Surface properties and conditions

Due to significant uncertainties associated with descriptions of the surface conditions, two variants, one humid and one dry, are analyzed. This is expected to yield a lower and upper limit for the permafrost and perennially frozen ground development, see further below.

As mentioned above, the 2D reconstruction of last glacial cycle permafrost conditions analyse the period from 115 to 70 kyrs BP, that is a ~85 kyr long period from the Eemian interglacial up to the first phase of glacial conditions as reconstructed for the Forsmark site /SKB 2006a/. Based on the Köppen climate classification /Lohmann et al. 1993/ and long-term observations /Eugster et al. 2000/ both climate variants may be divided into three climate zones: *Boreal*, *Subarctic* and *Arctic*, which may be characterized by the annual mean air temperature, the monthly mean maximum summer air temperature and the monthly mean minimum winter air temperature, together with the monthly mean maximum summer and winter precipitations (Table 3-11). The large ranges in the monthly mean air temperatures and precipitations are explained by the fact that the description and modelling of surface conditions involve significant uncertainties, see Appendix 1 and later in Section 3.4.

The shore-level development (Section 4.4.2) and evolution of lakes along the profile, as described in the SR-Site biosphere studies, are included in the modelling, see /Hartikainen et al. 2010 Appendix I/. As a result of isostatic uplift two lakes are formed along the profile, in the area today covered by the Baltic Sea (Figure 3-59).

The vegetation and snow cover are closely related to the prevailing climate conditions as well as to other landscape parameters. The presence of different vegetation types within different biomes has been described in numerous publications, e.g. /Breckle 2002, Archibold 1994/ and the regional response of vegetation types to e.g. periglacial climate conditions has been studied by /Kjellström et al. 2009b, Kjellström et al. 2010a/. In the present study, a detailed picture of the distribution of prevailing major vegetation types for *Boreal*, *Subarctic* and *Arctic* climate zones for the reconstruction of last glacial cycle conditions was described by using local variations in TWI (Table 3-9).

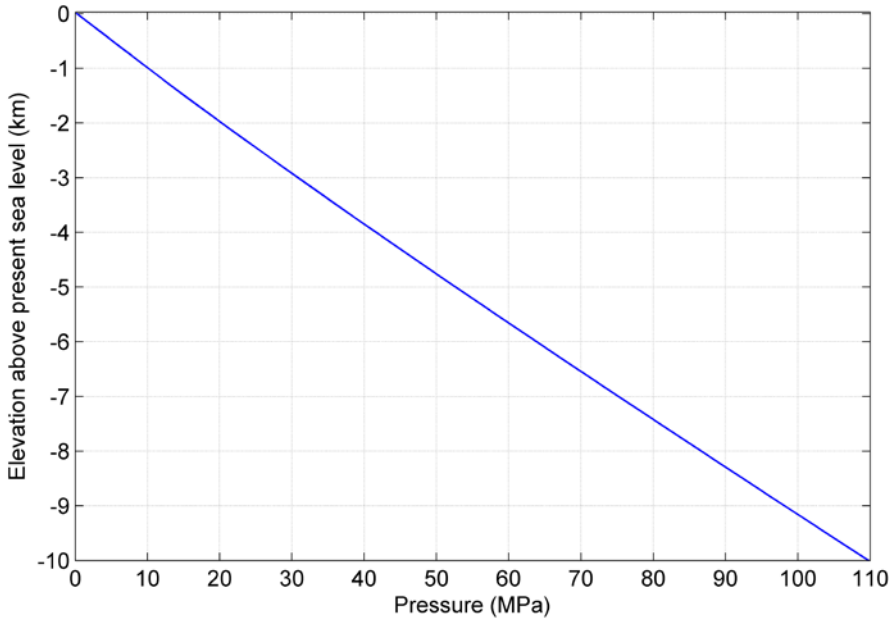

Figure 3-65. *Distribution of initial groundwater pressure associated with the temperature and salinity concentration shown in Figure 3-63 and 3-64.*

Table 3-9. Main vegetation cover types at Forsmark for three different climate zones and corresponding Topographic Wetness Index (TWI) values. For a more detailed description of the use of e.g. the TWI index in this study, see /Hartikainen et al. 2010 Appendix J/.

Climate zone	Vegetation cover type and TWI values				
	Forest	Shrubs	Grassland	Barren	Peatland
Boreal	Mixed	–	–	–	Peat
	TWI > 0				TWI > 13.2
Subarctic	Tree line/ tundra forest	Moderate/short	Short	–	Peat
	TWI > 13.2	10.9 ≤ TWI ≤ 13.2	TWI < 10.9		TWI > 13.2
Arctic	–	Short	Tussocks	Bare	Peat
		TWI > 13.2	10.9 ≤ TWI ≤ 13.2	TWI < 10.9	TWI > 13.2

Table 3-10. Freezing (winter) and thawing (summer) n-factors for the reconstruction of last glacial cycle conditions. See also /Hartikainen et al. 2010/. The numbers within brackets in the last four columns are Topographic Wetness Index (TWI) intervals.

Climatic zone	Season	Monthly mean max./min. air temperature (°C)	Monthly mean max. precipitation (mm/month)	*n*-factors for specified surface conditions and associated TWI intervals			
				Dry (< 10.9)	Fresh-moist (10.9–13.2)	Wet (> 13.2)	Peatland (> 13.2)
Boreal	summer	+10 – +20	10–60	1.2–1.4	1.2–1.4	1.2–1.4	1.0
	winter	–15 – +5	1–50	0.2–0.3	0.2–0.3	0.2–0.3	0.1
Subarctic	summer	+5 – +15	5–60	0.8–1.0	0.7–0.9	0.6–0.8	0.8–1.0
	winter	–25 – –10	1–40	0.5–0.9	0.4–0.8	0.2–0.6	0.1–0.4
Arctic	summer	< +5 – +10	5–60	1.0–1.2	0.5–0.8	0.4–0.7	0.6–0.9
	winter	–35 – –20	1–40	0.7–1.0	0.4–0.8	0.3–0.6	0.2–0.5

Table 3-11. Climate information for the reconstruction of last glacial cycle conditions.

Climate zone	Annual mean air temperature (°C)	Monthly mean max. summer air temperature (°C)	Monthly mean min. winter air temperature (°C)	Monthly mean max. summer precipitation (mm/month	Monthly mean max. winter precipitation (mm/month)
Boreal	> 0	+10 – +20	–15 – +5	10–60	1–50
Subarctic	0 – –6	+5 – +15	–25 – –10	5–60	1–40
Arctic	< –6	< +5 – +10	–35 – –20	5–60	1–40

The spatial resolution of the TWI information was 20·20 m. For a more detailed description of the adopted TWI approach, see /Hartikainen et al. 2010/.

The impact of vegetation, snow cover and other climate factors on the ground surface temperature and permafrost development is well investigated /Washburn 1979, Williams and Smith 1989, Yershov 1998, French 2007/. In general, an annual mean air temperature ranging between –9 and –1°C is required to build up permafrost for a majority of surface covers, depending on other climatic conditions and topography. The surface conditions can be modelled by thermodynamic and hydrodynamic models using surface energy and water balance equations and information on climate conditions and topography such as radiation, precipitation, cloudiness and wind, and their annual and diurnal variation /Riseborough et al. 2008/. However, these models are unsuitable for the long time spans associated with glacial cycles, since no climate data besides the air temperature can be adequately constructed. Therefore, an empirical approach based on *n*-factors /Lunardini 1978/, i.e. statistical correlations between air and ground surface temperature, has been used to construct the ground surface temperature from the reconstructed air temperature (Table 3-10). For a detailed motivation for and description of the *n*-factors approach as an approach to treatment of surface conditions, see /Hartikainen et al. 2010/.

When the site is submerged by the Baltic Sea or the two lakes, the ground surface temperature was set to +4°C for water depths greater than 6 m. For shallower depths the temperature was interpolated between the value of 4°C and the prevailing ground surface temperature.

Figure 3-66 exemplifies the evolution of modelled ground surface temperatures for the reconstruction of last glacial cycle conditions at one location along the profile with fresh-moist surface condi-

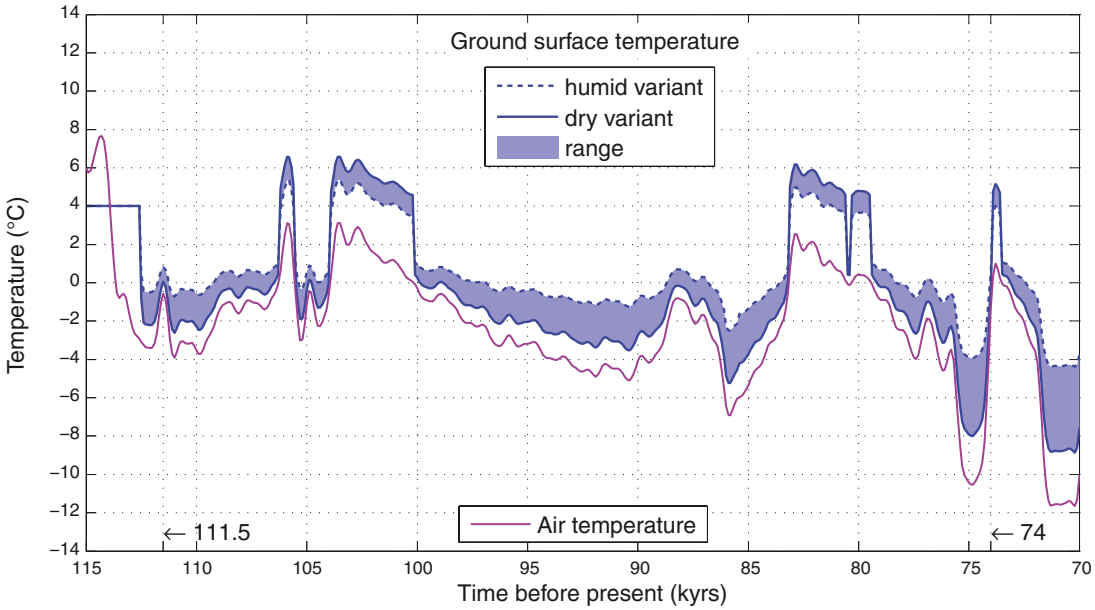

Figure 3-66. *Example of evolution of air temperature and modelled ground surface temperatures for a part of the profile with fresh-moist surface conditions (~4,800 m from the south-west side of the profile, above the repository, see Figure 3-59) for the reconstruction of last glacial cycle conditions.*

tions (at ~4,800 m from the south-west side). Examples of modelled ground surface temperatures for other surface condition types (wet, dry and peatland) are found in /Hartikainen et al. 2010/. Figure 3-67 illustrates the modelled ground surface temperatures along the profile at four different times during the last glacial cycle, considering different climate conditions: 111.5 kyrs BP – subarctic and partially submerged, 103.5 kyrs BP – boreal, 95 kyrs BP – subarctic, 70 kyrs BP – arctic. The results concerning the humid climate variant are obtained using the lowest *n*-factors of Table 2-7 and 2-8 in /Hartikainen et al. 2010/, whereas the highest *n*-factors from the same tables yield the results for the dry climate variant.

The ground surface temperature of +4°C indicates the times when the profile is submerged by the Baltic Sea or the two lakes. The dry surface condition type generates the lowest ground surface temperatures, and the peatland condition the highest ground surface temperatures in the subarctic and arctic climate zones. Furthermore, due to thin vegetation and snow cover, the dry variant of the reconstruction of last glacial cycle conditions results in the lowest ground surface temperatures in the subarctic and arctic climate zones but highest in the boreal climate zone.

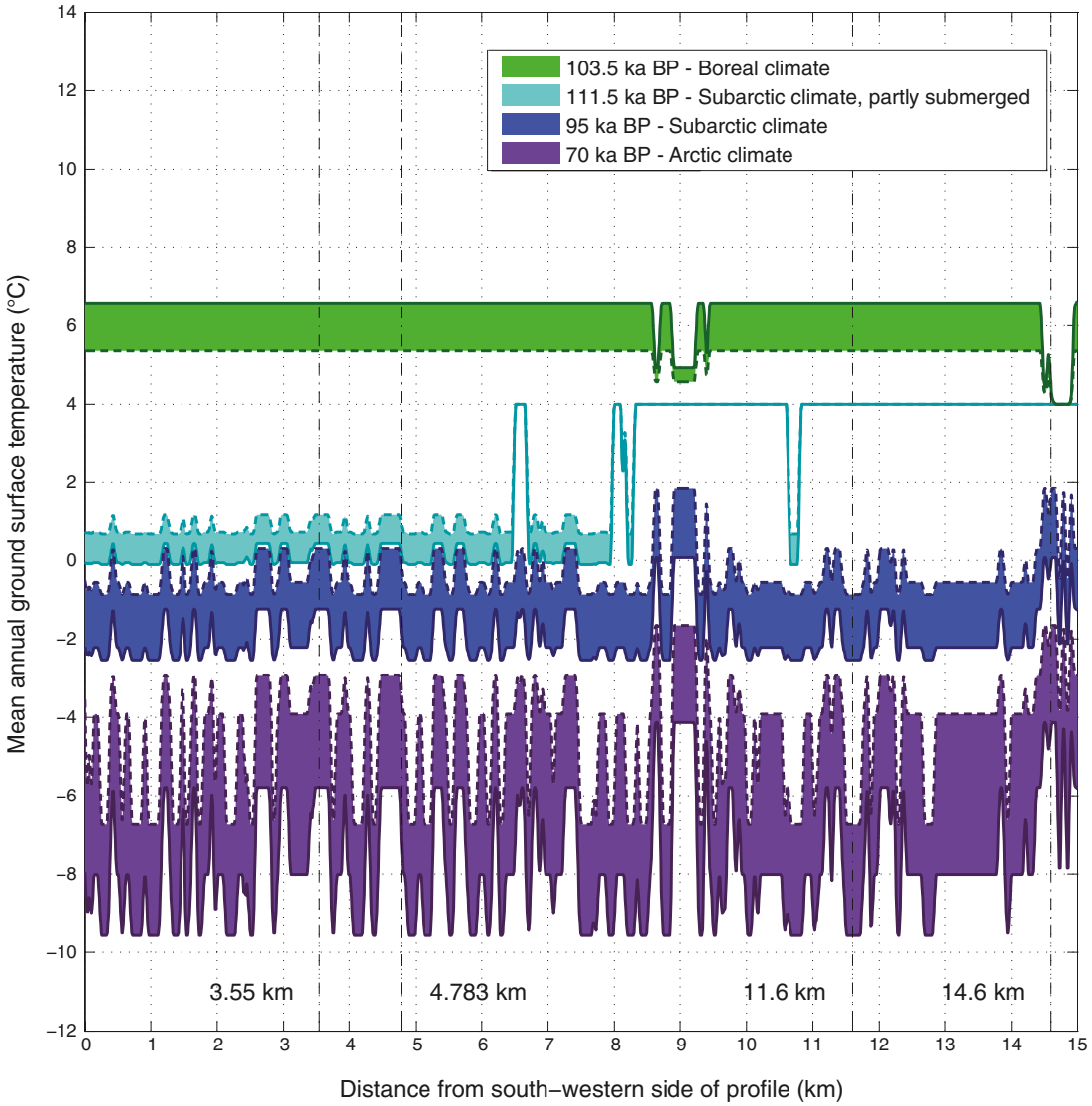

Figure 3-67. *Modelled ground surface temperatures along the profile at four different times for the last glacial cycle case considering different climate conditions: Boreal climate at 103.5 kyrs BP, Subarctic climate and partially submerged conditions at 111.5 kyrs BP, Subarctic climate at 95 kyrs BP, Arctic climate at 70 kyrs BP. The solid border lines of the shadowed areas indicate the dry variant of the climate case and dashed ones the humid variant of the reconstruction of last glacial cycle conditions. The dashed vertical line denotes the location used as example for the fresh-moist surface condition types (Figure 3-66).*

Descriptions of cases simulated with the 2D permafrost model

For the reconstruction of permafrost conditions for the last glacial cycle, two main simulations were made constituting one dry and one humid climate variant. The minimum values of *n*-factors shown in Table 3-10 describe the humid variant whereas their maximum values yield the dry variant. Mean subsurface properties and conditions are used for both variants (e.g. mean thermal and mechanical properties of soil and bedrock, and chemical properties of groundwater, see /Hartikainen et al. 2010/).

Main simulations:

1. Dry climate variant of last glacial cycle.
2. Humid climate variant of last glacial cycle.

The uncertainties related to surface conditions including moisture conditions, vegetation and snow cover as well as ground surface temperature are considered in the main simulations by means of the humid and dry variant of the climate cases studied. Variations in hydraulic properties and ionic composition of groundwater are considered to be of negligible significance in regard to permafrost development, and hence were not included in the sensitivity analyses. Following this approach, and taking results from previous studies into account /SKB 2006a/, the following sensitivity studies were done:

1. uncertainty in air temperature,
2. uncertainty in geothermal heat flow,
3. uncertainty in bedrock thermal conductivity,
4. uncertainty in bedrock thermal diffusivity,
5. combination of uncertainties in bedrock thermal properties,
6. combination of uncertainties in surface and bedrock thermal properties,
7. combination of uncertainties in air temperature, surface conditions and bedrock thermal properties,
8. influence of heat from the repository,
9. convective heat transfer by groundwater flow.

Description and results of main simulations

Resulting ground temperatures and extent of perennially frozen ground at times of 111.5, 95, 74, 70 kyrs BP are illustrated in Figure 3-68 and 3-69 for the humid and dry variant of the reconstruction of last glacial cycle conditions. The selected times in the figures represent the four different situations regarding climate zone, shore-level development and permafrost conditions:

- 111.5 kyrs BP: subarctic climate prevails, the profile is partially submerged by the Baltic and the exposed ground surface is partially underlain by permafrost. The temperature is at a maximum within the repository,
- 95 kyrs BP: subarctic climate prevails and discontinuous permafrost is developing,
- 74 kyrs BP: subarctic climate is turning into a warmer boreal climate and permafrost is degrading, changing from continuous or sporadic permafrost,
- 70 kyrs BP: arctic climate prevails and continuous permafrost reaches its maximum depth.

The evolution of maximum permafrost depth, maximum depth of perennially frozen ground and the maximum depths of the −2 and –4°C isotherms over the repository for the reconstruction of last glacial cycle conditions (both dry and humid climate variants) is shown in Figure 3-70. Figure 3-71 shows the same results for the whole profile and for the repository location, as well as the spatial extent of permafrost summarised along the investigated profile. The −2°C temperature corresponds to the temperature criterion used for freezing of the back-fill material in the deposition tunnels, while –4°C constitute the temperature criterion used in the safety assessment for freezing of the buffer clay /SKB 2011/.

The maximum permafrost depths, maximum depths of perennially frozen ground, and the extent of permafrost distribution are summarised in Tables 3-12 and 3-13. In addition, Table 3-14 and Table 3-15 show the evolution of permafrost depth and depth of perennially frozen ground over the repository and whole profile, respectively.

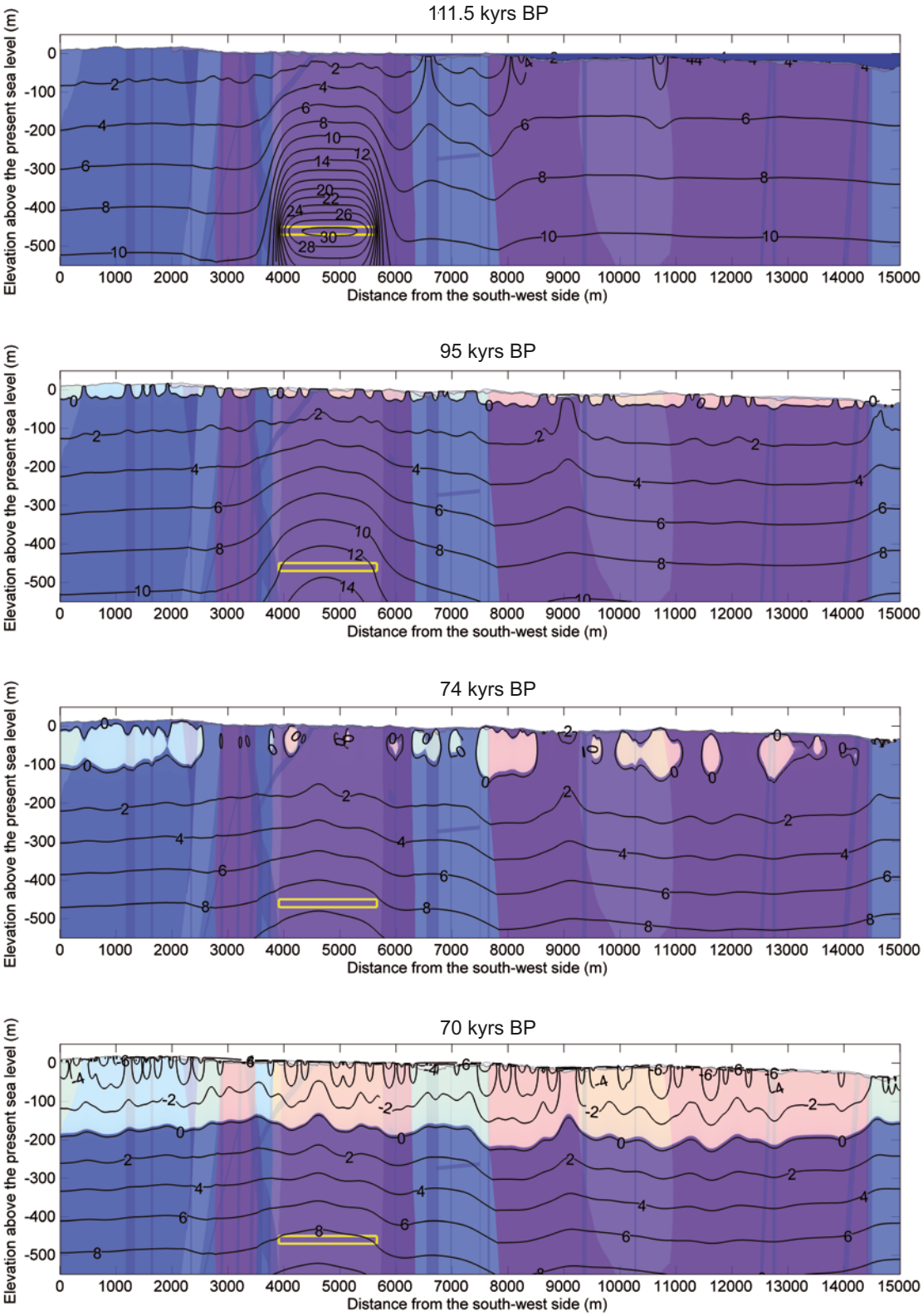

Figure 3-68. *Temperature contours in (°C) and the extent of perennially frozen ground (light colour) and permafrost (0°C isotherm) at times 111.5, 95, 74, 70 kyrs BP for the humid variant of the reconstruction of last glacial cycle conditions. Blue colour on the top of the profile at 111.5 BP kyrs shows the Baltic Sea. The yellow rectangle indicates the location of the repository.*

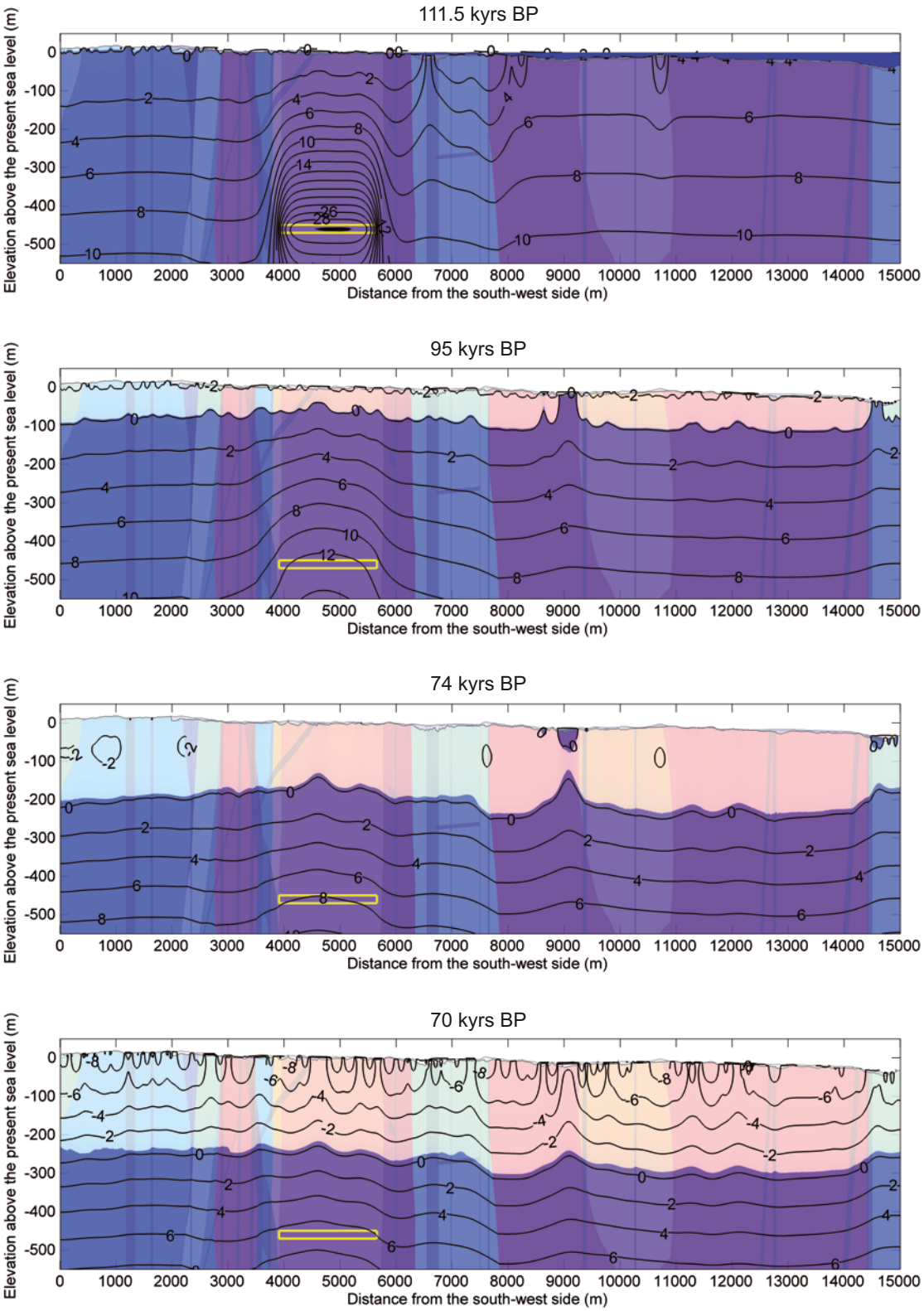

Figure 3-69. *Temperature contours in (°C) and the extent of perennially frozen ground (light colour) and permafrost (0°C isotherm) at times 111.5, 95, 74, 70 kyrs BP for the dry variant of the reconstruction of last glacial cycle conditions. Blue colour on the top of the profile at 111.5 kyrs BP shows the Baltic Sea. The yellow rectangle indicates the location of the repository.*

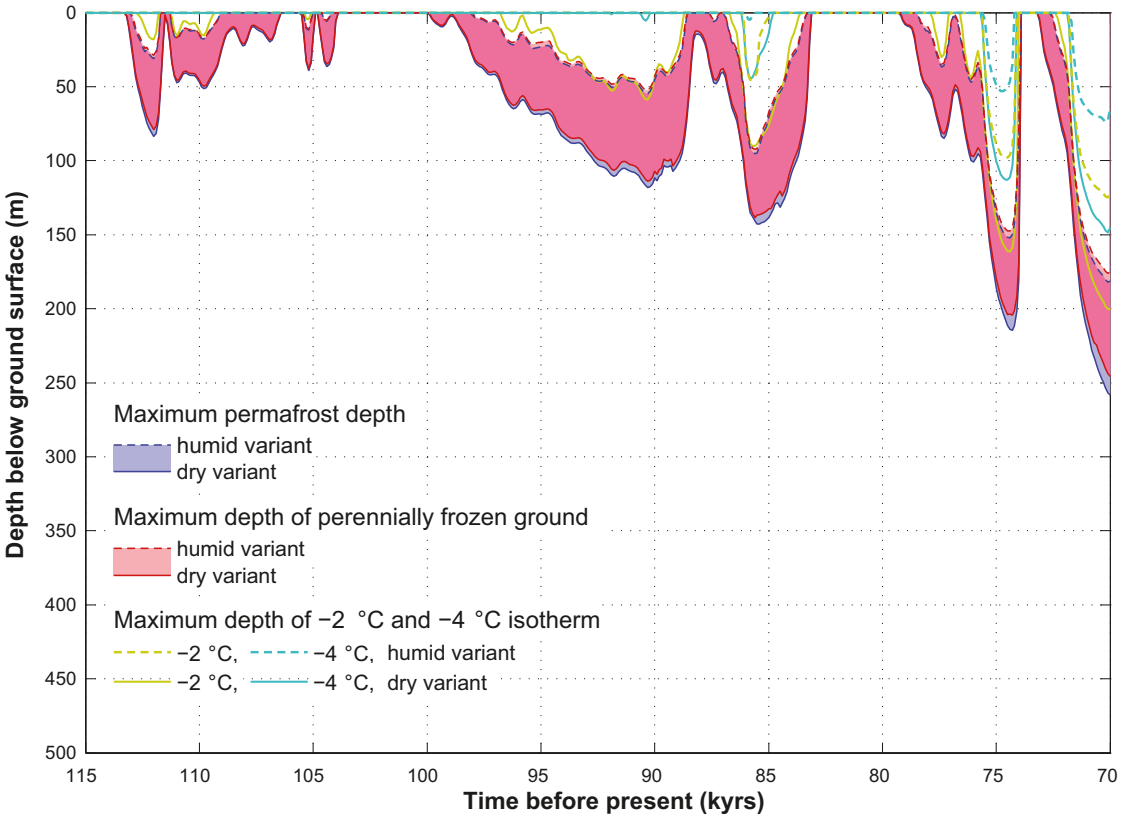

Figure 3-70. *Evolution of maximum permafrost depth, maximum depth of perennially frozen ground and maximum depths of the −2 and –4°C isotherms over the repository for the reconstruction of last glacial cycle conditions. The upper permafrost surface, for periods of degradation from above, is not shown. The shaded area in blue and red represents the range when considering the dry and humid climate variants. The lilac colour indicates that the results for permafrost and perennially frozen ground overlap.*

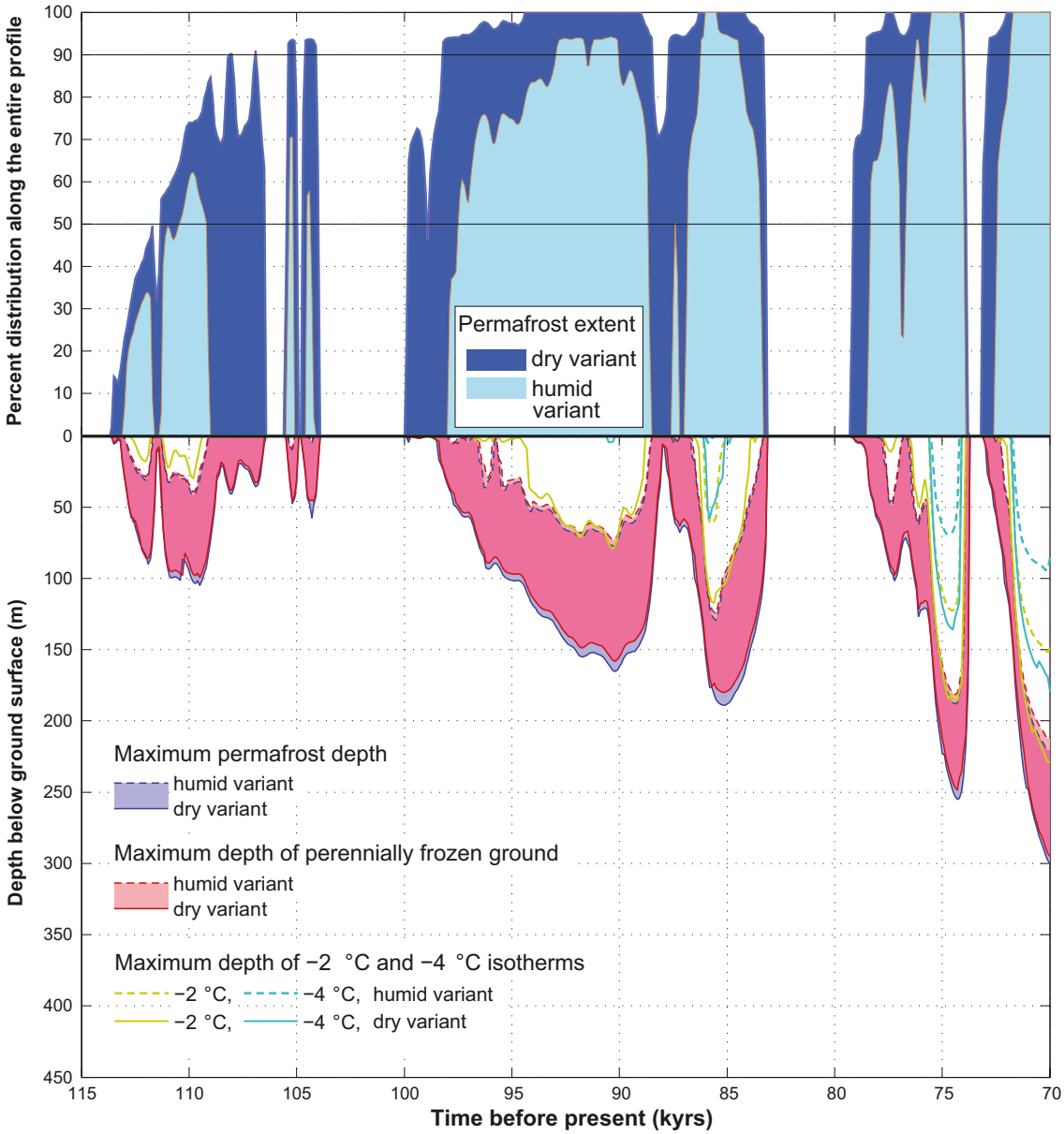

Figure 3-71. *Evolution of maximum permafrost depth, maximum depth of perennially frozen ground and maximum depth of −2 and –4°C isotherms over the whole profile for the reconstruction of last glacial cycle conditions. The figure also shows the percent permafrost distribution along the profile. The transition from sporadic to discontinuous permafrost occurs at 50% permafrost coverage and from discontinuous to continuous permafrost at 90% coverage. The upper permafrost surface, for periods of permafrost degradation from above, is not shown. The shaded area in blue and red represents the range when considering the dry and humid climate variants. The lilac colour indicates that the results for permafrost and perennially frozen ground overlap.*

Table 3-12. Times of permafrost occurrence and associated maximum permafrost depth and maximum depth of perennially frozen ground over the whole profile and over the repository for the humid variant reconstruction of last glacial cycle conditions. The table also gives the time and horizontal location of maximum permafrost depth and the percent extent of permafrost distribution.

Time periods of permafrost occurrence (kyrs BP)	Over the whole profile					Over the repository			
	Maximum permafrost depth (m)	Time of occurrence of maximum permafrost depth (ka BP)	Distance from the south-west side (m)	Maximum depth of perennially frozen ground (m)	Percent extent of permafrost distribution (%)	Maximum permafrost depth (m)	Time of occurrence of maximum permafrost depth (ka BP)	Distance from the south-west side (m)	Maximum depth of perennially frozen ground (m)
113–111.7	31	112	4,960	29	34	31	112	4,960	29
111.3–109.1	42	109.8	7,960	39	62	18	111	5,540	17
105.4–105.1	10	105.2	14,290	9	71	12	105.2	5,540	11
104.6–104.2	2	104.4	14,320	1	58	6	104.4	5,540	5
98–88.6	77	90.3	12,750	73	94	55	90.3	4,970	52
87.5–87.2	1	87.4	14,320	4	50	6	87.4	5,540	5
86.9–83.4	129	85.5	11,620	125	100	95	85.6	5,160	92
78.4–74	188	74.4	11,630	182	100	152	74.4	5,120	148
72.6–70	221	70	11,630	212	100	182	70.1	5,110	176

Table 3-13. Times of permafrost occurrence and associated maximum permafrost depth and maximum depth of perennially frozen ground over the whole profile and over the repository for the dry variant reconstruction of last glacial cycle conditions. The table also gives the time and horizontal location of maximum permafrost depth and the percent extent of permafrost distribution.

Time periods of permafrost occurrence (kyrs BP)	Over the whole profile					Over the repository			
	Maximum permafrost depth (m)	Time of occurrence of maximum permafrost depth (ka BP)	Distance from the south-west side (m)	Maximum depth of perennially frozen ground (m)	Percent extent of permafrost distribution (%)	Maximum permafrost depth (m)	Time of occurrence of maximum permafrost depth (ka BP)	Distance from the south-west side (m)	Maximum depth of perennially frozen ground (m)
113.6–106.4	104	109.7	7,950	98	74	84	112	4,100	79
105.5–104	48	104.4	13,970	46	94	39	105.2	5,540	38
99.9–83.2	189	85.1	12,770	180	100	143	85.5	5,652	137
79.2–73.8	255	74.3	12,810	249	100	215	74.3	5,650	204
73.1–70	301	70	12,820	295	100	259	70	5,650	246

Table 3-14. Evolution of maximum permafrost depth and maximum depth of perennially frozen ground over the repository modelled for the reconstruction of last glacial cycle conditions. The table also shows the prevailing mean annual air temperatures.

Time before present (kyr)	Mean annual air temperature (°C)	Maximum permafrost depth (m)		Maximum depth of perennially frozen ground (m)	
		Humid variant of the reconstruction of last glacial cycle	Dry variant of the reconstruction of last glacial cycle	Humid variant of the reconstruction of last glacial cycle	Dry variant of the reconstruction of last glacial cycle
112	–3.4	31	84	29	79
111.5	–0.6	0	3	0	1
110	–3.5	15	47	15	46
108	–1.5	0	22	0	21
106	2.5	0	0	0	0
104	–0.6	0	6	0	5
102	1.6	0	0	0	0
100	–0.3	0	0	0	0
98	–1.9	2	30	0	28
96	–2.9	18	62	16	60
95	–3.2	23	69	20	66
94	–3.9	35	84	33	81
92	–4.8	49	108	47	103
90	–4.1	45	112	43	107
88	–0.9	0	15	0	13
86	–6.4	73	116	71	113
84	–3.1	31	108	29	104
82	2.1	0	0	0	0
80	0.4	0	0	0	0
78	–2.5	12	52	10	50
76	–4.2	45	101	43	97
75	–10.4	135	186	131	179
74	–1.3	85	180	77	168
72	–3.6	33	86	31	82
70	–10	181	259	175	246

Table 3-15. Evolution of maximum permafrost depth and maximum depth of perennially frozen ground over the whole profile modelled for the reconstruction of last glacial cycle conditions. The table also shows the prevailing mean annual air temperatures.

Time before present (kyr)	Mean annual air temperature (°C)	Maximum permafrost depth (m)		Maximum depth of perennially frozen ground (m)	
		Humid variant of the reconstruction of last glacial cycle	Dry variant of the reconstruction of last glacial cycle	Humid variant of the reconstruction of last glacial cycle	Dry variant of the reconstruction of last glacial cycle
112	–3.4	31	84	29	86
111.5	–0.6	0	12	0	10
110	–3.5	37	95	34	89
108	–1.5	0	41	0	38
106	2.5	0	0	0	0
104	–0.6	0	23	0	20
102	1.6	0	0	0	0
100	–0.3	0	0	0	0
98	–1.9	0	34	0	32
96	–2.9	29	93	26	89
95	–3.2	34	101	31	97
94	–3.9	49	119	46	114
92	–4.8	70	151	66	145
90	–4.1	70	162	65	155
88	–0.9	0	7	0	6
86	–6.4	96	153	93	147
84	–3.1	50	155	46	147
82	2.1	0	0	0	0
80	0.4	0	0	0	0
78	–2.5	1	59	1	56
76	–4.2	55	122	52	117
75	–10.4	165	222	160	212
74	–1.3	150	239	140	222
72	–3.6	44	110	41	105
70	–10	221	301	212	295

Figure 3-72 and 3-73 show vertical bedrock temperature profiles in the middle of the repository location (with fresh-moist surface cover) for the humid and dry variants of the reconstruction of last glacial cycle conditions. Similar examples of vertical bedrock temperature profiles, including other surface cover types (wet, dry, peatland) are found in /Hartikainen et al. 2010/.

The modelling results for the reconstruction of last glacial cycle conditions show that annual mean ground surface temperature at the Forsmark site can vary considerably in time and location depending on the prevailing climate zone and surface moisture condition type, see Figures 3-66 and 3-67, and /Hartikainen et al. 2010/. For the first ~50 kyrs of the reconstructed last glacial cycle, the dry surface condition resulted in arctic climate zone ground surface temperatures below −11°C and boreal climate ground surface temperatures over +6°C. The wet surface condition yielded milder ground surface temperatures in both the arctic and boreal climate zones ranging from below −3°C to over +5°C over the same time period. Furthermore, the peatland surface condition, having the moistest surface conditions, resulted in even milder ground surface temperatures ranging approximately between −2°C and +4°C. In addition, the difference in ground surface temperature could be several degrees from place to

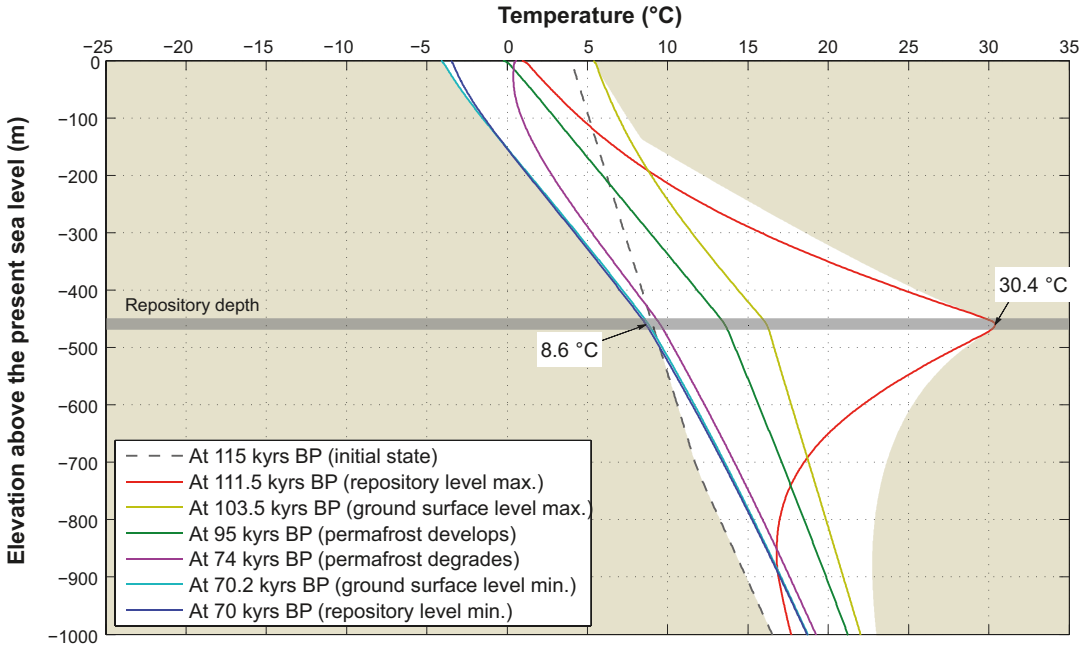

Figure 3-72. *Bedrock temperature along a vertical profile located in the middle of the repository at 4,783 m from the south-western side of the profile the for the humid variant of the reconstruction of last glacial cycle conditions. The surface cover type reflects fresh-moist conditions. The white colour envelope represents the range of bedrock temperature fluctuation, simulated over the time period of 115–70 kyrs BP. For more examples of modelled bedrock temperatures, see /Hartikainen et al. 2010/.*

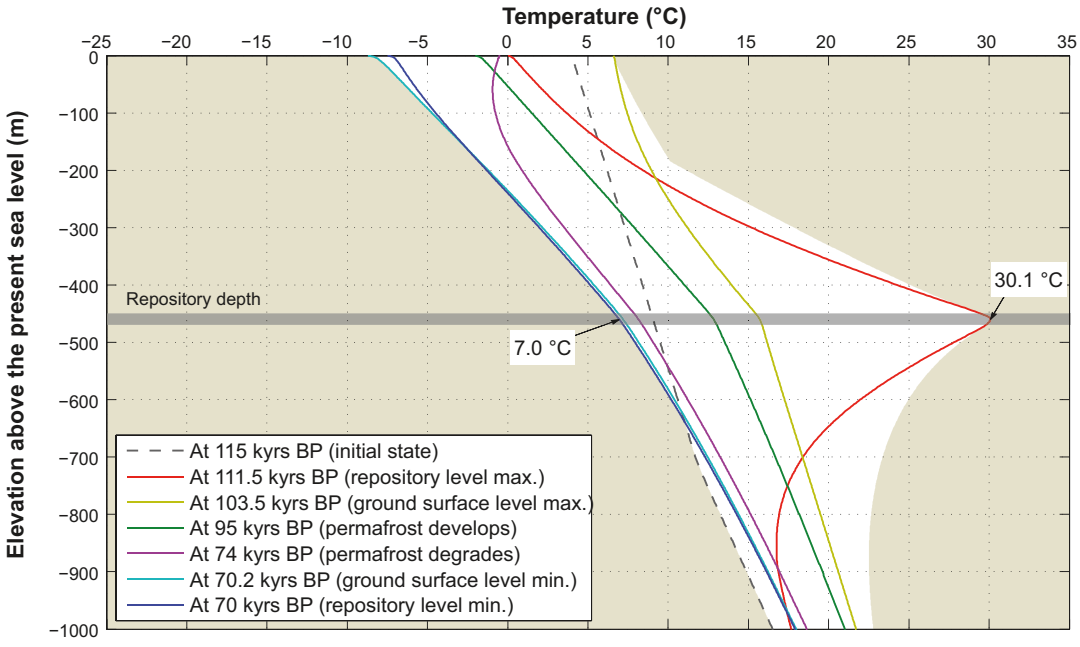

Figure 3-73. *Ground temperature along a vertical profile located in the middle of the repository at 4,783 m from the south-western side of the profile for the dry variant of the reconstruction of last glacial cycle conditions. The surface cover type reflects fresh-moist conditions. The white colour envelope represents the range of bedrock temperature fluctuation, simulated over the time period of 115–70 kyrs BP. For more examples of modelled bedrock temperatures, see /Hartikainen et al. 2010/.*

place along the investigated profile, see Figure 3-67. The same figure shows that the spatial fluctuation in ground surface temperature is largest in the arctic climate zone when the air temperature is lowest, and lowest in the boreal climate zone when the air temperature is close to 0°C.

The simulation results (Figure 3-70) demonstrate that development of discontinuous permafrost is characteristic for the humid climate variant of the reconstruction of last glacial cycle conditions whereas continuous permafrost development prevails for long periods of the dry climate variant. In all cases permafrost became a continuous spatial distribution when the annual mean air temperature decreased below –6°C and the maximum permafrost depth exceeded a depth of ~50 m.

During some periods, short distinct changes in climate results in phases of fast decay and growth of permafrost, such as at around 74 kyrs BP (Figure 3-71). Similar rates of permafrost growth and decay have been reported in /Delisle 1998, Kukkonen and Safanda 2001/.

The variation in ground surface temperature has the strongest effect on bedrock temperature fluctuations within the upper part of the vertical profile, see Figures 3-71 and 3-72 and /Hartikainen et al. 2010/. The fluctuation is largest at the surface and reduces considerably with depth except where the heat from the repository has a large influence.

Regarding the evolution of permafrost depth and depth of perennially frozen ground, the results for the reconstruction of the last glacial cycle that considered variations in surface moisture conditions and mean bedrock thermal properties indicated that permafrost (defined by the 0°C isotherm) can reach a depth between ~180 m and ~260 m over the repository (Figure 3-70) and a depth between ~220 m and ~300 m outside the repository (Figure 3-71) in a time frame of 45,000 years. The maximum depth of perennially frozen ground can range between ~180 m and ~250 m over the repository and between ~210 m and ~300 m over the whole site at the same time. As seen from the 1D permafrost simulations of the full last glacial cycle (Figure 3-56), these numbers represent the largest depths during the entire glacial cycle.

A comparison between results from the present 2D modelling for the reconstruction of last glacial cycle conditions and the corresponding 1D modelling simulation performed for SR-Can, see previous part of Section 3.4.4 and /SKB 2006a, Section 3.4/ shows a good agreement regarding the maximum permafrost depth at 70,000 years BP (Figure 3-74). The differences observed in Figure 3-74 reflect the higher thermal conductivity and lower geothermal heat flow values used in /SKB 2006a/ as well as differences in prescribed surface conditions.

Unfrozen water content and talik formation in reconstruction of last glacial cycle conditions

Figures 3-75 and 3-76 show the unfrozen water content within the frozen bedrock as well as the 2D groundwater flow (Darcy velocity) directions at a time of 90.4 kyrs BP for the humid and dry variants of the reconstruction of last glacial cycle conditions. The figures show the whole profile, and close-ups of the highly conductive deformation zone ZFMA2 at a distance of 4,000 m, and the near-by area of the two lakes at distances of 9,000 m and 14,600 m. The results show that during phases of the simulated time period, taliks form at these lake locations (Figures 3-69 and 3-76). The corresponding results for other time periods are found in /Hartikainen et al. 2010/.

The results show a maximum groundwater flow velocity of ~50 m/yr when no permafrost occurred and some metres per year beneath the perennially frozen ground. The results show that under continuous permafrost conditions both the local and regional groundwater flow are reduced considerably in the perennially frozen ground but also in the unfrozen ground beneath permafrost, see Figures 3-75 and 3-76 and /Hartikainen et al. 2010/. On the other hand, the results demonstrate that when the unfrozen groundwater content is greater than 10%, groundwater flow may occur through a continuous partially frozen permafrost zone, although the flow velocity is very low, only some millimetres per year (Figure 3-76). This indicate, that under continuous permafrost conditions taliks are able to form under lakes through perennially frozen ground down to ~50 m depth, if favourable groundwater flow conditions with open flow paths prevail. When the freezing of ground is advanced to a degree with unfrozen water content less than 10%, groundwater flow is reduced considerably, and thus a talik is not able to form or survive. A 2D model approach is in this context sufficient to justify the likelihood of talik occurrence, but not to determine their groundwater flow and precise geometrical characteristics.

Salinity concentration in reconstruction of last glacial cycle conditions

Given the permafrost and freezing results presented above, the associated results on salinity concentrations at times of 111.5, 95, 74, 70 kyrs BP are illustrated in Figures 3-77 and 3-78. Due to low salinity concentrations at shallow depths, the impacts of freezing on salinity exclusion and redistribution are difficult to see from the results. However, under more severe conditions when the air temperature is decreased exceptionally, i.e. by 8°C, the freezing occurs more intensively and an increase in salinity concentration due to the exclusion can be seen /Hartikainen et al. 2010/.

Groundwater flow is an integral part of the salinity transport modelling, which hence suffers from the same restrictions as the 2D groundwater flow modelling. However, the results for salinity concentration (Figure 3-78) and /Hartikainen et al. 2010 Figures 5-32 to 5-35/ show that freezing can induce salt exclusion and transport when perennially frozen ground development exceeds 200 m depth. This can be seen as increased salinity concentrations extending downwards in front of the partially frozen bedrock. At shallow depths the impacts of freezing cannot be seen since the salinity concentration of the groundwater has been diluted prior to the development of perennially frozen ground. The increased salinity concentration within the perennially frozen ground is mainly because salt transport occurs more slowly than the freezing zone advances.

Description and results of sensitivity experiments

Sensitivity experiment 1 – uncertainty in air temperature

In sensitivity experiment 1, the objective is to investigate the impact of the estimated uncertainty in the air temperature curve. The description of the temperature curve and its estimated uncertainty is found in Appendix 1. From this description, it is estimated that an uncertainty range of ±6°C is relevant for the temperature curve used as input. In addition, it was investigated how much the air temperature curve is required to be lowered to get the 0°C, −2°C and –4°C isotherms to reach the 450 m repository depth. Based on the SR-Can results /SKB 2006a/, temperature shifts of 4, 6, 8, 10, 12, 14 and 16°C were chosen (Figure 3-79). As a pessimistic case, the dry variant of the reconstruction of last glacial cycle conditions was simulated, since it results in deeper permafrost than the humid variant. The mean thermal properties of the subsurface were used.

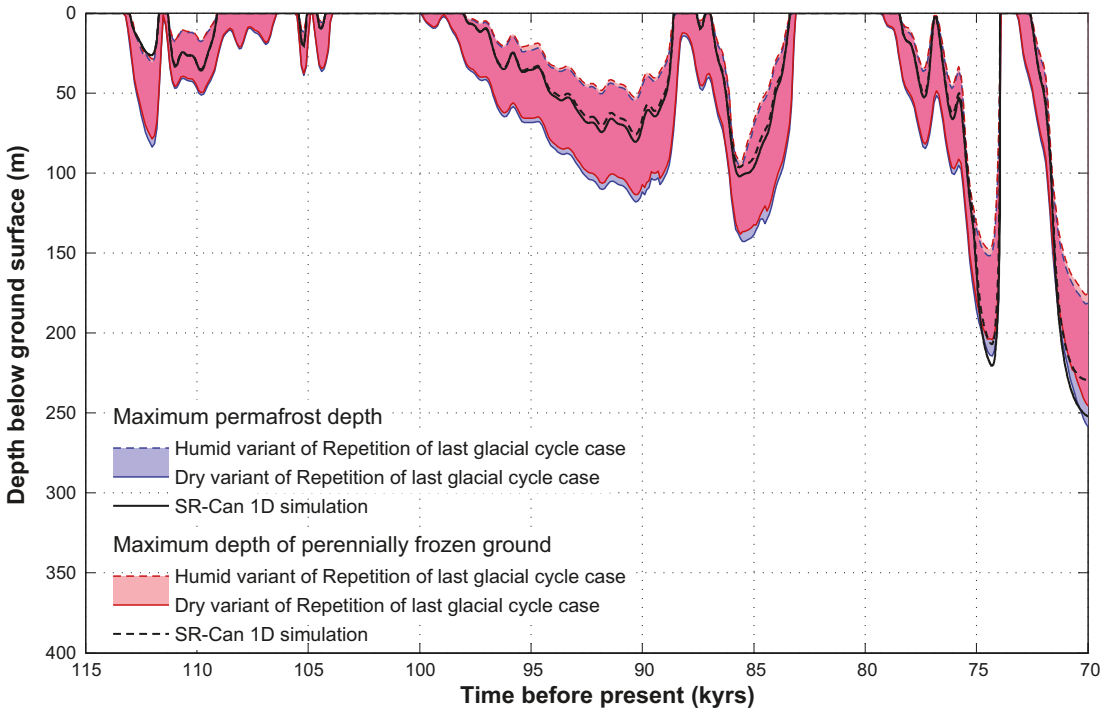

Figure 3-74. *Evolution of permafrost and frozen ground depth over the repository location from the 2D reconstruction of last glacial cycle conditions and from the 1D simulation of "the reference surface conditions of the base variant" from /SKB 2006a/. The results of the 1D and 2D permafrost models are in good agreement. The shaded area in blue and red represents the range when considering the dry and humid climate variants of the present study. The lilac colour indicates that the results for permafrost and perennially frozen ground overlap.*

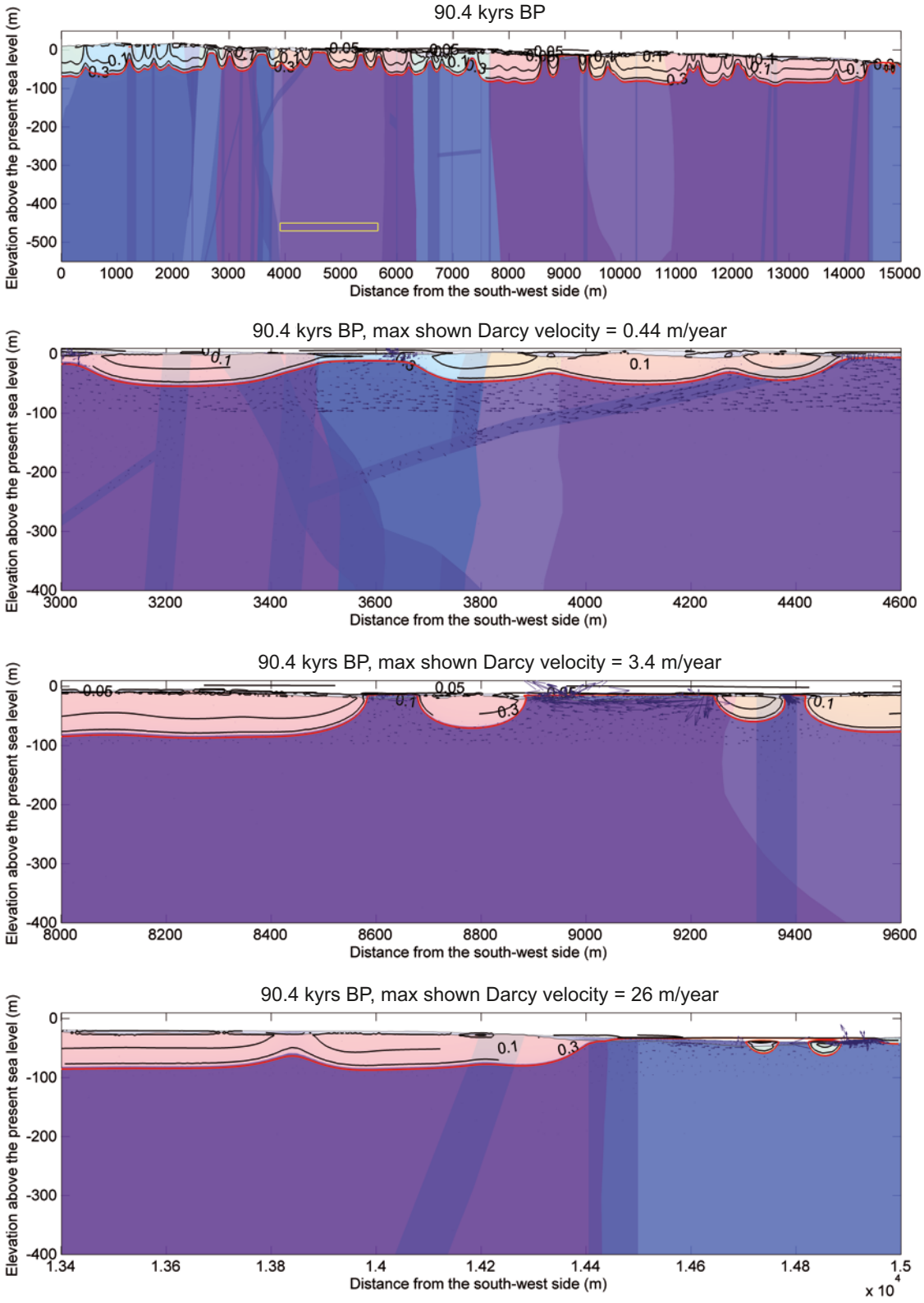

Figure 3-75. *Unfrozen volumetric (m^3/m^3) groundwater content contours and Darcy flow directions at 90.4 kyrs BP for the humid variant of the reconstruction of last glacial cycle conditions. The upper panel shows the whole profile, followed by close-ups of the deformation zone ZFMA2 at ~4,000 m, and the near-by area of the lakes at the distances 9,000 m and 14,600 m from the south-west side of the profile. Light colour shows the extent of perennially frozen ground, the red line shows the 0°C isotherm (i.e. permafrost depth), and the yellow box in the upper panel shows the repository. For further examples of these results, see /Hartikainen et al. 2010/.*

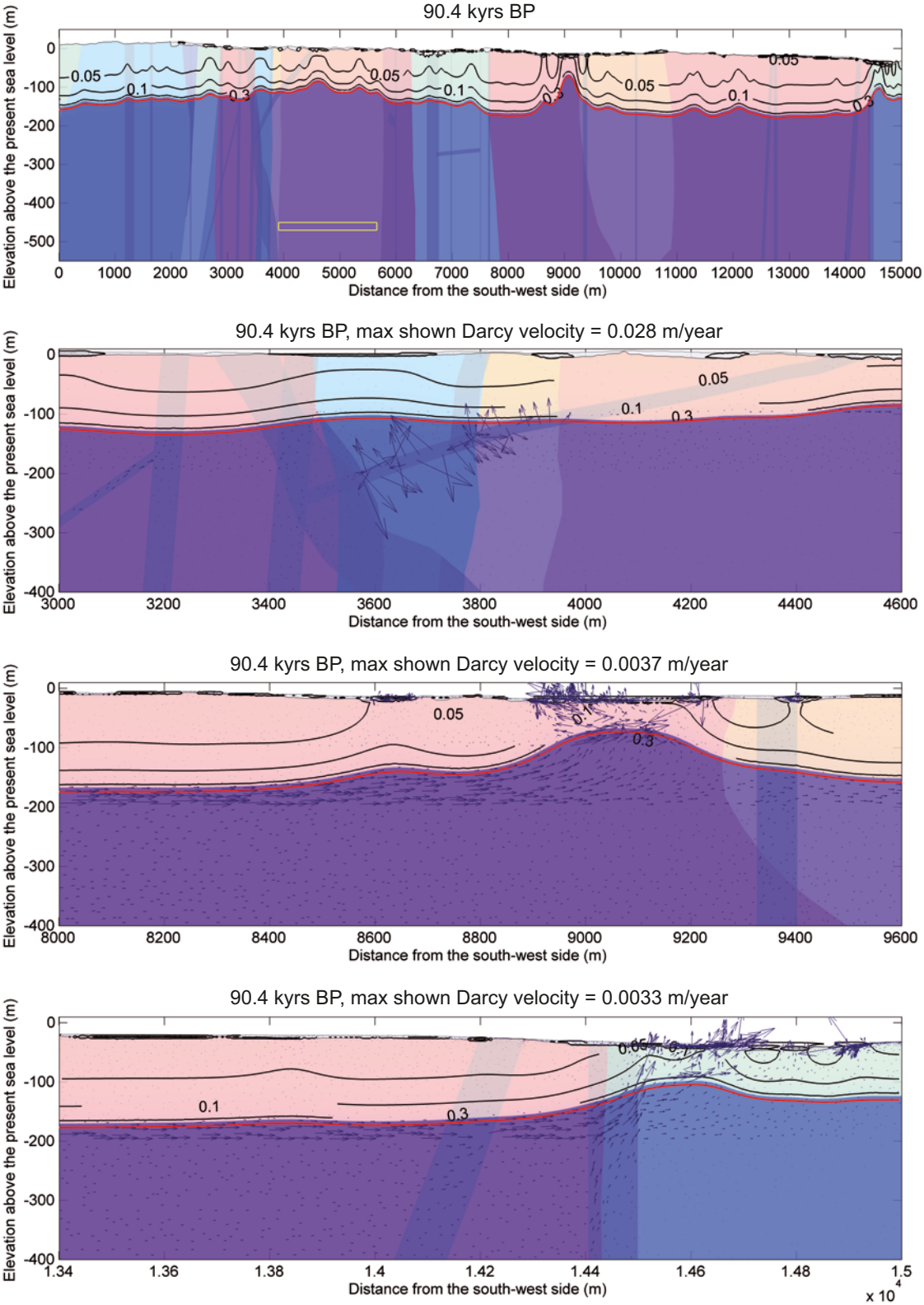

Figure 3-76. *Unfrozen volumetric (m^3/m^3) groundwater content contours and Darcy flow directions at 90.4 kyrs BP for the dry variant of the reconstruction of last glacial cycle conditions. The upper panel shows the whole profile, followed by close-ups of the deformation zone ZFMA2 at ~4,000 m, and the near-by area of the lakes at the distances 9,000 m and 14,600 m from the south-west side of the profile. Light colour shows the extent of perennially frozen ground, the red line shows the 0°C isotherm (i.e. permafrost depth), and the yellow box in the upper panel shows the repository. For further examples of these results, see /Hartikainen et al. 2010/.*

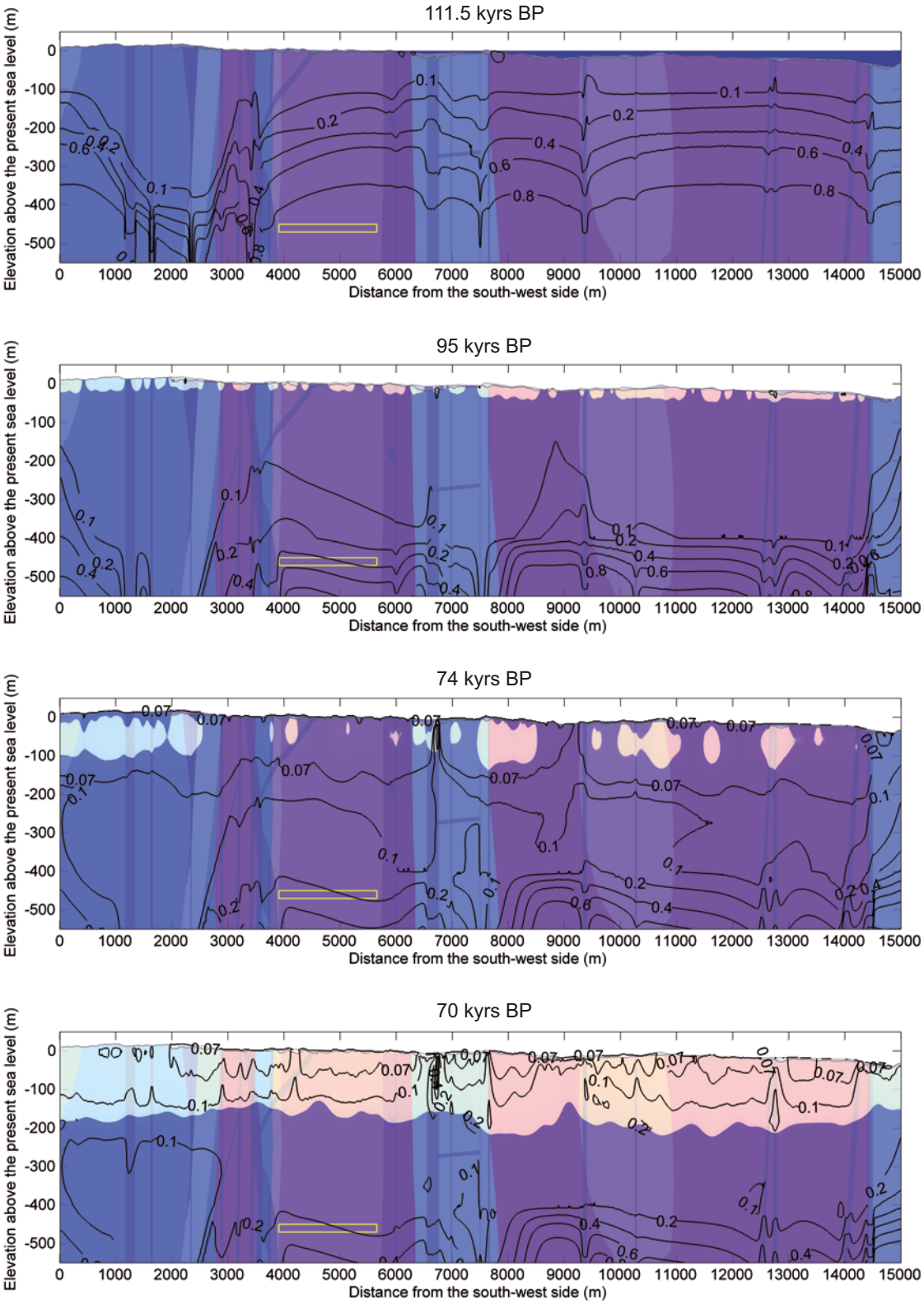

Figure 3-77. *Salinity concentration isolines in (mass-%) at times 111.5, 95, 74, 70 kyrs BP for the humid variant of the reconstruction of last glacial cycle conditions. The isolines show 0.07, 0.1, 0.2, 0.4, 0.6 and 0.8 mass-% salinity. Blue colour on the top of the profile at 111.5 kyrs BP shows the Baltic Sea and the light colour the extent of perennially frozen ground. For further examples of similar results, see /Hartikainen et al. 2010/.*

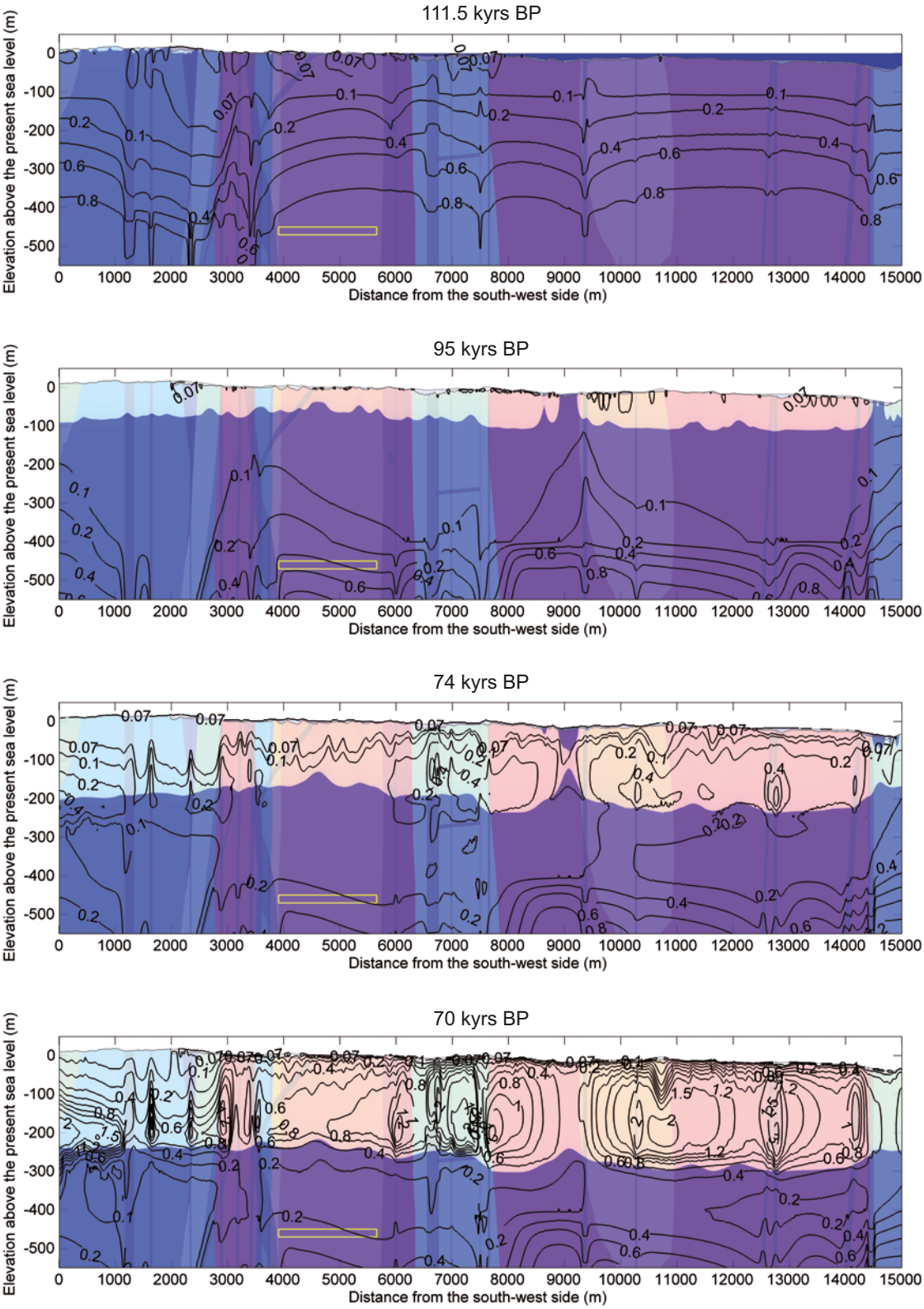

Figure 3-78. *Salinity concentration isolines in (mass-%) at times 111.5, 95, 74, 70 kyrs BP for the dry variant of the reconstruction of last glacial cycle conditions. The isolines show 0.07, 0.1, 0.2, 0.4, 0.6, 0.8, 1, 1.2, 1.5, 2 and 3 mass-% salinity. Blue colour on the top of the profile at 111.5 kyrs BP shows the Baltic Sea and the light colour the extent of perennially frozen ground. For further examples of similar results, see /Hartikainen et al. 2010/.*

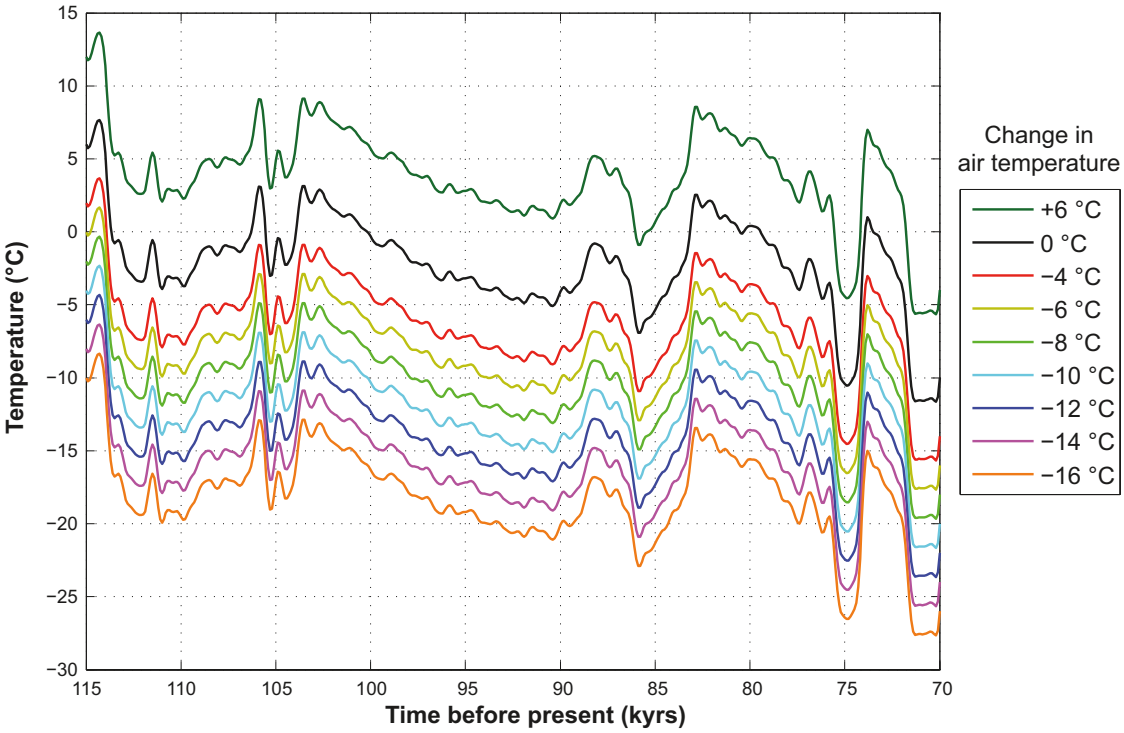

Figure 3-79. *Investigated temperature evolutions after shifting the entire reconstructed last glacial cycle temperature curve by −16, −14, −12, −10, –8, –6, –4, 0 and +6°C compared to the reconstruction of the last glacial cycle. The 0°C curve constitutes the temperature curve reconstructed for the last glacial cycle.*

The evolution of maximum permafrost depth and maximum depth of perennially frozen ground at the repository location considering mean thermal properties and the air temperature changed by –6, 0 and +6°C are shown in Figure 3-80. The evolution of maximum 0°C isotherm depth, i.e. maximum permafrost depth, and maximum depth of perennially frozen ground over the repository and the whole profile for the dry variant of the reconstruction of last glacial cycle conditions considering mean thermal properties and the air temperature changed by –4, –6, –8, −10, −12, −14 and −16°C are shown in Figure 3-81 and 3-82. The evolution of maximum −2°C and –4°C isotherm depth over the repository are shown in Figure 3-83 and 3-84, respectively. It can be seen that temperature shifts of ~8, ~10 and ~14°C are needed to get the 0°C, −2°C and –4°C isotherms to reach the repository at the time with deepest permafrost at 70 kyrs BP. For details on the setup and results of this experiment, see /Hartikainen et al. 2010/.

The results from the investigation of uncertainties in air temperature show that a 6°C lowering of the entire temperature curve reconstructed for the last glacial cycle (corresponding to the estimated maximum uncertainty in the temperature curve, Appendix 1) increased permafrost depth by almost 60%, from the range of ~180–260 m to ~290–410 m, while a corresponding change of the entire curve of +6°C reduce permafrost depth by 60 to 75%, to a range of ~40–100 m (Figure 3-80). A similar effect can be seen in the depth of perennially frozen ground, i.e. the temperature curve shift of –6°C results in a change from the range ~190–260 m to ~280–380 m, while a +6°C temperature shift reduces the range to ~40–100 m. In addition, the results in Figure 3-81 show that, for the dry variant of the last glacial cycle, the temperature curve reconstructed for the last glacial cycle needs to be lowered by almost 8°C to make permafrost reach the repository depth. Furthermore, the results show that a shift of the reconstructed temperature curve of ~10°C and ~14°C are needed to get the –2°C and –4°C isotherms to reach the repository depth (Figure 3-83 and 3-84). The major part of the difference (of up to more than 100 m) between results for the repository location and results from the entire profile (Figure 3-81 and 3-82) is due to the heat from the repository. The effect of topography is minor and further reduced with depth. A less important factor is that some rock domains (RFM026, RFM033, RFM034, RFM040) outside the repository have higher thermal conductivity (2.8%) than the one (RFM029) where the repository is located.

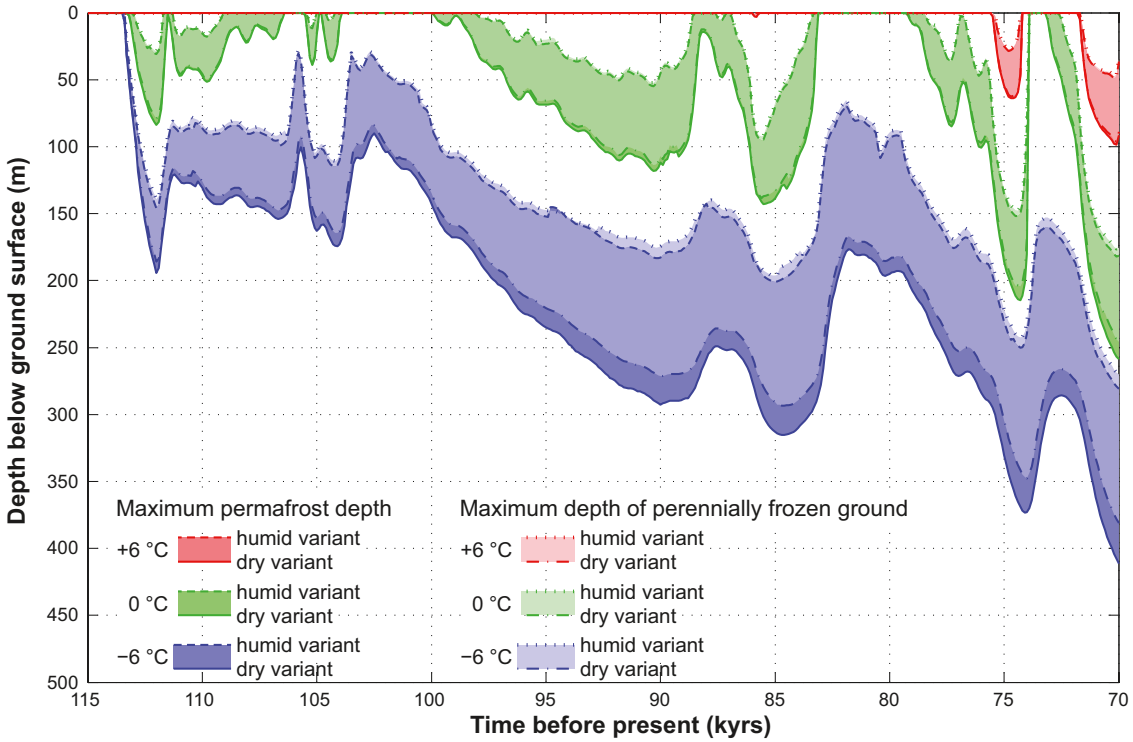

Figure 3-80. *Result of sensitivity experiment on uncertainty in air temperature. Evolution of maximum permafrost depth (solid lines) and maximum depth of perennially frozen ground (dashed lines) over the repository location considering mean thermal properties and the air temperature curve changed by –6, 0 and +6°C. The shaded areas in blue, green and red represents the range when considering the dry and humid climate variants. Note that the results for permafrost and perennially frozen ground overlap to a large degree.*

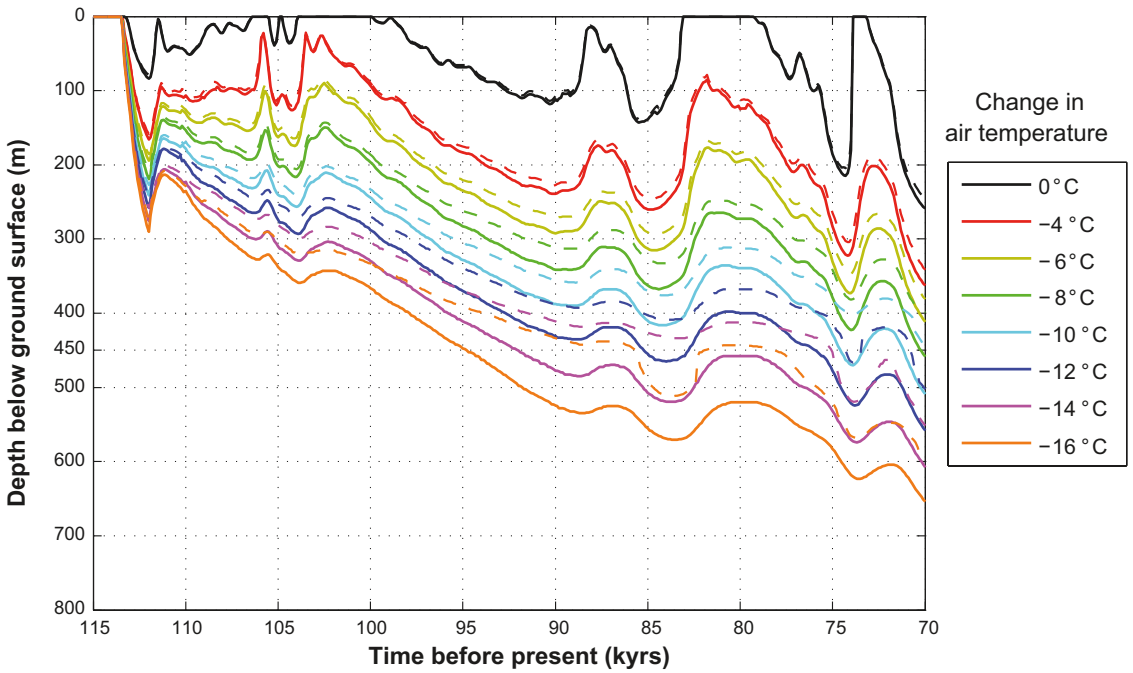

Figure 3-81. *Evolution of maximum permafrost depth (black solid line) and maximum depth of perennially frozen ground (black dashed line) at the repository location for the dry variant of the reconstruction of last glacial cycle conditions. The figure also show corresponding results with the air temperature curve lowered by –4, –6, –8, −10, −12, −14 and −16°C compared to the reconstruction of the last glacial cycle (coloured lines).*

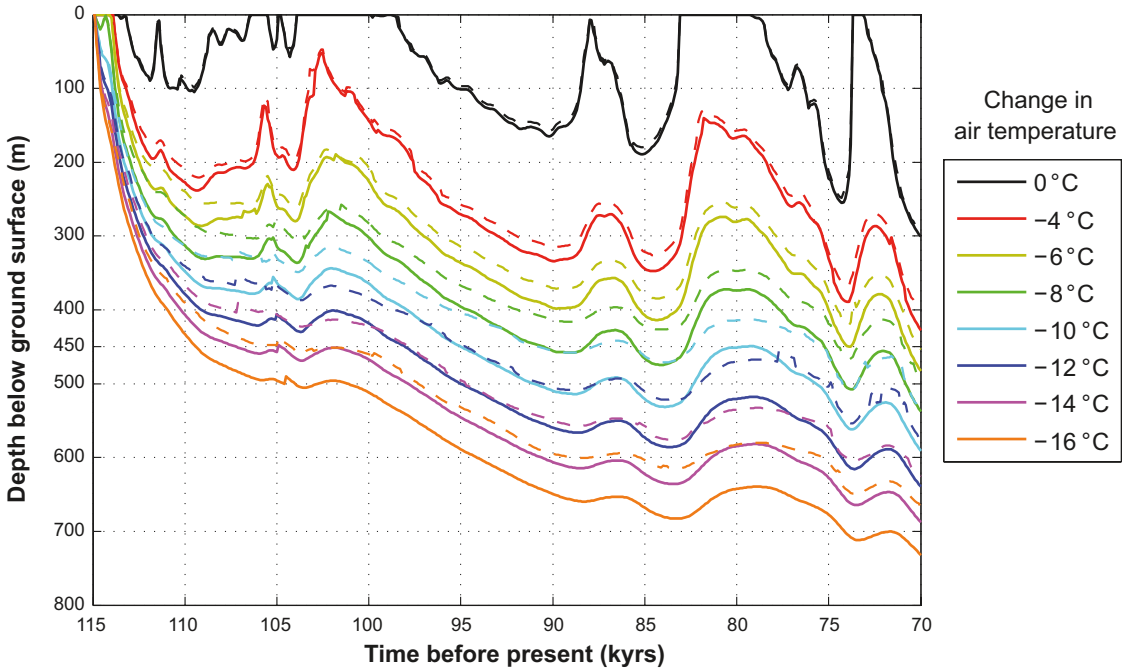

Figure 3-82. *Evolution of maximum permafrost depth (black solid lines) and maximum depth of perennially frozen ground (black dashed lines) over the whole profile for the dry variant of the reconstruction of last glacial cycle conditions. The figure also show corresponding results with the air temperature curve lowered by –4, –6, –8, −10, −12, −14 and −16°C (coloured lines).*

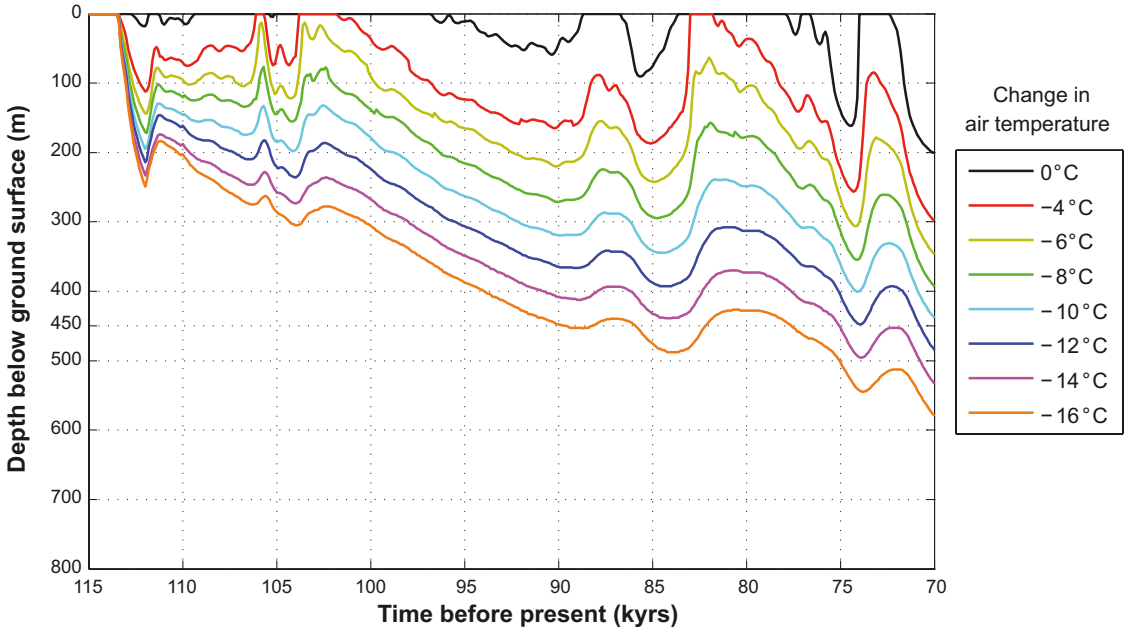

Figure 3-83. *Evolution of maximum −2°C -isotherm depth at the repository location for the dry variant of the reconstruction of last glacial cycle conditions (black line). The figure also show corresponding results with the air temperature curve lowered by –4, –6, –8, −10, −12, −14 and −16°C compared to the reconstruction of the last glacial cycle (coloured lines).*

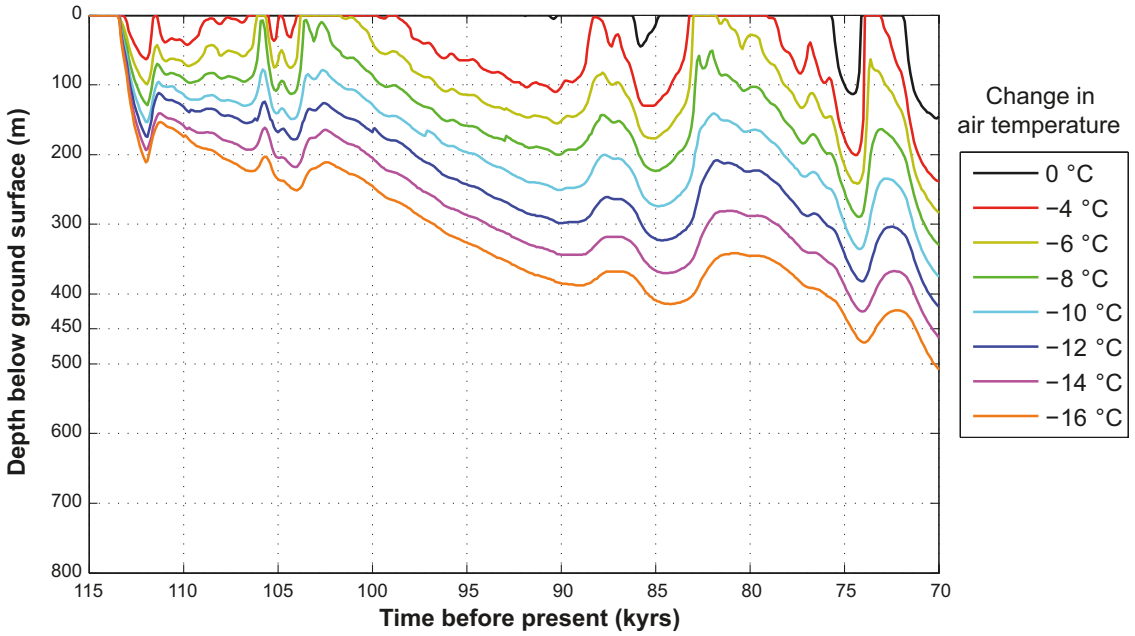

Figure 3-84. *Evolution of maximum –4°C -isotherm depth at the repository location for the dry variant of the reconstruction of last glacial cycle conditions (black line). The figure also show corresponding results with the air temperature curve lowered by –4, –6, –8, −10, −12, −14 and −16°C compared to the reconstruction of the last glacial cycle (coloured lines).*

Sensitivity experiment 2 – uncertainty in geothermal heat flow

Sensitivity experiment 2 investigates the effects of uncertainties in geothermal heat flow. The mean surface level value of 61 mW/m^2 and the range from –14% (minimum) to +12% (maximum) /Sundberg et al. 2009/ are used for the dry climate variant of the reconstruction of last glacial cycle conditions. For details on the setup of this experiment, see /Hartikainen et al. 2010/. The results show that a variation of –14% to +12% in geothermal heat flow can cause an approximate fluctuation of +8.0% to –6.3% (~280 m to ~240 m) in permafrost depth, and correspondingly an approximate fluctuation of +7.7% to –5.7% (~260 m to ~230 m) in the depth of perennially frozen ground.

Sensitivity experiment 3 and 4 – uncertainty in bedrock thermal conductivity and thermal diffusivity

Sensitivity experiment 3 was made in order to study the consequences of uncertainty in thermal conductivity (mean, minimum and maximum). In sensitivity experiment 4, the uncertainty is investigated in relation to the mean, minimum and maximum thermal diffusivities. In addition, the effect of heterogeneity of thermal properties on the development of permafrost and frozen ground is studied by the mixed thermal diffusivities, which are obtained by using values of highest difference for adjacent rock domains, see /Hartikainen et al. 2010/. For details on the setup of this experiment, see /Hartikainen et al. 2010/.

The results for thermal conductivity indicated that the mean variation of –6.1% to +8.6% in thermal conductivity can cause an approximate fluctuation of –4.6% to +2.7% (~250 m to ~270 m) in permafrost depth, and correspondingly an approximate fluctuation of –4.1% to +2.7% (~240 m to ~250 m) in perennially frozen ground depth. The uncertainty in thermal diffusivity causes a slightly larger variation in permafrost depth than solely the uncertainty in thermal conductivity. The results demonstrate that the mean variation of –11.5% to +14.6% in thermal diffusivity can cause an approximate fluctuation of –6.0% to +3.4% (~240 m to ~270 m) in permafrost depth, and correspondingly an approximate fluctuation of –5.5% to +3.4% (~230 m to ~250 m) in perennially frozen ground depth. In addition, the variation in thermal properties between adjacent rock domains has a minor effect on the development of permafrost and perennially frozen ground. The reason for this is probably the flat topography of the site, in consequence of which heat transfer mainly takes place vertically. This is also supported by the results for the ground temperature and perennially frozen ground (Figures 3-68 and 3-69) which show rather uniform permafrost development with depth when it occurs in continuous form.

Sensitivity experiment 5 – combination of uncertainties in bedrock thermal properties

In sensitivity experiment 5, the objective was to investigate the combination of uncertainties in dominant thermal properties of the bedrock. The limits for the uncertainty interval are obtained by combining the thermal properties that are anticipated, based on results from /SKB 2006a/, to enhance the permafrost development, i.e. maximum thermal conductivity, minimum heat capacity and minimum geothermal heat flow, as well as the thermal properties that are expected to diminish the permafrost development, i.e. minimum thermal conductivity, maximum heat capacity and maximum geothermal heat flow. The dry variant of the reconstruction of last glacial cycle conditions was simulated. For details on the setup of this experiment, see /Hartikainen et al. 2010/.The resulting evolution of maximum permafrost depth and maximum depth of perennially frozen ground over the repository are shown in Figure 3-85. The results show that the combined uncertainties can cause a variation of –8.9% to +12.2% (~240 m to ~290 m) in the permafrost depth and a variation of –6.2% to +14.4% (~230 m to ~280 m) in the depth of perennially frozen ground.

Sensitivity experiment 6 – combination of uncertainties in surface and bedrock thermal properties

In sensitivity experiment 6 the uncertainties in subsurface thermal properties from experiment 5 are combined with the uncertainties in surface conditions (excluding air temperature). For the reconstruction of last glacial cycle conditions, the uncertainty interval is obtained by combining the dry variant with the thermal properties enhancing permafrost development, and the humid variant of the same case with thermal properties diminishing permafrost development.

Figure 3-86 shows the evolution of maximum permafrost depth and maximum depth of perennially frozen ground over the repository for the reconstruction of last glacial cycle conditions considering combined uncertainties in surface conditions and thermal properties as described in /Hartikainen et al. 2010, Section 2.2 and 2.4, and Appendix E, H, I and J/. The calculated uncertainty range for the maximum permafrost depth at 70 kyrs BP is 170–290 m and for the maximum depth of perennially frozen ground 170–280 m. For details on the setup and results of this experiment, see /Hartikainen et al. 2010/.

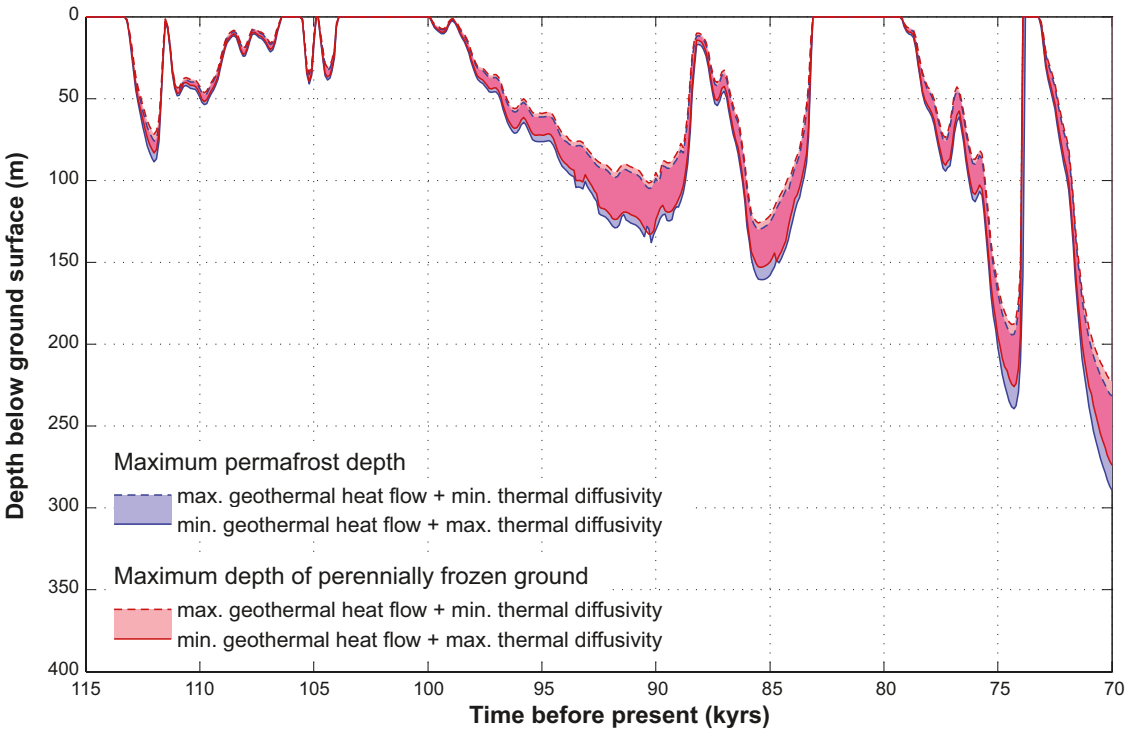

Figure 3-85. *Evolution of maximum permafrost depth and maximum depth of perennially frozen ground over the repository for the dry variant of the reconstruction of last glacial cycle conditions considering combined uncertainty in bedrock thermal conditions and geothermal heat flow. The shaded area in blue and red represents the range when considering the dry and humid climate variants. The lilac colour indicates that the results for permafrost and perennially frozen ground overlap.*

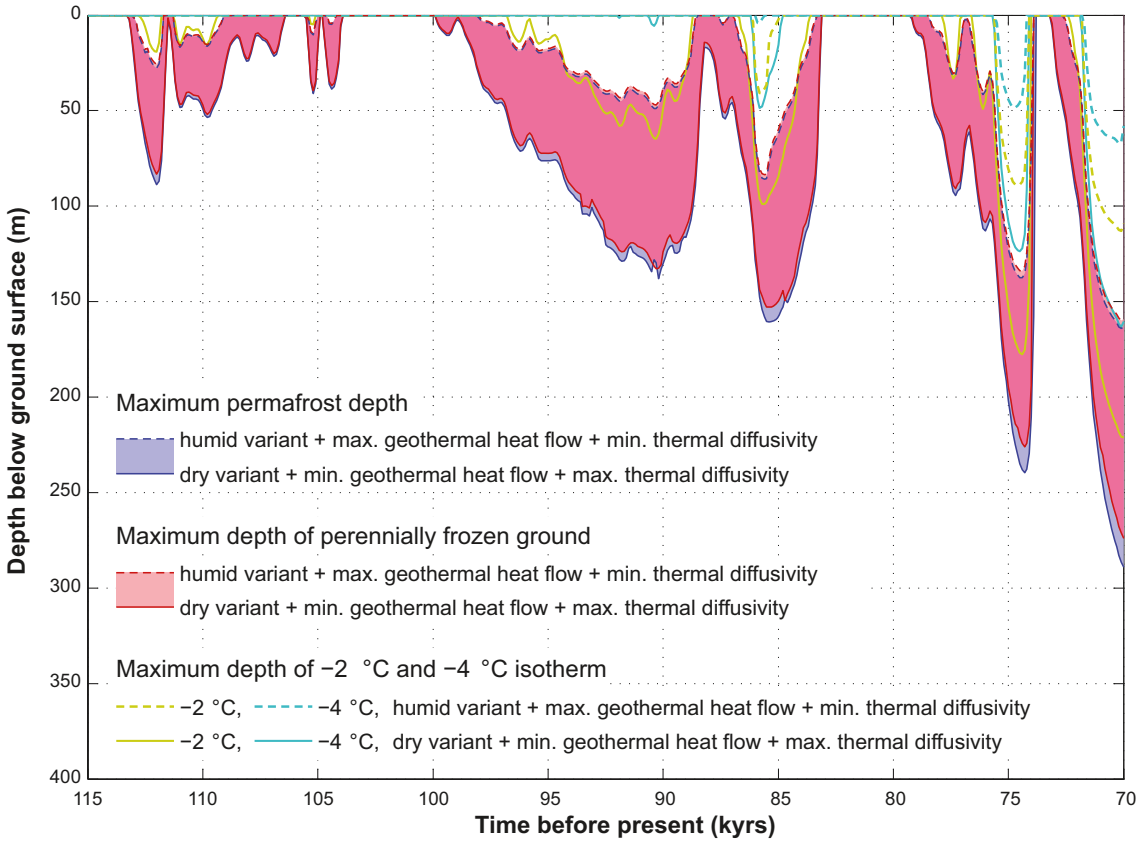

Figure 3-86. *Evolution of maximum permafrost depth, maximum depth of perennially frozen ground and maximum depth of −2 and –4°C isotherms over the repository for the reconstruction of last glacial cycle conditions considering combined uncertainties in surface conditions and bedrock thermal properties (including geothermal heat flow). The shaded area in blue and red represents the range when considering the dry and humid climate variants. The lilac colour indicates that the results for permafrost and perennially frozen ground overlap.*

Sensitivity experiment 7 – combination of uncertainties in air temperature, surface conditions and bedrock thermal properties

This case is studied in order to illustrate the effect of setting *all* known uncertainties to their extreme end (air temperature, surface conditions, geothermal heat flow and all thermal properties) so that they either promote or reduce permafrost growth. Note that the case is constructed for illustrational purposes, and that having this combination of parameter settings describes an almost unrealisable case. For this purpose both the dry and humid variants of the reconstruction of last glacial cycle conditions were used together with an air temperature change of ±6°C and all thermal properties and geothermal heat flow either enhancing or diminishing permafrost development, see /Hartikainen et al. 2010, Section 2.2 and 2.4, and Appendix E, H, I and J/. Based on the estimates of uncertainty in the air temperature curve (Appendix 1) and on the nature of the conceptual- and data uncertainty associated with the temperature curve /SKB 2010a/, it is considered adequate to lower the temperature curve reconstructed for the last glacial cycle (Figure 3-55) by 6° C as a most pessimistic case in the sensitivity analysis for examining the effect of the temperature curve uncertainty for the reconstruction of last glacial cycle conditions.

Figure 3-87 shows the resulting evolution of maximum permafrost depth and maximum depth of perennially frozen ground over the repository. The results show, as expected, a very large fluctuation in both permafrost depth (~40 m to ~460 m) and perennially frozen ground depth (~40 m to ~420 m). These two cases indicate that if all uncertainties have their most pessimistic settings, which is a quite unrealistic case, permafrost is able to reach the repository depth of 450 m in the reconstruction of last glacial cycle conditions.

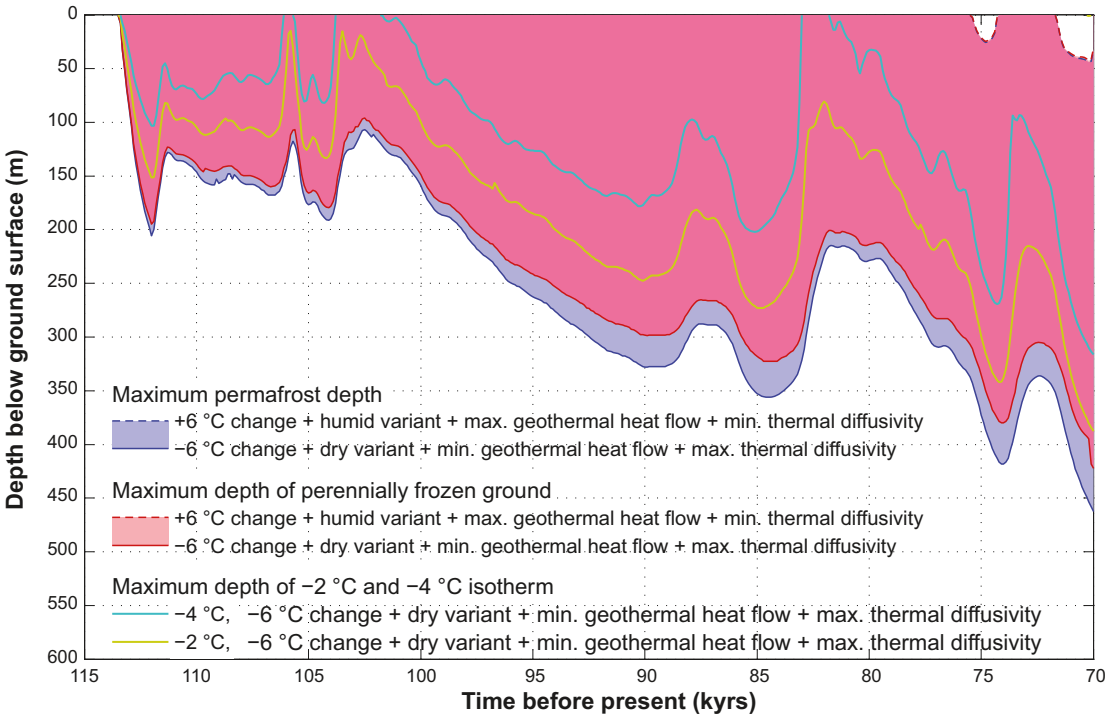

Figure 3-87. *Evolution of maximum permafrost depth, maximum depth of perennially frozen ground and maximum depth of –4°C isotherm over the repository for the reconstruction of last glacial cycle conditions considering the unrealistic combination of uncertainties in air temperature, surface conditions, geothermal heat flow and thermal properties all set in their most extreme position favoring permafrost growth.*

Sensitivity experiment 8 – repository heat

For illustrational purposes, sensitivity experiment 8 studies the effect of including or excluding the heat generated by the spent fuel. However, the heat from the repository should not be regarded an uncertainty. Cases with heat and without heat from the repository together with the dry variant of the reconstruction of last glacial cycle conditions were simulated. The resulting evolution of maximum permafrost depth and maximum depth of perennially frozen ground is illustrated in Figure 3-88. The results show, as expected, that the heat from the repository reduces the permafrost and perennially frozen ground depths, e.g. permafrost depth is reduced by ~38% at 109,700 years BP and by ~14% at 70,000 years BP (Figure 3-88). The calculated range for the maximum permafrost depth at 70 kyrs BP is 259–295 m and for the maximum depth of perennially frozen ground 246–280 m.

Sensitivity experiment 9 – convective heat transfer by groundwater flow

Sensitivity experiment 9 investigates the impact of convective heat transfer due to groundwater flow and salt transport on the evolution of permafrost and perennially frozen ground. Cases with and without 2D groundwater flow and salinity transport in the dry variant of the reconstruction of last glacial cycle conditions were simulated. The resulting evolution of maximum permafrost depth and maximum depth of perennially frozen ground over the repository with and without groundwater flow and salinity transport are shown in Figure 3-89.

The results show that the effect of convective heat transfer due to groundwater flow and salinity transport on the development of permafrost and perennially frozen ground is very weak. The permafrost depths in consideration of groundwater flow and salinity transport are less than a metre greater than those without it (for a permafrost depth of ~260 m). A somewhat larger difference in frozen depth (~5 metres) is possibly a consequence of reduced salinity concentration due to salt transport. It should again be emphasised that the results for groundwater flow and salinity are impaired by the 2D modelling approach. However, the topography of the site is rather flat and does not generate significant hydraulic gradients, suggesting that a 3D approach would only have a minor impact on the results for non-glacial conditions.

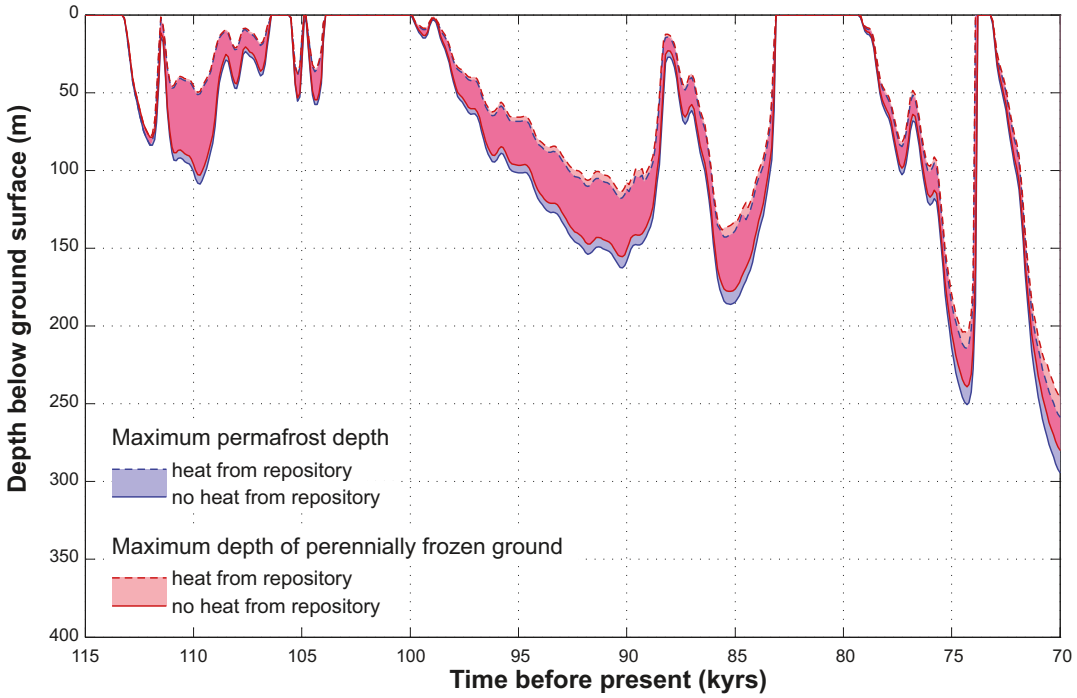

Figure 3-88. *Evolution of maximum permafrost depth and maximum depth of perennially frozen ground over the repository for the dry variant of the reconstruction of last glacial cycle conditions considering mean thermal properties and variable heat production from the repository from zero to the reference value, see /Hartikainen et al. 2010/. The shaded area in blue and red represents the range when considering the dry and humid climate variants. The lilac colour indicates that the results for permafrost and perennially frozen ground overlap.*

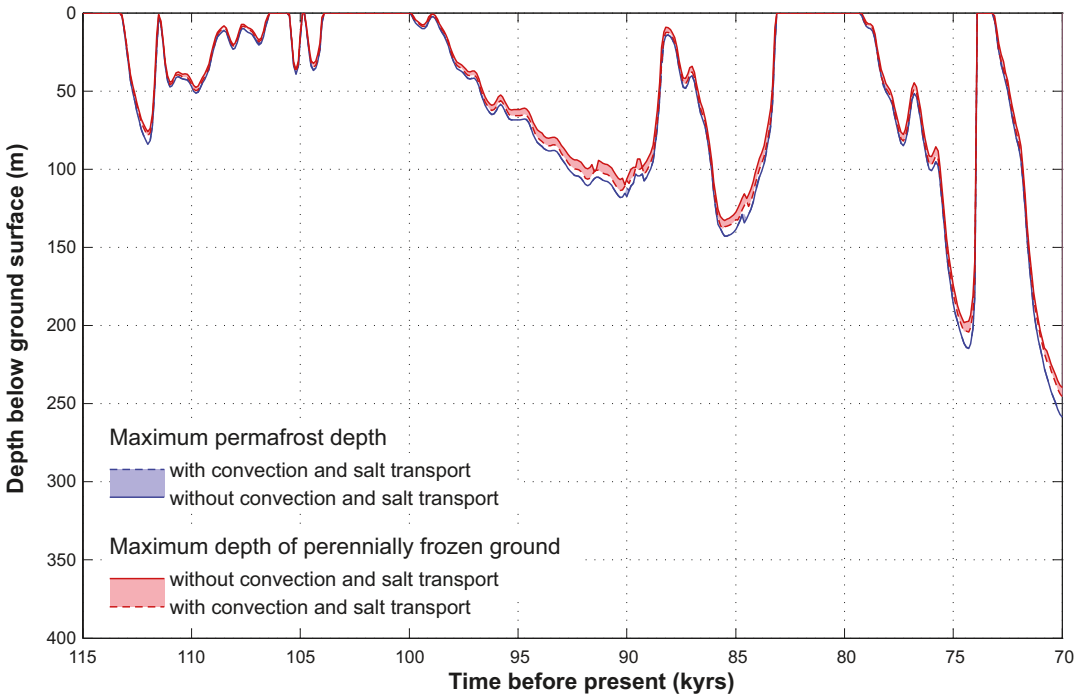

Figure 3-89. *Evolution of maximum permafrost depth and maximum depth of perennially frozen ground over the repository for the dry variant of the reconstruction of last glacial cycle conditions considering mean subsurface thermal conditions, and with and without 2D groundwater flow and salinity transport. The shaded area in blue and red represents the range within which a result is expected to lie when considering groundwater flow and salt transport between the reference case and case without groundwater flow and salt transport. The lilac colour indicates that the results for permafrost and perennially frozen ground overlap.*

A study dedicated at looking at 3D groundwater flow under permafrost conditions at Forsmark, using a simplified approach to model permafrost, is found in /Vidstrand et al. 2010/. The same study also includes a comparison between the results from the simplified permafrost solution (as used in DarcyTools), and the 2D permafrost study reported here and in /Hartikainen et al. 2010/.

Main conclusion from the 2D permafrost modelling study

The conclusion drawn from the 1D permafrost investigations /SKB 2006a/ that the surface conditions can be seen as the driving force for the development of permafrost has been strengthened by the 2D study. In addition, the conclusion that the subsurface conditions and the heat from the spent fuel act as either reducing or enhancing factors for the permafrost and perennially frozen ground development is also supported. The following main conclusions can be made from the 2D permafrost study:

- Given the temperature climate development reconstructed for the last glacial cycle, the study demonstrates how the site-specific spatial- and temporal development of permafrost and perennially frozen ground takes place at the Forsmark site, developing from sporadic-, to discontinuous- to continuous coverage in various combinations and extents.
- The study provides a full range of sensitivity analyses of uncertainties in sub-surface, and surface conditions, including the reconstructed input air temperature curve for the last glacial cycle.
- For the reconstruction of last glacial cycle conditions, the simulated maximum permafrost (the 0°C isotherm) depth over the repository is between 180 and 260 m depending on the surface conditions. The corresponding range for the entire investigated profile is from 220 to 300 m.
- For the reconstruction of last glacial cycle conditions, the simulated maximum depth of perennially frozen ground over the repository is between 180 and 250 m depending on the surface conditions. The corresponding range for the entire investigated profile is from 210 to 300 m.
- The prevailing surface conditions, such as temperatures and surface moisture conditions, are the main factors governing the spatial and temporal development of permafrost and perennially frozen ground at the Forsmark site.
- Subsurface conditions, such as bedrock thermal properties, geothermal heat flow and groundwater salinity, modify the spatial and temporal development of permafrost and perennially frozen ground, but are of secondary importance for modelled permafrost depths compared with surface conditions.
- The variation in thermal properties along the profile as well as 2D groundwater flow only have a slight influence on permafrost (the 0°C isotherm) development. Therefore the uncertainties introduced by excluding lateral variations in thermal properties, boundary conditions and convective heat transfer in the 1D model study /SKB 2006a/ are considered insignificant.
- If making the very pessimistic combination of setting all known uncertainties (in air temperature, surface conditions, bedrock thermal conductivity and heat capacity, and geothermal heat flow) in the position most favourable for permafrost growth, permafrost may extend to 450 m depth in 45,000 years in the reconstruction of last glacial cycle conditions. However, it should be noted that this combination of assumptions is very unrealistic.
- Under continuous permafrost conditions, the unfrozen groundwater content in the perennially frozen ground under lakes can exceed 10% down to a ~50 m depth. This may indicate that taliks are able to form under lakes through perennially frozen ground if favourable groundwater flow conditions with open flow paths prevail. When the unfrozen groundwater content decreases below 10%, groundwater flow is reduced considerably, and taliks are not longer able to form or survive.
- Freezing can induce salt exclusion and salt transport when perennially frozen ground develops deeper than ~200 m. At more shallow depths the impacts of freezing are difficult to see since the salinity of groundwater has been diluted prior to the development of perennially frozen ground. When salt transport occurs more slowly than the freezing zone advances, the salinity concentration is increased within the perennially frozen ground.
- The uncertainty dealing with groundwater flow with this permafrost model remains, since the 3D flow network is omitted in the 2D model. However, the topography of the site is rather flat to generate significant hydraulic gradients, suggesting that this would only have a minor impact on the results for non-glacial conditions.

- The model uncertainty regarding the neglect of salinity transport in the 1D model /SKB 2006a/ seems to be insignificant, mainly due to the low rock porosity, although the present 2D model is not able to describe the groundwater flow realistically.
- Based on the results and the investigations on ground temperature modelling by /Sundberg et al. 2009/ the uncertainty associated with determination of the ground surface temperature from the air temperature as well as with estimation of the in situ temperature and geothermal heat flow for the 1,000–10,000 m-depth for the thermal boundary and initial conditions of the model is reduced considerably.

Further results from the 2D modelling are found in the *severe permafrost case* (Section 5.5).

3.4.5 Time perspective

Changes in annual ground surface temperature due to climate change can lead to development of permafrost and freezing of the ground. If the mean annual ground surface temperature decreases constantly from the present day value to approximately –8°C, permafrost can develop to the depth of 400 m in a period of 26,000 years at Forsmark (Figure 3-52). Under periglacial conditions, permafrost can aggregate from some centimeters to some decimeters in a year whereas its degradation can take place several times faster than that (Figure 3-57), especially when the surface temperature is increased above 0°C and permafrost decays simultaneously from the bottom upwards and from the top downwards. Large degradation rates can occur also at the onset of glaciation when the surface temperature rises sharply to the freezing point beneath an advancing ice sheet.

3.4.6 Handling in the safety assessment SR-Site

The last-glacial-cycle evolution of permafrost is investigated by means of numerical modelling. The results were used to construct parts of the SR-Site *reference glacial cycle*. A broad range of sensitivity experiments are conducted in order to describe the effects of uncertainties in bedrock, surface or climate conditions. Two numerical permafrost models were used, a 1D model that was used for simulations of permafrost at the repository location, and a 2D model that investigated spatial development of permafrost along a profile that crossed the repository site. The permafrost models include a mathematical expression for freezing and thawing of saline-groundwater-saturated bedrock. The bedrock is considered as an elastic porous medium and the groundwater as an ideal solution of water and ionic solvents. The models are based on the principles of continuum mechanics, macroscopic thermodynamics and the theory of mixtures, and are capable of describing heat transfer, freezing of saline water, groundwater flow and deformations of bedrock. To capture the most important factors and parameters affecting the development of permafrost, sensitivity analyses have been performed considering the following issues:

- Surface conditions and climate.
- Subsurface conditions.
- Presence of the repository.

Surface temperatures, together with the influence of surface covers such as snow, vegetation and water bodies, have been included as factors of importance in the surface conditions. The investigated subsurface conditions are thermal properties of the bedrock and geothermal heat flow. The heat generated by the spent fuel has been included in most simulations. The calculations were carried out in two steps; 1) by using constant surface temperatures, and subsequently 2) using surface temperatures based on site-specific climate cases. For further, detailed information on the permafrost modelling, see the preceding parts of Section 3.4.4.

3.4.7 Handling of uncertainties in SR-Site

Uncertainties in mechanistic understanding

There are no major uncertainties in understanding of mechanistic processes regarding permafrost development. Minor uncertainties in the 1D modelling experiments are associated with the fact that the exclusion of salts in freezing of groundwater is not included. The process of freeze-out of salts is included in the 2D modelling performed.

Model simplification uncertainty

The major model simplification in the 1D permafrost modelling study is the exclusion of lateral variations in physical properties, boundary conditions and geometry. For example, full consideration of the anisotropy of thermal conductivity and heat capacity and the features of water bodies and topography, as well as the heat generation from the spent fuel, requires 3D modelling. However, this is to a large extent taken care of by the 2D modelling study reported here.

The 1D modelling approach could, in certain situations, result in somewhat higher temperatures than would be calculated using a 2D or full 3D approach. In the context of permafrost development, the effect of groundwater flow, cooling down the bedrock, is the most important factor here. However, compared with heat conduction, groundwater flow has only a minor role in permafrost development, as indicated by the 2D modelling results that included groundwater flow. Furthermore, the anisotropy of thermal properties is not a problem in 1D or 2D, since one can choose a combination of thermal properties that would give lowest temperatures, or at least very close to the lowest temperatures. Therefore, it is unlikely that 3D simulations would yield notably lower temperatures than the range obtained by the full series of 1D and 2D sensitivity modelling that have been performed.

The 2D modelling approach used for studying talik formation has limitations since the important 3D groundwater flow network is missing.

Input data and data uncertainty

Bedrock data

Some data uncertainty exists when it comes to thermal conductivity and heat capacity of rock at the Forsmark site. In the calculation of ground temperature and the rate of freezing, thermal conductivity is the most important input parameter in terms of thermal properties of the ground. Some uncertainty also exists in determination of hydraulic and mechanical properties of bedrock and salinity concentrations of groundwater versus depth, see appendices in /Hartikainen et al. 2010/ and references therein.

The *in situ* ground temperature has been measured in boreholes to a depth between 500 and 1,400 m. Between different boreholes the temperature deviates in a range of 2°C /SKB 2005a, 2006a, b/. A considerable uncertainty in the 1D permafrost study is associated with determination of the *in situ* temperature and geothermal heat flow in the depth range of 1,000–10,000 m for the thermal boundary and initial conditions of the model. Based on the results and the investigations on ground temperature modelling by /Sundberg et al. 2009/, the uncertainty associated with determination of the ground surface temperature from the air temperature as well as with estimation of the *in situ* temperature and geothermal heat flow for the 1,000–10,000 m-depth for the thermal boundary and initial conditions of the model have been reduced considerably in the 2D permafrost modelling study.

The uncertainty in geothermal heat flow was investigated and described in /Sundberg et al. 2009/.

In general the uncertainty in thermal characteristics of the bedrock and geothermal heat flow has a significantly smaller impact on modelled permafrost and freezing depths than uncertainties related to ground conditions and climate.

Surface conditions

As a complement to the 1D permafrost studies made for Forsmark (SKB 2006a, Section 3.4 and 4.4.1), the main objective of the 2D modelling study was to investigate impacts of surface conditions on the spatial (along the profile) development of permafrost and perennially frozen ground using site specific information on climate and landscape features including water bodies and topography. An approach based on TWI was introduced to describe the vegetation and snow cover in relation to the prevailing evolving climate and surface moisture conditions. TWI was used to identify and locate four relevant surface condition types, dry, moist-humid, wet and peatland, that could be expected to occur on the profile in Boreal-, Subarctic- and Arctic climate zones. Thereafter, ground surface temperatures were calculated from an air temperature curve by making use of *n*-factors that yield a statistical relation between the air and ground surface temperatures in consideration of climate and surface moisture conditions /Hartikainen et al. 2010/. Due to considerable uncertainties related in description of surface conditions by TWI and modelling of ground surface temperatures by means of *n*-factors, two variants, one humid and one dry for the reconstruction of last glacial cycle conditions and a *severe permafrost case* were analyzed.

Temperature curve

Major uncertainties exist in the temperature curve used for the permafrost modelling, including uncertainties for its representativity for the last glacial cycle climate as well as for its application to describe possible future climate cases. A detailed discussion and description of these uncertainties are found in Appendix 1 and /SKB 2010a/. To cover the estimated uncertainties in air temperature curve reconstructed for the last glacial cycle, a large range of sensitivity cases and alternative temperature climate variations of the temperature curve have been analyzed. This is also motivated by the fact that the variation in surface conditions and climate has a larger impact on modelled permafrost and freezing depth than bedrock thermal conditions and geothermal heat flow.

Input data for the permafrost modelling are described in /Hartikainen et al. 2010 Appendix H/ and /SKB 2010a/.

In addition, to cover the uncertainty in future climate development, a case with cold non-glaciated conditions, occurring during a significantly longer period than analysed here, is presented in Section 5.5.

Repository heat

In the 1D permafrost study made for SR-Can, repository heat was initiated at 120 kyrs BP, whereas in the 2D study made for SR-Site it was initiated at 112 kyrs BP. However, this temporal difference has a negligible effect on the timing of the first permafrost over the repository (see Figure 3-88) since it is the surface conditions that are the main factor for the initiation and development of permafrost. Furthermore, the difference in timing also has a negligible effect on the maximum permafrost and freezing depths, since, at the time when permafrost depths are largest (at ~70 kyrs BP), repository heat has declined very much (to ~ 0.3% of the initial value). If heat would have been initiated at 120 kyrs BP in the 2D study, it is estimated that the maximum permafrost and freezing depths would have been no more than a few metres deeper.

3.4.8 Adequacy of references

The SKB report produced for the handling of permafrost and freezing processes /Hartikainen et al. 2010/ has undergone the SR-Site QA system handling, including a documented factual review procedure. Also the SR-Can Climate report /SKB 2006a/, from which some of the studies are used, has undergone QA system handling including a factual review process. Other references used for the handling of the permafrost and freezing processes, in this report and in /Hartikainen et al. 2010/ , are either peer-reviewed papers from the scientific literature or the text books /Yershov 1998, Lide 1999, French 2007/.

3.5 Surface denudation

3.5.1 Overview/general description

The downwearing of the Earth's surface by exogenic processes is accomplished by weathering, erosion, and transportation of material. The combined effect of all weathering and erosion processes is referred to as denudation, i.e. denudation is the sum of the processes that results in the wearing away or the progressive lowering of continental relief. The energy needed for the denudation processes is gained from endogenic and exogenic sources. Glacial erosion is usually regarded as the main erosion process in Scandinavia during the Quaternary. However, as great parts of Scandinavia were not covered by ice during long periods of the Quaternary /Porter 1989/, other denudation processes must also be considered to get the complete picture /Lidmar-Bergström 1997, Lidmar-Bergström et al. 1997, Påsse 2004/.

Weathering

Weathering exerts the most fundamental control on denudation and is the driver of, or limiting factor, in landscape evolution /Turkington et al. 2005/. Weathering can be defined as structural and/or mineralogical break down of rock through the cumulative effects of physical, chemical and biological processes operating at or near the surface, e.g. /Reiche 1950, Selby 1993, Whalley and

Warke 2005/. The definition indicates that weathering occurs when minerals/rocks are exposed to temperatures, pressures and moisture conditions characteristic of the atmosphere and hydrosphere, that is in an environment that differs significantly from the conditions in which most igneous and metamorphic rocks as well as lithified sedimentary rocks were formed. Therefore, the alteration of rocks by weathering forms new materials (minerals) that are in equilibrium with conditions at or near the Earth's surface.

By definition weathering occurs *in situ* and does not directly involve erosion. This means that it leads to the formation of a residual material that differs from the parent, unweathered rock with respect to its physical and chemical properties. Weathering normally lowers the strength of rock and increases the permeability of the surface material and thus makes it more prone to mass wasting and easy to erode by running water, glaciers, wind etc. In addition, it is also an important prerequisite for the widespread development of flora and fauna on land by releasing nutrients for plants and other organisms.

Weathering is generally divided into physical-, chemical- and biological components. Physical or mechanical weathering occurs when volumetric expansion and related alteration of stresses lead to failure and disintegration of the rock. For example, volume changes due to decreased overburden and stresses can result in the creation of fractures at various scales. Crystallisation and volumetric alteration of salt crystals, freezing of water and freeze-thaw effects, as well as thermal fatigue due to repeated (diurnal) heating and cooling, may also cause physical weathering.

Chemical weathering comprises reactions between rock minerals and water. Examples are solution of minerals, carbonation, hydrolysis, hydration, and oxidation and reduction. Common to chemical weathering processes is that they depend on water composition, for example pH, salinity, CO_2 and redox potential. The prevailing temperature is another important parameter determining the type and efficiency of chemical weathering.

During temperate conditions in Sweden, weathering only occurs where the bedrock is exposed. /Swantesson 1992/ has estimated the postglacial weathering of bare bedrock surfaces in southern Sweden during the Holocene to be less than 0.02 m. Weathering rates in tropical climates range between 2 and 48 m Ma^{-1} /Thomas 1994/. Although the weathering rates reported by /Thomas 1994/ have a large span, due to differences in temperature and humidity conditions, it can be seen that weathering is a slow process even under the most favourable tropical climatic conditions. Weathering of fresh bedrock under temperate climate conditions is a considerably slower process.

For a description of climatological-, hydrological- and geological factors affecting weathering, see /Olvmo 2010, Section 3.3.3/. Estimated denudation rates for the Forsmark region are presented and discussed below.

Erosion

Erosion can be defined as the removal and transport of bedrock and earth materials by a moving natural agent, such as air, water or ice. Erosion is often preceded by weathering and followed by transport and sedimentation. Air or water flowing over a bed of loose particles generates a shear stress that tends to initiate particle movement /Collinson 2005a/. There is a critical boundary shear stress related to wind velocity and turbulence and water flow velocity above which particle movement occurs. With the exception of small grain sizes, the critical shear stress will increase as the grain size increases. For small grain sizes (less than 0.1 mm, silt and clay) increased cohesive strength and lower surface roughness means that higher velocities are required to initiate movement. In this section, a brief description is given of the main mechanisms of aeolian-, fluvial- and glacial erosion.

Aeolian erosion

Erosion of sediments by the wind, i.e. aeolian erosion, occurs in environments with sparse or non-existent vegetation, a supply of fine-grained sediments and strong winds, for example periglacial regions, semi-arid or arid regions, beaches and agricultural fields. Aeolian processes depend on weathering or other natural agents, e.g. rivers and waves, to supply sediments for transport. Particle movement is achieved due to wind shear stress and atmospheric turbulence. Particles begin to move when wind forces exceed the effect of weight and cohesion; the first particles to move dislodge or

impact other grains and the number of particles in movement increase exponentially. However, the particles reduce the near-bed velocity of the wind and the transport reaches a dynamic equilibrium state in a few seconds. The mass flux of particles is related to the wind shear velocity, abrasion and the impact of particles moved by saltation and creep. The latter mobilise fine-grained material affected by cohesion but easily carried by the wind. Thus, the transport rate is limited both by wind shear velocity and supply of particles.

Fluvial erosion

Less than 0.005% of the global water is stored in rivers nevertheless they are one of the most, if not the most, potent erosional forces operating on the Earth's surface. Rivers cut valleys, transport sediments and deposit their loads in a variety of depositional environments, such as flood plains and deltas. Vertical erosion by rivers is a striking feature of the world's mountainous areas where deep valleys dissect the landscape and form steep slopes, thereby creating the conditions for mass movement processes that are closely linked to fluvial vertical erosion.

Erosion and deposition of particles by water, i.e. fluvial erosion and deposition, is related to flow velocity. To generate water flow, a water supply and a flow gradient are required. Therefore, erosion by water generally requires a slope. However, erosion by water can also occur on bare surfaces as raindrops hit the surface and splash particles away. Fluvial erosion occurs on slopes, in ditches, brooks and rivers, and on beaches by wave action. Similar to wind erosion, erosion by water depends on shear stress and turbulence, and particles begin to move when water fluid forces exceed the effects of weight and cohesion. The relation between grain size, flow velocity and different modes of erosion and deposition are illustrated in a Hjulström-Sundborg diagram, see Figure 3-90.

The material is transported in two distinct ways, it is either carried along with the fluid or in intermittent contact with the bed, described in e.g. /Collinson 2005b/. In the first case, fine-grained particles are supported by the upwards component of turbulence and carried away with the fluid in suspension. In the second case, generally referred to as bedload transport, coarser-grained material rolls (creep or Erosion reptation) or bounces (saltation) on the bed. Particles carried in suspension will enhance the erosive capability of the fluid by abrasion and particles moved by saltation, creep or reptation will set other grains in motion.

Fluvial erosion occurs on slopes provides material that is transported to brooks and rivers, and into lakes and the sea. When freshwater reaches the sea, clay particles can flocculate into larger units and sedimentation is accelerated. Erosion by water on a slope increases with increased intensity of rain or snowmelt, increased inclination and length of the slope and decreased resistance to erosion of the soil. As for wind erosion, the presence of vegetation reduces the erosion rate.

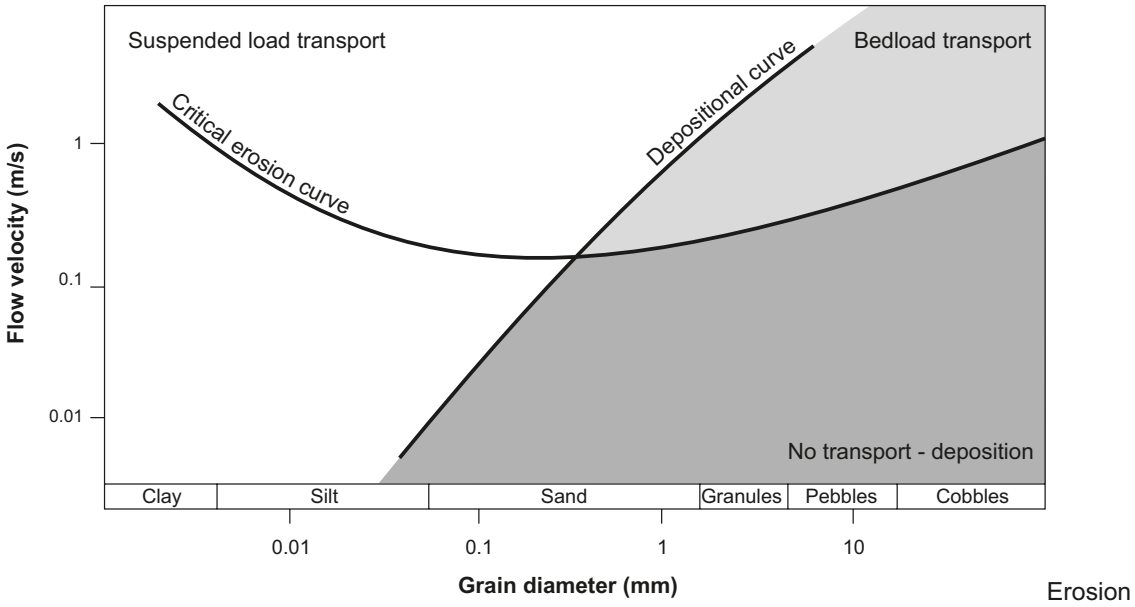

Figure 3-90. *A Hjulström-Sundborg diagram showing the relation between flow velocity, grain size and fluvial erosion.*

Erosion on slopes can also be the result of mud flows, landslides, creep processes and avalanches. These processes result from the movement of masses of snow, earth and debris down a slope under the influence of gravity and can occur at scales from a few metres to several kilometres and at rates from metres per year to metres per second. The material can move by creep, sliding, flowing and falling. The movement of material is generally triggered by increased water content (for example from snowmelt), but earthquakes and volcanic eruptions can also cause material to move down a slope.

For more information on fluvial erosion, see /Olvmo 2010, Section 4.1/ and references therein.

Glacial erosion

Glacial erosion is complex and depends on material properties of ice and rocks, ice thermodynamics, friction and lubrication, chemical effects and subglacial hydrology. In addition, a precondition for efficient glacial erosion in bedrock is that the bedrock has been subject to pre-glacial sub-aerial weathering processes.

In recent years, interpretations of geomorphological features e.g. /Kleman et al. 1997, 2008/ measurements of cosmogenic radionuclides, e.g. /Stroeven et al. 2002a/ and ice sheet modelling, e.g. /Näslund et al. 2003/ have resulted in a composite view on glacial erosion over Scandinavian. In some areas, over time dominated by basal frozen conditions, glacial erosion has been limited, whereas in other areas, where basal melting and sliding (see Section 3.1) have occurred, erosion may have been considerable.

Glacial erosion is traditionally divided into two components; plucking and abrasion. Plucking is the process by which rock fragment of different size are loosened, entrained and transported away from the glacier bed, while abrasion is the grinding of the substrate by rock fragments held in the moving glacier bed cf. /Sugden and John 1976, Benn and Evans 1998/. The former is responsible for the characteristic irregular and fractured surfaces of lee sides of bedrock bumps and small hills in formerly glaciated areas.

Failure leading to loosening of fragments is known to be caused by stresses set up by differential ice load and high water pressures at the ice-bedrock interface cf. /Sugden and John 1976, Drewry 1986, Benn and Evans 1998/. Many minor fracture features, such as chattermarks and crescentic gouges, observed on glacially affected rock surfaces, indicate that normal stress at the glacier bed may be sufficient to cause failure in some rocks. However, the role of pre-existing weakness, such as joints, cracks and foliation, and also pre-glacial weathering should not be underestimated cf. /Olvmo and Johansson 2002/. In addition, glacially induced cyclic water pressure variations may be important for bedrock crack propagation e.g. /Hooke 1991, Iverson 1991/, a process by which rock fragments may be formed and eroded from the bedrock. Melting of ice on the stoss side and refreezing of meltwater on the lee side of obstacles at the ice sheet bed may occur under certain thermal and pressure conditions. This so-called regelation process may also contribute to glacial erosion and transportation of subglacial till e.g. /Iverson 1993, 2000/.

Abrasion is the process whereby the bedrock beneath a glacier is scoured by debris carried in the basal layers of the glacier cf. /Sugden and John 1976, Drewry 1986/. The process leads to striation and polishing of bedrock surfaces cf. /Benn and Evans 1998/ and is typical of the stoss side of rock bumps in formerly glaciated terrain. Many factors control the effectiveness of glacial abrasion. The relative hardness of the overriding clast and the bedrock is important and the erosion process is most effective when the overriding clast is considerably harder than the substratum. The force pressing the clast against the bed is decisive and depends in turn on the shape of clast as well as the motion of the clast during transport. Other factors related to the availability of clasts in the basal ice layers, such as clast concentration, removal of debris and availability of basal debris are also of major importance.

Also glaciers and ice sheets that are cold-based could contribute to a restricted amount of glacial erosion /Cuffey et al. 2000, Waller 2001 Bennett et al. 2003/. This is achieved by e.g. movement, rotation and entrainment of debris in the basal ice at sub-freezing temperatures. However, this process is of very limited importance compared to other glacial erosional processes.

The magnitude of glacial erosion differs widely both in time and space. At a continental scale, the large-scale pattern of glacial erosion is controlled by ice sheet thermal regime and topography of the subglacial landscape. Based on a simple glaciological model /Sugden 1977, 1978/ made a reconstruction of the thermal regime of the Laurentide ice sheet. The reconstructed thermal pattern

shows an inner wet-based area and an outer cold-bed area, which broadly corresponds to the pattern of glacial erosion indicated by the distribution of erosional landforms. The most intense erosion as indicated by areas with high lake density coincide with the transition zone between wet-based and cold-based ice in the model, which probably favours plucking and debris entrainment.

/Näslund et al. 2003/ used a numerical ice sheet model to study regional ice flow directions and glacial erosion of the Weichselian ice sheet in Fennoscandia. A new quantity, basal sliding distance, was introduced, describing the accumulated length of ice that has passed over the landscape by basal sliding. It was suggested that this entity could be used as a proxy for glacial erosion. The results indicate high basal sliding distance values in SW Sweden/SE Norway, in Skagerrak, and along the Gulf of Bothnia, implying relatively large amounts of glacial erosion in these regions. On elevated parts of the Scandinavian mountain range and on adjacent plains in the east the basal sliding distance values are low, implying weaker glacial erosion, which is fairly in agreement with geological and geomorphological evidence cf. /Lagerbäck and Robertsson 1988, Riis 1996, Stroeven et al. 2002b, Olvmo et al. 2005/. The method of estimating glacial erosion by simulated basal sliding distance /Näslund et al. 2003/ was further developed by /Staiger et al. 2005/ who introduced a normalization of the sliding values by the duration of ice cover over a particular site. /Staiger et al. 2005/ also set up a relationship between normalized sliding distance and rate of glacial erosion.

Another approach to the issue of glacial erosion is presented by /Hallet et al. 1996/ who made a comprehensive review of glacial erosion rates based on sediment yields. They found that rates of glacial erosion vary by many orders of magnitude from 0.01 mm yr^{-1} for polar glaciers and thin temperate plateau glaciers on crystalline bedrock, to 0.1 mm yr^{-1} for temperate valley glaciers also on resistant crystalline bedrock in Norway, to 1.0 mm yr^{-1} for small temperate glaciers on diverse bedrock in the Swiss Alps, and to 10–100 mm yr^{-1} for large and fast-moving temperate valley glaciers in the tectonically active ranges of southeast Alaska. These major differences highlight the importance of the glacial basal thermal regime, glacial dynamics and topographic relief on the rates of glacial erosion.

Yet another approach was presented by /Påsse 2004/. In order to estimate the average glacial erosion in the bedrock in non-mountainous regions he used seismic data and well depth data on the thickness of the minerogenic Quaternary sediments in Sweden and Denmark. The average thickness of Quaternary sediments was estimated to be 16 m in the investigated area, which corresponds to 12 m of bedrock assuming that the whole volume is the result of glacial erosion of fresh bedrock. Since a great part of the sediments likely consist of glacially redistributed Tertiary regolith, this number probably is an overestimation of the glacial erosion depth in the bedrock. Considering this, Påsse concluded that the average glacial erosion during a full glacial period may be estimated to between 0.2 m and 4 m. This is in agreement with estimates of glacial erosion in the Precambrian basement based on geomorphological observations /Lidmar-Bergström 1997, Ebert 2009/. Lidmar-Bergström distinguishes the estimates of glacial erosion of Tertiary saprolites from glacial erosion of fresh bedrock. The glacial erosion of saprolites is estimated between 10 and 50 m and glacial erosion of fresh bedrock is estimated at some tens of metre /Lidmar-Bergström 1997/, although with great variations.

However, in Fennoscandia as a whole, large spatial differences in thicknesses of Quaternary deposits occur and distinct patterns of glacial scouring and deep linear erosion are observed in places. /Kleman et al. 2008/ point to the relative roles of mountain ice sheets and full-sized Fennoscandian ice sheets for this zonation and use spatio-temporal qualitative modelling of ice sheet extent and migration of erosion and deposition zones through the entire Quaternary to suggest an explanatory model for the current spatial pattern of Quaternary deposits and erosion zones.

Glacial meltwater erosion may be an effective agent both in subglacial and proglacial environments. The sediment concentrations of glacial meltwater streams are often high and the flow is often very rapid and turbulent, which mean that flows transitional between debris flows and normal stream flow are common /Benn and Evans 1998/. The erosivity of glacial streams is therefore often high both on bedrock and sediments. Apart from the high erosivity, the mechanisms of glacial meltwater erosion are the same as normal fluvial erosion including abrasion, cavitation, fluid stressing and particle entrainment from cohesionless beds as well as chemical erosion.

The relative efficacy of fluvial and glacial erosion, on a global basis, are presented in /Koppes and Montgomery 2009/. For a more detailed description of erosional and weathering processes relevant for Scandinavian conditions and the Forsmark area in a 0.1 to 1 Myr time perspective, see /Olvmo 2010/. Estimated denudation rates for the Forsmark region are presented and discussed below.

3.5.2 Controlling conditions and factors

As mentioned above, weathering and erosion are complex processes affected by the prevailing environmental conditions. Given the characteristics of the rock, the degree of weathering depends on the availability of weathering agents such as salt, moisture, biota (e.g. microorganisms and lichens), and on the microclimatic conditions to which the rock is exposed. Weathering occurs in all climates, but high temperatures and humid conditions increase weathering rates. In areas where frost and/or permafrost occur, freezing and freeze-thaw effects are important geomorphic processes. However, weathering in periglacial environments is also affected by salt (in combination with freezing), wetting and drying, thermal fatigue and biological agents /French 2007/.

During temperate climate conditions, the dominant process is fluvial erosion. During permafrost climate conditions, when the climate can be expected to be dryer and vegetation sparse, aeolian erosion may also be important. During spring when the snow melts, there may be significant erosion of sediments in the active layer in periglacial permafrost areas. During glacial climate conditions, the erosion is mainly affected by the basal conditions of the ice sheet. In areas where the ice is frozen to the bed, the ice acts to preserve its subsurface and practically no erosion occurs, whereas in areas of basal melting erosion of bedrock and pre-existing sediment is likely to occur, with more erosion generally associated with faster ice flow. In sub-glacial tunnels, where melt water flows towards the ice sheet margin, erosion of loose sediments and bedrock can be significant.

The topographic relief in Scandinavia is generally not dramatic outside the Scandinavian mountains, e.g. /Lidmar-Bergström and Näslund 2005/. The resistance to denudation of the Precambrian rocks that dominate in Scandinavia is rather uniform, as compared with, for example, the variation between the Caledonian bedrock types in the Scandinavian mountains. Although the relief locally may be steep at many places, the relatively homogeneous denudation resistance has contributed to the moderate to low relief of the Precambrian rock basement. The relative relief is exceptionally low (less than some tens of metre) along significant portions of the eastern Baltic Sea coastline of southern and south-central Sweden, due to the presence of the *sub-Cambrian peneplain* (a denudation surface formed in crystalline rock with a typical relief of less than 20 m /Rudberg 1954, Lidmar-Bergström 1995/, interpreted to have been formed down to sea-level prior to the Cambrian). The low relief favours low subaerial erosion rates, for example, the most important subaerial erosion process, fluvial erosion, increases with steeper topographical gradients.

One main reason why a deep dissection of the landscape could not occur by fluvial erosion in Forsmark is because of the coastal location of the site, situated just a few m above the Baltic Sea. The sea-level acts as the base-level for fluvial erosion, i.e. fluvial erosion cannot cut deeper than sea-level. The expected maximum lowering of the Baltic sea-level during glacial cycles (18 m, see Section 4.5.2) sets, together with the present altitude of the ground surface above the repository, a maximum limit to the amount future fluvial erosion at the Forsmark site.

Table 3-16 summarises how geosphere variables are influenced by surface denudation.

3.5.3 Natural analogues/observations in nature

The current landforms in Scandinavia are a result of the interaction between tectonic processes, weathering, erosion and sedimentation and consequently the traces of these processes can be observed and interpreted in nature. In Scandinavia, large-scale bedrock landforms outside the mountain range, such as denudation surfaces and landscapes of weathering and stripping of saprolites, are common, and reflect the varying phases of weathering, erosion, and sedimentation that have occurred in association with tectonic events and climate change e.g. /Lidmar-Bergström 1997, Lidmar-Bergström and Näslund 2002/.

During the late Cenozoic glacial cycles, ice sheets have repeatedly covered parts or the whole of Scandinavia, producing glacial erosional landforms in bedrock e.g. /Rudberg 1954/ and in surficial deposits e.g. /Kleman et al. 1997, 2008/. Traditionally, it has been thought that a considerable part of the bedrock relief is the result of glacial erosion. However, as mentioned above, it has been shown that the amount of glacial erosion of the Precambrian basement in general is on the order of a few tens of metres /Lidmar-Bergström 1997/, and in this context valleys are more eroded than the surrounding terrain. However, within the Scandinavian mountain range, valleys may have experienced several hundred metres of glacial erosion /Kleman and Stroeven 1997/. /Lidmar-Bergström 1997/ further estimated

Table 3-16. Influence of surface denudation on geosphere variables.

Geosphere variable	Influence present (Y/N)	Summary of influence
Groundwater flow	No	The process refers to weathering and erosion at the surface. Even if there is no absolute boundary between surface- and groundwater this process only includes the action of surface water.
Groundwater composition	Yes	Surface weathering may to some degree change groundwater composition. The effect is judged as negligible for the safety assessment.
Rock stresses	Yes	The removal of bedrock by denudation changes the stress field. However, since the denudation rate is very low, the influence is judged as negligible for the safety assessment period.
Fracture geometry	Yes	Weathering may change fracture aperture in the upper metre of bedrock, for instance by widening of fractures due to freezing. The influence is judged as negligible in relation to repository safety.

that denudation occurring during the Proterozoic (600–2,500 million years ago) was on the order of tens of kilometres, and during the Mesozoic (65–245 million years ago) and Tertiary (2.5–65 million years ago) up to 600 m at the most. Furthermore, during the last decades our understanding of ice sheet thermodynamics has showed that large portions of ice sheets may be cold-based and thus have a negligible erosive effect. Over the same period, numerous glacial geological studies have shown that the occurrence of preglacial saprolite remnants is solid evidence that ice sheets under certain circumstances cause very restricted glacial erosion, or even have a preserving effect on pre-glacial landforms /Lagerbäck 1988a, b/ and /Kleman 1994/, whereas under other conditions they may be fully erosive.

3.5.4 Model studies

Estimates of denudation rates can be made either through numerical models that *per se* describe the processes involved in the denudation, for instance the processes resulting in glacial erosion, or estimates may be based on interpretation and GIS-modelling of the development over time of landforms. A review of numerical modelling of glacial erosion is found in /Fisher 2009/, while the latter approach may be exemplified by /Olvmo 2010/, who has used this method in a study of long-term denudation history of southern Sweden.

The long-term denudation history of southern Sweden is interesting for two reasons. Firstly, it may be a guide to understand the denudation rate through time in the Forsmark area. Secondly, it is important because the different landforms and surfaces that have been recognized, such as the sub-Cambrian peneplain mentioned above, may be used as reference surfaces to understand, at least at a regional scale, the magnitude and patterns of glacial erosion, which is a important issue with respect to the time perspective of the safety assessment.

Some examples from Sweden of calculated long-term denudation rates can be found. Many of them use remnants of the sub-Cambrian peneplain as a reference surface. In eastern Småland and southern Östergötland, the maximum denudation of the tectonically uplifted sub-Cambrian peneplain is approximately 100 m. Once overlying sedimentary cover rocks had been removed, denudation and removal of the denudation products would have required a period of between 2 and 50 Myrs /Lidmar-Bergström et al. 1997/. On the Swedish west coast, a so-called *Sub-Cretaceous etch surface* has been incised into the sub-Cambrian peneplain by weathering. In places, it has resulted in a maximum bedrock lowering of 135 m. The time required for this amount of denudation has been suggested to be between 3 and 68 Myrs /Lidmar-Bergström et al. 1997/, with the denudation occurring during the Jurassic-Early Cretaceous. Finally, saprolite thicknesses of 50 m in Skåne were interpreted to have been produced by weathering over a time interval of 1–25 Myrs /Lidmar-Bergström et al. 1997/.

Given the specific tectonic and climatic evolution, including phases of denudation, sedimentation, and stripping of saprolites, the above examples clearly show that the evolution of the sub-Cambrian peneplain in southern Sweden into a younger incised landscape has been a very slow process, and that the total amount of material removed from the crystalline bedrock has not been large considering the

very long time periods involved. The total maximum denudation of bedrock in areas of Precambrian crystalline basement in southern Sweden during the last 540 Myrs is on the order of a few hundred metres. A significant part of this denudation took place during Mesozoic tropical climate conditions, considerably more favourable for chemical deep weathering than for instance a temperate climate.

A more detailed account of the long-term landform development and associated denudation in southern Sweden is given in /Olvmo 2010/.

A study on landform development and associated denudation in the Forsmark and Laxemar regions has been performed, reported in /Olvmo 2010/. In the following, a summary of the study in the Forsmark region is given.

From a geomorphological point of view the investigated region (Figure 3-91) can be divided into four distinctive areas, i) a central area, hosting the Forsmark site, characterized by very low topographic relief, ii) a coastal region SE of Forsmark with coast-parallel lineaments, iii) a southern part with more pronounced relief characterized by east-west trending fault scarps, and iv) an area with hilly relief in the northwest. The relief in the central area, including the Forsmark site, is characteristic of the sub-Cambrian peneplain and is consistent with the interpretation by /Lidmar-Bergström 1997/. The relative relief in this area is less than 20 m (Figure 3-91), although with some shallow valleys present in the peneplain. Around Forsmark (within c. 10 km) the relief is extremely low, often less than 10 m. South of this central flat area, a more dissected landscape appears. Here the peneplain is broken into blocks, tilted in different directions. Some of the blocks are elevated and partly dissected by weathering and erosion. In the southern part of the study area, the elevated rims of these uplifted blocks give rise to east-west trending horst ridges, whereas in the Stockholm region the peneplain is highly dissected and give rise to a *joint valley landscape*, consisting of plateaux bounded by shallow straight, structurally controlled valleys. In the coastal low lying areas between Forsmark and Uppsala, the relief is quite considerable along coast parallel tectonic lineaments. This is obvious in the relative relief map (Figure 3-91) where relative relief locally rises to 50 m along these fracture zones. In this area, some 15 km southeast of Forsmark, the coastal landscape is more dissected. The area coincide with areas with a high frequency of rock outcrops which may suggest that glacial erosion has been more effective in this region than at Forsmark, probably as a result of the closeness to the Baltic Sea depression which may have influenced the ice sheet flow.

The Forsmark area is situated on the sub-Cambrian Peneplain not far from the present extension of the Lower Palaeozoic sedimentary cover rocks. Exhumation of the peneplain has probably occurred during the Pleistocene glaciations and possibly as late as the Weichselian glaciation as indicated by the occurrence of clayey tills in the area. The major bedrock landforms in the area are probably close to the original peneplain surface. The area is extremely flat over large distances and many landforms in the Quaternary drift cover are prominent features in the landscape.

In this context it is worth noting that the relief map (Figure 3-91) shows the ground surface relief, i.e. it comprises the relief of both bedrock and overlying Quaternary deposits. The uncertainty introduced by not having removed these deposits in the analysis is however in general not large, exemplified by the fact that within the terrestrial parts of the Forsmark site (Figure 3-59), the average soil thickness is only 4 m /Lindborg 2010 Section 5.1.2/. Locally in the investigated area (Figure 3-91), larger sediment thicknesses of up to c. 100 m may occur, typically where large eskers are found. However, parts of these sediment thicknesses do have an expression in the relief map, such as the north-south trending eskers located north of Uppsala (Figure 3-91). If the esker sediments could be removed from the DEM, the resulting relative relief would not necessarily be greater than the one of the present eskers. Nevertheless, this uncertainty is taken care of by the analysis of a case with considerably higher relief than in Figure 3-91, see below.

Glacial erosion has reshaped some of the forms in the bedrock and may be responsible for evacuation of regolith along structurally controlled valleys. This is especially true in the coastal areas some 15 km southeast of Forsmark, where glacial erosion may have been comparably effective along fracture zones. Based on the conclusion that the sub-Cambrian peneplain is well-preserved and probably coincident with the present relief the total amount of glacial erosion caused by repeated Pleistocene glaciations in the area on average is probably less than 10 metres, but is probably above that number in the coastal zone southeast of Forsmark. The very low relief of the landscape today, together with the fact that the bedrock consists of crystalline basement rocks, implies that the present denudation rate is extremely low and corresponds to the low rates found in low relief shield areas reported in the literature.

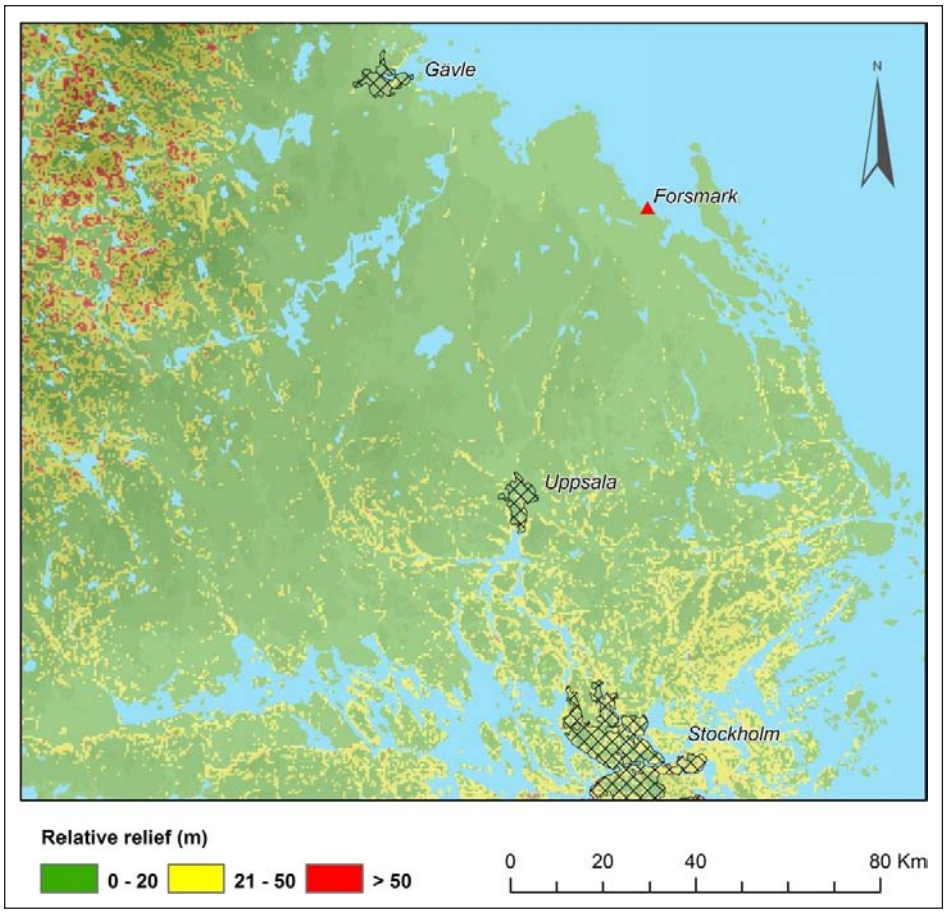

Figure 3-91. *Relative relief of the ground surface in the Forsmark study area.*

Future glacial erosion at Forsmark

The effect of a future glacial cycle would probably be very limited in areas dominated by the well-preserved sub-Cambrian peneplain, such as at Forsmark. Given the long-term denudation history up to present, the expected amount of glacial erosion during a future glacial cycle is probably very limited. For the Forsmark region, i.e. an area significantly larger than the specific repository location, /Olvmo 2010/ estimated that glacial erosion could amount to 2–5 m for a future glacial cycle comparable with the last one. /Lidmar-Bergström 1997/ estimated the *total* amount of glacial erosion for all Late Cenozoic ice sheets in low-land terrain in Sweden to be around 10 m. If extreme assumptions are excluded, which is valid approach for the low relief Forsmark site, about 1 m of glacial erosion for one glacial cycle was estimated by /Påsse 2004/. Based on all these estimates, and the topographic and geological characteristics of the repository location, the amount of glacial erosion in fresh bedrock for one glacial cycle is here estimated to 1–2 m at the repository location. More glacial erosion is expected in topographic low positions and/or along major fracture zones, especially if such features are located along the general ice flow direction. The dissected coastal areas south-east of Forsmark, with sometimes considerable relief, may experience stronger glacial erosion during a glaciation with a similar flow pattern as during the Late Weichselian. In this area, c. 15 km from Forsmark, glacial erosion of more than 10 m in one glacial cycle would be expected locally in low topographic positions /Olvmo 2010/.

Future non-glacial contribution to denudation at Forsmark in a 1 Myr time perspective

In order to evaluate the potential denudation in the Forsmark region in a 1 Myr time perspective, a potential denudation rate is calculated based on the relief of the area. The calculation is based on an empirical relationship between denudation and relief /Ahnert 1970/. The calculation excludes the effect of land uplift and glacial erosion and simply relates denudation to the local relief assuming

$$D = 0.1535h \qquad \text{Equation 3-12}$$

where D is the denudation rate, *h* is the relative relief and is a substitute for mean slope. The map of relative relief (Figure 3-91) was used for the calculation. The results show that the potential future, non-glacial component of denudation is between 0–5 m/Myr over most of the area (including the Forsmark site) (Figure 3-92), but might rise to between 5 and 10 m/Myr along uplifted fault scarps in the south, and to 10–25 m/Myr in the northwest where the contemporary relief is higher. The denudation rates resulting from this type of calculation are verified by a comparison of corresponding denudation rates for the Laxemar region with denudation and relief formation induced by the uplift of the so-called South Swedish Dome in the late Tertiary /Olvmo 2010/.

In order to show the effect of a change in relative relief by, for instance, a tectonic uplift occurring many millions of years into the future, a map of potential denudation after a five-fold increase of the relative relief was produced. This case also covers the uncertainty introduced by not having excluded sediment thicknesses from the relief map. This case does not significantly change the picture for the Forsmark site. Even if the local relief were raised to above 100 m, for instance by tectonic movement, the estimated non-glacial denudation is very low, up to 5–20 m/Myr /Olvmo 2010/.

Conclusions

The Forsmark area has a very low topographic relief and the repository location is not situated in a major fracture zone, resulting in a setting not prone to effective denudation. Given this, and the denudation rates estimated by /Lidmar-Bergström 1997, Påsse 2004, Olvmo 2010/, a glacial erosion value of 1–2 m per glacial cycle (similar to the last one), is used in the summary below. If looking only at the non-glacial component of denudation, the long-term denudation rate of the site is low as a consequence of the very low relief and the proximity to base level (sea-level). The numbers estimated for the long-term denudation rates /Olvmo 2010/ are in agreement with reports of denudation rates in geological shield areas and lie within the range 0 to 10 m/Myr.

A summary of expected future denudations rates at the Forsmark repository location is provided in Table 3-17. Locally, in topographic depressions away from the repository location, such as along larger valleys and fracture zones, denudation values may be higher than this. However, the Forsmark repository site is not located in a topographic low, nor in a major fracture zone, and therefore the estimated values in Table 3-17 are regarded as valid for the repository location.

3.5.5 Time perspective

Weathering, erosion and sedimentation are active processes over most of the Earth's surface. In Sweden, the maximum total denudation can be expected to be limited in lowland areas of low relative relief. For the region around Forsmark it is estimated to be up to 20 m Myr^{-1}. The rate of weathering and erosion vary in time and space.

3.5.6 Handling in the safety assessment SR-Site

Present-day knowledge on denudation processes suggests that denudation generally will be limited in lowland parts of Scandinavia during the assessment period. Areas where the bedrock is highly fractured and weathering and erosion can be expected to be significantly more rapid than the estimated averages do not apply for the repository location at Forsmark. The impact of weathering and erosion on groundwater flow and rock stresses is considered to be insignificant over the time period of relevance in assessments. In a very long time perspective, several million years, weathering and erosion may alter topography and rock stresses by redistribution of sediments and rock mass. In an even longer time perspective, many tens or hundreds of millions of years or longer, the repository may be brought to the ground surface due to tectonic uplift in conjunction with a combination of denudation processes.

Current knowledge, e.g. /Thomas 1994, Lidmar-Bergström 1997, 2007, Kleman 1994, Påsse 2004, Olvmo 2010/, supports the conclusion that the amount of future surface denudation is insignificant for repository safety in the time perspective of 100,000 years and one million years. The amount of denudation is estimated to be ~20 m or less for the Forsmark repository location during the coming 1 Myr (Table 3-17).

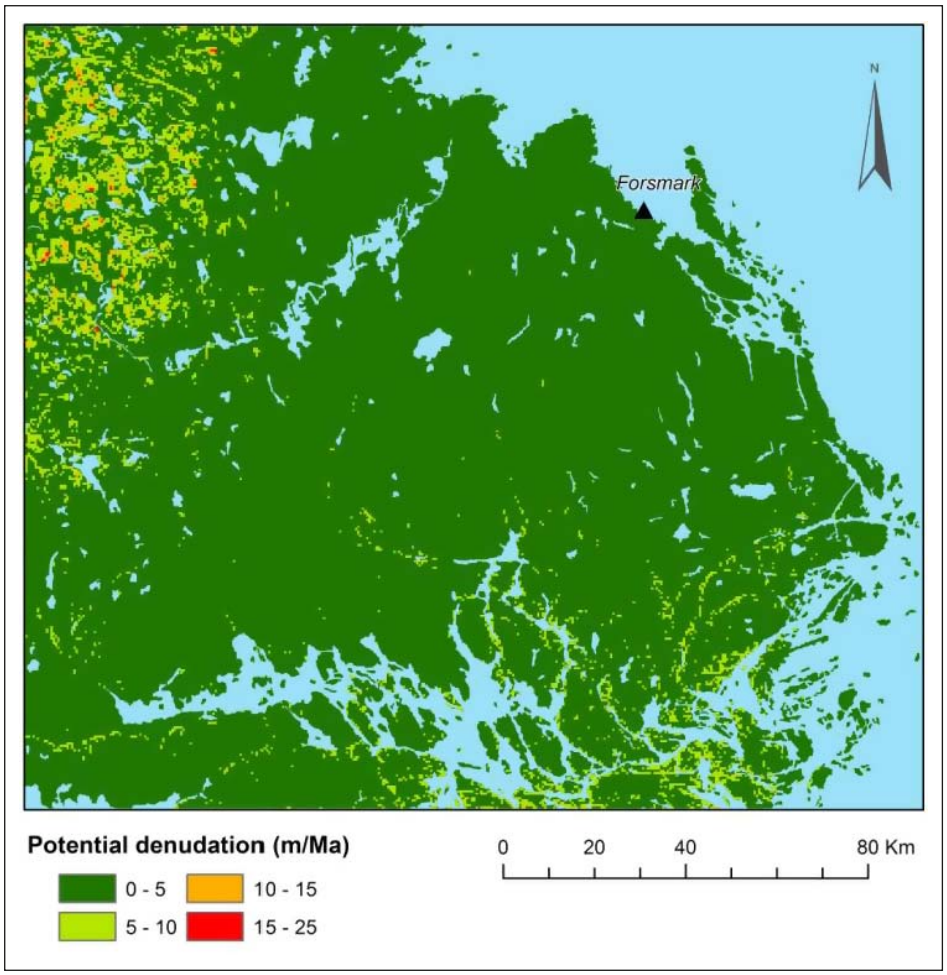

Figure 3-92. *Calculated potential future non-glacial denudation in the Forsmark region. At Forsmark, calculated values of the non-glacial denudation component are low, up to 5 m/Myr. From /Olvmo 2010/.*

Table 3-17. Expected future denudation at the repository location in Forsmark in a 100 kyr and 1 Myr time perspective. If looking at a larger region around Forsmark, locally higher denudation values are expected in topographic low positions and along major fracture zones. However, the Forsmark repository location is not located at a topographic low, nor in a major fracture zone, and therefore the estimated values are regarded as valid for the repository.

Parameter	~100 kyr timescale (one glacial cycle)	1 million year timescale (~8 glacial cycles)
A. Glacial erosion (average value over landscape)	1–2 m	8–16 m
B. Non-glacial denudation	(0–0.6)	0–5 m
C. Total denudation (A+B)	1 to 2.6 m	8–21 m

3.5.7 Handling of uncertainties in SR-Site

Rates of weathering and erosion vary as environmental conditions change. The rate of weathering and erosion also depends on rock and sediment characteristics and topography. In spite of the uncertainties in future environmental conditions, there is no reason to believe that denudation in the Forsmark region would diverge significantly from the values estimated above. The area has a low relief with low topographical gradients, in turn producing limited fluvial and glacial erosion at the site.

Uncertainties in mechanistic understanding

There are uncertainties in the understanding of the detailed mechanisms of weathering and erosion. However, for the safety assessment, the approach of using also indirect estimates of the amount of erosion and weathering over long time-scales (i.e. the development of large-scale landforms), the total knowledge is sufficient for estimating the amount of weathering and erosion of fresh bedrock during the assessment period.

Model simplification uncertainties in SR-Site

Not relevant for this process.

Input data and data uncertainties in SR-Site

Not relevant for this process.

3.5.8 Adequacy of references

The SKB report produced for the handling of surface denudation /Olvmo 2010/ has undergone the SR-Site QA system handling, including a documented factual review procedure. Also the SR-Can Geosphere process report /SKB 2006b/, from which some of the studies are used, have undergone QA system handling including a factual review process. Other references used for the handling of surface denudation processes are either peer-reviewed papers from the scientific literature or from text books /Sugden and John 1976, Drewry 1986, Paterson 1994, Thomas 1994, Benn and Evans 1998, French 2007/.

4 Climate and climate-related conditions for the SR-Site safety assessment

4.1 Rationale and general approach

As mentioned in Section 1.2, the main scenario of the safety assessment includes a *base case* and a *global warming variant* of climate evolution. The base case is based on a *reference glacial cycle* which in turn constitutes a repetition of conditions reconstructed for the last glacial cycle, the Weichselian and the Holocene, see Figure 1-3. By modifications of the *reference glacial cycle*, this evolution is used also for constructing additional climate cases with a potentially larger impact on repository performance. For example, by defining a longer period of glacial conditions, the *reference glacial cycle* has been used to construct an *extended ice sheet duration case* (Figure 1-3), used for analysis in the additional safety assessment scenarios of SR-Site.

In order to make relevant and well-motivated definitions of the climate cases, it is essential to first have good knowledge on the climate and glacial history of the Weichselian glacial cycle, i.e. the glacial cycle on which the *reference glacial cycle* is based and the additional climate cases are constructed (Figure 1-3). To this end, Section 4.2 describes the present knowledge on Weichselian climate and glacial history to a level required to give adequate input to the definition and description of the *reference glacial cycle* and the additional climate cases. The description in Section 4.2 is based both on geological information and climate modelling.

Section 4.3 gives an overview and detailed examples of climates that occurred during the last glacial cycle, from geological information and from climate modelling.

Section 4.4 presents the reconstruction of last glacial cycle conditions that subsequently are used for the *reference glacial cycle* and the base case of the SR-Site main scenario presented in Section 4.5, see also Figure 1-3. The global warming climate case is described in Section 5.1. Since it is not possible to describe an expected evolution of climate conditions for the time perspective of the safety assessment, the base case and global warming variant should not be seen as prognoses or attempts to predict future climate evolutions. Instead, they are *examples* of future evolutions that in a realistic way cover all relevant climate-related changes that can be expected in a 100 kyr time perspective. They are complemented with additional climate cases with a potentially larger impact on long-term repository safety, described in Chapter 5.

For the reconstruction of the last glacial cycle conditions in Section 4.4, an ice sheet model reconstruction of the Weichselian glacial is used (Section 3.1.4). Despite remaining uncertainties regarding the Weichselian glacial history, especially during the earlier phases of the glacial, see Section 4.2, the Weichselian is the best-known glacial cycle. This gives possibilities to use geological information for testing and constraining the adopted models. In line with the discussion above, the purpose is not to produce a “true picture” of the Weichselian evolution, a task that obviously is not possible to achieve, but rather to construct a scientifically reasonable starting point for the analysis of potential climate impacts on repository safety.

The reconstruction of last glacial cycle conditions, Section 4.4, extend over 120 kyrs. Three numerical models are used to yield boundary conditions for the reconstruction:

1. A dynamic ice sheet model.
2. A Glacial Isostatic Adjustment (GIA) model.
3. A permafrost model.

The ice sheet model is the University of Maine Ice Sheet Model (UMISM) (see Section 3.1.4), the GIA model was developed at the University of Durham (see Section 3.3.4) and the permafrost model at Helsinki University of Technology (see Section 3.4.4), see also /SKB 2010f/. The basis for the *reference glacial cycle* of climate-related conditions is a reconstruction of the Fennoscandian ice sheet during the Weichselian employing the ice sheet model. The generated ice sheet evolution has been used as input to the global isostatic adjustment (GIA) model. The third main component in the reconstruction of Weichselian conditions is the permafrost model, yielding permafrost depths given

the evolution of ice sheet, shore-level development, and other surface conditions. The main data flows between the ice sheet, GIA and permafrost models are shown in Figure 4-1.

The *reference glacial cycle*, described in Section 4.5 and used for the base case of the SR-Site main scenario (Figure 1-3) is one example of a conceivable evolution of climate and climate-related processes and covers conditions and sequences that could be expected in a 100 kyr time perspective. The *global warming case*, described in Section 5.1 and used for the Global warming variant of the main scenario, depicts an evolution with a warming climate due to an anthropogenically increased greenhouse effect. Other possible future climate evolutions are described in additional climate cases, described in other parts of Chapter 5. A summary of the climate cases is found in Table 4-1.

In Chapter 4, the sections on Weichselian climate and glacial history (Section 4.2) and reconstruction of last glacial cycle conditions (Section 4.4) describe *past* events, and therefore the time scale in the text and figures is time before present (BP). The sections on the SR-Site *reference glacial cycle* (Section 4.5), and the section on additional climate cases (Chapter 5) all describe possible *future* climate developments and therefore the time scale in these sections reflects this.

All in all, six climate cases depicting possible future climate development at the Forsmark site are presented (Table 4-1) and used for the analysis of long-term repository safety /SKB 2011/.

Table 4-1. Climate cases in the SR-Site safety assessment.

Case number (section in present report)	Climate case	Short description
1 (Section 4.5)	*Reference glacial cycle*	Repetition of reconstructed last glacial cycle conditions
2 (Section 5.1)	*Global warming*	Longer period of initial temperate conditions than in case 1
3 (Section 5.2)	*Extended global warming*	Longer period of initial temperate conditions than in case 2
4 (Section 5.3)	*Extended ice sheet duration*	Longer duration of ice sheet coverage than in case 1
5 (Section 5.4)	*Maximum ice sheet configuration*	Largest ice configuration in past two million years
6 (Section 5.5)	*Severe permafrost*	Favourable for early and deep permafrost growth

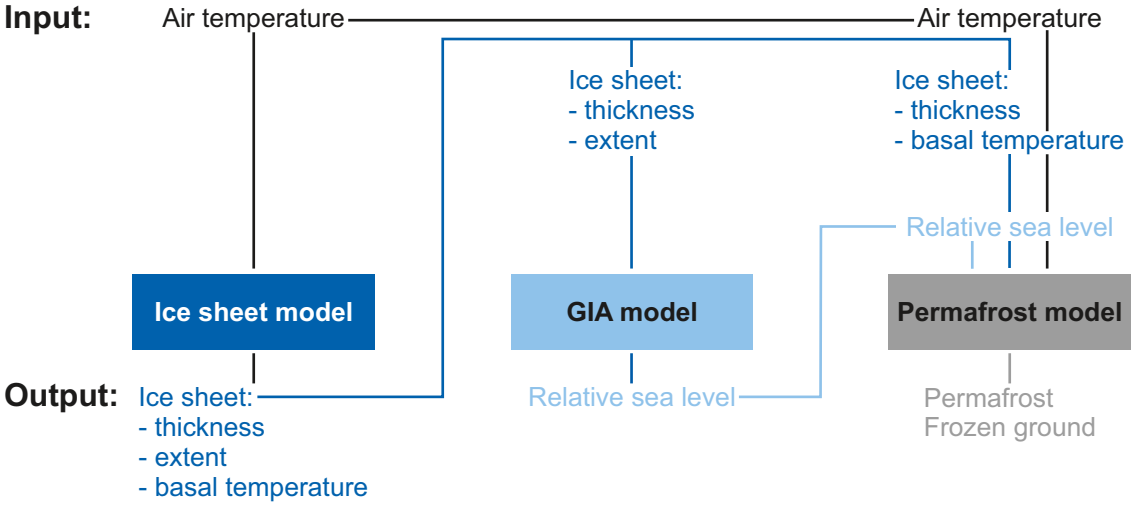

Figure 4-1. *Models used to provide boundary conditions for analysis of the impact of climate-related changes on the repository. Only input and output data shared between the models used to generate the boundary conditions are shown.*

4.2 Weichselian glacial history

In the previous sections, a reconstruction of Weichselian conditions of importance for the assessment of long-term repository safety has been made. Since the Weichselian constitutes the basis for the construction of the future *reference glacial cycle* in SR-Site, a brief description of the Weichselian glacial history is here presented. Special attention is given to describing ice margin stillstands documented from the Weichselian deglaciation, since such periods are of interest when assessing changes in groundwater flow around a KBS-3 repository /Vidstrand et al. 2010 and SKB 2011/.

4.2.1 Overview of Weichselian glacial history

A review of ice-marginal fluctuations during the Weichselian glaciation in Fennoscandia was presented in /Lokrantz and Sohlenius 2006/. The review is summarized below, and complemented with more recent information.

The Weichselian glaciation started 115 kyrs BP and ended at the transition to the Holocene 11.5 kyrs BP. Terrestrial and marine records show that ice volumes fluctuated drastically during the Weichselian. The marine isotope record contains information on global variations in climate and ice volume during the Weichselian and it has been used to divide the glacial into well-dated Marine Isotope Stages (MIS), MIS 5d to MIS 2 (Table 4-2, Figure 3-13). Dating of terrestrial records is often, however, problematic due to stratigraphical gaps and deposits that are difficult to date. In many areas, the timing of local and regional ice-marginal fluctuations, prior to the LGM, is therefore poorly understood. Age attribution of terrestrial deposits is often interpreted from bio- and lithostratigraphical information, which has been correlated to other records, e.g. marine stratigraphies.

The marine record from Early Weichselian (MIS 5d–5a, Table 4-2) shows two relatively warm interstadial periods at around 105–93 kyrs BP (MIS 5c) and 85–74 kyrs BP (MIS 5a). Stratigraphical data indicate at least two periods with ice-free conditions in northern Fennoscandia, which have been correlated with the two early Weichselian interstadials Brørup and Odderade (MIS 5c and 5a). Few absolute dates have, however, been obtained from deposits formed during these interstadials. It has been suggested that two ice advances occurred during the Early Weichselian and covered a large part of northern Fennoscandia. There are, however, different opinions regarding the southernmost extension of these ice sheets. It has also been suggested that large parts of northern Fennoscandia were free of ice from the onset of MIS 5c until the end of MIS 5a. A reconstruction of the Weichselian ice sheet 90–80 kyrs BP (MIS 5b) is seen in Figure 4-2 (lower left panel) and Figure 4-3 (upper panel). According to the /Lundqvist 1992/ reconstruction (Figure 4-2) the Forsmark region was covered by the ice sheet at this time, whereas according to /Svendsen et al. 2004/ (Figure 4-3) the Forsmark region was just barely ice free.

During the cold MIS 4, global ice volume increased, and the Weichselian ice sheet reached a large configuration covering entire Sweden, Finland and Norway (Figure 4-2 (lower right panel) and Figure 4-3 (middle panel)). At this time, south-central Sweden and the Forsmark region were ice covered.

Table 4-2. Marine Isotope Stages, ages, stadials and interstadials of the Weichselian. Regional variations from the denoted warm/cold state occur see /Lokrantz and Sohlenius 2006/, and there is a wide range of names used for each of the stadials/interstadials.

Marine Isotope Stage	Age (kyrs BP)	Stadial/ Interstadial	Warm/Cold	Name (other names are also used)	Weichselian phase
MIS 5d	117–105	Stadial	Cold	Herning	Early Weichselian
MIS 5c	105–93	Interstadial	Warm	Brørup	Early Weichselian
MIS 5b	93–85	Stadial	Cold	Rederstall	Early Weichselian
MIS 5a	85–74	Interstadial	Warm	Odderade	Early Weichselian
MIS 4	74–59	Stadial	Cold	Middle Weichselian stadial	Middle Weichselian
MIS 3	59–24	Interstadials/stadials	Warm/cold	Middle Weichselian interstadials	Middle Weichselian
MIS 2	24–12	Stadial	Cold	Stadial including Last Glacial Maximum	Late Weichselian

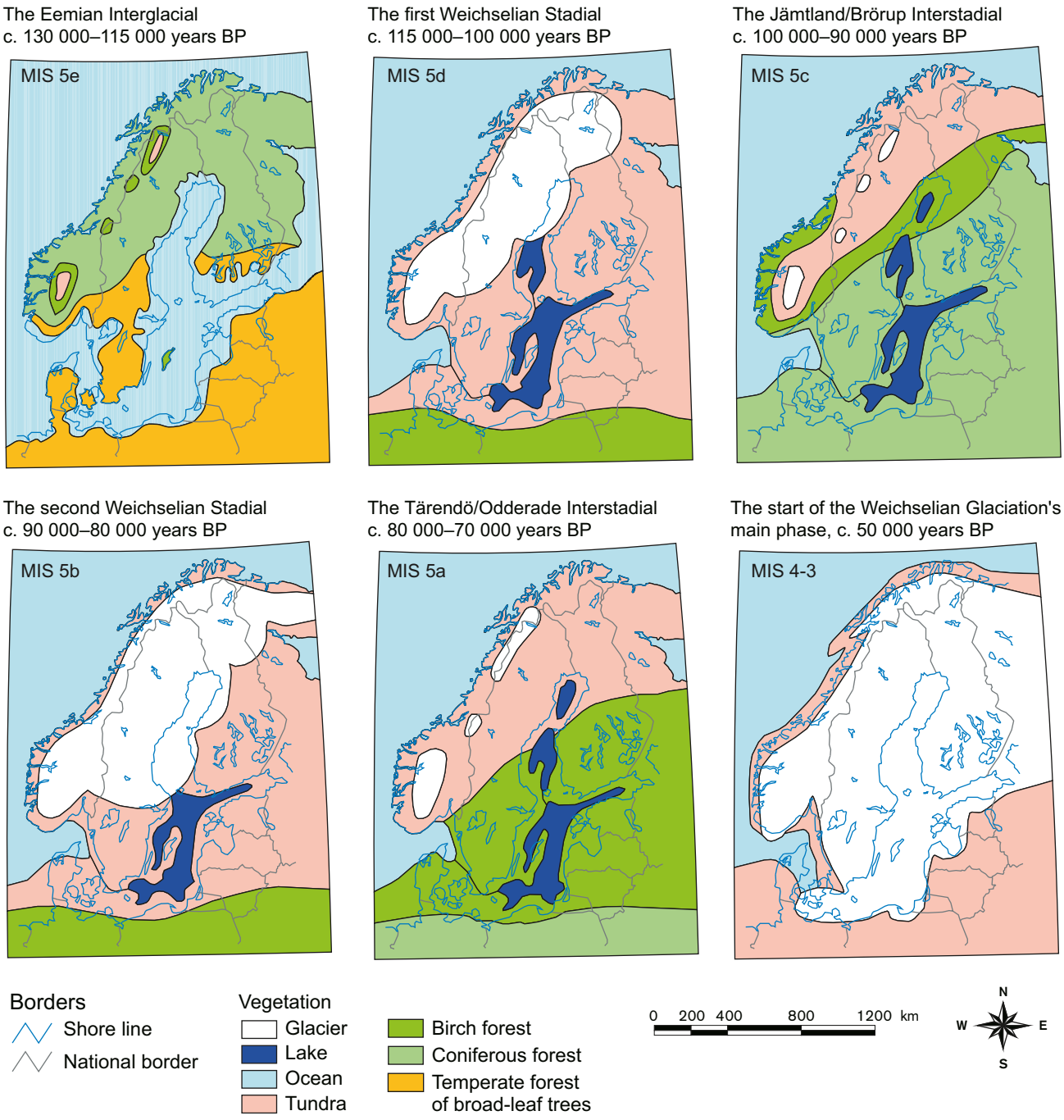

Figure 4-2. *Ice sheet and environmental development in northern Europe from the last interglacial (Eemian) to the Middle Weichselian stadial (MIS 4) according to /Lundqvist 1992/ in /Fredén 2002/. Each map shows a snapshot of the environment during each isotope stage. According to this reconstruction, there were two interstadials with ice-free conditions during Early Weichselian (Brørup and Odderade). Furthermore, in this reconstruction most of Fennoscandia was covered by ice from the Middle Weichselian until the deglaciation. More recent studies suggest that this view needs to be revised to include ice-free conditions over large parts of Fennoscandia during significant parts of MIS 3 (59–24 kyrs BP), see the text.*

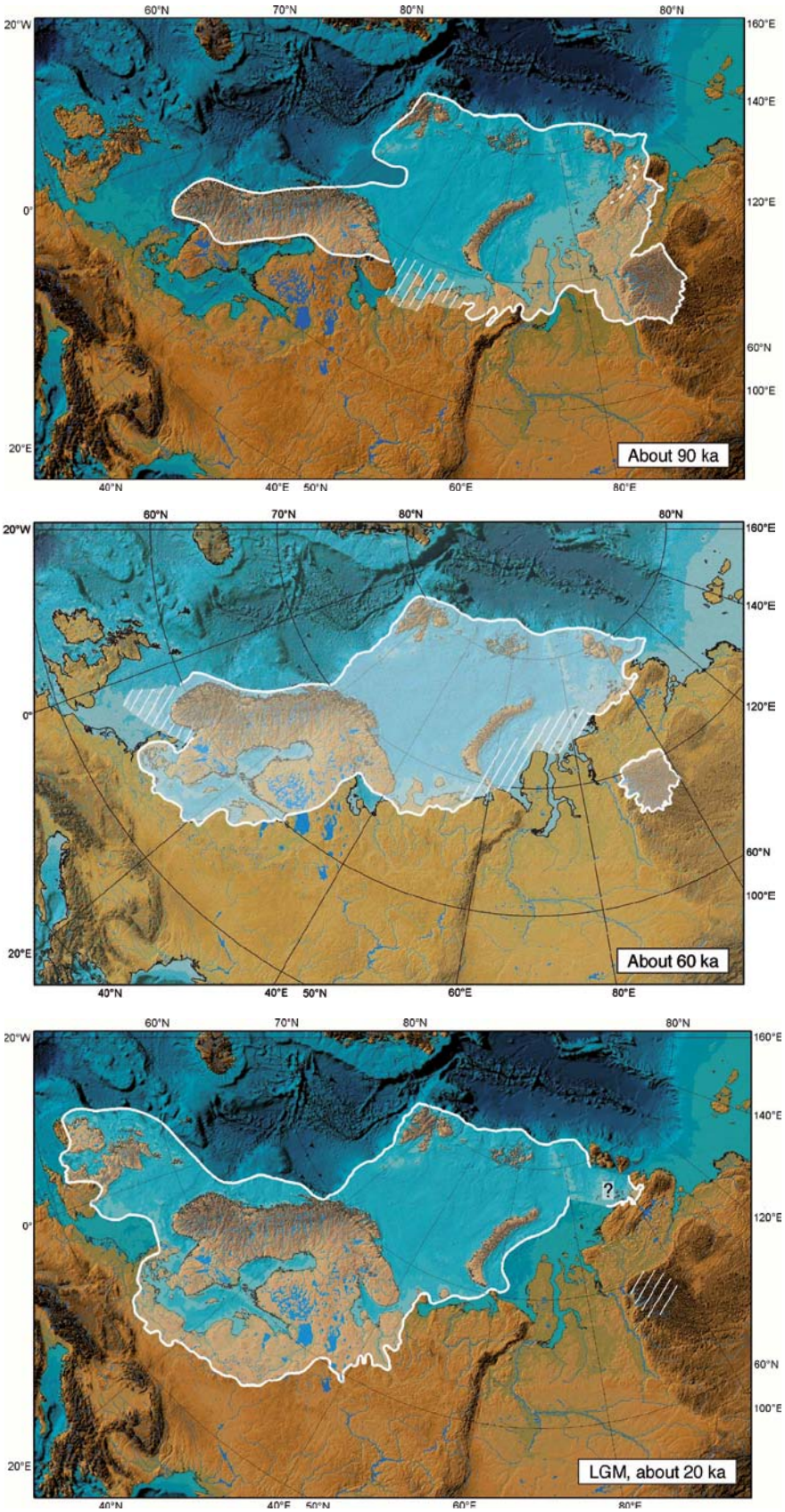

Figure 4-3. *Extent of the Eurasian ice sheet during the glacial maximum stages of the Early Weichselian (90–80 kyrs BP, MIS 5b), the Middle Weichselian (60–50 kyrs BP, MIS 4) and the Late Weichselian (LGM, around 20 kyrs BP, MIS 2) as reconstructed from Quaternary geology. From /Svendsen et al. 2004/. Between these stages of maximum ice sheet extent, the ice sheet had a more restricted configuration, see the text.*

According to the traditional view the ice sheet that was built up during MIS 4 remained large throughout the Middle Weichselian (74–24 kyrs BP), including MIS 3, up until the final deglaciation (Figure 4-2), e.g. /Lundqvist 1992/. However, MIS 3 was a long period characterized by distinct millennial-scale climate shifts (the so called Dansgaard-Oeschger events), which had a strong impact on the North Atlantic region. In addition, surges of Northern Hemisphere ice sheets prior to some of the longer interstadial events produced large amounts of ice-rafted debris in marine sediments, and led to a rise in global sea-level. Although surges of the Fennoscandian ice sheet could have contributed a significant amount of melt water, little is known about how and to what extent this ice sheet responded to these MIS 3 millennial-scale climate shifts. Data from Norway suggests that the youngest of the ice-free interstadials, traditionally correlated with MIS 5a, actually occurred during MIS 3. In line with this, several recent studies suggest ice-free conditions in large parts of Fennoscandia during MIS 3, e.g. /Helmens 2009a, Wohlfarth 2009, Wohlfarth and Näslund 2010, Mangerud et al. 2011/ and references therein. MIS 3 ice sheet scenarios for Fennoscandia thus range from an almost complete and persistent ice cover, to a significantly smaller ice sheet tentatively terminating in south-central Sweden. These different scenarios are discussed by /Wohlfarth 2010, Helmens and Engels 2010, Lambeck et al. 2010/.

There are still many unsolved questions related to an ice-free interstadial period during parts of MIS 3, many of them concerning the datings of various interstadial and ice advance phases, e.g. /Wohlfarth 2009, Wohlfarth and Näslund 2010/. Nevertheless, it is very likely that the Weichselian ice sheets were considerably more dynamic during the MIS 3 period of the Middle Weichselian than previously thought, in line with the variable climate (see also the description of possible MIS 3 climates in Fennoscandia below). One implication of such a revised MIS 3 glacial history is that the Forsmark site was free of ice for a considerable amount of time during the Middle Weichselian, prior to the LGM. If so, the climate at the end of MIS 3 at Forsmark probably was of a clear periglacial character, allowing for permafrost conditions, see below.

In this context it is also worth noting that the average Quaternary ice sheet configuration over Fennoscandia was considerably smaller than that of a full ice sheet configuration, and also considerably smaller than during the Younger Dryas. For average Quaternary ice sheet conditions, the ice sheet is centred over the Scandinavia mountain range, e.g. /Porter 1989, Kleman et al. 2008/, resulting in ice-free conditions in south-central Sweden including Forsmark.

After the MIS 3 period, during MIS 2, the ice sheet advanced to its maximum extent during the beginning of the Late Weichselian 24–12 kyrs BP. During the LGM the entire area of Fennoscandia was covered by the Weichselian ice sheet, including south-central Sweden and the Forsmark region (Figure 4-3 lower panel). The ice volume was at its largest during the LGM (~20–21 kyrs BP), with the ice margin located in Germany and Poland. The ice reached its maximum LGM position at different times in different regions.

After the LGM, the ice sheet started to retreat across e.g. northern Germany and Poland. The timing of the deglaciation is well dated and the ages have recently been converted into calibrated years. Several re-advances took place during the deglaciation of the Danish and Norwegian coast. There are several ice-marginal zones in south-west Sweden that indicate stillstands or re-advances of the ice front, see below. For instance, the deglaciation was interrupted during the Younger Dryas stadial (12.5–11.5 kyrs BP) and there were ice re-advances and stillstands in the middle part of Sweden and southern Finland, whereas coastal areas in the west were characterised by large re-advances. The ice-marginal deposits formed during the Younger Dryas can be followed around the entity of Fennoscandia. After the Younger Dryas, the ice retreated towards the Fennoscandian mountain range more or less continuously.

Deep weathered bedrock of Pre-Quaternary age occurs in parts of Småland and in the inner parts of northern Sweden. These deposits indicate low or negligible erosion in these regions. In the inner part of Norrbotten there are morphological features, Veiki moraines, which, according to several authors, were formed during the first Weichselian ice advance (MIS 5d). In Småland there are till-covered eskers, which may have been formed prior to the latest glacial advance. Areas with deep weathered bedrock and those with Quaternary deposits older than the last glaciation coincide to a large extent. These areas are indicators of cold-based ice and of low glacial erosion.

For more detailed descriptions of the Weichselian glacial history, see e.g. /Lokrantz and Sohlenius 2006, Lundqvist 2007, Wohlfarth 2010, Helmens and Engels 2010, Lambeck et al. 2010/. For recent examples of reconstructions of last glacial cycle Northern Hemisphere ice sheets, see e.g. /Peltier 2004, Svendsen et al. 2004, Peyaud et al. 2007, Charbit et al. 2007, Kleman et al. 2008, Bonelli et al. 2009, Clark et al. 2009/.

4.2.2 Ice-marginal stillstands

From Quaternary geological information it is known that temporary halts in the ice sheet retreat took place several times in southern and south-central Sweden during the Weichselian deglaciation, e.g. /Lundqvist and Wohlfarth 2000, Fredén 2002/. Similar, and in cases corresponding, halts are also documented from e.g. Finland, Denmark, Norway, Russia, Poland and Germany e.g. /Lagerlund et al. 1995, Marks 2002, Houmark-Nielsen and Kjær 2003, Lunkka et al. 2004/. At these locations, dated marginal moraines, once formed along the former ice sheet margin, indicate areas and periods when the ice margin was more or less stable at a certain location. No traces of such moraines, indicative of temporary halts, have been found from the growth phases of the Weichselian ice sheet. It is possible that stillstands did occur also during growth phases, but that resulting moraines have been obliterated by the subsequent ice coverage. However, during the Early Weichselian stadials, i.e. during Marine Isotope Stages 5d (117–105 kyrs BP) and 5b (93–85 kyrs BP), maximum ice configurations, with ice margins that may have been quasi stable for some period of time, have been envisaged for central Sweden /Lundqvist 1992/, see also /Lokrantz and Sohlenius 2006/.

The longest and most prominent halt during the last deglaciation took place during the cold Younger Dryas stadial. On the basis of data from the GRIP ice core from Greenland, the Younger Dryas stadial began around 12,800 years BP and ended around 11,500 BP, resulting in a ~1,300 year long Younger Dryas period. Quaternary geological information suggests that the associated Younger Dryas ice sheet margin stillstands in Sweden occurred during a period of around 900 years /Fredén 2002/. On glaciological grounds, /Fastook and Holmlund 1994/ concluded that the climatic event responsible for the Younger Dryas stillstand could have been short, even less than 500 years.

It should be noted however that during the Younger Dryas period, as well as for several other less prominent stillstands south of the Younger Dryas moraine complex, the position of the ice margin was not completely stable. Instead, as a response to climate variability and ice sheet dynamics, the ice front typically oscillated back and forward, in cases up to several tens of km, e.g. /Lundqvist and Wohlfarth 2000, Lunkka et al. 2004/. For the Younger Dryas, the resulting zone of ice-marginal deposits is typically around 20–25 km wide in central and eastern Sweden /Fredén 2002/. During shorter halts in the deglaciation, this zone may be considerably narrower or absent. During phases of maximum ice sheet configuration, such as during the LGM, the ice margin typically also oscillates back and forward as a response to ice sheet dynamics and climate variability.

South of the Younger Dryas zone, at least six older stillstands in the Weichselian deglaciation of southern Sweden have been documented /Lundqvist and Wohlfarth 2000/. At several of these sites, ice-marginal moraines have been suggested to have formed during periods of up to 100–200 years, such as the large Göteborg Moraine which formed sometime between 15,400 and 14,500 kyrs BP /Lundqvist and Wohlfarth 2000/. The suggested, often maximum, formation times of these moraines indicate that the ice margin was relatively stable for these periods or shorter. In southern Finland, it has been estimated that the largest Younger Dryas end moraine complexes, i.e. the First and Second Salpausselkä end moraines, as well as the younger Central Finland end-moraine, also were formed during periods up to a few hundred years long /Lunkka et al. 2004/. These estimates thus give an indication of the duration of periods with stable ice margin position during the last deglaciation.

In summary, it may be concluded that during the deglaciation of the Weichselian ice sheet, the general ice sheet retreat temporarily halted several times. This is seen from dated ice-marginal moraines, including the deposits from the Younger Dryas stadial. During such halts, the ice margin either oscillated back and forth or moved slowly within a zone that could be many km wide, in the case of the Younger Dryas, several tens of km. During the formation of individual moraine ridges, the ice margin is estimated to have been at stable positions for up to a few hundred years. It has to be assumed that similar types of stillstands may occur also during phases of ice sheet advance, see Section 4.5.1.

4.3 Examples of Weichselian climates

During the Weichselian, climate shifted many times between warmer and colder periods, as reflected in the growth and decay phases of the Weichselian ice sheet, see Section 4.2.1. The variability and range within which the climate shifted during the last glacial cycle could be expected also during future glacial cycles. Therefore, quantitative descriptions of prevailing climate conditions for periods with fundamentally different climates during the Weichselian are given below for Sweden and the Forsmark region, examples of climates that are of high relevance for e.g. the SR-Site *reference glacial cycle* presented in Section 4.5.

The aim of the following descriptions of Weichselian climates is not to give a full review of all that is known on climate and climate variability during the last glaciation. Instead, the intention is to provide examples that demonstrate a range within which the climate varied during the Weichselian by selecting climate reconstructions for both stadial and interstadial phases and to cover a broad time span of the glacial cycle.

4.3.1 Early Weichselian (117–74 kyrs BP)

The Fennoscandian climate during the Early Weichselian (MIS 5d–5a, 117–74 kyrs BP) varied significantly, as reflected in the glacial history with intervening stadial and interstadial conditions described above. Detailed quantifications of Fennoscandian climate conditions for these early periods are very rare. However, in northern Fennoscandia, quantifications of interstadial climate conditions have been made within an SR-Site project from the Sokli sediment sequence in Finnish Lapland, northern Fennoscandia e.g. /Helmens 2009a/. The sediment record at Sokli is one of the few well-dated sites in northern Europe that covers the Early Weichselian in high detail. The Sokli sequence consists of tills, glacio-fluvial beds, and fluvial beds, interlayered with fossil-rich lacustrine sediments that according to multiple accelerator mass spectrometer (AMS) ^{14}C and optically stimulated luminescence (OSL) datings extend from the present into the penultimate glacial, i.e. representing the last ~130 kyrs, e.g. /Helmens 2009a/.

Past environmental and climate conditions have been reconstructed for MIS 5d (the Herning stadial 117–105 kyrs BP, Table 4-2) by analysis of insect remnants and botanical and zoological macro remains /Engels et al. 2010/. The results show that, for the ice-free stadial conditions at the investigated site, the summer July air temperature may have been ~7°C, which is ~6°C colder than the present summer mean temperature (13°C), and indicative of arctic climate conditions.

During MIS 5c (the Brørup interstadial, 105–93 kyrs BP, Table 4-2), summer temperatures inferred from plant macrofossil remnants indicate surprisingly warm conditions for northern Fennoscandia /Väliranta et al. 2009, Engels et al. 2010/. Minimum July temperatures were as high as 16°C, which is 3°C warmer than at present /Väliranta et al. 2009/. At that time, open birch woodland existed at the site within a subarctic climate. This result is in contrast to other (lower-resolution) reconstructions from northern Fennoscandia indicate MIS 5c temperatures 6–7°C lower than present, see /Engels et al. 2010/. However, several central European sites indicate that there was a phase during the MIS 5d interstadial that was characterized by high summer temperatures, and a comparison between the high-resolution reconstructions from western Europe and the results presented in /Engels et al. 2010/ suggests that the north–south July air temperature gradient between the mid- and high-latitudes was much weaker during MIS 5c than at present.

One suggested reason for the warm climate conditions during this interstadial could be that the contemporary astronomical forcing resulted in a weaker north-south temperature gradient and a longer growing period, creating more favourable climate conditions that at present /Väliranta et al. 2009/.

4.3.2 Middle Weichselian (74–24 kyrs BP)

Examples of Fennoscandian climates during the MIS 3 interstadial (59–24 kyrs BP) have been studied by use of geological information /Helmens 2009a, Wohlfarth 2009/ and by climate modelling /Kjellström et al. 2009b (including erratum Feb 2010)/. MIS 3 covers a long time period that includes both rapid millennial-scale climate shifts and longer trends in changing climate, see /Wohlfarth 2009/. A few examples of climates occurring during MIS 3 are given below.

Early MIS 3 (at ~50 kyrs BP)

A comprehensive environmental reconstruction of early MIS 3 conditions, at around 50 kyrs BP, was made based on multi-proxy analysis on a two metre thick laminated, lacustrine clay-silt sequence obtained at the Sokli site in northern Finland /Helmens 2009a/. The analyses included lithological characteristics; organic content (loss-on-ignition, LOI); plant microfossils (pollen, spores, algal and fungal remains); macrofossils of plants (e.g. seeds, moss remains) and of aquatic animals (e.g. statoblasts of Bryozoa); head-capsules of chironomids (i.e. aquatic insects); and diatoms and other siliceous microfossils (e.g. phytolits, chrysophyte stomatocysts). Additionally, geomorphic evidence and analysis of DEM data are employed in the environmental reconstruction. Mean July temperatures were reconstructed by applying transfer functions to the pollen, chironomid and diatom records.

The results have been surprising in various aspects, seriously challenging previous concepts on environmental conditions during early MIS 3 in the near-central area of the Weichselian glaciation. Traditionally, the area is thought to have been ice covered throughout MIS 4–2, i.e. from around 60 kyrs BP to the final deglaciation, see above. /Helmens 2009a/ show not only ice-free interstadial conditions but also climate warming to present-day temperatures. The laminated sediments seem to have been deposited in a sheltered embayment of a glacial lake impounded along the ice front of the Weichselian ice sheet. Throughout the deposition of the lacustrine sediments, the reconstructed terrestrial ecosystem on the deglaciated land is low-arctic shrub tundra very similar in composition to modern tundra in the continental sector of northern Fennoscandia. The distributional ranges of pine and tree birch were probably only a few hundred kilometres south or south-east of the Sokli site. This is concordant with the sparse evidence for the presence of boreal tree taxa during MIS 3 in the Baltic countries and further east in Europe but contradicts with the commonly inferred treeless tundra or grass-dominated steppe conditions in central Europe.

Mean July air temperatures in the magnitude of present-day values are reconstructed by the chironomid and diatom records as well as by fossils from aquatic plants and Bryzoa. Temperature inferences based on the terrestrial pollen are consistently lower than the temperatures reconstructed from the fossil aquatic assemblages. It is possible that the regional terrestrial and the local aquatic systems responded differently to the climatic and landscape features at around 50 kyrs BP. Warmest and moistest conditions are recorded in the lower part of the laminated lacustrine sequence. This is consistent with the pattern of the Greenland millennium-scale Dansgaard-Oeschger interstadials in which abrupt warming is followed by a gradual cooling. The chironomid-inferred mean July air temperatures amount to around 13°C (i.e. the current temperature) ±1.15°C in the lower part of the lake sequence and to around 12±1.15°C in the upper part. The mean July air temperatures inferred from the terrestrial pollen data lie within the range of around 12±1.5°C (lower part of sequence) and around 11±1.5°C (higher part of sequence). High summer temperatures are ascribed in part to enhanced July insolation compared with present at the high latitude site of the site.

Comparison with recently published, well-dated sediment sequences in eastern and western Finland suggests ice-free and warm conditions in major part of eastern Fennoscandia at ~50 kyrs BP. Open birch forest seems to be registered in eastern Finland during part of the warming event. Direct evidence is lacking to reconstruct the total time span with ice-free conditions at the studied sites. It is argued that the Sokli site was glaciated during the overall colder late MIS 3. The absence of well-dated geological data in northern Sweden hampers a reconstruction of the total ice-marginal retreat in the continental sector of the Fennoscandian Ice Sheet during the early MIS 3 climate warming event. For more details on this study, see /Helmens et al. 2007a, Engels et al. 2008, Bos et al. 2009, Helmens 2009a, Helmens et al. 2009b, Helmens and Engels 2010, Engels et al. 2010/.

A warm climate during early MIS 3, such as reconstructed for northern Fennoscandia by e.g. /Helmens 2009a, is in line with, and probably necessary for, a deglaciation of the large ice sheet that existed during MIS 4, see above.

Middle MIS 3 (at 44 kyrs BP)

A comprehensive climate modelling study was made to investigate climate extremes within which the climate in Fennoscandia may vary on a 100 kyr time scale /Kjellström et al. 2009b, including erratum dated Feb 2010/. Three different periods were simulated, a cold glacial climate (at LGM,

~21 kyrs BP), a periglacial climate (at MIS 3, 44 kyrs BP) and a warm future climate dominated by global warming (a few thousands of years after present). In the present section, results from the periglacial climate simulation are presented. Results from the LGM climate simulation are presented in Section 4.3.3 whereas results from the global warming simulation are described in Section 5.1.7

In order to give a detailed example of a modelled periglacial MIS 3 climate over northern Europe, climate modelling was performed using the global climate model (GCM) that produced boundary conditions that were used by a regional climate model (RCM) /Kjellström et al. 2009b/. This model study was designed to also test whether a cold and dry climate favourable for permafrost growth would exist in the ice-free regions surrounding a Fennoscandian MIS 3 ice sheet with a restricted ice configuration. Based on forcing conditions for a selected period during MIS 3 (Greenland stadial 12 at 44 kyrs BP), a simulation of middle MIS 3 climate conditions was made with the climate models. For the simulations performed and analyzed within this study, atmospheric and land components of the CCSM3 used a grid spacing of approximately 2.8° in latitude and longitude. The vertical resolution is 26 levels in the atmosphere and 40 levels extending to 5.5-km depth in the ocean. The regional climate model used a horizontal resolution of 50 km and a time resolution of 30 minutes. For details on the models, how they were employed, and a discussion on climate model uncertainties, see /Kjellström et al. 2009b/.

The choice of period to simulate for MIS 3 followed from a workshop on MIS 3 organised by SKB in September 2007 /Näslund et al. 2008/ with the specific purpose of supporting this selection. Only limited and in some cases controversial, palaeo-information is available to reconstruct the extent of the Fennoscandian ice sheet during the different warm and cold intervals of MIS 3. We here assumed, in line with several recent studies, see above, that the southern part of Fennoscandia was ice free during some of the MIS 3 stadials.

The modelling activities included the use of; i) a fully coupled Atmosphere-Ocean General Circulation Model (AOGCM), ii) a Regional Climate Model (RCM), and iii) a dynamic vegetation model (DVM). The AOGCM was used to simulate the global climate in steady-state simulation for the selected time period. Even though AOGCMs are powerful models they are relatively coarse in their resolution due to computational limitations. Therefore, the output from the AOGCM was used as input to the RCM that provides output at a relatively high horizontal resolution for Europe. Both global and regional climate models hold descriptions of the land surface, including vegetation. In the regional model, it is important to describe the vegetation cover with a high degree of regional detail. Such details are missing in available global fields and details of the vegetation cover have to be estimated, based on the global fields and consideration of among other things land/sea distribution. In order to improve the representation of the regional vegetation, a dynamic vegetation model was used to simulate the European vegetation resulting from the RCM-simulated climate. In a subsequent step, the new vegetation was used in a new RCM simulation that provides the final climate output. For the studied MIS 3 period, data on relevant climate parameters was extracted from the regional model for the Forsmark area.

The global model simulation of the periglacial MIS 3 climate used a CO_2 concentration in the atmosphere of 200 ppm /Kjellström et al. 2009b/. An ice sheet with a restricted configuration was assumed, and in line with this, a simulated MIS 3 ice sheet configuration obtained from the Weichselian ice sheet reconstruction described in Section 3.1.4 was used /Kjellström et al. 2009b/. For a detailed description of the assumptions made in the modelling process, model forcing and initial conditions (such as astronomical and solar forcing, concentration of greenhouse gases and aerosols in the atmosphere, extents of ice sheets, distribution of land and sea, topography and vegetation), also see /Kjellström et al. 2009b/.

In addition to the modelling activities, an effort was made to collect palaeoclimatic information by compiling various MIS 3 and LGM proxy data from different sources /Kjellström et al. 2009b, Wohlfarth 2009/. An attempt to use part of this palaeoclimatic information to constrain the forcing conditions used in the climate models was made. Other proxy data were used for model evaluation purposes. Results from the global climate model were compared with proxy records of sea-surface temperatures and with terrestrial climate records. The regional climate model results have been compared with existing terrestrial palaeoclimate records from Europe.

Global climate

Figure 4-4 shows the simulated global warming climate from the middle MIS 3 simulation. Seasonal mean changes in temperature as compared with a simulation of the pre-industrial climate (with forcing conditions set at levels consistent with those preceding the 18th century) climate are also shown. Figure 4-5 shows the development over time of the simulated global mean temperature for this steady-state climate simulation. The figure also shows the temperature development of a LGM climate simulation that the MIS 3 simulation was initiated from.

The annual mean surface cooling in the MIS 3 simulation as compared with pre-industrial conditions is most pronounced over the Laurentide and the Fennoscandian ice sheets and over the Greenland-Iceland-Norwegian Sea, with a maximum cooling of 25°C (Figure 4-4). A large portion of the cooling over the Fennoscandian and Laurentide ice sheets is due to the increased elevation over the ice sheet. The cooling amounts to 5–10°C north of 40°N in the Atlantic Ocean, the Arctic Ocean and over Antarctica and the Southern Ocean. The sea-ice extent is increased in the MIS 3 simulation in the North Atlantic and north Pacific as compared with the pre-industrial simulation (Figure 4-4).

Even though proxy data for the period around 44 kyrs BP are sparse, comparison with available sea surface temperature data shows that the globally modelled temperatures and proxy data are in reasonable agreement. For further results and discussion of the MIS 3 simulation from the global climate model, and for details about the comparison with MIS 3 climate proxy data, see /Kjellström et al. 2009b/.

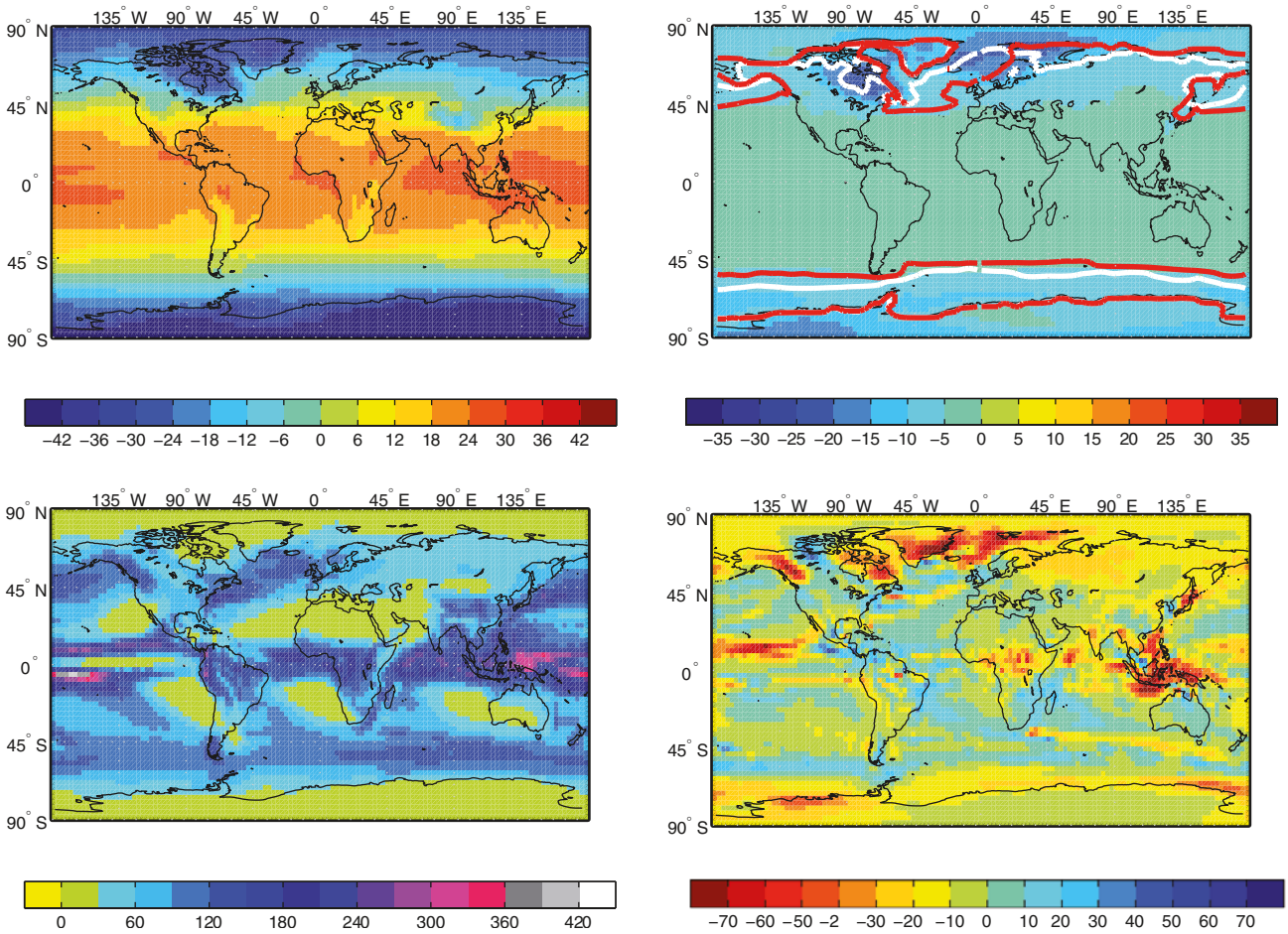

Figure 4-4. *Annual mean near-surface air temperature in the MIS 3 simulation (upper left) and the difference compared with a simulated pre-industrial climate (upper right). Units are °C. Also shown is the annual mean sea ice edge (defined at 10% areal sea ice cover) for the pre-industrial simulation (white; upper right)) and the MIS 3 simulation (red; upper right).The lower panels show the simulated precipitation (lower left) and the difference compared with the simulated pre-industrial climate (lower right). Units are mm/month. From /Kjellström et al. 2009b/.*

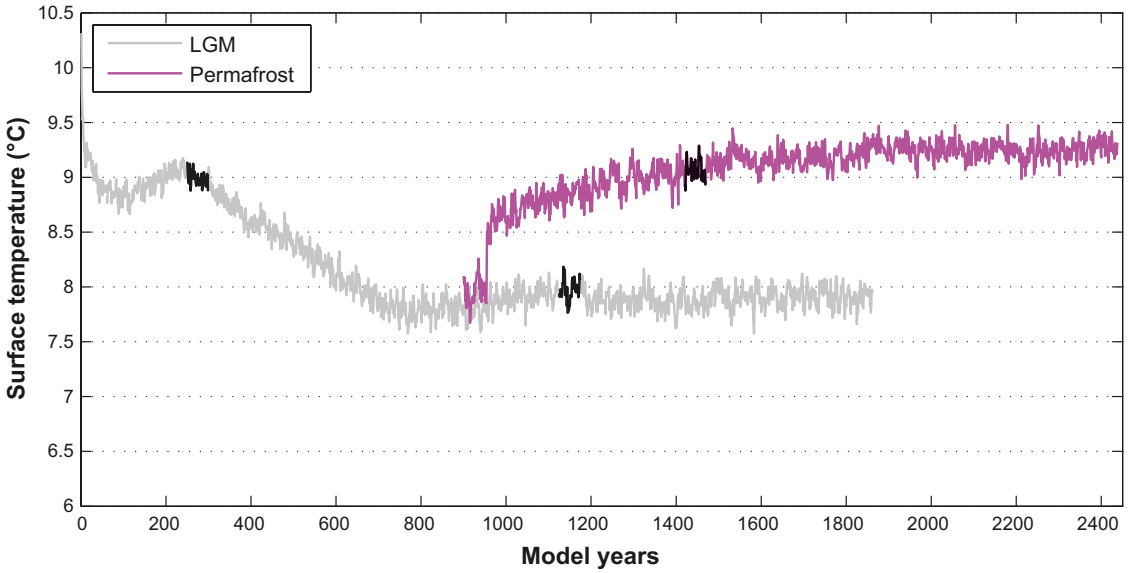

Figure 4-5. *Annual global mean near-surface air temperature in the MIS 3 (pink) and LGM (grey) climate simulation. Black parts of the curves marks the 50-year periods analysed in /Kjellström et al. 2010/ and presented here. Units are °C. From /Kjellström et al. 2009b erratum Feb 2010/.*

Climate in Europe and Sweden

The regional climate model was then used to downscale the model results of the global climate model in order to obtain a higher resolution data over Europe and Sweden. The resulting climate over Europe was used to produce a new vegetation distribution with the vegetation model. This vegetation was in turn, used as input to the regional climate model, to produce a climate in line with the new vegetation. An evaluation of the results from this iterative process is given in /Kjellström et al. 2009b/. Figure 4-6 and 4-7 presents selected results on temperature and precipitation from the regional modelling.

During this part of the middle Weichselian, the temperature climate is dominated by a very strong seasonal cycle (Figure 4-7) and a pronounced north-south gradient in the winter (Figure 4-6, upper row, middle panel). In the north, the effect of the Weichselian ice sheet is clearly seen in the isolines of temperature showing low temperatures in parts of Fennoscandia. The isotherm showing 0°C annual mean temperature goes south of Ireland, through England and the southern parts of Denmark, just south of Sweden and then eastwards (Figure 4-6, upper row, right panel). Compared with the present climate (1961–2000), the annual mean temperature in the MIS 3 simulation is ~5°C colder around the Mediterranean, 5–10°C colder in central Europe and more than 8°C colder in the ice-free parts of Fennoscandia (Figure 4-6, lower row, right panel). The same values as for difference in annual temperature apply for winter temperature in southern and central Europe. The winter temperature of the British Isles is 10–15°C colder and the southern tip of Fennoscandia around 15°C colder in comparison with the present climate (Figure 4-6, lower row, middle panel). Over the ice sheet in northern Fennoscandia, temperatures are at least 30°C colder than in the present climate (1961–2000) simulation. On Iceland and over the Norwegian Sea, the difference from the late 20th century is even larger. In summer, most of continental Europe is 0–5°C colder than in the late 20th century, western Europe and the British Isles are 5–10°C colder and northern Fennoscandia is 10–15°C colder than in the simulated present climate (Figure 4-6, lower row, left panel).

The annual mean precipitation in the MIS 3 simulation is characterized by considerably drier conditions than in the simulated present climate (1961–2000), by more than 360 mm/year in large parts of Fennoscandia and over the North Atlantic, and by an increase in precipitation of up to 360 mm/year in parts of the southwest (Figure 4-8, upper row right panel). In the rest of the model domain, differences are, with few exceptions, smaller.

The drier climate in northern Europe is reflected in the seasonal cycle of precipitation. For Sweden there is a reduction of more than a factor of two in winter and substantial reduction also during summer (Figure 4-9). Further south, the reduction is most evident in the winter half of the year whereas in southernmost Europe the changes relative to the present climate are small for all months.

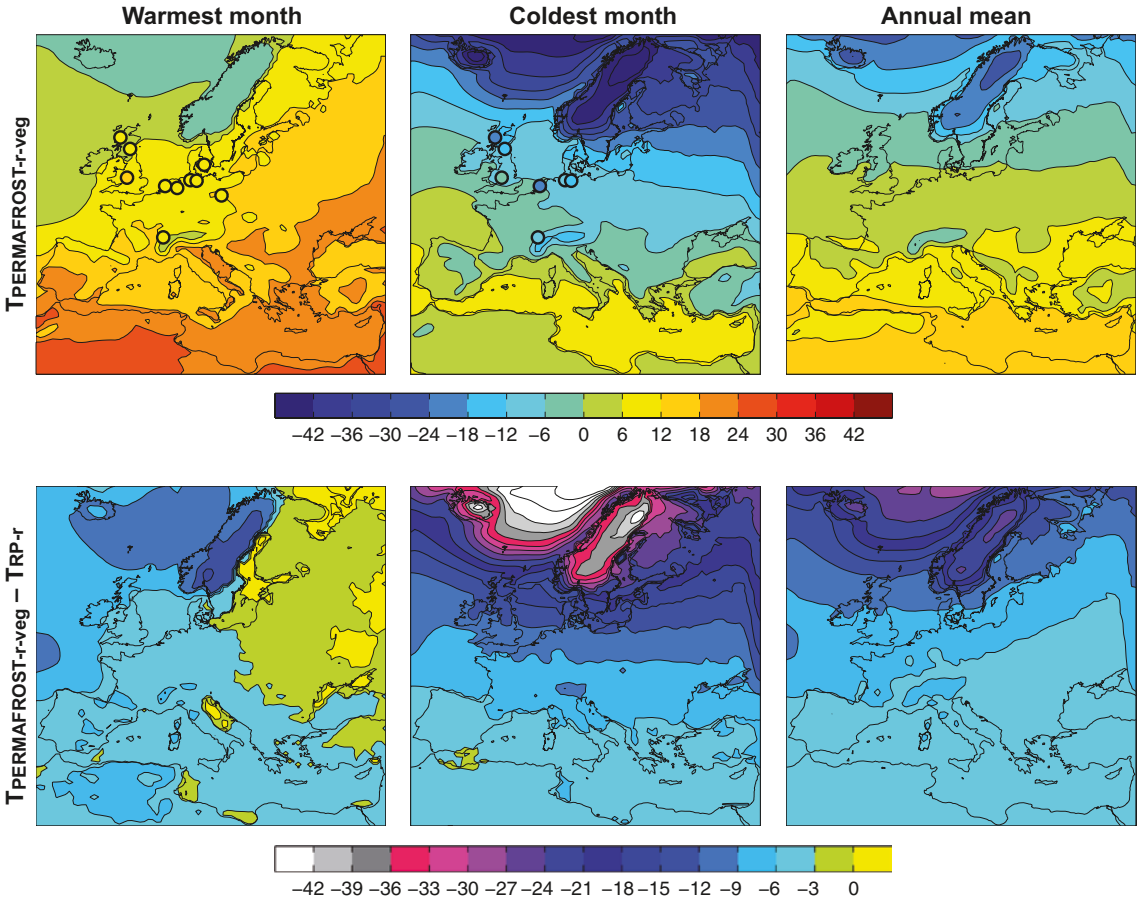

Figure 4-6. *Mean air temperatures of the warmest month, coldest month and annual mean in the MIS 3 simulation (top). Shown also are temperature estimates based on proxy data as described in /Kjellström et al. 2009b, Section 2.4/ (coloured circles). The lower row shows the differences between the simulated MIS 3 climate and a recent-past climate simulated for the period 1961–2000. From /Kjellström et al. 2009b/.*

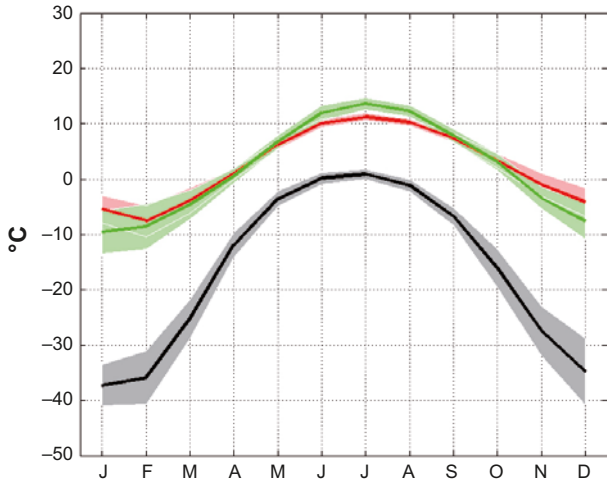

Figure 4-7. *Annual temperature range in Sweden for MIS 3 (black), simulated present climate (red) and according to the CRU (Climate Research Unit, East Anglia) observational data for the time period 1961–1990 (green). Shaded areas in corresponding colours indicate the ±1 standard deviation range of individual monthly averages in the three data sets. From /Kjellström et al. 2009b/.*

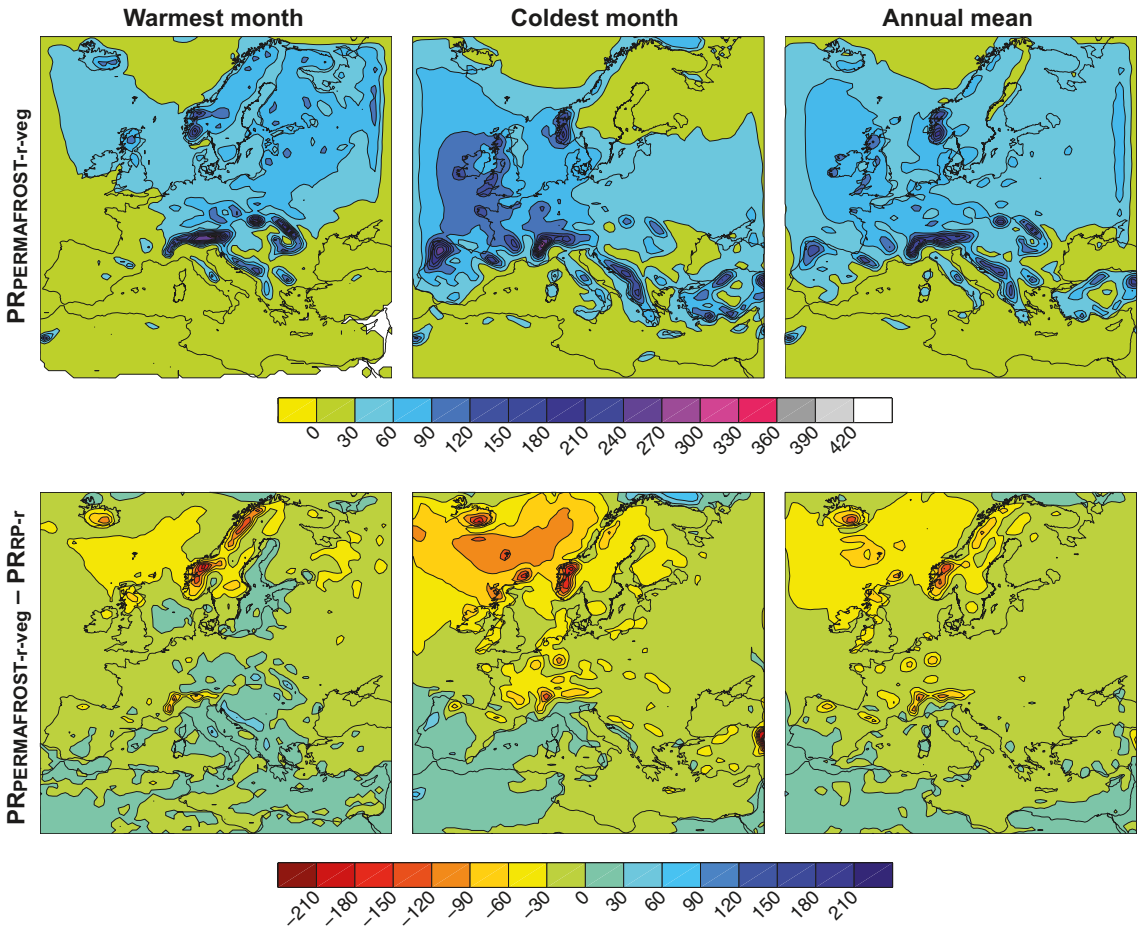

Figure 4-8. *Mean precipitation of the warmest month, coldest month and annual mean in the MIS 3 climate simulation (upper row). Also shown are differences between MIS 3 simulation and the simulation of the present (1961–2000) climate. Units are mm/month. From /Kjellström et al. 2009b/.*

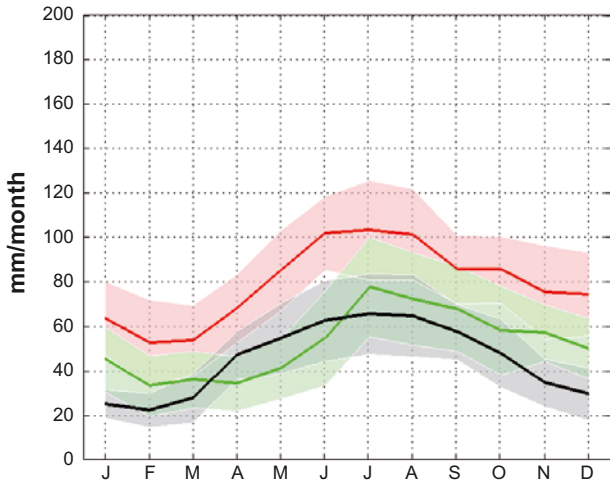

Figure 4-9. *Annual precipitation range in Sweden in the MIS 3 simulation (black), present climate simulation (1961–2000) (red) and according to the CRU observational data (green). Shaded areas in corresponding colours indicate the ±1 standard deviation range of individual monthly averages in the three data sets. From /Kjellström et al. 2009b/.*

For further results, on the European scale, from the MIS 3 climate simulations, including results and discussion of the simulations of MIS 3 vegetation , comparisons with climate proxy data, and comparisons with other model simulations of MIS 3 climates, see /Kjellström et al. 2009b/.

Do the results support a cold and dry climate favourable for permafrost growth? /Heginbottom et al. 1995/ examined the relation between ground temperature and permafrost continuity. An annual ground temperature of between –5 and –2°C is defined as the boundary for discontinuous permafrost (50–90% of landscape covered by permafrost) and –5°C and colder as the boundary for continuous permafrost (90–100%). However, it is also stated that a large part of areas with continuous permafrost has a ground temperature warmer than –5°C. Since the ground temperature differs from the near-surface air temperature by a few degrees, see Section 3.4, the simulated annual mean ground temperatures over Europe for MIS 3 are presented in Figure 4-10.

In central and northern Fennoscandia, outside of the prescribed ice sheet, the modelled MIS 3 annual average ground temperature is colder than –5°C (Figure 4-10), which suggest that the climate conditions are favourable for development of continuous permafrost. South of this, the modelled annual average ground temperature increases, reaching 0°C in the southernmost parts of Fennoscandia. The higher ground temperatures in the southern areas including northernmost Denmark, southern Sweden, Estonia and part of what today is the Baltic Sea and Gulf of Finland do not fulfil the thermal requirements for extensive permafrost. However, it is cold enough for sporadic permafrost (less than 50% of landscape covered), which may exist when the annual mean ground temperature is between 0 and –2°C. Based on these results of /Kjellström et al. 2009b/ it is concluded that conditions are favourable for permafrost growth in the inferred ice-free parts of Fennoscandia.

Do the results support a restricted MIS 3 Fennoscandian ice sheet? The global and regional climate models do not include dynamical modelling of ice sheets and thus an ice sheet cannot form in the models, even if the climate conditions are favourable for ice sheet growth. The snowpack is, however, allowed to build up in the model. If the snow depth increases in time in a specific region, we can take this as an indication that an ice sheet would grow in this region if such processes were included in the model. However, the opposite situation, a lack of snow accumulation in front of, or at the margins of, a prescribed ice sheet, does not necessarily mean that the ice sheet would not grow (simply the lowermost part of the ice sheet would have a net mass loss, which is typical for ice sheets ending on land). Growth of the ice sheet could still be possible if the precipitation over the ice sheet were large enough compared with its mass loss by melting, i.e. if conditions for the common pattern of ice sheet growth were satisfied.

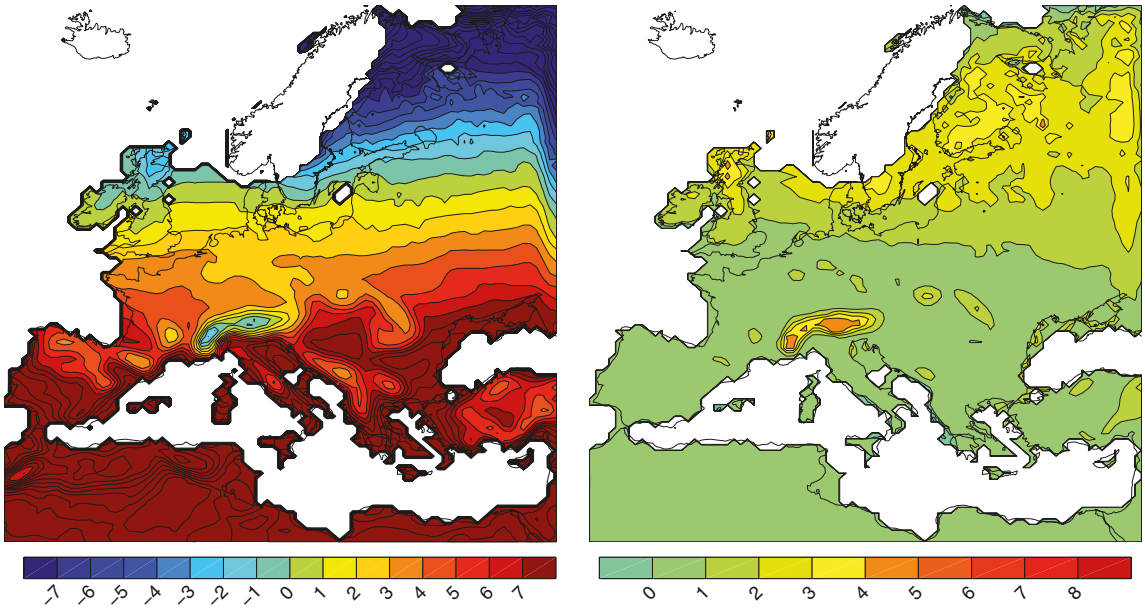

Figure 4-10. *Annual mean ground temperature (left) and difference between near-surface air temperature and the ground temperature (right) in the MIS 3 simulation. Units are °C. White areas in Fennoscandia are covered by the prescribed restricted MIS 3 ice sheet. From /Kjellström et al. 2009b/.*

In the middle MIS 3 simulation, the snow depth in eastern Sweden, including the Forsmark region, does not increase in time. The annual minimum snow depth (occurring in September) is close to zero (varying from 0–0.02 m equivalent water depth). For the issue of whether the simulated climate is in line with the prescribed restricted middle MIS 3 ice sheet configuration, with ice-free conditions in e.g. the Forsmark region (Figure 4-10), one can therefore conclude that 1) an ice sheet would not grow locally from the local precipitation in front of the ice margin, 2) the modelled temperature and precipitation climate in front of the ice sheet is consistent with the assumed ice-free conditions and restricted ice sheet coverage, but it does not exclude the possibility of a larger ice sheet.

Climate in the Forsmark region

Figure 4-11 and 4-12 show average air temperature and precipitation for a 50 year period of the simulated MIS 3 climate, and a comparison with the climate simulated for present conditions. The results show that the climate is significantly colder and drier than at present, with arctic climate conditions prevailing in the Forsmark region.

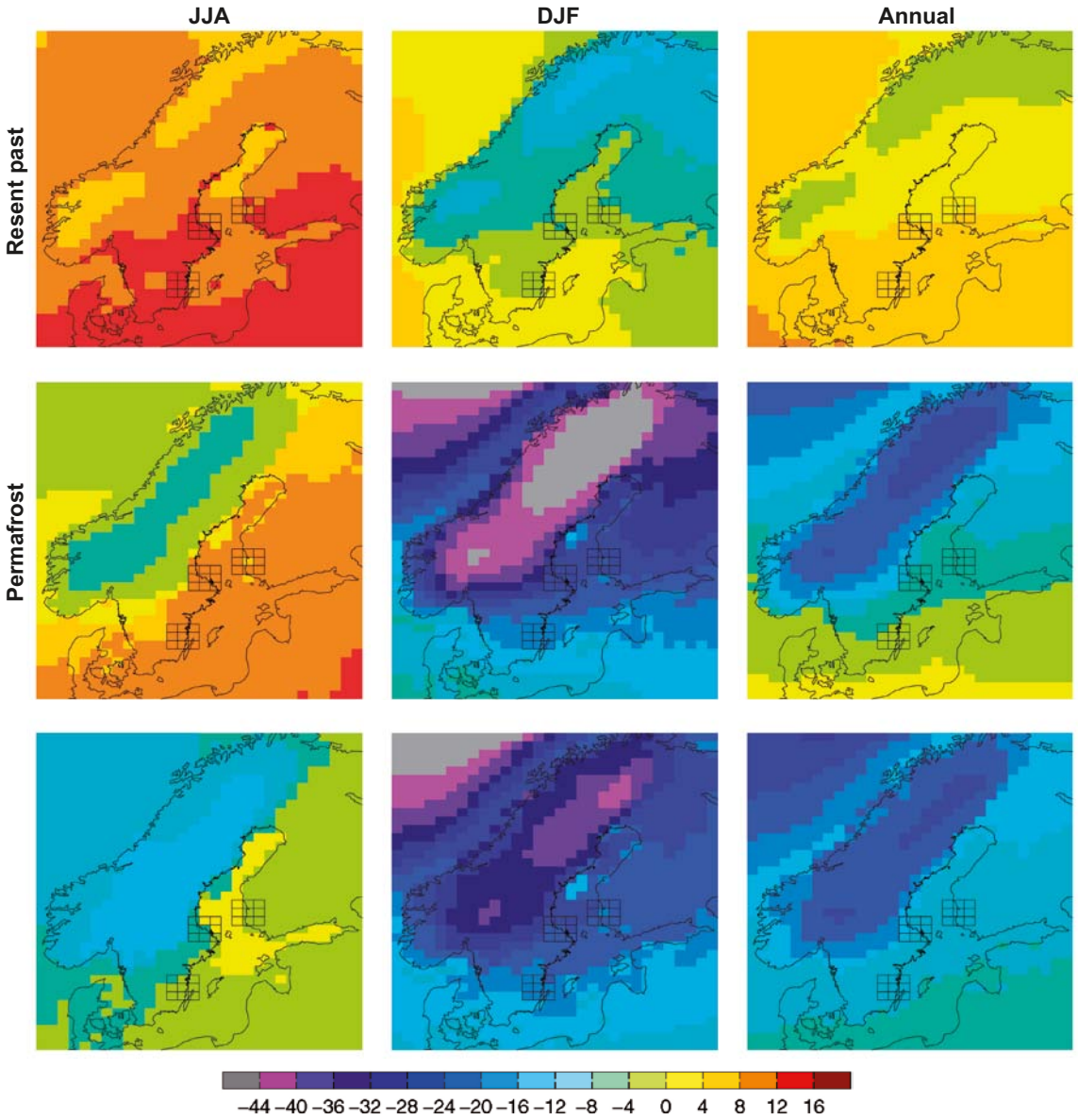

Figure 4-11. *Seasonal and annual mean temperature for the present (1961–2000) (upper row) and MIS 3 (middle row) climate simulations. The lower row shows the difference between the two. Units are °C. From /Kjellström et al. 2009b/.*

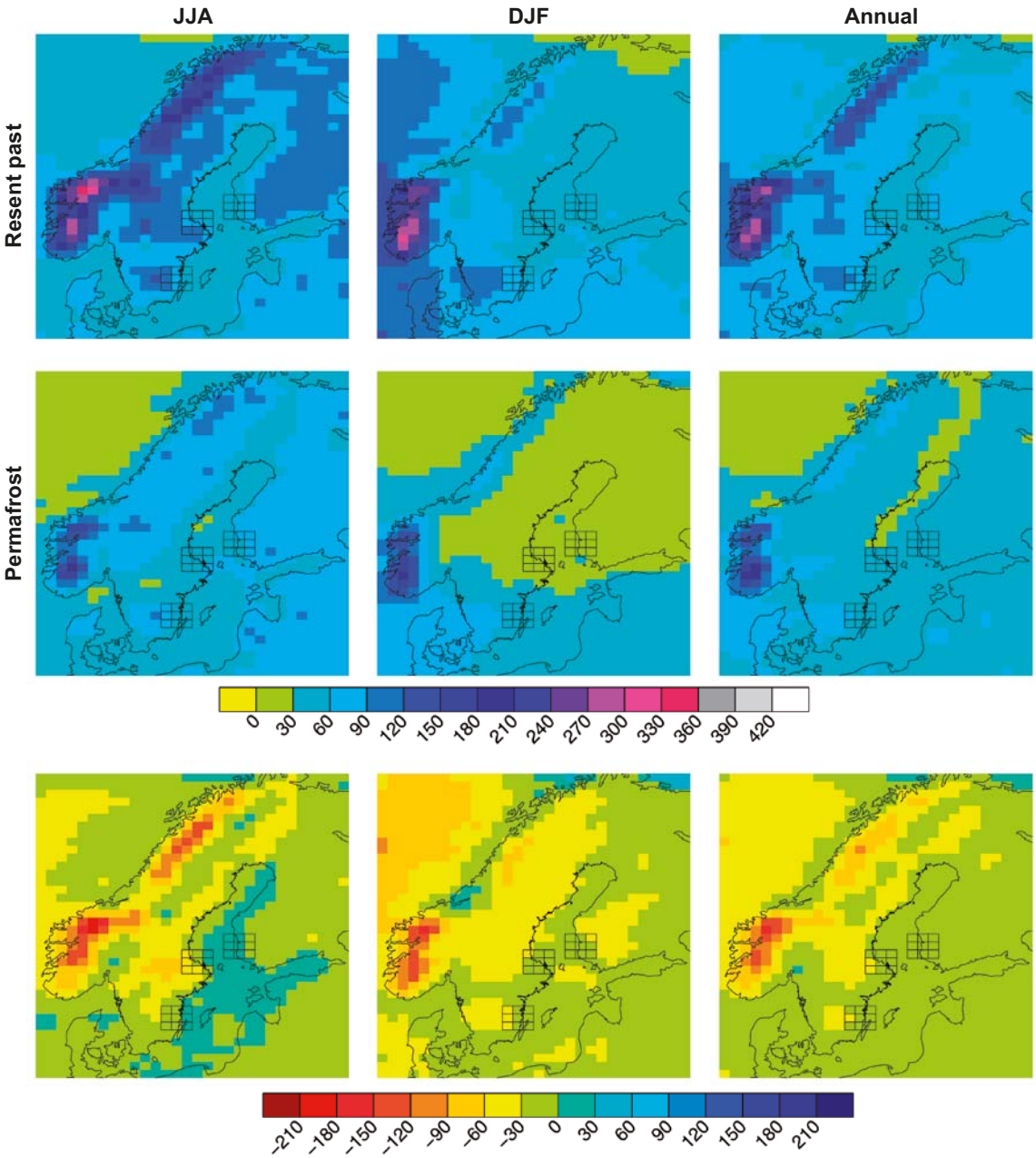

Figure 4-12. *Seasonal and annual mean precipitation in the present (1961–2000) (upper row) and MIS 3 (middle row) climate simulation. The lower row shows the difference between the two. Units are mm/month. From /Kjellström et al. 2009b/.*

The last step in the MIS 3 climate modelling study was to extract climatological data for the Forsmark region from these regional modelling results. Figure 4-13 shows the grid boxes used for extraction of data. Information was extracted from the model grid point located closest to the Forsmark site.

50-year averages values from the regional MIS 3 climate simulation show that the annual mean air temperature in the Forsmark region is –7.6°C during the inferred ice free stadial 44 kyrs ago. This is 12 degrees lower than in the simulated present climate (1961–2000). The largest difference compared with the simulated present climate in the seasonal cycle of temperature is seen in winter (Figure 4-14, upper row, second column).

The mean annual precipitation in the Forsmark region is 441 mm, which is 225 mm (or 30%) less compared with the simulated present climate. In this periglacial climate, the precipitation is lower than in the present climate for most parts of the year, and there is a very strong seasonal cycle in snow cover as the temperatures during summer get well above 0°C allowing complete snow melting

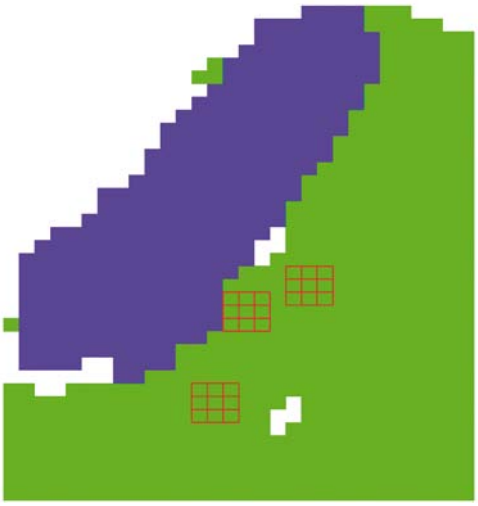

Figure 4-13. *Land (green), ice sheet (blue) and sea extent (white) in the Fennoscandian region used for the MIS 3 climate simulation. The 3·3-grids represent grid boxes covering the Forsmark, Oskarshamn and Olkiluoto sites (centre box) and the eight surrounding boxes. Grid boxes with a land fraction lower than 20% are not filled. Results from Oskarshamn and Olkiluoto are presented in /Kjellström et al. 2009b/. From /Kjellström et al. 2009b/.*

(Figure 4-14, upper and lower row, second column). The length of the completely snow-free season is three months and there is a more or less constant snow cover during at least 3 months.

The annual surface runoff is 139 mm in this exemplified periglacial climate, which is somewhat less (36 mm/year) than in the simulated present climate. In the MIS 3 climate, there is a clear spring peak in runoff connected with the snow melt which is more extensive than in the simulated present climate, since more snow is accumulated on the ground during the winter. During the remaining part of the year, the runoff is fairly small, due to the cold conditions during winter and the relatively small amounts of precipitation during summer. Given the uncertainties and assumptions used in the climate modelling, the model results thus show that the MIS 3 climate in the Forsmark region may be characterized by a significantly colder and drier climate than at present and also that the surface runoff is reduced.

The annual mean ground temperature is about –4°C in the Forsmark region (Figure 4-10). According to /Heginbottom et al. 1995/ these temperatures indicate that climate conditions are favourable for discontinuous permafrost (covering 50–90% of the landscape). The cold and dry climate with partially snow-free conditions implies that the climate is very favourable for permafrost growth.

In summary, the results from /Kjellström et al. 2009b, including erratum dated Feb 2010/ show that i) the climate models produce a cold and dry arctic climate in the Forsmark region for a stadial during MIS 3, ii) the resulting climate is in agreement with ice-free conditions in south-central Fennoscandia and iii) that this climate is suitable for permafrost growth in the Forsmark region.

The major uncertainties in the climate simulation are related to uncertainties in forcing, model formulation and natural variability. These uncertainty aspects are discussed in detail in /Kjellström et al. 2009b/. For further details on the setup, results, and discussion of the MIS 3 climate modelling results, see /Kjellström et al. 2009b (including erratum Feb 2010), Kjellström et al. 2010a, Brandefelt et al. 2011/. For other climate modelling studies focussing on MIS 3, see /Barron and Pollard 2002, van Huissteden and Pollard 2003, van Huisseden et al. 2003/ and references in /Kjellström et al. 2009b/ and /Wohlfarth 2009/.

Following the very warm temperatures reconstructed for *early* MIS 3, described above, which are suggested to have resulted in ice-free conditions over large parts of Fennoscandia during MIS 3, e.g. /Helmens et al. 2009b, Wohlfarth 2009, Wohlfarth and Näslund 2010/, the low air temperatures simulated for Fennoscandia for the middle MIS 3 stadial (44 kyrs BP) are in line with the view that the Weichselian ice sheet needs to re-grow to attain the known large MIS 2 (LGM) ice configuration in a relatively short time.

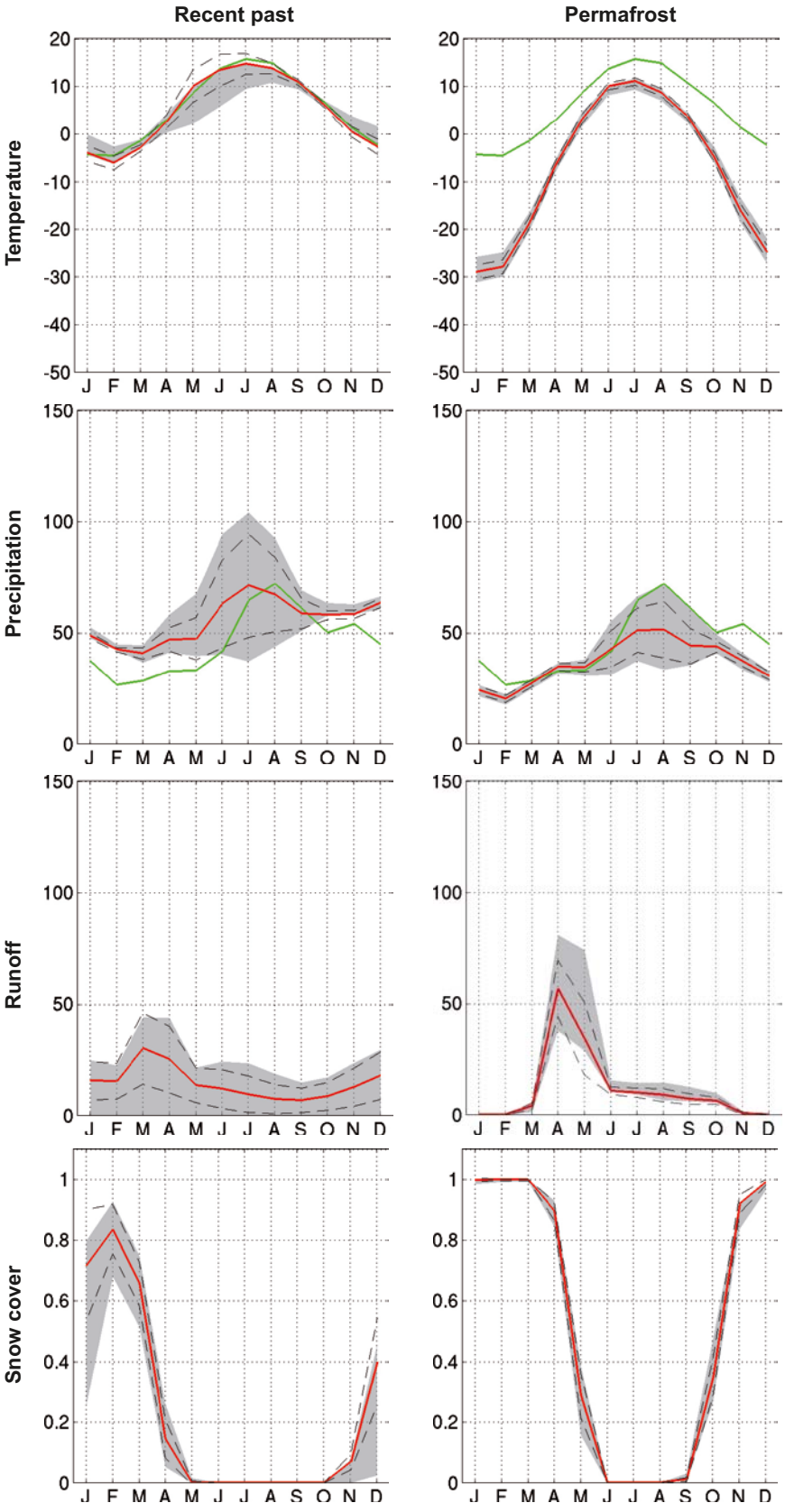

Figure 4-14. *Simulated seasonal cycles of temperature (°C), precipitation (mm/month), runoff (mm/month) and snow fraction (dimensionless ranging from 0 to 1) at the grid box closest to the Forsmark site (red line). The spatial variability in the 3·3-grids (Figure 4-13) is displayed with the dashed lines representing ±1 standard deviation calculated from the 9 grid boxes, and the grey area representing the absolute maximum and minimum, of the 9 grid boxes. The green line for temperature and precipitation is the observed seasonal cycle from the CRU data set in the period 1961–1990, see /Kjellström et al. 2009b/. From /Kjellström et al. 2009b/.*

4.3.3 Late Weichselian including LGM (24–12 kyrs BP)

All of Fennoscandia was covered by the Weichselian ice sheet during the Last Glacial Maximum (LGM), which occurred during the Late Weichselian (Figure 4-3, lower panel). At that time, air temperatures were among the lowest of the last glacial cycle /Jouzel et al. 2007/ and Figure 3-13. In order to study the climate during the LGM in a consistent way with the simulation of a periglacial climate, the same models and modelling approach as for the periglacial climate modelling described in Section 4.3.2 was used for LGM simulations. The LGM climate model simulations were set up to resemble conditions at the time of LGM in a way as similar as possible to what was done in the Palaeoclimate Modelling Intercomparison Project /Joussaume and Taylor 2000, Harrison et al. 2002/. This choice facilitates comparisons with other GCM results. It also allows the use of pre-existing long simulations with the general circulation model CCSM3 performed at the National Centre for Atmospheric Research (NCAR) in the USA /Otto-Bliesner et al. 2006/, reducing the model spin-up time needed for this study. Further, as the LGM is part of the most recent Weichselian glacial period, there is a better possibility of finding climate proxy data than for earlier cold stadials during the Weichselian. The orbital year 21 kyrs BP and a CO_2 level of 185 ppm were used in the LGM simulation. Ice sheet configurations were the same as in the PMIP-2 project /Harrison et al. 2002/, which were based on the ICE-5G data /Peltier 2004/. For a description of the set up of all other forcing conditions, see /Kjellström et al. 2009b/.

Global climate

The global LGM simulation is a continuation of a LGM simulation performed at NCAR /Otto-Bliesner et al. 2006/. The simulation was originally initiated from a simulation of pre-industrial climate, except for the ocean which was initiated by adding three-dimensional anomalies of ocean temperature and salinity derived from a LGM simulation with the Climate System Model version 1.4 (CSM1.4) /Shin et al. 2003/ to the CCSM3 pre-industrial simulation. The simulation was first run for 400 years at NCAR, and was then continued for another 856 years within the present study. The annual global mean surface temperature reaches quasi-equilibrium after 100–150 years, then it continues to cool and reaches a new quasi-equilibrium after a total of 750–800 years. This second quasi-equilibrium extends until the simulation is ended at model year 1,538 /Kjellström et al. 2009b erratum Feb 2010/. The annual global mean surface temperature is 9.0°C in the first quasi-equilibrium and 7.9°C in the second LGM equilibrium, i.e. 4.5°C and 5.6°C colder than the corresponding simulated pre-industrial temperature /Kjellström et al. 2009b, Brandefelt and Otto-Bliesner 2009/. The second equilibrium also results in a 30% reduction in the strength of the Atlantic Meridional Overturning Circulation (AMOC) compared with the first quasi steady-state /Brandefelt and Otto-Bliesner 2009/.

The global climate model LGM simulation thus shows that the global mean air temperature during the LGM could have been more than one degree colder than previously thought, and also that the variability in global mean temperature was larger. The variability is attributed to coupled ocean-atmosphere-sea ice variations in the North Atlantic region. The difference between globally warm and cold years is focussed over oceans in the Northern Hemisphere outside the tropics. The largest difference between cold and warm years is found over Greenland and Northern Europe, with a maximum of 6.8°C. The total amount of precipitation is up to 32% higher over the North Atlantic and North Pacific region in warm years than in cold years at the LGM. Furthermore, the sinking branch of the AMOC is shifted further north in globally warm years as compared with cold years. Further results, and discussions of their significance, are found in /Kjellström et al. 2009b, including erratum dated Feb 2010/.

Significant effort was made to compile LGM climate proxy data for model validation. For the comparison between global LGM model results and marine and terrestrial LGM climate proxy data, see /Kjellström et al. 2009b, Section 3.2.1/.

Climate over Europe and Sweden

A very cold LGM climate, with annual mean temperatures below 0°C in all of Europe north of about 50°N and also in high-altitude regions in southern Europe is clearly seen in the regional climate model results (Figure 4-15, upper row right). In winter the situation is even more striking with the 0°C line encompassing basically all of continental Europe and monthly mean temperatures below –40°C over the northern parts of the ice sheet (Figure 4-15, upper row middle). During summer,

the area with the lowest temperatures is more confined to the ice sheet, the extent of which is readily visible in Figure 4-15 (upper left). In winter when most parts of Europe are snow covered, the gradient is less pronounced as there is no abrupt shift from snow-covered to snow-free conditions. The annual mean temperature in the LGM simulation is 25–30°C lower than the simulated present climate. Over the southern parts of the ice sheet (British Isles, southern Fennoscandia) the annual mean temperature is around 15°C lower than today. At the edge of the ice sheet, there is a strong gradient towards smaller temperature differences. Central Europe is around 8°C colder than today and southern Europe around 6°C colder. In winter the temperature over the Fennoscandian ice sheet is around 40°C colder than present Fennoscandian temperatures.

Annual mean precipitation has its maximum over the North Atlantic and over parts of western Europe (Figure 4-16, upper right). Relatively small amounts of precipitation are simulated in the northern parts of Fennoscandia and over the Mediterranean Sea and North Africa. Compared with the simulated present climate (1961–2000), Fennoscandia, the British Isles and Iceland are drier (Figure 4-16, lower right). More precipitation than at present is seen in southernmost Europe (the Iberian Peninsula, Italy) and northwest Africa. Fennoscandia and western Europe receive less precipitation than in the present climate. The steep coastlines of western Fennoscandia and Scotland which today are facing the ocean and therefore get a lot of precipitation were, during the LGM, parts of the ice sheet that extended further westward. Without the strong orographic effect, precipitation is considerably smaller in this region during the LGM. In summer, as in winter, precipitation is less than in the present climate in most parts of northern Europe. However, more precipitation in the LGM simulation is seen on the edge of the Weichselian ice sheet northwest of Fennoscandia and the British Isles (Figure 4-16, upper and lower left panels). Another area with more precipitation than in the present climate is the area of what is today the Baltic Sea. During the LGM this area partly coincided with the most elevated parts of the ice sheet in which the regional climate model produces large amounts of precipitation during summer.

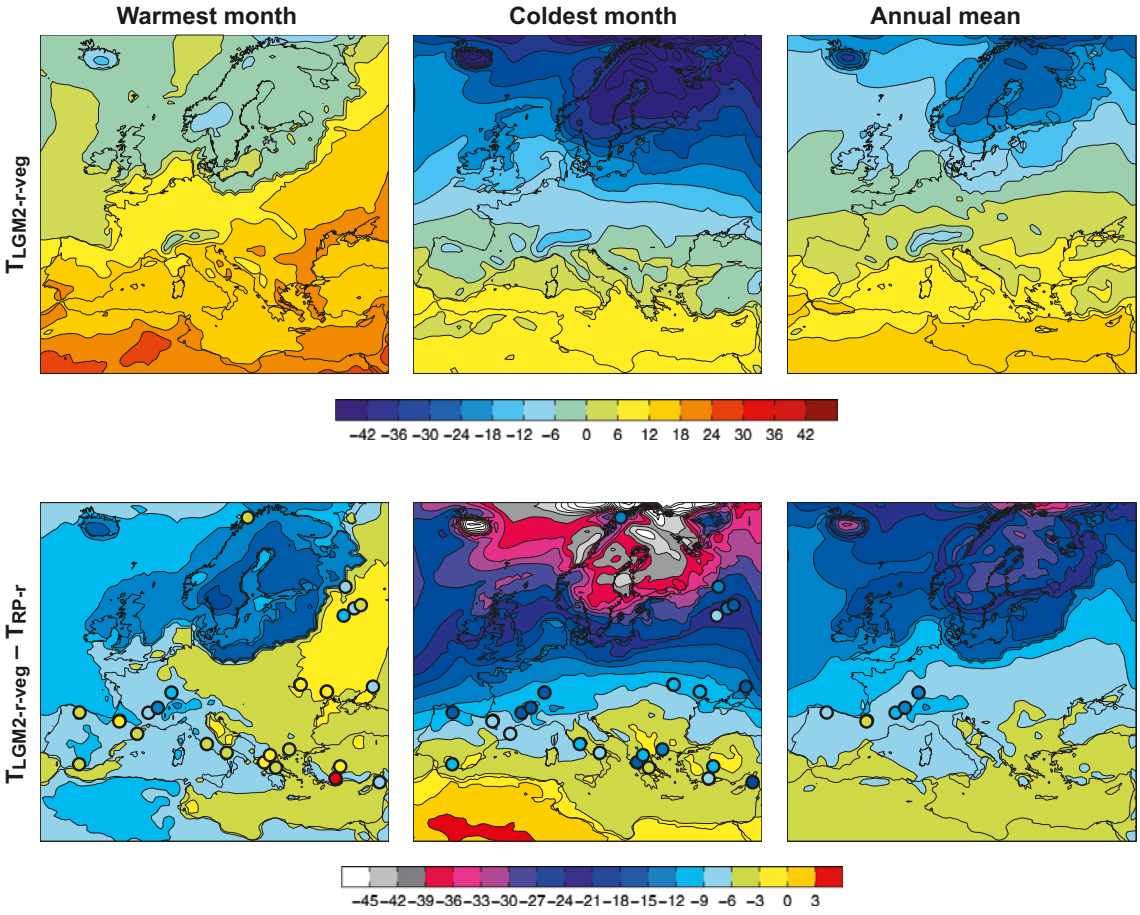

Figure 4-15. *Mean temperatures of the warmest and coldest month and annual mean for the LGM simulation (denoted LGM2-r-veg) (upper row). Also shown are differences between LGM simulation and the simulations of the present climate (years 1961–2000) (denoted RP-r) (lower row). Climate proxy based temperature reconstructions are denoted in the filled circles. Units are °C. From /Kjellström et al. 2009b/.*

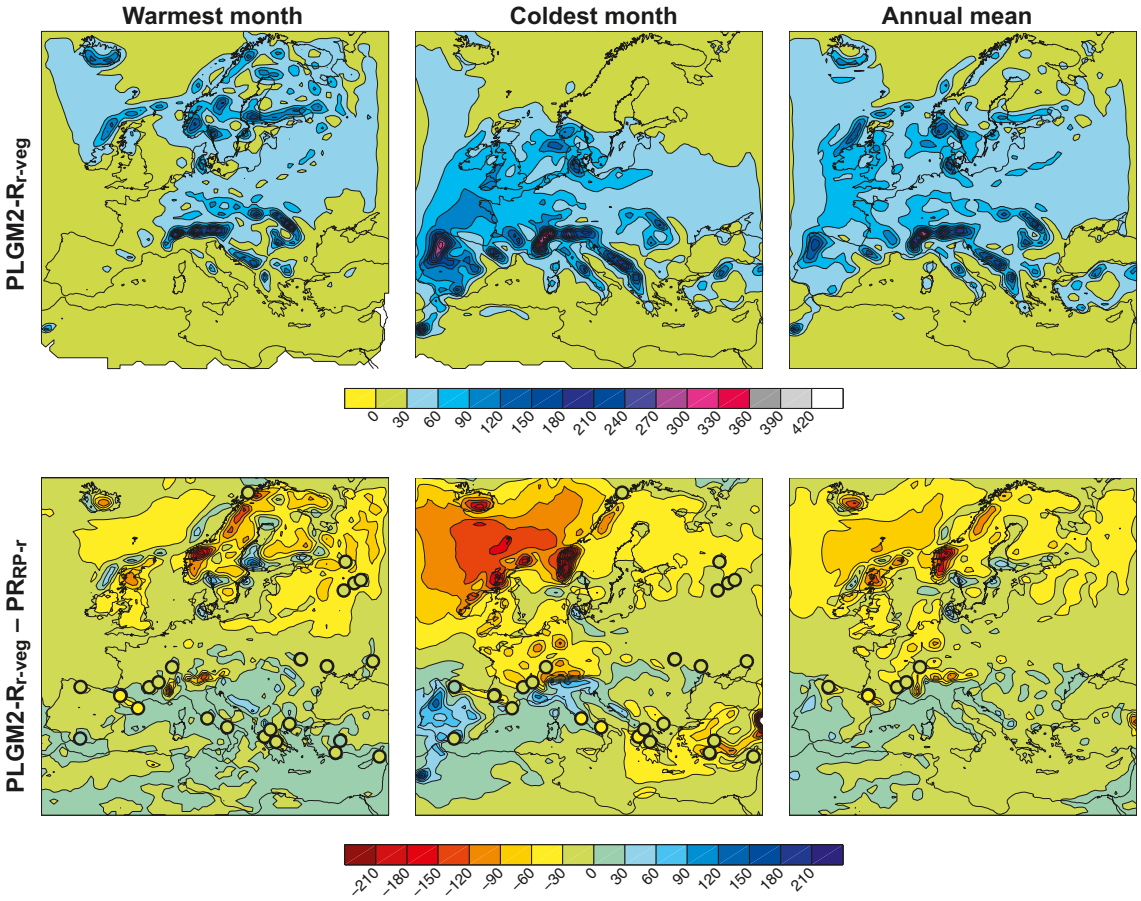

Figure 4-16. *Mean precipitation of the warmest month, coldest month and annual mean in the LGM simulation (denoted PLGM2-r-veg) (upper row). Also shown are differences between the LGM simulation and the simulation of the present (year 1961–2000) (denoted RP-r) (lower row). Units are mm/month. From /Kjellström et al. 2009b/.*

Comparison to other model simulations

The simulated annual global mean temperature in the LGM simulation (i.e. the second quasi-equilibrium described in the beginning of this section) is 6.9°C lower than in the present climate. This is a stronger response than in most of the PMIP1 (full range is 1.85–9.17°C colder than in the present climate) and PMIP2 simulations (3.4–5.46°C colder than the pre-industrial climate) presented by /Kageyama et al. 2006/. The results indicate that much of the strong cooling is associated with low Sea Surface temperatures (SSTs) (up to 6°C colder than some proxy data indicates) and extensive sea-ice cover in the North Atlantic and North Pacific.

These changes in sea-ice extent are a result of the changes in the temperature climate, but they also act to amplify the changes, as increased sea-ice extent leads to a colder climate through the feedback mechanisms involving increased surface albedo and reduced heat fluxes from the ocean to the atmosphere. This connection between low SSTs at high northern latitudes and the global mean temperature for the LGM simulation is in contrast with the PMIP simulations discussed by /Kageyama et al. 2006/. They find that winter and summer temperature changes over the North Atlantic, Europe and western Siberia do not relate closely to global temperature changes. Another uncertainty relates to the response of the Atlantic Meridional Overturning Circulation (AMOC). This has previously been shown to differ among different PMIP2 models for the LGM; one model gives an unchanged AMOC, whereas two models give an increased AMOC strength /Otto-Bliesner et al. 2007/. The simulations presented in /Kjellström et al. 2009b/ indicate a relatively severe weakening of the AMOC; the strength is reduced by more than 50% in the LGM simulation compared with the pre-industrial climate.

Regardless of possible biases in SSTs, the simulated changes in annual mean temperatures over Europe in the global model are similar to those obtained in the high-resolution atmosphere-only CCM3-simulations by /Kim et al. 2008/. In both our global and regional models, the coldest month of the year is warmer than proxy data indicate. This is a result also shown for the PMIP1 and PMIP2 simulations /Ramstein et al. 2007, Kageyama et al. 2006/. However, even though the models are warmer than the proxy data indicates, /Ramstein et al. 2007/ conclude that they are within the confidence interval of the proxy based reconstructions. /Wu et al. 2007/ suggest that LGM winter temperatures were ~10–17°C lower than today outside the ice sheet margin in Eurasia, with a more significant decrease in northern regions. This is in line with the results by /Kjellström et al. 2009b/.

For a description of the results concerning using an improved European vegetation for the regional LGM climate simulations, as well as for a detailed description of the comparison with climate proxy data, see /Kjellström et al. 2009b/.

Just as for the simulation of a periglacial climate (Section 4.3.2), results from the regional climate modelling were extracted for the Forsmark region also for the LGM simulation. However, for this situation, the results naturally show the climate conditions prevailing at the ice sheet surface, high above that overridden Forsmark landscape. They are thus of less importance for the present report and are therefore not included here. The interested reader is referred to /Kjellström et al. 2009b/.

4.3.4 Climate variability during the last glacial cycle

The difference between the present warm interglacial temperatures and the *coldest* temperatures during the last glacial cycle as recorded in the GRIP ice core is on the order of 12°C (Figure 3-13). Using an alternative way of interpreting $\delta^{18}O$ values from the ice core in terms of air temperature, /Lang et al. 1999/ suggested that this cold event reflects a temperature change of 16°C, which is several degrees more than proposed in /Dansgaard et al. 1993/. From the LGM climate modelling study described in Section 4.3.3, annual air temperatures in front of the southern sector of the ice sheet are around 9–12°C colder than at present (Figure 4-15, lower right) while further towards northeast, annual air temperatures are around 12–15°C lower than at present. The largest difference compared to present occurs during the winter season (Figure 4-15, middle).

In a similar way, the air temperature simulated for the Forsmark region for an prescribed ice-free MIS 3 stadial at 44 kyrs BP (see Section 4.3.2) are low, 12.5 degrees lower than at present (Figur 4-11, lower right). Also for this situation, the largest change compared to present occurs during the winter season.

As exemplified by the climate development around the modelled cold stadial at 44 kyrs BP, such cold events were relatively short lived, around a few thousands of years long, and alternated with warmer interstadials. A striking climate variability was found also in the simulated LGM climate (Section 4.3.3). These results, from geological archives and from climate modelling, illustrate a typical feature of the last glacial cycle, namely that the climate was highly variable on both long and short time scales. This is also described in for instance the section on abrupt climate change in the description on palaeoclimate characteristics in /IPCC 2007/. The last glacial cycle climate variability is also seen for example if looking at the full GRIP temperature proxy record (Figure 3-13).

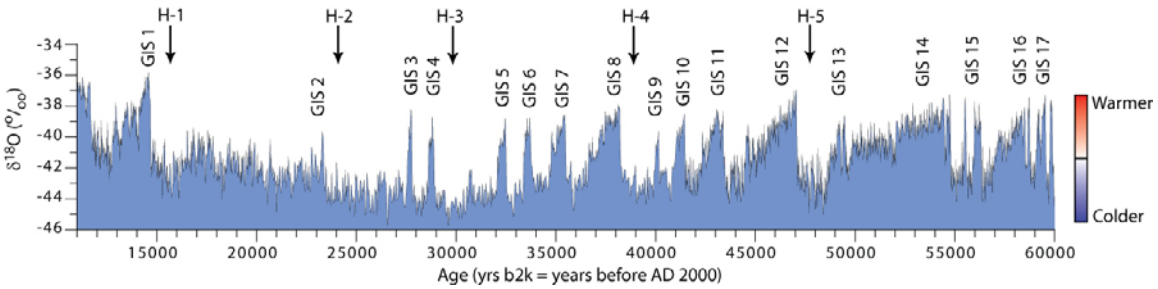

Figure 4-17. *The NorthGRIP oxygen isotope ($\delta^{18}O$) stratigraphy for MIS 2 and 3. Warmer Greenland interstadials were succeeded by colder stadial intervals. Heinrich (H) events 1–5, which have been described from North Atlantic marine sequences, occurred after a series of progressively colder interstadials and in the coldest phase of a stadial. From /Wohlfarth 2009/, modified after /Krogh Andersen et al. 2006/.*

When severe cold conditions occur, these conditions do not persist for long periods of time. Such climate variability is observed also in frequency analysis of climate records /Moberg et al. 2005, Witt and Schumann 2005/.

How low could temperatures have been in the Forsmark region during the last glacial cycle? The simulated temperatures for the MIS 3 stadial suggest that the annual mean air temperature in the Forsmark region was –7.6°C, which is 12.5°C lower than at present. If looking at the air temperature curve produced for the region (Figure 3-13), transferred from Greenland conditions to regional conditions in Sweden in a rather simplistic way (Appendix 1), the curve suggests that annual mean air temperatures during the ice-free stadials of the last glacial cycle may have been around −10 to −11°C in the Forsmark region (Figure 3-13), that is c. 2–3 degrees colder than the temperature modelled for MIS 3 (Greenland Stadial 12) at 44 kyrs BP. However, considering the uncertainties in e.g. the transfer functions between $\delta^{18}O$ and temperature when constructing the temperature proxy curve (Appendix 1), temperatures could even have been lower.

The climate variability seen during the last glacial cycle, e.g. (Figure 3-13 and 4-17) was caused by the combined effect of variations in external orbital forcing (Section 2.2.2) and internal feedback mechanisms within and between the atmosphere, ocean, cryosphere and vegetation systems (Section 2.3). These mechanisms will continue to operate also in the future. Therefore, it is reasonable to assume that a similar climate variability that was characteristic for the last glacial cycle would be characteristic also for future glacial cycles.

For further descriptions of last glacial cycle temperatures, see Appendix 1. Descriptions of geological climate archives from various parts of the last glacial cycle found in Fennoscandia and Europe are presented in e.g. /Hohl 2005, Kjellström et al. 2009b, Wohlfarth 2009, Helmens 2009a/.

4.4 Reconstructed last glacial cycle conditions at Forsmark

In this section, results from Sections 3.1.4, 3.3.4 and 3.4.4 are summarized to present key parameters (development of ice sheet, shore-level, and permafrost) for the reconstruction of last glacial cycle conditions at Forsmark. Additional results from these simulations are presented in Section 4.5, where the results have been used for the construction of the future *reference glacial cycle*. Section 4.5 also presents the resulting evolution of climate domains, as defined in Section 1.2.3.

4.4.1 Ice sheet evolution

In Section 3.1.4, an ice sheet model simulation of the Weichselian ice sheet was made, based on e.g. the temperature reconstruction of the last glacial cycle (Appendix 1). The modelled ice sheet configurations during Weichselian stadials were calibrated against the known maximum ice margin positions for these periods. In the Weichselian ice sheet reconstruction, the overall behaviour of the ice sheet can be characterised as being distinctly dynamic throughout the glacial cycle (Figure 3-14). For instance, during the MIS 3 period (which was *not* used for model calibration), large parts of Fennoscandia were modelled to be ice free (Figure 3-14), in line with several recent independent Quaternary geological studies (Section 4.2.1).

From the ice sheet simulation, data on ice sheet thickness was extracted for the Forsmark region (Figure 4-18). The Forsmark region was subject to two phases of ice sheet coverage, during the cold stadials of MIS 4 and 2. During the last glacial maximum, the ice sheet thickness reached ~2,900 m. Further description and discussion of this ice sheet evolution is given when these data are used to construct the future SR-Site *reference glacial cycle* (Section 4.5).

In this ice sheet reconstruction, the two very short phases of ice sheet coverage at Forsmark at around 70 kyrs BP (with 40 and 750 m of ice thickness occurring over 500 and 1900 yrs) are considered very uncertain. They are the result of two short and severe cold phases existing in the palaeotemperature curve used to run the ice sheet model. However, the ice sheet model response to these very rapid and strong temperature events is considered uncertain. Therefore these short phases of ice coverage are not included here, nor in the construction of the SR-Site *reference glacial cycle* (Section 4.5). However, a case with longer periods of ice sheet coverage than in the *reference glacial cycle* is described in the *extended ice sheet duration case* (Section 5.3). Further uncertainties related to the ice sheet model simulation are discussed in Section 3.1.4, 3.1.7 and Appendix 1.

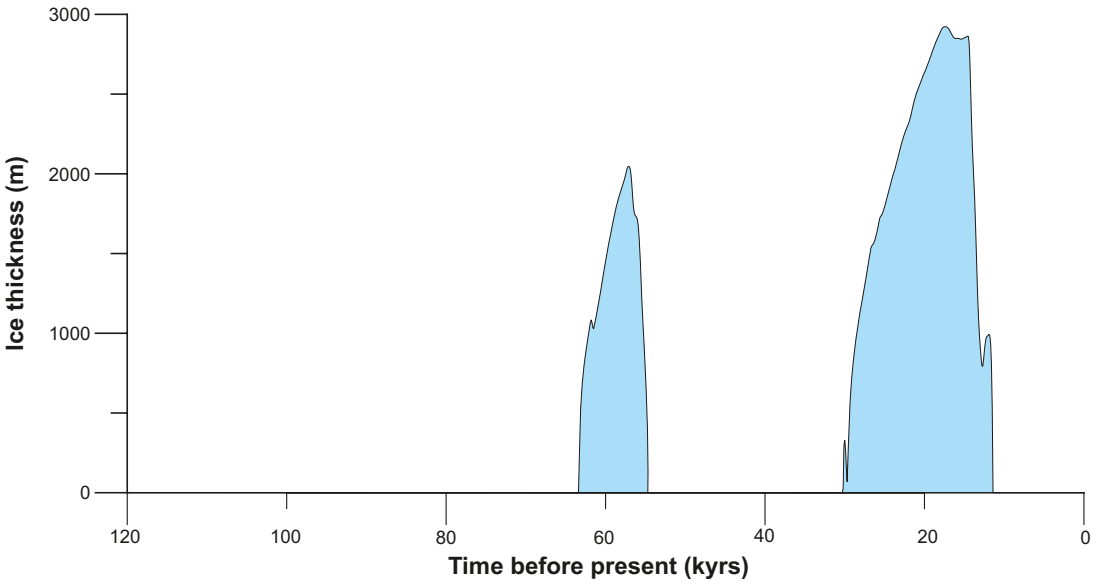

Figure 4-18. *Reconstructed ice sheet thickness over Forsmark for the last glacial cycle using ice sheet modelling (Section 3.1.4).*

4.4.2 Shore-level evolution

In Section 3.3.4, a GIA model was used to reconstruct changes in shore-level during the last glacial cycle, given input from various Earth models as well as ice load history from Section 3.1.4. Shore-level data were extracted for the Forsmark region (Figure 4-19) showing that the area was submerged after both reconstructed phases of ice sheet coverage (Figure 4-18). At times of maximum isostatic depression, the Forsmark region was covered by the Weichselian ice sheet. The uncertainties in reconstructed levels are rather large (Section 3.3.4). This has resulted in that, at the time of deglaciation (10,800 BP), the inferred water depth at Forsmark in Figure 4-19 probably is too large /Söderbäck 2008/. The results from the GIA modelling have for the following part of the Holocene been combined with results from other shore-level estimates /Påsse 2001/ in order to decrease the uncertainty (Section 4.5.2).

Further description and discussion of this shore-level displacement, and the associated development of the Baltic Sea, is given when these data are used to construct the future SR-Site *reference glacial cycle* (Section 4.5). Uncertainties related to the GIA model simulation are discussed in Section 3.3.4.

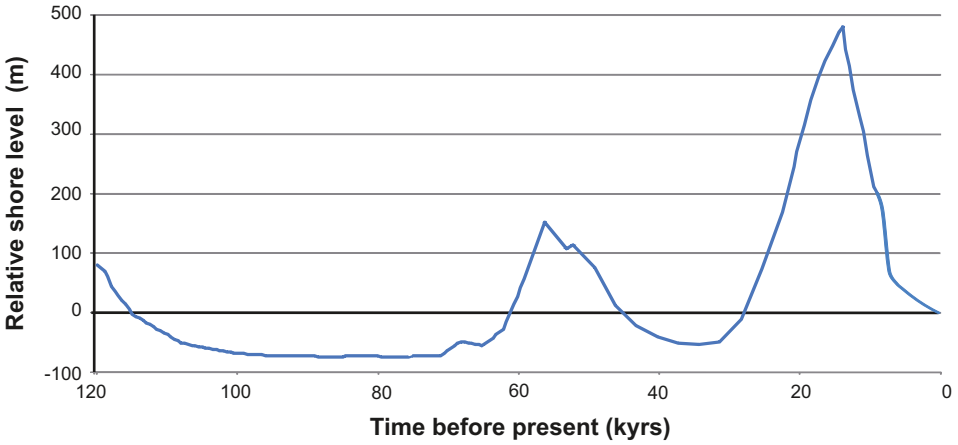

Figure 4-19. *Reconstructed shore-level displacement at Forsmark for the last glacial cycle using GIA modelling (Section 3.3.4) and Holocene data /Påsse 2001/. Positive values mean that the area is submerged under the contemporary level of the Baltic Sea. Note that during periods of maximum isostatic depression, the area is situated under the ice sheet.*

4.4.3 Permafrost evolution

In Section 3.4.4, reconstructions of permafrost and freezing depths for the last glacial cycle at Forsmark were made using two permafrost models (Figure 4-20 and 4-21). The simulations were made by employing the air temperature curve reconstruction for the last glacial cycle (Appendix 1 and Section, 3.1.4) together with site-specific data on e.g. bedrock, soil, groundwater, lakes and shore-level development, see Section 3.4.4 and /Hartikainen et al. 2010/.

The maximum Weichselian permafrost depth at the Forsmark repository location is ~250 m and it occurs around 70 kyrs BP, prior to the MIS 4 ice sheet advance over the region (Figure 4-20 and 3-69). The maximum permafrost in the surrounding region, here represented by a 15 km long profile, is ~300 m and it occurs at the same time (Figure 4-21 lower part). At this time the area is subject to continuous permafrost coverage (more than 90% spatial coverage), see Figure 4-21, upper part. During periods of ice sheet coverage, permafrost declines, especially during periods when the ice sheet is warm-based (Figure 4-22). At the time of the deglaciations, there is no permafrost or frozen ground present.

The values estimated for last glacial cycle air temperatures at ground level (Section 3.4.4 and Appendix 1) are typically 2–4°C lower than mean annual temperature in the uppermost part of the ground for the same climate, see Section 3.4.4 and Figure 4-10. As discussed above, really low air temperatures during the last glacial cycle only prevailed during stadials which had a restricted duration. During cold ice-free periods, permafrost developed at the Forsmark site, but climate variability with alternating cold and warm periods, e.g. Figures 3-54 and 3-65, as well as the presence of the ice sheet (e.g. Figure 4-18), prevented permafrost from developing to great depths (Figure 4-20 and 4-21) and Section 3.4.4. Further description and discussion of this permafrost evolution is given when these data are used to construct the future SR-Site *reference glacial cycle* (Section 4.5).

It should be noted that in the reconstruction of last glacial cycle permafrost development, heat from the repository has been included in order to make the results useful for the subsequent construction of a future *reference glacial cycle* with a repository present. The difference between including and excluding heat from the repository has also been evaluated, see Figures 3-51, 3-87, as well as /SKB 2006a, Figure 3-59/. All uncertainties related to the permafrost simulations are examined in detail in Section 3.4.4 and in /Hartikainen et al. 2010/.

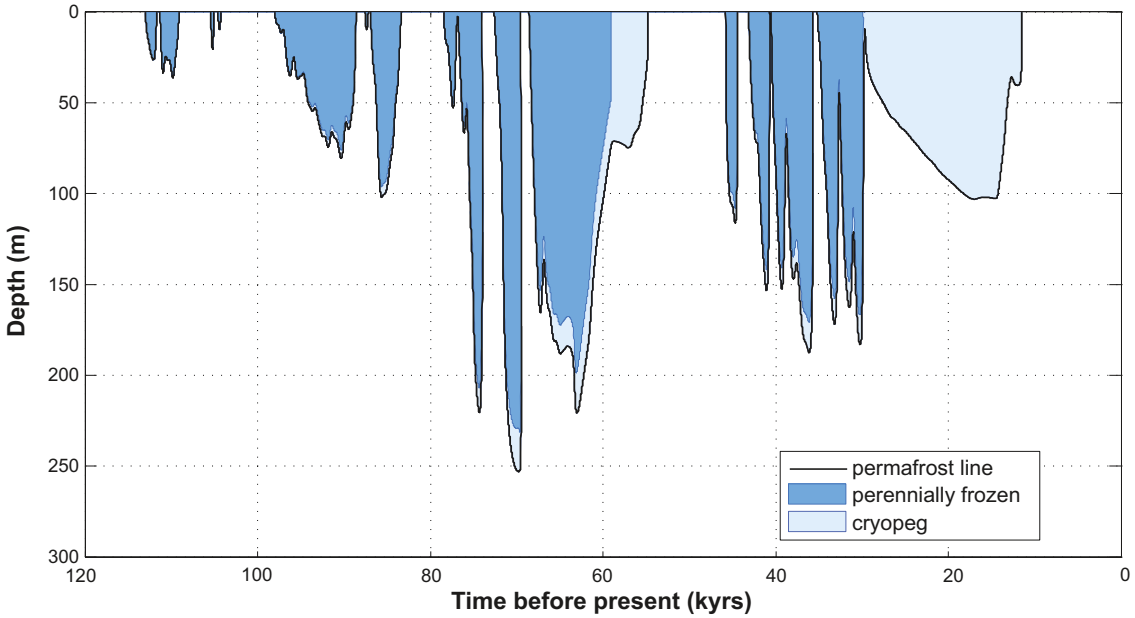

Figure 4-20. *Evolution of permafrost and perennially frozen ground depth for the reconstruction of last glacial cycle conditions for the repository location in Forsmark. The results were obtained using a 1D permafrost model (Section 3.4.4). Due to the high sub-glacial pressure, a thick unfrozen cryopeg exists within the permafrost (defined by the 0°C isotherm) after 60 kyrs and after 30 kyrs before present (including the LGM). For the corresponding 2D modelling results see Figure 3-69.*

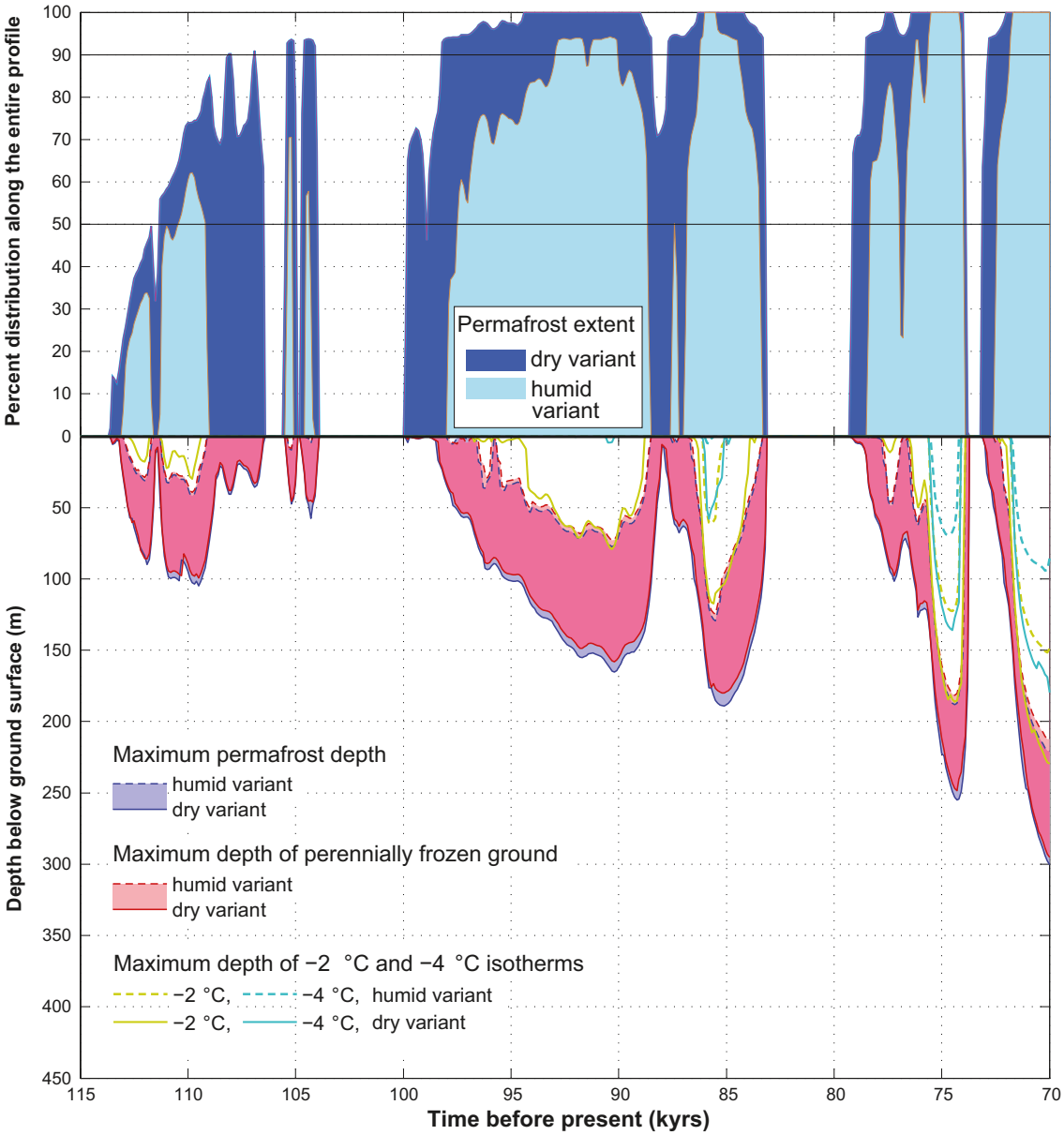

Figure 4-21. *Reconstructed evolution of maximum permafrost depth, maximum freezing depth and percent permafrost distribution over a 15 km long transect over the Forsmark area for the first 50 kyrs of the last glacial cycle, see Section 3.4.4 . Upper panel: the transition from sporadic to discontinuous permafrost occurs at 50% spatial coverage and from discontinuous to continuous permafrost at 90% coverage. Lower panel: the shaded area in blue and red represents the range obtained when considering one dry and one humid climate variant. The lilac colour indicates that the results for permafrost and perennially frozen ground overlap.*

4.4.4 Combined reconstructed last glacial cycle parameters

Figure 4-22 shows the combined evolution of ice sheet thickness, shore-level changes, permafrost- and frozen ground depth at Forsmark as reconstructed in Sections 3.1.4, 3.3.4, 3.4.4 and above. This reconstruction was used to construct the SR-Site *reference glacial cycle* for the coming 120 kyrs (Section 4.5).

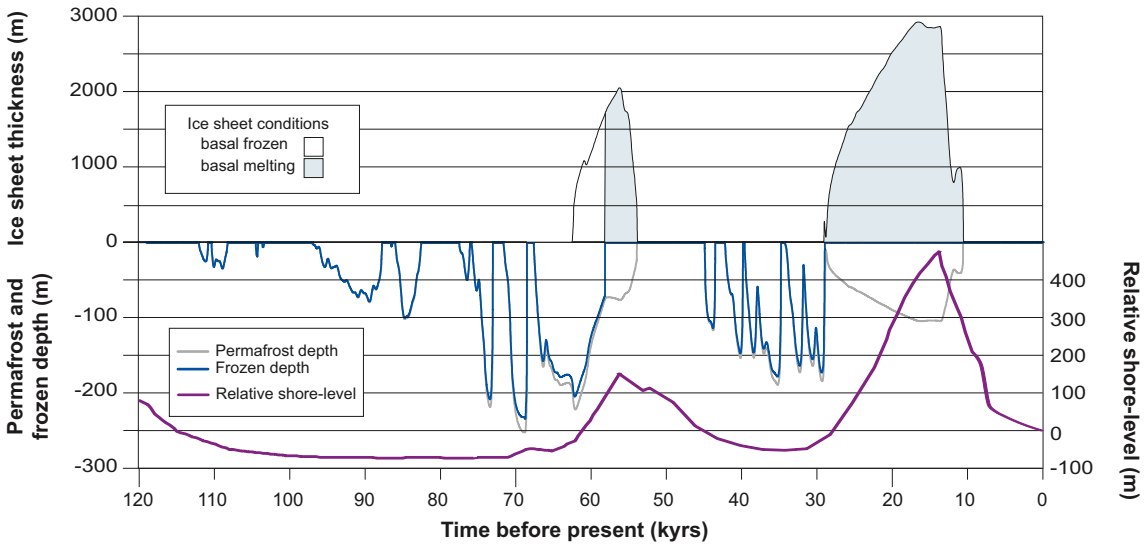

Figure 4-22. *Reconstructed Weichselian evolution of ice sheet, shore-level, permafrost and frozen ground at Forsmark. This evolution was used to construct the SR-Site reference glacial cycle.*

4.5 Reference glacial cycle

The SR-Site *reference glacial cycle* describes a conceivable future evolution of climate and climate-related conditions and sequences that could be expected in a 100 kyr time perspective. It is constructed by repeating the reconstructed conditions for the last glacial cycle described in Section 4.4. The *reference glacial cycle* constitutes a climate evolution fully dominated by natural climate change, i.e. without anthropogenic influence on climate. Therefore, the length of the present temperate interglacial period is assumed to be within the range of interglacial durations as observed within the past 800 kyr /Tzedakis et al. 2009/, see further Section 4.5.4. The case of having a climate evolution e.g. affected by increased amounts of greenhouse gases in the atmosphere due to human activity, resulting in a longer duration of the present interglacial period, is dealt with in Section 5.1 and 5.2.

In the SR-Site safety assessment the *reference glacial cycle* is used for constructing the base case of the Main scenario, see Figure 1-3.

The climate evolution of the *reference glacial cycle* starts in the present warm interglacial climate, characterized as a temperate, humid cold climate with year-round precipitation. For a description of the present climate at Forsmark, see Section 2.4.2.

4.5.1 Ice sheet evolution

In the *reference glacial cycle*, the lowering of air temperature during the onset of the glacial results in ice sheet inception. Following the ice sheet evolution in the model reconstruction of the Weichselian glacial, see Section 3.1 and 4.4, the evolution of ice covered area and ice volume for the *reference glacial cycle* are shown in Figure 4-23. The corresponding ice configurations for selected time slices, depicting future stadial and interstadial configurations in the *reference glacial cycle*, are shown in Figure 4-24. During the glacial cycle, the ice sheet grows progressively larger in a number of distinct growth phases, with intervening phases of more restricted ice coverage. The Glacial Maximum (corresponding to the LGM of the Weichselian glaciation), is reached at around 100 kyrs into the future. As described in the previous section, the overall behaviour of the ice sheet can be characterised as being distinctly dynamic throughout the glacial cycle.

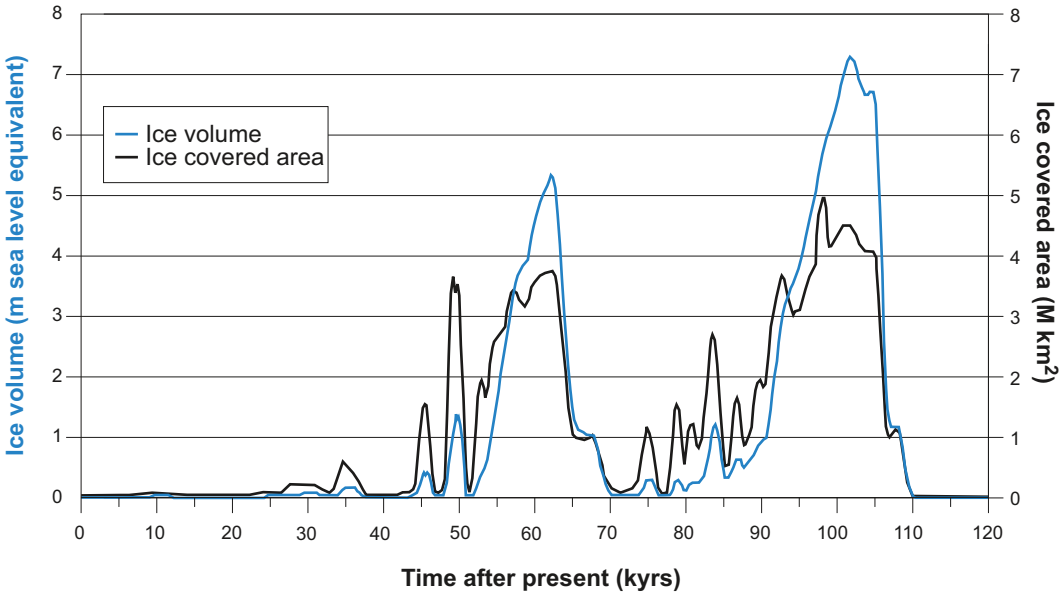

Figure 4-23. *Ice sheet volume and ice covered area for the reference glacial cycle.*

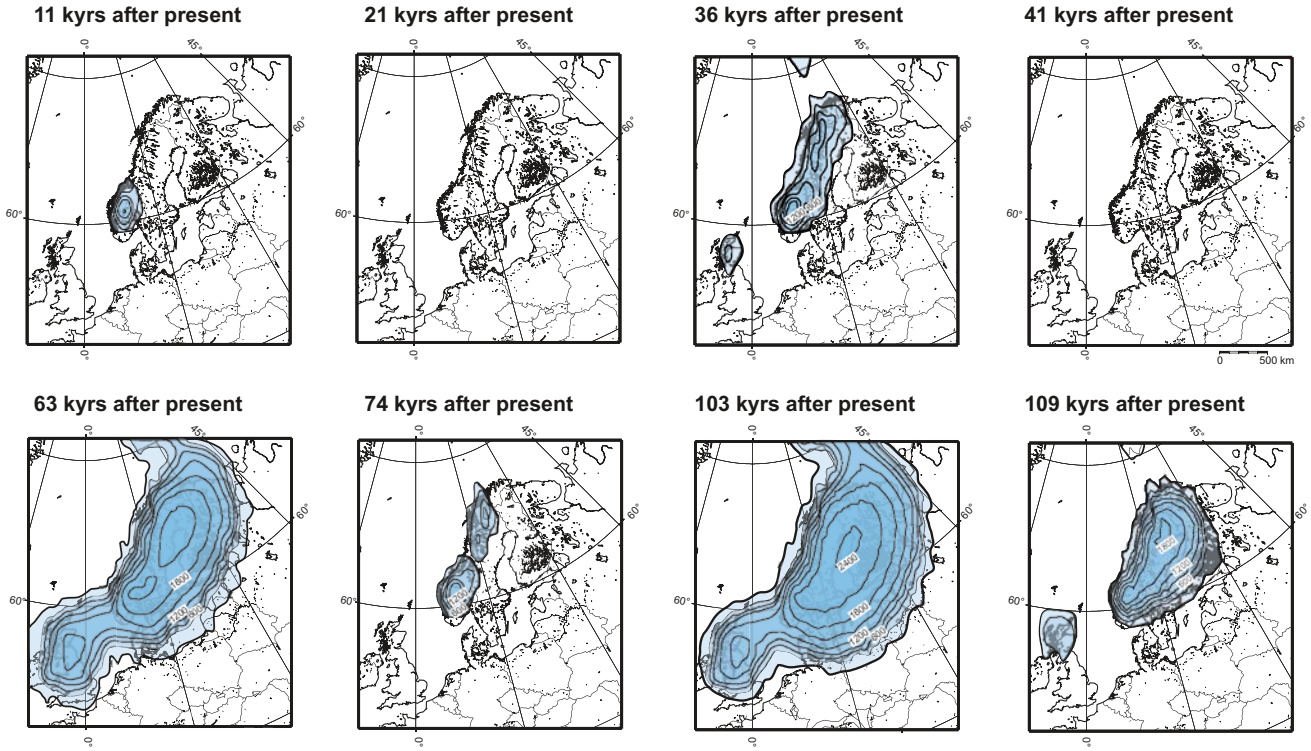

Figure 4-24. *Ice sheet configurations at stadials and interstadials for the reference glacial cycle. Contour lines show ice surface elevation with a 300 m interval. All maps show present day shoreline position.*

The dynamic behaviour of the ice sheet during the glacial cycle is seen also at the Forsmark site. The site is covered by ice during the cold stadials at around 60 and 100 kyrs after present (Figure 4-25). Between these stadials, the site experiences ice-free warmer interstadial conditions (corresponding to Marine Isotope Stage 3 in the reconstructed Weichselian glacial cycle). Advances of the Fennoscandian ice sheet during stadials around 14 and 38 kyrs after present do not reach the Forsmark site (Figure 4-24), although the ice sheet margin is close to Forsmark during latter stage. Note that even though an ice sheet is present in Fennoscandia during most of the glacial cycle (Figure 4-23), the Forsmark site, located in south-central Sweden, is not covered by the ice sheet for the majority of the time (Figure 4-25).

In the *reference glacial cycle*, the Forsmark region is covered by the ice sheet for a total time of ~30 kyrs. For most of the ice-covered time, the numerical ice sheet modelling suggests that the site is covered by warm-based ice with free water present at the ice-bed interface. Forsmark is covered by wet-based ice for ~23 kyrs, corresponding to about 75% of the ice-covered time. This means that during most of the time when the ice sheet covers the site in the *reference glacial cycle*, meltwater is present at the ice sheet bed, typically produced at rates of a few mm/year, up to ~10 mm/year, and hence groundwater recharge by glacial meltwater takes place.

The short periods of cold-based conditions, with no basal water production, always follow immediately after each time the sites become ice covered. During these periods, as well as during deglaciation periods when the site is close to becoming ice free, water from *surface* melting may still reach the bed. However, in cases when the ice sheet margin is located over permafrost ground, this melt water would not contribute significantly to groundwater recharge. The prerequisites for groundwater flow under glacial- and permafrost conditions are further discussed below. A study of groundwater flow under glacial- and permafrost conditions is found in /Vidstrand et al. 2010/.

During the glacial maximum of the *reference glacial cycle*, at around 100 kyrs after present, the maximum ice sheet thickness over Forsmark is ~2,900 m (Figure 4-25). It is worth noting that the modelled ice sheet reaches significant thickness over the site not only during the glacial maximum, but also during the cold stadial at around 60 kyrs after present. At that time, the modelled maximum ice thickness is ~2,000 m.

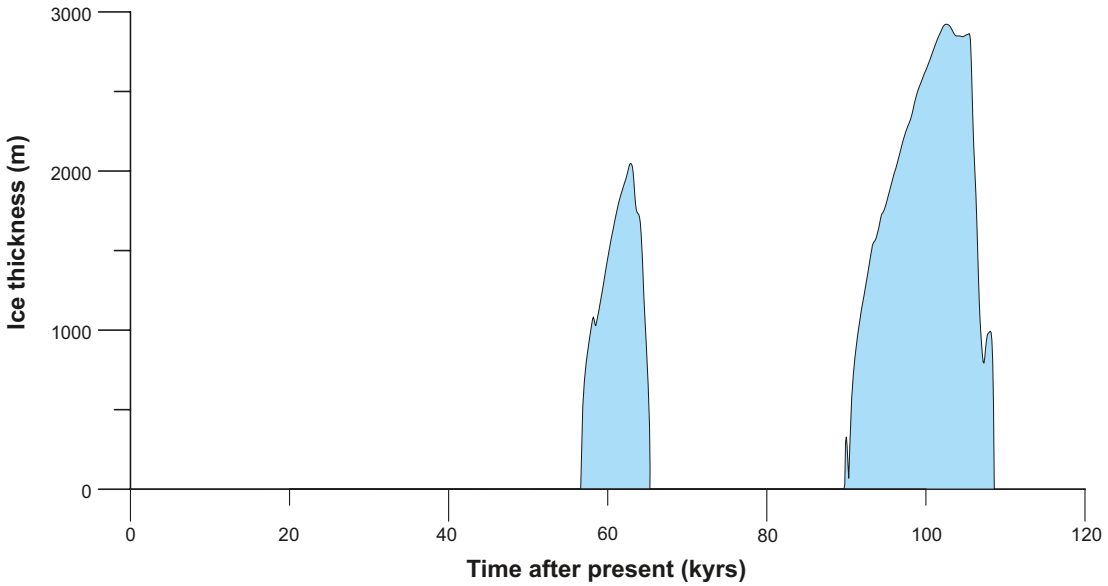

Figure 4-25. *Development of ice sheet thickness at the Forsmark site in the SR-Site reference glacial cycle. Note that even though an ice sheet is present in Fennoscandia during most of the glacial cycle (Figure 4-23) the Forsmark site, located in south-central Sweden, is not covered by the ice sheet for the majority of the time.*

The groundwater pressure at repository depth is, for non-glacial conditions, determined by the depth of the repository, and for glacial conditions by the repository depth as well as an additional pressure induced by the ice load. The ice sheet thickness sets a limit to the maximum hydrostatic pressure that may occur at the ice sheet/bed interface. The additional hydrostatic pressure related to the maximum thickness in the *reference glacial cycle* (Figure 4-25) is 26 MPa for Forsmark. This value is listed in Table 5-6 together with other estimates of *maximum* possible ice loads and associated *maximum* hydrostatic pressures.

Ice-marginal stillstands

Although not the case during the deglaciation of the Weichselian ice sheet, or in the SR-Site *reference glacial cycle*, future periods of ice sheet-frontal stillstands cannot be excluded for the Forsmark site during ice advance, maximum or retreat phases, given suitable climate conditions. An extreme case in terms of hydraulic gradients and associated increased groundwater flow would occur if the ice front came to a temporary halt with the frontal part of the ice sheet situated above the repository. According to /Vidstrand et al. 2010/ there is an approximately one km wide zone of high groundwater fluxes in front of the ice sheet margin and a similarly wide zone of increased flux behind the ice sheet margin, i.e. two km wide influence area with significantly increased groundwater flux. This situation is valid when there is no permafrost at the Forsmark site. If continuous permafrost is present, which is the case in the SR-Site *reference glacial cycle*, and also very likely during a future glaciation of the Forsmark site, a zone of increased groundwater flow is significantly less pronounced /Vidstrand et al. 2010/. Using a two km wide near-frontal zone with significantly increased groundwater flux is therefore a pessimistic choice for an analysis of the probability for a future situation with an ice margin stillstand over the repository.

Assuming that future periods of ice margin stillstands would have the same characteristics as the stillstands associated with the last deglaciation described above, one could make an estimate of the probability of having such a situation occurring at the Forsmark site. By generalizing the development of the last deglaciation, one could postulate ten temporary halts of shorter duration and one major halt of longer duration, corresponding to the Younger Dryas event, for a deglaciation of a full-sized ice sheet equivalent to the one of the LGM. For halts of short duration, completely stable ice margin conditions are set to persist for 200 years, while during the major stillstand a completely stable position of the ice margin is pessimistically set to a full 1,000 years. This is somewhat longer than the time period that the ice margin was located somewhere within the 20–25 km wide Younger Dryas zone in Sweden, which lasted around 900 years. In reality, it is likely that, during such long phases, the ice margin would move slowly and/or oscillate within an ice-marginal zone. Nevertheless, in order to cover uncertainties in future ice sheet behaviour, a completely stable margin position for 1,000 years is assumed for the major stillstand. In this way, the major stillstand constitutes a pessimistically chosen case in terms of the duration of a high hydraulic gradient and associated high groundwater fluxes.

The deglaciation of the Weichselian ice sheet, from its LGM position in Poland and Germany to the Scandinavian mountain range, occurred over a distance of ~2,500 km /Fredén 2002/. For each of the postulated stillstands, there is a ~2 km wide frontal zone with significantly increased groundwater fluxes /Vidstrand et al. 2010/. For each advance- or deglaciation phase, the probability of having a 200 year long stillstand at Forsmark is therefore 0.008 (10·2 km/2,500 km), while the probability of having the postulated 1,000 year long stillstand at Forsmark is 0.0008 (2 km/2,500 km). For a complete glacial cycle with two phases of ice advance and two phases of deglaciation over Forsmark, i.e. a glacial cycle similar to the SR-Site *reference glacial cycle*, the probabilities for the 200 year and 1,000 year ice margin stillstands at Forsmark are 0.03 (0.008·4) and 0.003 (0.0008·4), respectively. For the full assessment period of 1 million years, comprising eight repeated identical glacial cycles, the probabilities grow correspondingly larger. There is thus a relatively low probability that the ice margin zone with high groundwater flux would come to a temporary halt above the repository, especially when considering the rarer stillstands of long duration. In this context, it should again be pointed out that the assumption of a completely stable ice margin over the repository for 1,000 years is a highly pessimistic case compared to what is known from the last deglaciation.

4.5.2 Evolution of the Baltic Sea and the Forsmark shore-level

At the start of a GIA model run, the Earth is assumed to be in isostatic equilibrium. In reality, the Earth is unlikely to reach such a state if glaciations occur with similar periodicity as in the past. To correct for this, the GIA-modelling, Section 3.3.4, has been initiated by a glacial loading history yielding shore-levels comparable to those reported by /Funder et al. 2002/ at the peak of marine inundation in the Early Eemian about 130 kyrs before present. This gives shore-levels similar to the present at the early phase of the *reference glacial cycle*. However, during the first 1,000 years after present, and for the analysis of biosphere and hydrological evolution during the initial period of temperate climate domain, the shore-level evolution is extrapolated from shore-level data /Påsse 2001/. From about 8 kyrs after present to the end of the *reference glacial cycle*, the shore-level evolution is based on the GIA modelling described in Section 3.3.4.

The evolution of the Baltic Sea

During the initial phase of the *reference glacial cycle*, when climate is getting colder and ice sheets expand globally, global sea-levels fall. At the same time, the rate of isostatic rebound from the last glacial cycle decreases. However, even if the rate is low, the amount of remaining uplift for parts of Fennoscandia is significant. For the central parts of the Fennoscandian ice sheet it has been estimated to ~100 m, and in the distal parts to ~25 m. As long as the Baltic Sea is connected to the Atlantic, the relative shore-level along the Baltic Sea coast is determined by isostatic rebound and global sea-level change. If and when the relative sea-level at Darss sill, in the southern Baltic Sea south of Denmark, falls below the sill depth (at present 18 m below mean sea-level), the Baltic Sea is transformed into a lake. The surface level of this lake is determined by the altitude of the contemporary Darss sill.

In the *reference glacial cycle*, results from the GIA simulations (Section 3.3.4) indicate that the Baltic Sea is isolated from the Atlantic around 9 kyrs after present. However, due to the uncertainties in the GIA modelling, discussed in Section 3.3.4, it is likely that the suggested timing for this isolation is too early. Given these uncertainties, the salinity of the Baltic Sea could thus remain high for a considerably longer period than 9 kyrs after present. If extrapolation of present observed relative sea-level trends /Påsse 2001/ is made, it seems unlikely that isolation of the Baltic Sea from the Atlantic would occur at all, even if excluding the possibility of a considerable future global sea-level rise due to global warming.

In addition, the northern part of the Baltic Sea, i.e. the Gulf of Bothnia at which the Forsmark site is located, will be isolated from the rest of the Baltic Sea due to the remaining isostatic uplift. This occurs around 25 kyrs after present /SKB 2010d/, i.e. well before the onset of the first phase of glacial conditions in the Forsmark region in the *reference glacial cycle* (after 60 kyrs after present), see Figure 4-25. The salinity in the Gulf of Bothnia is reduced as a consequence of this isolation, since the Gulf at this stage constitutes a large lake fed by freshwater from surrounding terrestrial regions. This freshwater stage is formed regardless of the isostatic and eustatic conditions in the southern Baltic Sea (Darss sill). Note that at his stage, the Forsmark site is situated far from the shoreline of the Gulf of Bothnia due to land uplift /SKB 2010d/.

In the *reference glacial cycle*, the isostatic load from the first major ice sheet advance, at ~60 kyrs after present (Figure 4-25), most likely depresses the Gulf of Bothnia lake threshold so that the Gulf of Bothnia regains contact with the southern part of the Baltic Sea. However, it is uncertain if the Baltic Sea has contact with the Atlantic or not at this stage. The uncertainties in the GIA simulations for the southern Baltic Sea region are too large to give useful information for that region at this time. However, according to modelling studies by /Lambeck et al. 2010/, the Baltic may have constituted a freshwater lake during MIS 3 of the Weichselian, which corresponds to the period following the deglaciation of the first glacial period of the *reference glacial cycle*.

Following the deglaciation of the second and larger ice sheet coverage, at around 110 kyrs after present (Figure 4-25) the Baltic regains contact with the Atlantic. Given that the *reference glacial cycle* is based on the repetition of conditions reconstructed for the last glacial cycle (including the Holocene), the development of the Baltic Sea for this future post-glacial period is envisaged to follow the Holocene development, which includes both saline and freshwater stages. After this deglaciation, large parts of southern Sweden are submerged by a predominantly saline Baltic Sea. At the end of the *reference glacial cycle*, and as isostatic rebound proceeds, the Baltic Sea is transformed to an inland brackish sea, similar to today's situation.

Shore-level displacement in Forsmark

For the first 30–40 kyrs of the *reference glacial cycle*, the Forsmark site continues to rise due to post-glacial isostatic uplift. When the isostatic uplift is completed, the site is, according to the GIA simulations (Section 3.3.4), elevated ~70 m above the contemporary sea-level (Figure 4-26).

During the first glaciated period of the *reference glacial cycle*, at 60–70 kyrs after present, the Forsmark site is isostatically depressed by the weight of the ice sheet (Figure 4-26). The glacial phase is followed by interstadial ice-free conditions around 65–90 kyrs after present. In connection with the deglaciation that follows the first glaciated period, the isostatic depression results in the Forsmark site being situated below the Baltic Sea water level, at around 70 kyrs after present (Figure 4-26). In line with the description of the development of the Baltic Sea above, it is uncertain if the site during this stage is submerged by a freshwater lake only, or if the water is more saline as a result of a contact with the Atlantic.

Subsequently during this future interstadial, isostatic recovery results in the Forsmark site rising above the Baltic water level, after 75 kyrs after present. At this time in the *reference glacial cycle*, the Forsmark site is situated above sea-level, and is free of ice, for approximately 15 kyrs.

During the second and main phase of glaciated conditions around 100–110 kyrs after present (Figure 4-25) the Forsmark site is again isostatically depressed (Figure 4-26). After the deglaciation that follows this glaciated period, at around 110 kyrs after present, the Baltic Sea is in contact with the Atlantic and the Forsmark site is submerged by a saline sea. In line with the development of the Baltic Sea presented above, the development of salinity over the Forsmark site during this submerged period follows that of the Holocene. The site finally rises above the Baltic Sea-level again during a brackish phase at around 120 kyrs after present (corresponding to present-day conditions).

During periods of maximum salinity in the Baltic Sea, generally following sometime after periods of maximum glaciation, the Forsmark site is submerged (Figure 4-26). A more detailed description of the development of salinity in the Baltic Sea for this submerged period of the *reference glacial cycle* is found in /SKB 2010d/.

The most important factor affecting modelled shore-level displacement is the Earth structure and ice loading history, primarily the near-field history. The uncertainty in modelled shore-level mainly manifests itself in that reported relative sea-level values are too high, resulting from an overestimation of isostatic depression during glaciated periods, see Section 3.3.4. The size of the uncertainty varies over the modelled glacial cycle. Postulating that the ice sheet evolution is correct, the mean overestimation of relative sea-level over the whole glacial cycle may be up to 45 m for Forsmark.

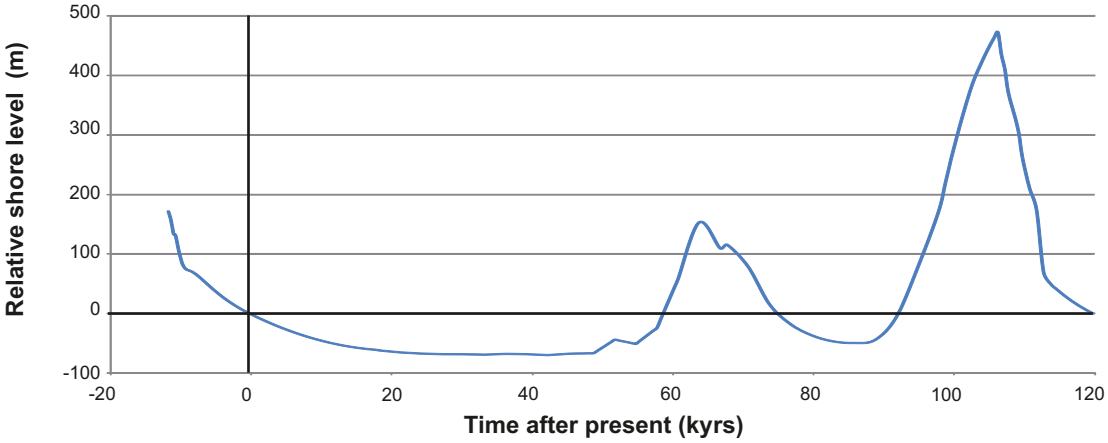

Figure 4-26. *Shore-level displacement at Forsmark during the reference glacial cycle. The first c. 8,000 years of the future period are based on observed relative sea-level data /Påsse 2001/ whereas the following part of the curve is constructed from Glacial Isostatic Adjustment modelling (Section 3.3.4). The shore-level is expressed relative to the contemporary Baltic sea-level. Positive numbers indicate that the site is submerged and vice versa. Note that for most of the time when the figure show submerged conditions, the site is covered by an ice sheet (Figure 4-25). The figure also includes the relative shore-level from the time of deglaciation up to present, used in e.g. the SR-Site biosphere programme.*

4.5.3 Permafrost evolution

The permafrost modelling is described in Section 3.4.4. The input data of geological, hydrogeological, geothermal, geochemical and geomechanical properties are based on site-specific descriptions and are summarised in /SKB 2006a/ and /Hartikainen et al. 2010/. In the reconstruction of last glacial cycle conditions, permafrost develops during the progressively colder phases of the glacial cycle. When the ice sheet subsequently comes to cover an area of permafrost, the permafrost typically stops developing and starts to slowly diminish. When the ground is re-exposed to a cold climate permafrost starts to grow again.

In the SR-Site *reference glacial cycle*, the development of permafrost at Forsmark starts about 7 kyrs after present (Figure 4-27 and 4-28). The 1D modelling approach used for the results in Figure 4-27 could, in certain situations, result in somewhat higher temperatures than would be calculated using a multi-dimensional model. However, a comparison between the 1D modelling results /SKB 2006a/ and the results from the 2D model /Hartikainen et al. 2010/, using the same air temperature curve as input, shows that the results for this site and settings are in line with each other (Figure 4-28). Since lateral groundwater flow only has a minor role in permafrost development compared to heat conduction, e.g. /Hartikainen 2010/, it is likely that modelling including a 3D groundwater flow (instead of the used 2D groundwater flow, and the 1D approach without groundwater flow) would only contribute with minor changes of the permafrost and perennially frozen depths.

When permafrost starts to grow over the site, it starts as sporadic permafrost (i.e. with a spatial coverage less than 50%). As climate gets colder, discontinuous permafrost (with a spatial coverage between 50 and 90%) and continuous permafrost (more than 90% spatial coverage) form over the site (Figure 4-29). Examples of permafrost development along the investigated profile (for profile location, see Figure 3-58) for the dry climate variant of the *reference glacial cycle* are seen in Figure 4-30. The upper panel in Figure 4-30 shows the situation at 8.5 kyrs after present when a Subarctic climate prevails at the site. The profile is partially submerged by the Baltic and sporadic permafrost has started to grow at the site (too shallow to be seen in the figure). At this time the temperature is at its maximum within the repository, which has a large influence on the temperature of surrounding bedrock. Figure 4-30 middle panel shows the situation at 25 kyrs after present in the *reference glacial cycle*, with discontinuous permafrost coverage over the site. In Figure 4-30 lower panel, the situation 50 kyrs after present is shown. At this time an Arctic climate prevails at the site which has resulted in a continuous permafrost cover. At this time the permafrost reaches its maximum depth in the *reference glacial cycle*. As seen from the temperature contours, the heat from the repository has decreased considerably at this time.

During periods of permafrost an unfrozen active layer develops above the permafrost during summer conditions. The thickness of the active layer could typically be c. 40–70 cm deep, depending on the vegetation and soil. For a bare surface the active layer thickness is greater, up to ~1 m.

During the permafrost development prior to the first ice sheet advance, unfrozen taliks are formed under the two future lakes that are located along the profile (Figure 3-58).This is exemplified by the dry climate variant of the *reference glacial cycle* (Figure 4-31). The upper panel shows the situation at 25 kyrs after present when the taliks have formed 9 and 15 km from the south-western starting point of the profile. Groundwater recharge and/or discharge is likely to occur in such taliks. The lower panel of Figure 4-31 shows the situation at 46 kyrs after present. At this time permafrost growth has developed further and none of the taliks reach through the permafrost anymore. In this situation groundwater flow is heavily reduced or stopped.

The permafrost and frozen ground depth reach a maximum prior to the first major glacial advance, at about 50 kyrs after present. At this time the maximum modelled permafrost depth reaches ~260 m at Forsmark (Figure 4-27 and 4-28). The perennially frozen depth is, at the same time, a few tens of metres shallower. When the ice sheet advances over the site, the permafrost stops developing and instead starts to diminish, for example around 60 kyrs after present. Subsequently, permafrost develops again at the site during the ice-free interglacial period between the two major ice advances, but at this time to a somewhat shallower depth, about 180 m (Figure 4-27). During the major phase of ice coverage, including the ice sheet maximum at more than 100 kyrs after present, the maximum permafrost depth (defined by the 0°C isotherm) is around 100 m at Forsmark. Note that, at this time, the permafrost consists only of a completely unfrozen cryopeg due to the insulation effect of the ice sheet and due to the high pressure induced by ice load. Hence all bedrock is at this time at the pressure melting point temperature (Figure 4-27).

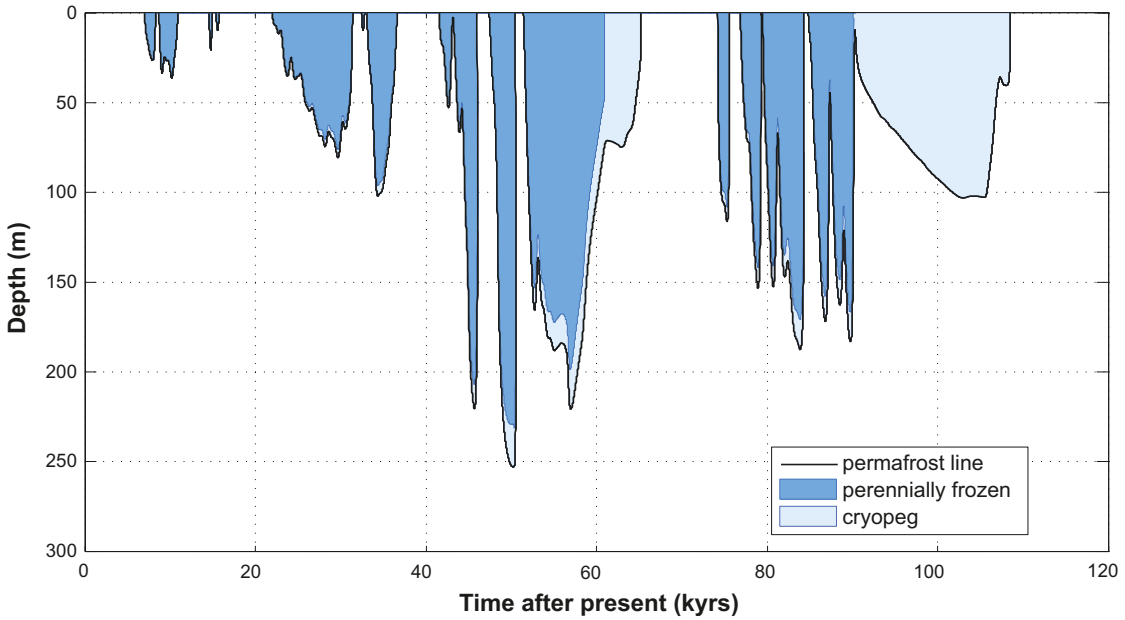

Figure 4-27. *Evolution of permafrost and perennially frozen ground depth for the reference glacial cycle for the repository location in Forsmark. The results were obtained using a 1D permafrost model (Section 3.4.4). Due to the high pressure, a thick unfrozen cryopeg exists within the permafrost (defined by the 0°C isotherm) after 60 kyrs and 90 kyrs after present.*

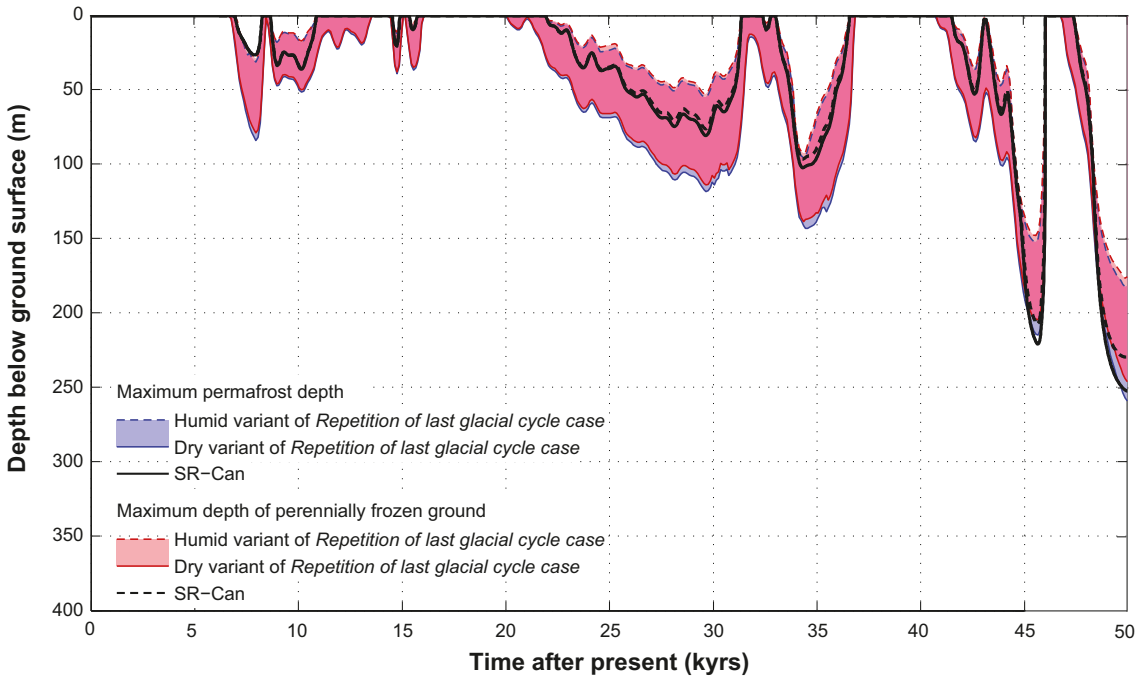

Figure 4-28. *Evolution of permafrost and perennially frozen ground depth at the repository location for the first 50 kyrs of the reference glacial cycle as simulated by the 2D and 1D permafrost models (Section 3.4.4). The shaded area in blue and red represents the range obtained from the 2D modelling when considering one wet and one humid climate variant. Further uncertainties in the permafrost modelling are discussed in Section 3.4.4. Both model simulations show that permafrost starts to grow around 7 kyrs after present and that the maximum permafrost depth is ~250 m around 50 kyrs after present.*

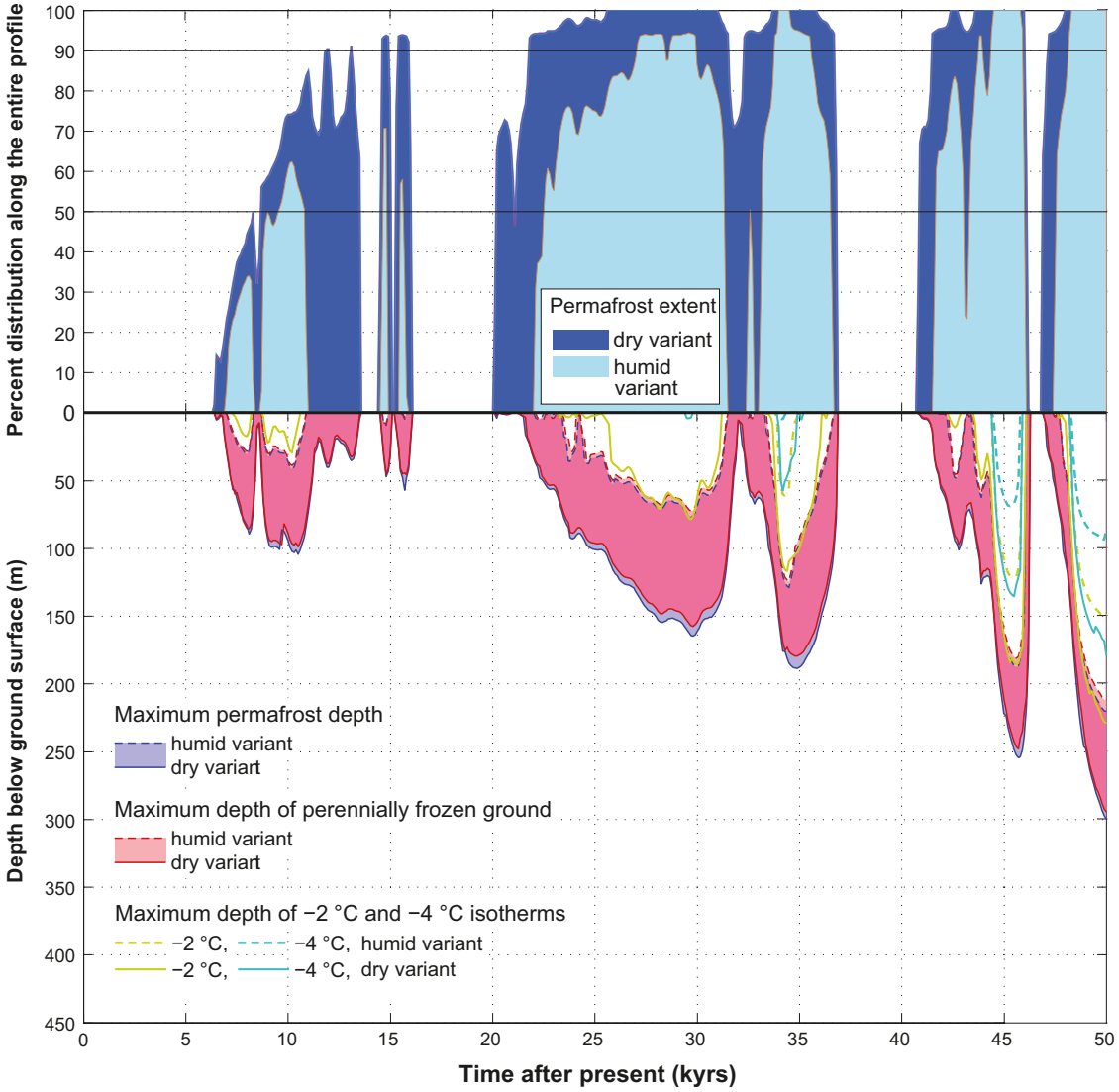

Figure 4-29. *Evolution of maximum permafrost depth, maximum freezing depth and percent permafrost distribution over the entire investigated profile (Figure 3-58) for the first 50 kyrs of the reference glacial cycle. Upper panel: the transition from sporadic to discontinuous permafrost occurs at 50% spatial coverage and from discontinuous to continuous permafrost at 90% coverage. Lower panel: the shaded area in blue and red represents the range obtained when considering one dry and one humid climate variant of the reference glacial cycle. The lilac colour indicates that the results for permafrost and perennially frozen ground overlap.*

Some of the input data for the permafrost simulations are associated with significant uncertainty. The largest uncertainly relates to the air temperature curve reconstructed for the Forsmark site for last glacial cycle, which is estimated up to ±6°C (Appendix 1). If this uncertainty in air temperature is combined with the uncertainty in climate humidity, the permafrost (e.g. 0°C isotherm) uncertainty range in the *reference glacial cycle* reach a maximum depth of ~410 m, while the uncertainty range for the perennially frozen ground reaches ~380 m (Figure 3-79).

Uncertainties related to other surface conditions (vegetation type, surface wetness, snow cover) and subsurface conditions (thermal conductivity and diffusivity, and geothermal heat flow) have a smaller impact on the simulated permafrost results. If they all are combined with the uncertainty in climate humidity, they result in a permafrost uncertainty interval down to between ~170 to ~290 m depth (Figure 3-85).

Setting *all* known uncertainties (in air temperature curve, climate humidity, surface wetness, vegetation, snow cover, bedrock thermal conductivity and diffusivity, and geothermal heat flux) at their most extreme values favourable for permafrost growth, the permafrost uncertainty range reaches a

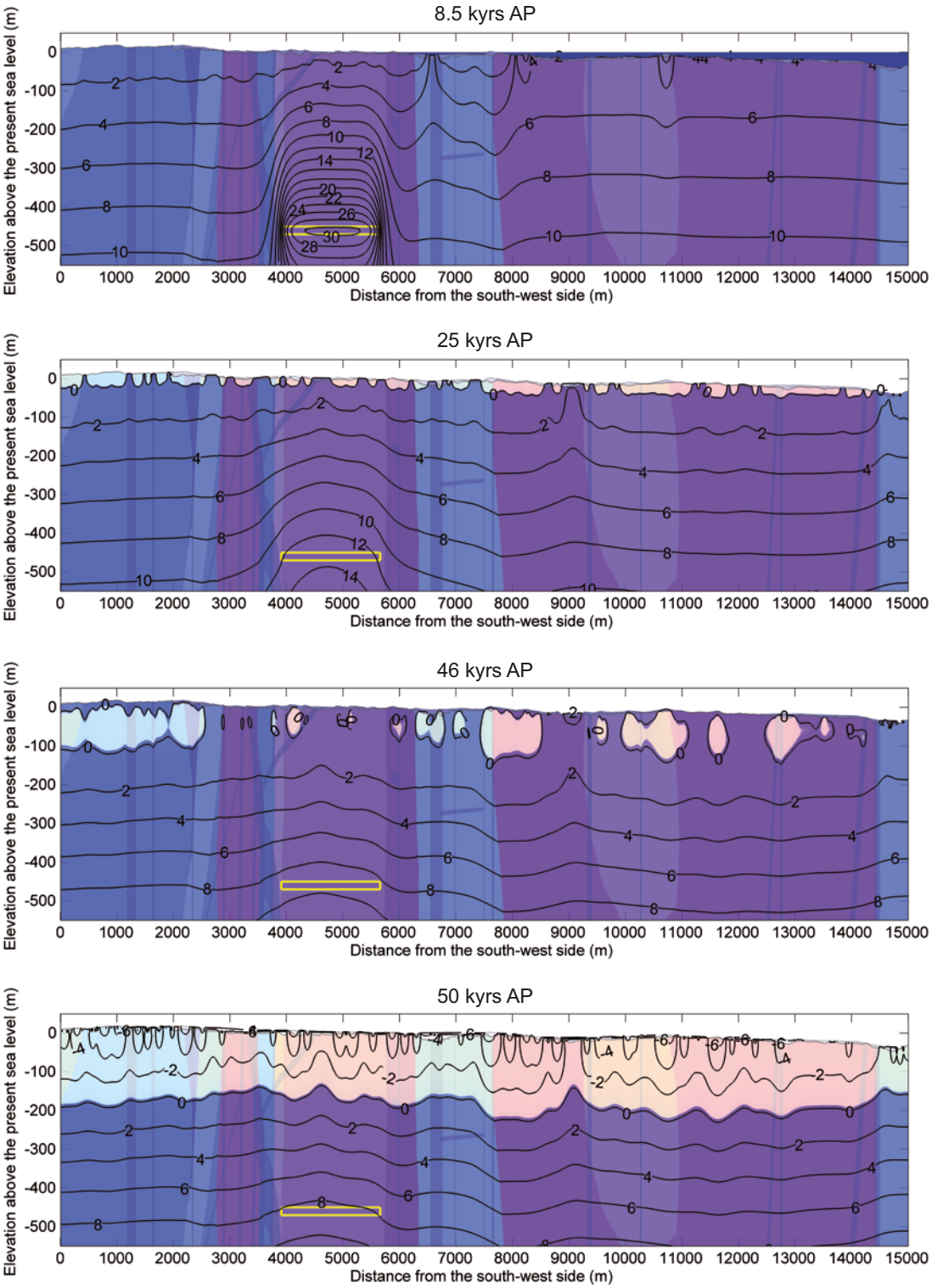

Figure 4-30. *Temperature contours in (°C) and the extent of perennially frozen ground (light colour) and permafrost (0°C isotherm) at times 8.5, 25, 46 and 50 kyrs after present for the reconstruction of last glacial cycle conditions (humid climate variant, see Section 3.4.4). Blue colour on the top of the profile at 8.5 kyrs after present shows the Baltic Sea. The yellow rectangle indicates the location of the repository. Vertical areas with various light colours denote different rock domains. At 8.5 kyrs after present (upper panel) a subarctic climate prevails. At this time the profile is partially submerged and the exposed ground surface is partially underlain by permafrost (too thin to be seen in the figure). At this time the ground temperature is at its maximum within the repository. At 25 kyrs after present (middle panel) a subarctic climate prevails and discontinuous permafrost is developing. At 50 kyrs after present (lower panel) an arctic climate prevails and continuous permafrost reaches its maximum depth in this humid climate variant of the reference glacial cycle. In the dry climate variant, the permafrost grows deeper (Figure 4-29 and 4-31).*

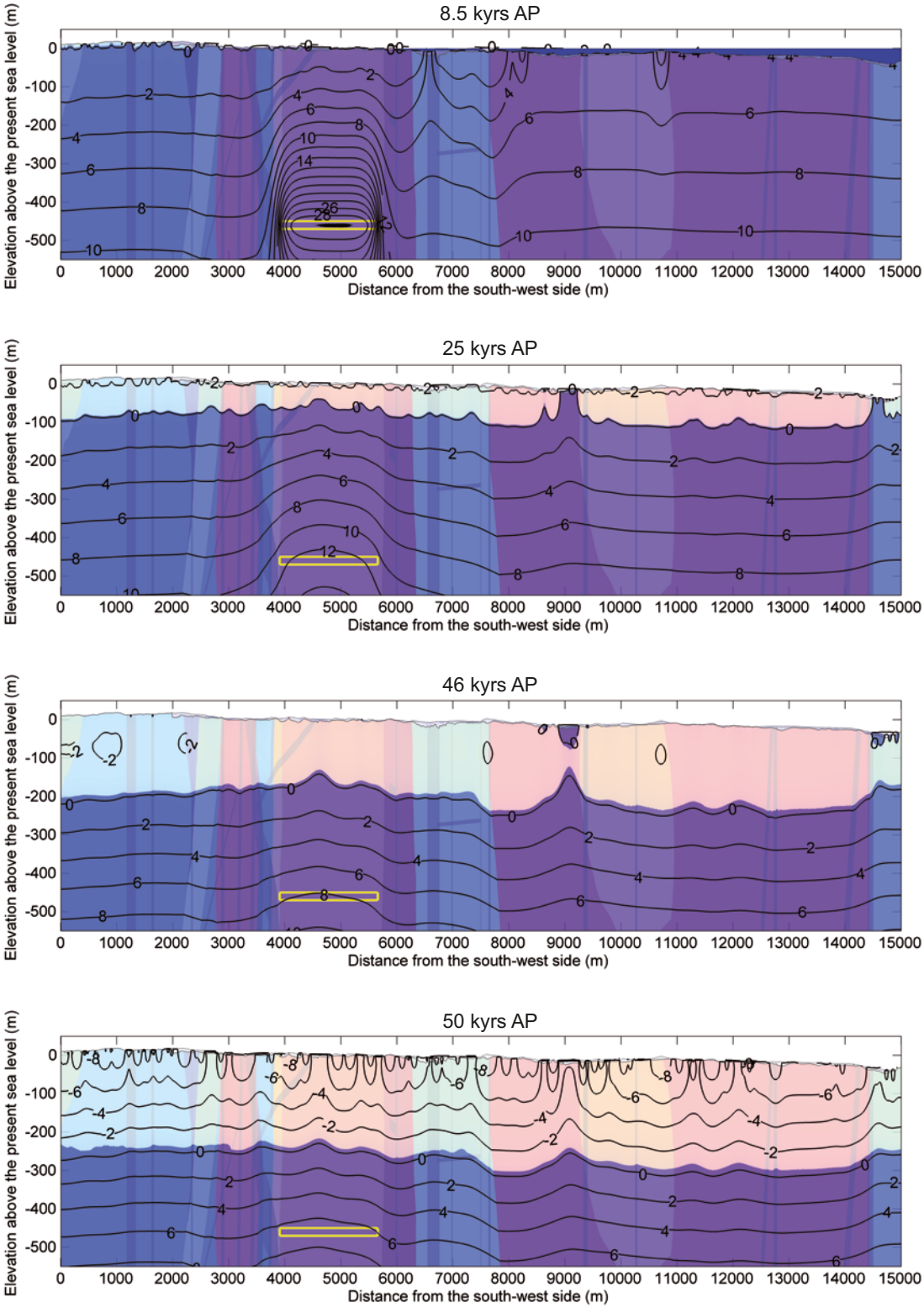

Figure 4-31. *Temperature contours in (°C) and the extent of perennially frozen ground (light colour) and permafrost (0°C isotherm) at times 8.5, 25, 46 and 50 kyrs after present for the reference glacial cycle (dry climate variant, see Section 3.4.4). The yellow rectangle indicates the location of the repository. Vertical areas with various light colours denote different rock domains. At 25 kyrs after present (Upper panel) a subarctic climate prevails and continuous permafrost has developed. Two major taliks have formed under the future lakes located at c. 9,000 and 14,600 m along the profile. At 46 kyrs after present (middle panel), the taliks are shallow, and not in contact with the deep groundwater. At 50 kyrs after present (lower panel) an arctic climate prevails and continuous permafrost reaches its maximum depth in the reference glacial cycle. The maximum permafrost depth is shallower in the humid climate variant (Figure 4-29 and 4-30).*

maximum depth of ~460 m, whereas the uncertainty range for the perennially frozen ground reaches a maximum depth of ~420 m (Figure 3-86). It must be noted, however, that this most extreme combination of uncertainties is quite unrealistic. Given that the uncertainty in the maximum depth of perennially frozen ground does not reach 450 m depth even in the most extreme combination of all uncertainties, freezing of groundwater at repository depth is excluded in the *reference glacial cycle*. For a more detailed description of e.g. individual contributions of uncertainty from various parameters affecting permafrost growth, see Section 3.4.4 and /Hartikainen et al. 2010/.

The presence of permafrost and perennially frozen ground may impact the buffer and backfill material. The temperature criterion used in SR-Site for buffer freezing is −4°C /SKB 2011/. However, in reality it is likely that buffer clay material freezes at even lower temperatures /Birgersson et al. 2010/. The criterion used for freezing of the material to be used for filling of e.g. deposition tunnels is –2°C /SKB 2011/. The reference glacial cycle evolution of the 0°C isotherm (e.g. permafrost depth) and the −4°C isotherm for the repository location are shown in Figure 4-32. The figures show results from the dry climate variant, i.e. the climate variant with deeper permafrost. The 0°C and −4°C isotherms reach a maximum depth at prior to the first major ice advance, around 50 kyrs after present. As previously mentioned the 0°C isotherm (permafrost) reaches a maximum depth of 250 m, whereas the −4°C isotherm reaches a maximum depth of 150 m (Figure 4-32) in the *reference glacial cycle*.

Table 4-3 summarizes the maximum permafrost depths, frozen depths, and depths of the −2°C isotherm and −4°C isotherm for the *reference glacial cycle*, and also presents the maximum depth of the associated uncertainty intervals.

In this context it should be noted that the depths presented above and in Table 4-3, which were calculated including the (declining) contribution of heat from the repository, are relevant for the first future glacial cycle. In SR-Site, the full safety assessment period is 1 Myrs. This means that for the second and following glacial cycles, the permafrost and frozen depths will be somewhat deeper (~37 m), see Figure 3-87, since the heat contribution from the repository has become insignificant. This issue is included in the analysis in the SR-Site buffer freezing scenario /SKB 2011, Section 12.3/.

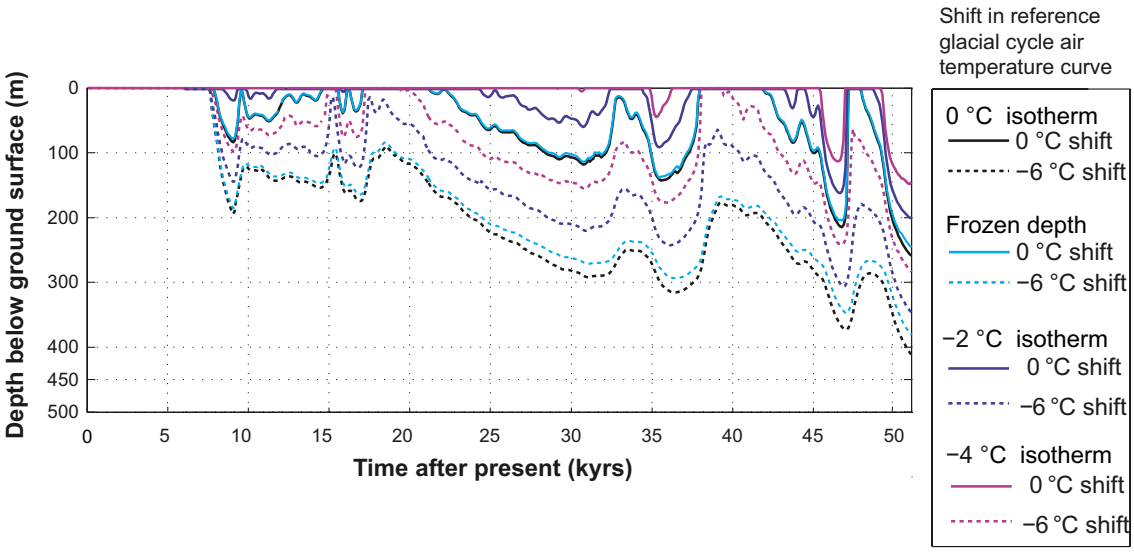

Figure 4-32. *Evolution of 0°C isotherm (permafrost depth), perennially frozen ground and −2 and −4°C isotherms at the Forsmark repository location for the first ~50,000 years of the reference glacial cycle (solid lines, i.e. 0°C shift of reference glacial cycle air temperature curve). Dashed lines show the lower boundaries of the corresponding uncertainty intervals when considering the maximum uncertainty in air temperature (±6°C) (Appendix 1). The results are from the dry climate variant, i.e. the variant with deeper permafrost, see Section 3.4.4. For corresponding results for other shifts of the temperature curve, see /Hartikainen et al. 2010/.*

Table 4-3. Maximum depths of permafrost (0°C isotherm), perennially frozen ground, −2°C isotherm and −4°C isotherm for the reference glacial cycle calculated using the 2D permafrost model /Hartikainen et al. 2010/. The uncertainty interval includes the unlikely combination of having all uncertainties, including air temperature, set at the most pessimistic values favouring permafrost growth.

	Maximum permafrost depth (0°C isotherm) [max uncertainty interval]	Maximum depth perennially frozen ground [max uncertainty interval]	Maximum depth −2°C isotherm [max uncertainty interval]	Maximum depth −4°C isotherm [max uncertainty interval]
Reference glacial cycle	259 m [down to 463 m]	246 m [down to 422 m]	200 m [down to 388 m]	148 m [down to 316 m]

The climate that may prevail in the Forsmark region during periods of periglacial climate domain was as previously described, studied by climate modelling /Kjellström et al. 2009b, including erratum Feb 2010/, see Section 4.3.2.

The results show that, given a prescribed restricted ice sheet coverage during the interstadial between the two phases of ice sheet coverage (Figure 4-25), the climate at Forsmark is subject to dry and cold periglacial conditions at the end of the interstadial. For the selected modelled time period (44 kyrs BP), the climate in the Forsmark region is considerably colder and drier than at present. The modelled mean annual air temperature is 12°C colder than at present whereas the precipitation is reduced by more than 30% (Section 4.3.2). The results of the study thus show that climate conditions are clearly favourable for permafrost growth during this cold stadial of the *reference glacial cycle*. These climatological description, and several other climatic parameters reported in /Kjellström et al. 2009b/, together give one detailed example of the climatic characteristics that may prevail at the Forsmark site during periods of periglacial climate domain. In addition to the climate modelling performed by /Kjellström et al. 2009b/, the same study also simulated vegetation types associated with the different climate cases studied. The results of the vegetation simulations for e.g. the periglacial climate case are reported in /Kjellström et al. 2009b/ and /SKB 2010d/.

Some general conclusions about the site-specific evolution of permafrost and perennially frozen ground for the *reference glacial cycle* can be drawn.

- Permafrost (i.e. the 0°C isotherm) reaches a depth of ~250 m in the *reference glacial cycle*.
- If considering the combined uncertainties related to surface conditions (vegetation types, snow cover and climate humidity) and subsurface conditions (e.g. bedrock thermal conditions and geothermal heat flow), the uncertainty range for the perennially frozen ground reaches a maximum depth of ~290 m (Figure 3-85).
- If considering the uncertainties in climate (in air temperature curve and humidity), the uncertainty range for the perennially frozen ground reaches a maximum depth of 380 m (Figure 3-79).
- If considering the extreme and unrealistic combination of setting *all* known uncertainties (in air temperature curve, climate humidity, surface wetness, vegetation, snow cover, bedrock thermal conductivity and diffusivity, and geothermal heat flux) at their values most favourable for permafrost growth, the uncertainty range for the permafrost depth reaches a maximum depth of ~460 m and for the perennially frozen ground ~420 m (Figure 3-86).
- The maximum depth of the −4°C isotherm reaches a depth of ~150 m over the repository in the *reference glacial cycle* (Figure 3-69).
- If including the extreme and unrealistic combination of setting *all* uncertainties (in air temperature curve, climate humidity, surface wetness, vegetation, snow cover, bedrock thermal conductivity and diffusivity, and geothermal heat flux) in their most favourable setting for permafrost growth, the uncertainty range for the −4°C isotherm reach a maximum depth of ~320 m (see Figure 3-86).

Given these results, freezing of groundwater at repository depth is excluded in the *reference glacial cycle*.

The maximum depths of permafrost, frozen ground, −2°C isotherm, −4°C isotherm, and uncertainties for both the *reference glacial cycle* are summarised in Table 4-3. For a detailed description of the uncertainties associated with the permafrost modelling, see Section 3.4.4.

4.5.4 Evolution of climate domains

Based on the above evolutions of ice sheet, shore-level and permafrost, the climate development at the Forsmark site for the *reference glacial cycle* can be described as successions of climate domains and submerged periods (Figure 4-33). The temporal evolution of all climate domains relevant for Forsmark in the SR-Site *reference glacial cycle* is presented in Figure 4-34. Considering that the development of permafrost in Figure 4-34 has been simulated specifically for the repository location (Section 3.4.4 and 4.5.3), the development of climate domains in Figure 4-33 and 4-34 also refers specifically to the repository location and not to the entire Forsmark site (Figure 3-58). For a description of the spatial representativity and development of the climate domains, see the description on *Transitions between climate domains* below in this section.

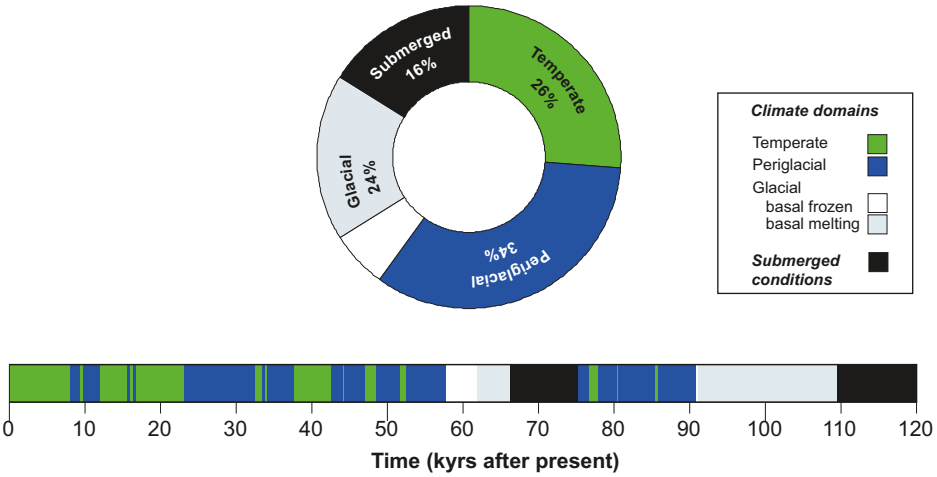

Figure 4-33. *Duration of climate domains and submerged conditions at Forsmark in the SR-Site reference glacial cycle, expressed as percentage of the total time of the reference glacial cycle. The bar below the pie chart shows the development of climate-related conditions for the reference glacial cycle as a time series of climate domains and submerged periods. Other possible future climate developments are described in Chapter 5.*

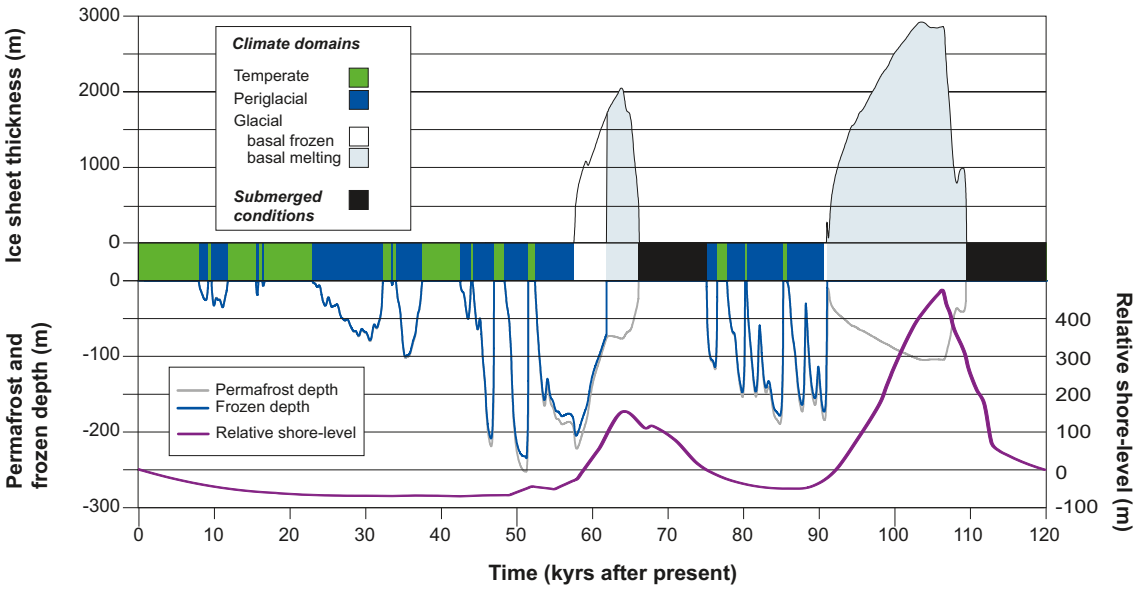

Figure 4-34. *Evolution of important climate-related variables at Forsmark for the coming 120 kyrs in the SR-Site reference glacial cycle. Other possible future climate developments are described in Chapter 5.*

At Forsmark, periods with periglacial climate domain correspond to 34% of the total time of the *reference glacial cycle* (Figure 4-33), whereas periods with temperate climate domain occupies 26%, the glacial climate domain 24% and periods with submerged conditions 16% of the *reference glacial cycle*, see also Table 4-4.

Table 4-4. Duration of climate domains in the SR-Site reference glacial cycle.

Climate domain	Duration (% of reference glacial cycle)	Duration (years)
Temperate climate domain	26%	31,200
Periglacial climate domain	34%	40,800
Glacial climate domain	24%	28,200
Submerged conditions	16%	19,200

The climate succession bar in Figure 4-33 shows that the Forsmark site is dominated by temperate climate conditions for the first ~25 kyrs, although shorter periods of periglacial climate domain occur around 10 kyrs after present. Subsequently, up to the first period of glacial climate domain, temperate conditions are gradually replaced by periglacial conditions. The ice-free interstadial period around 80–90 kyrs after present in the *reference glacial cycle* is dominated by permafrost conditions. The trend with gradually more dominating permafrost conditions is a natural result of the progressively colder climate during the glacial cycle. An exception to this trend is the short period after the submerged phase that follows the final deglaciation, at the very end of the scenario. At that time, ice-free conditions are again dominated by temperate conditions in a warm interglacial climate. Yet another effect of the progressively colder climate during the glacial cycle is the increasing length of the periods with glacial climate domain.

Periods of temperate climate domain occurs in Forsmark in the early phase of the glacial cycle, during short periods of the interstadial between the two major ice advances, and during the interglacial period following the glacial maximum. The periods of temperate climate domain in the early phases of the *reference glacial cycle* are generally warmer and longer than those occurring during interstadials in the later part of the glacial.

During the first 50 kyrs of the *reference glacial cycle*, and in the period between the two ice advances, the increasingly colder climate results in progressively longer periods of periglacial conditions. The total duration of the periglacial climate domain at Forsmark is about 41 kyrs (Table 4-4). During the most severe permafrost periods in the *reference glacial cycle*, at around 70 kyrs BP (Figure 4-34), the permafrost at the repository location develops to between ~180 and ~250 m depth depending on assumed ground cover. The corresponding depths of perennially frozen conditions are between ~180 and ~250 m. The maximum permafrost depth along the entire profile investigated for permafrost development (Figure 4-21) is between 220 and 300 m for the same simulation. The maximum depth of perennially frozen ground along the profile is from 210 to 300 m. The uncertainties related to the simulated permafrost depths are described in Section 3.4.4 and 4.4.3.

Forsmark is exposed to two major ice advances and retreats during the *reference glacial cycle*, the first advance occurs around 60 kyrs after present and the second after about 90 kyrs after present (Figure 4-34). Prior to both of these glaciated periods, the Forsmark site is situated above sea-level with prevailing permafrost conditions when the ice sheet advances towards and over the site. A period of basal frozen conditions initiates the first major period of glacial climate domain. The period of basal frozen conditions is ~4 kyrs long.

After the first glacial period, the site is submerged under the Baltic Sea (Figure 4-34). Following from the warm climate conditions reconstructed for the first part of MIS 3 during the Weichselian (Section 4.3.2), with present-day air temperatures during summer in northern Fennoscandia, temperate climate conditions are envisaged to prevail at Forsmark during the first several thousands of years of the submerged period (not seen in Figure 4-34). That is, if the site were not submerged after the first glacial period, due to a thinner ice sheet and less isostatic depression, subaerial temperate climate conditions would prevail at the site for considerable amount of time after ~66 kyrs after present.

The landscape is in a state of continuous permafrost coverage during the time of the first ice advance over the site, at around 70 kyrs after present (Figures 4-29 and 4-34). At this time, all present and future lakes at the Forsmark site are infilled /SKB 2010d/, and hence there are no taliks present under lakes. Nevertheless, a hypothetical situation with an ice sheet co-existing with taliks under lakes at the Forsmark site is investigated by groundwater modelling in /Vidstrand et al. 2010/.

When the ice sheet expands over the site, it insulates the ice sheet bed from the cold air temperatures and in time induces ice sheet basal melting conditions. During periods of ice sheet coverage, the development of subglacial permafrost is more restricted than permafrost development during ice-free conditions (Figure 4-34). The total length of periods of glacial climate domain in the *reference glacial cycle* is 28 kyrs at Forsmark (Table 4-4). During this time, basal melting conditions dominate.

For detailed examples of how the climate may be characterized in Sweden and in the Forsmark region under periglacial and glacial conditions, see the exemplified climates of the Weichselian glacial cycle in Section 4.3.

The climate simulations /Kjellström et al. 2009b/, show that there is a large range in possible climates for the Fennoscandian region in a 100 kyr time perspective. Excluding the situation when the region is covered by an ice sheet, annual mean air temperatures for the Forsmark region differ from the simulated cold MIS 3 stadial climate (Section 4.3.2) to the future warm climate (Section 5.1.7) by 12–15°C. Correspondingly, annual mean precipitation is almost a factor two higher in the future warm climate compared with MIS 3 at these sites.

Figure 4-35 shows both the first and second repetition of conditions reconstructed for the last glacial cycle (i.e. the *reference glacial cycle*), illustrating how glacial cycles are envisaged to follow each other in the 1million year time perspective of the safety assessment reference evolution see /SKB 2011/.

The first full interglacial period, following the present one, is shown at around 110 to 130 kyrs after present (Figure 4-35). The onset and ending of this future interglacial period, as well as the corresponding onset and ending of the Holocene, is here defined from the development in the Forsmark region; the onsets of the interglacials are defined by the timing of the deglaciation of the area, whereas the ending is defined by the first occurrence of permafrost in the *reference glacial cycle* (Figure 4-35). The timing and duration of the Holocene and future interglacial period in Figure 4-35 is thus determined from the development in the *reference glacial cycle*, which for this part of the glacial cycle is based on site-specific observations and modelling. The resulting, *locally defined*, Holocene interglacial and future interglacial periods have a length of ~18 kyrs. This duration is in line with the longer of the two types of interglacials, with durations roughly of either ~20 kyrs or ~10 kyrs, that have occurred during the past eight glacial cycles /Tzedakis et al. 2009/.

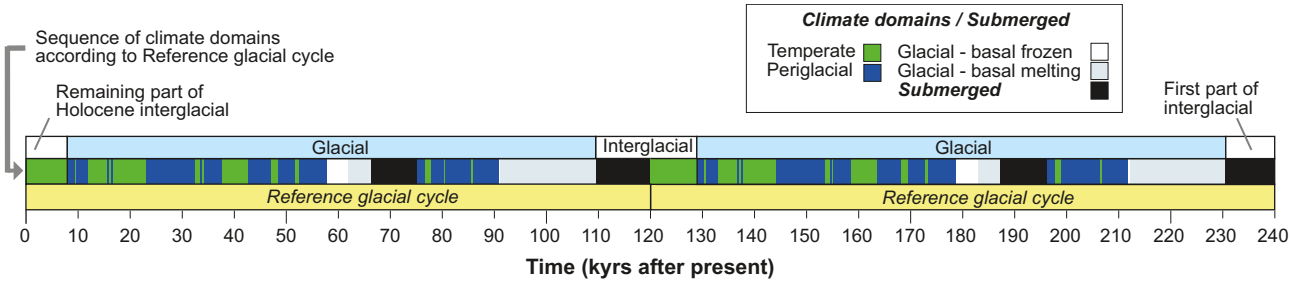

Figure 4-35. *Evolution of climate at Forsmark for the coming 240 kyrs using repetitions of the reference glacial cycle. The figure illustrates how the reference glacial cycle is repeated in order to finally cover the 1 million year time perspective of the SR-Site reference evolution see /SKB 2011/. The resulting duration of the locally defined interglacial periods, see the text, is in this case approximately 19 kyrs. For approximately half of that interglacial time, the Forsmark site is submerged under the Baltic water level. Other possible future climate developments are described in Chapter 5.*

The uncertainties in the *actual* length of the present and future interglacial periods are naturally very large. Given these uncertainties, it is again emphasized that the evolution of climate domains as described in the *reference glacial cycle* (Figures 4-33, 4-34, 4-35), and corresponding base case of the SR-Site main scenario (Figure 1-3), is not an *expected* future climate evolution. It is one relevant example of an evolution covering the climate-related conditions that can be met in a 100 kyr time perspective. Other possibilities for the length of the present interglacial period are handled in the additional climate cases, including the *global warming case* and *extended global warming case* (Chapter 5).

The sequence of main climate-related events for the *reference glacial cycle*, including times of transitions between events and corresponding climate domains, is summarized in Table 4-5.

For the set up of the groundwater modelling, a simplified climate development for the reference glacial cycle has been produced (Figure 4-36, Table 4-6). In the simplified reference glacial cycle, climate periods of short duration have been removed and longer periods are used to describe the general climate development in Figure 4-33 and 4-34. In the simplified reference glacial cycle, the total duration of each climate domain is however the same as in the detailed reference glacial cycle presented in Table 4-4.

Table 4-5. Sequence of climate-related events for the reference glacial cycle, including the full Holocene. The same sequence of events is seen in Figure 4-33 and 4-34.

Event	Time for transition between events	Climate domain
Deglaciation/ Start Holocene interglacial (locally defined as time of deglaciation of Forsmark)	10,800 before present (BP) (8800 BC)	–
Holocene interglacial	–	Temperate climate domain (incl. submerged conditions)
Present	0 BP	
End of Holocene interglacial (locally defined as first occurrence of permafrost in reference glacial cycle)	7000 after present (AP) (9000 AD)	–
Periglacial and temperate conditions (progressively longer periods of permafrost conditions)	–	Periglacial- and temperate climate domains (progressively shorter phases of temperate climate conditions)
End of periglacial and temperate conditions. Start of glacial conditions	57,600 AP (59,600 AD)	–
First phase with glacial conditions	–	Glacial climate domain
Deglaciation at site. Start interstadial conditions	66,200 AP (68,200 AD)	–
Interstadial conditions	–	Mainly periglacial climate domain (incl. submerged conditions and short temperate periods)
End of interstadial conditions. Start of glacial conditions	90,800 AP (92,800 AD)	–
Second and main phase with glacial conditions	–	Glacial climate domain
Deglaciation/start of interglacial (locally defined as time of deglaciation of Forsmark)	109,500 AP (111,500 AD)	–

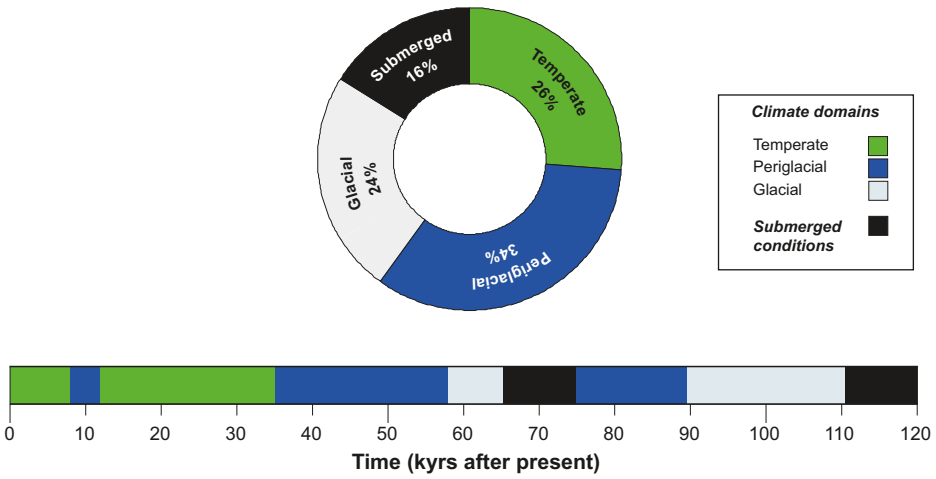

Figure 4-36. *Simplified reference glacial cycle. The total durations of the climate domains are the same as in the detailed reference glacial cycle seen in Figure 4-33.*

Table 4-6. Simplified climate development for the reference glacial cycle.

Climate domain/ Submerged conditions	Time (kyrs after present)	Duration (kyrs)
Temperate	0–8	8
Periglacial	8–12	4
Temperate	12–35	23
Periglacial	35–58	23
Glacial	58–65	7
Submerged	65–75	10
Periglacial	75–89	14
Glacial	89–111	22
Submerged	111–120	9

Transitions between climate domains

Depending on what spatial scale is considered, the transitions between climate domains need to be described differently. If considering the repository site only, or even the central part of the repository, the transitions between climate domains (temperate-, periglacial-, glacial domain and submerged conditions) may be described as more or less instantaneous in time, as perceived from the way the succession of climate domains are depicted in Figure 4-34. This is in line with the fact that the permafrost modelling used for Figure 4-8 was conducted specifically for the repository site, see Section 3.4.4 and 4.5.3. (The ice sheet and GIA modelling used for Figure 4-34 were done on a much coarser spatial scale, but the results from the larger model grid cells are here taken to represent the ice sheet- and shore-level development at the repository location).

However, if looking at Forsmark on a site-scale, i.e. several hundreds of square km (see Figure 4-37), the transition between climate domains is of a gradual nature, both spatially and temporally. The main transitions within the *reference glacial cycle* occur when the site goes from i) temperate climate domain to periglacial climate domain, ii) periglacial climate domain to glacial climate domain, iii) glacial domain to submerged conditions and finally iv) from submerged conditions back to temperate climate domain.

The transient nature of the change from temperate climate domain to periglacial climate domain is illustrated in Figure 4-29. Sporadic permafrost starts to grow more or less simultaneously over the site. Subsequently, if climate allows, the permafrost may develop to a discontinuous- and continuous spatial coverage. The duration of such a full transition in the *reference glacial cycle*, i.e. the development from a landscape without permafrost to a landscape with a permafrost coverage of 90% or more at the Forsmark site, is approximately between 2 and 5 kyrs (Figure 4-29).

The transition from periglacial- to glacial climate domain manifests itself as an ice sheet margin that advances over the site. A spatially transient change takes place in one specific direction over the Forsmark site, by which the periglacial climate domain is replaced with glacial climate domain following the advance of the ice sheet front. In the *reference glacial cycle,* the ice sheet margin advances over the site at a speed of ~50 m/year. The duration of this transition in the *reference glacial cycle*, i.e. the time it takes for the ice sheet to advance over the Forsmark site, is around 250 years. Note that permafrost may still exist under the ice sheet for some of the time that the site is assigned to the glacial climate domain (Figure 4-34).

The transition from glacial to submerged conditions constitutes the deglaciation phases of the site, when ice sheet conditions are replaced by submerged conditions. The retreat rate of the ice sheet margin during deglaciation of the Forsmark site is, in the *reference glacial cycle,* ~300 m/year. The duration of this transition, i.e. the time during which one deglaciation occurs over the Forsmark site in the reference glacial cycle, is around 50 years.

According to the model reconstruction of the last phase of ice sheet coverage in the Forsmark area (Section 3.1.4), the ice flow direction during the MIS 2 ice sheet advance was approximately from north, while the ice flow direction during the deglaciation was from north-west. This is in line with the interpretation of glacial striae, with a northerly direction recorded both in the oldest glacial striae and the oldest documented directional transport of the till material as recorded in clast fabric analysis /Sundh et al. 2004/, and with an overall dominating younger striae system showing transport and deposition from the north-west /Sohlenius et al. 2004/. This demonstrates that the transition to and from the glacial climate domain may be spatially different during phases of ice sheet growth and decay.

The transition from submerged conditions to temperate climate domain is manifested by the shore-level displacement caused by the isostatic rebound that follows deglaciation. The duration of this transition in the *reference glacial cycle*, i.e. the time it takes from the very first appearance of land at the site (Figure 4-37) until the last remnants of sea have disappeared from the site is around 12 kyrs /SKB 2010d/. This is the transition that is occurring at the Forsmark site at present, manifested by the slow movement of the shore line across the site. The transient nature of shore-level displacement over the site is further described in /SKB 2010d/.

The durations of the four transitions above are summarised in Table 4-7.

Given the climate evolution of the *reference glacial cycle*, the assumptions made in all modelling exercises (Chapter 3), and the physiographical characteristics of the site, the glacial processes result in the fastest transition between climate domains (Table 4-7). The transition from glacial climate domain to submerged conditions for the Forsmark site is around 50 years. The transition from periglacial to glacial climate domain is about five times slower. These two fastest transitions relate to the glacial climate domain, i.e. to the relatively fast processes of ice sheet advance and decay. The transition from temperate- to periglacial climate domain with continuous permafrost is 40 to 100 times slower than the transition from glacial climate domain to submerged conditions (Table 4-7). The slowest transition is the one from submerged conditions back to temperate climate domain, which, in the *reference glacial cycle,* is around 240 times slower than the transition from glacial climate domain to submerged conditions. This is due to very slow glacial isostatic adjustment of the Earth's crust to the unloading associated with the ice sheet deglaciation (Section 3.3).

Table 4-7. Approximate durations of full transitions between climate domains over the Forsmark site (as shown in Figure 4-37) for the SR-Site reference glacial cycle. In order to compare the duration of the transitions from and to various climate domains, the relative duration time of the transitions are in the last column expressed as numbers compared to the duration that takes place during the deglaciation of the site.

Transition	Approximate duration in reference glacial cycle	Relative duration of transition
Temperate- to periglacial climate domain with continuous permafrost coverage	~2,000 to ~5,000 years	40 to 100·
Periglacial- to glacial climate domain	~250 years	5·
Glacial climate domain to submerged conditions (deglaciation)	~50 years	1·
Submerged conditions to temperate climate domain	~12,000 years	240·

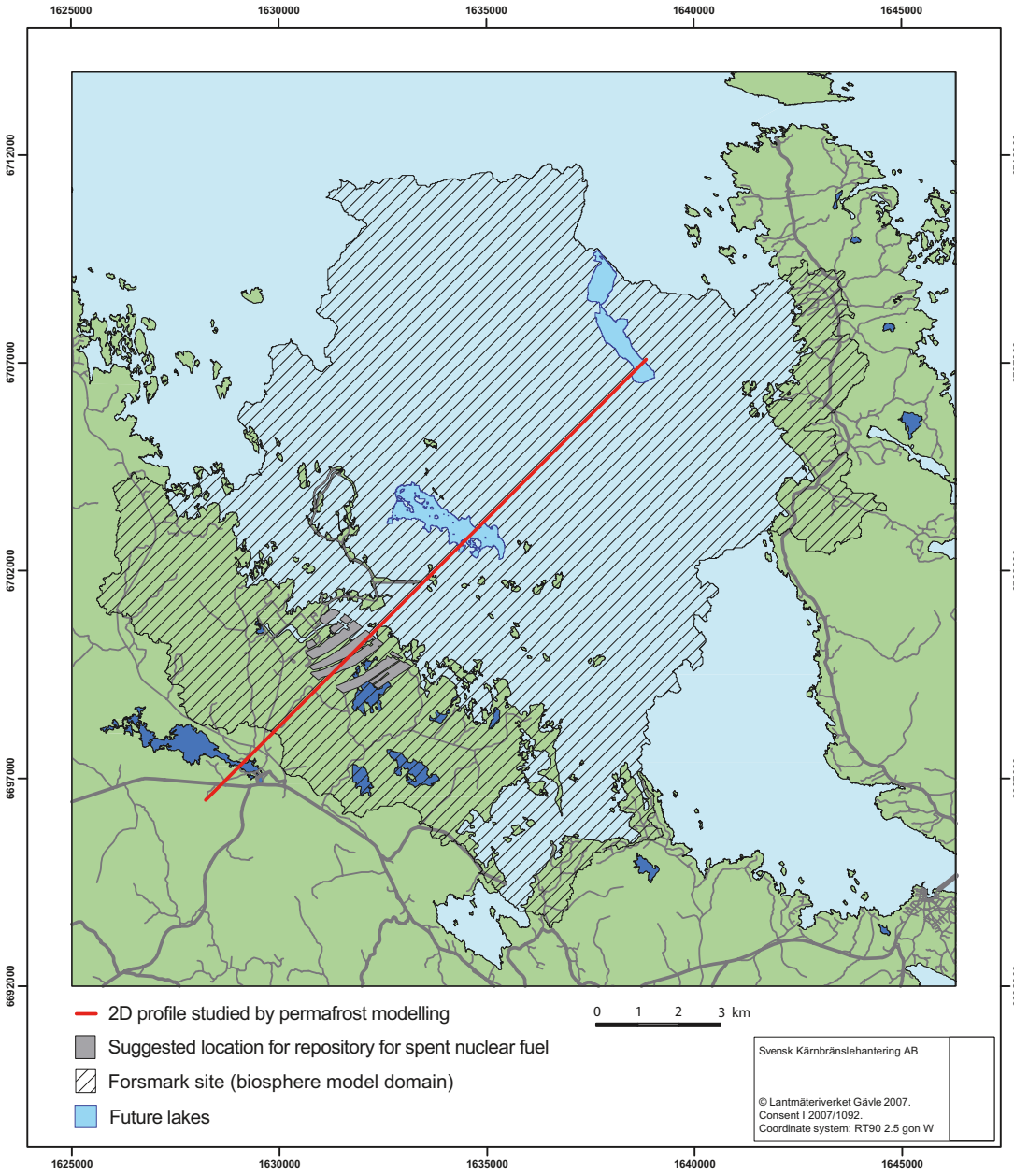

Figure 4-37. *The Forsmark site as defined and analysed in the SR-Site biosphere programme (stippled) /SKB 2010d, e/ and the location of the profile studied by 2D permafrost modelling (red line) (Section 3.4.4 and 5.5). The figure is the same as Figure 3-58.*

Note that for any given time during these transitions, the Forsmark site (Figure 4-37) contains more than one type of climate domain. For instance, parts of the site may be subject to the periglacial climate domain, having permafrost conditions without an ice sheet, at the same time as another part of the site may be overridden by an ice sheet and thus being subject to the glacial climate domain. Also note that the transition from one climate domain to another over the site does not need to be a full transition (as in the above examples). For instance, discontinuous permafrost may start to form within the site due to lower air temperatures, transforming the affected areas to periglacial climate domain. Thereafter, climate may become warmer and permafrost (and the periglacial climate domain) diminishes and disappears.

The hydrogeological consequences of the ongoing transition from submerged conditions to temperate climate domain at Forsmark is analysed in /Salas et al. 2010/. The hydrogeological consequences of transitions between temperate-, periglacial- and glacial climate domains are analysed in /Vidstrand et al. 2010/.

4.5.5 Evolution of hydrological conditions and groundwater

In SR-Site, dedicated groundwater flow modelling has been performed for all types of climate domains that occur in the *reference glacial cycle*. Groundwater flow modelling of periods with temperate climate conditions are found in /Joyce et al. 2010/, while groundwater modelling of periods with periglacial and glacial conditions are found in /Vidstrand et al. 2010/. The geochemical development during the different climate conditions are presented in /Salas et al. 2010/. An overview of the hydrological and groundwater conditions of the *reference glacial cycle* is given below.

A schematic section through an arbitrary south-western sector of a Fennoscandian ice sheet large enough to cover the Forsmark site is shown in the upper panel of Figure 4-38. A zone of basal melting reaches some hundreds of kilometres from the ice margin in the southeast. The production of basal melt water here varies between 1 and 10 mm/year and can be regarded as constant over the year. In the ablation area below the equilibrium line, melt water from the ice surface and rain is brought to the ice sheet bed through crevasses and moulins. In the *reference glacial cycle* (Figures 4-23 and 4-24) surface melt water production in the ablation area typically varies up to 4–8 m of water per year.

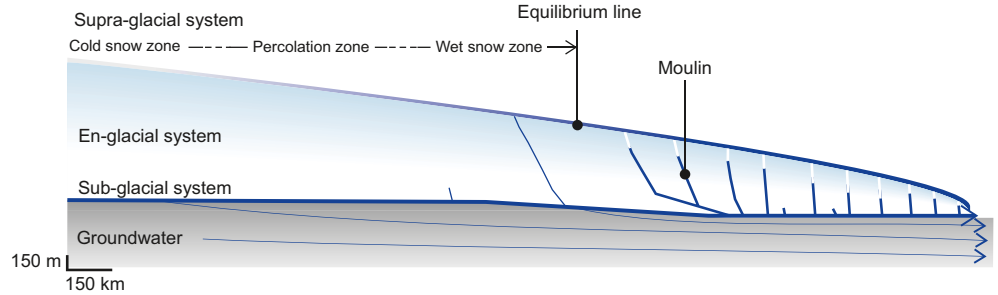

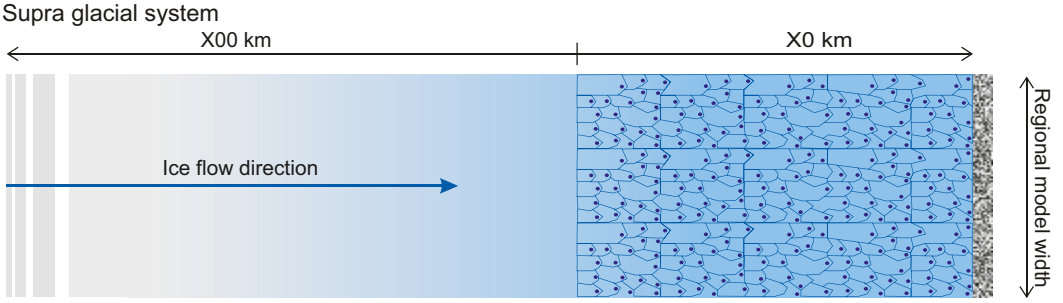

In the ablation area, downstream of the equilibrium line, a system of catchment areas is assumed. Each catchment area is assumed to be connected to the en- and sub-glacial systems through which surface melt water is assumed to reach the bed.

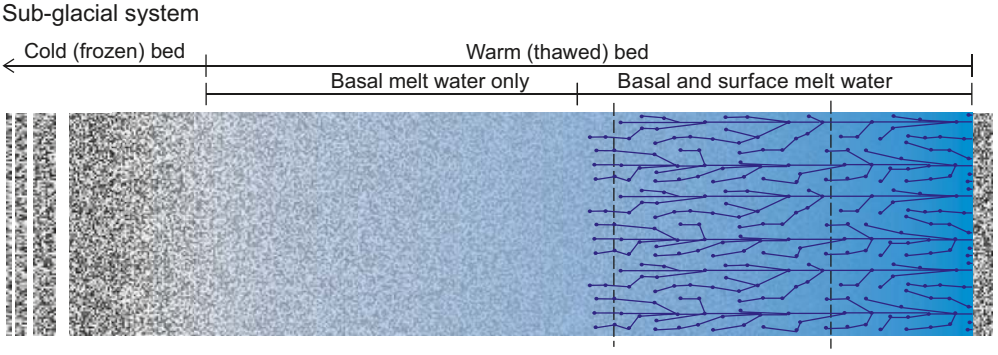

In the area of basal melting, where the water supply is from basal melting only, a slow system is assumed. In the ablation area, downstream the equilibrium line, where both basal and surface melt water are assumed to reach the bed, a fast system with channels or tunnels is assumed.

Figure 4-38. *Conceptual model of the ice sheet hydrological system. Upper panel: arbitrary south-western section through a Fennoscandian ice sheet. Middle and lower panels: possible configurations of the supra- and sub-glacial hydrological systems. At present it is not known if water generated at the surface could reach the bed also upstream of the equilibrium line.*

More ice melts in lower parts of the ice sheet, and less ice closer to the equilibrium line. During the final deglaciation of the ice sheet in this *reference glacial cycle*, a maximum modelled surface melt rate of 14 m/year occurs. The modelled typical surface melt rate values of 4–8 m/year can be compared with observed present average surface ablation rates of the Greenland ice sheet of a few metres/year /Krabill et al. 2000/ up to ~10 m/year /Bøggild et al. 2004/. During the deglaciation of the Weichselian ice sheet, melt rates of more than 10 m/year may have occurred /Humlum and Houmark-Nielsen 1994/.

During periods of temperate climate domain, the groundwater flow pattern is similar to the present ice free situation, with a mixture of local areas of groundwater recharge, typically at topographically high positions, and discharge, typically in low positions. The groundwater flow is at this time to a large degree driven by topographic gradients in the landscape.

During the initial periods of periglacial climate domain, the permafrost distribution in the Forsmark region is first sporadic followed by discontinuous spatial permafrost coverage, see section on permafrost development above. This results in a modified pattern of groundwater flow, but still with significant groundwater recharge and discharge taking place. When climate gradually gets colder, permafrost grows progressively thicker and more widespread (see section on permafrost development above and Section 4.5.3). When the climate is cold enough, continuous permafrost forms. When continuous permafrost occurs, the precipitation recharge of groundwater is strongly reduced or even stopped, since permafrost influences subsurface hydrology by drastically reducing the hydraulic conductivity of the frozen unit /Burt and Williams 1976, Vidstrand et al. 2010, Hartikainen et al. 2010/. At locations of future deep lakes, unfrozen taliks may exist where groundwater recharge and discharge takes place, see section on permafrost development above and Section 4.5.3. Details on the permafrost and hydrological conditions during such situations are found in /Hartikainen et al. 2010, Vidstrand et al. 2010/.

In this context it is worth noting that even in cases when continuous permafrost is present in the landscape, it is unlikely that the permafrost layer has zero permeability for groundwater flow. A zero permeability would probably require a uniform and very deep permafrost distribution. In many cases, the permeability of the frozen ground could instead be large enough to allow for some groundwater flow through the permafrost. In addition, the increased groundwater flow associated with an advancing ice sheet margin over permafrost terrain is likely to enhance the creation of taliks.

During the first period of glacial climate domain, the ice sheet overrides ground with permafrost (Figure 4-34). In line with the situation with ordinary permafrost, subglacial permafrost under the ice sheet margin acts as a hydrological barrier for groundwater flow /King-Clayton et al. 1997/. Therefore, this phase is characterised by a period with no groundwater recharge under the frontal near part of the ice sheet. Groundwater recharge may still take place further in under the ice sheet, where permafrost may have melted. Even though the ice sheet is cold-based in its frontal-near parts at this time, water from surface melting may still reach the glacier bed or forefield. However, since permafrost is present, this water does not contribute significantly to groundwater recharge.

Even if the 2D permafrost modelling (Section 3.4.4) did not indicate any taliks at the time of ice sheet overriding (at 50 kyrs after present in the *reference glacial cycle*) it is probably not correct to assume an effective large-scale permeability of zero for the pro-glacial landscape at this time. The permeability of the frozen ground can in places be large enough to allow some groundwater flow through the permafrost, and furthermore, the increased groundwater flow due to the large pressure gradient associated with an advancing ice sheet /Vidstrand et al. 2010/ could enhance a creation of taliks.

After the initial cold-based period, subglacial groundwater recharge again takes place at the Forsmark site, this time under the ice sheet due to melting of basal ice (Figure 4-34). In local areas of former groundwater discharge, groundwater recharge typically occurs under glacial conditions e.g. /Breemer et al. 2002/. This results in a dominant subglacial groundwater flow directed downwards under the major part of the warm-based ice sheet, recharging the groundwater aquifer. Subglacial groundwater discharge may possibly occur close to the ice margin /Breemer et al. 2002, Vidstrand et al. 2010/. Even if the permeability of the bedrock were to decrease under the load of an ice sheet, the increased physical and hydraulic gradient, especially associated with passages of the ice sheet margin, would likely increase groundwater flow in bedrock compared to temperate climate domain conditions /Hökmark et al. 2010, Vidstrand et al. 2010/.

As known from present glaciers and ice sheets e.g. /Jansson and Näslund 2009, Jansson et al. 2007/, as well as from the esker and geomorphological record in e.g. Sweden, subglacial ice tunnels may be present at the ice sheet bed. The reason why an ice tunnel may form, and is kept open, is the presence of a high enough basal water pressure and water flux. From observations from glaciers, it is known that atmospheric pressure may exist in parts of the tunnels during parts of the year, typically at the end of the melting season when the input of surface melt water is reduced or stopped, and the ice deformation has not yet reduced the size of the tunnel. However, the tunnel width and length are reduced during the winter season due to the ice deformation and since no meltwater from the surface system is entering the glacial en- and subglacial hydrological system. There are very few observations of these processes from ice sheets. However, it is likely that this closing process is more efficient some distance away from an ice sheet margin, where the ice thickness is greater and associated ice deformation faster. Over one full year, it is likely that the major stretch of subglacial tunnels under ice sheets is dominated by water pressures higher than atmospheric pressure.

The first direct observation of these processes from an ice sheet was made by Wadham et al., see /GAP team members 2009/. For summer conditions at the Russel Glacier, located in the marginal zone of the Greenland ice sheet (Figure 4-39), they concluded that meltwater generated in the lower ablation zone was routed by an efficient, channelized basal drainage system during the height of the melt season. At this time, the conduits were water filled, except for a few km near the ice sheet margin where the tunnels were at atmospheric pressure. The water-filled conduits fluctuated between open and closed channel flow over timescales of days to weeks, as a response to the varying melt water fluxes. Given the information from theory and from observations at smaller glaciers and the Greenland ice sheet, it is unrealistic to envisage large open subglacial ice channels at atmospheric pressure stretching many tens of km in under the ice sheet at Forsmark, and that such channels would stay constantly open for many years.

After the first period of glacial climate domain, the Forsmark site is submerged for up to 9 kyrs (Figure 4-34). When the site subsequently is situated above sea-level during this interstadial at around 80–90 kyrs after present (Figure 4-34), climate is generally cold, which induces new long

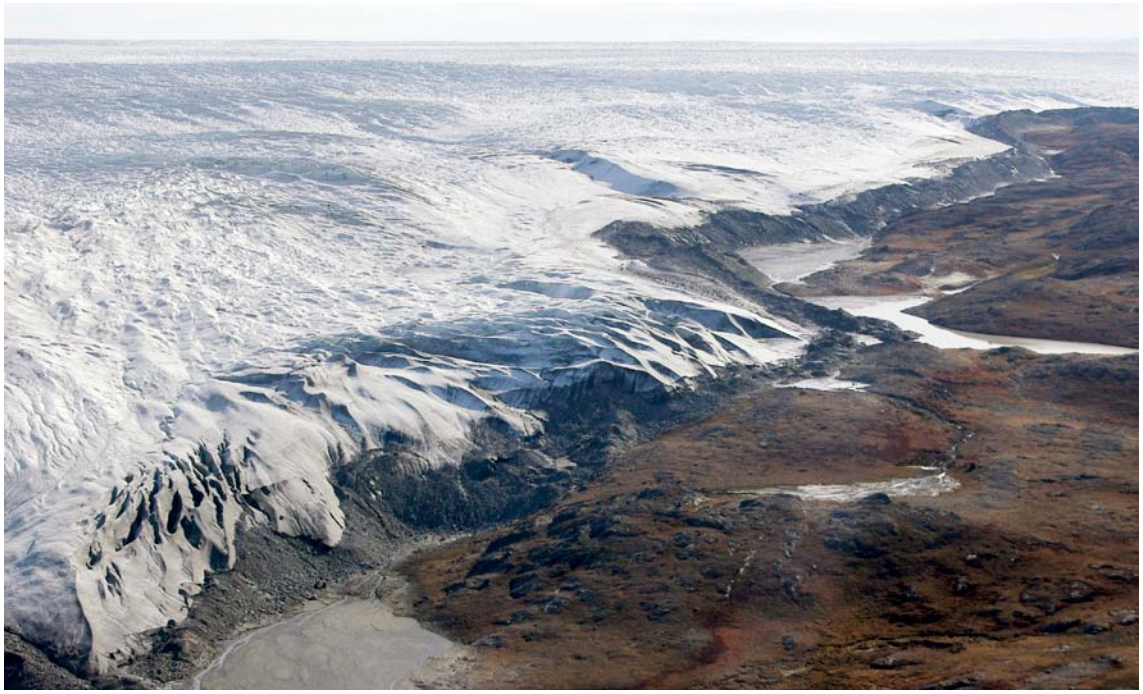

Figure 4-39. *Part of the Greenland ice sheet in the Kangerlussuaq region, west Greenland. During summer conditions, subglacial channels are here water filled except for a few km near the ice sheet margin where the tunnels were at atmospheric pressure, see Wadham et al. in /GAP team members 2009/. The proglacial area is characterized by continuous permafrost with sub-lake taliks that penetrate the permafrost down to the deep groundwater system. Within this region, SKB, Posiva and NWMO carry out the Greenland Analogue project (GAP) in order to study questions on glacial hydrology and hydrogeology. Photo: Jens-Ove Näslund.*

periods of deep permafrost, and associated reduced conductivity in the upper part of the bedrock. During the short temperate conditions during this interstadial, groundwater flow may again be characterized by local areas of recharge and discharge.

During the second and most severe glacial phase, starting around 90 kyrs after present, the ice sheet is cold-based for a considerably shorter initial time than during the first major glacial phase (Figure 4-34). This makes water from surface and basal melting available for groundwater recharge during most of this period of ice sheet coverage. As in the case of the first ice-covered period, steeper physical and hydraulic gradients, especially associated with the passage of the ice sheet front, may, for a limited period, induce more rapid and substantial groundwater flow than under present ice-free conditions, see /Vidstrand et al. 2010/.

Thereafter, at the very end of the *reference glacial cycle*, an evolution corresponding to the Holocene occurs, with Forsmark first being submerged after deglaciation for around 10 kyrs. When the site emerges above sea-level, the climate is much warmer than during the non-submerged period between the two major glacial advances. The Forsmark site is again dominated by temperate climate conditions, with groundwater flow similar to present-day conditions. For a description of the geochemical evolution in this scenario, see /SKB 2011/**.**

4.5.6 Evolution of mechanical conditions

During the *reference glacial cycle* (Figure 4-23 and 4-24) the temporal evolution of the ice sheet will cause time-varying stresses and deformations in the Earth /Lund et al. 2009/. Due to the long time spans both elastic and viscous deformation occurs. Properties of the ice sheet controlling the deformation and stress change are duration, areal extent, thickness and slope of the ice margin. The evolution of stresses in the crust during a glacial cycle has been studied by /Lund et al. 2009/, who used numerical finite-element modelling of the glacially induced stresses based on the ice sheet development in the *reference glacial cycle*. As the ice sheet advances and the load from the ice increases, the vertical and horizontal stresses will both increase in direct and immediate response to the increasing load. The elastic lithosphere will bend and the viscoelastic mantle will flow laterally. This will, on a large scale, result in a depression beneath the load, where crustal flexure will give an additional slow increase in horizontal stresses in the upper crust. Outside the ice sheet margin, crustal flexure will result in an up-warping peripheral bulge (see also Section 3.3.4), in which the horizontal stresses are reduced. The thicker the ice sheet and the longer duration an area is covered by ice, the larger the induced bending stresses will become. When the growth rate of the ice sheet decreases, the induced horizontal stresses under the load grow larger than the vertical stress and remain so during times of steady-state ice conditions and all through the deglaciation phase. As the ice sheet retreats during deglaciation, the depressed lithosphere will experience isostatic rebound, which is a much slower process than the ice load removal process. Consequently, high horizontal stresses remain in the lithosphere for a significant amount of time after the ice sheet induced vertical stress has disappeared.

The pore pressures in the crust are increased during glaciation as a result of the consolidation of the bedrock, the recharge of meltwater available at the base of the ice sheet and the additional hydrostatic pressure induced by the ice sheet itself. Furthermore, increased pore pressure-levels may also potentially develop beneath an impermeable permafrost layer in front of an approaching ice sheet, cf. /Lönnqvist and Hökmark 2010/. Estimates of the magnitude of the glacially induced pore pressure at different depths and during different phases of a glacial cycle have been made by /Hökmark et al. 2010/.

The discussion on glacially induced stresses and pore pressures implies that the effective rock stress (i.e. the normal stress reduced by the water pressure) varies both with changes in the mechanical load and changes in the pore pressure produced by the ice sheet. The evolution and magnitude of the effective stress during the different parts of the glacial cycle will dictate the mechanical behaviour of rock fractures, and hence, also their water-conducting ability, see /Hökmark et al. 2010/. In general, the increase in total stress during ice sheet advance will act to reduce the transmissivity of fractures and fracture zones. But since the vertical stress increases more rapidly than the horizontal stresses, upper crustal stress axes may rotate so that the vertical stress is the intermediate or largest principal stress. These stress changes, together with the increase in pore pressure as compared with non-glacial hydrostatic conditions, may result in changed transmissivity anisotropy.

Outside the edge of the ice sheet, the reduction in horizontal stresses may give rise to a decreased normal stress acting across steeply dipping fractures, leading to an increase in transmissivity. In the absence of reduced temperatures or increased pore pressure levels due to proglacial permafrost, calculations by /Hökmark et al. 2010/ indicate that the increase will be modest. /Hökmark et al. 2010/ also consider two cases associated with the scenario of proglacial permafrost coinciding with the forebulge stress regime. Firstly, they consider the possibility of increased pore pressure-levels beneath the permafrost layer. Secondly, a further reduction of the horizontal stresses due to reduced temperatures /Hartikainen et al. 2010/ is considered in combination with high pore pressures. /Hökmark et al. 2010/ found that, for the former case, the transmissivity will increase by a factor 2–3 at most. For the latter case, significant transmissivity increases of some vertical fracture orientations (factor around 7) were found at shallow depths. For repository depth more moderate increases by a factor 2–3 were found for identically oriented fractures.

Increased deviatoric stresses may also give rise to shearing of critically oriented fractures, which in turn can yield larger fracture apertures and increased transmissivities. The same effect may also result from elevated pore pressures that will act to reduce the shear strength. However, /Hökmark et al. 2010/ argue that transmissivity increases resulting from shear displacements taking place at high normal stress (>6–7 MPa) are negligible. As described by /Lönnqvist and Hökmark 2010/, hydraulic jacking of fractures is also possible, but most likely not deeper than at most 200 metres.

In general, the emplacement of a large ice sheet stabilises faults in the crust and suppresses earthquake activity. During deglaciation, however, the rapid decrease in vertical stress tends to destabilise the crust. Crustal pore pressures are of great significance in the faulting process, since an increased pore pressure decreases the effective normal stress on faults, and hence, reduces their shear strength. If the pore pressure is still enhanced at the end of glaciation, when the vertical load from the ice disappears, fault stability will be further reduced. Observations of large end- or postglacial faults in northern Scandinavia show that such a process was indeed active at the end of the last glaciation.

4.5.7 Surface denudation

For the *reference glacial cycle*, the total amount of surface denudation, i.e. the combined effect of surface erosion and weathering, is expected to be 1–2.6 m for the repository location in Forsmark (Section 3.5.4, Table 3-17).

The major part of this denudation is a result of glacial erosion, occurring during phases of warm-based ice sheet coverage. These warm-based periods of glacial erosion occur after 60 kyrs, and between 90 and 110 kyrs into the *reference glacial cycle* (Figure 4-34). The amount of glacial erosion at the repository location is estimated to 1–2 m for this glacial cycle (Table 3-17). This relatively low amount of expected glacial erosion is a result of the very flat topography in the area, and that the erosional capacity of the ice sheet is relatively small (compared with considerably more active erosion by more active ice sheets or smaller glaciers in other climatological and topographic settings, such as along the Norwegian coast or alpine environments. For examples of various glacial erosion rates from different climatological and topographic environments, see /Olvmo 2010/, and references therein).

The non-glacial component of surface denudation, resulting from all other active erosion and weathering processes, such as weathering and fluvial erosion during temperate- and periglacial climate conditions, is estimated to amount up to 0.6 m for the *reference glacial cycle* (Table 3-17).

All in all, the total denudation for the *reference glacial cycle* is estimated to be limited at Forsmark (less than 3 m), since the area is dominated by the well-preserved sub-Cambrian peneplain (Section 3.5.4). The dissected area with sometimes considerable relief in the coastal areas, some 25 km south-east of Forsmark, may experience more efficient glacial erosion during a glaciation with a similar erosional characteristics as during the Weichselian. In this area, glacial erosion of more than 10 m is expected locally in low topographic positions. However, this is not the case for Forsmark and the repository location.

The removal of bedrock by surface denudation results in a reduction of the repository depth. A reduced repository depth could in turn lead to permafrost and frozen ground reaching closer to the repository. However, a total denudation of less than 3 m for the *reference glacial cycle* (Table 3-17) has a negligible effect, in terms of repository safety, on the estimated permafrost- and freezing depths presented in Section 4.5.3 and 5.5.3. In this context, also the estimated total denudation of around 20 m over the repository in a 1 Myr time perspective (Table 3-17) is insignificant in terms of repository safety.

5 Additional climate cases for the safety assessment SR-Site

In order to cover the uncertainty in future climate development, the *reference glacial cycle* (Section 4.5) has been used to construct additional climate cases with a potentially larger impact on repository safety than the reference cycle, see Figure 1-3. Consequently, they form the basis for the global warming variant of the main SR-Site safety assessment scenario, and also for other additional safety assessment scenarios, see Figure 1-3 and /SKB 2011/. The climate-related issues having the greatest impact on repository safety functions are:

- Maximum permafrost and ground freezing depth;
- Maximum hydrostatic pressure;
- Penetration of oxygen to deep groundwater;
- Occurrence of dilute or extremely saline groundwater;
- Reduction of retardation in the geosphere due to high groundwater fluxes and/or mechanical influences on permeability.

These issues are mainly related to extremes within the temperate-, periglacial-, and glacial climate domains. For a description of the strategy for using and selecting the additional climate cases, see the section on *Strategy for managing long-term evolution of climate-related processes* (Section 1.2.3), and the section on *Rationale and general approach* (Section 4.1). For the SR-Site safety assessment, the climate cases presented in Table 5-1 are considered.

Chapter 5 describes climate cases 2–6 in Table 5-1 and Figure 1-3. In addition to the description of the parameters that the climate cases were designed to take care of, for instance maximum thick ice sheets, a description of expected changes in surface denudation are also described for each case. The removal of bedrock by surface denudation affects the repository depth, which in turn may affect e.g. the possibility for permafrost- and frozen ground to reach the repository. Climate cases with an expected larger total denudation than in the *reference glacial cycle* are therefore considered more important, and are thus described in more detail, compared with cases with an expected denudation smaller than in the *reference glacial cycle*, which are described only briefly.

5.1 Global warming case

5.1.1 Background

There is a large range of potential future climate developments when considering the combined effect of natural and anthropogenic climate change. One such case is described in the present *global warming case*. This case describes a future climate development influenced by both natural climate variability and climate change induced by anthropogenic emissions of greenhouse gases, with the latter resulting in weak to moderate global warming. In order to cover a reasonably broad array of future climate developments based on present knowledge, a case of *extended global warming* is also included in the SR-Site safety assessment (Section 5.2), describing a situation with stronger and longer-lasting global warming.

Table 5-1. Climate cases considered in the SR-Site safety assessment. Cases 2 to 6 are described in the present chapter of the report. The table contains the same information as Table 4-1.

Case number (section in present report)	Climate case	Description
1 (Section 4.5)	*Reference glacial cycle*	Repetition of reconstructed last glacial cycle conditions
2 (Section 5.1)	*Global warming*	Longer period of initial temperate conditions than in case 1
3 (Section 5.2)	*Extended global warming*	Longer period of initial temperate conditions than in case 2
4 (Section 5.3)	*Extended ice sheet duration*	Longer duration of ice sheet coverage than in case 1
5 (Section 5.4)	*Maximum ice sheet configuration*	Largest ice configuration in past two million years
6 (Section 5.5)	*Severe permafrost*	Favourable for early and deep permafrost growth

The purpose of the *global warming case* and the *extended global warming case* is to give a picture of the possible impact of global warming on the repository and also to cover extremes of warm conditions with respect to repository safety. In general, temperate climate conditions are not negative for the repository safety, as the conceivable conditions occurring within the temperate domain have limited impact on repository safety functions. However, if for some reason, a release from the repository does occur, previous safety analyses have shown that peak doses occur during periods when the area above the repository is situated above sea-level, and areas of discharge are located within that area. In addition, prolonged periods of temperate climate conditions above sea-level may result in lower groundwater salinity. The effects of this also needs to be assessed in terms of e.g. buffer stability /SKB 2011/.

There is a large amount of published information on various aspects of global warming in recent literature. The intention with this section and the section on the *extended global warming case* is not to give a comprehensive description of the present status on knowledge in the global warming issue (with its causes, effects, uncertainties etc). Instead, the aim is to include information and data that support the treatment of this complex topic at a level required for the safety assessment. To this end, both general scientific literature is used as well as dedicated studies performed for SR-Site. For further descriptions of the topic of global warming, the reader is referred to the compilations by /IPCC 2007, Bates et al. 2008, Jol et al. 2008, Allison et al. 2009, Richardson et al. 2009, Rummukainen and Källén 2009, Arndt et al. 2010/, and references therein. Detailed descriptions of global warming and its effects specifically on Sweden and the Baltic region is found in /SOU 2007, Miljövårdsberedningen 2007, BACC author team 2008/.

In SR-Site, there are two main reasons for analysing cases of climates warmer than the *reference glacial cycle*; i) modelling studies of the climate response to increased greenhouse gas emissions, mainly CO_2, indicate that global temperatures will increase in the future under such conditions, e.g. /IPCC 2007, Kjellström et al. 2009b/, and ii) natural long-term climate cycles are believed to be driven mainly by changes in solar insolation (Section 2.2). The coming 100 kyr period is initially characterised by exceptionally small amplitudes of insolation variations /Berger 1978/, suggesting that the present interglacial may be exceptionally long. If considering the known future changes in insolation, /Loutre and Berger 2000/ and /Berger and Loutre 2002/ suggest that the interglacial may end ~50 kyrs after present. This is illustrated in Figure 5-1, showing modelled Northern Hemisphere ice sheet volumes for the coming 130 kyrs, based on a model forcing only by future variations in insolation and natural as well as anthropogenically increased CO_2 levels. Given this insolation forcing, the model results suggest that a growth of the Greenland-, Eurasian- and North American ice sheets would not start until after 50 kyrs after present even without increased CO_2 levels.

However, /Müller and Pross 2007/ suggest that under natural climate forcing conditions, the present insolation minimum holds the potential to terminate the Holocene interglacial. This supports a hypothesis by /Ruddiman 2003/ which proposes that early anthropogenic greenhouse gas emissions prevented the inception of a glacial that otherwise already would have started.

In addition to handling future variations in insolation, the *global warming case* also includes the effect of low to moderate global warming from an anthropogenic increase of atmospheric CO_2 levels, e.g. /IPCC 2007/. (Higher levels of greenhouse gas concentrations, also described by e.g. /IPCC 2007/, with an associated longer period of temperate climate conditions, are treated in the *extended global warming case*, see Section 5.2). In the *global warming case*, peak air temperatures are envisaged to be reached within the first hundreds to thousands of years. Mean annual air temperatures several degrees warmer than at present then occur in central Sweden and Forsmark. Subsequently, following a decline in atmospheric CO_2 concentrations, air temperatures are envisaged to show a general slow decline for the rest of the long initial period with temperate climate conditions.

The reduction of atmospheric CO_2 concentrations, following peak values, is a very slow process, e.g. /Archer 2005, Lenton and Britton 2006, Tyrell et al. 2007, Archer and Brovkin 2008, Schaffer et al. 2009/. This suggests that the onset of colder climate conditions, after the initial temperate period, also would be a gradual and slow process. Therefore, it is appropriate to use the mild onset of colder climate conditions reconstructed for the last glacial cycle (Section 4.5.4) for the climate development following the initial temperate period. In order to describe the combined effect of known variations in insolation and a low- to moderate global warming, the *global warming case* therefore assumes

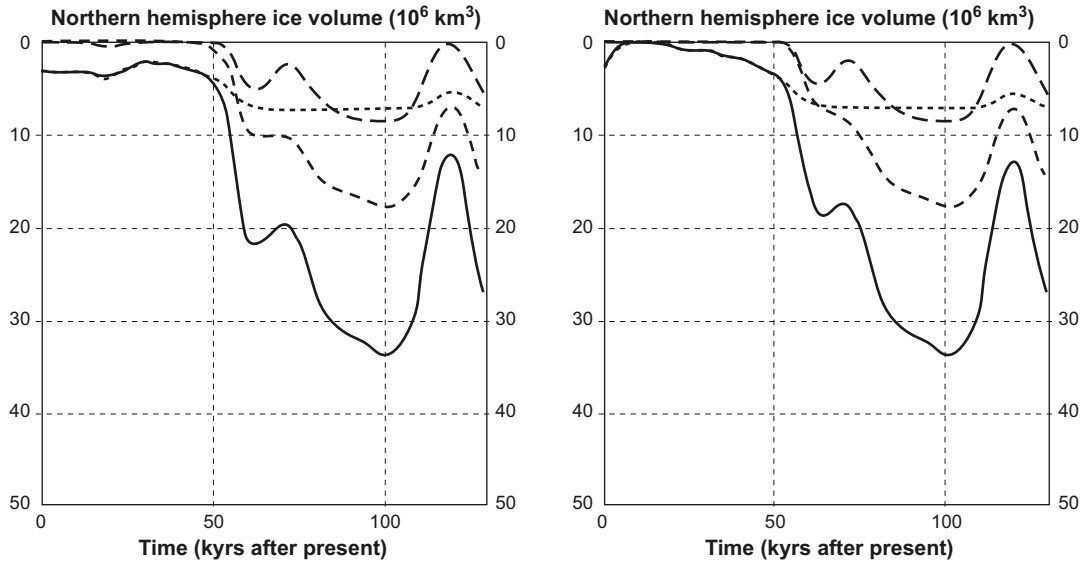

Figure 5-1. *Simulated ice volume of the Northern Hemisphere over next 130 kyr using model forcing only by variations in insolation and natural CO_2 levels (left). The right figure shows a corresponding simulation but with a global warming scenario with an atmospheric CO_2 concentration peak of 750 ppmv within 200 yrs. Ice volume of the Northern Hemisphere (full line), Greenland ice sheet (dotted line), North American ice sheet (dashed line) and Eurasian ice sheet (long-dashed line). The initial Greenland ice sheet corresponds to the present one. Modified from /Loutre and Berger 2000/.*

that the present temperate climate domain, albeit with higher initial air temperatures, will prevail for 50,000 years longer than in the *reference glacial cycle*. Following the first 50 kyrs of additional temperate climate conditions, the first 70 kyrs of the *reference glacial cycle* is assumed to follow. This results in c. 60 kyrs of temperate climate conditions at Forsmark before the ending of the present interglacial (the ending locally defined as the time of first occurrence of periglacial conditions with permafrost, see Section 4.5.4). This development is in broad agreement with results simulated for two global warming cases within the BIOCLIM project /BIOCLIM 2003/.

5.1.2 Ice sheet evolution

In this case of low to moderate global warming, colder climates again arise in the latter half of the coming 120 kyrs. The climate cooling associated with a slow reduction in atmospheric greenhouse gas concentrations results in a Fennoscandian ice sheet forming in the same way as in the *reference glacial cycle*, but in this case 50,000 years later. In the *reference glacial cycle*, two main phases of ice sheet coverage took place at Forsmark. In the *global warming case*, only the first of these two phases occurs, around 110 kyrs after present. The characteristics of this glacial period are identical to the first major glacial period of the *reference glacial cycle*. The maximum ice sheet thickness during this event is just above 2,000 m. The glacial climate domain persists for around 10 kyrs, of which the first half consists of cold-based ice sheet conditions, without local formation of groundwater, whereas the second half consists of warm-based ice sheet conditions with active sub-glacial groundwater formation at Forsmark. Prior to the ice sheet overriding, periglacial conditions with permafrost exist at the site.

5.1.3 Shore-level evolution

The main process of importance for repository safety in the temperate climate domain is changes in shore-level. Due to the near-coastal location of Forsmark, one question related to future global warming is the response of the present glaciers and ice sheets, and associated changes in sea-level and shore-level.

Ice sheets and sea-level

At present, there are major uncertainties in the estimates of future sea-level rise due to global warming. A major part of this uncertainty relates to the response of the cryosphere to increased temperatures. Given the location in a warmer climate at present, the Greenland ice sheet may be more sensitive to increases in air temperature than are the Antarctic ice sheets, especially the East Antarctic ice sheet. After the publication of the fourth assessment report from the Intergovernmental Panel on Climate Change (IPCC) /IPCC 2007/, a wealth of scientific literature has highlighted aspects of the Greenland ice sheet response to climate change, e.g. /Hall et al. 2008, Hanna et al. 2008, Howat et al. 2008, Mernild et al. 2009, van den Broeke et al. 2009, Vinther et al. 2009, Wake et al. 2009, Robinson et al. 2010, Stone et al. 2010b/, including the role of oceanographic warming e.g. /Holland et al. 2008, Hanna et al. 2009, Rignot et al. 2010, Straneo et al. 2010/ and the coupling between climate, ice sheet dynamics and glacial hydrology, e.g. /van de Wal et al. 2008, Joughin et al. 2008, Price et al. 2008/. A summary of various aspects of the Greenland ice sheet in a warming climate is found in /AMAP 2009/. The sea-level contribution from glacial sources are specifically dealt with in e.g. /Gregory and Huybrechts 2006, Meier et al. 2007, Shepherd and Wingham 2007, Pfeffer et al. 2008, Velicogna 2009, Bamber and Riva 2010/.

The present volume of the Greenland ice sheet corresponds to a global sea-level rise of 7.3 m /Bamber et al. 2001/, whereas the maximum contribution to future global sea-level change from melting glaciers and ice caps (i.e. excluding the Greenland and Antarctic ice sheets) is considerably smaller, no more than 0.5 metres (corresponding to the total volume of water stored in glaciers and ice caps at present) /IPCC 2007/.

In some studies, the decay of the Greenland ice sheet under global warming is a relatively smooth function of the temperature increase /Huybrechts and de Wolde 1999/. However, many recent studies have highlighted that the response of the Greenland ice sheet is a complex process, involving internal ice sheet processes as well as the interaction between the cryosphere, atmosphere and ocean, e.g. /Huybrechts et al. 2004, Howat et al. 2008, Thomas et al. 2009, Wake et al. 2009, Vinther et al. 2009, Rignot et al. 2010/. According to /Gregory and Huybrechts 2006/ an increase in annual temperature of 4.5±0.9° or more over Greenland, corresponding to a global temperature increase of 3.1±0.8°, could result in an irreversibly collapsing Greenland ice sheet. In the most pessimistic CO_2 scenario of /IPCC 2007/, with a 4° global climate warming by the year 2100 (compared to the period 1980–1999), with a likely range of 2.4°–6.4°, the warming would in the long run be sufficient to lead to a complete Greenland ice sheet collapse /Huybrechts and de Wolde 1999, Gregory et al. 2004, Alley et al. 2005a, Gregory and Huybrechts 2006, Lunt et al. 2008, 2009, Stone et al. 2010a, b/, and eventually a global mean sea-level rise by 7 m. According to these model simulations, which are acknowledged to not properly represent the dynamics of fast-flowing ice streams, this could happen within a few millennia. If proper ice stream dynamics could have been considered, the ice sheet response to a warmer climate could perhaps be faster than this.

One crucial aspect of sea-level rise due to ice sheet collapse is that the effect of the rising sea-level is not distributed evenly over the seas and along continental coasts. This is due to changes in the gravity field associated with the melting of ice sheets and water entering the ocean basins /Milne et al. 2009**,** Whitehouse 2009, Bamber and Riva 2010/. For instance, a complete collapse of the Greenland ice sheet would result in gravitational changes that counteracts the sea-level rise in the near field of the collapsed ice sheet, resulting in a *lower* sea-level, in the near field, than when the ice sheet was present /Milne et al. 2009/. This aspect is one key aspect of the GIA model used for SR-Site, see below. /Milne et al. 2009/ studied this spatially-variable change in sea-level assuming a complete melting of the Greenland ice sheet, and they predicted a ~0 mm/yr sea-level change in the region of Fennoscandia.

Even if considered less sensitive to global warming, several studies have been published, since the publication of /IPCC 2007/, on the possible contribution to sea-level rise by the West Antarctic ice sheet e.g. /Mitrovica et al. 2009, Bamber et al. 2009, Ivins 2009, Rignot et al. 2008/. According to the literature reviewed in /IPCC 2007/, a collapse of the West Antarctic ice sheet could contribute with a maximum of ~5 m of global sea-level rise. A more recent study suggests that the potential maximum rise in global mean sea-level from the West Antarctic Ice Sheet is 3.3 m /Bamber et al. 2009/. The effects of a collapse of the West Antarctic ice sheet was studied by /Mitrovica et al. 2009/ and /Bamber et al. 2009/. By using the traditional ice volume value for West Antarctica,

corresponding to 5 m of global mean sea-level rise, /Mitrovica et al. 2009/ estimated that a collapse of the West Antarctic ice sheet would result in a sea-level rise around Fennoscandia of 5±1 m, when including the gravitational effects associated with the ice sheet collapse. However, using the revised West Antarctic ice volume value, corresponding to 3.3 m of global mean sea-level rise, /Bamber et al. 2009/ suggested that a full collapse of the West Antarctic ice sheet would give a sea-level rise around Fennoscandia of around 3 m, gravitational effects taken into account.

Sea-level rise up to year 2100

The fourth assessment report from IPCC did a summary of expected future global mean sea-level rise given various greenhouse gas emission scenarios. The maximum global mean sea-level rise for year 2100 was estimated to +59 cm /IPCC 2007/. The maximum corresponding value reported by IPCC in 2001 amounted to +88 /Church et al. 2001/. The difference between these two estimates is dependent on how the risks of global sea-level changes are evaluated. Primarily, in /IPCC 2007/, the contribution response to global warming from internal ice sheet dynamics was excluded from the estimate of sea-level rise because of its large uncertainty.

In addition to the studies mentioned under the ice sheets and sea-level heading, many studies have attempted to improve the numbers and approach to address the question on future sea-level rise since /IPCC 2007/, e.g. /Rahmstorf 2007, Grinsted et al. 2009, Sidall et al. 2009, Cazenave et al. 2009/. /Rahmstorf 2007/ predicted a maximum global sea-level rise by year 2100 of +138 cm (relative to the level year 1990). This is considerably higher than the value reported by /IPCC 2007/, a difference that is mainly due to the different methodological approach taken by /Rahmstorf 2007/. In /Rahmstorf 2007/, a semi-empirical relationship is used to connect global sea-level rise to global mean surface temperature, proposing that the rate of sea-level rise is roughly proportional to the magnitude of warming above the temperature of the pre-Industrial Age. In a study by /Pfeffer et al. 2008/, the Greenland and Antarctic ice sheet dynamic response to global warming is estimated and included. Also in this study the large uncertainty in sea-level rise is emphasised. /Pfeffer et al. 2008/ points to two probable cases of global sea-level rises by year 2100 (relative to the level year 2000) amounting to +79 and +83 cm, respectively. /Pfeffer et al. 2008/ also describe a less probable, but still possible, worst case where a calculated *maximum* ice discharge from the Greenland and West Antarctic ice sheets result in a global sea-level rise of +200 cm by year 2100, i.e. +141 cm above the /IPCC 2007/ estimate (that excluded this process).

The short term effect (by year 2100) of these worst case estimates of global sea-level rise for the Forsmark site is described in the *extended global warming case*, Section 5.2.3, and in /Brydsten et al. 2009/.

Sea-level rise beyond year 2100

The long-term sea-level response to global warming is naturally also associated with major uncertainties, and is for instance not discussed in /IPCC 2007/ which does not describe events more than 3,000 years into the future. It is clear however, that global sea-level would continue to rise far beyond year 2100 as a response to global warming. The effects on sea-level related to the response of the Greenland and West Antarctic ice sheets to global warming are discussed above, where a full collapse of the Greenland and West Antarctic ice sheets are suggested to contribute with a sea-level rise around Fennoscandia of ~0 and ~3 m respectively. There are major uncertainties related to the amount of global warming and the associated amount of ice sheet disintegration, as well as on the timing of such events.

/Rohling et al. 2009/ showed the (non-linear) relationship between Antarctic temperatures and sea-level elevation for the past five glacial cycles, indicating that the equilibrium sea-level for the present day CO_2 concentration in the atmosphere lie within the broad range of 0 and +25 (±5) m, and that such levels might be reached within the next two to five millennia. The higher CO_2 levels that result from future emissions, results in even higher equilibrium sea-levels.

Another uncertainty relates to the long-term response from thermal expansion of ocean (thermosteric sea-level rise) due to a global warming climate. The rate of global sea-level rise from thermal expansion of ocean water would initially be low and then increase. /IPCC 2007/ estimated the total

sea-level increase due to thermal expansion in year 2300 to be 0.3–0.8 m (A1B emission scenario), and to be 0.5–2 m in year 3000 AD compared with year 2000 AD. Because of the large heat capacity of the ocean, thermal expansion would continue for many centuries after a warmer climate has stabilised. The final maximum contribution to sea-level change from thermal expansion would thus be considerably larger than at the time of peak climate warming.

There is thus a large uncertainty in the future long-term response of global sea-level on global warming. Despite these uncertainties, it is clear that the final sea-level rise resulting from global warming is reached several thousands of years into the future, and that the global mean sea-level rise could amount to several tens of metres.

GIA modelling

Despite the large uncertainty in future sea-level rise, reflected in the references above, many researchers believe that substantial long term sea-level rise will continue for centuries as a result of global warming, e.g. /IPCC 2007, Overpeck and Weiss 2009/. For the *global warming case* it is not meaningful or possible to assign probabilities to the various predictions of future global sea-level change above. Instead, for the GIA model simulations, it is adequate to assume a complete collapse of the Greenland ice sheet as a response to global warming. It is assumed that this ice sheet completely melts away at a linear rate during the coming 1,000 years, resulting in 7 m of global sea-level rise. If the rate would be different, or if the ice sheet response would be non-linear and more complex, which is very likely, this does not influence the modelled long-term (glacial cycle time scale) shore-level signal at the Forsmark site.

Just as for the reconstruction of last glacial cycle conditions (Section 3.3.4) and the resulting *reference glacial cycle* (Section 4.5.2), the effect of sea-level rise on the development of the Baltic shore-level was for the *global warming case* investigated by GIA modelling. In the GIA simulations made for the reconstruction of last glacial cycle conditions there was a discrepancy between the GIA results on modelled present-day uplift rates and present uplift rates as observed by GPS measurements. In Section 3.3.4 and in /Whitehouse 2009/ it was shown that the discrepancy was partly due to the fact that a laterally homogeneous Earth model (2D Earth model) was used in the GIA simulations. A 3D modelling approach significantly reduces this discrepancy (Section 3.3.4 and Whitehouse 2009). Another contributing factor to the discrepancy can be a too large an ice load provided to the GIA model from the ice sheet model (Section 3.1.4). By sensitivity tests made in SR-Can using the GIA model, it was found that a reduction in ice thickness to 80% of the value in the *reference glacial cycle* yielded GIA results on present uplift rates that were in accordance with the observed present-day uplift. Even if a large part of the discrepancy now can be attributed to the 2D GIA modelling approach (Section 3.3.4), the *global warming case* for SR-Site uses the 2D GIA model simulation together with an 80% reduction in ice sheet thickness. However, this is judged as not having a large impact on the usefulness of the results on relative sea-level, given the large uncertainty interval presented for the results.

In line with the approach used in the GIA modelling of the *reference glacial cycle*, the GIA model was initiated by running one full glacial cycle in order to obtain realistic initial uplift rates for the greenhouse scenario. This was followed by linear melting of the Greenland ice sheet over 1,000 years, inducing corresponding changes in global sea-levels. This was followed by a 50 kyr long period of no change to the loading model, simulating a warm global warming climate without a Fennoscandian ice sheet forming. Finally a second full glacial cycle was added in the simulation. No contribution from thermal expansion of oceans was included, which adds an uncertainty to the results, see below.

After the GIA simulation, the relative shore-level curve from the GIA model was combined with observed shore-level data for the present day /Påsse 2001/ in order to produce the final shore-level curve for the global warming variant (Figure 5-2). In the GIA simulation, the rise in global sea-level due to the melting of the Greenland ice sheet does not result in a sea transgression at Forsmark. This is due to the counterbalancing gravitational effect associated with the removal of the mass of the Greenland ice sheet mentioned above, in Section 3.3 and in /Milne et al. 2009, Whitehouse 2009/.

As mentioned above, /Milne et al. 2009/ studied the spatially-variable change in sea-level assuming a melting of the Greenland ice sheet, and predicted a ~0 mm/yr sea-level change in the region

of Fennoscandia. This is in line with the results of the GIA modelling performed for the *global warming case*, where the isostatic rebound is larger than the sea-level rise even when including a 1,000 year long complete melting of the Greenland ice sheet. The results show that the Forsmark site is situated above sea-level basically for the entire coming 120 kyrs in the *global warming case*.

However, here it is important to note that there are large uncertainties in the shore-level curve presented in Figure 5-2. They relate to uncertainties and assumptions made in the GIA modelling and also to the uncertainties in present knowledge on future global sea-level rise discussed above. The main uncertainty in future global sea-level rise is, as described above, related to the uncertain response of the Greenland and West Antarctic ice sheets to global warming and to the contribution from thermal expansion. The assumed complete collapse of the Greenland ice sheet covers the uncertainty of the most sensitive ice sheet. The uncertainty in the shore-level curve may thus be up to several tens of metres, see also Section 3.3.4.

Given the uncertainties described above, it is possible that, in contrast to what is shown in Figure 5-2, there might be an initial period of sea transgressions at the Forsmark site in the *global warming case*, lasting some thousands of years, before the isostatic uplift component starts to dominate. After an early phase with these large uncertainties in the *global warming case*, the results of the GIA modelling suggest that in the long run the Forsmark site is situated above sea-level until the end of the 120 kyr period (Figure 5-2).

Situations with worst case scenarios for global sea-level rise up until year 2100, and the resulting effect on shoreline migration at the Forsmark site, are described in Section 5.2.3 and /Brydsten et al. 2009/.

Another expected effect of a global warming climate is that the increased precipitation in the Baltic drainage basin leads to increased surface runoff to the Baltic Sea, with less saline conditions in the Baltic as result, e.g. /BACC author team 2008/.

5.1.4 Permafrost evolution

In the *global warming case,* the evolution of permafrost is postponed 50 kyrs compared to the development in the *reference glacial cycle*. After the first 50 kyrs, the development of the temporal pattern and depths of permafrost is identical to the development in the *reference glacial cycle*. The permafrost starts to develop at around 60 kyrs after present. After that, progressively longer periods of permafrost conditions and shorter periods of temperate climate conditions occur, up until the glacial period at around 110 kyrs after present. The maximum permafrost depth is, in this climate case, the same as in the *reference glacial cycle*, ~260 m (with a maximum uncertainty interval down to ~460 m), but it occurs later, c. 100 kyrs after present. At the same time, the depth of the frozen ground is somewhat shallower than the permafrost depth, due to the pressure and salinity; ~245 m (with a maximum uncertainty interval down to ~420 m).

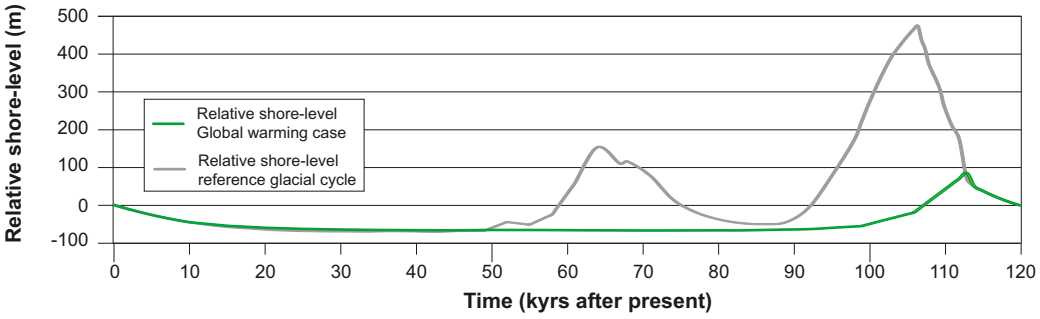

Figure 5-2. *Shore-level evolution at Forsmark for the global warming case. For comparison, the shore-level evolution for the reference glacial cycle (Section 4.5.2) is also shown. Negative numbers indicate that the area is situated above the contemporary sea-level. The curve was constructed by GIA modelling combined with results from observations of present-day uplift rates /Påsse 2001/. There are significant uncertainties in the future shore-level development, which, in contrast to what is shown in the figure, may result in a sea transgression at Forsmark during the first thousands of years of the evolution.*

5.1.5 Evolution of climate domains

The development of climate domains for the *global warming case* is shown in Figure 5-3 and 5-4. Given the assumption of a long initial period of temperate climate conditions, the temperate climate domain is dominating. Temperate conditions prevail for ~78,000 years (65% of the time), permafrost conditions for ~28,000 years (23% of the time), glacial conditions for ~11,000 years (9% of the time) and submerged conditions prevail for ~3,000 years (~3% of the time).

In this climate case, the climate at Forsmark is dominated by the initial ~60 kyr long period with temperate climate conditions. The variation in air temperature and precipitation is considerable within this temperate period, with air temperatures and precipitation rates considerably higher than at present in the early phase of the 120 kyr period. A detailed example of the characteristics of a climate dominated by global warming in Forsmark is given below, derived from the climate modelling study by /Kjellström et al. 2009b/. In time the high temperatures are slowly reduced, as a response to the slow decrease in atmospheric CO_2 concentrations. During the initial long temperate period, climate

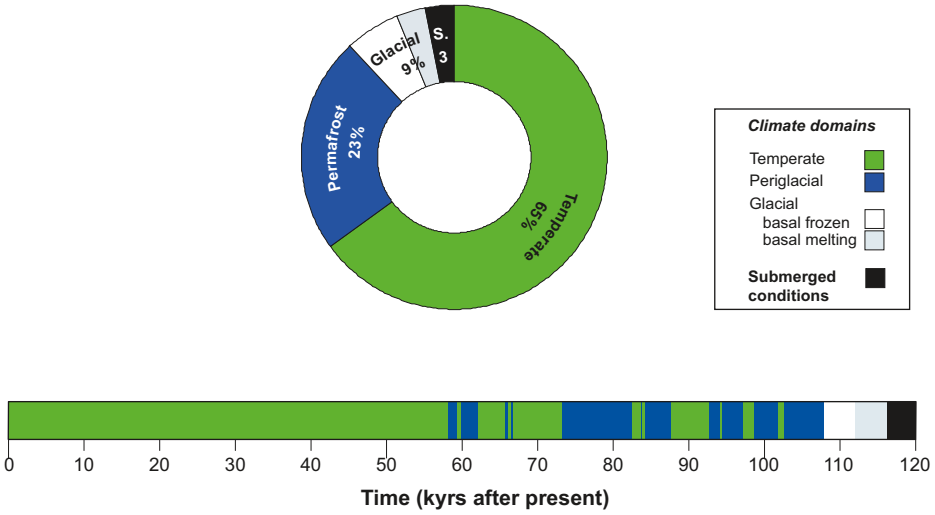

Figure 5-3. *Duration of climate domains at Forsmark, expressed as percentage of the total time for the global warming case. The bar below the pie chart shows the development of climate as a future time series of climate domains and submerged periods.*

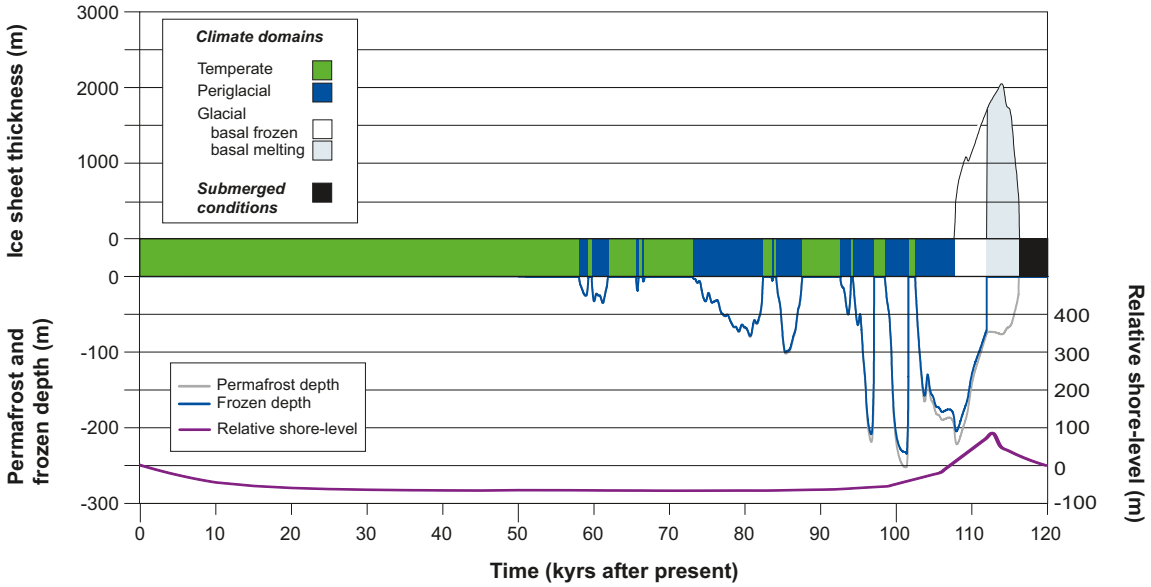

Figure 5-4. *Evolution of climate-related conditions at Forsmark as a time series of climate domains and submerged periods for the global warming case.*

varies within a range that is larger than that during the preceding parts of the Holocene. The length of the initial period of temperate climate domain should not be taken as a prediction or statement on how a future global warming climate will manifest itself. Under a future warming climate, this period could be shorter or longer than that described here. One such alternative case, with an even longer duration of temperate climate conditions, is described in the *extended global warming case*, see Section 5.2.

Between ~60 kyrs after present and more than 100 kyrs after present, periods of periglacial conditions with permafrost occur and get progressively more severe (Figure 5-4). The first major ice sheet advance in the *global warming case* occurs at around 110 kyrs after present. The maximum ice sheet thickness, around 2,000 m, occurrs at around 115 kyrs after present. Table 5-2 summarizes the sequence of events for the *global warming case*.

During the second half of the *global warming case* (Figure 5-3 and 5-4), climate varies within the same range as during the first part of the *reference glacial cycle* (Section 4.5), and consequently the climate-related processes act in the same way as in the *reference glacial cycle*. The global warming variant reduces the effects of climate-related processes of importance for repository safety that are related to cold climate conditions, i.e. in the periglacial- and glacial climate domains.

Another possible course of events within a generally warming global climate, is that the annual mean Atlantic Meridional Overturning Circulation (AMOC) in the North Atlantic is reduced, e.g. /Wu et al. 2004, IPCC 2007, Zickfeld et al. 2007, Drijfhout et al. 2008/. This would result in less heat being transported towards Fennoscandia by the North Atlantic Drift sea current, which in theory could lead to a regional cooling over Fennoscandia. However, in the global warming climate simulations by /Kjellström et al. 2009b (including erratum Feb 2010)/, the AMOC is reduced by up to 22% compared with the control period (1961–2000). These changes are not large enough to cause regional cooling over Fennoscandia. This results is in general agreement with the Atmosphere Ocean General Circulation Model (AOGCM) simulations of the 21st century as presented by /Meehl et al. 2007/. They show that the AOGCMs suggest a decreased intensity of the AMOC in the 21st century in the range from 0 to 50%. As in the simulations by /Kjellström et al. 2009b/, none of these AOGCM simulations indicates a cooling over Fennoscandia.

However, it is believed that the general warming would be considerably larger than such a cooling effect, resulting in net warming in Fennoscandia /IPCC 2007, Kjellström et al. 2009b/. Nevertheless, a case with a more severe permafrost development than in the *reference glacial cycle* is investigated in the *severe permafrost case* (Section 5.5).

Table 5-2. Sequence of climate-related events for the global warming case.

Event	Transition date	Climate domain
Deglaciation/ Start Holocene interglacial (locally defined)	–9,500 after present	–
Holocene interglacial	–	Temperate climate domain (incl. submerged conditions)
End of Holocene interglacial (locally defined)	c. 59,400 after present	–
Periglacial conditions (progressively longer periods of permafrost conditions)	–	Periglacial climate domain (incl. progressively shorter phases of temperate climate conditions)
End of periglacial conditions Start of glacial conditions	109,600 after present	–
First phase with glacial conditions	–	Glacial climate domain
Deglaciation at site, Start interstadial conditions	118,200 after present	–
Interstadial conditions (corresponding to MIS 3)	–	Periglacial climate domain (incl. submerged conditions and short temperate periods)

In the global warming climate variant, the warmer annual mean air temperatures do not affect repository safety functions. Furthermore, the increase in precipitation would not affect groundwater formation significantly, since, on a regional scale, the major part of the groundwater aquifer is filled already by present-day precipitation rates. Instead surface-runoff is increased, discussed further under the section on surface denudation. However, low groundwater salinity due to persistent infiltration of meteoric water during the prolonged temperate periods in the greenhouse variant may have a potential effect on the function of the clay buffer /SKB 2011/.

5.1.6 Surface denudation

The relative importance of different denudation processes, as well as the resulting amount of surface denudation, is expected to change in the *global warming case* as compared with the *reference glacial cycle*. The major difference between the *global warming case* and the *reference glacial cycle* is that glacial conditions with warm-based erosive ice only exist for a few thousands of years in the former case compared with around 24,000 years in the latter case. Glacial erosion is identified as the most important denudation process in the *reference glacial cycle*, with the largest contribution to the total denudation rate (Section 4.5.7). Since the duration of periods with glacial erosion is significantly shorter in the *global warming case*, the expected amount of glacial erosion is also significantly smaller in this case compared with the *reference glacial cycle*.

In the *global warming case*, the annual air temperature and precipitation are expected to increase in Forsmark during the initial part of the temperate climate domain, see above. For the first tens of thousands of years of this climate case, increased precipitation results in increased surface runoff, see above and /Kjellström et al. 2009b/, which probably leads to increased fluvial erosion. In this global warming variant, with 50,000 initial extra years of temperate climate conditions, the effect of this increased fluvial erosion is most probably significantly smaller than the effect of the anticipated decrease in glacial erosion. The increased fluvial erosion most probably has a minor impact on total denudation rates for this climate case. Even if the fluvial erosion process were to have been large, the resulting amount of fluvial erosion is limited by the fact that fluvial erosion cannot erode deeper than the level of the Baltic Sea and that the site is located at sea-level today. The period of increased precipitation is accompanied by a slowly regressing, stationary or even transgressing sea-level (Section 5.1.3), which further precludes deep fluvial erosion during the period influenced by increased precipitation.

Increased temperatures in a global warming climate could lead to somewhat higher weathering rates. Some studies suggest that such climate change feedbacks may be weaker than previously thought and in fact could even accelerate the recovery from fossil fuel CO_2 perturbations /Lenton and Britton 2006/. However, given the large expected reduction in glacial erosion, and a considerably smaller expected effect of increased weathering rates, the feedback mechanisms between climate, weathering and vegetation, are not further treated in the present report.

Other, minor, differences compared with the *reference glacial cycle* relate to periglacial conditions, which have a shorter duration in this climate case than in the *reference glacial cycle*. Aeolian erosion is therefore expected to contribute even less to the total denudation in the global warming variant.

All in all, the relative importance of various erosion and denudation processes are changed in the *global warming case*, with the overall result that total denudation is more restricted in this climate case than in the *reference glacial cycle*. The one process that could give a relevant contribution to increased denudation, fluvial erosion, is limited by the near-sea-level location of the site. The *reference glacial cycle* is judged as resulting in a larger surface denudation that the *global warming case*, mainly because of the reduction in duration of periods with the most efficient denudation process (glacial erosion), as identified in Section 3.5.4.

A climate case with an estimated larger amount of surface denudation than in the *reference glacial cycle* is described in the *extended ice sheet duration case* (Section 5.3).

5.1.7 Exemplified climate conditions for the global warming case

In order to give a detailed example of how a climate influenced by global warming could appear in Forsmark, climate modelling was used to describe a situation with a temperate climate with increased greenhouse gas concentrations in the atmosphere (750 ppm), a few thousands of years from now /Kjellström et al. 2009b, including erratum Feb 2010/. According to /Lenton et al. 2006/, a 750 ppm CO_2 level still means that all "conventional" fossil fuel resources (including coal, oil, and gas) need not have been used.

In the climate modelling simulations, a complete loss of the Greenland ice sheet was assumed. Since this deglaciation is a process that may take up to a couple of thousand years, it is very uncertain what other climate-related conditions may be prevailing at that time. According to climate-change scenarios from simulations with GCMs, irreversible melting of the Greenland ice sheet may start at a time when the global mean temperature has increased by about 1.9–5.1°C above today's conditions and the temperature over Greenland has increased by about 3–6.5°C /Gregory et al. 2004, Gregory and Huybrechts 2006/. Recent studies indicate that the ice sheet might be more sensitive to increased concentrations of atmospheric greenhouse gases than previously thought /Stone et al. 2010a, b/.

Increases in temperature large enough for making the Greenland ice sheet collapse are projected by GCMs within the 21st century for some emission scenarios /Meehl et al. 2007/. If such high temperatures persist for a long enough time (several hundreds to a couple of thousand years depending on the degree of warming) the Greenland ice sheet will eventually collapse and disappear. In this time perspective, CO_2 levels will start to decrease again (when emissions cease). Nevertheless, at one thousand years from now, the atmospheric CO_2 concentrations will remain considerably higher than today /Lenton et al. 2006/. Here, the time period for the global warming simulation was chosen as a compromise between a high level of CO_2 (needed to simulate a warm climate that melts the Greenland ice sheet), and a not too high level (that remains in the atmosphere a long time after the emissions have ceased). Thus, the simulations can be considered as representative of the climate a few thousand years into the future after a complete melting of the Greenland ice sheet and a partial recovery towards lower background CO_2 concentrations.

For these simulations, a global GCM model (Community Climate System Model version 3, CCSM3), a regional climate model (Rossby Centre Regional Climate Model RCA 3) and a vegetation model (LPJ-GUESS) were used. For the simulations performed and analyzed within this study, atmospheric and land components of the CCSM3 used a grid spacing of approximately 2.8° in latitude and longitude. The vertical resolution is 26 levels in the atmosphere and 40 levels extending to 5.5-km depth in the ocean. The regional climate model used a horizontal resolution of 50 km and a time resolution of 30 minutes. For details on the models, how they were employed, and a discussion on model uncertainties, see /Kjellström et al. 2009b/. The simulation of the global warming climate used a CO_2 concentration in the atmosphere of 750 ppm. In order to include the effect of also other greenhouse gases in the RCA 3 model, a CO2 equivalent value of 841 ppm was used /Kjellström et al. 2009b/. For a detailed description of the assumptions made in the modelling process, model forcing and initial conditions (such as astronomical and solar forcing, concentration of greenhouse gases and aerosols in the atmosphere, extents of ice sheets, distribution of land and sea, topography and vegetation), also see /Kjellström et al. 2009b/.

The simulated global warming climate should not be taken as a prediction or prognosis on how a future global warming climate will manifest itself. Instead, it is *a detailed example* of how such a climate may be manifested. Given another model forcing, for instance using a lower or higher CO_2 concentration, the resulting climate would have been different. However, the model results are useful for exemplifying a climate affected by global warming, also for Forsmark. In this context it is worth noting that the results of /Kjellström et al. 2009b/ resemble those for many of the scenarios for the 21st century from the climate model intercomparison project (CMIP3) /Meehl et al. 2007/. For a detailed discussion and comparison with other climate model results, see /Kjellström et al. 2009b, Section 3.1.4/.

Global climate

Figure 5-5 shows the simulated global warming climate from the GCM simulations. Seasonal mean changes in temperature in the global warming simulation as compared with a simulation of the present (1961–2000) climate are also shown in Figure 5-5. The removal of the Greenland ice sheet

produces a strong heating of up to 17°C over Greenland in both summer and winter. This heating is primarily due to a combination of i) the lowering of the surface by up to 3,000 m and ii) the decrease in surface albedo and changes in heat fluxes between the atmosphere and the ground produced by the replacement of the glacier ice surface by tundra /Kjellström et al. 2009b/. Similar to all greenhouse warming scenarios presented in the IPCC AR4 report /Meehl et al. 2007/, the Arctic region exhibits strong heating by up to 15°C in winter (due to a substantial decrease in the Arctic sea-ice cover and a decrease in the snow cover). The seasonal mean temperature is up to 5°C warmer in summer and up to 7.5°C warmer in winter over Fennoscandia in the global warming simulation as compared with the simulation of the present climate. Seasonal mean summer temperatures in Sweden vary in the range 12–18°C and winter temperatures vary in the range 0–6°C. Sensitivity to changes in vegetation in these GCM simulations is discussed in /Kjellström et al. 2009b/.

The change in precipitation in the global warming simulation as compared with the simulation of the present climate is also shown in Figure 5-5. The removal of the Greenland ice sheet leads to a 25% decrease in precipitation in particular over south-eastern Greenland in both summer and winter, indicating that much of the precipitation in that area in today's climate is triggered by the steep ice sheet topography. Similar to all greenhouse-warming scenarios presented in the IPCC AR4 report /Meehl et al. 2007/, precipitation is increased over mid-latitude Northern Hemisphere continents and the Arctic. For Fennoscandia there is an increase in precipitation, most notably in the north.

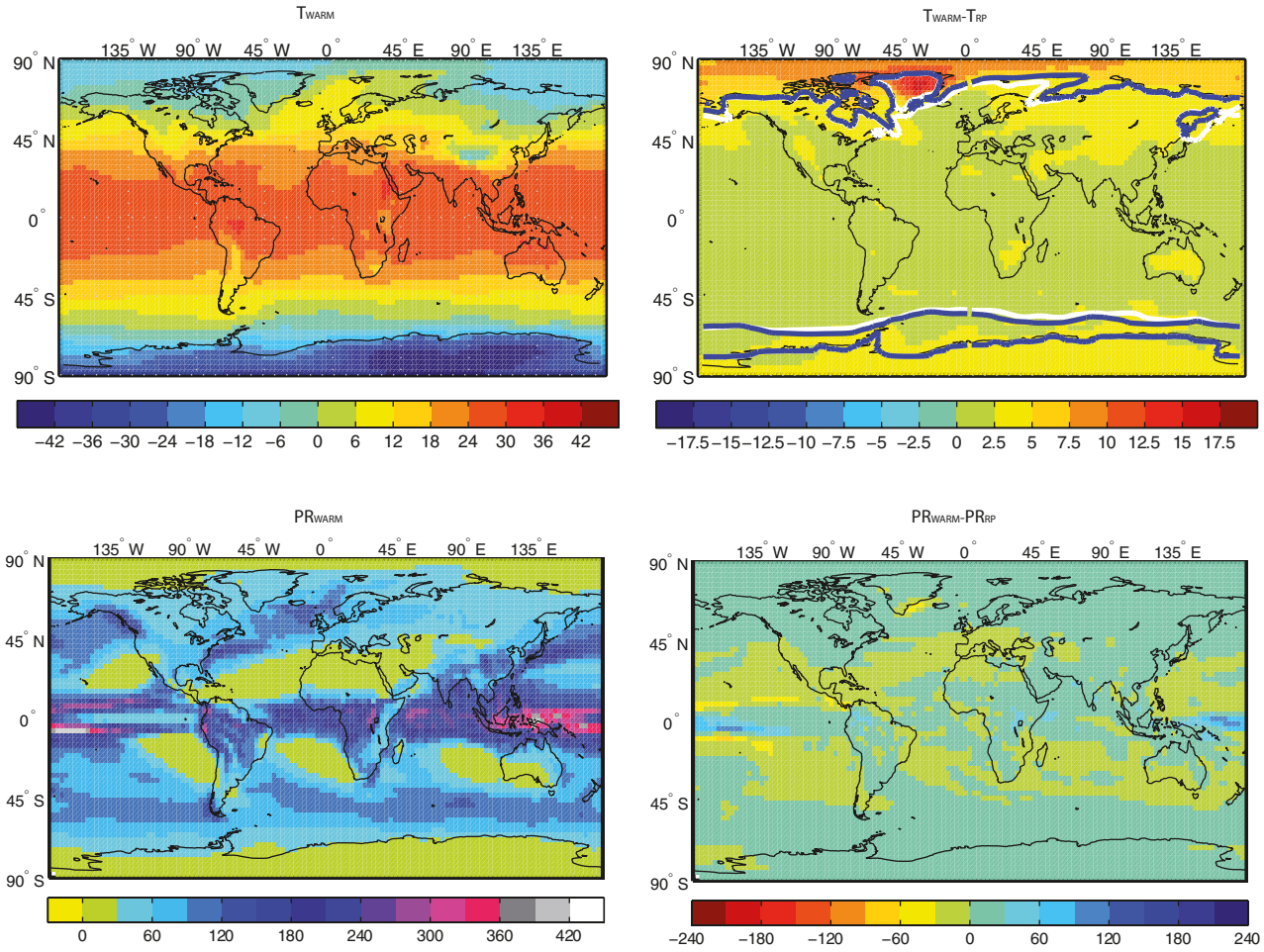

Figure 5-5. *Upper panels: Simulated near-surface air temperature in the global warming simulation (T_{WARM}) and the difference compared with the simulated present climate (T_{RP}) (1961–2000). Units are °C. Also shown by isolines in the rightmost panels is the extent of sea-ice in the simulation of the present climate (white) and in the global warming simulation (blue). Lower panels: Precipitation in the global warming simulation (PR_{WARM}) and the difference compared with the simulated present climate (PR_{RP}). Units are mm/month. From /Kjellström et al. 2009b/.*

Climate in Europe and Sweden

The regional climate model was then used to downscale the model results of the global climate model in order to obtain higher resolution data over Europe and Sweden. The resulting climate over Europe was used to produce a new vegetation distribution with the vegetation model. This vegetation was in turn, used as input to the regional climate model, to produce a climate in line with the new vegetation. An evaluation of the results from this iterative process is given in /Kjellström et al. 2009b/. Figures 5-6, 5-7 and 5-8 present selected results on temperature and precipitation from the regional modelling.

In the regional global warming simulation, the warming compared with the simulated present climate (1961–2000) is strongest over northern Europe in winter. The simulated temperature increase for the coldest month is more than 5°C in northern Fennoscandia (Figure 5-6, second row, middle panel). In southern Europe the warming is stronger in summer, where the temperature of the warmest month increases with more than 4°C in large areas (Figure 5-6, second row, left panel). The stronger warming in the areas of the Bothnian Bay, Bothnian Sea and in the Gulf of Finland in summer in this experiment is due to the land uplift converting sea to land in those areas. The same phenomenon is also responsible for the weaker warming in these areas in winter. Differences between the results of the global and regional model simulations are discussed in /Kjellström et al. 2009b/.

As expected, the simulated climate of the *global warming case* clearly resembles many of the scenarios for the 21st century from the climate model intercomparison project (CMIP3) as presented by IPCC /Meehl et al. 2007/. Seasonal mean changes in precipitation and temperature from a large number of the CMIP3 scenarios have been analysed for Sweden by /Lind and Kjellström 2008/.

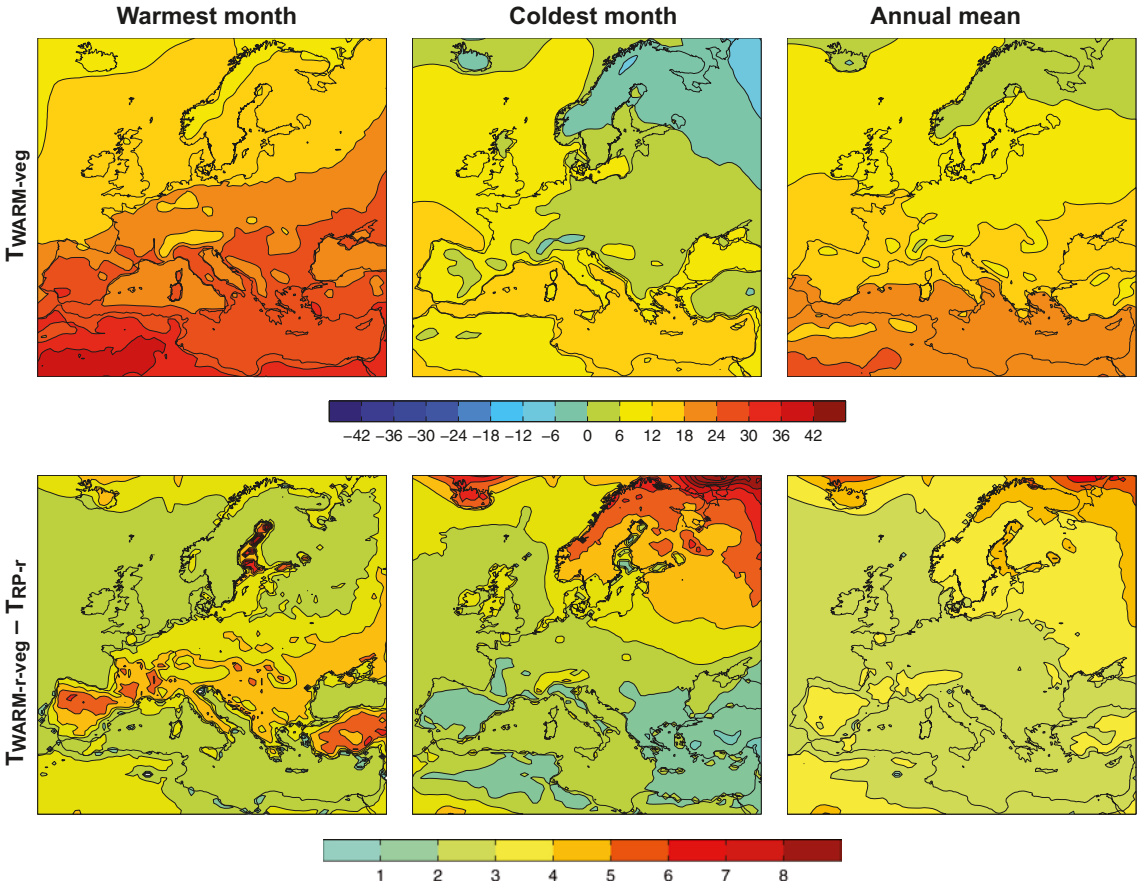

Figure 5-6. *Mean near-surface air temperatures of the warmest month, coldest month and annual mean in the global warming simulation with improved vegetation (upper row). Also shown are differences between the global warming simulation and the simulations of the present climate (RP-r) (1961–2000) (lower row). Units are °C. From /Kjellström et al. 2009b/.*

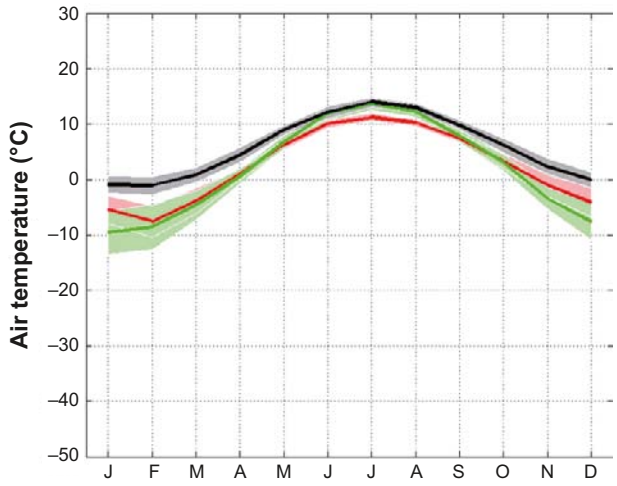

Figure 5-7. *Annual cycle of temperature for Sweden in the global warming (black line) and simulated present climate (1961–2000) (red line). Also shown is the CRU observational data from 1961–1990 (green line). Shaded areas in corresponding colours indicate the ±1 standard deviation calculated for the range of individual monthly averages in the three data sets. From /Kjellström et al. 2009b/.*

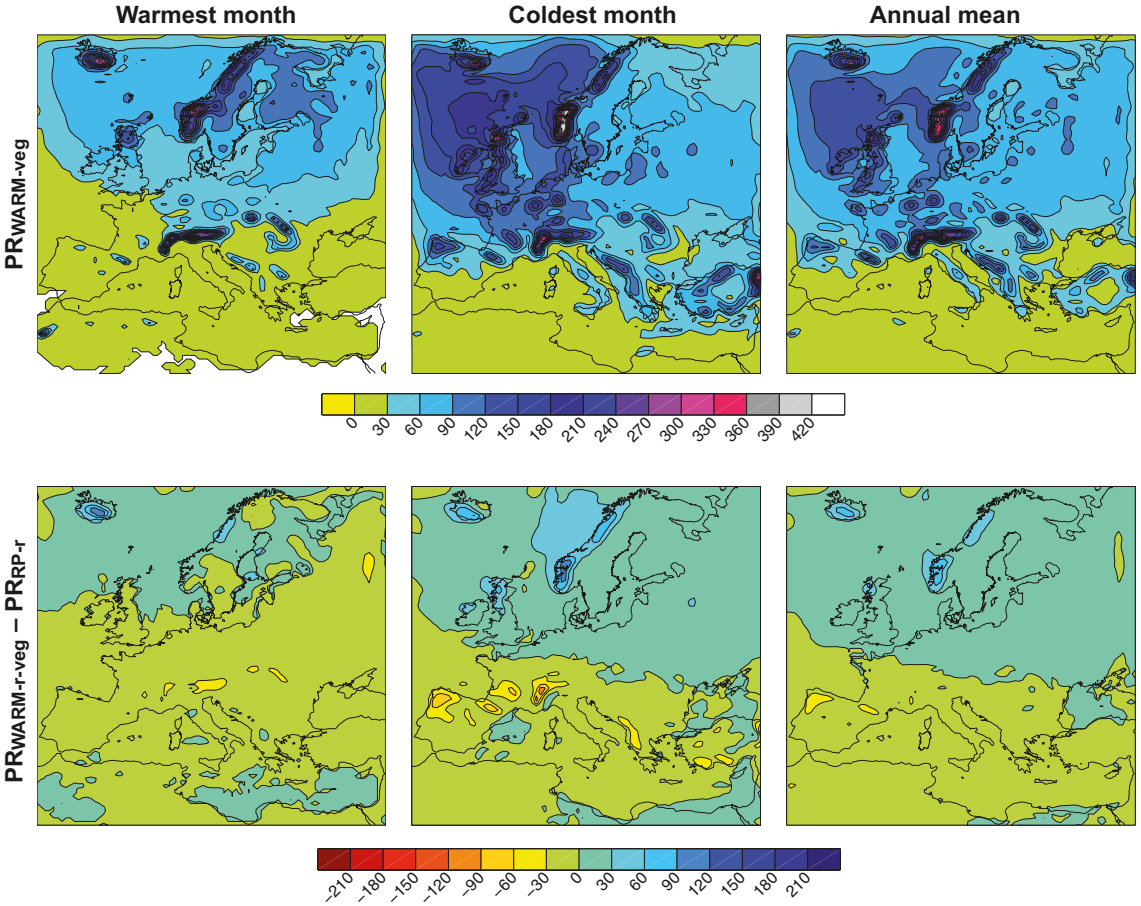

Figure 5-8. *Mean precipitation of the warmest month, coldest month and annual mean in the global warming simulation. Also shown are differences between the global warming simulation and the simulated present climate (RP-r) (1961–2000). Units are mm/month. From /Kjellström et al. 2009b/.*

/Lind and Kjellström 2008/ report increased temperatures of 4–6°C by the end of the 21st century in northern Sweden and about 3°C in southern Sweden relative to the 1961–1990 period. The corresponding increases in precipitation are about 25% in the north and only a small average increase in the south albeit with a large spread between the models. These changes are annual averages over a range of different emission scenarios. As noted in /Kjellström et al. 2009b/, the uncertainties related to the future forcing in the global warming simulation are large and substantially lower or higher greenhouse-gas concentrations than the one used cannot be ruled out. Considering the large spread between the emission scenarios and the uncertainty related to the climate models one cannot rule out that a future warmer climate can be warmer than the one simulated in /Kjellström et al. 2009b/. However, the high-end emission scenarios (A1FI and A2) /Nakićenović and Swart 2000/ may have CO_2 concentrations that are too high to be sustained over the long period that it takes to melt the Greenland ice sheet, which was part of the set-up here. But, even so, the CO_2 concentrations may very well reach levels high enough to sustain long-term (i.e. multi-century) temperature anomalies exceeding those simulated here.

Clearly, the results from the regional model gives a climate change signal that is within the range defined by the global model results for southern Sweden compiled in /Lind and Kjellström 2008/, see Figure 3-15 in /Kjellström et al. 2009b/. The climate change signal for entire Sweden is +4°C in winter and +3.5°C in summer and the corresponding numbers for precipitation are +37% in winter and no change (±0%) in summer. Further model results and discussion for all of Sweden from the global- and regional climate modelling and from the vegetation modelling are presented in /Kjellström et al. 2009b/.

The vegetation simulated by LPJ-GUESS for the global warming climate is reported in the context of the biosphere studies /SKB 2010d/.

Here it is also worth noting that the Greenland summer temperatures are well above 0°C, clearly indicating that there is no chance of ice sheet regeneration under these circumstances once the ice has been removed. A similar result was obtained previously for the pre-industrial climate when the Greenland ice sheet was removed in the Hadley Centre HadCM3 coupled model /Toniazzo et al. 2004/.

Climate in the Forsmark region

In the last step in the climate modelling study of the global warming climate, climatological data for the Forsmark region were extracted from the regional modelling. Figure 5-9 shows the grid boxes used for extraction of data. Information was extracted from the grid point located closest to the Forsmark site. As there is a high degree of spatial heterogeneity in land-sea distribution and topography, information from the surrounding eight grid boxes were also used to discuss uncertainties related to these inhomogeneities.

In addition to the results from the modelled case, data from the simulation of the present climate (1961–2000) (RP-r) and from the CRU observations representing conditions in the late 20th century are also shown for the Forsmark region (Figure 5-10). In addition to this, results from three other climate-change simulations with RCA3 for the 21st century as described in /Persson et al. 2007/ are also shown. These simulations follow the A2, A1B and B2 emission scenarios /Nakićenović and Swart 2000/. The A1B emission scenario leads to greenhouse gas concentrations close to the one in the *global warming case* by the end of the 21st century. The two other scenarios have more (A2) or less (B2) emissions than the A1B scenario.

The fairly small annual temperature range in the present climate is even smaller in the future global warming climate for the Forsmark region (Figure 5-10, upper row, first column). This reduction in the seasonal cycle of temperature is a consequence of the future warming being stronger in winter than in summer. The snow season is much shorter, or even totally absent, in the warm climate. The seasonality of the runoff is closely connected to the presence or absence of snow. In the warmer future climate, the spring peak in runoff is absent and there is now a more widespread wintertime maximum related to the large amounts of precipitation for that season.

In the global warming simulation, the spread in the presented variables due to differences in geographical location is reduced compared with that in the simulation of the present climate. This is partly a result of the land uplift turning two of the Baltic Sea grid boxes east of Forsmark into land

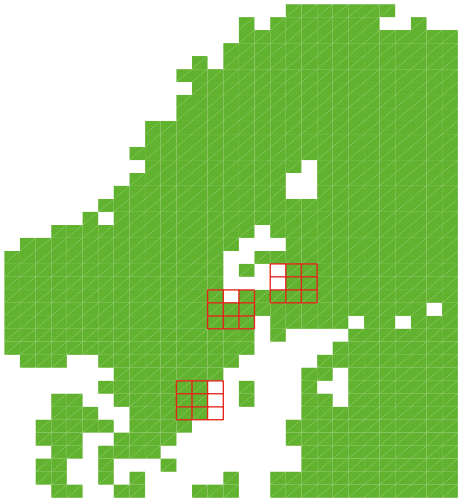

Figure 5-9. *Land (green) sea extent (white) in the regional climate model in the Fennoscandian region used for the global warming climate simulation. The 3·3-grids represent grid boxes covering the Forsmark, Oskarshamn and Olkiluoto sites (centre box) and the eight surrounding boxes. Grid boxes with a land fraction lower than 20% are not filled. Results from Oskarshamn and Olkiluoto are presented in /Kjellström et al. 2009b/.*

in the *global warming case*. Thereby, the surrounding area becomes more homogeneous than in the present-day situation. When including also the uncertainty ranges based on results from the three other climate simulations for the 21st century, also simulated with RCA3 /Persson et al. 2007/, it is seen that the weakening of the annual cycle is a robust trend when going to a warmer climate.

50-year averages values from the regional global warming climate simulation show that the annual mean air temperature in the Forsmark region is +8.3°C. This is a temperature increase of 3.6°C compared with the simulated present climate (1961–2000). The future warming is stronger in winter than in summer and there is an associated reduction in the seasonal cycle amplitude in temperature. The mean annual precipitation in the region is 804 mm, which is an increase of 138 mm (or 20%) compared with the simulated present climate. Most of the precipitation increase occurs during the winter season (DJF). The snow season is much shorter than at present or even totally absent (Figure 5-10). Finally, the annual surface runoff is 337 mm in this exemplified global warming climate, which is an increase of 162 mm compared with the present climate. Given the uncertainties and assumptions used in the climate modelling, and the CO_2 level chosen, the model results thus show that the global warming climate in the Forsmark region, may be characterized by a clearly warmer and wetter climate than at present, and also that the surface runoff is significantly increased.

The major uncertainties in the climate simulation are related to uncertainties in forcing, model formulation and natural variability. These uncertainty aspects are discussed in detail in /Kjellström et al. 2009b/.

Another recent study that focussed on regional climate modelling is /Kjellström et al. 2010b/ where changes in seasonal mean temperature, precipitation and wind over Europe were studied in an ensemble of 16 regional climate model simulations for 1961–2100. The study used the A1B emission scenario /Nakićenović and Swart 2000/ in which the CO_2 equivalents in RCA 3 were set to 902 ppm, somewhat higher than the 841 ppm used in /Kjellström et al. 2009b/. Six-member ensemble means of winter season (DJF) conditions suggest an increase in temperature by c. 4°C and precipitation by 20–30% in south central Sweden, including the Forsmark region, by year 2100. Corresponding model ensemble means for the summer season (JJA) indicate an air temperature increase of 2–3°C and a precipitation increase of c. 10%. The study also shows that the climate-change signal gets stronger the larger the forcing becomes, i.e. more greenhouse-gas emissions leads to a stronger warming and larger changes in precipitation. The results of the A1B-scenario-simulations are thus in line with the detailed results described above from /Kjellström et al. 2009b/. Similar results were obtained also in the SWECLIM project /Rummukainen 2003, Tjernström et al. 2003/. Other modelling results that give similar pictures of future global warming climates are reported in /BIOCLIM 2003, Meehl et al. 2007 and Lind and Kjellström 2008/.

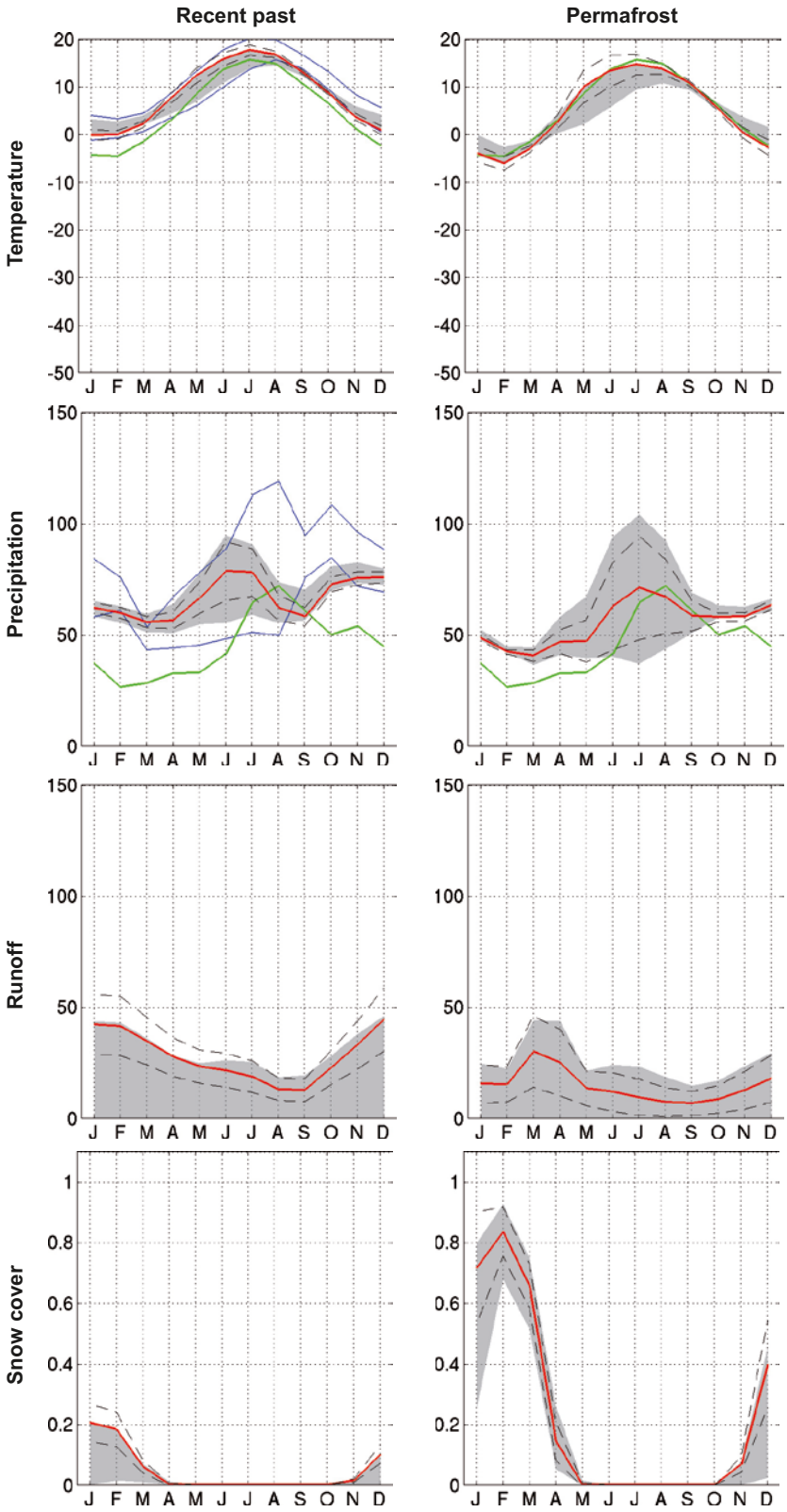

Figure 5-10. *Simulated seasonal cycles of temperature (°C), precipitation (mm/month), runoff (mm/month) and snow fraction (dimensionless ranging from 0 to 1) at the grid box closest to the Forsmark site (red line). The spatial variability in the 3·3-grid (Figure 5-9) is displayed with the dashed lines representing ±1 standard deviation calculated from the 9 grid boxes, and the grey area representing the absolute maximum and minimum, of the 9 grid boxes. The green line for temperature and precipitation is the observed seasonal cycle from the CRU data set in the period 1961–1990. In the global warming case (left column), an additional uncertainty range defined by ±1 standard deviation of the data calculated from the 9 surrounding grid boxes from three additional simulations for the 21st century with RCA3 is shown with blue full lines. From /Kjellström et al. 2009b/.*

5.2 Extended global warming case

5.2.1 Background

There is a large range of potential future climate developments when considering the combined effect of natural climate variability and anthropogenic climate change, e.g. /IPCC 2007, Archer and Brovkin 2008, Kjellström et al. 2010b/ and references therein. One such case is the *global warming case* described in Section 5.1. In order to cover a reasonably broad array of future climate developments based on present knowledge, an *extended global warming case* is also included in the SR-Site safety assessment. This case describes a future climate heavily influenced by anthropogenic emissions of greenhouse gases, resulting in strong global warming. In this case, all fossil fuel sources are envisaged to have been used, resulting in that peak CO_2 levels might reach above 1,000 ppm, cf. /Rahmstorf and Ganopolski 1999, IPCC 2007/, before the CO_2 concentration again start to decline. One consequence of this, together with the known future insolation changes from the orbital cycles, is the possibility of a very long duration of the present interglacial period, prior to the onset of ice sheet growth.

One case of long-lasting global warming is described in /Archer and Ganopolski 2005/, suggesting that a release of 1,000 Gton of greenhouse gases together with orbital variations would result in the present interglacial persisting for another 130 kyrs, before ice sheet growth commences on the Northern Hemisphere. A larger release is suggested to results in an even longer interglacial. Naturally, such estimates of the length of the present interglacial are associated with very large uncertainties. They relate both to the uncertain amount of future greenhouse gases in the atmosphere, and to poorly known feed-back mechanisms in the ice sheet-, climate-, vegetation- and carbon cycle system, and how, or if, these mechanisms are implemented in the models.

In order to cover a reasonable wide range of possibilities, an additional 100 kyrs of temperate climate conditions is added prior to the slow onset of a *reference glacial cycle* for the *extended global warming case*. This results in a temporal development of climate and ice sheet growth very similar to the case with 130 kyrs until the next glaciation as described by /Archer and Ganopolski 2005/, see below, and it is also in broad agreement with results in /BIOCLIM 2003/.

For a more detailed motivation for addressing climate cases of global warming and a long interglacial, see Section 5.1.1.

5.2.2 Ice sheet evolution

This climate case results in there being no ice sheets present at the Forsmark site during the coming 120 kyrs. The first glacial conditions at Forsmark occur at ~160 kyrs (158 kyrs) after present.

5.2.3 Shore-level evolution

Given the envisaged strong global warming for the *extended global warming case*, also the sea-level response to the warming is envisaged to be strong. And just as in the *global warming case*, there are significant uncertainties in the estimated sea-level changes and associated shore-level displacement.

Sea-level rise up to year 2100

In order to investigate worst-case scenarios for sea-level and shore-level displacement at Forsmark for year 2100, /Brydsten et al. 2009/ conducted a study that included estimates of global sea-level rise, local isostasy (e.g. ongoing isostatic rebound) and their trends, as well as regional (North Sea) and local (Baltic Sea) annual extremes of today's sea-levels and those in year 2100. The aim of the study was to illustrate the location of the shoreline at Forsmark if applying worst-case assumptions on global- and local sea-level from the literature, together with short-term effects that increase the shore-level during severe storms. The most uncertain factor of the various input parameters is the future global sea-level change, and specifically the contribution by ice sheets (see Section 5.1.3). Possible future developments on global sea-level rise were included from /IPCC 2007, Rahmstorf 2007, Pfeffer et al. 2008/.

/Rahmstorf 2007/ estimated the maximum global sea-level rise by year 2100 to be +138 cm relative to the year 1990. In the study by /Pfeffer et al. 2008/, the Greenland and Antarctic ice sheet response to global warming is estimated and included. Also in this study the large uncertainty in sea-level rise is emphasised. /Pfeffer et al. 2008/ points to two probable cases of global sea-level rises by year 2100 (relative to the level year 2000) amounting to +79 and +83 cm, respectively. /Pfeffer et al. 2008/ also describe a less probable, but still possible, worst case where a calculated *maximum* ice discharge from the Greenland and West Antarctic ice sheets result in a global sea-level rise of +200 cm by year 2100, i.e. +141 cm above the /IPCC 2007/ estimate (that excluded this process).

According to model simulations reported by /IPCC 2007/, the North Sea is expected to have a +20 cm higher level than the global mean on a permanent basis, which is termed *interregional* distribution. The *intraregional* distribution within the North Sea area has been modelled by /Woth et al. 2006/ and amounts at most to +7 cm in the Skagerrak. In order to estimate the worst case, this episodic contribution was also included, even if it is unlikely that it would occur with sufficient duration and at times that could accentuate extreme sea-levels in the Baltic Sea.

The global sea-level rise is locally compensated for by the glacial isostatic rebound that occurs at Forsmark. With the shore-level displacement equation for the site /Söderbäck 2008/, the future course of the isostasy can be calculated by subtracting the eustasy from the shore-level displacement. In this way Rahmstorf's prediction of future global sea-level rise was adjusted for local isostasy (Figure 5-11).

Besides the changing global eustasy and local isostasy, sea-level variations of short duration occur due to temporary weather systems (atmospheric pressure, winds etc). The highest sea-level measured in Forsmark occurred in 2004 and amounted to +144 cm above mean sea-level, equivalent to +141 in the height system RH70. This value was included in the assessment of extreme shore line values for Forsmark.

Future climate change may also lead to increasing wind speeds. This means that the local sea-level rises generated by weather systems in the future may be higher than the values measured so far, a process also accounted for in the study by /Brydsten et al. 2009/. For a more detailed description of the methodology and handling of global sea-level, isostasy, and for a discussion on return periods and storm surges at Forsmark, see /Brydsten et al. 2009/.

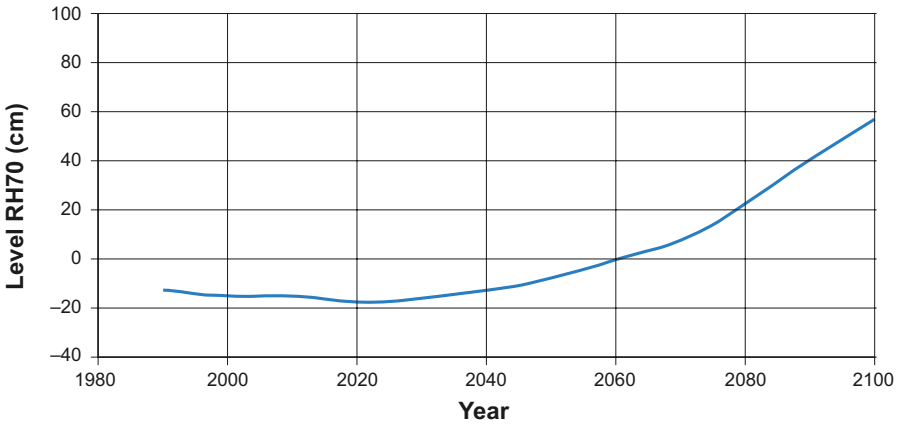

Figure 5-11. *Prediction of sea-level according to /Rahmstorf 2007/ adjusted for local isostasy at Forsmark and corrected to the height system RH70. Modified from /Brydsten et al. 2009/.*

The calculated extreme values on possible future sea-level elevations for Forsmark in the year 2100 are summarized in Table 5-3. For a description of the contribution from local variation in North Sea and Baltic Sea, see /Brydsten et al. 2009/. The maximum sea-level during storm events in year 2100, based on the maximum sea-level rise estimate by /Rahmstorf 2007/, is +254 cm. The uncertainty in this value is large. In addition to the estimate of maximum global sea-level change by /Rahmstorf 2007/, the /IPCC 2007/ and /Pfeffer et al. 2008/ global sea-level estimates may be used to illustrate the uncertainties in future sea-level rise.

/IPCC 2007/ predicted a 79 cm lower sea-level compared with /Rahmstorf 2007/ by year 2100, whereas /Pfeffer et al. 2008/ estimated a maximum theoretical global sea-level value 62 cm higher than /Rahmstorf 2007/. Using the /IPCC 2007/ and /Pfeffer et al. 2008/ values, the resultant total sea-level in 2100 at Forsmark, with unchanged values for the other constituent processes, is seen in Table 5-4. Figure 5-12 summarizes the various contributions to extreme sea-levels at Forsmark for year 2100. In relation to /Rahmstorf's 2007/ maximum value for year 2100 (+138 cm), the difference relative to the /IPCC's 2007/ estimate (–79 cm) is similar to the difference relative to the maximum value given by /Pfeffer et al. 2008/ (+62 cm). These differences can therefore serve as a measure of the present-day uncertainty of future global sea-level rise (see Figure 5-12).

Figures 5-13 to 5-15 show which areas will be flooded at Forsmark if the sea-level, during short events, reaches +175, 254 and 316 cm above the reference level in the height system RH70 (Table 5-4). The consequences are relatively small at a level of +175 cm, whereas more serious consequences result from levels of +254 cm and +316 cm.

The estimates on maximum sea-levels presented in Table 5-4 and Figure 5-12 to 5-15 describe what might happen due to the cumulative worst-case effects of possible future processes spanning over the global, regional and local scales. The numbers apply for occasions of short duration during heavy storms. The selected processes are characterized by the fact that they are unfavourable as regards a possible raised water level, but they can at present not be dismissed as unrealistic. However, it should again be emphasised that research on e.g. possible future global sea-level rise is in a very intensive phase, and that major uncertainties still exist in this field. Nevertheless, these uncertainties should be considered when planning to build near the present day coast-line.

Table 5-3. Maximum sea-level at Forsmark in year 2100 during storm events, based on e.g. the maximum global sea-level rise as estimated by /Rahmstorf 2007/.

Process	Forsmark	Source
Global eustasy	138	/Rahmstorf 2007/
Local isostasy	–82	/Söderbäck ed. 2008/
Global variation in North Sea	20	/IPCC 2007)
Local variation in North Sea	7	/Woth et al. 2006/
Local variation in Baltic Sea	171	/Meier 2006 and Nerheim 2008/
Total 2100	254	

Table 5-4. Resultant maximum sea-levels (cm in RH70) at Forsmark in the year 2100 based on three different estimates of future global sea-level rise.

Source	Forsmark
/IPCC 2007/	175
/Rahmstorf 2007/	254
/Pfeffer et al. 2008/	316

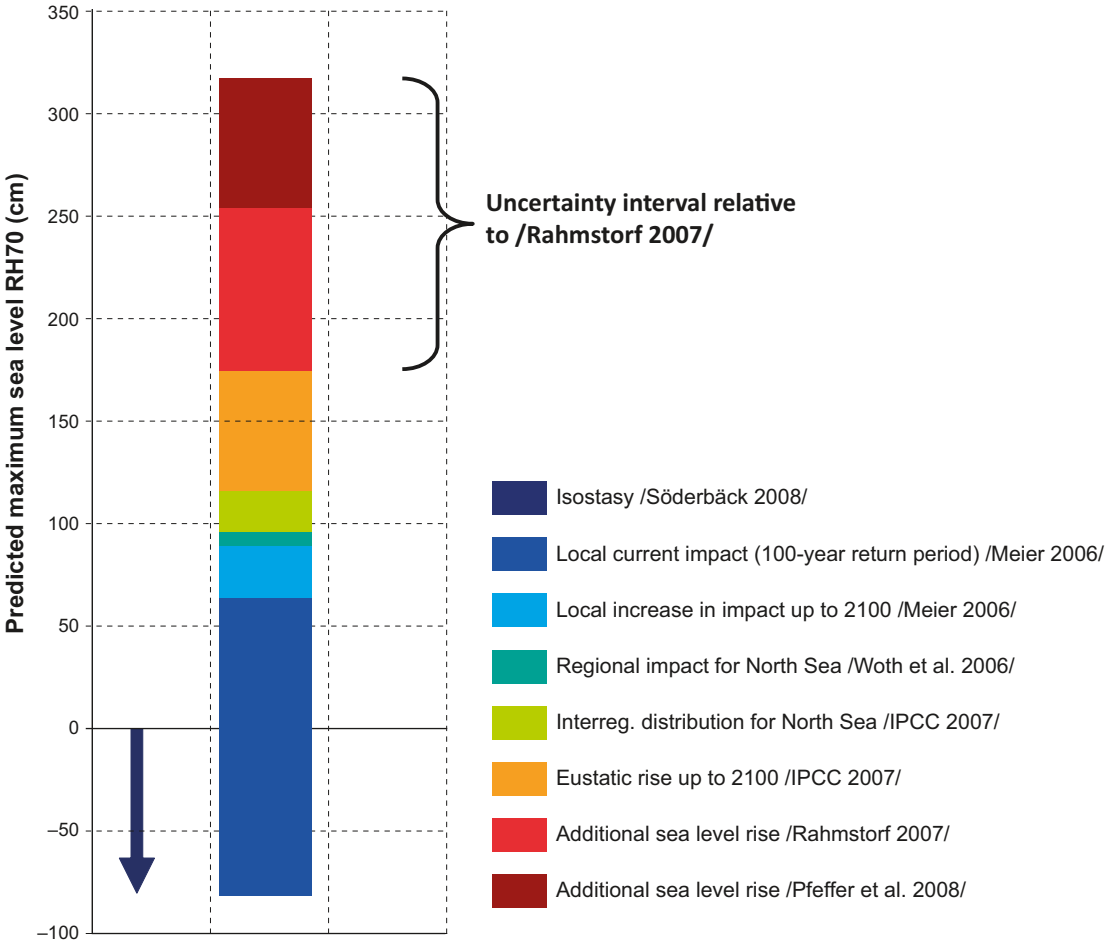

Figure 5-12. *Graphic presentation of the compilation of estimated contributions to possible extreme sea-level at Forsmark in year 2100. The isostasy is indicated by downward arrows according to the colour scale. Elevations are expressed in the height system RH70. A first-order expression of uncertainty in global sea-level rise is indicated by a bracket centred on the maximum estimate of /Rahmstorf 2007/, which corresponds to the top edge of the red bar. The numbers apply for the worst possible case in regard to future sea-level rise, and for occasions of short duration during heavy storms. In this context it is important to note that the data on which these estimates are based are the subject of intense research, and that revisions are therefore to be expected.*

Sea-level rise beyond year 2100

In the present climate case, air temperatures are raised more than in the *global warming case*. The Greenland ice sheet is envisaged to experience a total collapse, contributing 7.3 m to global mean sea level rise /Bamber et al. 2001/. Also a West Antarctic ice sheet collapse is envisaged included in this case, contributing with 3.3 m of global mean sea level rise /Bamber et al. 2009/. The net results of the collapse of the Greenland ice sheet may be a ±0 mm/yr sea level change around Fennoscandia /Milne et al. 2009/, whereas the collapse of the West Antarctic ice sheet could result in a sea level rise around Fennoscandia of ~3 m /Bamber et al. 2009/. A 0.5 m sea level contribution from melting of all glaciers and ice caps are also envisaged for this case. The thermosteric sea level rise is larger in this case than in the *global warming case*, due to the larger temperature increase, amounting to several metres.

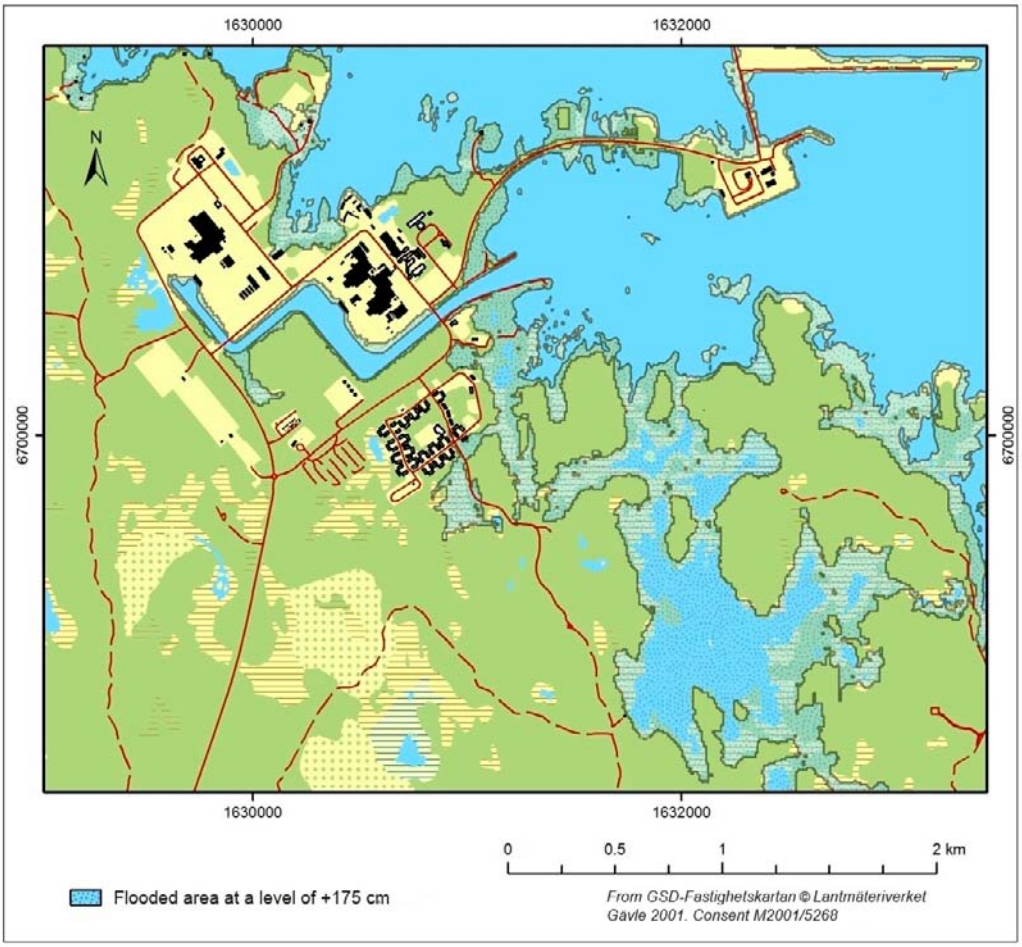

Figure 5-13. *Area at risk of flooding at an extreme level of +175 cm in Forsmark in year 2100 AD. Note that these results show extreme situations when assumed worst cases from the present scientific literature are combined with local effects also set to pessimistic values. From /Brydsten et al. 2009/.*

Given these contributions and the assumed extreme global warming, equilibrium sea-levels at Forsmark of up to around 10 metres may be possible. This results in an initial period with a sea-level rising faster than the isostatic uplift at the Forsmark site, resulting in submerged conditions for several thousands of years. Following the results of /Rohling et al. 2009/, that equilibrium sea-levels for the present day CO_2 concentration could be reached within the next two to five millennia, submerged conditions are somewhat arbitrarily set to prevail for 10 kyrs in this *extended global warming case*. The duration of this initial submerged period is uncertain; it could be shorter or longer than this.

After this transgression, isostatic rebound, and in time a slow lowering of global sea-level, mainly due to cooling and associated thermal contraction of sea water, results in the site again emerging from the sea. Subsequently, the site is situated above sea-level for the rest of the 120 kyr climate case, in line with the GIA modelling results on shore-level changes in the *global warming case (*Figure 5-4).

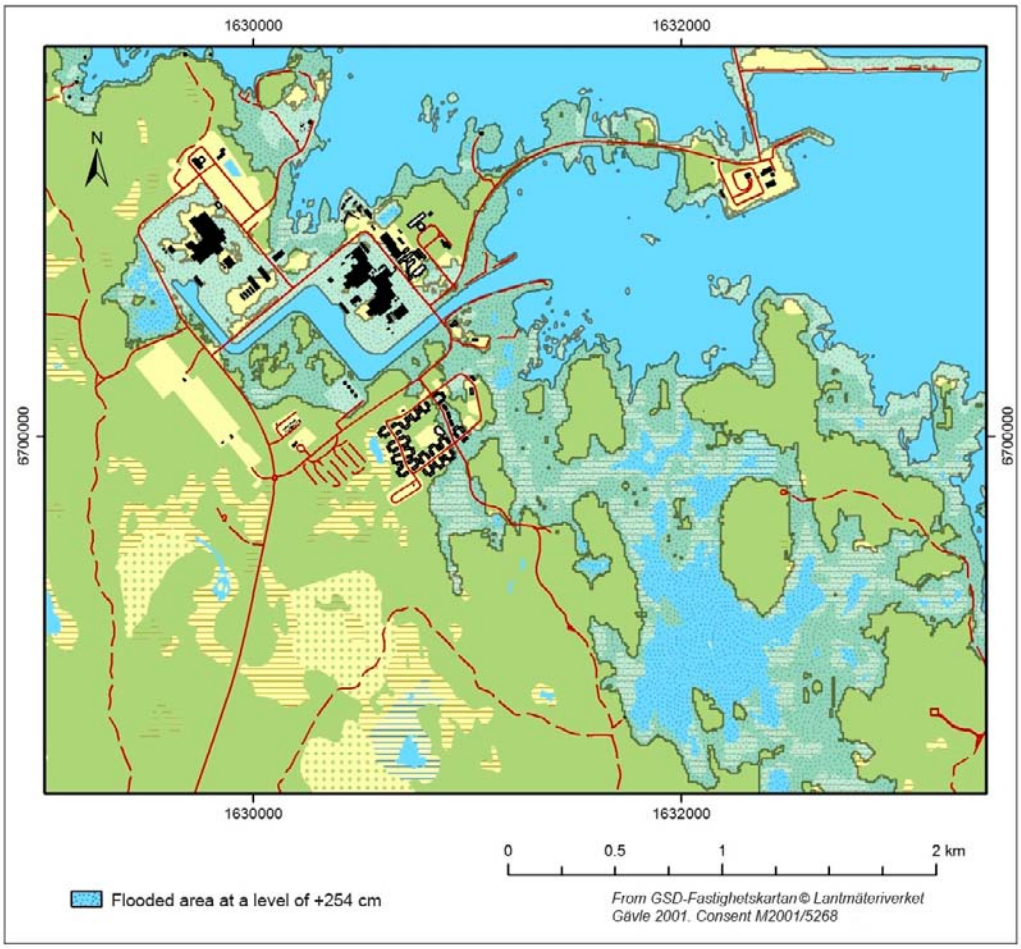

Figure 5-14. *Area at risk of flooding at an extreme level of +254 cm in Forsmark in year 2100 AD. Note that these results show extreme situations when assumed worst cases from the present scientific literature are combined with local effects also set to pessimistic values. From /Brydsten et al. 2009/.*

In the long run, around 130–140 kyrs after present, the growth of ice sheets results in a general lowering of global sea-level.

5.2.4 Permafrost evolution

In the *extended global warming case*, the very long period of temperate climate conditions is followed by permafrost develop at the Forsmark repository location at ~110 kyrs (107 kyrs) after present. Subsequently, temperate climate conditions develop again before the ending of the first 120 kyrs. Given the local definition of the ending of the present interglacial (by the development of permafrost at the repository location, see Section 4.5.4), the Holocene ends per definition at ~110 kyrs after present in this climate case. Periglacial conditions with permafrost prevail for c. 4 kyrs (3%) of the coming 120 kyrs.

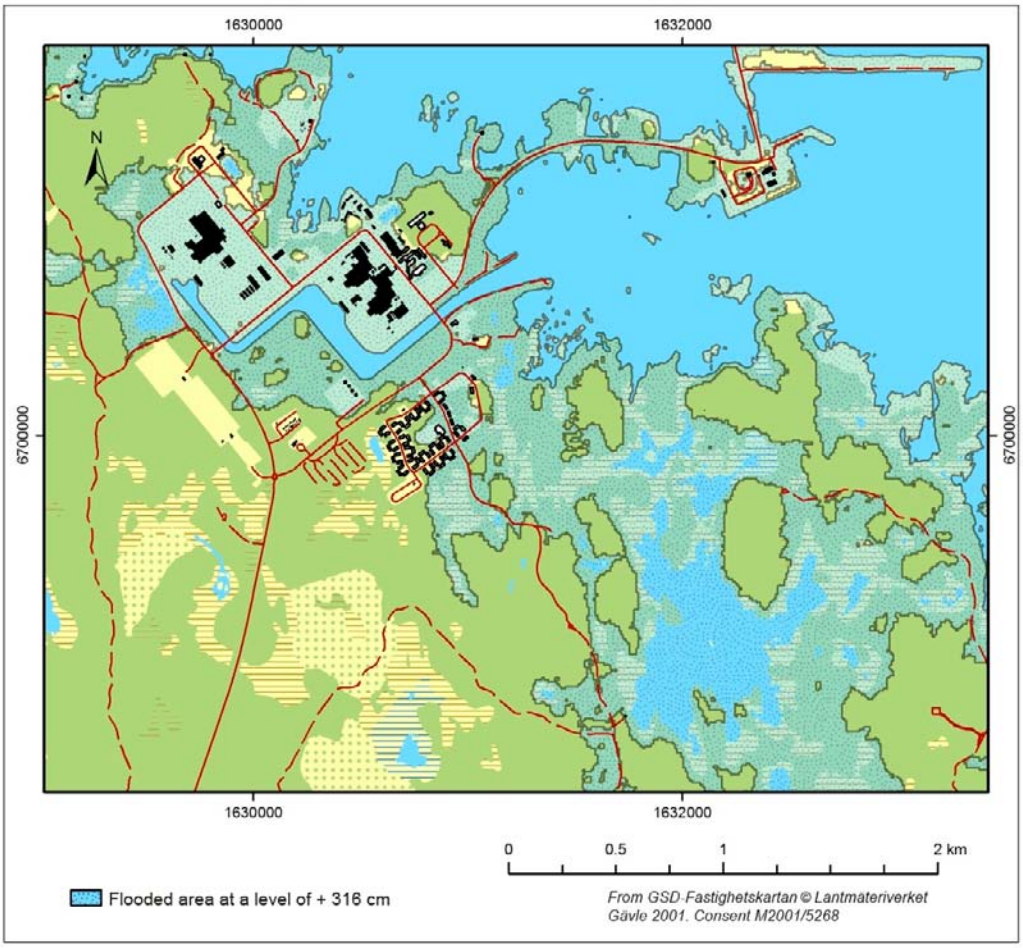

Figure 5-15. *Area at risk of flooding at an extreme level of +316 cm in Forsmark in year 2100 AD. Note that these results show extreme situations when assumed worst cases from the present scientific literature are combined with local effects also set to pessimistic values. From /Brydsten et al. 2009/.*

5.2.5 Evolution of climate domains

As mentioned above, a 100 kyr long period of temperate climate conditions is added before a slow onset of the first *reference glacial cycle* for the *extended global warming case*. After these additional 100 kyrs of temperate conditions, regular Late Pleistocene glacial cycles, represented by the *reference glacial cycle* described in Section 4.5, are envisaged to follow (Figure 5-16). This results in there being ~160 kyrs before the first glacial conditions occur at the Forsmark site, while the first permafrost occurs at ~110 kyrs after present. The climate development in the *extended global warming case* thus describes a situation without periglacial- or glacial climate conditions in central Sweden, including Forsmark, for a very long period of time.

Peak air temperatures are envisaged to be reached within the first hundreds to thousands of years as a result of anthropogenic greenhouse-gas emissions. Mean annual air temperatures several degrees warmer than at present then occur at Forsmark. In line with the results of /Kjellström et al. 2010b/, higher atmospheric greenhouse gas concentrations than in the *global warming case* are envisaged to give, at peak global warming conditions, air temperatures in excess of the global warming temperatures modelled for the Forsmark region (annual mean air temperature of +3.6°C a few thousands of years into the future) by /Kjellström et al. 2009b/. The changes in climate also result in a larger initial increase in precipitation than the +20% modelled for the Forsmark region /Kjellström et al. 2009b/.

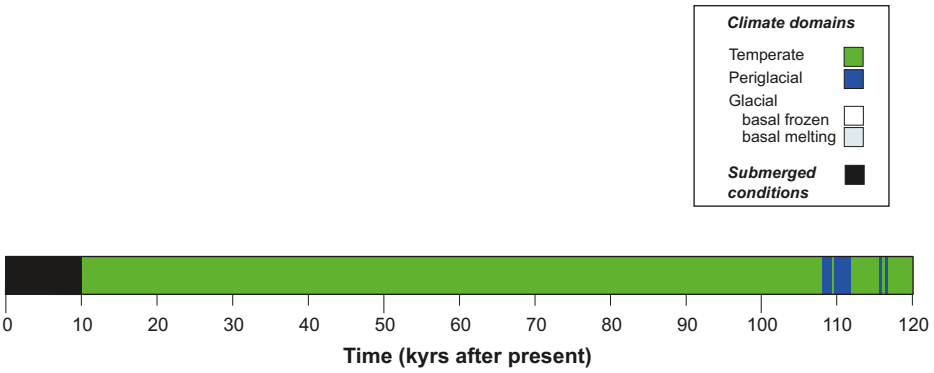

Figure 5-16. *Evolution of climate conditions at Forsmark for the extended global warming case. Following from the assumption of this case, temperate climate conditions prevail at the site for the coming 120 kyrs, except for an initial period of submerged conditions and for a few thousands of years at the end of the period. The duration of the initial period of submerged conditions is uncertain; it could be shorter or longer than indicated in the figure. Note that there is a very large range in e.g. temperature, precipitation and other climate parameters within these temperate conditions, ranging from strong global warming conditions to conditions with temperatures significantly cooler than at present (prior to the development of periglacial conditions). For a detailed example of more moderate global warming conditions at Forsmark than envisaged for this case, see Section 5.1.7.*

Following the reduction in e.g. CO_2 emissions, air temperature and precipitation are envisaged to slowly decline for the rest of the long interglacial period, in response to the slow decline in atmospheric CO_2 concentration e.g. /Archer 2005, Lenton and Britton 2006, Tyrell et al. 2007, Archer and Brovkin 2008, Schaffer et al. 2009/.

The cryosphere response to the extreme global warming results in raised global sea-levels and submerged conditions at the Forsmark site at the start of the period (Figure 5-16). The length of the initial submerged period is uncertain; it could be shorter or longer than illustrated in Figure 5-16.

5.2.6 Surface denudation

Since the *extended global warming case* envisages an even larger fossil fuel CO_2 climate perturbation than in the *global warming case*, fluvial erosion and chemical weathering in the wetter and warmer climate are anticipated to be more efficient than in the *global warming case* (Section 5.1). For a description of denudation processes that are anticipated to change compared with the *reference glacial cycle*, see the description of denudation under the *global warming case*.

Even if fluvial erosion and chemical weathering increase in this climate case compared with the *reference glacial cycle*, the *extended global warming case* mainly comprises temperate climate conditions for the entire 120,000 years, and consequently completely excludes the most efficient denudation process (glacial erosion) as defined in Section 3.5.4. Given this, and that feedback-mechanisms between climate, weathering and vegetation, e.g. /Lenton and Britton 2006/ could partly counteract the climate perturbation, the expected total amount of denudation for the present climate case is considered smaller, or at least not larger, than in the *reference glacial cycle*. Surface denudation is therefore not described and treated further in the *extended global warming case*. A climate case with an anticipated *larger* amount of surface denudation than in the *reference glacial cycle* is described in the *extended ice sheet duration case* (Section 5.3).

5.3 Extended ice sheet duration case

5.3.1 Background

In order to cover the uncertainty in duration of ice sheet coverage for the coming 120 kyrs, a climate case with extended ice sheet duration is constructed, describing a situation with a longer time of ice sheet coverage than in the *reference glacial cycle*. To this end, a climate evolution similar to that of the *reference glacial cycle* is used, with the important exception that the long interstadial with ice-free conditions between the two ice advances does not occur at Forsmark. In the *reference glacial cycle*, interstadial conditions, dominated by periglacial climate conditions with permafrost, occur between 66 and 91 kyrs (Table 4-5, Figure 4-34). In the present case, no ice-free conditions occur during this period. Accordingly, the scenario with extended ice sheet coverage describes one long single phase of ice sheet coverage at Forsmark, with a timing of glaciation and deglaciation according to Table 5-5.

This ice sheet evolution is similar to the Weichselian glacial history presented by /Lundqvist 1992/. In /Lundqvist 1992/, the main phase of the Weichselian glaciations starts ~50 kyrs BP with the ice sheet envisaged to cover Sweden continuously up to the final Weichselian deglaciation, see the literature review on ice-marginal fluctuations during the Weichselian glaciation by /Lokrantz and Sohlenius 2006/. Several recent studies suggest that there was a long period of ice free-interstadial conditions over large parts of Fennoscandia during MIS 3 (59–24 kyrs BP), i.e. in the middle of the main phase of glaciation as traditionally suggested, see Section 4.2.

The duration of ice sheet coverage over the Forsmark region in the *extended ice sheet duration case* is comparable with the total time of ice sheet coverage as coarsely deduced from the Weichselian reconstruction by /Lundqvist 1992/. In the Lundqvist reconstruction, most of Scandinavia is covered by ice from the mid-Weichselian (around 50 kyrs BP) until the deglaciation (around 10 kyrs BP), and during a phase of the early Weichselian (90–80 kyrs BP), which gives a total time of ice sheet coverage for the major part of Scandinavia of roughly 50 kyrs. Acknowledging that the Lundqvist reconstruction was not intended to give a detailed picture of ice sheet durations, the *approximate* duration in the Lundqvist reconstruction is similar to the duration of ice sheet coverage at Forsmark (60 kyrs) in the present climate case. In line with the ice sheet reconstruction by /Lundqvist 1992/, the Fennoscandian ice sheet is assumed to have started to grow considerably earlier than the time of ice sheet overriding at Forsmark. For a compilation of information on Weichselian glacial history, see Section 4.2 and references therein.

5.3.2 Ice sheet evolution

As an illustration of a situation with a persistent ice sheet coverage over the site for a long time (also during the ice-free phase corresponding to MIS 3 during the Weichselian glaciation, 70–90 kyrs ago), ice thickness data from an uncalibrated ice sheet model reconstruction of the Fennoscandian ice sheet are used (Figure 5-17). The data were produced by the same ice sheet model that was used for the simulation of the calibrated ice sheet development used for the *reference glacial cycle* (Section 3.1.4). In this climate case, the precise evolution of the ice thickness is not important. Therefore, the uncalibrated ice sheet simulation may be used to illustrate the ice sheet development for the case when it covers the Forsmark site without interstadial conditions between the two glacial phases in the *reference glacial cycle*.

As during the initial 4 kyrs of the first glacial phase of the *reference glacial cycle* (Figure 4-34), cold-based conditions with subglacial permafrost are envisaged to exist under the first 4 kyrs of glacial conditions in this case. Subsequently, the subglacial permafrost melts, and the ice sheet becomes warm-based at around 56 kyrs and remains so for the rest of the glacial period.

Table 5-5. Duration of climate domains at the Forsmark site in the extended ice sheet duration case.

Temperate climate domain [kyrs] (percent of time of glacial cycle)	Periglacial climate domain [kyrs] (percent of time of glacial cycle)	Glacial climate domain [kyrs] (percent of time of glacial cycle)	Submerged conditions [kyrs] (percent of time of glacial cycle)
28 kyrs (23%)	22 kyrs (18%)	60 kyrs (50%)	10 kyrs (8%)

The ice sheet evolution for this case starts with glacial conditions at c. 50 kyrs after present (Figure 5-17), i.e. around 7 kyrs earlier than in the *reference glacial cycle*. Glacial conditions persist until c. 110 kyrs after present when the site is deglaciated (Figures 5-17 and 5-18). The duration of all climate domains is summarized in Table 5-5. The ice thicknesses in this uncalibrated model run are somewhat smaller than in the *reference glacial cycle*. In this context, it should be noted that the maximum possible ice thickness over Forsmark, used for the safety assessment scenario for canister failure due to isostatic load /SKB 2011/, is not derived from this climate case or the *reference glacial cycle*, but from the case describing a maximum ice sheet configuration (Section 5.4).

In light of recent results indicating that the Weichselian ice sheet exhibited a more dynamic behaviour during the middle Weichselian than traditionally assumed (see above and Section 4.2), the ice sheet development in Figure 5-17 is considered a pessimistic estimate of the duration of ice sheet coverage for the coming 120 kyrs. The degree of pessimism in this case may also be seen in the light of the inferred present global warming, which may result in a longer than usual interglacial, and consequently shorter time of glacial conditions than in the *reference glacial cycle* (Section 4.5 and 5.2).

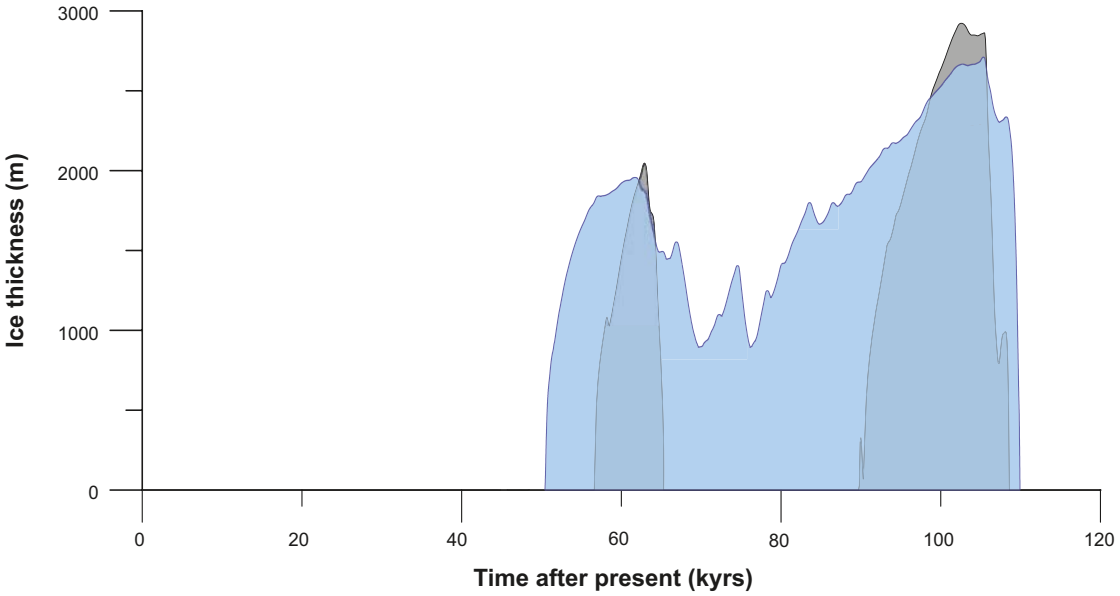

Figure 5-17. *Ice sheet coverage over Forsmark in the extended ice sheet duration case (blue). For comparison, the ice sheet development of the reference glacial cycle, based on a reconstruction of Weichselian conditions, is also shown (grey).*

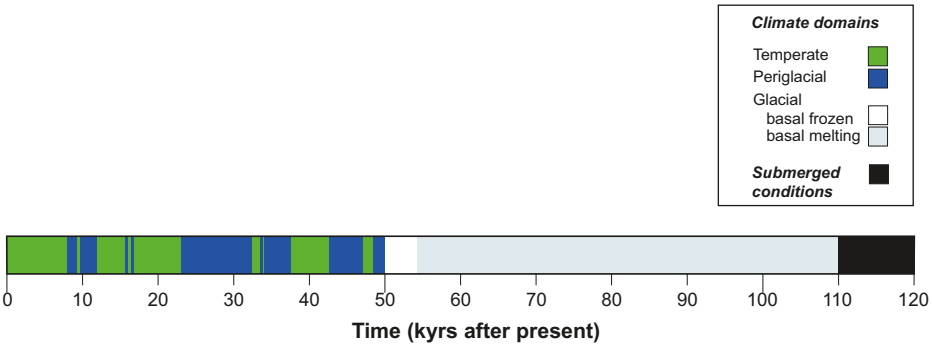

Figure 5-18. *Evolution of climate conditions at Forsmark as a time series of climate domains and submerged conditions for the extended ice sheet duration case. Glacial conditions start earlier and lasts considerably longer than in the reference glacial cycle (Section 4.5.4).*

5.3.3 Surface denudation

The *extended ice sheet duration case* results in the period with warm-based ice sheet conditions, and associated glacial erosion over the repository, being longer than in the *reference glacial cycle* (Section 4.5.4. and 4.5.7). Given that the ice sheet duration is about twice as long in this case (Figure 5-17) compared with the *reference glacial cycle* (Section 4.5.4), the amount of glacial erosion is estimated to be around doubled compared with the *reference glacial cycle*. The maximum amount of glacial erosion in fresh bedrock could thus be up to 2–4 m at the repository location for this case. However, if periods of cold-based, non-erosive, conditions would be longer in this climate case, which could be the case if climate conditions are colder, the duration of periods with glacial erosion would be shorter and the amount of erosion smaller.

The amount of non-glacial denudation is somewhat less than in the *reference glacial cycle*, since the time of temperate- and periglacial (mainly periglacial) climate conditions are shorter than in the *reference glacial cycle*. However, if the estimated amount of non-glacial surface denudation pessimistically is kept at the same value as for the *reference glacial cycle*, the resulting total denudation for the glacial cycle with extended ice sheet duration is still less than 5 m (4 m of glacial erosion and up to 0.6 m of non-glacial denudation, Table 3-17).

Surface denudation results in a reduction of the repository depth. A reduced repository depth could in turn lead to that permafrost and frozen ground reach closer to the repository. However, a 5 m reduction in repository depth for a glacial cycle with prolonged ice sheet duration has a negligible effect, in terms of repository safety, on the estimated permafrost- and freezing depths presented in Section 4.5.3 and 5.5.3. Also in the 1 Myr time perspective, a pessimistic use of the case of prolonged glacial conditions and the associated amount estimated glacial erosion (4 m of erosion in fresh bedrock) for each of the 8 glacial cycles, combined with the estimated 5 m of non-glacial denudation in 1 million years (Table 3-17), results in a limited amount of total denudation, less than 40 m, over the repository.

5.4 Maximum ice sheet configuration case

5.4.1 Background

For glacial conditions an additional hydrostatic pressure related to the ice sheet thickness is added to the hydrostatic pressure for ice-free conditions. The extremes regarding hydrostatic pressure in the glacial climate domain depend on the ice sheet configuration and on its hydraulic systems. Under the Antarctic ice sheet, sub-glacial lakes have been observed. The hydrostatic pressure in these lakes is assumed to correspond to the ice overburden pressure. A hydro-thermo-mechanical balance is assumed, where supply of basal melt water, re-freezing and ice deformation result in a hydrostatic equilibrium where the ice sheet rests, or floats, on the water surface, e.g. /Pattyn et al. 2004/. As further justified below, it is reasonable to assume that also for the Fennoscandian ice sheet, the maximum ice sheet thickness sets a limit to the maximum hydrostatic pressure that may occur at the ice sheet-substrate interface. To find and analyze the effects of the extremes regarding ice sheet thickness additional simulations were performed with the ice sheet model used to construct the ice sheet development of the *reference glacial cycle*.

5.4.2 Ice sheet evolution

To investigate the maximum ice sheet thickness that may occur in Fennoscandia, the UMISM ice sheet model (Section 3.1.4) was used for a sensitivity test to see what ice configurations were possible with different degrees of climate cooling. The sensitivity experiment used the same model setup as used for the reconstruction of last glacial cycle conditions (Section 3.1.4). However, the model was not run using the palaeo-temperature curve for the last glacial cycle, but instead by using a set of temperature evolutions in which annual air temperatures decreased linearly by 1° per 2 kyrs, from present-day temperatures down to various constant levels. In these sensitivity tests, temperatures were lowered between 4 and 16° (Figure 5-19). Model uncertainties and simplifications are described in Section 3.1.7.

Ice sheet growth started at a temperature lowering of 6 to 7°. If temperature is lowered by 9° or more, the ice sheet covers the Forsmark site. Warmer cases did not produce an ice sheet. In all cases

of ice sheet growth, the model simulated a total period of 100 kyrs, after which approximately steady-state conditions were obtained with little further change in ice volume and area. The results indicate that cold climate conditions with annual mean temperatures lowered by 10°C are required for the ice sheet to advance to and over the Forsmark site. The resulting maximum ice sheet thicknesses from the sensitivity simulations are shown in Figure 5-20.

As expected, the maximum ice sheet thickness increases with colder climates (Figure 5-20, black line). However, the degree of increase in thickness with temperature lowering declines as colder cases are considered. For a temperature lowering of more than approximately 13°C, colder climates do not generate thicker ice sheets. This result is in general agreement with what is known of Antarctic ice sheet variations, see below.

These simulated temperature cases (Figure 5-19) are extreme as regards their prolonged duration. Variations in temperature of this magnitude have occurred in the past, e.g., but never of this long duration without interruptions, see Appendix 1 and references therein. The extreme nature of these sensitivity cases is reflected also in the resulting ice sheet configurations. For the colder cases, the ice sheet covers all of northern and central Europe, and extends southward all the way to the Alps. Geological observations of traces from Fennoscandian ice sheets show that such large ice configurations have never occurred during the last 2 million years e.g. /Ehlers and Gibbard 2004/, and can thus be considered unrealistic for the time scale of interest for the safety assessment.

The maximum ice thickness at Forsmark in the *reference glacial cycle* was 2,920 m (Section 4.5). In the sensitivity tests, the maximum ice sheet thickness developed over Forsmark was 3,670 m. The uniform and high values reflect that the Forsmark site has an interior location within these unrealistically large ice sheets.

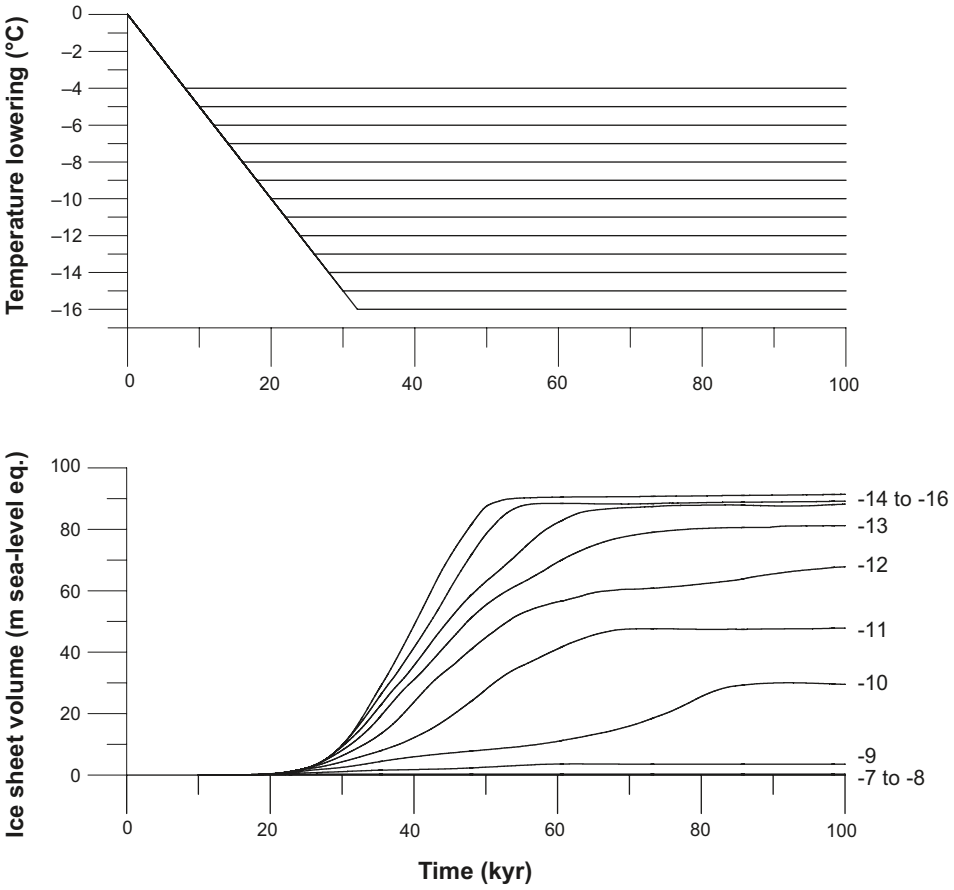

Figure 5-19. *Temperature lowering schemes (upper graph) and resulting development of Fennoscandian/ Eurasian ice sheet volumes (lower graph) in the sensitivity test on air temperatures and ice sheet configurations. The volume of the ice sheets is expressed as metres sea-level contribution.*

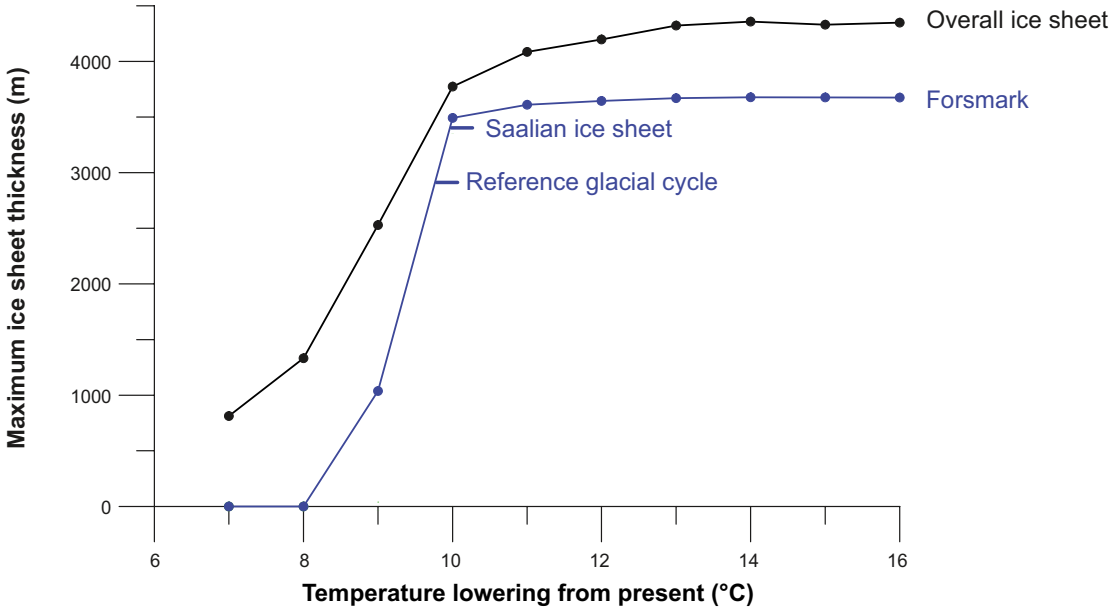

Figure 5-20. *Maximum modelled ice sheet thicknesses for the ice sheets modelled using the schematic climate evolutions in Figure 5-19. The blue curve represents maximum ice thicknesses extracted specifically over the Forsmark region. The overall largest ice thicknesses for these ice sheets are shown in black. The short line marked Reference glacial cycle show the maximum ice thickness of the ice sheet in the reference glacial cycle (Section 4.5.1), whereas the line marked Saalian ice sheet shows the maximum ice thickness for the largest Fennoscandian ice sheet configuration supported by geological observation for the past 2 million years.*

Estimate of maximum ice thickness during the past 2 million years

From geological information, it is known that the maximum ice extents of Pleistocene Fennoscandian ice sheets (i.e. those occurring during the past ~2 million years) were larger than that of the Weichselian ice sheet, and occurred during the Saalian glaciation, e.g. /Svendsen et al. 1999, 2004, Lambeck et al. 2006, Colleoni et al. 2009/. At the peak of the Saalian glaciation, around 140 kyrs BP, the ice sheet reached up to c. 200 km further south and more than 1,000 km further east than the Weichselian ice sheet. Modelling of the maximum Saalian ice sheet configuration (Section 5.4.2) indicated that the maximum ice thickness of this ice sheet was c. 3,100 m over the Forsmark region. According to /Lambeck et al. 2006/ the maximum Saalian ice thickness over the Forsmark region at 140 kyrs BP was around 3,400 m. Similar values may be inferred from /Colleoni et al. 2009/. Based on this information, the maximum expected ice sheet thickness for Forsmark is set to 3,400 m.

From the results of the extreme cases in the sensitivity test (Figure 5-20), it is unlikely that the ice thickness at Forsmark could under any circumstance exceed 3,700 metres. The results of the sensitivity tests can be considered as high values since it is unlikely that the Fennoscandian ice sheet would, in reality, ever reach its maximum equilibrium size, i.e. the size simulated in these experiments.

In the climate cooling sensitivity tests, the maximum simulated *overall* thickness of the ice sheets is 4,360 metres. This is 1,000 m more than the maximum overall ice thickness for the *reference glacial cycle* which is 3,300 m. Estimating the maximum thickness of the largest geologically feasible Pleistocene ice sheet yields a maximum *overall* Saalian ice thickness of 3,600 m. Other simulations of the Saalian ice sheet result in a maximum ice thickness of 4,500 m, over the Kara Sea in the Arctic /Lambeck et al. 2006/.

For comparison, the maximum ice sheet thickness occurring on Earth today is ~4,500 m for parts of the East Antarctic ice sheet /Lythe et al. 2001/. The Greenland ice sheet has a maximum thickness of ~3,400 m /Bamber et al. 2001/. In a colder glacial climate, the maximum ice thickness of the Antarctic ice sheet will probably not change significantly. In a colder climate, the marginal parts of the Antarctic ice sheet grow significantly, whereas, at the same time, more interior parts of the ice sheet keep the same thickness or even gets thinner due to moisture starvation /Huybrechts 1990, Näslund et al. 2000/. Therefore, it is likely that the maximum thickness of the Antarctic ice sheet seen also over an entire glacial cycle is around 4,500 m. This value is close to the largest overall ice thickness obtained in the sensitivity test, 4,360 metres (Figure 5-20). These results are also in line with a largest inferred thickness of the Laurentide ice sheet of 4,300 metres (Tarasov and Peltier 2004). These observations and results suggest that Pleistocene ice sheets up to date have not grown thicker than approximately 4,500 m, which gives an upper limit for ice sheet thickness.

Hydrostatic pressures exceeding ice overburden pressure

Hydrostatic pressures exceeding ice overburden can occur in some situations, for example in relation to jökulhlaups, i.e. large sudden outburst floods of glacial melt water from subglacial or supraglacial ice-dammed water reservoirs /Roberts et al. 2000/. In a few cases, higher pressures of non-jökulhlaup origin have been registered also in the ablation area of smaller glaciers. These high pressures are of artesian character, with the amount of pressure being ultimately determined by upglacier ice thickness and the presence of meltwater. This may also occur in near-frontal parts of ice sheets /Roberts 2005/. However, during times of maximum ice sheet thickness over Forsmark, e.g. during the Last Glacial Maximum, this site is located within the ice sheet interior, far from the ablation area and the margin. For this ice sheet configuration, surface melting is thus absent or negligible above and upstream of the Forsmark site, due to the high ice surface elevation and associated low air temperatures. In addition, climate is at its coldest at this time during the glacial cycle, also precluding surface melt in these high-polar regions of the ice sheet. Therefore, it is reasonable to assume that maximum hydrostatic pressures at Forsmark are dependent only on the local ice thickness during periods of maximum ice thickness, and not on ice thickness and surface melting upstream of the site.

Conclusions

For the *reference glacial cycle*, the additional hydrostatic pressure related to ice thickness over Forsmark is 26 MPa (Table 5-6). The *maximum* expected additional hydrostatic pressure, pessimistically derived from the largest ice sheet configuration during the past 2 million years, as supported by geological observations, is 30 MPa. Maximum ice thicknesses of the more extreme and unrealistic ice sheet configurations discussed above, with associated additional hydrostatic pressures, are also presented in Table 5-6.

Table 5-6. Maximum ice sheet thickness and associated additional hydrostatic pressure at Forsmark for various Fennoscandian ice sheet configurations.

	Maximum ice thickness (m)	Hydrostatic pressure contribution (MPa)
Reference glacial cycle	2,920	26
Largest Fennoscandian ice sheet during past 2 Myrs (Saalian ice sheet)	3,400	30
Extreme ice sheets from climate sensitivity test	3,670	32

5.4.3 Surface denudation

The large size of this ice sheet would take a longer time to build than the maximum ice sheet of the *reference glacial cycle* (Section 4.5.1), but not a longer time than the 60 kyrs of ice sheet presence in the *extended ice sheet duration case* (Section 5.3). Therefore, the present climate case does not contribute to a longer time of glacial erosion, or resulting larger total amount of denudation, than the *extended ice sheet duration case*. For that reason, surface denudation is not described and treated further in the *extended global warming case*.

5.5 Severe permafrost case

5.5.1 Background

The main factors of importance for repository safety in the permafrost climate domain are the permafrost- and frozen depths, the depth of the isotherm at which the buffer and backfill freezes, and the possible freezing out of salt that may result in a zone with high salinity beneath the freeze front. The prevailing climate conditions are the main factor determining the evolution of permafrost, see Section 3.4.4 and /Hartikainen et al. 2010/. A mean annual air temperature well below 0°C for long periods is a prerequisite for the development of permafrost to greater depth, Section 3.4.4.

In order to investigate remaining uncertainties within the periglacial climate domain that were not studied in the permafrost simulations reported in Section 3.4.4 and 4.5, a *severe permafrost case* was investigated /Hartikainen et al. 2010/. These remaining uncertainties mainly consist of the possibility of having a cold dry climate at Forsmark, but without the presence of an ice sheet. An assumption of a cold periglacial climate is here combined with an assumption of a very dry climate in order to favour permafrost growth. In this climate case, the dry climate also limits ice sheet growth so that an ice sheet does not reach the Forsmark site during the first glacial cycle. If an ice sheet covers the site, any pre-existing permafrost decays due to the insulating effect of the ice sheet, especially if the ice sheet is warm-based (Section 4.5.4). In line with the dry and cold assumption, and that no ice sheet forms over the site, it is further assumed that no post-glacial periods of submerged conditions occur, and that no insulating winter snow and vegetation cover exist.

In addition to the simulation using the above assumptions, a number of sensitivity studies have also been done in order to investigate the climate conditions required to develop permafrost and perennially frozen ground to repository depth.

5.5.2 Ice sheet evolution

One of the main assumptions in the *severe permafrost case* is that there is no ice sheet coverage over the Forsmark site for the coming 120 kyrs, and consequently there is no ice sheet development in this climate case.

5.5.3 Permafrost evolution

The *severe permafrost case* is analysed with the same 2D permafrost model that was used for the *reference glacial cycle* and for the sensitivity experiments on surface, subsurface and air temperature parameters (Section 3.4.4). The *severe permafrost case* was simulated for a full glacial cycle, from 115 kyrs BP to present. However, for the present section the results have been projected for a future glacial cycle, in the same way as the reconstruction of last glacial cycle conditions (Section 3.4.4) were used to construct a future *reference glacial cycle* (Section 4.5).

In this context it should be noted that the exact way in which the start of the previous reconstructed glacial cycle is taken to form the start of the present climate case will affect the detailed timing of permafrost events, such as the detailed timing of the first permafrost development. However, for the safety assessment of a KBS-3 repository, the precise timing of permafrost and freezing events is not central. Instead it is the maximum simulated permafrost and freezing *depths* that are of importance. Therefore, the temporal uncertainties arising from the onset of the future glacial cycle in the *severe permafrost case* do not affect the analysis of e.g. the SR-Site freezing scenario /SKB 2011/.

The following assumptions were made for the *severe permafrost case*:

- The climate is so dry that no ice sheet forms that is large enough to reach the Forsmark site at any time during the glacial cycle, i.e. ice free conditions prevail during the entire glacial cycle.
- In line with the above assumption, it is assumed that the repository location is not isostatically depressed below sea-level.
- The climate is so dry that there is no insulating snow cover during winter.
- There is no vegetation to insulate the ground from low air temperatures.
- The temperature curve reconstructed for the last glacial cycle, but without a presence of ice sheets and submerged conditions (Figure 3-54, red line) was employed for calculating ground surface temperatures.

Initial conditions are assumed to correspond to the present-day conditions (temperature, salinity and groundwater pressure). Heat generated by the radioactive decay of the spent fuel in the repository is included in the simulation. The modelled 2D profile is seen in Figure 3-58.

Regarding the choice of using the temperature curve reconstructed for the last glacial cycle also for the analysis of a *severe permafrost case*, the following needs to be considered. Northern Hemisphere mid-latitude ice sheets form essentially as a response to low air temperatures, see Section 2.1 and 3.1. In line with this, there is a correlation between cold interstadial periods during glacial cycles and large ice sheet configurations. In the *severe permafrost case*, the main assumption is that the climate is cold but without an ice sheet reaching the Forsmark site, see above. This means that the maximum ice sheet configuration for this hypothetical case does not reach middle central Sweden anytime during the glacial cycle. This ice sheet thus has very much smaller ice sheet configurations, at all times, than the Weichselian ice sheet had. This, in turn, strongly implies that that air temperatures during the fictive glacial cycle of the *severe permafrost case* would be higher than in the reconstruction of the last glacial cycle that hosted the Weichselian ice sheet (but still significantly colder than temperate climate conditions). If temperatures were to be the same during the *severe permafrost case* as during the Weichselian, a larger ice sheet would form and cover the Forsmark site for parts of the glacial cycle. It is difficult to estimate what temperatures would correspond to a glacial cycle as envisaged for the *severe permafrost case*. The temperature curve used for permafrost simulations for the *severe permafrost case* should, in line with the above reasoning, be considerably warmer than the one used for the reconstruction of the last glacial cycle.

On the other hand, the temperature curve reconstructed for the last glacial cycle also has a significant uncertainty interval, see Appendix 1. The comparison of the reconstructed last glacial cycle temperature curve with (the few) existing quantitative proxy data on Weichselian temperatures from the Fennoscandian region seems, however, to indicate that the reconstructed temperature curve is in broad agreement with proxy data, see Appendix 1. Furthermore, the comparison suggests that the temperature curve does not overestimate temperatures for the compared last glacial cycle stadials and interstadials. Instead, the general picture from the comparison with Fennoscandian proxy data is that the reconstructed temperature curve gives roughly correct or slightly too low temperatures by a few degrees.

In order to make a reasonable choice of temperature curve for the *severe permafrost case*, with the above issues in consideration, air temperatures were pessimistically assumed to fall according to the reconstructed temperature curve for the *reference glacial cycle*, but without a presence of ice sheets and submerged conditions (Figure 3-54).

Surface and subsurface properties and conditions

Just as for the 2D permafrost modelling for the *reference glacial cycle* (Section 3.4.4), the significant uncertainties associated with descriptions of the surface conditions motivate the analysis of two climate variants of the *severe permafrost case*, one humid and one dry. This is to yield a lower and upper limit for the permafrost and perennially frozen ground development, see further below.

Based on the Köppen climate classification /Lohmann et al. 1993/ and long-term observations /Eugster et al. 2000/ the climate of the *severe permafrost case* may be divided into three climate zones: *Boreal*, *Subarctic* and *Arctic*, which may be characterized by the annual mean air temperature, the monthly mean maximum summer air temperature and the monthly mean minimum winter air temperature, together with the monthly mean maximum summer and winter precipitations (Table 5-7), see /Hartikainen et al. 2010/. The large ranges in the monthly mean air temperatures and precipitations are explained by the fact that the description and modelling of surface conditions involve significant data-, conceptual- and model uncertainties, see /Hartikainen et al. 2010/.

Other surface properties and conditions are the same as in the 2D permafrost modelling of the *reference glacial cycle* (Section 3.4.4). All subsurface properties for the *severe permafrost case* are the same as for the 2D permafrost modelling of the *reference glacial cycle* (Section 3.4.4).

In order to construct an air temperature curve for a full glacial cycle without the presence of an ice sheet at the Forsmark site, the site-specific air temperature curve reconstructed for the last glacial cycle (Figure 3-54 blue line) was used together with the ice sheet surface elevations of the *reference glacial cycle* to making a correction for the difference in elevation between the height of the ice sheet and that of the ice-free ground surface (see also Appendix 1). Subsequently, by using the same n-factor approach as in the modelling of the *reference glacial cycle*, calculations of ground-surface temperatures were made from air temperature (Section 3.4.4). The resulting air temperature curve for the *severe permafrost case* is seen in /Hartikainen et al. 2010, Figure 2-15/.

Figure 5-21 exemplifies modelled ground surface temperatures along the profile at four different times for the *severe permafrost case* considering different climate conditions: 8.5 kyrs after present – Subarctic and partially submerged, 16.5 kyrs after present – Boreal, 25 kyrs after present – Subarctic, 50 kyrs after present – Arctic. The partially submerged conditions at 8.5 kyrs after present refer to locations away from the repository location, the repository location is never submerged in this climate case. For details on the setup of the *severe permafrost case*, see /Hartikainen et al. 2010/.

The extent of perennially frozen ground over the Forsmark site for the *severe permafrost case* is exemplified by time slices at 8.5, 25, 46, 50 kyrs after present in Figures 5-22 and 5-23. The evolution of maximum permafrost depth and depth of perennially frozen ground at the repository location is shown in Figure 5-24. Figure 5-25 shows the same results over the whole profile, as well as the extent of permafrost summarised along the investigated profile.

Table 5-7. Climate information for the severe permafrost case. Summer precipitation is close to 5 mm/month for dry case while it is close to 50 mm/month for the humid case. The winter precipitation is the same (< 1) for both cases.

Climate zone	Annual mean air temperature (°C)	Monthly mean max. summer air temperature (°C)	Monthly mean min. winter air temperature (°C)	Monthly mean max. summer precipitation (mm/month	Monthly mean max. winter precipitation (mm/month)
Boreal	> 0	+10 – +20	–15 – +5	5 – 50	< 1
Subarctic	0 – –6	+5 – +15	–25 – –10	5 – 50	< 1
Arctic	< –6	< +5 – +10	–35 – –20	5 – 50	< 1

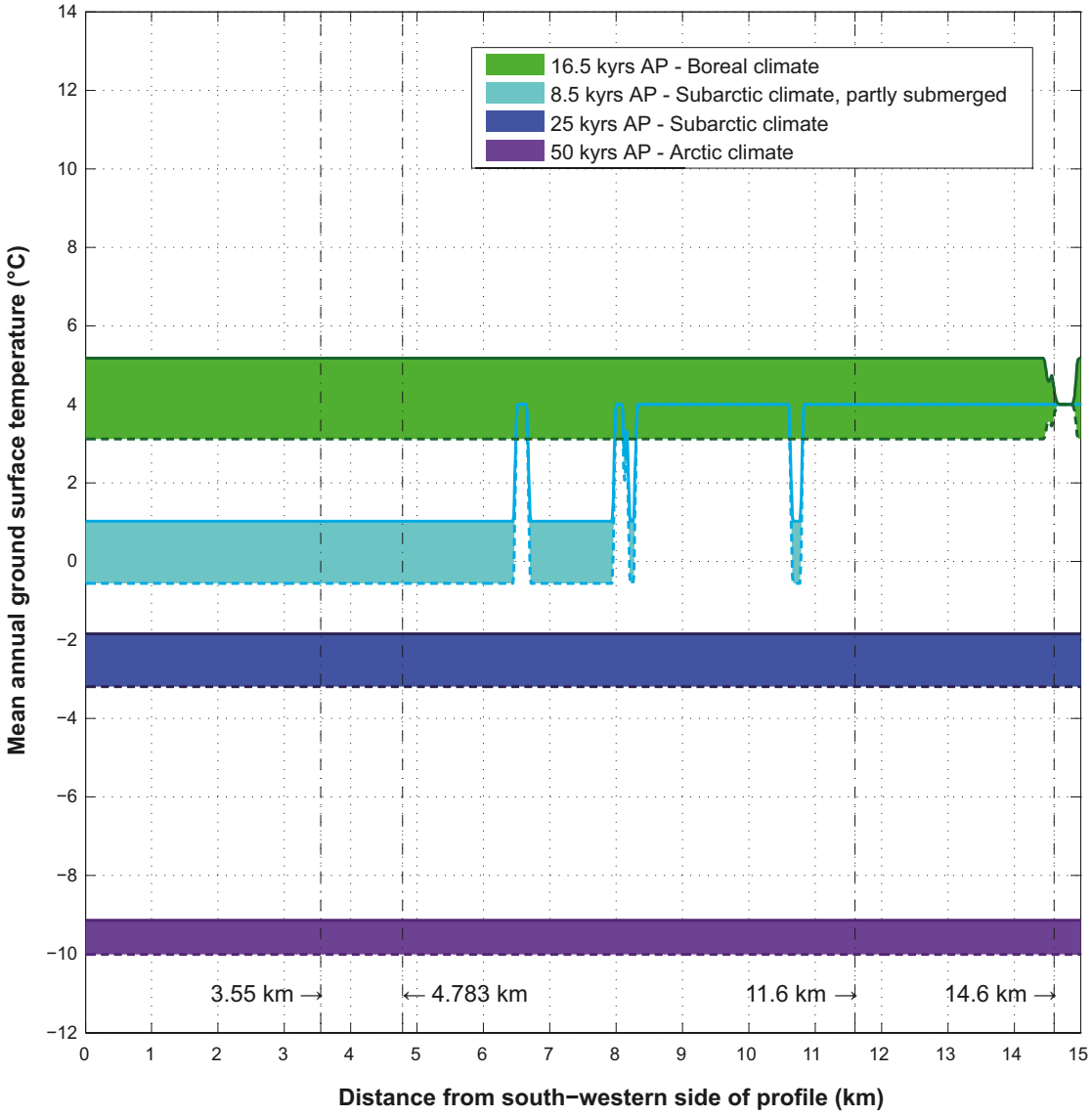

Figure 5-21. *Modelled ground surface temperatures along the profile at four different times for the severe permafrost case considering different climate conditions: 8.5 kyrs after present – Subarctic and partially submerged, 16.5 kyrs after present – Boreal, 25 kyrs after present – Subarctic, 50 kyrs after present – Arctic. The solid border lines of the coloured areas indicate the dry variant of the climate case and dashed ones the humid variant of the same case. For details on the calculations of ground surface temperatures, see /Hartikainen et al. 2010/.*

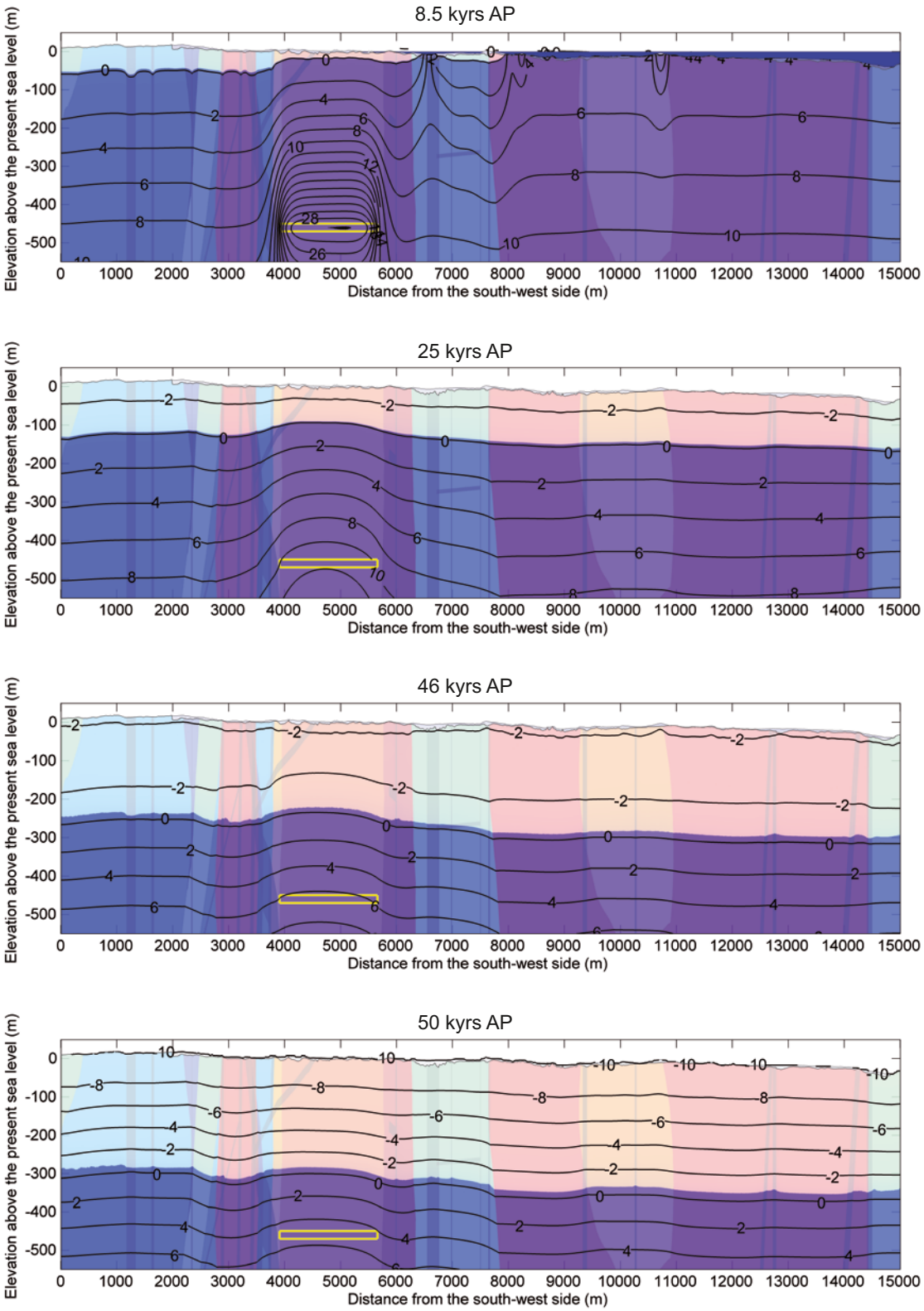

Figure 5-22. *Exemplified temperature contours in (°C) and the extent of perennially frozen ground (light colour) within permafrost (0°C isotherm) at times 8.5, 25, 46, 50 kyrs after present for the humid variant of the severe permafrost case. Blue colour blue on the top of the profile at 8.5 kyrs after present shows the Baltic Sea. The yellow rectangle indicates the location of the repository.*

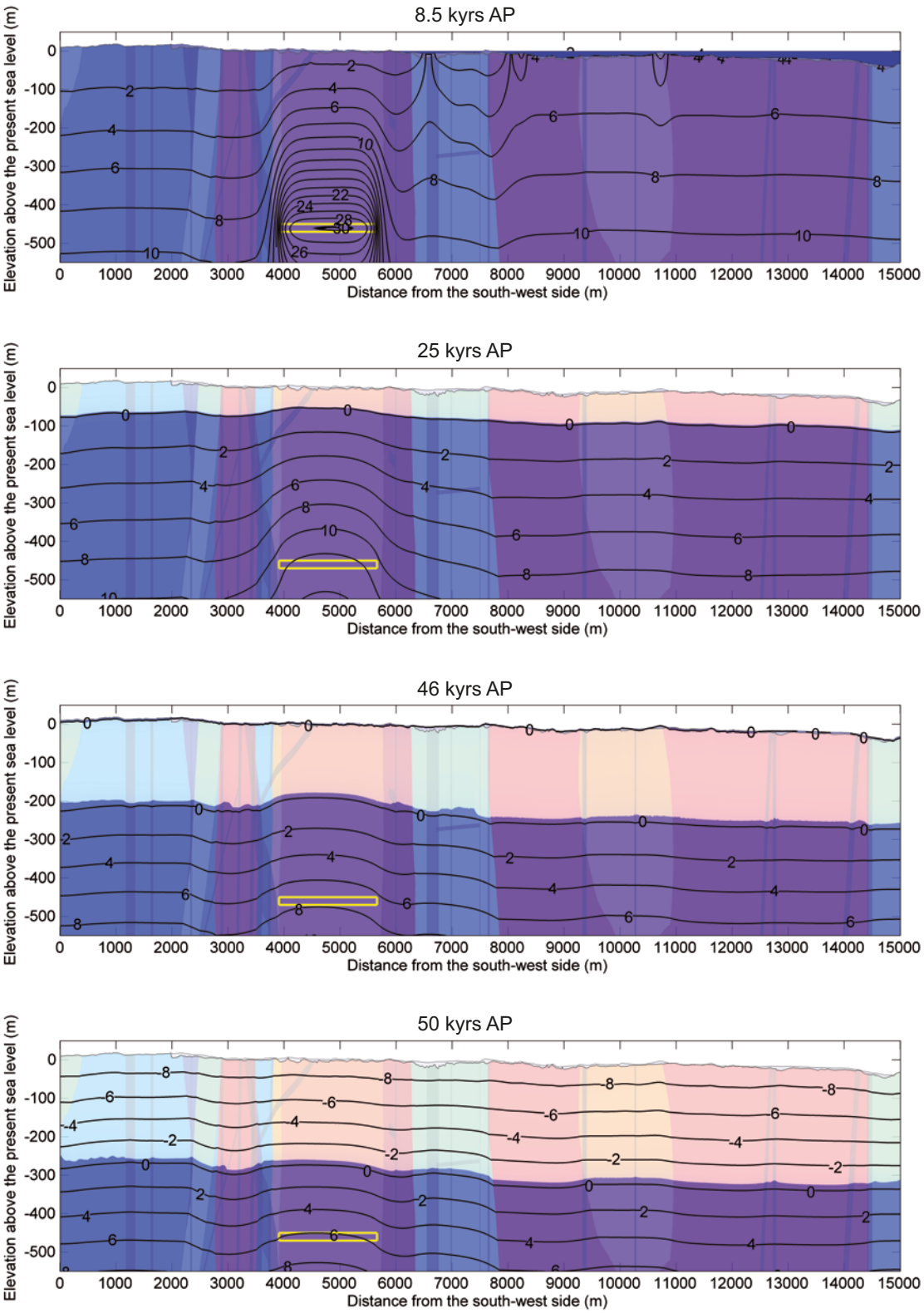

Figure 5-23. *Exemplified temperature contours in (°C) and the extent of perennially frozen ground (light colour) within permafrost (0°C isotherm) at times 8.5, 25, 46, 50 kyrs after present for the dry variant of the severe permafrost case. Blue colour blue on the top of the profile at 8.5 kyrs after present shows the Baltic Sea. The yellow rectangle indicates the location of the repository.*

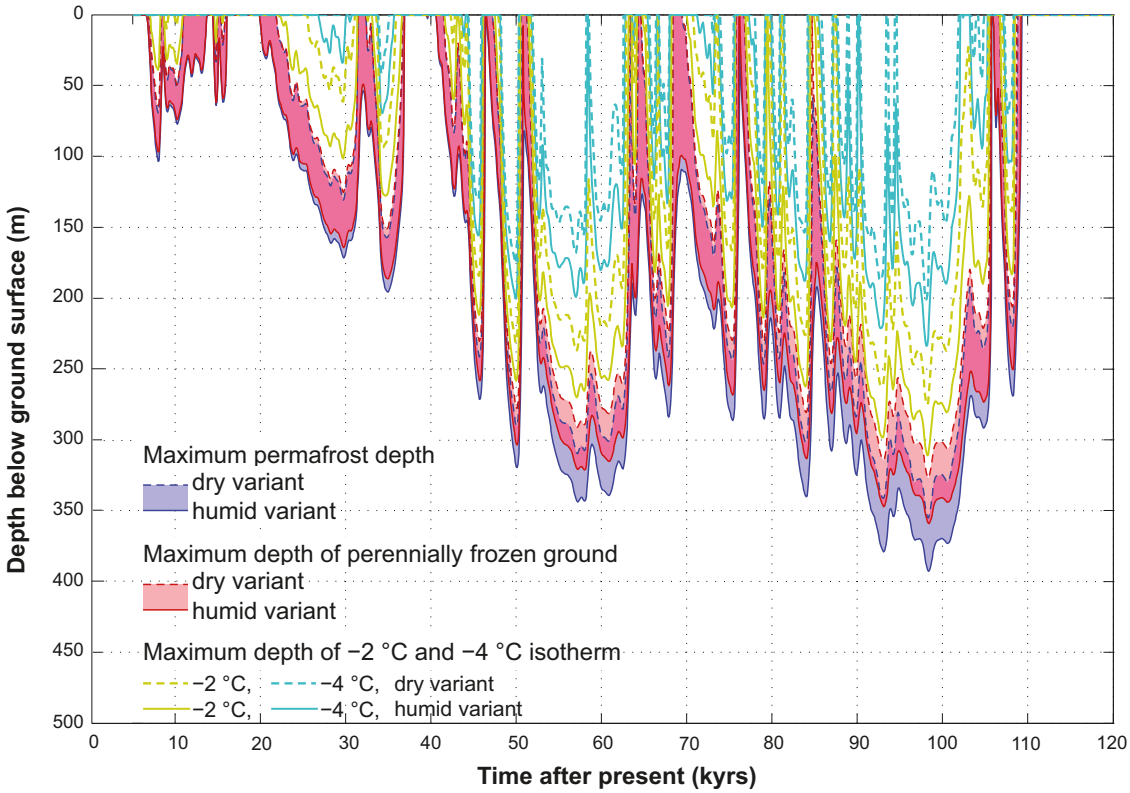

Figure 5-24. *Evolution of maximum permafrost depth, maximum depth of perennially frozen ground and maximum depth of –2 and –4°C isotherms over the repository for the severe permafrost case. The upper permafrost surface, for periods of permafrost degradation from above, is not shown. The shaded area in blue and red represents the range when considering the dry and humid climate variants of the severe permafrost case. The darker lilac colour indicates that the results for permafrost and perennially frozen ground overlap.*

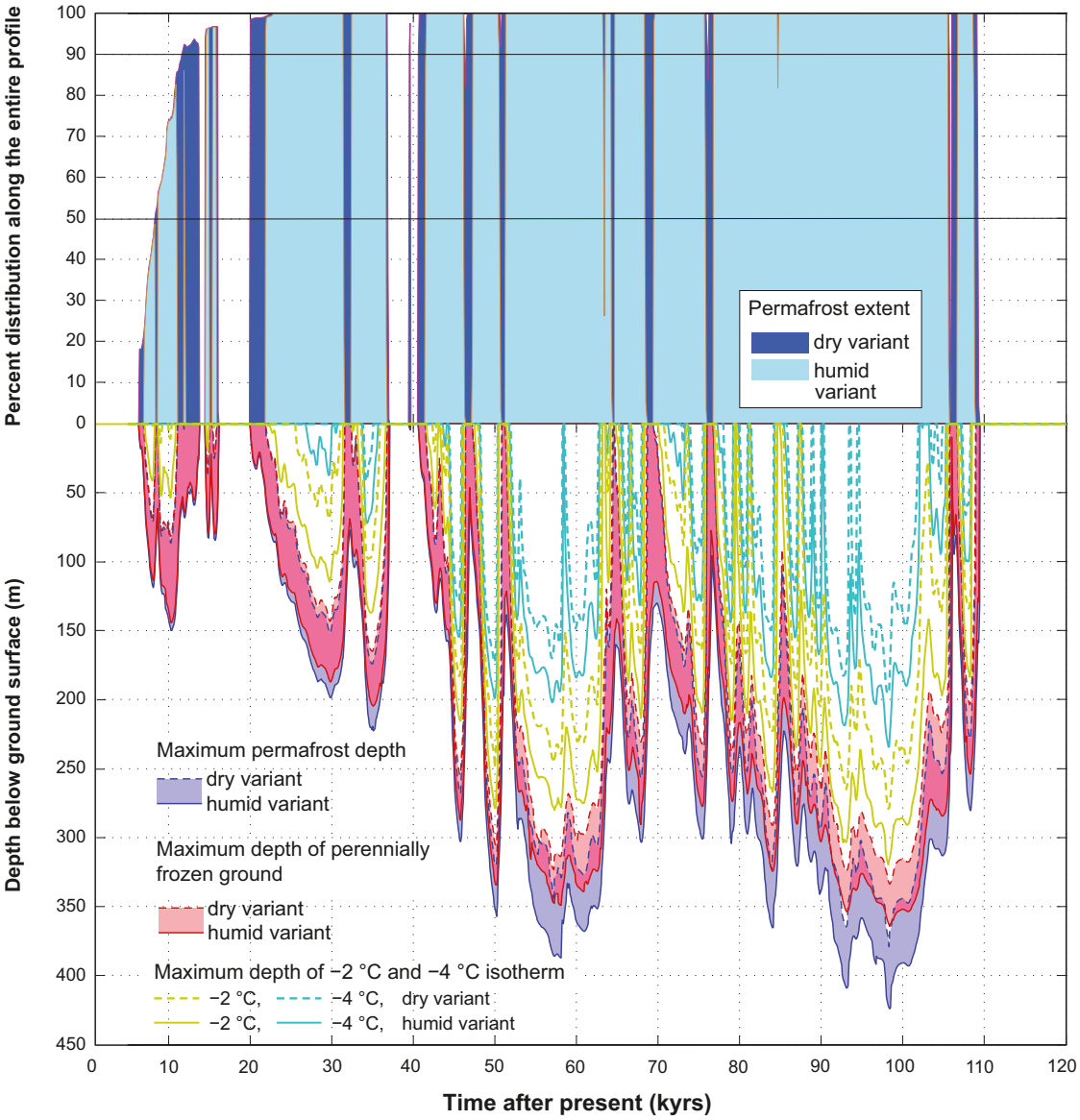

Figure 5-25. *Evolution of maximum permafrost depth, maximum depth of perennially frozen ground and maximum depth of –2 and –4°C isotherms over the whole profile for the severe permafrost case. The figure also shows the percent permafrost distribution along the profile. The transition from sporadic to discontinuous permafrost occurs at 50-% coverage and from discontinuous to continuous permafrost at 90-% coverage, indicated by two horizontal lines. The upper permafrost surface, for periods of degradation from above, is not shown. The shaded area in blue and red represents the range when considering the dry and humid climate variants. The darker lilac colour indicates that the results for permafrost and perennially frozen ground overlap.*

The maximum permafrost depths, maximum depths of perennially frozen ground, and the extent of permafrost distribution have been summarised in Tables 5-8 and 5-9. In addition, Table 5-10 describes the evolution of permafrost depth and depth of perennially frozen ground at the repository site. For a corresponding table for the entire profile, see /Hartikainen et al. 2010/.

The results show that development of continuous permafrost is characteristic for both the dry and humid variants of the *severe permafrost case* (Figure 5-25). As expected this is a difference compared with the *reference glacial cycle* where longer periods of discontinuous permafrost prevailed both in the dry and humid climate variants (Figure 4-29).

Table 5-8. Times of permafrost occurrence and associated maximum permafrost depth and maximum depth of perennially frozen ground over the whole profile and over the repository location for the future humid variant of the severe permafrost case. The table also gives the time and horizontal location of maximum permafrost depth and the percent extent of permafrost distribution.

Time periods of permafrost occurrence (kyrs after present, AP)	Over the whole profile					Over the repository			
	Maximum permafrost depth (m)	Time of occurrence of maximum permafrost depth (ka AP)	Distance from the south-west side (m)	Maximum depth of perennially frozen ground (m)	Percent extent of permafrost distribution (%)	Maximum permafrost depth (m)	Time of occurrence of maximum permafrost depth (ka AP)	Distance from the south-west side (m)	Maximum depth of perennially frozen ground (m)
6.4 – 13.7	150	10.3	100	144	75	104	8	3,950	97
14.5 – 16.1	85	15.7	12,280	80	97	64	14.8	5,650	62
19.9 – 37	223	35.1	14,910	205	100	196	34.9	5,650	186
39.5 – 39.6	5	39.6	14,870	3	95	3	39.6	5,610	1
40.6 – 109.4	424	98.4	12,240	364	100	393	98.4	5,650	359

Table 5-9. Times of permafrost occurrence and associated maximum permafrost depth and maximum depth of perennially frozen ground over the whole profile and over the repository location for the future dry variant of the severe permafrost case. The table also gives the time and horizontal location of maximum permafrost depth and the percent extent of permafrost distribution.

Time periods of permafrost occurrence (kyrs after present, AP)	Over the whole profile					Over the repository			
	Maximum permafrost depth (m)	Time of occurrence of maximum permafrost depth (ka AP)	Distance from the south-west side (m)	Maximum depth of perennially frozen ground (m)	Percent extent of permafrost distribution (%)	Maximum permafrost depth (m)	Time of occurrence of maximum permafrost depth (ka AP)	Distance from the south-west side (m)	Maximum depth of perennially frozen ground (m)
7 – 8.3	72	8	3,020	68	44	69	8	3,950	64
8.7 – 11	87	10.3	7,990	81	74	52	10.2	5,650	50
11.8 – 12	4	11.9	12,360	1	79	2	11.9	5,620	0
14.6 – 15	36	14.8	14,280	35	96	33	14.8	5,650	32
15.4 – 15.8	25	15.6	14,280	22	97	21	15.6	5,650	20
21.9 – 31.5	152	29.8	14,840	143	100	131	29.7	5,650	125
32.4 – 36.7	174	34.9	14,880	165	100	157	34.8	5,650	151
41.5 – 46.3	268	45.7	13,890	255	100	242	45.7	5,650	231
47.2 – 50.8	320	50.1	13,790	306	100	290	50	5,650	277
51.3 – 64.4	326	58	14,890	314	100	310	57.2	5,650	291
64.7 – 68.6	257	67.9	14,980	231	100	241	67.8	5,650	224
69.5 – 75.9	256	75.4	14,980	232	100	244	75.4	5,650	230
76.8 – 105.7	379	98.3	13,940	333	100	355	98.3	5,650	327
106.7 – 108.9	229	108.2	14,980	204	100	221	108.2	5,650	206

Table 5-10. Evolution of maximum permafrost depth and maximum depth of perennially frozen ground at the repository site for the severe permafrost case. For comparison the table also include the results from the reference glacial cycle. The table also shows the prevailing mean annual air temperatures. For a table describing model results for the full glacial cycle of the severe permafrost case, see /Hartikainen et al. 2010 Appendix K/.

Time (kyrs after present)	Mean annual air temperature (°C)	Maximum permafrost depth (m)				Maximum depth of perennially frozen ground (m)			
		Humid variant of the reference glacial cycle case	Dry variant of the reference glacial cycle case	Humid variant of the severe permafrost case	Dry variant of the severe permafrost case	Humid variant of the reference glacial cycle case	Dry variant of the reference glacial cycle case	Humid variant of the severe permafrost case	Dry variant of the severe permafrost case
8	–3.4	31	84	104	69	29	79	97	64
8.5	–0.6	0	3	30	0	0	1	27	0
10	–3.5	15	47	71	46	15	46	68	44
12	–1.5	0	22	44	0	0	21	42	0
14	2.5	0	0	0	0	0	0	0	0
16	–0.6	0	6	33	0	0	5	30	0
18	1.6	0	0	0	0	0	0	0	0
20	–0.3	0	0	7	0	0	0	5	0
22	–1.9	2	30	55	9	0	28	52	8
24	–2.9	18	62	102	56	16	60	97	53
25	–3.2	23	69	110	64	20	66	105	61
26	–3.9	35	84	127	86	33	81	122	82
28	–4.8	49	108	158	117	47	103	151	113
30	–4.1	45	112	168	123	43	107	161	118
32	–0.9	0	15	54	0	0	13	49	0
34	–6.4	73	116	155	120	71	113	149	115
36	–3.1	31	108	164	105	29	104	156	98
38	2.1	0	0	0	0	0	0	0	0
40	0.4	0	0	0	0	0	0	0	0
42	–2.5	12	52	88	37	10	50	84	35
44	–4.2	45	101	147	102	43	97	140	98
45	–10.4	135	186	232	204	131	179	219	194
46	–1.3	85	180	256	211	77	168	241	198
48	–3.6	33	86	130	78	31	82	124	74
50	–10	181	259	319	290	175	246	303	277

For the *severe permafrost case*, i.e. when considering no ice sheet, sea, vegetation or snow cover over the Forsmark site throughout the glacial cycle, permafrost (0 ºC isotherm) can reach a depth between ~360 m and ~390 m over the repository and between ~380 m and ~420 m outside the repository, in a time frame of 100,000 years. Meanwhile, the maximum depth of perennially frozen ground may vary between ~330 m and ~360 m over both the repository and the rest of the profile, see Figure 5-24 and 5-25.

Examples of vertical profiles of bedrock temperature at one selected location (in the middle of the repository location, at 4,783 m along the profile) corresponding the fresh-moist surface cover types are presented in Figures 5-26 (humid climate variant) and 5-27 (dry climate variant). The white colour envelope represents the range of bedrock temperature fluctuation simulated over the glacial cycle. Other examples of vertical bedrock temperature profiles, with other surface cover types (wet, dry, peatland) are found in /Hartikainen et al. 2010/.

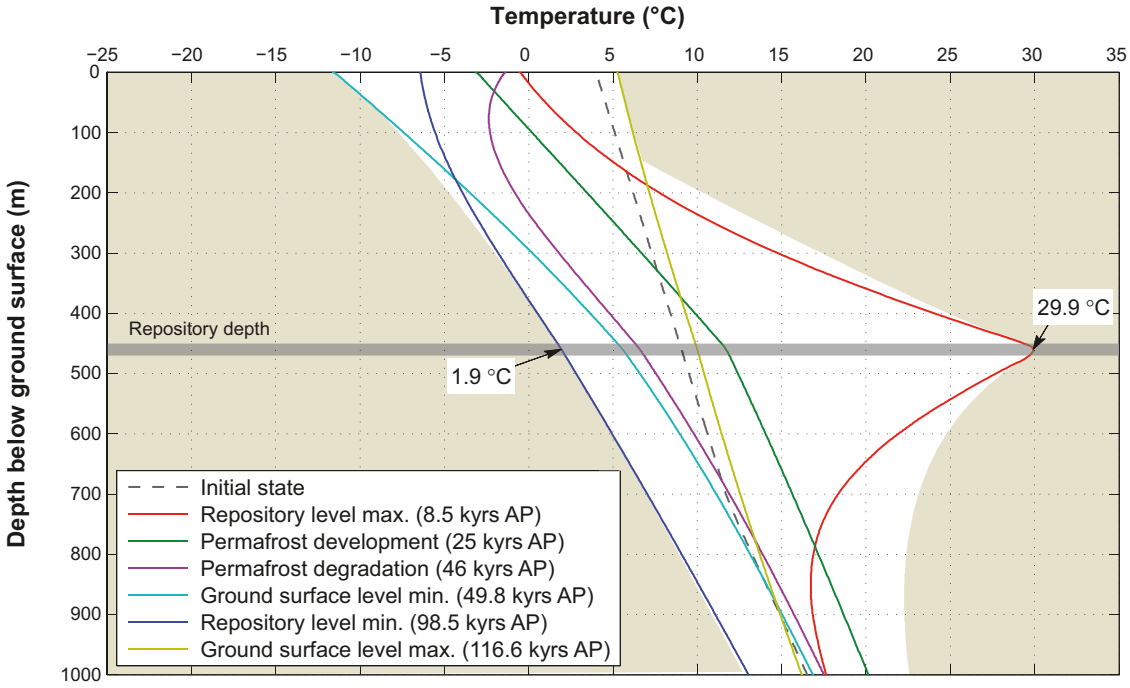

Figure 5-26. *Ground temperature along a vertical profile located in the middle of the repository for the humid variant of the severe permafrost case and dry surface condition type. The white colour envelope represents the range of bedrock temperature fluctuation simulated over the glacial cycle.*

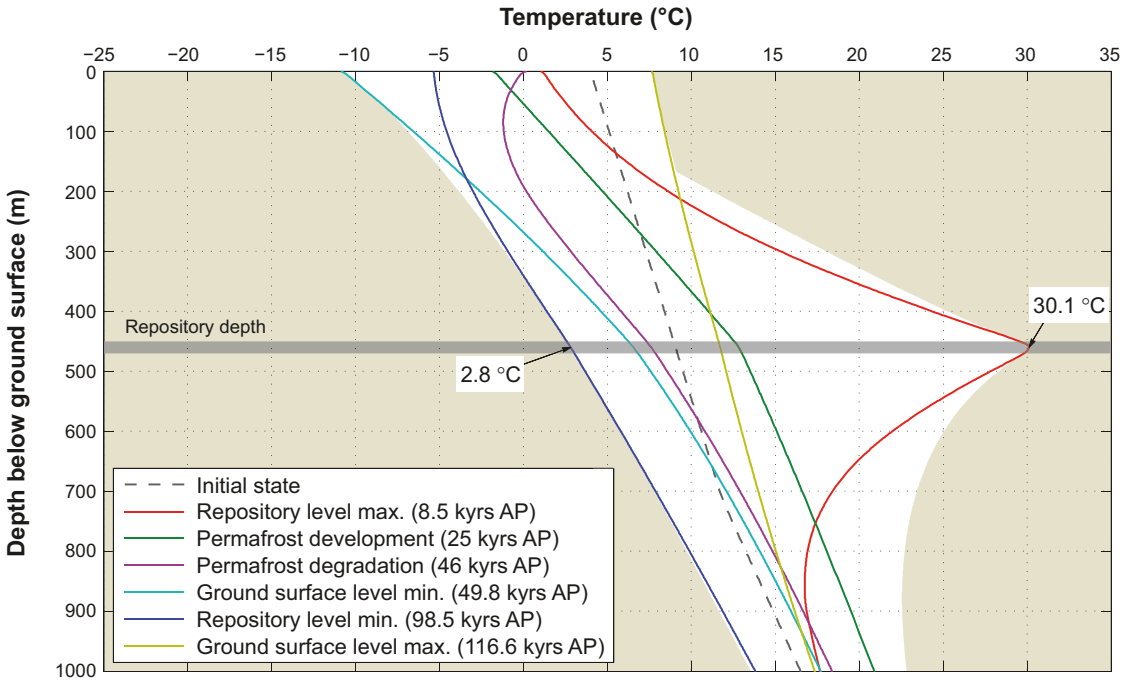

Figure 5-27. *Ground temperature along a vertical profile located in the middle of the repository for the dry variant of the severe permafrost case and dry surface condition type. The white colour envelope represents the range of bedrock temperature fluctuation simulated over the glacial cycle.*

Given the permafrost and freezing results presented above for the *severe permafrost case*, the associated results on salinity concentration are illustrated in Figures 5-28 and 5-29. In this study, the effect of freezing-out of salt is small. Due to low salinity concentrations at shallow depths, the impacts of freezing on salinity exclusion and redistribution are difficult to see from the results. However, under more extreme conditions than simulated in the *severe permafrost case*, if the air temperature curve reconstructed for the last glacial cycle is lowered by 8°C, the freezing occurs more intensively and an increase in salinity concentration due to salt exclusion can be seen (Figure 5-30).

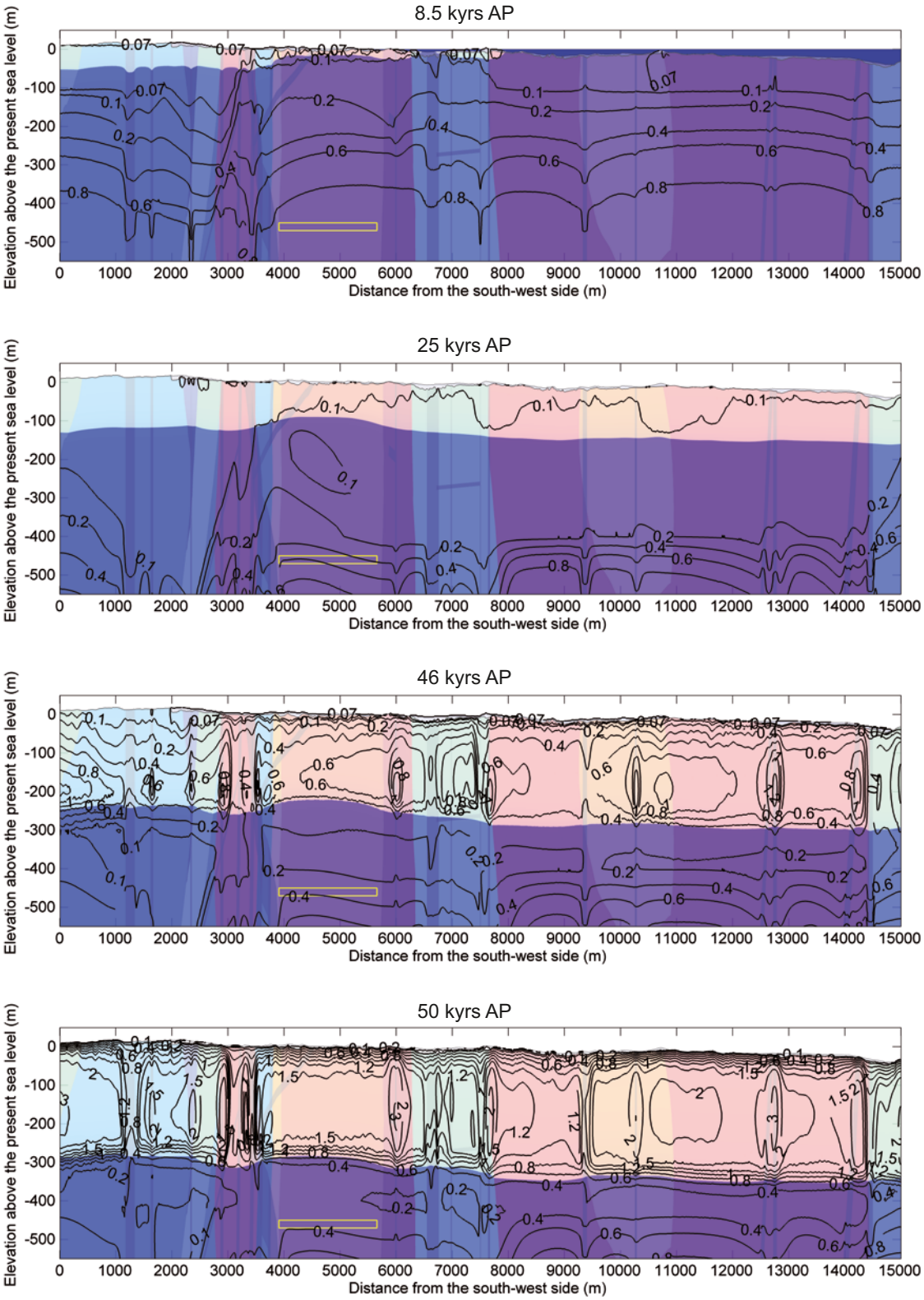

Figure 5-28. *Salinity concentration isolines at times 8.5, 25, 46, 50 kyrs after present for the humid variant of the severe permafrost case. The isolines show salinity concentrations of 0.07, 0.1, 0.2, 0.4, 0.6, 0.8, 1, 1.2, 1.5, 2, 3, 4, 5 mass-%. Blue colour blue on the top of the profile at 8.5 kyrs after present shows the Baltic Sea and the light colour the extent of perennially frozen ground.*

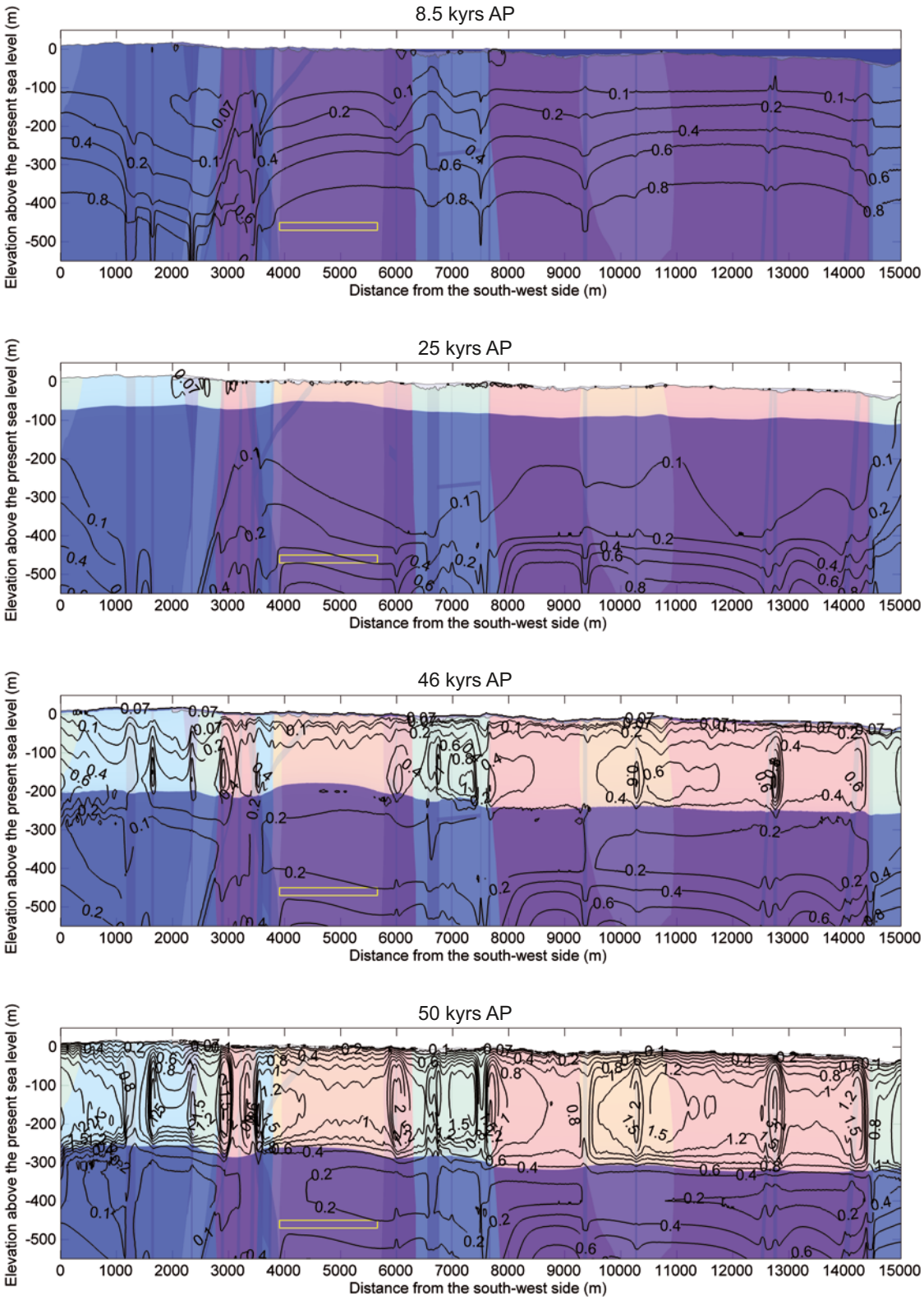

Figure 5-29. *Salinity concentration isolines for the dry variant of the severe permafrost case at times 8.5, 25, 46, 50 kyrs after present. The isolines show salinity concentrations of 0.07, 0.1, 0.2, 0.4, 0.6, 0.8, 1, 1.2, 1.5, 2, 3, 4, 5 mass-%. Blue colour on the top of the profile at 8.5 kyrs after present shows the Baltic Sea and the light colour the extent of perennially frozen ground.*

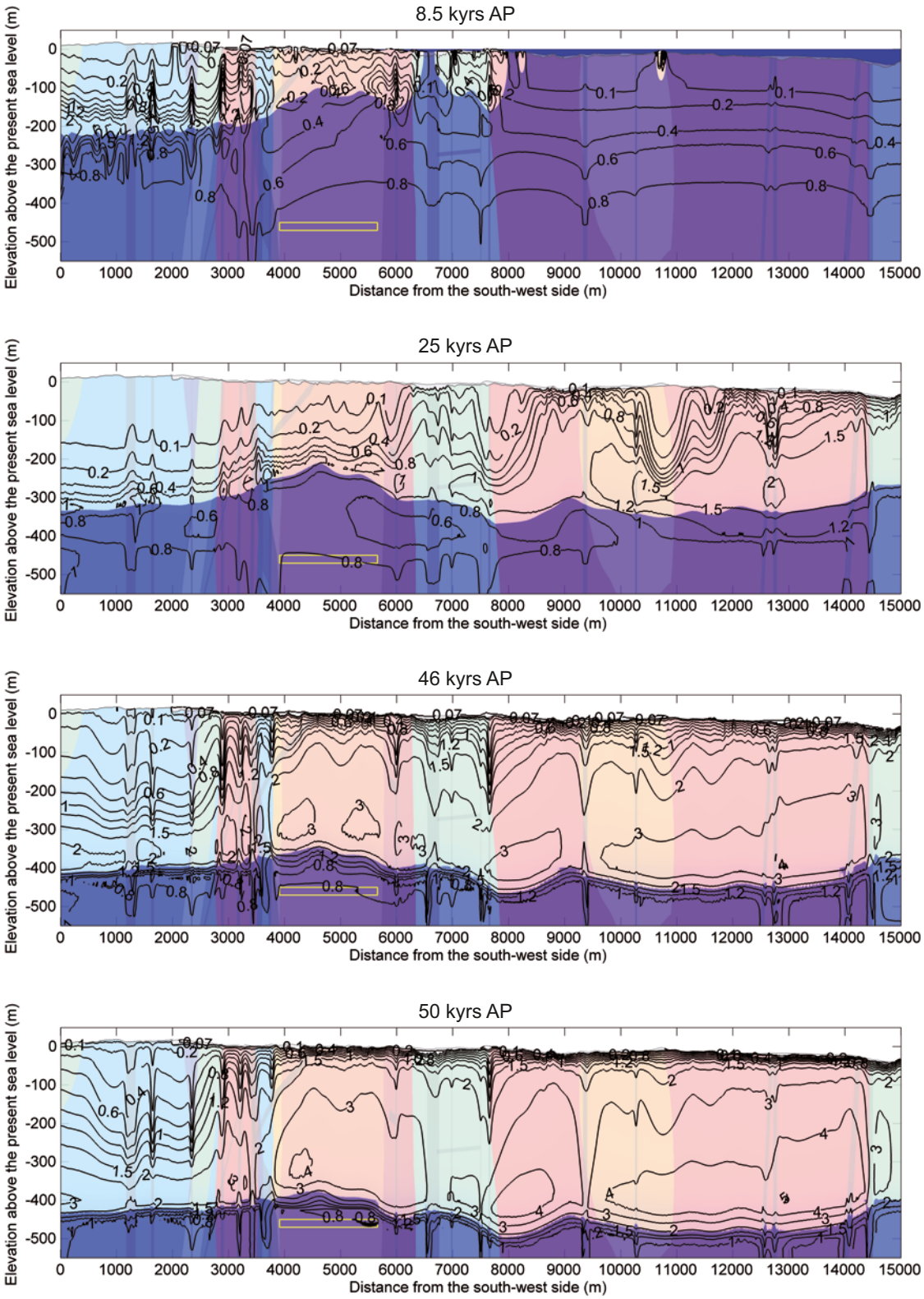

Figure 5-30. *Salinity concentration isolines at times 8.5, 25, 46, 50 kyrs after present for the humid variant of the severe permafrost case and air temperature decreased by 8°C. The isolines show the salinity concentrations 0.07, 0.1, 0.2, 0.4, 0.6, 0.8, 1, 1.2, 1.5, 2, 3, 4, 5 mass-%. Blue colour blue on the top of the profile at 8.5 kyrs after present shows the Baltic Sea and the light colour the extent of perennially frozen ground.*

Sensitivity experiments

In addition to the *severe permafrost case* simulations described above, a sensitivity experiment was made to study the effects of uncertainties in bedrock thermal properties together with uncertainties in surface conditions (excluding air temperature) for this case, i.e. the same experiment as sensitivity experiment number 6 conducted for the *reference glacial cycle*. To this end, the uncertainty interval is obtained by combining the dry climate variant with the thermal properties enhancing permafrost development, and the humid climate variant with thermal properties diminishing permafrost development, see Section 3.4.4. The resulting evolution of maximum permafrost depth and maximum depth of perennially frozen ground over the repository are shown in Figure 5-31.

Sensitivity studies have also been made to investigate the climate conditions required to develop permafrost and perennially frozen ground to repository depth /Hartikainen et al. 2010/. Based on the results of a similar study performed in SR-Can /SKB 2006a/, this was made by lowering the entire temperature curve reconstructed for the last glacial cycle by 4, 6, 8, 10, 12, 14 and 16°C, see Figure 3-63. A temperature of 0°C corresponds to the freezing point of fresh water at normal pressure. A temperature of –2°C corresponds to the freezing point of the backfill material in the deposition tunnels, whereas a temperature of –4°C constitutes the temperature criterion used in the safety assessment for freezing of the buffer clay /SKB 2011/.

The results show that if the reconstructed temperature curve for the last glacial cycle is lowered by 8°C, the 0°C isotherm (permafrost) reach repository depth (450 m) (Figure 5-32). The temperature curve needs to be lowered by more than 10°C in order to make the −2°C isotherm reach repository depth (Figure 5-33), and it needs to be lowered by as much as 14°C in order make the −4°C isotherm reach repository depth (Figure 5-34).

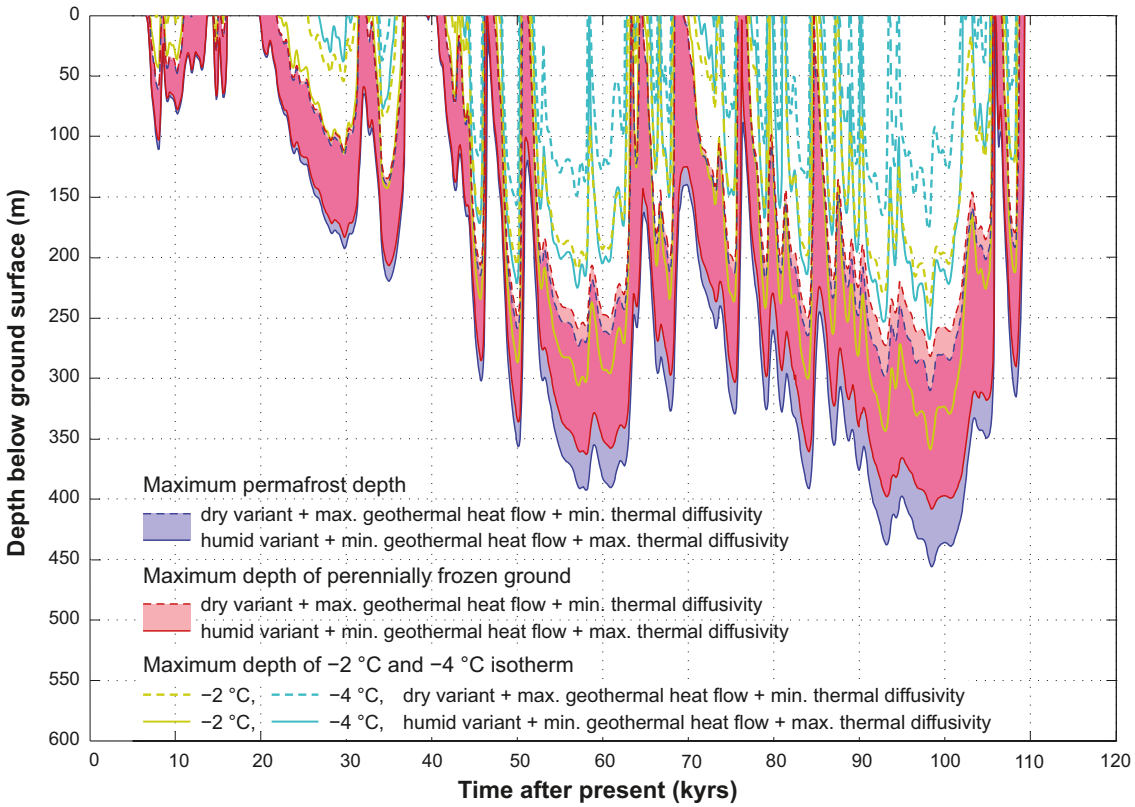

Figure 5-31. *Evolution of maximum permafrost depth, maximum depth of perennially frozen ground and maximum depth of –2 and –4°C isotherms over the repository for the severe permafrost case when considering combined uncertainties in surface conditions and thermal properties favourable for permafrost growth. The shaded area in blue and red represents the range when considering the dry and humid climate variants. The darker lilac colour indicates that the results for permafrost and perennially frozen ground overlap.*

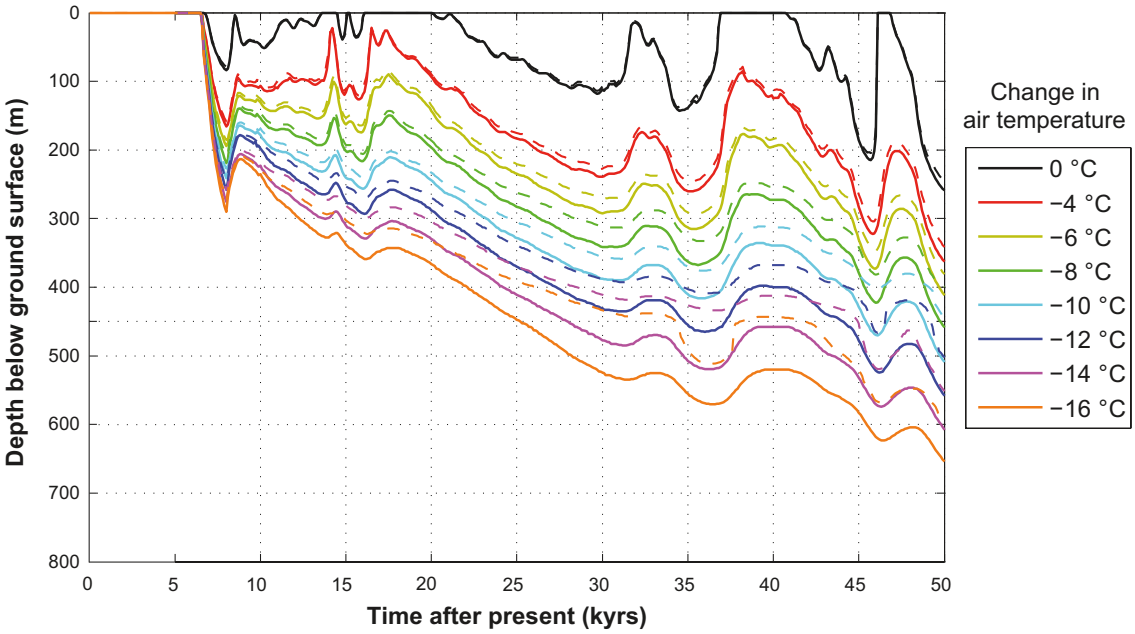

Figure 5-32. *Evolution of 0°C isotherm (permafrost) depth (black solid line) and depth of perennially frozen ground (black dashed line) at the repository location for the reference glacial cycle (dry climate variant, see Section 3.4.4). The figure also show corresponding results for simulations where the temperature curve reconstructed for the last glacial cycle has been lowered by –4, –6, –8, –10, –12, –14 and –16°C compared to the reference glacial cycle.*

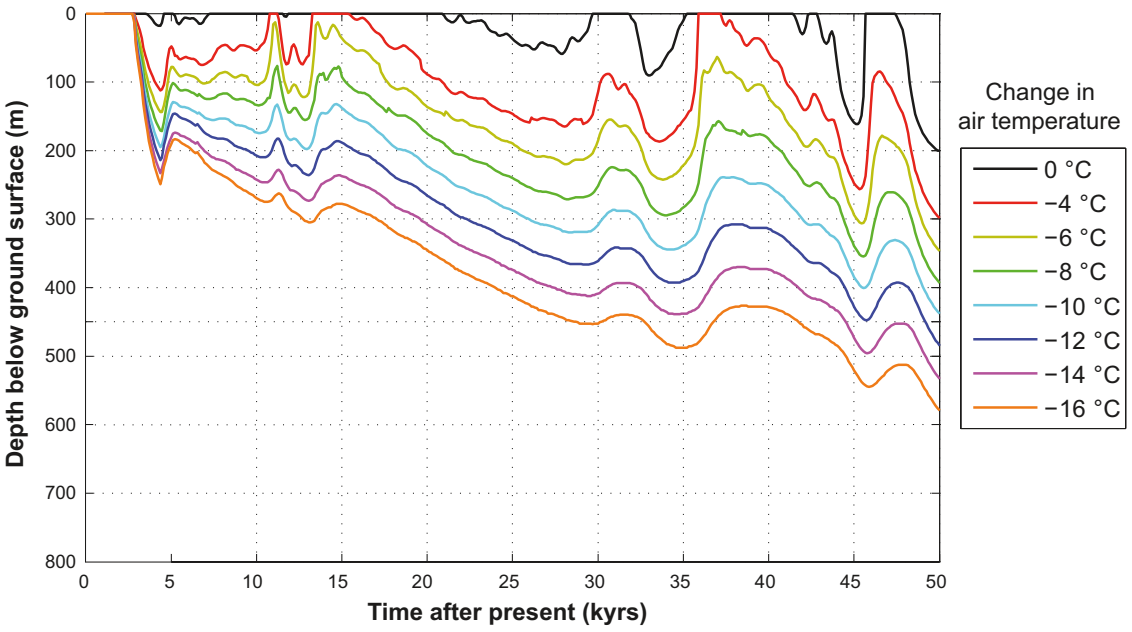

Figure 5-33. *Evolution of –2°C-isotherm depth at the repository location for the reference glacial cycle (dry climate variant, see Section 3.4.4) (black line). The figure also shows corresponding results for simulations where the temperature curve reconstructed for the last glacial cycle has been lowered by –4, –6, –8, –10, –12, –14 and –16°C compared to the reference glacial cycle (coloured lines).*

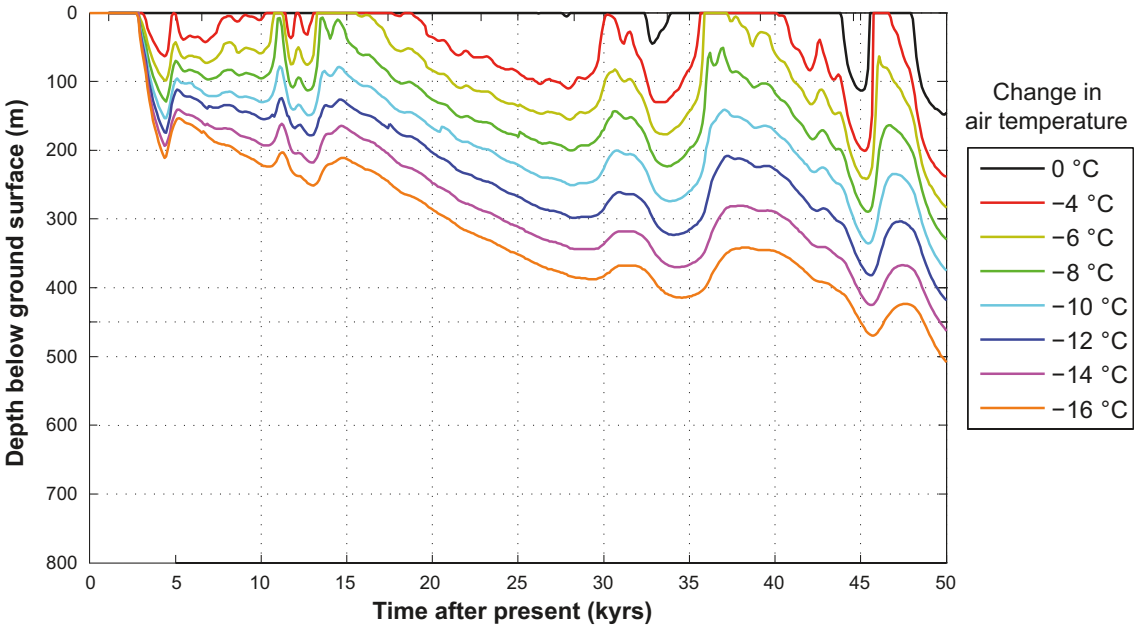

Figure 5-34. *Evolution of –4°C-isotherm depth at the repository location for the reference glacial cycle ((dry climate variant, see Section 3.4.4) (black line). The figure also shows corresponding results for simulations where the temperature curve reconstructed for the last glacial cycle has been lowered by –4, –6, –8, –10, –12, –14 and –16°C compared to the reference glacial cycle (coloured lines).*

The evolution of subsurface temperatures and residual pore water pressures at a depth of 400 m at Forsmark for a case similar to the *severe permafrost case* described above is found in /SKB 2006a, Figure 3-64/.

Summary of the *severe permafrost case* and sensitivity studies

In the following, the main conclusions from the *severe permafrost case* and the sensitivity studies are summarized. When assuming a glacial cycle without any cover of ice sheet, sea, vegetation or snow, the range for the maximum permafrost depth (the 0°C isotherm) over the repository is 360–390 m depending on the surface conditions. The corresponding range for the entire investigated profile is 380-420 m. Likewise, for the same assumptions, the maximum depth of perennially frozen ground over the repository and the entire profile ranges between 330 and 360 m depending on the surface conditions. Very low surface temperatures are required in order to give an increase in salinity concentration due to salt exclusion. Making the unrealistic combination of the *severe permafrost case* (which assumes no ice sheet, winter snow, vegetation or sea coverage during the entire glacial cycle), with maximum thermal conductivity and minimum heat capacity for the subsurface, as well as using the minimum geothermal heat flow value, the simulated maximum permafrost depth over the repository may extend to 450 m depth in 95,000 years. However, it should be noted that this combination of assumptions is unrealistic. Assuming a similar climate variability as during the last glacial cycle, the temperature curve reconstructed for the last glacial cycle needs to be lowered by 8°C order in order to make the 0°C isotherm (permafrost) reach repository depth, while the temperature curve needs to be lowered by as much as 14°C in order make the −4°C isotherm reach repository depth. Also when considering the significant estimated maximum uncertainty in the reconstructed air temperature curve (±6 ºC, Appendix 1), this corresponds to an unrealistically large change in glacial climate conditions.

It should here be remembered that the *severe permafrost case* was designed to take care of remaining uncertainties (mainly related to ice sheet coverage) that was not covered in the extensive investigation of uncertainties reported in the *reference glacial cycle* (Section 4.5 and 3.4.4). Therefore, the resulting maximum uncertainty interval for e.g. permafrost and frozen depths (Table 5-11), may reach deeper in the *reference glacial cycle* than in the *severe permafrost case* (whereas calculated depths without the uncertainty interval are deeper for the *severe permafrost case*).

Table 5-11. Maximum depths of permafrost (0°C isotherm), perennially frozen ground, −2°C isotherm and −4°C isotherm for the severe permafrost case and the reference glacial cycle. The uncertainty interval for the severe permafrost case includes all uncertainties (set to their most pessimistic values) except air temperature, since lower air temperatures are not compatible with the main assumption of having no ice sheet development over the site. The uncertainty interval for the reference glacial cycle includes the unlikely combination of having all uncertainties, including air temperature, set to their most pessimistic values favouring permafrost growth.

	Maximum permafrost depth (0°C isotherm) [max uncertainty interval]	Maximum depth perennially frozen ground [max uncertainty interval]	Maximum depth −2°C isotherm [max uncertainty interval]	Maximum depth −4°C isotherm [max uncertainty interval]
Severe permafrost case	393 [down to 456]	359 [down to 408]	311 [down to 359]	234 [down to 268]
Reference glacial cycle	259 m [down to 463 m]	246 m [down to 422 m]	200 m [down to 388 m]	148 m [down to 316 m]

The information on freezing depths from the *severe permafrost case* and the *reference glacial cycle* is used to assess the potential for freezing of groundwater, buffer clay and deposition tunnel backfill material in the safety assessment freezing scenario /SKB 2011/.

The development of climate domains for the *severe permafrost case* is shown in Figure 5-35. For this construction, the dry climate variant, with most permafrost, was chosen. Temperate climate conditions prevail for 24 kyrs or 20% of the time, whereas periglacial conditions prevail for 96 kyrs or 80% of the time. There are no periods of glacial conditions.

5.5.4 Surface denudation

In the *severe permafrost case*, the main assumption is that there is no ice sheet present at Forsmark during the glacial cycle, and consequently the denudation process that contributed to the largest amount of denudation in the *reference glacial cycle* (glacial erosion) does not take place. In line with this, it is assumed that the amount of surface denudation in the present climate case is smaller than in the *reference glacial cycle*, and definitely smaller than in the case of extended ice sheet duration. Therefore, surface denudation is not described and treated further in the *severe permafrost case*.

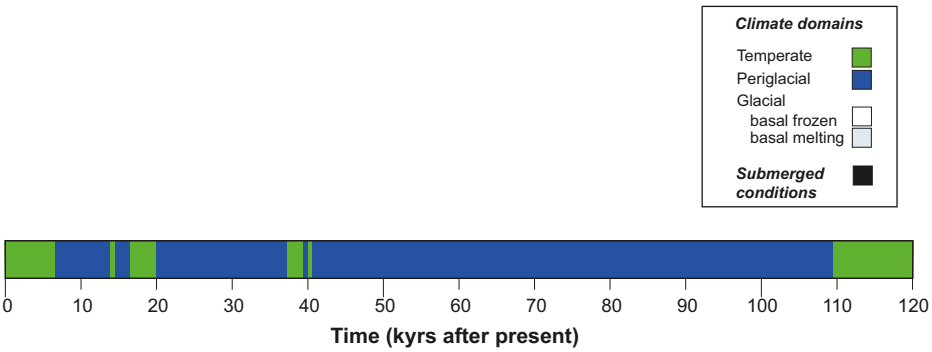

Figure 5-35. *Evolution of climate conditions at the Forsmark repository location as a time series of climate domains for the severe permafrost case. Following from the assumptions used for this climate development, there are no periods of glacial or submerged conditions. The glacial cycle is dominated by periglacial conditions, with longer-lasting temperate climate conditions during periods that correspond to interglacial conditions.*

5.6 Summary of climate cases for the SR-Site safety assessment

As stated in Section 1.2, a single most likely future climate evolution cannot be predicted with enough confidence and detail for the analyses of long-term safety of repositories for spent nuclear fuel. The longest safety assessment time scales range up to around 100,000 years and 1 million years /SKB 2011/. The 100,000 year time scale corresponds to the time scale of glacial cycles during the past 700,000 years. The selected approach in the SR-Site safety assessment, as well as in previous SKB safety assessments such as SR-Can, is therefore to use a reasonable future climate evolution, consisting of a repetition of conditions reconstructed for the last glacial cycle, as well as complementary climate evolutions with potentially larger impacts on repository safety (Section 1.2 and Figure 1-3). Given that the safety assessment needs to analyse repository safety on these very long time scales, the existing uncertainties in future climate development result in a wide range of possible climate developments that need to be addressed. Figure 5-36 and Table 5-12 summarise the climate developments included in the SR-Site safety assessment. These cases are based on the processes that have been identified as important for long-term KBS-3 repository safety and on the present scientific knowledge and uncertainties of future climate development with focus on these processes. The climate cases in Figure 5-36 are used as input to the description and analysis of various SR-Site safety assessment scenarios, see Figure 1-3 and /SKB 2011/.

The *reference glacial cycle* (Figure 5-36 and Section 4.5) contributes with a reasonable development of climate and climate-related conditions for the coming 120 kyrs, whereas the *global warming case* (Section 5.1) contributes with a variant of this development. The longest period of temperate climate conditions for the coming 120 kyrs, including an initial period with the warmest and wettest climate conditions, highest sea-level, as well as longest period of groundwater formation from precipitation, is found in the *extended global warming case (*Section 5.2). The most extended period of periglacial climate conditions, with longest periods of permafrost at Forsmark, is found in the *severe permafrost case* (Section 5.5). The deepest permafrost and frozen ground is also found in the *severe permafrost case.* The largest uncertainty for the development of permafrost and frozen ground, which is future air temperature, is however connected to the *reference glacial cycle*, resulting in the deepest uncertainty interval for freezing being documented in this climate case. The longest period of glacial conditions, and associated period of groundwater formation from glacial meltwater, is found in the *extended ice sheet duration case* (Section 5.3). The maximum future ice sheet thickness, and resulting largest increase in hydrostatic pressure at repository depth, is found in the *maximum ice sheet configuration case* (Section 5.4) (a case not depicted in Figure 5-36). The six climate cases together cover the expected maximum range within which climate and climate-related conditions of importance for long-term repository safety may vary within the time scales analysed in the SR-Site safety assessment.

In light of present-day knowledge on climate, some of the climate cases in Figure 5-36 might be regarded as more likely than others. However, the adopted approach in the SR-Site safety assessment is to handle *all* possible future climate developments relevant for repository safety. Therefore, there is in the safety assessment no need to quantify the probabilities of the identified individual climate developments. The *actual* development of climate and climate-related processes at the Forsmark site for the coming 120 kyrs are expected to lie within the range covered by the six climate cases presented in Figure 5-36.

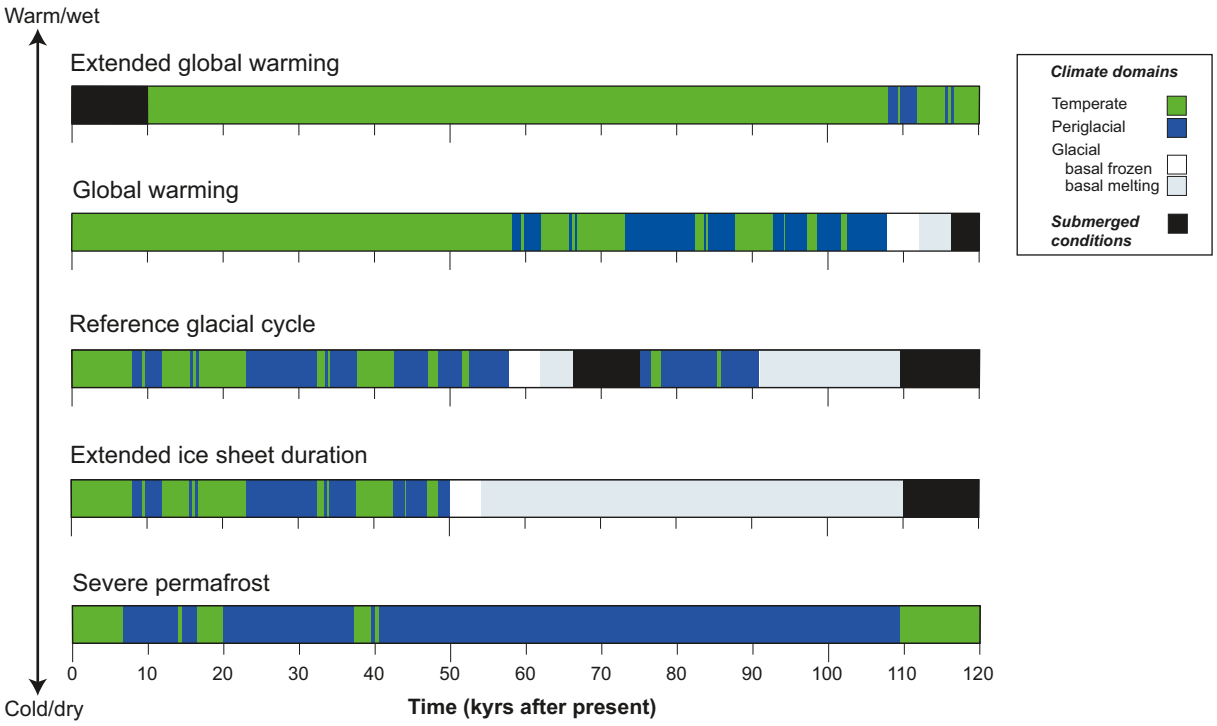

Figure 5-36. *Summary of future climate cases analysed in the SR-Site safety assessment. The cases go from warmer/wetter climates at the top to colder/dryer climates at the bottom. The maximum ice sheet configuration case, with maximum ice thicknesses, is not shown. However, it could be contained within the temporal development of the extended ice sheet duration case.*

Table 5-12. Summary of duration of climate domains for the six climate cases in SR-Site. For definitions of the climate domains, see Section 1.2.3.

Climate case	Temperate climate domain [kyrs] (percent of time of glacial cycle)	Periglacial climate domain [kyrs] (percent of time of glacial cycle)	Glacial climate domain [kyrs] (percent of time of glacial cycle)	Submerged conditions [kyrs] (percent of time of glacial cycle)
Extended global warming (Section 5.2)	106 kyrs (89%)	4 yrs (3%)	0 yrs (0%)	10 kyrs (8%)
Global warming (Section5.1)	78 kyrs (65%)	28 kyrs (23%)	11 kyrs (9%)	3 kyrs (c. 3%)
Reference glacial cycle (Section 4.5)	31 kyrs (26%)	41 kyrs (34%)	28 kyrs (24%)	19 kyrs (16%)
Extended ice sheet duration (Section 5.3)	28 kyrs (23%)	22 kyrs (18%)	60 kyrs (50%)	10 kyrs (8%)
Severe permafrost (Section 5.5)	24 kyrs (20%)	96 kyrs (80%)	0 kyrs (0%)	0 kyrs (0%)

6 List of abbreviations

Except expressions in equations, chemical expressions and common units

1D	One dimensional
2D	Two dimensional
3D	Three dimensional
A1B	IPCC emission scenario
A1FI	IPCC emission scenario
A2	IPCC emission scenario
ACIA	Arctic Climate Impact Assessment
AD	Anno Domini
AMAP	Arctic Monitoring and Assessment Programme
AMS	Accelerator Mass Spectrometer
AMOC	Atlantic Meridional Overturning Circulation
AOGCM	Atmosphere-Ocean General Circulation Model
AP	After Present
AR4	Fourth Assessment Report of IPCC
B2	IPCC emission scenario
BACC	BALTEX Assessment of Climate Change for the Baltic Sea Basin
BC	Before Christ
BIFROST	Baseline Inferences for Fennoscandian Rebound, Sea-level, and Tectonics
BIOCLIM	Modelling sequential BIOsphere systems under CLIMate change for radioactive waste disposal
BP	Before Present
CCSM3	Community Climate System Model 3
CRU	Climate Research Unit (East Anglia)
CSM	Climate System Model
CMIP3	Climate Model Intercomparison Project, phase 3
DEM	Digital Elevation Model
Dfb	Köppen climate classification class (temperate, humid cold climate with year-round precipitation)
dGPS	Differential Global Positioning System
DJF	December, January, February (winter season)
DO event	Dansgaard-Oeschger event
DVM	Dynamic Vegetation Model
EAIS	East Antarctic Ice Sheet
EISMINT	European Ice Sheet Modeling Initiative
ELA	Equilibrium Line Altitude
EPICA	European Project for Ice Coring in Antarctica
FEP	Features, Events and Processes
GAP	Greenland Analogue Project
GCM	General Circulation Model, Global Circulation Model
GIA	Glacial Isostatic Adjustment
GIS	Geographical Information System
GISP2	Greenland Ice Sheet project 2
GPS	Global Positioning System
GRACE	Gravity Recovery and Climate Experiment

GRIP	European Greenland Ice Core Project
GS 12	Greenland Stadial number 12
HadCM3	Hadley Centre Coupled Climate Model, version 3
HFD	Heat Flow Density, *or* geothermal heat flow
ICE-3G	Global ice sheet reconstruction
ICE-5G	Global ice sheet reconstruction
InSAR	Interferometric Synthetic Aperture Radar
IPCC	Intergovernmental Panel on Climate Change
JJA	June, July, August (summer season)
KTH	Royal Institute of Technology (Stockholm)
LGM	Last Glacial Maximum
ka	kilo annum (thousands of years)
KBS-3	Kärnbränslesäkerhet 3 (method for final storage of spent nuclear fuel)
kyr	kilo year (thousand years)
kyrs	kilo years (thousands of years)
LPJ-GUESS	A dynamic vegetation model
Ma	Mega annum (millions of years)
MIS	Marine Isotope Stage
MX-80	Bentonite clay
Myr	million year (million years)
Myrs	Millions of years (millions of years)
NCAR	National Centre for Atmospheric Research
NEA	Nuclear Energy Agency
NGRIP	North Greenland Ice core Project
NorthGRIP	North Greenland Ice core Project
NSF	National Science Foundation
NWMO	Nuclear Waste Management Organization
OSL	Optically Stimulated Luminescence
PMIP1	Paleoclimate Modelling Intercomparison Project, phase 1
PMIP2	Paleoclimate Modelling Intercomparison Project, phase 2
PREM	Preliminary Reference Earth Model
QA	Quality assurance
RCA 3	Rossby Centre Regional Climate Model
RCM	Regional Circulation Model
RH70	Rikets höjdsystem 1970 (national elevation system in Sweden)
RT-90	Rikets Triangelnät 1990 (national coordinate system in Sweden)
ScanSAR	Scanning Synthetic Aperture Radar
SCAR	Scientific Committee on Antarctic Research
SGU	Geological Survey of Sweden
SKB	Swedish Nuclear Fuel and Waste Management Organisation
SMHI	Swedish Meteorological and Hydrological Institute
SSTs	Sea Surface temperatures
SWECLIM	Swedish Regional Climate Modelling Programme
THM	Thermo-Hydro-Mechanical
TWI	Topographic Wetness Index
UMISM	University of Maine Ice Sheet Model
UNFCCC	United Nation’s Framework Convention on Climate Change
WAIS	West Antarctic Ice Sheet

7 References

SKB's (Svensk Kärnbränslehantering AB) publications can be found at www.skb.se/publications.

ACIA, 2005. Arctic Climate Impact Assessment. Cambridge: Cambridge University Press.

Ahnert F, 1970. Functional relationships between denudation, relief, and uplift in large, mid-latitude drainage basins. American Journal of Science, 268, pp 243–263.

Ahonen L, 2001. Permafrost: occurrence and physicochemical processes. Helsinki: Posiva.

Ahrens C D, 1994. Meteorology today: an introduction to weather, climate and the environment. 5th ed. Minneapolis/St. Paul: West Publishing Company.

Allen D, Michel F, Judge A, 1988. Paleoclimate and permafrost in the Mackenzie Delta. In: Proceedings of the fifth international conference on permafrost. Trondheim, 2–5 August 1988. Vol 1. Trondheim: Tapir.

Alley R B, 1992. Flow-law hypotheses for ice-sheet modeling. Journal of Glaciology, 38, pp 245–256.

Alley R B, Clark P U, Huybrechts P, Joughin I, 2005a. Ice-sheet and sea-level changes. Science, 310, pp 456–460.

Alley R B, Dupont T K, Parizek B R, Anandakrishnan S, 2005b. Access of surface meltwater to beds of sub-freezing glaciers: preliminary insights. Annals of Glaciology, 40, pp 8–14.

Alley R B, Dupont T K, Parizek B R, Anandakrishnan S, Lawson D E, Larson G J, Evenson E B, 2006. Outburst flooding and the initiation of ice-stream surges in response to climatic cooling. Geomorphology, 75, pp 76–89.

Allison I, Bindoff N L, Bindschadler R A, Cox P M, de Noblet N, England M H, Francis J E, Gruber N, Haywood A M, Karoly D J, Kaser G, Le Quéré C, Lenton T M, Mann M E, McNeil B I, Pitman A J, Rahmstorf S, Rignot E, Schellnhuber H J, Schneider S H, Sherwood S C, Somerville R C J, Steffen K, Steig E J, Visbeck M, Weaver A J, 2009. The Copenhagen diagnosis, 2009: updating the world on the latest climate science. Sydney: The University of New South Wales Climate Change Research Centre (CCRC).

AMAP, 2009. The Greenland ice sheet in a changing climate: snow, water, ice and permafrost in the Arctic (SWIPA) 2009. Oslo : Arctic Monitoring and Assessment Programme.

Ampel L, Bigler C, Wohlfarth B, Risberg J, Lotter A F, Veres D, 2010. Modest summer temperature variability during DO cycles in western Europe. Quaternary Science Reviews, 29, pp 1322–1327.

Andersen B G, Mangerud J, 1989. The last interglacial-glacial cycle in Fennoscandia. Quaternary International, 3-4, pp 21–29.

Andersen K, Azuma N, Barnola J-M, Bigler M, Biscaye P, Caillon N, Chappellaz J, Clausen H B, Dahl-Jensen D, Fischer H, Flückiger J, Fritzsche D, Fujii Y, Goto-Azuma K, Grønvold K, Gundestrup N S, Hansson M, Huber C, Hvidberg C S, Johnsen S J, Jonsell U, Jouzel J, Kipfstuhl S, Landais A, Leuenberger M, Lorrain R, Masson-Delmotte V, Miller H, Motoyama H, Narita H, Popp T, Rasmussen S O, Raynaud D, Röthlisberger R, Ruth U, Samyn D, Schwander J, Shoji H, Siggaard-Andersen M-L, Steffensen J P, Stocker T, Sveinbjörnsdóttir A E, Svensson A, Takata M, Tison J-L, Thorsteinsson T, Watanabe O, Wilhelms F, White J W C, 2004. High-resolution record of Northern Hemisphere climate extending into the last interglacial period. Nature, 431, pp 147–151.

Andrews J T, Barber D C, 2002. Dansgaard-Oeschger events: is there a signal off the Hudson Strait Ice Stream? Quaternary Science Reviews, 21, pp 443–454.

Archer D, 2005. Fate of fossil fuel CO_2 in geologic time. Journal of Geophysical Research, 110, C09S05, doi:10.1029/2004JC002625.

Archer D, Brovkin V, 2008. The millennial atmospheric lifetime of anthropogenic CO_2. Climatic Change, 90, pp 283–297.

Archer D, Ganopolski A, 2005. A movable trigger: Fossil fuel CO_2 and the onset of the next glaciation. Geochemistry, Geophysics, Geosystems, 6, Q05003, doi:10.1029/2004GC000891.

Archibold O W, 1994. Ecology of world vegetation. New York: Springer.

Árnadóttir T, Lund B, Jiang W, Geirsson H, Björnsson H, Einarsson P, Sigurdsson T, 2009. Glacial rebound and plate spreading: results from the first countrywide GPS observations in Iceland. Geophysical Journal International, 177, pp 691–716.

Arndt D S, Baringer M O, Johnson M R (eds), 2010. State of the climate in 2009. Bulletin of the American Meteorological Society, 91, pp 1–222.

Arnold N, Sharp M, 2002. Flow variability in the Scandinavian ice sheet: modelling the coupling between ice sheet flow and hydrology. Quaternary Science Review, 21, pp 485–502.

Arnold N, Richards K, Willis I, Sharp M, 1998. Initial results from a distributed, physically based model of glacier hydrology. Hydrological Processes, 12, pp 191–219.

Artemieva I M, Mooney W D, 2001. Thermal thickness and evolution of Precambrian lithosphere: a global study. Journal of Geophysical Research, 106, pp 16387–16414.

BACC author team 2008. Assessment of climate change for the Baltic Sea basin. Berlin, Heidelberg: Springer Verlag. (Regional climate studies)

Balling N, 1984. Gravity and isostasy in the Baltic Shield. In: Galson D A, Mueller S, Munch B (eds). Proceedings of the first workshop on the European Geotraverse Project (EGT): The northern segment. Strasbourg: European Science Foundation, pp 53–66.

Bamber J L, Riva R E M, 2010. The sea-level fingerprint of 21st century ice mass flux. The Cryosphere Discussions, 4, pp 1593–1606.

Bamber J L, Layberry R L, Gogineni S P, 2001. A new ice thickness and bed data set for the Greenland ice sheet. 1. Measurement, data reduction, and errors. Journal of Geophysical Research, 106, pp 33773–33780.

Bamber J L, Alley R B, Joughin I, 2007. Rapid response of modern day ice sheets to external forcing. Earth and Planetary Science Letters, 257, pp 1–13.

Bamber J L, Riva R E M, Vermeersen B L A, LeBrocq A M, 2009. Reassessment of the potential sea-level rise from a collapse of the West Antarctic ice sheet. Science, 324, pp 901–903.

Barber D C, Dyke A, Hillaire-Marcel C, Jennings A E, Andrews J T, Kerwin M W, Bilodeau G, McNeely R, Southon J, Morehead M D, Gagnon J-M, 1999. Forcing of the cold event of 8,200 years ago by catastrophic drainage of Laurentide lakes. Nature, 400, pp 344–348.

Bard E, Hamelin B, Fairbanks R G, 1990. U-Th ages obtained by mass spectrometry in corals from Barbados: sea-level during the past 130,000 years. Nature, 346, pp 456–458.

Bard E, Hamelin B, Arnold M, Montaggioni L, Cabioch G, Faure G, Rougerie F, 1996. Deglacial sea-level record from Tahiti corals and the timing of global meltwater discharge. Nature, 382, pp 241–244.

Barron E, Pollard D, 2002. High-resolution climate simulations of oxygen isotope stage 3 in Europe. Quaternary Research, 58, pp 296–309.

Bassett S E, Milne G A, Mitrovica J X, Clark P U, 2005. Ice sheet and solid Earth influences on far-field sea-level histories. Science, 309, pp 925–928.

Bates B C, Kundzewicz Z W, Wu S, Palutikof J P (eds), 2008. Climate change and water. Technical paper of the Intergovernmental Panel on Climate Change. Geneva: IPCC Secretariat.

Bauder A, Mickelson D M, Marshall S J, 2003. Modelling ice sheet permafrost interaction around the southern Laurentide ice sheet. EGS - AGU - EUG Joint Assembly. Abstracts from the meeting held in Nice, France, 6–11 April 2003, abstract 12348.

Beardsmore G R, Cull J P, 2001. Crustal heat flow: a guide to measurement and modelling. Cambridge: Cambridge University Press.

Bell R E, 2008. The role of subglacial water in ice-sheet mass balance. Nature Geoscience, 1, pp 297–304.

Benn D I, Evans D J A, 1998. Glaciers & glaciation. London: Arnold.

Bennett M R, Waller R I, Midgley N G, Huddart D, Gonzalez S, Cook S J, Tomio A, 2003. Subglacial deformation at sub-freezing temperatures? Evidence from Hagafellsjökull-Eystri, Iceland. Quaternary Science Reviews, 22, pp 915–923.

Benson C S, 1961. Stratigraphic studies in the snow and firn of the Greenland ice sheet. Folia Geographica Danica, 9, pp 13–37.

Berger A, 1978. Long-term variations of daily insolation and Quaternary climatic changes. Journal of the Atmospheric Sciences, 35, pp 2362–2367.

Berger A, Loutre M F, 2002. An exceptionally long interglacial ahead? Science, 297, pp 1287–1288.

Bhattacharya I, Jezek K C, Wang L, Liu H, 2009. Surface melt area variability of the Greenland ice sheet: 1979–2008. Geophysical Research Letters, 36, L20502, doi:10.1029/2009GL039798.

Bills B G, James T S, 1996. Late Quaternary variations in relative sea level due to glacial cycle polar wander. Geophysical Research Letters, 23, pp 3023–3026.

Bintanja R, van de Wal R S W, 2008. North American ice-sheet dynamics and the onset of 100,000-year glacial cycles. Nature, 454, pp 869–872.

BIOCLIM, 2003. Deliverable D7. Continuous climate evolution scenarios over western Europe (1000 km scale). Work package 2: Simulation of the future evolution of the biosphere system using the hierarchical strategy. Châtenay-Malabry: Agence Nationale pour la Gestion des Dechets Radioactifs (ANDRA).

Birch F, Roy R F, Decker E R, 1968. Heat flow and thermal history in New England and New York. In: Zen E-an (ed). Studies of Appalachian geology: northern and maritime. New York: Interscience, pp 437–451.

Birgersson M, Karnland O, Nilsson U, 2008. Freezing in saturated bentonite – a thermodynamic approach. Physics and Chemistry of the Earth, Parts A/B/C, 33, S527–S530.

Birgersson M, Karnland O, Nilsson U, 2010. Freezing of bentonite. Experimental studies and theoretical considerations. SKB TR-10-40, Svensk Kärnbränslehantering AB.

Björck S, 1995. A review of the history of the Baltic Sea, 13.0–8.0 ka BP. Quaternary International, 27, pp 19–40.

Björck S, Noe-Nygaard N, Wolin J, Houmark-Nielsen M, Hansen H J, Snowball I, 2000. Eemian lake development, hydrology and climate: a multi-stratigraphic study of the Hollerup site in Denmark. Quaternary Science Reviews, 19, pp 509–536.

Bogren J, Gustavsson T, Loman G, 1998. Klimatförändringar: naturliga och antropogena orsaker. Lund: Studentlitteratur (in Swedish).

Bonelli S, Charbit S, Kageyama M, Woillez M-N, Ramstein G, Dumas C, Quiquet A, 2009. Investigating the evolution of major Northern Hemisphere ice sheets during the last glacial-interglacial cycle. Climate of the Past Discussions, 5, pp 1013–1053.

Bos J A A, Bohncke S J P, Engels E, Helmens K F, Coope G R, 2007. Abrupt climatic events during MIS3 recorded in terrestrial sediments in NW Europe: multi-proxy approach. XVII INQUA congress. Cairns, Australia, 28 July–3 August 2007.

Bos J A A, Helmens K F, Bohncke S J P, Seppä H, Birks H J B, 2009. Flora, vegetation and climate at Sokli, northeastern Fennoscandia, during the Weichselian Middle Pleniglacial. Boreas, 38, pp 335–348.

Bosson E, Sassner M, Sabel U, Gustafsson L-G, 2010. Modelling of present and future hydrology and transport - SR Site Biosphere. SKB R-10-02, Svensk Kärnbränslehantering AB.

Bougamont M, Bamber J L, Greuell W, 2005. A surface mass balance model for the Greenland Ice Sheet. Journal of Geophysical Research, 110, F04018, doi:10.1029/2005JF000348.

Boulton G S, Clark C D, 1990. The Laurentide Ice Sheet through the last glacial cycle: the topology of drift lineations as a key to the dynamic behaviour of former ice sheets. *Transactions of the Royal Society of Edinburgh: Earth Sciences*, 81, pp 327–347.

Boulton G S, Payne A, 1992. Simulation of the European ice sheet through the last glacial cycle and prediction of future glaciation. SKB TR 93-14, Svensk Kärnbränslehantering AB.

Boulton G S, Kautsky U, Morén L, Wallroth T, 2001a. Impact of long-term climate change on a deep geological repository for spent nuclear fuel. SKB TR-99-05, Svensk Kärnbränslehantering AB.

Boulton G S, Zatsepin S, Maillot B, 2001b. Analysis of groundwater flow beneath ice sheets. SKB TR-01-06, Svensk Kärnbränslehantering AB.

Brandefelt J, Strandberg G, 2007. Simulating extreme climate conditions in Sweden in a 100,000 year perspective, abstract ICESM2007-A-00035 for the Second International Conference on Earth System Modelling (ICESM).

Brandefelt J, Otto-Bliesner B L, 2009. Equilibrium and variability in a Last Glacial Maximum climate simulation with CCSM3. Geophysical Research Letters 36, L19712, doi:10.1029/2009GL040364.

Brandefelt J, Kjellström E, Näslund J-O, Smith B, Strandberg G, Voelker A H L, Wohlfarth B, 2011. A coupled climate model simulation of Marine Isotope Stage 3 stadial climate. Climate of the Past Discussions, 7, pp 79–118. Manuscript under review for Climate of the Past.

Brandefelt J, Kjellström E, Näslund J-O, Strandberg G, Voelker A, Wohlfarth B, 2010. The importance of equilibration in glacial climate simulations. EGU2010-12736, EGU General Assembly 2010. Geophysical Research Abstracts, 12.

Breckle S-W, 2002. Walter's vegetation of the earth: the ecological systems of the geo-biosphere. 4th ed. Berlin: Springer.

Breemer C W, Clark P U, Haggerty R, 2002. Modeling the subglacial hydrology of the late Pleistocene lake Michigan Lobe, Laurentide Ice Sheet. Geological Society of America Bulletin, 114, pp 665–674.

Broecker, 1991. In: Watson R T, Zinyowera M C, Moss R H (eds). Climate change 1995. Impacts, adaptations and mitigation of climate change: scientific-technical analyses. Contribution of working group 2 to the second assessment report of the intergovernmental panel on climate change. Cambridge: Cambridge University Press.

Brydsten L, Engqvist A, Näslund J-O, Lindborg T, 2009. Expected extreme sea levels at Forsmark and Laxemar-Simpevarp up until year 2100. SKB TR-09-21, Svensk Kärnbränslehantering AB.

Burroughs W J, 2001. Climate change: a multidisciplinary approach. Cambridge: Cambridge University Press.

Burn C R, 2002. Tundra lakes and permafrost, Richards Island, western Arctic coast, Canada. Canadian Journal of Earth Sciences, 39, pp 1281–1298.

Burt T P, Williams P J, 1976. Hydraulic conductivity in frozen soils. Earth Surface Processes, 1, pp 349–360.

Bøggild C E, Mayer C, Podlech S, Taurisano A, Nielsen S, 2004. Towards an assessment of the balance state of the Greenland Ice Sheet. Geological Survey of Denmark and Greenland Bulletin, 4, pp 81–84.

Calcagnile G, 1982. The lithosphere asthenosphere system in Fennoscandia. Tectonophysics, 90, pp 19–35.

Catania G A, Neumann T A, 2009. Persistent englacial drainage features in the Greenland Ice Sheet. Geophysical Research Letters, 37, L02501, doi:10.1029/2009GL041108.

Catania G A, Neumann T A, Price S F, 2008. Characterizing englacial drainage in the ablation zone of the Greenland ice sheet. Journal of Glaciology, 54, pp 567–578.

Cazenave A, Dominh K, Guinehut S, Berthier E, Llovel W, Ramillien G, Ablain M, Larnicol G, 2009. Sea-level budget over 2003–2008: a reevaluation from GRACE space gravimetry, satellite altimetry and Argo. Global and Planeraty Change, 65, pp 83–88.

Čermák V, Balling N, Kukkonen I, Zui V I, 1993. Heat flow in the Baltic Shield – results of the lithospheric geothermal modelling. Precambrian Research, 64, pp 53–65.

Chappell J, Polach H, 1991. Post-glacial sea-level rise from a coral record at Huon Peninsula, Papua New Guinea. Nature, 349, pp 147–149.

Chappell J, Omura A, Esat T, McCulloch M, Pandolfi J, Ota Y, Pillans B, 1996. Reconciliation of late Quaternary sea levels derived from coral terraces at Huon Peninsula with deep sea oxygen isotope records. Earth and Planetary Science Letters, 141, pp 227–236.

Charbit S, Ritz C, Phillippon G, Peyaud V, Kageyama M, 2007. Numerical reconstructions of the Northern Hemisphere ice sheets through the last glacial-interglacial cycle. Climate of the Past, 3, pp 15–37.

Chen J L, Wilson C R, Tapley B D, 2006. Satellite gravity measurements confirm accelerated melting of Greenland ice sheet. Science, 313, pp 1958–1960.

Cheng H, Edwards L, Broecker W S, Denton G H, Kong X, Wang Y, Zhang R, Wang X, 2009. Ice age terminations. Science, 326, pp 248–252.

Christoffersen P, Tulaczyk S, Wattrus N J, Peterson J, Quintana-Krupinski N, Clark C D, Sjunneskog C, 2008. Large subglacial lake beneath the Laurentide ice sheet inferred from sedimentary sequences. Geology, 36, pp 563–566.

Church J A, 35 others, 2001. Greenland and Antarctic Ice Sheets. In: Houghton J T (ed). Climate Change 2001: the scientific basis. New York: Cambridge University Press, ch 11.2.3.

Clark J A, Farrell W E, Peltier W R, 1978. Global changes in postglacial sea level: a numerical calculation. Quaternary Research, 9, pp 265–287.

Clark P U, Mix A C, 2002. Ice sheets and sea level of the Last Glacial Maximum. Quaternary Science Reviews 21, pp 1–7.

Clark P U, Walder J S, 1994. Subglacial drainage, eskers, and deforming beds beneath the Laurentide and Eurasian ice sheets. Geological Society of America Bulletin, 106, pp 304–314.

Clark P U, Alley R B, Keigwin L D, Licciardi J M, Johnsen S J, Wang H X, 1996. Origin of the first global meltwater pulse following the Last Glacial Maximum. Paleoceanography, 11, pp 563–577.

Clark P, Archer D, Pollard D, Blum J, Rial J, Brovkin V, Mix A C, Pisias N, Roy M, 2006. The middle Pleistocene transition: characteristics, mechanisms, and implications for long-term changes in atmospheric pCO_2, Quaternary Science Reviews, 25, pp 3150–3184.

Clark P U, Dyke A S, Shakun J D, Carlson A E, Clark J, Wohlfarth B, Mitrovica J X, Hostetler S W, McCabe A M, 2009. The Last Glacial Maximum. Science, 325, pp 710–714.

Clarke G, Leverington D, Teller J, Dyke A, 2003. Superlakes, megafloods, and abrupt climate change. Science, 301, pp 922–923.

Clauser C, Huenges E, 1995. Thermal conductivity of rocks and minerals. In: Ahrens T J (ed). Rock physics and phase relations: handbook of physical constants. Washington, D.C.: American Geophysical Union, pp 105–126.

Colleoni F, Krinner G, Jakobsson M, Peyaud V, Ritz C, 2009. Influence of regional parameters on the surface mass balance of the Eurasian ice sheet during the peak Saalian (140 kya). Global and Planetary Change, 68, pp 132–148.

Collinson J, 2005a. Erosional sedimentary structures. In: Selley R C, Cocks L R M, Plimer I R (eds). Encyclopedia of geology. Amsterdam: Elsevier Academic Press.

Collinson J, 2005b. Depositional sedimentary structures. In: Selley R C, Cocks L R M, Plimer I R (eds). Encyclopedia of geology. Amsterdam: Elsevier Academic Press.

Cuffey K M, Alley R B, Grootes P M, Bolzan J M, Anandakrishnan S, 1994. Calibration of the $\delta^{18}O$ isotopic paleothermometer for central Greenland, using borehole temperatures. Journal of Glaciology, 40, pp 341–349.

Cuffey K M, Conway H, Gades A M, Hallet B, Lorrain R, Severinghaus J P, Steig E J, Vaughn B, White J W C, 2000. Entrainment at cold glacier beds. Geology, 28, pp 351–354.

Dahl-Jensen D, Gundestrup N, Gogineni S P, Miller H, 2003. Basal melt at NorthGRIP modeled from borehole, ice-core and radio-echo sounder observations. Annals of Glaciology, 37, pp 207–212.

Danielson E W, Levin J, Abrams E, 2003. Meteorology. 2nd ed. New York: McGraw-Hill.

Dansgaard W, Johnsen S J, Clausen H B, Dahl-Jensen D, Gundestrup N S, Hammer C U, Hvidberg C S, Steffensen J P, Sveinbjörnsdottir A E, Jouzel J, Bond G, 1993. Evidence for general instability of past climate from a 250-kyr ice-core record. Nature, 364, pp 218–220.

Das S B, Joughin I, Behn M D, Howat I M, King M A, Lizarralde D, Bhatia M P, 2008. Fracture propagation to the base of the Greenland ice sheet during supraglacial lake drainage. Science, 320, pp 778–781.

Davis J L, Mitrovica J X, 1996. Glacial isostatic adjustment and the anomalous tide gauge record of eastern North America. Nature, 379, pp 331–333.

Davis J L, Mitrovica J X, Scherneck H G, Fan H, 1999. Investigations of Fennoscandian glacial isostatic adjustment using modern sea level records. Journal of Geophysical Research, 104, pp 2733–2747.

Delisle G, 1998. Numerical simulation of permafrost growth and decay. Journal of Quaternary Science Vol. 13, pp 325–333.

Denton G H, Hughes T J (eds), 1981. The last great ice sheets. New York: John Wiley.

Denton G E, Sugden D E, 2005. Meltwater features that suggest Miocene ice-sheet overriding the Transantarctic Mountains in Victoria Land, Antarctica. Geografiska Annaler, 87A, pp 67–85.

Drewry D, 1986. Glacial geologic processes. London: Arnold.

Drijfhout S, Hazeleger W, Selten F, Haarsma R, 2008. Future changes in internal variability of the Atlantic Meridional Overturning Circulation. Climate Dynamics, 30, pp 407–419.

Duval P, Ashby M F, Anderman I, 1983. Rate-controlling processes in the creep of polycrystalline ice. Journal of Physical Chemistry, 87, pp 4066–4074.

Dziewonski A M, Anderson D L, 1981. Preliminary reference earth model. Physics of the Earth and Planetary Interiors, 25, pp 297–356.

Ebert K, 2009. Cenozoic landscape evolution in northern Sweden: geomorphological interpretation within a GIS-framework. Ph.D. thesis. Department of Physical Geography and Quaternary Geology, Stockholm University. (Dissertations from the Department of Physical Geography and Quaternary Geology 19)

Ehlers J, Gibbard P L (eds), 2004. Quaternary glaciations: extent and chronology. Part I: Europe. Amsterdam: Elsevier. (Developments in quaternary science 2)

Ekman M, 1991. A concise history of postglacial land uplift research (from its beginning to 1950). Terra Nova, 3, pp 358–365.

Engelhardt H, Kamb B, 1998. Basal sliding of Ice Stream B, West Antarctica. Journal of Glaciology, 44, pp 223–230.

Engelhardt H, Humphrey N, Kamb B, Fahnestock M, 1990. Physical conditions at the base of a fast moving Antarctic ice stream. Science, 248, pp 57–59.

Engels S, Bohncke S J P, Boss J A A, Helmens K F, Heiri O, 2006. A chironomid-based Middle Weichselian climate reconstruction from an unusual location: Finnish Lapland. Nederlands Aardwetenschappelijk Congres 8. Veldhoven, 24–25 April 2006.

Engels S, Bohncke S J P, Bos J A A, Brooks S J, Heiri O, Helmens K F, 2008a. Chironomid-based palaeotemperature estimates for northeast Finland during Oxygen Isotope Stage 3. Journal of Palaeolimnology, 40, pp 49–61.

Engels S, Bohncke S J P, Bos J A A, Helmens K F, Heiri O, 2008b. Chironomid-based inferences of local and regional environmental change during the early Middle Weichselian in Northeast Finland. In: Proceedings of the 16th International Chironomid Symposium, Funchal, Madeira, Portugal, 25–28 July 2006. Boletim do Museu municipal do Funchal, Suppl. 13, pp 191–196.

Engels S, Helmens K F, Bohncke S J P, Bos J A A, Brooks S J, Heiri O, Väliranta M, 2008c. A multi-proxy record of environmental and climate changes during Oxygen Isotope Stages-3 and -5C from an unusual location: Finnish Lapland. Geophysical Research Abstracts, 10, EGU2008-A-08467.

Engels S, Bohncke S J P, Heiri O, Vandenberghe J, 2008d. Exploring Middle Weichselian climate variability in NW Europe by applying chironomids as a proxy. Geophysical Research Abstracts, 10, EGU2008-A-08604.

Engels S, Helmens K F, Väliranta M, Brooks S J, Birks H J B, 2010. Early Weichselian (MIS 5d and 5c) temperatures and environmental changes in northern Fennoscandia as recorded by chironomids and macroremains at Sokli, northeast Finland. Boreas, 39, pp 689–704.

EPICA community members, 2004. Eight glacial cycles from an Antarctic ice core. Nature, 429, pp 623–628.

Eronen M, Gluckert G, Hatakka L, van de Plassche O, van der Plicht J, Rantala P, 2001. Rates of Holocene isostatic uplift and relative sea-level lowering of the Baltic in SW Finland based on studies of isolation contacts. Boreas, 30, pp 17–30.

Eugster W, Rouse W R, Pielke R A Mcfadden J P, Baldocchi D D, Kittel T G F, Chapin F, Stuart F, Liston G E, Vidale P L, Vaganov E, Chambers S, 2000. Land-atmosphere energy exchange in Arctic tundra and boreal forest: available data and feedbacks to climate. Global Change Biology, 6 (Suppl. 1), pp 84–115.

Evatt G W, Fowler A C, Clark C D, Hulton N R J, 2006. Subglacial floods beneath ice sheets. Philosophical Transactions of the Royal Society A, 364, pp 1769–1794.

Fahnestock M, Abdalati W, Joughin I, Brozena J, Gogineni P, 2001. High geothermal heat flow, basal melt, and the origin of rapid ice flow in central Greenland. Science, 294, pp 2338–2342.

Fairbanks R G, 1989. A 17,000-year glacio-eustatic sea level record: influence of glacial melting rates on the Younger Dryas event and deep-ocean circulation. Nature, 342, pp 637–642.

Farrell W E, Clark J A, 1976. On postglacial sea level. Geophysical Journal of the Royal Astronomical Society, 46, pp 647–667.

Fastook J L, 1990. A map-plane finite-element program for ice sheet reconstruction: a steady-state calibration with Antarctica and a reconstruction of the Laurentide ice sheet for 18,000 BP. In: Brown H U (ed). Computer assisted analysis and modelling on the IBM 3090. White Plains, N.Y.: IBM Scientific and Technical Computing Department.

Fastook J L, 1994. Modeling the Ice Age: the finite-element method in glaciology. Computing Science and Engineering, 1, pp 55–67.

Fastook J L, Chapman J E, 1989. A map plane finite-element model: three modeling experiments. Journal of Glaciology, 35, pp 48–52.

Fastook J L, Holmlund P, 1994. A glaciological model of the Younger Dryas event in Scandinavia. Journal of Glaciology, 40, pp 125–131.

Fastook J L, Prentice M, 1994. A finite-element model of Antarctica: sensitivity test for meteorological mass-balance relationship. Journal of Glaciology, 40, pp 167–175.

Fetterer F, Knowles K, Meier W, Savoie M, 2002, updated until 2010. Sea ice index. Boulder, Colorado: National Snow and Ice Data Center. Digital media.

Fisher U H, 2009. Glacial erosion: a review of its modelling. Nagra Arbeitsbericht NAB 09-23, National Cooperative for the Disposal of Radioactive Waste, Switzerland.

Fischer H, Goto-Azuma K, Hansson M E, Ruth U, 2006. A new Greenland ice core chronology for the last glacial termination. Journal of Geophysical Research, 111, D06102, doi:10.1029/2005JD006079.

Fjeldskaar W, 1994. The amplitude and decay of the glacial forebulge in Fennoscandia. Norsk Geologisk Tidsskrift, 74, pp 2–8.

Fleming K, Johnston P, Zwartz D, Yokoyama Y, Lambeck K, Chappell J, 1998. Refining the eustatic sea-level curve since the Last Glacial Maximum using far- and intermediate-field sites. Earth and Planetary Science Letters, 163, pp 327–342.

Flowers G E, Clarke G K C, 2002a. A multicomponent coupled model of glacier hydrology. 1. Theory and synthetic examples. Journal of Geophysical Research, 107, 2287, doi:10.1029/2001JB001122.

Flowers G E, Clarke G K C, 2002b. A multicomponent coupled model of glacier hydrology. 2. Application to Trapridge Glacier, Yukon, Canada. Journal of Geophysical Research, 2288, doi:10.1029/2001JB001124.

Forsström P-L, Sallasmaa O, Greve R, Zwinger T, 2003. Simulation of fast-flow features of the Fennoscandian ice sheet during the Last Glacial Maximum. Annals of Glaciology, 37, pp 383–389.

Forsström P-L, 2005. Through a glacial cycle: simulation of the Eurasian ice sheet dynamics during the last glaciation. Ph. D. thesis. University of Helsinki, Faculty of Science, Department of Geology, Geology and Palaeontology and Center for Scientific Computing.

Fotiev S M, 1997. Permafrost groundwater Russian Literature Review. In: Haldorsen S, Liebman M, Nelson G, van Everdingen R O, Boike J, 1997: State-of-the-art report on saturated water movement in permafrost areas. Report No 4/97 (lnr 54). Ås: Norges landbrukshøgskole.

Fountain A G, Walder J S, 1998. Water flow through temperate glaciers. Reviews of Geophysics, 36, pp 299–328.

Fountain A G, Jacobel R W, Schlichting R, Jansson P, 2005a. Fractures as the main pathways of water flow in temperate glaciers. Nature, 433, pp 618–621.

Fountain A G, Schlichting R, Jansson P, Jacobel R W, 2005b. Observations of englacial flow passages: a fracture dominated system. Annals of Glaciology, 40, pp 25–30.

Fredén C (ed), 2002. Sveriges nationalatlas. Berg och Jord. Stockholm: SNA publishing (in Swedish).

French H M, 2007. The periglacial environment. 3rd ed. Chichester: John Wiley and Sons.

Fronval T, Jansen E, 1996. Late Neogene paleoclimates and paleoceanography in the Iceland-Norwegian Sea: evidence from the Iceland and Vøring plateaus. In: Thiede J, Myhre A M, Firth J V, Johnson G L, Ruddiman W F (eds). Proceedings of the Ocean Drilling Program, Scientific results, 151, pp 455–468.

Funder S, Demidov I, Yelovicheva Y, 2002. Hydrography and mollusc faunas of the Baltic and the White Sea-North Sea seaway in the Eemian. Palaeogeography, Palaeoclimatology, Palaeoecology 184, pp 275–304.

Furlong K P, Chapman D S, 1987. Crustal heterogeneities and the thermal structure of the continental crust. Geophysical Research Letters, 14, pp 314–317.

GAP team members, 2009. The Greenland Analogue Project (GAP) Annual report 2009. SKB R-10-59, Svensk Kärnbränslehantering AB.

Garisto F, Avis J, Chshyolkova T, Gierszewski P, Gobien M, Kitson C, Melnyk T, Miller J, Walsh R, Wojciechowski L, 2010. Glaciation scenario: safety assessment for a deep geological repository for used fuel. NWMO TR-2010-10, Nuclear Waste Management Organization, Canada.

Gascoyne M, 2000. A review of published literature on the effects of permafrost on the hydrogeochemistry of bedrock. SKB R-01-56, Svensk Kärnbränslehantering AB.

Giovinetto M B, Zwally H J, 2000. Spatial distribution of net surface accumulation on the Antarctic ice sheet. Annals of Glaciology, 31, pp 171–178.

Glen J W, 1955. The creep of polycrystalline ice. Proceedings of the Royal Society of London, Series A, 228, pp 519–538.

Global Warming Art, 2007. Five Myr climate change. Figure prepared by Robert A. Rohde / Global Warming Art. [Online]. Available at: http://www.globalwarmingart.com/wiki/File:Five_Myr_Climate_Change_Rev_png. [26 November 2010].

Goodess C M, Palutikof, J P, Davies T D, 1992. The Nature and causes of climate change: assessing the long-term future. London: Belhaven.

Gregory J M, Huybrechts P, 2006. Ice-sheet contributions to future sea-level change. Philosophical Transactions of the Royal Society A, 364, pp 1709–1731.

Gregory J M, Huybrechts P, Raper S C B, 2004. Threatened loss of the Greenland ice sheet. Nature, 428, p 616.

Greve R, Hutter K, 1995. Polythermal three-dimensional modelling of the Greenland ice sheet with varied geothermal heat flux. Annals of Glaciology, 21, pp 8–12.

Grinsted A, Moore J C, Jevrejeva S, 2009. Reconstructiong sea-level from paleo and projected temperatures 2000 to 2100 AD. Climate Dynamics, 34, pp 461–472.

Hagdorn M K M, 2003. Reconstruction of the Past and Forecast of the Future European and British Ice Sheets and Associated Sea–Level Change. Academic Dissertation, 2003, University of Edinburgh, School of GeoScience. 175 p.

Hagdorn M, Hulton N, Payne A J, Rutt I, Boulton G, 2005. Introducing GLIMMER – a 3D thermomechanical ice sheet model. Poster presented at European Geosciences Union General Assembly 2005, Vienna, Austria, April 24–29 2005.

Hall D K, Williams R S, Luthcke S B, Digirolamo N E, 2008. Greenland ice sheet surface temperature, melt and mass loss: 2000-06. Journal of Glaciology, 54, pp 81–93.

Hallet B, Hunter L, Bogen J, 1996. Rates of erosion and sediment evacuation by glaciers: a review of field data and their implications. Global and Planetary Change, 12, pp 213–235.

Hambrey M J, Barrett P J, Ehrmann W U, Larsen B, 1992. Cainozoic sedimentary processes on the Antarctic continental margin and the record from deep drilling. Zeitschrift für Geomorphologie, Suppl. 86, pp 77–103.

Han D, Wahr J, 1989. Post-glacial rebound analysis for a rotating Earth. In: Cohen S, Vanicek P (eds). Slow deformations and transmission of stress in the Earth. Washington D.C.: American Geophysical Union. (AGU Monograph Series 49), pp 1–6.

Hanebuth T, Stattegger K, Grootes P M, 2000. Rapid flooding of the Sunda Shelf: a late-glacial sea-level record. Science, 288, pp 1033–1035.

Hanna E, Huybrechts P, Steffen K, Cappelen J, Huff R, Shuman C, Irvine-Fynn T, Wise S, Griffiths M, 2008. Increased runoff from melt from the Greenland ice sheet: a response to global warming. Journal of Climate, 21, pp 331–341.

Hanna E, Cappelen J, Fettweis X, Huybrechts P, Luckman A, Ribergaard M H, 2009. Hydrologic response of the Greenland ice sheet: the role of oceanographic warming. Hydrological Processes, 23, pp 7–30.

Haq B U, Hardenbol J, Vail P R, 1987. Chronology of fluctuating sea levels since the Triassic. Science, 235, pp 1156–1165.

Harrison S P, Braconnot P, Joussaume S, Hewitt C, Stouffer R J, 2002. Comparison of palaeoclimate simulations enhances confidence in models. EOS, 83, p 447.

Hartikainen J, 2004. Permafrost modeling in DECOVALEX III for BMT3. In: Eloranta E (ed). DECOVALEX III, 1999–2003. An international project for the modelling of coupled thermo-hydro-mechanical processes for spent fuel disposal. Finnish national contributions. STUK-YTO-TR 209, Finnish Centre for Radiation and Nuclear Safety (STUK), Helsinki.

Hartikainen J, Mikkola M, 2006. Thermomechanical modelling for freezing of solute saturated soil. In: Gladwell G M L, Huyghe J M , Raats P A C, Cowin S C (eds). IUTAM Symposium on the mechanics of physicochemical and electromechanical interactions in porous media, pp 335–341.

Hartikainen J, Kouhia R, Wallroth T, 2010. Permafrost simulations at Forsmark using a numerical 2D thermo-hydro-chemical model. SKB TR-09-17, Svensk Kärnbränslehantering AB.

Hays J D, Imbrie J, Shackleton N, 1976. Variations in the Earth's orbit: pacemaker of the ice ages, Science, 194, pp 1121–1132.

Heginbottom J A, Dubreuil M A, Harker P A, 1995. Canada – Permafrost. In: National Atlas of Canada, 5th ed. Ottawa: National Atlas Information Service, Natural Resources Canada.

Heinrich H, 1988. Origin and consequences of cyclic ice rafting in the northeast Atlantic Ocean during the past 130,000 years. Quaternary Research, 29, pp 142–152.

Helmens K F, 2009a. Climate, vegetation and lake development at Sokli (northern Finland) during early MIS 3 at ~50 kyr: Revising earlier concepts on climate, glacial and vegetation dynamics in Fennoscandia during the Weichselian. SKB TR-09-16, Svensk Kärnbränslehantering AB.

Helmens K F, 2009b. Late Quaternary climate variability in high latitude northern Europe: data-model comparison. 4th BBCC (Bert Bolin Climate Centre, Stockholm University) annual meeting, Stockholm, Sweden, 14–15 September 2009.

Helmens K F, Engels S, 2010. Ice-free conditions in eastern Fennoscandia during early Marine Isotope Stage 3: lacustrine records. Boreas, 39, pp 399–409.

Helmens K F, Bos J A A, Engels S, Van Meerbeeck C J, Bohncke S J P, Renssen H, Heiri O, Brooks S J, Seppä H, Birks H J B, Wohlfarth B, 2007a. Present-day temperatures in northern Scandinavia during the last glaciation. Geology, 35, pp 987–990.

Helmens K F, Bos J A A, Engels E, Seppä H, Bohncke S J P, Van Meerbeeck C J, Renssen H, Risberg J, Wohlfarth B, 2007b. Ice free and warm conditions in the central area of the Scandinavian glaciations during MIS 3. XVII INQUA congress. Cairns, Australia, 28 July–3 August 2007.

Helmens K F, Bos J A A, Engels S, Van Meerbeeck C J, Seppä H, Birks H J B, Brooks S J, Risberg J, Wohlfarth B, 2007c. Present-day temperatures at Sokli (northern Finland) during MIS 3 recorded by high-resolution multi-proxy analysis and climate modeling. 1st NEPAL (Nordic Network on Palaeoclimatology) workshop. Palmse, Estonia, 10–12 May 2007.

Helmens K F, Seppä H, Bos J A A, Engels S, Väliranta M, Birks H J B, 2008. Weichselian vegetation dynamics in the central area of the Scandinavian glaciations recorded in a long sediment sequence from Sokli (N-Finland). 33rd IGC congress. Oslo, 6–14 August 2008.

Helmens K F, Engels S, Väliranta M, Bergman J, 2009a. Environmental and climate conditions at Sokli (N Finland) during MIS 5d-c: first integration of multi-proxy evidence. 3rd NEPAL (Nordic Network of Palaeoclimatology) workshop. Bergen, Norway, 3–5 June 2009.

Helmens K F, Risberg J, Jansson K N, Weckström J, Berntsson A, Kaislahti Tillman P, Johansson P W, Wastegård S, 2009b. Early MIS 3 glacial lake evolution, ice-marginal retreat pattern and climate at Sokli (northeastern Fennoscandia). Quaternary Science Reviews, 28, pp 1880–1894.

Helmens K F, Väliranta M, Engels S, Luoto T P, Self A, submitted. Dramatic shifts in Early Glacial climate regimes recorded by multi-proxy data from the high latitude site Sokli (N Finland). XVIII INQUA congress. Bern, Switzerland, 20–27 July 2011.

Hemming S R, 2004. Heinrich events: massive late Pleistocene detritus layers of the North Atlantic and their global climate imprint. Reviews of Geophysics, 42, RG1005, doi:10.1029/2003RG000128.

Henton J A, Craymer M R, Ferland R, Dragert H, Mazotti S, Forbes D L, 2006. Crustal motion and deformation monitoring of the Canadian landmass. Geomatica, 60, pp 173–191.

Hindmarsh R C A, Boulton G S, Hutter K, 1989. Modes of operation of thermo-mechanically coupled ice sheets. Annals of Glaciology, 12, pp 57–69.

Hock R, 1998. Modelling of glacier melt and discharge. Zürich: Geographisches Institut ETH. (Zürcher Geographische Schriften 70)

Hock R, 2005. Glacier melt: a review of processes and their modelling. Progress in Physical Geography, 29, pp 362–391.

Hock R, Jansson P, 2005. Modelling glacier hydrology. In: Anderson M G, McDonnell J (eds). Encyclopedia of hydrological sciences. Chichester: John Wiley and Sons, vol 4, pp 2647–2655.

Hock R, Jansson P, Braun L, 2005. Modelling the response of mountain glacier discharge to climate warming. In: Huber U M, Bugmann H K M, Reasoner M A (eds). Global change and mountain regions: an overview of current knowledge. Dordrecht: Springer, pp 243–252.

Hohl V, 2005. Northern European long term climate archives. SKB TR-05-01, Svensk Kärnbränslehantering AB.

Hohmann M, 1997. Soil freezing – the concept of soil water potential. State of the art. Cold Regions Science and Technology, 25, pp 101–110.

Holland D M, Thomas R H, de Young B, Ribergaard M H, Lyberth B, 2008. Acceleration of Jakobshavn Isbræ triggered by warm subsurface ocean waters. Nature Geoscience, 1, pp 659–664.

Holmlund P, Fastook J, 1995. A time dependent glaciological model of the Weichselian ice sheet. Quaternary International, 27, pp 53–58.

Holmlund P, Jansson P, 2003. Glaciologi (in Swedish). Stockholm: Stockholm University and the Swedish Research Council.

Hooke R LeB, 1977. Basal temperatures in polar ice sheets: a qualitative review: Quaternary Research, 7, pp 1–13.

Hooke R LeB, 1984. On the role of mechanical energy in maintaining subglacial water conduits at atmospheric pressure. Journal of Glaciology, 30, pp 180–187.

Hooke R LeB, 1989. Englacial and subglacial hydrology: a qualitative review. Arctic and Alpine Research, 21, pp 221–233.

Hooke R LeB, 1991. Positive feedbacks associated with erosion of glacial cirques and overdeepenings. Geological Society of America Bulletin, 103, pp 1104–1108.

Hooke R LeB, 2004. Principles of glacier mechanics. Second edition. Cambridge: Cambridge University Press.

Hooke R LeB, Lauman T, Kohler J, 1990. Subglacial water pressures and the shape of subglacial conduits. Journal of Glaciology, 36, pp 67–71.

Houmark-Nielsen M, 2009. MIS 3 interstadial climate and rapid ice advances in the south-western Baltic. SKB P-09-10, Svensk Kärnbränslehantering AB.

Houmark-Nielsen M, Kjær K H, 2003. Southwest Scandinavia, 40–15 kyr BP: palaeogeography and environmental change. Journal of Quaternary Science, 18, pp 769–786.

Howat I M, Joughin I, Tulaczyk S, Gogineni S, 2005. Rapid retreat and acceleration of Helheim Glacier, east Greenland. Geophysical Research Letters, 32, L22502, doi:10.1029/2005GL024737.

Howat I M, Joughin I, Scambos T A, 2007. Rapid changes in ice discharge from Greenland outlet glaciers. Science, 315, pp 1559–1561.

Howat I M, Joughin I, Fahnestock M, Smith B E, Scambos T A, 2008. Synchronous retreat and acceleration of southeast Greenland outlet glaciers 2000-06: ice dynamics and coupling to climate. Journal of Glaciology, 54, pp 646–660.

Hubbard B, Nienow P, 1997. Alpine subglacial hydrology. Quaternary Science Reviews, 16, pp 939–955.

Huber C, Leuenberger M, Spahni R, Flückiger J, Schwander J, Stocker T F, Johnsen S, Landais A, Jouzel J, 2006. Isotope calibrated Greenland temperature record over Marine Isotope Stage 3 and its relation to CH_4. Earth and Planetary Science Letters, 243, pp 504–519.

Humlum O, Houmark-Nielsen M, 1994. High deglaciation rates in Denmark during the late Weichselian – implications for the palaeoenvironment. Geografisk Tidsskrift, 94, pp 26–37.

Huybrechts P, 1986. A three dimensional time-dependent numerical model for polar ice sheets: some basic testing with a stable and efficient finite difference scheme. Report 86-1, Geografisch Instituut, Vrije Universiteit Brussel, Belgium.

Huybrechts P, 1990. A 3D model for the Antarctic ice sheet: a sensitivity study on the glacial-interglacial contrast. Climate Dynamics, 5, pp 79–92.

Huybrechts P, 2006. Numerical modeling of ice sheets through time. In: Knight P G (ed). Glacier science and environmental change. Malden: Blackwell Publishing, pp 406–412.

Huybrechts P, de Wolde J, 1999. The dynamic response of the Greenland and Antarctic ice sheets to multiple-century climate warming. Journal of Climate, 12, pp 2169–2188.

Huybrechts P, T'siobbel S, 1995. Thermomechanical modelling of northern hemisphere ice sheets with a two-level mass-balance parameterization. Annals of Glaciology, 21, pp 111–116.

Huybrechts P, Payne T, EISMINT Intercomparison Group, 1996. The EISMINT benchmarks for testing ice-sheet models. Annals of Glaciology, 23, pp 1–12.

Huybrechts P, Gregory J, Janssens I, Wild M, 2004. Modelling Antarctic and Greenland volume changes during the 20th and 21st centuries forced by GCM time slice integrations, Global and Planetary Change, 42, pp 83–105.

Hökmark H, Lönnqvist M, Fälth B, 2010. T-H-M issues in repository rock. Thermal, mechanical, thermo-mechanical and hydro-mechanical evolution of the rock at the Forsmark and Laxemar sites. SKB TR-10-23, Svensk Kärnbränslehantering AB.

Hönisch B, Hemming N G, Archer D, Siddall D, Mcmanus J F, 2009. Atmospheric carbon dioxide concentrations across the mid-Pleistocene transition. Science, 324, pp 1551–1554.

Imbrie J, Boyle E A, Clemens S C, Duffy A, Howard W R, Kukla G, Kutzbach J, Martinson D G, McIntyre A, Mix A C, Molfino B, Morley J J, Peterson L C, Pisias N G, Imbrie J, Hays J D, Martinson D G, McIntyre A, Mix A C, Morley J J, Pisias N G, W L Prell, Shackleton N J, 1984. The orbital theory of Pleistocene climate: support from a revised chronology of the marine $\delta^{18}O$ record. In: Berger A L, Imbrie J, Hays J D, Kukla G, Saltzman B (eds). Milankovitch and climate: understanding the response to astronomical forcing. Dordrecht: Reidel, pp 269–305.

Imbrie J, Boyle E A, Clemens S C, Duffy A, Howard W R, Kukla G, Kutzbach J, Martinson D G, McIntyre A, Mix A C, Molfino B, Morley J J, Peterson L C, Pisias N G, Prell W L, Raymo M E, Shackleton N J, Toggweiler J R, 1992. On the structure and origin of major glaciation cycles. 1. Linear responses to Milankovitch forcing. Paleoceanography, 7, pp 701–738.

IPCC, 2001. Climate change 2001: the scientific basis. Contribution of Working Group I to the third assessment report of the Intergovernmental Panel on Climate Change. New York: Cambridge University Press.

IPCC, 2007. Climate change 2007: the physical science basis. Contribution of Working Group I to the fourth assessment report of the Intergovernmental Panel on Climate Change. Cambridge: Cambridge University Press.

Isaksen K, Holmlund P, Sollid J L, Harris C, 2001. Three deep alpine-permafrost boreholes in Svalbard and Scandinavia. Permafrost and Periglacial Processes, 12, pp 13–26.

Iverson N R, 1991. Potential effects of of subglacial water-pressure fluctuations on quarrying. Journal of Glaciology, 37, pp 27–36.

Iverson N R, 1993. Regelation of ice through debris at glacier beds: implications for sediment transport. Geology, 21, pp 559–562.

Iverson N R, 2000. Sediment entrainment by a soft-bedded glacier: a model based on regelation into the bed. Earth Surface Processes and Landforms, 25, pp 881–893.

Iverson N R, Hanson B, Hooke R LeB, Jansson P, 1995. Flow mechanism of glaciers on soft beds. Science, 267, pp 80–81.

Ivins E R, 2009. Ice sheet stability and sea-level. Science, 324, pp 888–889.

Jansen E, Sjøholm J, 1991. Reconstruction of glaciation over the past 6 Myr from ice-borne deposits in the Norwegian Sea. Nature, 349, pp 600–603.

Jansson P, 2010. Ice sheet hydrology from observations. SKB TR-10-68, Svensk Kärnbränslehantering AB.

Jansson P, Näslund J-O, 2009. Spatial and temporal variations in glacier hydrology on Storglaciären, Sweden. SKB TR-09-13, Svensk Kärnbränslehantering AB.

Jansson P, Hock R, Schneider T, 2003. The concept of glacier storage: a review. Journal of Hydrology, 282, pp 116–129.

Jansson P, Näslund J-O, Rodhe L, 2007. Ice sheet hydrology – a review. TR-06-34, Svensk Kärnbränslehantering AB.

Jaquet O, Siegel P, 2006. Regional groundwater flow model for a glaciation scenario. Simpevarp subarea – version 1.2. SKB R-06-100, Svensk Kärnbränslehantering AB.

Jaquet O, Namar R, Jansson P, 2010. Groundwater flow modelling under ice sheet conditions: scoping calculations. SKB R-10-46, Svensk Kärnbränslehantering AB.

Johansson J M, Davis J L, Scherneck H-G, Milne G A, Vermeer M, Mitrovica J X, Bennett R A, Jonsson B, Elgered G, Elósegui P, Koivula H, Poutanen M, Rönnäng B O, Shapiro I I, 2002. Continuous GPS measurements of postglacial adjustment in Fennoscandia. 1. Geodetic results. Journal of Geophysical Research 107, pp 400–428.

Johansson P-O, 2008. Description of surface hydrology and near-surface hydrogeology at Forsmark. Site descriptive modelling, SDM-Site Forsmark. SKB R-08-08, Svensk Kärnbränslehantering AB.

Johnsen S J, Dahl-Jensen D, Dansgaard W, Gundestrup N, 1995. Greenland palaeotemperatures derived from GRIP bore hole temperature and ice core isotope profiles. Tellus, 47B, pp 624–629.

Johnsen S J, Dahl-Jensen D, Gundestrup N, Steffensen J P, Clausen H B, Miller H, Masson-Delmotte V, Sveinbjörnsdottir A E, White J, 2001. Oxygen isotope and palaeotemperature records from six Greenland ice-core stations: Camp Century, Dye-3, GRIP, GISP2, Renland and NorthGRIP. Journal of Quaternary Science, 16, pp 299–307.

Johnson J, 1994. A basal water model for ice sheets. Ph. D. thesis. University of Minnesota.

Johnson J, 2004. Estimating basal melt rate in Antarctica. International Symposium on Ice and Water Interactions: processes across the phase boundary. Portland, Oregon, 26–30 July 2004.

Johnston, P, 1993. The effect of spatially non-uniform water loads on predictions of sea-level change. Geophysical Journal International, 114, pp 615–634.

Jol A, Šťastný P, Raes F, Lavalle C, Menne B, Wolf T, 2008. Impacts of Europe's changing climate: 2008 indicator-based assessment. EEA report 4/2008. Copenhagen: European Environment Agency.

Joughin I, Tulaczyk S, 2002. Positive mass balance for the Ross Ice Streams, West Antarctica. Science, 295, pp 476–480.

Joughin I, Tulaczyk S, Fahnestock M, Kwok R, 1996. A mini-surge on the Ryder Glacier, Greenland, observed by satellite radar interferometry. Science, 274, pp 228–230.

Joughin I, Abdalati W, Fahnestock M, 2004. Large fluctuations in speed on Greenland's Jakobshavn Isbræ glacier. Nature, 432, pp 608–610.

Joughin I, Das S B, King M A, Smith B E, Howat I M, Moon T, 2008. Seasonal speedup along the western flank of the Greenland Ice Sheet. Science, 320, pp 781–783.

Joussaume S, Taylor K E, 2000. The paleoclimate modeling intercomparison project. In: Braconnot P (ed). Proceedings of the third Paleoclimate Modelling Intercomparison Project (PMIP) workshop. La Huardière, Canada, 4–8 October 1999. (WCRP-111, WMO/TD-1007)

Jouzel J, Stiévenard M, Johnsen S J, Landais A, Masson-Delmotte V, Sveinbjornsdottir A, Vimeux F, von Grafenstein U, White J W C, 2007. The GRIP deuterium-excess record. Quaternary Science Reviews, 26, pp 1–17.

Joyce S, Simpson T, Hartley L, Applegate D, Hoek J, Swan D, Marsic N, Follin S, 2010. Groundwater flow modelling of periods with temperate climate conditions – SR-Site Forsmark. SKB R-09-20, Svensk Kärnbränslehantering AB.

Kageyama M, Laîné A, Abe-Ouchi A, Braconnot P, Cortijo E, Crucifix M, de Vernal A, Guiot J, Hewitt C D, Kitoh A, Kucera M, Marti O, Ohgaito R, Otto-Bliesner B, Peltier W R, Rosell-Melé A, Vettoretti G, Weber S L, Yu Y, MARGO project members, 2006. Last Glacial Maximum temperatures over the North Atlantic, Europe and western Siberia: a comparison between PMIP models, MARGO sea-surface temperatures and pollen-based reconstructions. Quaternary Science Reviews, 25, pp 2082–2102.

Kahr G, Kraehenbuehl F, Stoeckli H F, Müller-Vonmoos M, 1990. Study of the water-bentonite system by vapour adsorption, immersion calorimetry and X-ray techniques: II. Heats of immersion, swelling pressures and thermodynamic properties. Clay Minerals, 25, pp 499–506.

Kaislahti-Tillman P, Berntsson A, Risberg J, Helmens K F, Jansson K, 2007. Diatom stratigraphy of the MIS 3 deposit at Sokli, Northern Finland. Nordic Diatomists Meeting. Lillehammer, Norway, 11–14 May 2007.

Kamb B, 1987. Glacier surge mechanism based on linked cavity configuration of the basal water conduit system. Journal of Geophysical Research, 92, pp 9083–9100.

Kamb B, 2001. Basal zone of the West-Antarctic ice streams and its role in their rapid motion. In: Alley R B, Bindschadler R A (eds). The West Antarctic ice sheet: behavior and environment. Washington D.C.: American Geophysical Union, pp 157–200.

Kamb B, Echelmeyer K A, 1986. Stress-gradient coupling in glacier flow: IV. Effects of the "T" term. Journal of Glaciology, 32, pp 342–349.

Kapitsa A P, Ridley J K, Robin G de Q, Siegert M J, Zotikov I A, 1996. A large deep freshwater lake beneath the ice of central East Antarctica. Nature, 381, pp 684–686.

Karnland O, Olsson S, Nilsson U, 2006. Mineralogy and sealing properties of various bentonites and smectite-rich clay materials. SKB TR-06-30, Svensk Kärnbränslehantering AB.

Karnland O, Olsson S, Dueck A, Birgersson M, Nilsson U, Hernan-Håkansson T, Pedersen K, Nilsson S, Eriksen T E, Rosborg B, 2009. Long term test of buffer material at the Äspö Hard Rock Laboratory, LOT Project. Final report on the A2 test parcel. SKB TR-09-29, Svensk Kärnbränslehantering AB.

Karunaratne K C, Burn C R, 2004. Relations between air and surface temperature in discontinuous permafrost terrain near Mayo, Yukon Territory. Canadian Journal of Earth Sciences, 41, pp 1437–1451.

Kaufmann G, Lambeck K, 2002. Glacial isostatic adjustment and the radial viscosity profile from inverse modeling. Journal of Geophysical Research, 107, 2280, doi:10.1029/2001JB000941.

Kaufmann G, Wu P, 1998. Lateral asthenospheric viscosity variations and postglacial rebound: a case study for the Barents Sea. Geophysical Research Letters, 25, pp 1963–1966.

Kaufmann G, Wu P, 2002. Glacial isostatic adjustment in Fennoscandia with a three-dimensional viscosity structure as an inverse problem. Earth and Planetary Science Letters, 197, pp 1–10.

Kaufmann G, Wu P, Li G Y, 2000. Glacial isostatic adjustment in Fennoscandia for a laterally heterogeneous earth. Geophysical Journal International, 143, pp 262–273.

Kendall R A, Mitrovica J X, Milne G A, 2005. On post-glacial sea level – II. Numerical formulation and comparative results on spherically symmetric models. Geophysical Journal International, 161, pp 679–706.

Kim S-J, Crowley T J, Erickson D J, Govindasamy B, Duffy P B, Lee B Y, 2008. High-resolution climate simulation of the last glacial maximum. Climate Dynamics, 31, pp 1–16.

King L, 1984. Permafrost in Skandinavien: Untersuchungsergebnisse aus Lappland, Jotunheimen und Dovre/Rondane. Heidelberg: Geographisches Institut der Univ. (Heidelberger geographische Arbeiten 76)

King-Clayton L (ed), Chapman N, Ericsson L O, Kautsky F, 1997. Glaciation and hydrogeology, Proceedings of the workshop on the impact of climatic change and glaciations on rock stresses, groundwater flow and hydrochemistry: past, present and future. Hässelby, Sweden, 17–19 April 1996. SKI Report 97:13, Statens kärnkraftinspektion (Swedish Nuclear Power Inspectorate).

Kjellström E, Brandefelt J, Strandberg G, Smith B, Wohlfarth B, Näslund J-O, 2008. Global and regional climate model simulations of extreme climate conditions in Sweden in a 100,000 year perspective. EGU2008-A-02249. Abstracts of the contributions of the EGU General Assembly 2008. Geophysical Research Abstracts, 10.

Kjellström E, Brandefelt J, Strandberg G, Smith B, Wohlfarth B, Näslund J-O, 2009a. Global and regional climate model simulations of extreme climate conditions in Sweden in a 100,000 year perspective. UN Climate Change Conference March 2009, Copenhagen. Theme 1: Exploring the risks: understanding climate change. Session: Informing the future by understanding the past.

Kjellström E, Strandberg G, Brandefelt J, Näslund J-O, Smith B, Wohlfarth B, 2009b. Climate conditions in Sweden in a 100,000-year time perspective. SKB TR-09-04, Svensk Kärnbränslehantering AB.

Kjellström E, Brandefelt J, Näslund J-O, Smith B, Strandberg G, Voelker A H L, Wohlfarth B, 2010a. Simulated climate conditions in Europe during a Marine Isotope Stage 3 stadial. Boreas, 39, pp 436–456.

Kjellström E, Nikulin G, Hansson U, Strandberg G, Ullerstig A, 2010b. 21st century changes in the European climate: uncertainties derived from an ensemble of regional climate model simulations. Tellus A, doi: 10.1111/j.1600-0870.2010.00475.x.

Kleman J, 1994. Preservation of landforms under ice sheets and ice caps. Geomorphology, 9, pp 19–32.

Kleman J, Glasser N F, 2007. The subglacial thermal organisation (STO) of ice sheets. Quaternary Science Reviews, 26, pp 585–597.

Kleman J, Hättestrand C, 1999. Frozen-based Fennoscandian and Laurentide ice sheets during the last glacial maximum. Nature, 402, pp 63–66.

Kleman J, Stroeven A P, 1997. Preglacial surface remnants and Quaternary glacial regimes in north-western Sweden. Geomorphology, 19, pp 35–54.

Kleman J, Hättestrand C, Borgström I, Stroeven A, 1997. Fennoscandian palaeoglaciology reconstructed using a glacial geological inversion model. Journal of Glaciology, 43, pp 283–299.

Kleman J, Stroeven A, Lundqvist J, 2008. Patterns of Quaternary ice sheet erosion and deposition in Fennoscandia and a theoretical framework for explanation. Geomorphology, 97, pp 73–90.

Klene A E, Nelson F E, Shiklomanov N I, Hinkel K M, 2001. The N-factor in natural landscapes: Variability of air and soil-surface temperatures, Kuparuk River Basin, Alaska. Arctic, Antarctic, and Alpine Research, 33, pp 140–148.

Kohler J, 1995. Determining the extent of pressurized flow beneath Storglaciären, Sweden, using results of tracer experiments and measurements of input and output discharge. Journal of Glaciology, 41, pp 217–231.

Koppes M N, Montgomery D R, 2009. The relative efficacy of fluvial and glacial erosion over modern to orogenic timescales. Nature Geoscience, 2, pp 644–647.

Krabill W, Abdalati W, Frederick E, Manizade S, Martin C, Sonntag J, Swift R, Thomas R, Wright W, Yungel J, 2000. Greenland ice sheet: high elevation balance and peripheral thinning. Science, 289, pp 428–430.

Krawczynski M J, Behn M D, Das S B, Joughin I, 2009. Constraints on the lake volume required for hydro-fracture through ice sheets. Geophysical Research Letters, 36, L10501, doi:10.1029/2008GL036765.

Krinner G, Genthon C, Jouzel J, 1997. GCM analysis of local influence on ice core δ signals. Geophysical Research Letters, 24, pp 2825–2828.

Krogh Andersen K, Svensson A, Rasmussen S O, Steffensen J P, Johnsen S, Bigler M, Röthlisberger R, Ruth U, Siggaard-Andersen M-L, Dahl-Jensen D, Vinther B M, Clausen H B, 2006. The Greenland ice core chronology 2005, 15–42 kyr. Part 1: constructing the time scale. Quaternary Science Reviews, 25, pp 3246–3257.

Kukkonen, I, 1989. Terrestrial heat flow and radiogenic heat production in Finland, the central Baltic Shield. Tectonophysics, 164, pp 219–230.

Kukkonen I T, Šafanda J, 2001. Numerical modelling of permafrost in bedrock in northern Fennoscandia during the Holocene. Global and Planetary Change, 29, pp 259–274.

Lachenbruch A H, 1968. Preliminary geothermal model of the Sierra Nevada. Journal of Geophysical Research, 73, pp 6977–6989.

Lagerbäck R, 1988a. The Veiki moraines in northern Sweden – widespread evidence of an Early Weichselian deglaciation. Boreas, 17, pp 469–486.

Lagerbäck R, 1988b. Periglacial phenomena in the wooded areas of northern Sweden – relicts from the Tärendö Interstadial. Boreas, 17, pp 487–499.

Lagerbäck R, Robertsson A-M, 1988. Kettle holes – stratigraphical archives for Weichselian geology and palaeoenvironment in northernmost Sweden. Boreas, 17, pp 439–468.

Lagerlund E, Persson K M, Krzyszkowski D, Johansson P, Dobracka E, Dobracki R, Panzig W-A, 1995. Unexpected ice flow directions during the Late Weichselian deglaciation of the South Baltic area indicated by a new lithostratigrapy in NW Poland and NE Germany. Quaternary International, 28, pp 127–144.

Lambeck K, 1995. Late Devensian an Holocene shorelines of the British Isles and North Sea from models of glacio-hydroisostatic rebound. Journal of the Geological Society, 152, pp 437–448.

Lambeck K, 1999. Shoreline displacements in southern-central Sweden and the evolution of the Baltic Sea since the last maximum glaciation. Journal of the Geological Society, 156, pp 465–486.

Lambeck K, Chappell J, 2001. Sea level change through the last glacial cycle. Science, 292, pp 679–686.

Lambeck K, Nakada M, 1990. Late Pleistocene and Holocene sea-level change along the Australian coast. Palaeogeography, Palaeoclimatology, Palaeoecology, 89, pp 143–176.

Lambeck K, Smither C, Johnston P, 1998. Sea-level change, glacial rebound and mantle viscosity for northern Europe. Geophysical Journal International, 134, pp 102–144.

Lambeck K, Yokoyama Y, Purcell T, 2002. Into and out of the Last Glacial Maximum: sea-level change during Oxygen Isotope Stages 3 and 2. Quaternary Science Reviews, 21, pp 343–360.

Lambeck K, Purcell A, Funder S, Kjær K H, Larsen E, Möller P, 2006. Constraints on the Late Saalian to early Middle Weichselian ice sheet of Eurasia from field data and rebound modelling. Boreas, 35, pp 539–575.

Lambeck K, Purcell A, Zhao J, Svensson N-O, 2010. The Scandinavian Ice Sheet: from MIS 4 to the end of the Last Glacial Maximum. Boreas, 39, pp 410–435.

Lambert A, Courtier N, Sasagawa G S, Klopping F, Winester D, James T S, Liard J O, 2001. New con-straints on Laurentide postglacial rebound from absolute gravity measurements. Geophysical Research Letters, 28, pp 2109–2112.

Landström O, Larsson, S Å, Lind G, Malmqvist D, 1979. Geothermal investigations in the Bohus granite area in southwestern Sweden. Tectonophysics, 64, pp 131–162.

Lang H, 1987. Forecasting meltwater runoff from snow-covered areas and from glacier basins. In: Kraijenhoff D A, Moll J R (eds). River flow modelling and forecasting. Dordrecht: D. Reidel, pp 99–127.

Lang C, Leuenberger M, Schwander J, Johnsen S, 1999. 16°C rapid temperature variation in central Greenland 70,000 years ago. Science, 286, pp 934–937.

Latychev K, Mitrovica J X, Tamisiea M E, Tromp J, Moucha R, 2005a. Influence of lithospheric thickness variations on 3D crustal velocities due to glacial isostatic adjustment. Geophysical Research Letters, 32, L01304, doi:10.1029/2004GL021454.

Latychev K, Mitrovica J X, Tromp J, Tamisiea M E, Komatitsch D, Christara C C, 2005b. Glacial isostatic adjustment on 3D Earth models: a finite-volume formulation. Geophysical Journal International, 161, pp 421–444.

Lemieux J-M, Sudicky E A, Peltier W R, Tarasov L, 2008a. Dynamics and groundwater recharge and seepage over the Canadian landscape during the Wisconsinian glaciation. Journal of Geophysical Research, 113, F01011, doi:10.1029/2007JF000838.

Lemieux J-M, Sudicky E A, Peltier W R, Tarasov L, 2008b. Simulating the impact of glaciations on continental groundwater flow systems: 1. Relevant processes and model formulation. Journal of Geophysical Research, 113, F03017, doi:10.1029/2007JF000928.

Lemieux J-M, Sudicky E A, Peltier W R, Tarasov L, 2008c. Simulating the impact of glaciations on continental groundwater flow systems: 2. Model application to the Wisconsinian glaciation over the Canadian landscape. Journal of Geophysical Research 113, F03018, doi:10.1029/2007JF000929.

Lenton T M, Britton C, 2006. Enhanced carbonate and silicate weathering accelerates recovery from fossil fuel CO_2 pertubations. Global Biogeochemical Cycles, 20, GB3009, doi:10.1029/2005GB002678.

Lenton T M, Williamson M S, Edwards N R, Marsh R, Price A R, Ridgwell A J, Shepherd J G, Cox S J, The GENIE team, 2006. Millennial timescale carbon cycle and climate change in an efficient Earth system model. Climate Dynamics, 26, pp 687–711.

Lewis A R, Marchant D R, Kowalewski D E, Baldwin S L, Webb L E, 2006. The age and origin of the labyrinth, western Dry Valleys, Antarctica: evidence for extensive middle Miocene subglacial floods and freshwater discharge to the Southern Ocean. Geology, 34, pp 513–516.

Lidberg M, 2007. Geodetic reference frames in presence of crustal deformations. Ph.D. thesis. Department of Radio and Space Science, Chalmers University of Technology.

Lide D R (ed), 1999. CRC handbook of chemistry and physics: a ready-reference book of chemical and physical data. 80th ed. Cleveland, Ohio: CRC Press.

Lidmar-Bergström K, 1995. Relief and saprolites through time on the Baltic shield. Geomorphology, 12, pp 45–61.

Lidmar-Bergström K, 1997. A long-term perspective on glacial erosion. Earth Surface Processes and Landforms, 22, pp 297–306.

Lidmar-Bergström K, Näslund J-O, 2002. Landforms and uplift in Scandinavia. In: Doré A G, Cartwright J A, Stoker M S, Turner J P, White N (eds). Exhumation of the North Atlantic margin: timing, mechanisms, and implications for petroleum exploration. London: Geological Society. (Special publication 196), pp 103–116.

Lidmar-Bergström K, Näslund J-O, 2005. Major landforms and bedrock. In: Seppälä M (ed). The physical geography of Fennoscandia, Oxford: Oxford University Press.

Lidmar-Bergström K, Olsson S, Olvmo M, 1997. Palaeosurfaces and associated saprolites in southern Sweden. In: Widdowson M (ed). Palaeosurfaces: recognition, reconstruction and palaeoenvironmental interpretation. London: Geological Society. (Special publication 120), pp 95–124.

Lind P, Kjellström E, 2008. Temperature and precipitation changes in Sweden: a wide range of model-based projections for the 21st century. Norrköping: Sveriges meteorologiska och hydrologiska institut (Swedish Meteorological and Hydrological Institute). (SMHI reports. Meteorology and Climatology 113)

Lindborg T (ed), 2010. Landscape Forsmark – data, methodology and results for SR-Site. SKB TR-10-05, Svensk Kärnbränslehantering AB.

Lisiecki L E, Raymo M E, 2005. A Pliocene-Pleistocene stack of 57 globally distributed benthic $\delta^{18}O$ records. Paleoceanography, 20, pp 1–17.

Lockwood J G, 1979. Causes of climate. Edward Arnold, London.

Lohmann U, Sausen R, Bengtsson L, Cubasch U, Perlwitz J, Roeckner E, 1993. The Köppen climate classification as a diagnostic tool for general circulation models. Climate Research, 3, pp 177–193.

Lokrantz H, Sohlenius G, 2006. Ice-marginal fluctuations during the Weichselian glaciation in Fennoscandia, a literature review. SKB TR-06-36, Svensk Kärnbränslehantering AB.

Loutre M F, Berger A, 2000. Future climatic changes: are we entering an exceptionally long interglacial? Climatic Change, 46, pp 61–90.

Luckman A, Murray T, de Lange R, Hanna E, 2006. Rapid and synchronous ice-dynamic changes in East Greenland. Geophysical Research Letters, 33, L03503, doi:10.1029/2005GL025428.

Lunardini V J, 1978. Theory of n-factors and correlation of data. In: Proceedings of the 3rd International Conference on Permafrost. Edmonton, Alta, 10–13 July 1978. Ottawa: National Research Council of Canada, vol 1, pp 40–46.

Lunardini V J, 1981. Heat transfer in cold climates. New York: Van Nostrand Reinhold.

Lunardini V J, 1995. Permafrost formation time. CRREL Report 95-8, U.S. Army Cold Regions Research and Engineering Laboratory.

Lund B, Näslund J-O, 2009. Glacial isostatic adjustment: implications for glacially induced faulting and nuclear waste repositories. In: Connor C B, Chapman N A, Connor L J (eds). Volcanic and tectonic hazard assessment for nuclear facilities. Cambridge: Cambridge University Press, pp 142–155.

Lund B, Schmidt P, Hieronymus C, 2009. Stress evolution and fault stability during the Weichselian glacial cycle. SKB TR-09-15, Svensk Kärnbränslehantering AB.

Lundqvist J, 1992. Glacial stratigraphy in Sweden. Geological Survey of Finland Special Paper, 5, pp 43–59.

Lundqvist J, 2007. Surging ice and break-down of an ice dome – a deglaciation model for the Gulf of Bothnia. Geologiska Föreningens i Stockholm Förhandlingar, 129, pp 329–336.

Lundqvist J, Wohlfarth B, 2000. Timing and east-west correlation of south Swedish ice-marginal lines during the Late Weichselian. Quaternary Science Reviews, 20, pp 1127–1148.

Lunkka J P, Johansson P, Saarnisto M, Sallasmaa O, 2004. Glaciation of Finland. In: Ehlers J, Gibbard P L (eds). Quaternary glaciations: extent and chronology. Part I: Europe. Amsterdam: Elsevier. (Developments in Quaternary Science 2), pp 93–100.

Lunt D J, Foster G L, Haywood A M, Stone E J, 2008. Late Pliocene Greenland glaciation controlled by a decline in atmospheric CO_2 levels. Nature, 454, pp 1102–1105.

Lunt D J, Haywood A M, Foster G L, Stone E J, 2009. The Arctic cryosphere in the Mid-Pliocene and the future. Philosophical Transactions of the Royal Society A: Mathematical, Physical and Engineering Sciences, 367, pp 49–67.

Luthcke S B, Zwally H J, Abdalati W, Rowlands D D, Ray R D, Nerem R S, Lemoine F G, Mccarthy J J, Chinn D S, 2006. Recent Greenland ice mass loss by drainage system from satellite gravity observations. Science, 314, pp 1286–1289.

Lythe M B, Vaughan D G, the BEDMAP Consortium, 2001. BEDMAP: a new ice thickness and subglacial topographic model of Antarctica. Journal of Geophysical Research, 106, pp 11335–11351.

Löfgren A (ed), 2010. The terrestrial ecosystems at Forsmark and Laxemar-Simpevarp. SKB TR-10-01, Svensk Kärnbränslehantering AB.

Lönnqvist M, Hökmark H, 2010. Assessment of potential for glacially induced hydraulic jacking at different depths. SKB R-09-35, Svensk Kärnbränslehantering AB.

Mackay J R, 1997. A full-scale field experiment (1978–1995) on the growth of permafrost by means of lake drainage, western Arctic coast: a discussion of the method and some results. Canadian Journal of Earth Sciences, 34, pp 17–33.

Mai H, Thomsen T, 1993. Permafrost studies in Greenland. In: Proceedings of the sixth international conference on permafrost. Beijing, 5–9 July 1993. Guangzhou: South China University of Technology, vol 2.

Malmqvist D, Larson S Å, Landström O, Lind G, 1983. Heat flow and heat production from the Malingsbo granite, central Sweden. Bulletin of the Geological Institutions of the University of Uppsala, 9, pp 137–152.

Mangerud J, Gyllencreutz R, Øystein L, Svendsen J I, 2011. Glacial history of Norway. In: Ehlers J, Gibbard P L (eds). Quaternary glaciations: extent and chronology. Part IV: a closer look. Amsterdam: Elsevier.

Marchant D R, Denton G H, Sugden D E, Swisher C C, 1993. Miocene glacial stratigraphy and landscape evolution of the western Asgard Range, Antarctica. Geografiska Annaler, 75A, pp 303–330.

Marshall S J, Clarke G K C, 1997. A continuum mixture model of ice stream thermodynamics in the Laurentide Ice Sheet. 1. Theory. Journal of Geophysical Research, 102, pp 20599–20614.

Marks L, 2002. Last Glacial Maximum in Poland. Quaternary Science Reviews, 21, pp 103–110.

Masson-Delmotte M, Jouzel J, Landais A, Stievenard M, Johnsen S J, White J W C, Werner M, Sveinbjörnsdottir A, Fuhrer K, 2005. GRIP deuterium excess reveals rapid and orbital-scale changes in Greenland moisture origin. Science, 309, pp 118–121.

McConnell R K, 1968. Viscosity of the mantle from relaxation time spectra of isostatic adjustment. Journal of Geophysical Research, 73, pp 7089–7105.

McIntyre K, Delaney M L, Ravelo A C, 2001. Millennial-scale climate change and oceanic processes in the late Pliocene and early Pleistocene. Paleoceanography, 16, pp 535–543.

Meehl G A, Stocker T F, Collins W D, Friedlingstein P, Gaye A T, Gregory J M, Kitoh A, Knutti R, Murphy J M, Noda A, Raper S C B, Watterson I G, Weaver A J, Zhao Z-C, 2007. Global climate projections. In: IPCC, 2007. Climate change 2007: the physical science basis. Contribution of Working Group I to the fourth assessment report of the Intergovernmental Panel on Climate Change. Cambridge: Cambridge University Press.

Meese D A, Gow A J, Alley R B, Zielinski G A, Grootes P M, Ram M, Taylor K C, Mayewski P A, Bolzan J F, 1997. The Greenland Ice Sheet Project 2 depth-age scale: methods and results. Journal of Geophysical Research, 102, pp 26411–26423.

Meier M F, Dyurgerov M B, Rick U K, O'Neel S, Pfeffer W T, Anderson R S, Anderson S P, Glazovsky A F, 2007. Glaciers dominate eustatic sea-level rise in the 21st century. Science, 317, pp 1064–1067.

Mernild S H, Liston G E, Hiemstra C A, Steffen C, Hanna E, Christensen J H, 2009. Greenland ice sheet surface mass-balance modelling and freshwater flux for 2007, and in a 1995–2007 perspective. Hydrological Processes, 23, pp 2470–2484.

Miljövårdsberedningen, 2007. Vetenskapligt underlag för klimatpolitiken: rapport från vetenskapliga rådet för klimatfrågor (in Swedish). Stockholm: Miljövårdsberedningen. (Miljövårdsberedningens rapport 2007:03).

Milne G A, 1998. Refining models of the glacial isostatic adjustment process. Ph. D. thesis. University of Toronto.

Milne G A, Mitrovica J X, 1998. Postglacial sea-level change on a rotating Earth. Geophysical Journal International, 133, pp 1–19.

Milne G A, Mitrovica J X, Davis J L, 1999. Near-field hydro-isostasy: the implementation of a revised sea-level equation. Geophysical Journal International, 139, pp 464–482.

Milne G A, Davis J L, Mitrovica J X, Scherneck H-G, Johansson J M, Vermeer M, Koivula H, 2001. Space-geodetic constraints on glacial isostatic adjustment in Fennoscandia. Science, 291, pp 2381–2385.

Milne G A, Mitrovica J X, Schrag D P, 2002. Estimating past continental ice volume from sea-level data. Quaternary Science Reviews, 21, pp 361–376.

Milne G A, Mitrovica J X, Scherneck H G, Davis J L, Johansson J M, Koivula H, Vermeer M, 2004. Continuous GPS measurements of postglacial adjustment in Fennoscandia: 2. Modeling results. Journal of Geophysical Research, 109, B02412, doi:10.1029/2003JB002619.

Milne, G A, Gehrels W R, Hughes C W, Tamisiea M E, 2009. Identifying the causes of sea-level change. Nature Geoscience, 2, pp 471–478.

Ministry of the Environment, 2001. Sweden's third national communication on Climate Change: under the United Nations Framework Convention on Climate Change. Stockholm: Ministry of the Environment. (Ds 2001:71)

Mitrovica J X, 2003. Recent controversies in predicting post-glacial sea-level change. Quaternary Science Reviews, 22, pp 127–133.

Mitrovica J X, Forte A M, 1997. Radial profile of mantle viscosity: results from the joint inversion of convection and postglacial rebound observables. Journal of Geophysical Research, 102, pp 2751–2769.

Mitrovica J X, Forte A M, 2004. A new inference of mantle viscosity based upon joint inversion of convection and glacial isostatic adjustment data. Earth and Planetary Science Letters, 225, pp 177–189.

Mitrovica J X, Milne G A, 2002. On the origin of late Holocene sea-level highstands within equatorial ocean basins. Quaternary Science Reviews, 21, pp 2179–2190.

Mitrovica J X, Milne G A, 2003. On post-glacial sea level: I. General theory. Geophysical Journal International, 154, pp 253–267.

Mitrovica J X, Peltier W R, 1991. On post-glacial geoid subsidence over the equatorial oceans. Journal of Geophysical Research, 96, pp 20053–20071.

Mitrovica J X, Davis J L, Shapiro I I, 1994. A spectral formalism for computing three-dimensional deformations due to surface loads. 2. Present-day glacial isostatic-adjustment. Journal of Geophysical Research, 99, pp 7075–7101.

Mitrovica J X, Milne G A, Davis J L, 2001a. Glacial isostatic adjustment on a rotating earth. Geophysical Journal International, 147, pp 562–579.

Mitrovica J X, Tamisiea M E, Davis J L, Milne G A, 2001b. Recent mass balance of polar ice sheets inferred from patterns of global sea-level change. Nature 409, pp 1026–1029.

Mitrovica J X, Wahr J, Matsuyama I, Paulson A, 2005. The rotational stability of an ice-age Earth. Geophysical Journal International, 161, pp 491–506.

Mitrovica J X, Gomez N, Clark P U, 2009. The sea-level fingerprint of West Antarctic Collapse. Science, 323, p 753.

Moberg A, Sonechkin D M, Holmgren K, Datsenko N M, Karlén W, 2005. Highly variable Northern Hemisphere temperatures reconstructed from low- and high-resolution proxy data. Nature, 433, pp 613–617.

Moberg A, Gouirand I, Wohlfarth B, Schoning K, Kjellström E, Rummukainen M, de Jong R, Linderholm H, Zorita E, 2006. Climate in Sweden during the past millennium – Evidence from proxy data, instrumental data and model simulations. SKB TR-06-35, Svensk Kärnbränslehantering AB.

Montagnat M, Duval P, 2000. Rate controlling processes in the creep of polar ice, influence of grain boundary migration associated with recrystallization. Earth and Planetary Science Letters, 183, pp 179–186.

Montenegro A, Brovkin V, Eby M, Archer D, Weaver A J, 2007. Long term fate of anthropogenic carbon. Geophysical Research Letters, 34, L19707, doi:10.1029/2007GL030905.

Moon T, Joughin I, 2007. Changes in ice front position on Greenland's outlet glaciers from 1992 to 2007. Journal of Geophysical Research, 113, F02022, doi:10.1029/2007JF000927.

Munro-Stasiuk M J, 2003. Subglacial Lake McGregor, south-central Alberta, Canada. Sedimentary Geology, 160, pp 325–350.

Müller F, 1962. Zonation in the accumulation area of the glaciers of Axel Heiberg Island, N.W.T, Canada. Journal of Glaciology, 4, pp 302–313.

Müller U C, Pross J, 2007. Lesson from the past: present insolation minimum holds potential for glacial inception. Quaternary Science Reviews, 26, pp 3025–3029.

Mäkinen J, Engfeldt A, Harsson B G, Routsalainen H, Strykowski G, Oja T, Wolf D, 2005. The Fennoscandian land uplift gravity lines 1966–2003. In: Jekeli C, Bastos L, Fernades J (eds). Gravity, geoid and space missions. Berlin: Springer. (International Association of Geodesy symposia 129), pp 328–332.

Mörner N-A, 1977. Past and present uplift in Sweden: glacial isostasy, tectonism and bedrock influence. Geologiska föreningen i Stockholms förhandlingar, 99, pp 48–54.

Mörner N-A, 1979. The Fennoscandian uplift and Late Cenozoic geodynamics: geological evidence. GeoJournal, 3, pp 287–318.

Naish T, Powell R, Levy R, Wilson G, Scherer R, Talarico F, Krissek L, Niessen F, Pompilio M, Wilson T, Carter L, DeConto R, Huybers P, McKay R, Pollard D, Ross J, Winter D, Barrett P, Browne G, Cody R, Cowan E, Crampton J, Dunbar G, Dunbar N, Florindo F, Gebhardt C, Graham I, Hannah M, Hansaraj D, Harwood D, Helling D, Henrys S, Hinnov L, Kuhn G, Kyle P, Läufer A, Maffioli P, Magens D, Mandernack K, McIntosh W, Millan C, Morin R, Ohneiser C, Paulsen T, Persico D, Raine I, Reed J, Riesselman C, Sagnotti L, Schmitt D, Sjunneskog C, Strong P, Taviani M, Vogel S, Wilch T, Williams T, 2009. Obliquity-paced Pliocene West Antarctic ice sheet oscillations. Nature, 458, pp 322–328.

Nakada M, Lambeck K, 1989. Late Pleistocene and Holocene sea-level change in the Australian region and mantle rheology. Geophysical Journal International, 96, pp 497–517.

Nakićenović N, Swart R (eds), 2000. Special report on emissions scenarios. A Special Report of Working Group III of the Intergovernmental Panel on Climate Change. Cambridge: Cambridge University Press.

Nerheim S, 2008. Extrema vattenstånd för ett högt klimatscenario perioden 2071–2100 för Forsmark och Oskarshamn. SMHI rapport 2008–80. 5 sid.

Nienow P, Sharp M, Willis I, 1998. Seasonal changes in the morphology of the subglacial drainage system, Haut Glacier d'Arolla, Switzerland. Earth Surface Processes and Landforms, 23, pp 825–843.

NorthGRIP community members, 2004. High-resolution record of the Northern Hemisphere climate extending into the last interglacial period. Nature, 431, pp 147–151.

NSF, 2000. GEO 2000 Full Report. NSF 00-27, National Science Foundation.

Nye J F, 1976. Water flow in glaciers: jökulhlaups, tunnels and veins. Journal of Glaciology, 17, pp 181–207.

Näslund J-O, 1997. Subglacial preservation of valley morphology at Amundsenisen, western Dronning Maud Land, Antarctica. Earth Surface Processes and Landforms, 22, pp 441–455.

Näslund J-O, 1998. Ice sheet, climate, and landscape interactions in Dronning Maud Land, Antarctica. Ph. D. thesis. Department of Physical Geography, Stockholm University. (Dissertation series 11)

Näslund J-O, 2001. Landscape development in western and central Dronning Maud Land, East Antarctica. Antarctic Science, 13, pp 302–311.

Näslund J-O, Fastook J L, Holmlund P, 2000. Numerical modelling of the ice sheet in western Dronning Maud Land, East Antarctica: impact of present, past, and future climates. Journal of Glaciology, 46, pp 54–66.

Näslund J-O, Rodhe L, Fastook J L, Holmlund P, 2003. New ways of studying ice sheet flow directions and glacial erosion by computer modelling – examples from Fennoscandia. Quaternary Science Reviews, 22, pp 245–258.

Näslund J-O, Jansson P, Fastook J L, Johnson J, Andersson L, 2005. Detailed spatially distributed geothermal heat-flow data for modeling of basal temperatures and meltwater production beneath the Fennoscandian ice sheet. Annals of Glaciology, 40, pp 95–101.

Näslund J-O (ed), Wohlfarth B (ed), Alexanderson H, Helmens K, Hättestrand M, Jansson P, Kleman J, Lundqvist J, Brandefelt J, Houmark-Nielsen M, Kjellström E, Strandberg G, Knudsen K L, Krogh Larsen N, Ukkonen P, Mangerud J, 2008. Fennoscandian paleo-environment and ice sheet dynamics during Marine Isotope Stage (MIS) 3. Report of a workshop held September 20–21, 2007 in Stockholm, Sweden. SKB R-08-79, Svensk Kärnbränslehantering AB.

Näslund J-O, Fastook J, Jansson P, 2010. A numerical model reconstruction of the Weichselian ice sheet. SKB TR-09-19. Svensk Kärnbränslehantering AB.

Olvmo M, 2010. Review of denudation processes and quantification of weathering and erosion rates at a 0.1 to 1 Ma time scale. SKB TR-09-18, Svensk Kärnbränslehantering AB.

Olvmo M, Johansson M, 2002. The significance of rock structure, lithology, and pre-glacial deep weathering for the shape of intermediate-scale glacial erosional landforms. Earth Surface Processes and Landforms, 27, pp 251–268.

Olvmo M, Lidmar-Bergström K, Ericson K, Bonow J M, 2005. Saprolite remnant as indicators of pre-glacial landform genesis in southeast Sweden. Geografiska annaler, 87A, pp 447–460.

O'Neill K, Miller R D, 1985. Exploration of rigid ice model of frost heave. Water Resources Research, 21, pp 281–296.

Oswald G K A, Gogineni S P, 2008. Recovery of subglacial water extent from Greenland radar survey data. Journal of Glaciology, 54, pp 94–106.

Otto-Bliesner B L, Brady E C, Clauzet G, Thomas R, Levis S, Kothavala Z, 2006. Last glacial maximum and Holocene climate in CCSM3. Journal of Climate, 19, pp 2526–2544.

Otto-Bliesner B L, Hewitt C D, Marchitto T M, Brady E, Abe-Ouchi A, Crucifix M, Murakami S, Weber S L, 2007. Last Glacial Maximum ocean thermohaline circulation: PMIP2 model intercomparisons and data constraints. Geophysical Research Letters, 34, L12706, doi:10.1029/2007GL029475.

Overpeck J, Weiss J, 2009. Projections of future sea level becoming more dire. Proceedings of the Natural Academy of Sciences of the United States of America, 106, pp 21461–21462.

Paananen M, Ruskeeniemi T, 2003. Permafrost at Lupin: Interpretation of SAMPO electromagnetic soundings at Lupin. Report YST-117, Geological Survey of Finland.

Padilla F, Villeneuve J-P, 1992. Modelling and experimental studies of frost heave including solute effects. Cold Regions Science and Technology, 20, pp 183–194.

Paillard D, 2001. Glacial cycles: toward a new paradigm. Reviews of Geophysics, 39, pp 325–346.

Paterson W S B, 1994. The physics of glaciers. 3rd ed. Oxford: Pergamon.

Pattyn F, 2003. A new three-dimensional higher-order thermomechanical ice sheet model: basic sensitivity, ice-stream development, and ice flow across subglacial lakes. Journal of Geophysical Research, 108, 2382, doi:10.1029/2002JB002329.

Pattyn F, Huybrechts P, Decleir H, 1989. Modelling glacier fluctuations in the Sør Rondane, Dronning Maud Land, Antarctica. Zeitschrift fur Gletscherkunde und Glazialgeologie, 25, pp 33–47.

Pattyn F, de Smedt, B, Souchez R, 2004. Influence of subglacial Vostok lake on the regional ice dynamics of the Antarctic ice sheet: a model study. Journal of Glaciology, 50, pp 583–589.

Paulson A, Zhong S, Wahr J, 2005. Modelling post-glacial rebound with lateral viscosity variations. Geophysical Journal International, 163, pp 357–371.

Payne A J, 1995. Limit cycles in the basal thermal regime of ice sheets. Journal of Geophysical Research, 100, pp 4249–4263.

Payne A J, Baldwin D J, 1999. Thermomechanical modelling of the Scandinavian ice sheet: implications for ice-stream formation. Annals of Glaciology, 28, pp 83–89.

Payne A J, Dongelmans P W, 1997. Self-organization in the thermomechanical flow of ice sheets. Journal of Geophysical Research, 102, pp 12219–12234.

Payne A J, Huybrechts P, Abe-Ouchi A, Calov R, Fastook J L, Greve R, Marshall S J, Marsiat I, Ritz C, Tarasov L, Thomassen M P A, 2000. Results from the EISMINT model intercomparison: the effects of thermomechanical coupling. Journal of Glaciology, 46, pp 227–238.

Peltier W R, 1994. Ice age palaeotopography. Science, 265, pp 195–201.

Peltier W R, 1998. Postglacial variations in the level of the sea: implications for climate dynamics and solid-earth geophysics. Reviews of Geophysics, 36, pp 603–689.

Peltier W R, 2002. On eustatic sea level history: Last Glacial Maximum to Holocene. Quaternary Science Reviews, 21, pp 377–396.

Peltier W R, 2004. Global glacial isostasy and the surface of the ice-age Earth: the ICE-5G (VM2) model and GRACE. Annual Review of Earth and Planetary Science, 32, pp 111–149.

Peltier W R, 2005. On the hemispheric origins of meltwater pulse 1a. Quaternary Science Reviews, 24, pp 1655–1671.

Peltier W R, Drummond R, 2002. A "broad-shelf effect" upon postglacial relative sea level history. Geophysical Research Letters 29, 1169, doi:10.1029/2001GL014273.

Peltier W R, Farrell W E, Clark J A, 1978. Glacial isostasy and relative sea level: a global finite element model. Tectonophysics, 50, pp 81–110.

Pérez-Gussinyé M, Lowry A R, Watts A B, Velicogna I, 2004. On the recovery of effective elastic thickness using spectral methods: examples from synthetic data and from the Fennoscandian Shield. Journal of Geophysical Research, 109, B10409, doi:10.1029/2003JB002788.

Person M, McIntosh J, Bense V, Remenda V H, 2007. Pleistocene hydrology of North America: the role of ice sheets in reorganizing groundwater flow systems. Reviews of Geophysics, 45, RG3007, doi:10.1029/2006RG000206.

Persson G, Bärring L, Kjellström E, Strandberg G, Rummukainen M, 2007. Climate indices for vulnerability assessments. Norrköping: Sveriges meteorologiska och hydrologiska institut (Swedish Meteorological and Hydrological Institute). (SMHI reports. Meteorology and Climatology 111)

Peyaud V, Ritz C, Krinner G, 2007. Modelling the early Weichselian Eurasian ice sheets: role of ice shelves and influence of ice-dammed lakes. Climate of the Past Discussions, 3, pp 221–247.

Pfeffer W T, Harper J T, O'Neel S, 2008. Kinematic constraints on glacier contributions to 21st-century sea-level rise. Science, 321, pp 1340–1343.

Placidi L, Greve R, Seddik H, Faria S H, 2010. Continuum-mechanical, Anisotropic Flow model for polar ice masses, based on an anisotropic Flow Enhancement factor. Continuum Mechanics and Thermodynamics, 22, pp 221–237.

Pollack H N, Hurter S J, Johnson, J R, 1991. A new global heat flow compilation. [Online]. Available at: http://www.wdcb.ru/sep/data/hdata/hf_global.dat.

Pollack H N, Hurter S J, Johnson J R, 1993. Heat flow from the Earth's interior: analysis of the global data set. Reviews of Geophysics, 31, pp 267–280.

Porter S C, 1989. Some geological implications of average Quaternary glacial conditions. Quaternary Research, 32, pp 245–261.

Poudjom Djomani Y H, Fairhead J D, Griffin W L, 1999. The flexural rigidity of Fennoscandia: reflection of the tectonothermal age of the lithospheric mantle. Earth and Planetary Science Letters, 174, pp 139–154.

Price S F, Payne A J, Catania G A, Neumann T A, 2008. Seasonal acceleration of inland ice via longitudinal coupling to marginal ice. Journal of Glaciology, 54, pp 213–219.

Påsse T, 2001. An empirical model of glacio-isostatic movements and shore-level displacement in Fennoscandia. SKB R-01-41, Svensk Kärnbränslehantering AB.

Påsse T, 2004. The amount of glacial erosion of the bedrock. SKB TR-04-25, Svensk Kärnbränslehantering AB.

Raab B, Vedin H, 1995. National Atlas of Sweden. Climate, Lakes and Rivers. Stockholm: SNA publishing.

Radtke U, Grün R, Schwarcz H P, 1988. Electron spin resonance dating of the Pleistocene coral reef tracts of Barbados. Quaternary Research, 29, pp 197–215.

Rahmstorf S, Ganopolski A, 1999. Long-Term Global Warming Scenarios Computed with an Efficient Coupled Climate Model. Climatic Change, 43 (2), pp 353–367. DOI: 10.1023/A:1005474526406

Rahmstorf S, 2007. A semi-empirical approach to projecting future sea-level rise. Science, 315, pp 368–370.

Ramillien G, Lombard A, Cazenave A, Ivins E R, Llubes M, Remy F, Biancale R, 2006. Interannual variations of the mass balance of the Antarctica and Greenland ice sheets from GRACE. Global and Planetary Change, 33, pp 198–208.

Ramstein G, Kageyama M, Guiot J, Wu H, Hély C, Krinner G, Brewer S, 2007. How cold was Europe at the Last Glacial Maximum? A synthesis of the progress achieved since the first PMIP model-data comparison. Climate of the Past, 3, pp 331–339.

Rasmussen S O, Andersen K K, Svensson A M, Steffensen J P, Vinther B, Clausen H B, Siggaard-Andersen M-L, Johnsen S J, Larsen L B, Dahl-Jensen D, Bigler M, Röthlisberger R, Fisher H, Goto-Azuma K, Hansson M E, Ruth U, 2006. A new Greenland ice core chronology for the last glacial termination. Journal of Geophysical Research, 111, D06102, doi:10.1029/2005JD006079.

Rasmussen S O, Seierstad I K, Andersen K K, Bigler M, Dahl-Jensen D, Johnsen S J, 2008. Synchronization of the NGRIP, GRIP, and GISP2 ice cores across MIS 2 and palaeoclimatic implications. Quaternary Science Reviews, 27, pp 18–28.

Raymo M E, Nisancioglu K, 2003. The 41 kyr world: Milankovitch's other unsolved mystery, Paleoceanography, 18, 1011, doi:10.1029/2002PA000791.

Raymo M E, Ganley K, Carter S, Oppo D W, McManus J, 1998. Millennial-scale climate instability during the early Pleistocene epoch. Nature, 392, pp 699–702.

Raymond C F, Harrison W D, 1975. Some observations on the behaviour of the liquid and gas phases in temperate glacier ice. Journal of Glaciology, 14, pp 213–234.

Reiche P, 1950. Survey of weathering processes and products. (University of New Mexico publications in geology 3)

Remy F, Minster J F, 1993. Precise altimetric topography in ice-sheet flow studies. Annals of Glaciology, 17, pp 195–200.

Rial J A, 2004. Abrupt climate change: chaos and order at orbital and millennial time scales. Global and Planeraty Change, 41, pp 95–109.

Richardson C, 2004. Spatial characteristics of snow accumulation in Dronning Maud Land, Antarctica. Global and Planetary Change, 42, pp 31–43.

Richardson K, Steffen W, Schellnhuber H J, Alcamo J, Barker T, Kammen D M, Leemans R, Liverman D, Munasinghe M, Osman-Elasha B, Stern N, Wæver O, 2009. Synthesis report from CLIMATE CHANGE - Global risks, challenges and decisions. Copenhagen, 10–12 March 2009. Copenhagen: University of Copenhagen.

Riddihough R P, 1972. Regional magnetic anomalies and geology in Fennoscandia: a discussion. Canadian Journal of Earth Sciences, 9, pp 219–232.

Ridley J K, Huybrechts P, Gregory J M, Lowe J A, 2005. Elimination of the Greenland ice sheet in a high CO_2 climate. Journal of Climate, 18, pp 3409–3427.

Rignot E, Kanagaratnam P, 2006. Changes in the velocity structure of the Greenland ice sheet. Science, 311, pp 986–990.

Rignot E J, Gogineni S P, Krabill W B, Ekholm S, 1997. North and Northeast Greenland ice discharge from satellite radar interferometry. Science, 276, pp 934–937.

Rignot E, Bamber J L, van den Broeke M R, Davis C, Li Y, van de Berg W J, van Meijgaard E, 2008. Recent Antarctic ice mass loss from radar interferometry and regional climate modelling. Nature Geoscience, 1, pp 106–110.

Rignot E, Koppes M, Velicogna I, 2010. Rapid submarine melting of the calving faces of West Greenland glaciers. Nature Geoscience, 3, pp 187–191.

Riis F, 1996. Quantification of Cenozoic vertical movements of Scandinavia by correlation of morphological surfaces with offshore data. Global and Planetary Change, 12, pp 331–357.

Riseborough D W, Shiklomanov N, Etzelmüller B, Gruber S, Marchenko S, 2008. Recent advances in permafrost modelling. Permafrost and Periglacial Processes, 19, pp 137–156.

Ritz C, Fabre A, Letreguilly A, 1996. Sensitivity of a Greenland ice sheet model to ice flow and ablation parameters: Consequences for evolution through the last climatic cycle. Climate Dynamics, 13, pp 11–24.

Roberts M J, 2005. Jökulhlaups: a reassessment of floodwater flow through glaciers. Reviews of Geophysics, 43, RG1002, doi:10.1029/2003RG000147.

Roberts M J, Russell A J, Tweed F S, Knudsen Ó, 2000. Ice fracturing during jökulhlaups: implications for englacial floodwater routing and outlet development. Earth Surface Processes and Landforms, 25, pp 1429–1446.

Robinson A, Calov R, Ganopolski A, 2010. An efficient regional energy-moisture balance model for simulation of the Greenland Ice Sheet response to climate change. The Cryosphere, 4, pp 129–144.

Rohling E J, Grant K, Bolshaw M, Roberts A P, Siddall M, Hemleben C, Kucera M, 2009. Antarctic temperature and global sea level closely coupled over the past five glacial cycles. Nature Geoscience, doi:10.1038/ngeo557.

Rudberg S, 1954. Västerbottens berggrundsmorfologi: ett försök till rekonstruktion av preglaciala erosionsgenerationer i Sverige. Ph. D. thesis. Uppsala University. (Geographica 25)

Ruddiman W F, 2001. Earth's climate: past and future. New York: Freeman.

Ruddiman W F, 2003. The anthropogenic greenhouse era began thousands of years ago. Climate Change, 61, pp 261–293.

Rummukainen M, 2003. The Swedish regional climate modeling program, SWECLIM, 1996–2003. Final report. Norrköping: Sveriges meteorologiska och hydrologiska institut (Swedish Meteorological and Hydrological Institute). (SMHI Meteorologi 104)

Rummukainen M, Källén E, 2009. Ny klimatvetenskap 2006–2009. Komissionen för hållbar utveckling, Regeringskansliet (in Swedish).

Ruskeeniemi T, Paananen M, Ahonen L, Kaija J, Kuivamäki A, Frape S, Moren L, Degnan P, 2002. Permafrost at Lupin: report of Phase I. Report YST-112, Geological Survey of Finland.

Ruskeeniemi T, Ahonen L, Paananen M, Frape S, Stotler R, Hobbs M, Kaija J, Degnan P, Blomqvist R, Jensen M, Lehto K, Moren L, Puigdomenech I, Snellman M, 2004. Permafrost at Lupin: report of Phase II. Report YST-119, Geological Survey of Finland.

Röthlisberger H, 1972. Water pressure in intra- and subglacial channels. Journal of Glaciology, 11, pp 177–203.

Röthlisberger H, Lang H, 1987. Glacial hydrology. In: Gurnell A M, Clark M J (eds). Glacio-fluvial sediment transfer: an alpine perspective. Chichester: Wiley.

Salas J, Gimeno M J, Molinero J, Auqué L F, Gómez J, Juárez I, 2010. SR-Site. Hydrogeochemical evolution of the Forsmark site. SKB TR-10-58, Svensk Kärnbränslehantering AB.

Sawagaki T, Hirakawa K, 1997. Erosion of bedrock by subglacial meltwater, Soya Coast, East Antarctica. Geografiska Annaler, 79A, pp 223–238.

SCAR, 2007. A need for more realistic ice-sheet models. SCAR report 30, Scientific Committee on Antarctic Research.

Scherneck H-G, Johansson J M, Vermeer M, Davis J L, Milne G A, Mitrovica J X, 2001. BIFROST project: 3D crustal deformation rates derived from GPS confirm postglacial rebound in Fennoscandia. Earth Planets Space, 53, pp 703–708.

Schneider T, 2000. Hydrological processes in the wet-snow zone of glaciers: a review. Zeitschrift fur Gletscherkunde und Glazialgeologie, 36, pp 89–105.

Seipold U, 1995. The variation of thermal transport properties in Earth's crust. Journal of Geodynamics, 20, pp 145–154.

Selby M J, 1993. Hillslope materials and processes. 2nd ed. Oxford: Oxford University Press.

Shackleton N J, Kennett J P, 1975. Paleotemperature history of the Cenozoic and the initiation of Antarctic glaciation: oxygen and carbon isotopic analyses in DSDP sites 277, 279, and 281. In: Kennett J P, Houtz R (eds). Initial reports of the Deep Sea Drilling Project, 29, pp 743–755.

Shaffer G, Olsen S M, Pedersen J O P, 2009. Long-term ocean oxygen depletion in response to carbon dioxide emissions from fossil fuels. Nature Geoscience, 2, pp 105–109.

Shala S, Helmens K F, Risberg J, Löwemark L, Jansson K, Kuhry P, submitted. Early Holocene glacial-lake evolution in northern Finland – a multi-proxy approach. XVIII INQUA congress. Bern, Switzerland, 20–27 July 2011.

Sharp R P, 1960. Glaciers. Eugene: University of Oregon Press. (Condon lectures 1960).

Shepherd A, Wingham D, 2007. Recent sea-level contribution of the Antarctic and Greenland ice sheets. Science, 315, pp 1529–1532.

Shepherd A, Hubbard A, Nienow P, King M, McMillan M, Joughin I, 2009. Greenland ice sheet motion coupled with daily melting in late summer. Geophysical Research Letters, 36, L01501, doi:10.1029/2008GL035758.

Shin S-I, Liu Z, Otto-Bliesner B, Brady E C, Kutzbach J E, Harrison S P, 2003. A simulation of the Last Glacial Maximum climate using the NCAR-CSM. Climate Dynamics, 20, pp 127–151.

Shreve R, 1972. Movement of water in glaciers. Journal of Glaciology, 11, pp 205–214.

Shur Y L, Slavin-Borovskiy V B, 1993. N-factor maps of Russian permafrost region. Proceedings of the sixth international conference on permafrost. Beijing, 5–9 July 1993. Guangzhou: South China University of Technology, pp 564–568.

Siddall M, Rohling E J, Almogi-Labin A, Hemleben C, Meischner D, Schmelzer I, Smeed D A, 2003. Sea-level fluctuations during the last glacial cycle. Nature, 423, pp 853–858.

Siddall M, Stocker T F, Clark P U, 2009. Constraints on future sea-level rise from past sea-level change. Nature Geoscience, 2, pp 571–575.

Siegert M J, 2005. Lakes beneath the ice sheet: the occurence, analysis and future exploration of Lake Vostok and other Antarctic subglacial lakes. Annual Review of Earth and Planetary Sciences, 33, pp 215–245.

Siegert M J, Dowdeswell J A, 1996. Spatial variations in heat at the base of the Antarctic ice sheet from analysis of the thermal regime above subglacial lakes. Journal of Glaciology, 42, pp 501–509.

Siegert M J, Dowdeswell J A, Gorman M R, McIntyre N F, 1996. An inventory of Antarctic sub-glacial lakes. Antarctic Science, 8, pp 281–286.

Siegert M J, Carter S, Tabacco I, Popov S, Blankenship D D, 2005. A revised inventory of Antarctic subglacial lakes. Antarctic Science, 17, pp 453–460.

Simons M, Hager B H, 1997. Localization of the gravity field and the signature of glacial rebound. Nature, 390, pp 500–504.

Six D, Letréguilly A, Reynaud L, 2001. Greenland ice-sheet mass-balance distribution: a variance analysis of existing field data. Journal of Glaciology, 47, pp 441–451.

SKB, 2005a. Preliminary site description. Forsmark area – version 1.2. SKB R-05-18, Svensk Kärnbränslehantering AB.

SKB, 2006a. Climate and climate-related issues for the safety assessment SR-Can. SKB TR-06-23, Svensk Kärnbränslehantering AB.

SKB, 2006b. Geosphere process report for the safety assessment SR-Can. SKB TR-06-19, Svensk Kärnbränslehantering AB.

SKB, 2010a. Data report for the safety assessment SR-Site. SKB TR-10-52, Svensk Kärnbränslehantering AB.

SKB, 2010b. FEP-report for the safety assessment SR-Site. SKB TR-10-45, Svensk Kärnbränslehantering AB.

SKB, 2010c. Geosphere process report for the safety assessment SR-Site. SKB TR-10-48, Svensk Kärnbränslehantering AB.

SKB, 2010d. Biosphere assessment of SR-Site Forsmark – synthesis and summary of results. SKB TR-10-09, Svensk Kärnbränslehantering AB.

SKB, 2010e. Comparative analysis of safety related site characteristics. SKB TR-10-54, Svensk Kärnbränslehantering AB.

SKB 2010f. Model summary report for the safety assessment SR-Site. TR-10-51, Svensk Kärnbränslehantering AB.

SKB, 2011. Long-term safety for the final repository for spent nuclear fuel at Forsmark. Main report of the SR-Site project. SKB TR-11-01, Svensk Kärnbränslehantering AB.

Skinner L C, 2008. Revisiting the absolute calibration of the Greenland ice-core age-scales. Climate of the Past, 4, pp 295–302.

SMHI, 2001. Temperaturen och nederbörden i Sverige 1961–1990: referensnormaler. 2. utg. Norrköping: Sveriges meteorologiska och hydrologiska institut (Swedish Meteorological and Hydrological Institute). (SMHI Meteorologi 99)

Smith M W, Riseborough D W, 1996. Permafrost monitoring and detection of climate change, Permafrost and Periglacial Processes, 7, pp 301–309.

Sohlenius G, Hedenström A, Rudmark L, 2004. Forsmark site investigation. Mapping of unconsolidated Quaternary deposits 2002–2003. Map description. SKB R-04-39, Svensk Kärnbränslehantering AB.

SOU 2007. Klimat- och sårbarhetsutredningen. Sverige inför klimatförändringarna: hot och möjligheter (in Swedish). Stockholm: Fritzes. (Statens offentliga utredningar 2007:60)

Spada G, Antonioli A, Cianetti S, Giunchi C, 2006. Glacial isostatic adjustment and relative sea-level changes: the role of lithospheric and upper mantle heterogeneities in a 3D spherical Earth. Geophysical Journal International, 165, pp 692–702.

Spring U, Hutter K, 1981. Numerical studies of jökulhlaups. Cold Regions Science and Technology, 4, pp 227–244.

Staiger J K W, Gosse J C, Johnson J V, Fastook J, Gray J T, Stockli D F, Stockli L, Finkel R, 2005. Quaternary relief generation by polythermal glacier ice. Earth Surface Processes and Landforms, 30, pp 1145–1159.

Steffen K, Nghiem S V, Huff R, Neumann G, 2004. The melt anomaly of 2002 on the Greenland Ice Sheet from active and passive microwave satellite observations. Geophysical Research Letters, 31, L20402, doi:10.1029/2004GL020444.

Stone E J, Lunt D J Rutt I C, Hanna E, 2010a. The effect of more realistic forcings and boundary conditions on the modelled geometry and sensitivity of the Greenland ice-sheet. The Cryosphere Discussion, 4, pp 233–285.

Stone E J, Lunt D J, Rutt I C, Hanna E, 2010b. Investigating the sensitivity of numerical model simulations of the modern state of the Greenland ice sheet and its future response to climate change. The Cryosphere, 4, pp 379–417.

Strandberg G, Brandefelt J, Kjellström E, 2008. Modelling last glacial maximum climate variability with a high resolution regional climate model. EGU2008-A-03244. Abstracts of the contributions of the EGU General Assembly 2008. Geophysical Research Abstracts, 10.

Strandberg G, Brandefelt J, Kjellström E, 2009a. High-resolution regional climate model simulations for a 50-year period under Last Glacial Maximum conditions. Abstracts of the contributions of the EGU General Assembly 2009. Geophysical Research Abstracts, 11.

Strandberg G, Brandefelt J, Kjellström E, Smith B, 2009b. Simulating cold palaeo climate conditions in Europe with a regional climate model. In: Rockel B, Bärring L, Reckermann M (eds). Proceedings from WCRP workshop on regional climate modelling. Lund, 4–8 May 2009. (International BALTEX Secretariat publication 41), pp 280–281.

Strandberg G, Brandefelt J, Kjellström E, Smith B, 2010. High resolution simulation of Last Glacial Maximum climate and vegetation in Europe. Tellus, doi: 10.1111/j.1600-0870.2010.00485.x.

Straneo F, Hamilton G S, Sutherland D A, Stearns L A, Davidson F, Hammill M O, Stenson G B, Rosing-Asvid A, 2010. Rapid circulation of warm subtropical waters in a major glacial fjord in East Greenland. Nature Geoscience, 3, pp 182–186.

Stroeven A P, Fabel D, Hättestrand C, Harbor J, 2002a. A relict landscape in the centre of Fennoscandian glaciation: cosmogenic radionuclide evidence of tors preserved through multiple glacial cycles. Geomorphology, 44, pp 145–154.

Stroeven A P, Fabel D, Hättestrand C, Kleman J, 2002b. Quantifying the erosional impact of the Scandinavian ice sheet in the Torneträsk-Narvik corridor, northern Sweden, based on cosmogenic radionuclide data. Geografiska Annaler, 84A, pp 275–287.

Sugden D E, 1977. Reconstruction of the morphology, dynamics and thermal characteristics of the Laurentide ice sheet at its maximum. Arctic and Alpine Research, 9, pp 27–47.

Sugden D E, 1978. Glacial erosion by the Laurentide ice sheet. Journal of Glaciology, 20, pp 367–391.

Sugden D E, John B S, 1976. Glaciers and landscape: a geomorphological approach. London: Arnold.

Sundberg J, 1988. Thermal properties of soils and rocks. Ph. D. thesis. Chalmers tekniska högskola. (Geologiska institutionen publ. A 57)

Sundberg J, Back P-E, Ländell M, Sundberg A, 2009. Modelling of temperature in deep boreholes and evaluation of geothermal heat flow at Forsmark and Laxemar. SKB TR-09-14, Svensk Kärnbränslehantering AB.

Sundh M, Sohlenius G, Hedenström A, 2004. Forsmark site investigation. Stratigraphical investigation of till in machine cut trenches. SKB P-04-34, Svensk Kärnbränslehantering AB.

Svendsen J I, Mangerud J, 1987. Late Weichselian and Holocene sea-level history for a cross-section of western Norway. Journal of Quaternary Science, 2, pp 113–132.

Svendsen J I, Astakhov V I, Bolshiyanov D Y, Demidov I, Dowdeswell J A, Gataullin V, Hjort C, Hubberten H W, Larsen E, Mangerud J, Melles M, Möller P, Saarnisto M, Siegert M J, 1999. Maximum extent of the Eurasian ice sheets in the Barents and Kara Sea region during the Weichselian. Boreas, 28, pp 234–242.

Svendsen J I, Alexanderson H, Astakhov V I, Demidov I, Dowdeswell J A, Funder S, Gataullin V, Henriksen M, Hjort C, Houmark-Nielsen M, Hubberten H W, Ingólfsson O, Jakobsson M, Kjær K H, Larsen E, Lokrantz H, Lunkka J P, Lyså A, Mangerud J, Matiouchkov A, Murray A, Moller P, Niessen F, Nikolskaya O, Polyak L, Saarnisto M, Siegert C, Siegert M J, Spielhagen R F, Stein R, 2004. Late Quaternary ice sheet history of northern Eurasia. Quaternary Science Reviews, 23, pp 1229–1271.

Svensson A, Andersen K K, Bigler M, Clausen H B, Dahl-Jensen D, Davies S M, Johnsen S J, Muscheler R, Parrenin F, Rasmussen S O, Röthlisberger R, Seierstad I, Steffensen J P, Vinther B M, 2008. A 60 000 year Greenland stratigraphic ice core chronology. Climate of the Past, 4, pp 47–57.

Svensson P D, Hansen S, 2010. Freezing and thawing of montmorillonite – a time resolved X-ray diffraction study. Applied Clay Science, 49, pp 127–134.

Swantesson J O H, 1992. Recent micro-weathering phenomena in southern and central Sweden. Permafrost and Periglacial Processes, 3, pp 275–292.

Söderbäck B, 2008. Geological evolution, palaeoclimate and historical development of the Forsmark and Laxemar-Simpevarp areas. Site descriptive modelling. SDM-Site. SKB R-08-19, Svensk Kärnbränslehantering AB.

Tamisiea M E, Mitrovica J X, Milne G A, Davis J L, 2001. Global geoid and sea level changes due to present-day ice mass fluctuations. Journal of Geophysical Research, 106, pp 30849–30863.

Tamisiea M E, Mitrovica J X, Davis J L, Milne G A, 2003. Long wavelength sea level and solid surface perturbations driven by polar ice mass variations: fingerprinting Greenland and Antarctic ice sheet flux. Space Science Reviews, 108, pp 81–93.

Tarasov L, Peltier W R, 2004. A geophysically constrained large ensemble analysis of the deglacial history of the North American ice-sheet complex. Quaternary Science Reviews, 23, pp 359–388.

Tarbuck E J, Lutgens F K, 1999. Earth: an introduction to physical geology. 6th ed. Upper Saddle River, N.J.: Prentice Hall.

Taylor A E, 1995. Field measurements of n-factors for natural forest areas, Mackenzie Valley, Northwest Territories. Geological Survey of Canada, Current Research, 1995-B, pp 89–98.

Taylor A E, 2001. Relationship of ground temperatures to air temperatures in forests. Geological Survey of Canada, Bulletin, 547, pp 111–117.

Thomas M F, 1994. Geomorphology in the tropics: a study of weathering and denudation in low latitudes. Chichester: Wiley.

Thomas R, Frederick, E, Krabill W, Manizade S, Martin C, 2009. Recent changes on Greenland outlet glaciers. Journal of Glaciology, 55, pp 147–162.

Thomsen H H, Thorning L, Olesen O B, 1989. Applied glacier research for planning hydroelectric power, Ilulissat/Jakobshavn, West Greenland. Annals of Glaciology, 13, pp 257–261.

Tjernström M, Rummukainen M, Bergström S, Rodhe J, Persson G, 2003. Klimatmodellering och klimatscenarier ur SWECLIMS perspektiv (in Swedish). Norrköping: Sveriges meteorologiska och hydrologiska institut (Swedish Meteorological and Hydrological Institute). (SMHI reports. Meteorology and Climatology 102)

Toniazzo T, Gregory J M, Huybrechts P, 2004. Climatic impact of a Greenland deglaciation and its possible irreversibility. Journal of Climate, 17, pp 21–33.

Turcotte D L, 1980. On the thermal evolution of the Earth. Earth and Planetary Science Letters, 48, pp 53–58.

Turkington A V, Phillips J D, Campbell S W, 2005. Weathering and landscape evolution. Geomorphology, 67, pp 1–6.

Tushingham A M, Peltier W R, 1991. ICE-3G: a new global model of Late Pleistocene deglaciation based upon geophysical predictions of post-glacial relative sealevel change. Journal of Geophysical Research, 96, pp 4497–4523.

Tyrell T, Sheperd J G, Castle S, 2007. The long-term legacy of fossil fuels. Tellus B, 59, pp 664–672.

Tzedakis P C, Raynaud D, McManus J F, Berger A, Brovkin V, Kiefer T, 2009. Interglacial diversity. Nature Geoscience, 2, pp 751–755.

Tziperman E, Gildor H, 2003. On the mid-Pliocene transition to 100-kyr glacial cycles and the asymmetry between glaciation and deglaciation times. Paleoceanography 18, 1001, doi:10.1029/2001pa000627.

UNEP/GRID-Arendal, 2005. Permafrost distribution in the Arctic. UNEP/GRID-Arendal Maps and Graphics Library. [Online]. Available at: http://maps.grida.no/go/graphic/permafrost-distribution-in-the-arctic. [26 November 2010].

van de Wal R S W, 1996. Mass-balance modelling of the Greenland ice sheet: a comparison of an energy-balance model and a degree-day model. Annals of Glaciology, 23, pp 36–45.

van de Wal R S W, Boot W, van den Broeke M R, Smeets C J P P, Reijmer C H, Donker J J A, Oerlemans J, 2008. Large and rapid meltinduced velocity changes in the ablation zone of the Greenland Ice Sheet. Science, 321, pp 111–113.

van den Broeke M, Bamber J, Ettema J, Rignot E, Schrama E, van de Berg W J, van Meijgaard E, Velicogna I, Wouters B, 2009. Partitioning recent Greenland mass loss. Science, 326, pp 984–986.

van der Veen C J, 1998a. Fracture mechanics approach to penetration of surface crevasses on glaciers. Cold Regions Science and Technology, 27, pp 31–47.

van der Veen C J, 1998b. Fracture mechanics approach to penetration of bottom crevasses on glaciers. Cold Regions Science and Technology, 27, pp 213–223.

van der Veen C J, 2007. Fracture propagation as means of rapidly transferring surface meltwater to the base of glaciers. Geophysical Research Letters, 34, L01501, doi:10.1029/2006GL028385.

van Huissteden K, Pollard D, 2003. Oxygen isotope stage 3 fluvial and eolian successions in Europe compared with climate model results. Quaternary Reseach, 59, pp 223–233.

van Huissteden K, Vandenberghe J, Pollard D, 2003. Palaeotemperature reconstructions of the European permafrost zone during oxygen isotope Stage 3 compared with climate model results. Journal of Quaternary Science, 18, pp 453–464.

Van Meerbeeck C J, Renssen H, Roche D M, Wohlfarth B, Bohncke S J P, Bos J A A, Engels S, Helmens K F, Sánchez-Goñi M F, Svensson A, Vandenberghe J, submitted. The nature of MIS 3 stadial-interstadial transitions in Europe: new insights from model-data comparisons. Submitted to Quaternary Science Reviews.

Van Tatenhove F G M, Huybrechts P, 1996. Modelling of the thermal conditions at the Greenland ice sheet margin during Holocene deglaciation: boundary conditions from moraine formation. Geografiska Annaler, 78A, pp 83–99.

Velicogna I, 2009. Increasing rates of ice mass loss from the Greenland and Antarctic ice-sheets revealed by GRACE. Geophysical Research Letters, 36, L19503, doi:10.1029/2009GL040222.

Velicogna I, Wahr J, 2006. Acceleration of Greenland ice mass loss in spring 2004. Nature, 443, pp 329–331.

Vidstrand P, 2003. Surface and subsurface conditions in permafrost areas – a literature review. SKB TR-03-06, Svensk Kärnbränslehantering AB.

Vidstrand P, Follin S, Zugec N, 2010. Groundwater flow modelling of periods with periglacial and glacial conditions – SR-Site Forsmark. SKB R-09-21, Svensk Kärnbränslehantering AB.

Vinther B M, Buchardt S L, Clausen H B, Dahl-Jensen D, Johnsen S J, Fisher D A, Koerner R M, Raynaud D, Lipenkov V, Andersen K K, Blunier T, Rasmussen S O, Steffensen J P, Svensson A M, 2009. Holocene thinning of the Greenland ice sheet. Nature, 461, pp 385–388.

Väliranta M, Helmens K F, 2007. Palaeobotanical and lithological review of a 7-m-thick sediment sequence, dated to MIS 5d-c, from Sokli, Finnish Lapland: preliminary results and interpretation. 1st NEPAL (Nordic Network on Palaeoclimatology) workshop. Palmse, Estonia, 10–12 May 2007.

Väliranta M, Birks H H, Engels S, Helmens K F, 2008. Early Weichselian botanical features in Finnish Lapland. 33rd IGC congress. Oslo, 6–14 August 2008.

Väliranta M, Birks H H, Helmens K F, Engels S, Piirainen M, 2009. Early-Weichselian interstadial (MIS 5c) summer temperatures were higher than today in northern Fennoscandia. Quaternary Science Reviews (rapid communications), 28, pp 777–782.

Waddington E D, 1987. Geothermal heat flux beneath ice sheets. In: Waddington E D, Walder J S (eds). The physical basis of ice sheet modelling. Wallingford, Oxfordshire: International Association of Hydrological Sciences. (IAHS Publication 170), pp 217–226.

Wadham J L, Lis G P, Bartholomew I, Sole, A, Nienow P, Mair D, Hubbard A, Watson A, Das S, Stibal M, Lawson E, Dubnick A, Criscitiello A, Barnett M, submitted. Observed rapid meltwater drainage via channels beneath the GIS. Submitted to Science.

Waelbroeck C, Labeyrie L, Michel E, Duplessy J C, McManus J F, Lambeck K, Balbon E, Labracherie M, 2002. Sea-level and deep water temperature changes derived from benthic foraminifera isotopic records. Quaternary Science Reviews, 21, pp 295–305.

Wake L M, Huybrechts P, Box J E, Hanna E, Janssens I, Milne G A, 2009. Surface mass-balance changes of the Greenland ice sheet since 1866. Annals of Glaciology, 50, pp 178–184.

Walder J S, Fowler A, 1994. Channelized subglacial drainage over a deformable bed. Journal of Glaciology, 40, pp 3–15.

Waller R I, 2001. The influence of basal processes on the dynamic behaviour of cold-based glaciers. Quaternary International, 86, pp 117–128.

Washburn A L, 1979. Geocryology: a survey of periglacial processes and environments. 2nd ed. London: Arnold.

Watts A B, 2001. Isostasy and flexure of the lithosphere. Cambridge: Cambridge University Press.

Weart S R, 2003. The discovery of global warming. Cambridge: Harvard University Press.

Weertman J, 1972. General theory of water flow at the base of a glacier or ice sheet. Reviews of. Geophysics and Space Physics, 10, pp 287–303.

Weertman J, 1973. Can a water-filled crevasse reach the bottom surface of a glacier? In: Symposium on the Hydrology of Glaciers, Cambridge, 7–13 September 1969. Wallingford, Oxfordshire: International Association of Hydrological Sciences. (IAHS Publication 95), pp 139–145.

Werner M, Heimann M, Hoffman G, 2001. Isotopic composition and origin of polar precipitation in present and glacial climate simulations. Tellus, 53B, pp 53–71.

Whalley W B, Warke P A, 2005. Weathering. In: Selley R C, Cocks L R M, Plimer I R (eds.) Encyclopedia of geology. Amsterdam: Elsevier.

Whitehouse P, 2009. Glacial isostatic adjustment and sea-level change. State of the art report. SKB TR-09-11. Svensk Kärnbränslehantering AB.

Whitehouse P, Latychev K, Milne G A, Mitrovica J X, Kendall K, 2006. Impact of 3D Earth structure on Fennoscandian glacial isostatic adjustment: Implications for space-geodetic estimates of present-day crustal deformations. Geophysical Research Letters 33, L13502, doi:10.1029/2006GL026568.

Williams P J, Smith M W, 1989. The frozen earth: fundamentals of geocryology. Cambridge: Cambridge University Press.

Wingham D J, Wallis D W, Shepherd A, 2009. Spatial and temporal evolution of Pine Island Glacier thinning, 1995–2006. Geophysical Research Letters, 36, L17501, doi:10.1029/2009GL039126.

Witt A, Schumann A Y, 2005. Holocene climate variability on millennial scales recorded in Greenland ice cores. Nonlinear Processes in Geophysics, 12, pp 345–352.

Wohlfarth B, 2009. Ice-free conditions in Fennoscandia during Marine Oxygen Isotope Stage 3? SKB TR-09-12, Svensk Kärnbränslehantering AB.

Wohlfarth B, 2010. Ice free conditions in Sweden during Marine Oxygen Isotope Stage 3? Boreas, 39, pp 377–398.

Wohlfarth B, Näslund J-O (eds), 2010. Fennoscandian ice sheet in MIS 3. Boreas, 39, pp 325–456.

Woth K, Weisse R, von Storch H, 2006. Climate change and North Sea storm surge extremes: an ensemble study of storm surge extremes expected in a changed climate projected by four different regional climate models. Ocean Dynamics, 56, pp 3–15.

Wouters B, Chambers D, Schrama E J G, 2008. GRACE observe small-scale mass loss in Greenland. Geophysical Research Letters, 35, L20501, doi:10.1029/2008GL034816.

Wu P, Peltier W R, 1983. Glacial isostatic adjustment and the free air gravity anomaly as a constraint on deep mantle viscosity. Geophysical Journal of the Royal Astronomical Society, 74, pp 377–449.

Wu P, Wood R, Stott P, 2004. Does the recent freshening trend in the North Atlantic indicate a weakening thermohaline circulation? Geophysical Research Letters, 31, L02301, doi:10.1029/2003GL018584.

Wu P, Wang H, Schotman H, 2005. Postglacial induced surface motions, sea-levels and geoid rates on a spherical, self-gravitating laterally heterogeneous earth. Journal of Geodynamics, 39, pp 127–142.

Wu H, Guiot J, Brewer S, Guo Z, 2007. Climatic changes in Eurasia and Africa at the last glacial maximum and mid-Holocene: reconstruction from pollen data using inverse vegetation modelling. Climate Dynamics, 29, pp 211–229.

Yershov E D, 1998. General Geocryology. Cambridge: Cambridge University Press.

Yin Q Z, Berger A, 2010. Insolation and CO2 contribution to the interglacial climate before and after the Mid-Brunhes Event. Nature Geoscience, 3, pp 243–246.

Yokoyama Y, Lambeck K, De Deckker P, Johnston P, Fifield L K, 2000. Timing of the last glacial maximum from observed sea level minima. Nature, 406, pp 713–716.

Zickfeld K, Levermann A, Morgan M G, Kuhlbrodt T, Rahmstorf S, Keith D W, 2007. Expert judgement on the response of the Atlantic meridional overtuning circulation to climate change. Climate Change, 82, pp 235–265.

Zwally H J, Abdalati W, Herring T, Larson K, Saba J, Steffen K, 2002. Surface melt-induced acceleration of Greenland ice-sheet flow. Science, 297, pp 218–222.

Zweck C, Huybrechts P, 2003. Modeling the marine extent of northern hemisphere ice sheets during the last glacial cycle. Annals of Glaciology, 37, pp 173–180.

Appendix 1

Air temperature data

A1.1 Introduction

With the approach used to handle climate issues in the safety assessment, Section 1.2, estimates of past and possible future temperature variations are necessary for various studies within the safety assessment, such as simulations of ice sheet and permafrost development. The approach taken in SR-Site is to reconstruct temperatures for the last glacial cycle and use them to construct a *reference glacial cycle* for the coming 100 kyrs, Section 1.2. This *reference glacial cycle* is not a forecast of the future climate that will occur at Forsmark, but instead i) one relevant example of a possible future climate, and ii) a starting point for the construction of complementary, and more pessimistic, climate cases also to be analysed in the safety assessment.

In the following text the term *air temperature* is used as representing annual mean air temperatures, while *ground surface temperature* describes the annual mean temperature on the ground surface below vegetation including the humus layer. The ground can be mineral or organic soil or rock. *Subglacial temperature* describes the temperature at the interface between the basal part of an ice sheet and its bed, while *submerged temperature* describes an assumed water temperature at the sea bed during periods when the site is submerges by the Baltic Sea.

A1.2 Greenland proxy data on last glacial cycle temperatures used for ice sheet modelling

In the absence of a complete last glacial cycle palaeotemperature curve from Fennoscandia, proxy data on palaeotemperatures from the GRIP ice core /Dansgaard et al. 1993, Johnsen et al. 1995/ are typically used in model simulations of the Weichselian ice sheet e.g. /Fastook and Holmlund 1994, Holmlund and Fastook 1995, Hagdorn 2003, Hagdorn et al. 2005, Forsström 2005/. The ice sheet modelling performed for SR-Site also uses palaeotemperature information from the GRIP core (Section 3.1.4). Figure A1-1 (red line) shows the GRIP temperature curve (50 year average values plotted on the on the ss09 time scale, see below) used as input to the SR-Site ice sheet modelling performed with the University of Maine Ice Sheet Model (UMISM).

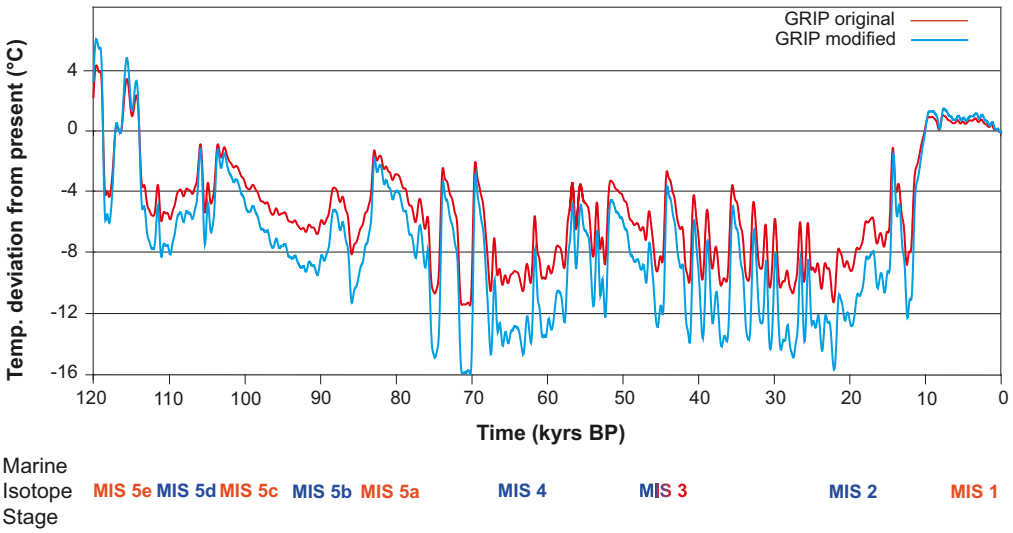

Figure A1-1. *Palaeotemperature curve from the GRIP ice core /Johnsen et al. 1995/ (red) and modified temperature curve resulting from the ice sheet model calibration (blue). Cold stadials and warm interstadials are shown in blue and red text respectively, denoted by their Marine Isotope Stage (MIS) numbers. The uncertainty of the temperature curves is discussed in Section A1.5.*

Although $\delta^{18}O$ values from ice cores are useful temperature proxies, transferring $\delta^{18}O$ values to air temperatures and using them as proxy data for palaeotemperatures is not straightforward e.g. /Cuffey et al. 1994, Huber et al. 2006/. In part, this is because of changes in the source of precipitation over time and changes in the distribution of snow on the ice sheet. Also seasonal variations in temperature and precipitation affect the isotopic composition of the ice core /Krinner et al. 1997/. Studies of $\delta^{15}N$ isotopes from the NorthGRIP (NGRIP) ice core /NorthGRIP community members 2004/ has shown that the $\delta^{18}O$ – Temperature relationship changes over time, for instance between glacial and interglacial periods and between stadials and interstadials /Huber et al. 2006/. The results by /Huber et al. 2006/ may be used as input in an estimation of the errors present in the GRIP temperature curve. This is discussed in Section A1.5 together with the errors associated with using the GRIP temperature curve for reconstructing Fennoscandian temperatures. Despite the uncertainties, the temperature reconstructions from the Greenland ice cores are one of the best continuous archives of palaeoclimate information available in the vicinity of Fennoscandia.

In the simulation of the Weichselian ice sheet, the modelled ice sheet configurations were calibrated against known dated ice-marginal positions (Section 3.1.4). The calibration was done by making systematic changes of the entire input GRIP temperature curve. The resulting modified temperature curve after calibration is shown in Figure A1-1. Keeping all other input data constant in the calibration process, the modified temperature curve after model calibration results in Late and Middle Weichselian ice sheet configurations in good agreement with dated stadial ice-marginal positions from glacial geology and Early Weichselian configurations in reasonably good agreement with geological interpretations. The main difference between the original GRIP curve and the temperature curve after calibration is that the latter shows generally colder conditions during stadials (Figure A1-1). The temperatures during interstadials are similar.

A1.3 Reconstructed last glacial cycle temperatures in the Forsmark region

A1.3.1 Air temperatures with and without a Weichselian ice sheet

From the calibrated ice sheet model, a regional temperature curve was extracted for the terrestrial grid cell closest to the Forsmark site (Figure A1-2, blue line). This local temperature curve thus originates from the modified GRIP curve of Figure A1-1. For periods without an ice sheet cover over the Forsmark region, the extracted temperature curve shows air temperature in the Forsmark region as represented in the ice sheet model simulation. For periods with ice sheet cover over Forsmark, the curve shows the simulated basal ice temperatures from the ice sheet model.

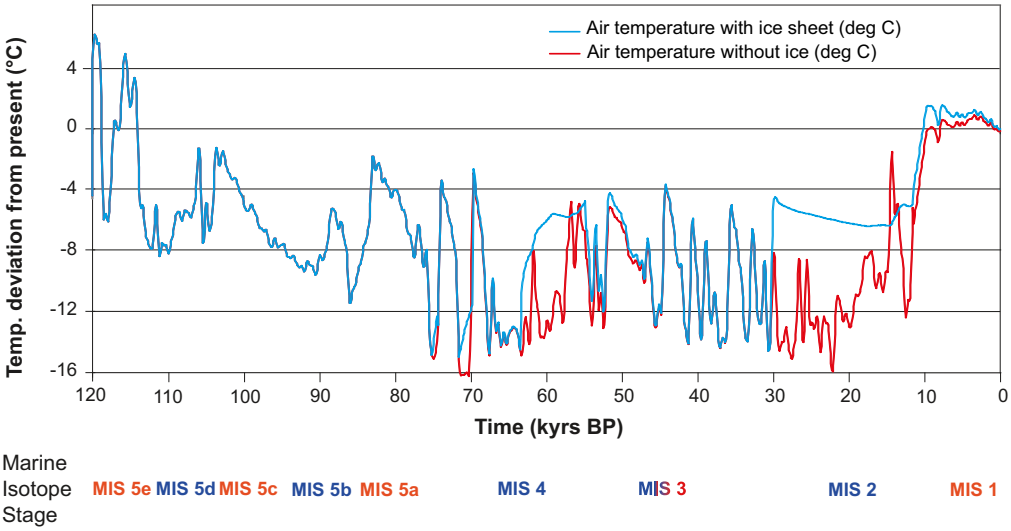

Figure A1-2. *Extracted air temperature curve for the Forsmark region for the past 120 kyrs, obtained from the calibrated ice sheet model (Section 3.1.4). The blue line shows the temperatures as obtained from the ice sheet model, comprising ground-level temperatures for ice free periods and basal ice temperatures for glaciated periods. A temperature curve constructed to show conditions without the presence of the ice sheet is shown by the red line. The uncertainty of the temperature curves is discussed in Section A1.5.*

In addition to the temperature curve containing ice covered periods, a temperature curve was calculated to show glacial cycle temperatures *without* the presence of an ice sheet. First, a calculation of the annual air temperature that would prevail at the ground-level if the ice sheet was not present was made for the glaciated periods. This was done by applying an atmospheric lapse rate temperature dependence to the ice sheet surface temperatures and ice surface elevation variations. The resulting ground-level air temperatures were subsequently combined with the ground-level air temperatures for ice-free periods resulting in a temperature evolution without ice sheet temperatures (Figure A1-2).

A1.3.2 Adjustment of Forsmark air temperature curves to include estimated Eemian, Mid-Weichselian and Holocene conditions

Eemian conditions

In the temperature reconstruction for the past 120 kyrs (Figure A1-2), the likely environmental conditions in the Forsmark region during interglacials and interstadials also need to be considered. Following the deglaciation of the large Saalian ice sheet (with a maximum ice configuration at around 140 kyrs BP), it is very likely that the Forsmark site was submerged by the Baltic Sea during a large part of the Eemian interglacial, much in the same way as following the Weichselian glaciation. The reconstructed temperature curve (Figure A1-2) was adjusted to reflect these submerged conditions. According to /Björck et al. 2000/, the Eemian interglacial period started at 127 kyrs BP and ended at 116 kyrs BP, resulting in an 11 kyrs long Eemian period. Other studies define the start of the Eemian at 133 and 130 kyrs BP. The length of the Eemian in the GRIP ice core is more than 15 kyrs, although with poor dating /Dansgaard et al. 1993/. It can be concluded that the length and timing, especially the starting time, of the Eemian period from geological data is uncertain. However, in order to make a locally defined Eemian period for the Forsmark site, the ending of the Eemian is selected to occur at the time of the first permafrost development in the SR-Site permafrost simulations, at 114 kyrs BP.

Based on the Saalian glaciation having been more severe than the Weichselian, and with a thicker ice sheet over e.g. Fennoscandia (Section 5.4), it was assumed that the Forsmark site was submerged for several thousands of years longer during the Eemian than in the Holocene. The uncertainty of how much longer the site may have been submerged is of course large. In accordance with this reasoning, the air temperature curve (Figure A1-2) was adjusted to show a mean water temperature of +4°C during the period –120 to –115,000 kyrs at Forsmark (Figure A1-3). The Eemian temperatures for the period following submerged conditions were kept the same as in Figure A1-2.

One result of including, the very likely, submerged conditions in the Forsmark region for the main part of the Eemian interglacial is that not much of the warm Eemian temperatures are seen in the resulting ground temperature curve (Figure A1-3). After 115 kyrs BP, there is a 1,000 year long period of warm Eemian terrestrial conditions before temperatures start to drop. It should be emphasized that this is a coarse reconstruction of Eemian conditions, both in terms of timing, length and prevailing conditions. Nevertheless it is very likely that this reconstruction provides a better estimate of Eemian conditions for the Forsmark region than simply applying the air temperature curve without submerged conditions (Figure A1-2). In addition, the assumption of a submerged temperature of +4°C for the major part of the Eemian constitutes a pessimistic assumption of thermal conditions for the permafrost simulations, see Section 3.4.4 and /Hartikainen et al. 2010/. Keeping a long period of very warm terrestrial conditions would have heated the bedrock prior to cooling and resulted in less permafrost than with the approach taken here.

In the 1D permafrost reconstructions of Weichselian permafrost conditions, see Section 3.4.4 and /SKB 2006a/, the correction for submerged conditions at Forsmark during the Eemian was not made, whereas the temperature curve adjusted for submerged Eemian conditions was used for the 2D permafrost reconstructions (/Hartikainen et al. 2010/ and Section 3.4.4).

Mid-Weichselian conditions

In the reference glacial cycle, ice sheet modelling (Section 3.1.4) resulted in ice-free conditions at Forsmark during Marine Isotope Stage 3, between c. 55 and 30 kyrs BP (Section 4.4). According to the results of the Glacial Isostatic Adjustment (GIA) model simulations (Section 3.3.4), the Forsmark region remained submerged beneath the Baltic Sea for the initial ~8 kyrs of this interstadial period (Section 4.4). Therefore, a submerged temperature of +4°C was set for the first part of this ice-free period of MIS 3 (Figure A1-3, blue curve).

Holocene conditions

The starting time for the Holocene period is here locally defined as the time of the Weichselian deglaciation of Forsmark, occurring at c. 8,800 BC (10,800 years ago) /Söderbäck 2008/. In line with the method above, the temperature curve has been adjusted to show a submerged temperature of +4°C from that time up to near-present conditions (Figure A1-3).

At present, the Forsmark site is located at the Baltic Sea shore. The past and future isostatic land uplift affects the site gradually, discussed in e.g. the section on transition between climate domains (Section 4.5.4). Detailed studies of how the land uplift is affecting the Forsmark site are presented in /SKB 2010d/. However, for the present temperature reconstruction it is sufficient to use the estimate that the repository site in Forsmark emerged from the sea ~1,000 years ago, and adjust the temperature curves accordingly (Figure A1-3).

A1.3.3 Ground surface temperatures

As mentioned in e.g. Section 3.4 and in Figure 4-10, the annual mean ground surface temperature is typically a few degrees warmer that the annual mean air temperature. Therefore, the air temperature curve in Figure A1-3 was used to calculate ground surface temperatures using the 1D permafrost model /SKB 2006a/ (Figure A1-4). This ground surface temperature has been used in the SR-Site studies of /Sundberg et al. 2009/ and /Vidstrand et al. 2010/. For details on how the ground surface temperature was derived, see /SKB 2006a/.

In the 2D permafrost simulations made for SR-Site (see /Hartikainen et al. 2010/ and Sections 3.4.4 and 5.5.3), ground surface temperatures were constructed from the same air temperature curve but in a more detailed way accounting for e.g. dry/wet climate conditions and various surface cover types, see /Hartikainen et al. 2010/. An example of the resulting ground surface temperatures is seen in Figure A1-5. These ground surface temperatures were used to simulate the 2D permafrost development described in Section 3.4.4 and 5.5.

The more simplified ground surface temperature reconstruction (Figure A1-4) typically lies within the range of ground surface temperatures reconstructed in a more detailed way (Figure A1-5).

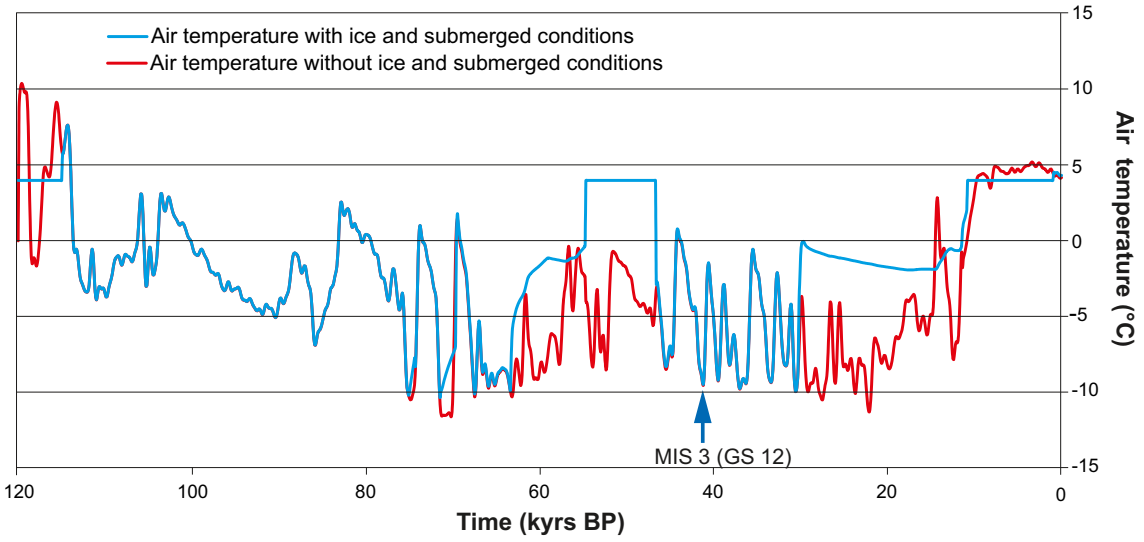

Figure A1-3. *Reconstructed air temperature curve for the Forsmark region for the past 120 kyrs, including estimated submerged periods of the Eemian, Mid-Weichselian and Holocene (blue line). The red line shows last glacial cycle air temperatures without the presence of an ice sheet and submerged periods. The temperature scale shows absolute temperatures. The curves have been used as input to e.g. the 1D and 2D permafrost simulations /SKB 2006a, Hartikainen et al. 2010/, see Section 3.4.4 and5.5. The uncertainties of the temperature curves are discussed in the present appendix, Section A1.5, and the implications for modelled permafrost depths in Section 3.4.4 (sensitivity studies made with the 2D model).*

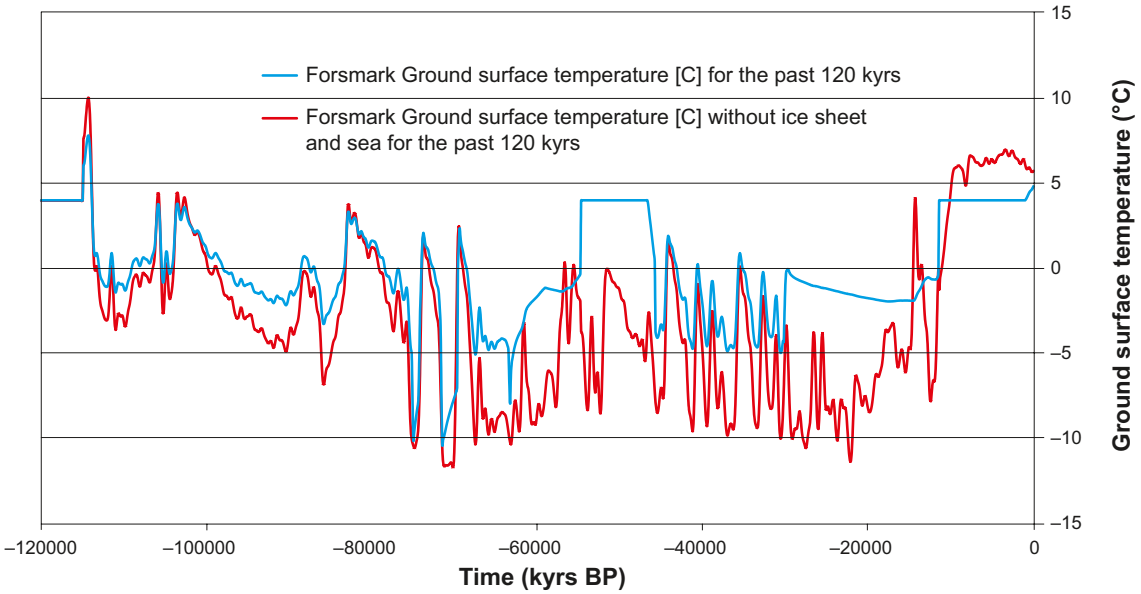

Figure A1-4. *Ground surface temperature for Forsmark for the past 120 kyrs with ice sheet (blue) and without ice sheet and sea (red) reconstructed with the 1D permafrost model /SKB 2006a/. The ground surface temperature data has been used as input to /Sundberg et al. 2009/ and /Vidstrand et al. 2010/. The temperature scale shows absolute temperatures. The uncertainty of the temperature curves is discussed in Section A1.5.*

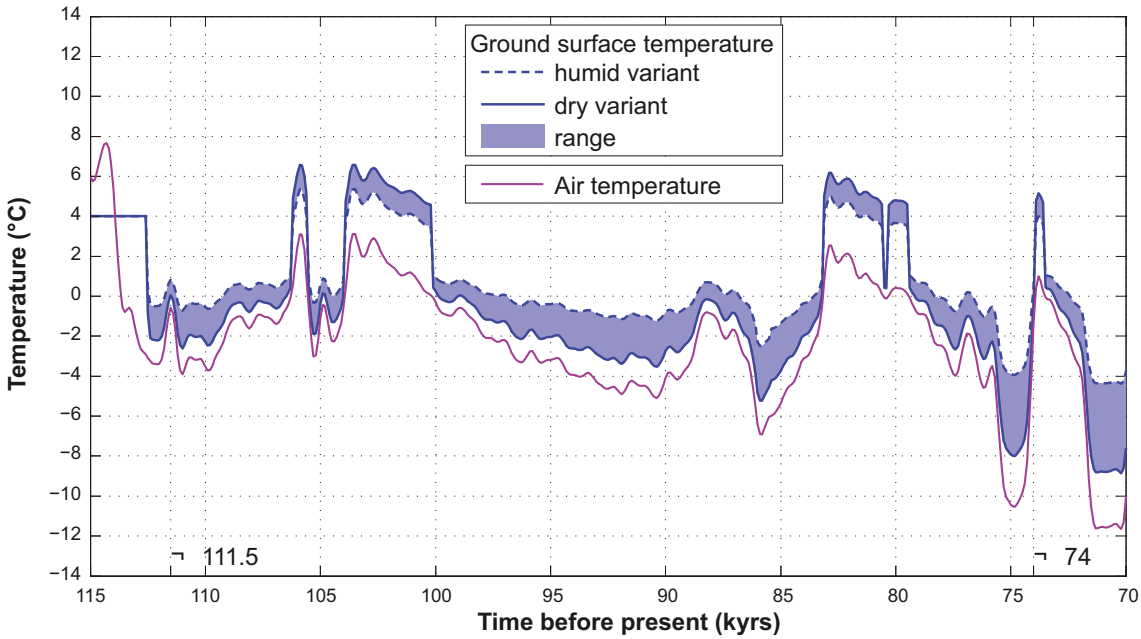

Figure A1-5. *Examples of reconstructed ground surface temperatures for Forsmark for the first part of the last glacial cycle (see Section 3.4.4 and /Hartikainen et al. 2010/). The ground surface temperatures cover a range of dry/humid climate conditions, see /Hartikainen et al. 2010/. The example is for one part of the 15 km long investigated profile, with fresh-moist surface conditions just above the repository location (~4,800 m from the south-west side of the profile in Figure 3-58).*

A1.4 Temperature conditions during the Holocene and reference glacial cycle

A1.4.1 The ending and duration of the Holocene interglacial in the reference glacial cycle

In the *reference glacial cycle* (Section 4.5), reconstructed last glacial cycle conditions (Section 4.4) are assumed to be repeated during the coming 120 kyrs. To this end, the present day is selected to correspond to 120 kyrs BP in the reconstructed last glacial cycle. This, together with the local definition of the ending of the Holocene (defined as the time of the first occurrence of permafrost at the Forsmark repository location, see Section 4.5.4), results in a total duration of the Holocene period of ~18 kyrs (Table 4-5). This duration is in line with the longer of the two types of interglacials, with durations roughly of either ~20 kyrs or ~10 kyrs, that have occurred during the past eight glacial cycles /Tzedakis et al. 2009/.

This way of defining the ending and duration of the Holocene interglacial is a simple way of treating a complicated subject. For instance, the *reference glacial cycle* described here should be seen as a climate development dominated by natural climate change, i.e. without anthropogenic warming. As mentioned in Section 4.5.4, the uncertainties in the *actual* length of the present interglacial period are naturally very large. Given this uncertainty, it is again emphasized that the evolution of climate domains as described in the *reference glacial cycle* (Figures 4-33, 4-34, 4-35) is not an *expected* future climate evolution. It is one relevant example of an evolution covering the climate-related conditions that can be met in a 100 kyr time perspective. Other possibilities for the length of the present interglacial period are handled in the additional climate cases, such as the *global warming case* (Section 5.1) and *extended global warming case* (Section 5.2).

Looking at Fennoscandia as a whole, glacial and permafrost conditions at other places would come and go at other times, which would result in shorter or longer locally defined interglacial periods if the same approach were to be applied. This way of using locally defined times for start and end of the interglacial results in that the Holocene in northern Sweden being many thousand years shorter in duration than in southern Sweden. From the safety assessment point of view, this is a proper approach to defining interglacial periods, since it is specifically the local conditions, such as the disappearance of an ice sheet or development of permafrost, that are of importance for other relevant processes such as e.g. groundwater flow and chemistry, biosphere conditions, and thermo- mechanical conditions in the bedrock.

As mentioned above, the *reference glacial cycle* assumes that the reconstructed development of ice sheets, permafrost and shore-level are repeated during the coming 120 kyrs. Given this and the treatment of the onset of the last glacial cycle conditions described above, there is no need to explicitly repeat also the temperature curves reconstructed for the last glacial cycle into the future. This is also motivated by the fact that the temperatures at the ground surface, as such, are not of importance for repository safety. The temperature curves reconstructed for the last glacial cycle formed the basis for the reconstruction of last glacial cycle ice sheet and permafrost development, and therefore also the basis for the corresponding development during the future *reference glacial cycle*. Therefore, the temperature curves of Figure A1-3 and A1-4 do not need to be repeated for the future *reference glacial cycle*.

In this context it is important to notice that the uncertainties estimated for the temperature curve reconstructed for the last glacial cycle (Figure A1-3), discussed in Section A1.5, are dealt with: i) in dedicated sensitivity tests in the permafrost simulations (Section 3.4.4), and ii) in a indirect way by e.g. the complementary climate case dealing with larger future ice sheets than those reconstructed for the last glacial cycle.

A1.4.2 Holocene temperatures

From extrapolations of measured temperature bore hole loggings in Forsmark, the present-day ground surface temperature is estimated as +6.5°C /Sundberg et al. 2009/. This value lies between the present ground surface temperatures suggested by the 2D permafrost modelling, which yields a value of +6.1°C for the evolution with dry climate, and +7.4°C for the evolution humid climate variant /Hartikainen et al. 2010/. A future Holocene ground surface temperature of around +6.5°C could therefore be envisaged for the remaining part of the Holocene. This estimate of *reference glacial cycle* conditions (which is completely dominated by natural climate change, see Section 1.2.3 and 4.5) thus excludes the anthropogenic contribution to the ~0.7 degrees of climate warming that has taken place during the last 100 years /IPCC 2007/. For the climate cases with global warming, air- and ground surface temperatures are considerably higher than in the *reference glacial cycle*, see Sections 5.1 and 5.2.

As mentioned above, in the adopted approach to repeating last glacial cycle reconstructions of ice sheet, permafrost and shore-level development for the coming 120 kyrs, there is no need to explicitly repeat also the air temperature curve used for these reconstructions. If such a projection were to be made, it would be very similar to the curve seen in Figure A1-3 (blue line), with the exception that initial temperatures would not reflect submerged conditions (as the initial conditions in the last glacial cycle reconstruction). Submerged temperature conditions would however prevail later on in the development (as in Figure A1-3 blue line).

A1.5 Estimates of uncertainties in the reconstructed temperature curve

There are a number of different uncertainties and assumptions that contribute to the overall uncertainty in the air temperature curve reconstructed for the Forsmark region for the last glacial cycle (Figure A1-3): i) uncertainties in the calculations of air temperatures from $\delta^{18}O$ vales in the GRIP ice core, ii) temporal uncertainties in the time scales used for the ice core data, iii) the representativity of GRIP ice core data for Fennoscandian conditions.

A1.5.1 Uncertainties in the GRIP temperature curve

Uncertainties in calculated Greenland temperatures

The isostopic record used for the calculation of GRIP temperatures (Figure A1-1, red line) is the one used in /Johnsen et al. 1995/. For the transformation of $\delta^{18}O$ values to air temperatures, /Johnsen et al. 1995/ used the relationship:

$$T = 1.5\ (\delta^{18}O + 35.27) \qquad \text{Equation A1-1}$$

where T is the temperature deviation from year 1989, and $\delta^{18}O$ is the oxygen isotope value recorded in the ice core. Equation A1-1 represents a *present day* $\delta^{18}O$-T relationship averaged for the last 50 years up to 1989, and assuming that the temperature over these 50 years is the same as in 1989 /Johnsen et al. 1995/. As previously mentioned, it has been shown that the present day $\delta^{18}O$ – T relationship is less suitable for glacial conditions, and that this relationship also changes between stadials and interstadials /Huber et al. 2006/. Changes in the $\delta^{18}O$ – T relationship over time are caused by several factors such as changes in the source of precipitation /Masson-Delmotte et al. 2005/, changes in the distribution of precipitation on the ice sheet /Werner et al. 2001/, and by seasonal variations in temperature and precipitation /Krinner et al. 1997/. This introduces errors in the temperature curve when produced according to /Johnsen et al. 1995/.

Results of /Huber et al. 2006/ show that the $\delta^{18}O$ – T relationships during last glacial cycle interstadials are closer to the present-day relationship, used by /Johnsen et al. 1995/, than is the $\delta^{18}O$ – T relationship during last glacial cycle stadials. It is therefore expected that stadial temperatures in the /Johnsen et al. 1995/ temperature curve (Figure A1-1, red line) contain a larger error than the warmer interstadial temperatures. The uncertainty in the temperature estimates for Marine Isotope Stage 3 (MIS 3) by /Huber et al. 2006/ is minimum c. 3 degrees and maximum c. 6 degrees. From $\delta^{15}N$ measurements a symmetric uncertainty of ±3°C would be applicable for these periods /Huber et al. 2006/.

For a comparison with the temperatures reconstructed for the NGRIP ice core /Huber et al. 2006/, $\delta^{18}O$ values from the NGRIP ice core /NorthGRIP community members 2004/ were transformed to tentative temperatures using the same transfer function (Equation A1-1) as used in the production of the GRIP temperature curve. The resulting curve is seen in Figure A1-6 (green line), together with the original GRIP curve and the temperature curve modified in the ice sheet model calibration process (Section A1.2 and Figure A1-1). It is important to note that the temperatures calculated from the NorthGRIP data within the present study are not to be taken as solid scientific results. They are included only to make the first-order analysis of the errors introduced by using the present day $\delta^{18}O$ – temperature relationship for the GRIP data.

Table A1-1 summarizes the temperature amplitudes of individual Dansgaard-Oeschger (DO) events during MIS 3 from /Huber et al. 2006/ together with corresponding temperature amplitudes from using the present day $\delta^{18}O$ – T relationship of /Johnsen et al. 1995/ on the NGRIP $\delta^{18}O$ data (Figure A1-6, green line). The results show that, during the MIS 3 DO events studied by /Huber el al. 2006/, the temperature lowering is underestimated by between c. 20 and 40% or c. 2–4°C (Table A1-1) when using the present-day $\delta^{18}O$ – T relationship in the reconstruction of GRIP ice core Greenland temperatures (Figure A1-1, red line).

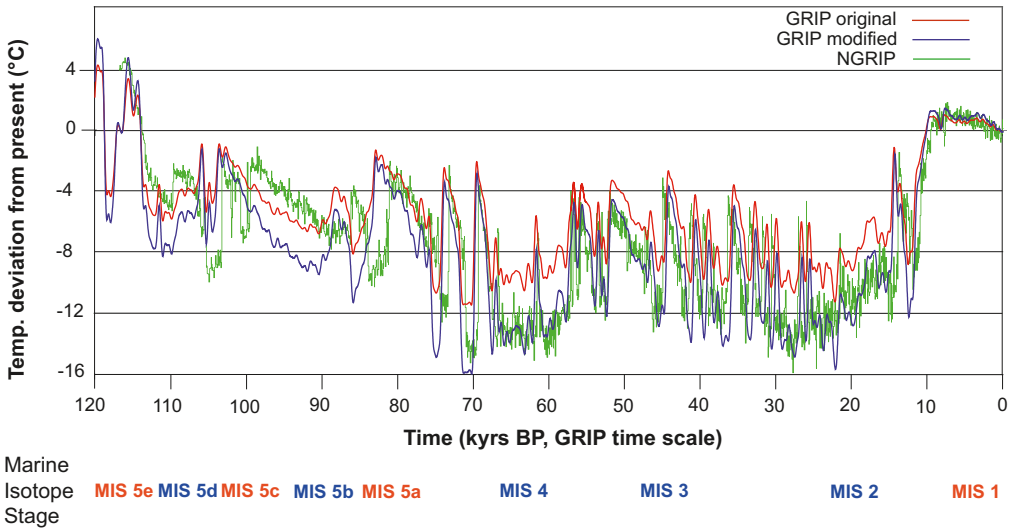

Figure A1-6. *Palaeotemperature curve from the GRIP ice core /Johnsen et al. 1995/ (red) and modified GRIP temperature curve resulting from the ice sheet model calibration (blue). For comparison, a tentative temperature record from the NGRIP ice core /NorthGRIP community members 2004/ is shown in green, see the text. The NGRIP temperature curve was constructed within the present study. Note that the time scale only applies for the GRIP data. The NGRIP data is not plotted on the same time scale, which contributes to a temporal mismatch between GRIP and NGRIP results in the plot. However, the tentative NGRIP curve is here included only for general comparison of temperature amplitudes between the two ice cores.*

This means that the temperature curve used for the ice sheet model calibration (Figure A1-1, red line) probably underestimates Greenland air temperatures during cold stadial periods by c. 2–4°C due to the use of the present day $\delta^{18}O$ – T relationship. This uncertainty needs to be considered in the overall estimate of uncertainty in the temperature curve reconstructed for Forsmark for the last glacial cycle (Figure A1-3), see below. Given the result by /Huber et al. 2006/, using the present day $\delta^{18}O$ – T relationship for warmer interstadial periods most probably introduces a considerably smaller error.

An additional error is introduced by the treatment of the air temperatures from the GRIP ice core as annual mean air temperatures when they in fact are affected by a seasonality signal /Krinner et al. 1997/.

Table A1-1. Difference in temperature amplitude for Dansgaard-Oeschger (DO) events during MIS 3 between the NGRIP curve as described by /Huber et al. 2006/ and if applying the simple present-day $\delta^{18}O$-Temperature relationship used for the GRIP data. The results indicate that the GRIP data (Figure A1-1 and A1-6) may underestimate the temperature amplitude associated with DO-events by up to 3–4 degrees. However, this also assumes that the climate signal in the NGRIP and GRIP temperature curves are the same.

Dansgaard-Oeschger event	Mean ΔT (°C) from NGRIP data /Huber et al. 2006/	ΔT if applying simple GRIP $\delta^{18}O$-T relationship on NGRIP $\delta^{18}O$ data	Difference (°C and percent)
9	9	7	2 (–22%)
10	11.5	8	3.5 (–30%)
12	12.5	9.5	3 (–24%)
14	12.5	8	4 (–32%)
15	10	6	4 (–40%)
16	9	5	4 (–44%)
17	12	8	4 (–33%)

It is also worth noting that the modified GRIP temperature curve (from the ice sheet model calibration process) (Figure A1-6, blue line) specifically has resulted in that temperatures during stadial are colder than in the original GRIP curve, whereas warm interstadial temperatures are similar. This shows that the ice sheet model calibration process has reduced the error introduced from using the present day $\delta^{18}O$ – T relationship for the original GRIP temperature curve.

Temporal uncertainties in the ice core data

In the Greenland ice cores, such as GRIP, NGRIP, GISP2 etc, temporal uncertainties exist in the timing of individual climatic events. From the beginning, different ice cores were dated by different methods, which yielded inherited differences in the resulting time-scales. The actual climate information also differs between the cores, which contributes to the difficulties in matching them against each other.

The most commonly used ice core time scales are the Meese-Sowers GISP2 stratigraphic time scale /Meese et al. 1997/ and the modelled "ss09sea" time scale that was applied to the GRIP and NGRIP ice cores /Johnsen et al. 2001/. The glacial section of the GRIP core (Figure A1-1) was dated by employing an ice flow model with an empirical $\delta^{18}O$-accumulation relationship and two dated fix-points /Dansgaard et al. 1993, Johnsen et al. 1995/. This resulted in the improved ss09sea time scale /Johnsen et al. 2001/. According to /Svensson et al. 2008/, these time scales agree within 750 years back to 40 kyrs, but further back in time the disagreement becomes several thousands of years. Further adjustments of the time scales used for ice core data are also made, e.g. /Skinner 2008, Svensson et al. 2008/.

There are still significant temporal uncertainties related to the Greenland ice cores, e.g. /Rasmussen et al. 2006 and 2008, Skinner 2008, Svensson et al. 2008/. For example, /Skinner 2008/ showed that the NGRIP age scale probably is missing up to 1,200 years for the last glaciation period. Any reconstruction of last glacial cycle conditions that are based on these ice core data also includes these uncertainties. However, in the safety assessment work, the *exact* temporal development of temperature during the last glacial cycle, and more specifically the exact temporal development of other processes that are dependent on the temperature such as ice sheets and permafrost, is of minor importance for repository safety (Section 1.2.3). Furthermore, the reconstructed last glacial cycle conditions (including their temporal uncertainties) are used to construct a future *reference glacial cycle*, which in turn is complemented by other possible future climate developments in which e.g. permafrost and ice sheets may develop at other times than in the *reference glacial cycle*.

A1.5.2 Uncertainties in the reconstructed Forsmark region temperature curve – comparison with other data on Fennoscandian palaeotemperatures

As previously mentioned, the modified GRIP temperature curve (Figure A1-1, blue line) was subsequently used to extract a temperature curve for the Forsmark region (Figure A1-2 and A1-3). Other independent proxy data and model data on Fennoscandian temperatures during the last glacial cycle may be used for a first-order check of the validity of this reconstructed Forsmark region temperature curve (Figure A1-3). In such comparisons, it is important to remember that both climate proxy data and modelled climate data may contain significant uncertainties, e.g. /Kjellström et al. 2010b/. The temperature curve reconstructed for Forsmark is compared with other palaeoclimate data for the MIS 5d stadial, the MIS 5c interstadial, the early MIS 3 interstadial, and the middle MIS 3 stadial, see Section 4.2 and 4.3.

The palaeoclimate data from the Sokli site in northern Fennoscandia e.g. /Helmens 2009a, Väliranta et al. 2009, Engels et al. 2010/, used in the comparisons, consists of reconstructed summer (July) air temperatures, whereas the temperature curve reconstructed for the Forsmark region (Figure A1-3) reflects annual mean air temperatures. Therefore, the comparison between the two regions does not make use of absolute temperatures, but instead the *temperature difference* to present climate conditions in each region for each period. With this approach, potential differences between the sites in terms of the amount of change in seasonal temperature cycle between present conditions and the past is neglected. However, it is considered that this is of minor importance and that the comparisons still contribute with important information.

Early Weichselian (MIS 5d stadial)

During ice-free stadial conditions of MIS 5d (the Herning stadial 117–105 kyrs BP), July summer temperatures of +7°C were reconstructed for the Sokli site in northern Finland, see Section 4.3.1 and /Engels et al. 2010/. This is c. 6°C colder than the present summer mean temperature of +13°C.

The reconstructed air temperature curve for the Forsmark region indicate MIS 5d annual mean air temperatures from c. –1°C down to c. –4°C (Figure A1-3), i.e. around 6 down to 9°C colder than at present.

Early Weichselian (MIS 5c interstadial)

During MIS 5c (the Brørup interstadial, 105–93 kyrs BP), summer temperatures inferred from plant macrofossil remnants indicate warm conditions in northern Fennoscandia. Reconstructed July temperatures for this period are as high as +16°C, which is 3°C warmer than at present /Väliranta et al. 2009, Engels et al. 2010/. Other (lower-resolution) MIS 5c reconstructions from northern Fennoscandia indicate summer temperatures 6–7°C lower than present, see /Engels et al. 2010/. However, several central European sites indicate that there was a phase during the MIS 5d interstadial that was characterized by high summer temperatures, see /Engels et al. 2010/.

The reconstructed annual air temperature for the Forsmark region during the MIS 5c interstadial (105–93 kyrs BP) is from c. +2°C down to c. –4°C (Figure A1-3), i.e. between 3 and 9°C lower than at present.

Middle Weichselian (early MIS 3 interstadial)

Mean July air temperatures for early MIS 3 (at ~50 kyrs BP) in northern Fennoscandia, inferred from fossil chironomides, are 12–13 ± 1.15°C /Helmens 2009a/. This corresponds to the present-day summer temperature (13°C) in the region. Mean July air temperatures inferred from terrestrial pollen data from the same site lie within the range of 11–12 ±1.5°C /Helmens 2009a/. The reconstructed high summer temperatures are in part ascribed to enhanced July insolation compared with present at the high latitude site of the site. Warm early MIS 3 temperatures are in line with the ice-free conditions in northern Fennoscandia and elsewhere (Section 4.2 and 4.3.2).

In the reconstructed annual air temperature curve (Figure A1-3), the Forsmark region is submerged under the Baltic Sea during early MIS 3 (at ~50 kyrs BP). However, the values for non-submerged conditions amount to around –1 to –4°C, which is between c. 6 and 9°C lower than at present.

Middle Weichselian (middle MIS 3 stadial)

Simulated temperatures for the MIS 3 (Greenland Stadial 12) period (44 kyrs BP), see Section 4.3.2 and /Kjellström et al. 2009b/, suggest that the annual mean air temperature in the Forsmark region was –7.6°C during this cold stadial. This is c. 12.5°C colder than the present annual mean air temperature.

The reconstructed last glacial cycle air temperature curve for Forsmark suggests that the annual air temperature during the same stadial was c. −9°C (Figure A1-3, blue arrow), or c. 14°C colder than at present.

Discussion

In this comparison, it should be emphasized that all data on palaeotemperatures, from proxy data and from climate modelling, including the temperature curve reconstructed for the Forsmark region, contain uncertainties. Nevertheless, a comparison between the temperature reconstructions contributes with an overall picture of how the reconstructed curve for the Forsmark region (Figure A1-3) relates to other independent estimates of palaeotemperatures.

Table A1-2 summarizes the estimated approximate temperature difference between present day conditions and the conditions during the four last glacial cycle stadials and interstadials as described above.

Table A1-2. Estimated approximate temperature difference between present day conditions and conditions during four last glacial cycle stadials and interstadials as reflected in the reconstructed temperature curve for the Forsmark region (Figure A1-3) and in other palaeoclimate proxy- and model data (see the text). It should be noted that many of the reconstructed palaeotemperatures should be regarded with caution, such as the MIS 5d value for Northern Fennoscandia /Engels et al. 2010/.

	Approximate ΔT MIS 5d stadial – present	Approximate ΔT MIS 5c interstadial – present	Approximate ΔT Early MIS 3 interstadial – present	Approximate ΔT Middle MIS 3 stadial – present
Northern Fennoscandia (Sokli region)	6°C colder	3°C warmer	0–2°C colder	–
Other Fennoscandian MIS 5c sites	–	6–7°C colder	–	–
South-central Sweden from modelling (Forsmark region)	–	–	–	12.5°C colder
South-central Sweden from temp curve (Forsmark region)	6–9°C colder	3–9°C colder	6–9°C colder	c. 14°C colder

The only comparison above which uses the same geographical region, as well as estimates of absolute numbers on annual mean air temperature in both reconstructions, is the one for the middle MIS 3 stadial, where climate model results from the Forsmark region are compared with the reconstructed Forsmark region air temperature curve (Figure A1-3). This comparison shows that, for this cold stadial period 44 kyrs ago, the reconstructed temperature curve gives a ~1.5°C lower temperature than the climate model simulation (Table A1-2), and thus that these two independent temperature estimates of temperature in the Forsmark region are well in line with each other. This suggests that, although the temperature curve for Forsmark was constructed in a crude way, the resulting Middle Weichselian stadial temperatures in the Forsmark region curve may well be realistic.

For the Early Weichselian MIS 5d stadial and MIS 5c interstadial, values from the reconstructed Forsmark temperature curve indicates a similar, or some degrees larger, lowering of temperature than the other proxy data (Table A1-2).

For the early MIS 3 interstadial (at ~50 kyrs BP), proxy data e.g. /Helmens 2009a/ suggests present-day summer temperature conditions in northern Fennoscandia. When such warm interstadial conditions prevail in northern Fennoscandia, similar near-present temperature conditions would be expected also in south-central Sweden, given that the region is free of ice such as in the *reference glacial cycle*. However, for early MIS 3, the temperature in the reconstructed curve (Figure A1-3) is c. 6–9°C colder than at present, i.e. far from present-day temperatures. This might be due to several reasons, i) similar near-present temperatures did occur also in south-central Sweden (including the Forsmark region), but the warm conditions over Fennoscandia did not have a corresponding rise in temperature over Greenland, and are thus not found in the ice core record, ii) the climate in south-central Sweden was significantly colder than in northern Fennoscandia during this period, iii) one (or both) of the reconstructions may have a large error in reconstructed temperatures for this period (the temperature estimate by /Helmens 2009a/ has an uncertainty of only ±1.5°C, which in this case would indicate that the temperature reconstruction for the Forsmark region has temperatures that are much too low for this period), or iv) a combination of the above reasons.

The resulting overall picture from the comparisons is that the reconstructed temperature curve (Figure A1-3) is in agreement with or gives somewhat lower temperatures (by some degrees) than the other reconstructions. The comparison thus suggests that the reconstructed temperature curve for Forsmark probably does not overestimate the temperatures during the investigated last glacial cycle stadials and interstadials.

A1.5.3 Estimated temperature uncertainty and treatment of this uncertainty in SR-Site

The modified GRIP temperature curve (after ice sheet model calibration) (Figure A1-1) has reduced uncertainties present in the original GRIP curve, but there still remains a significant uncertainty of several degrees in this curve (Table A1-1). When this curve was used to construct the temperature

curve for the Forsmark region (Figure A1-3), it is, as expected, obvious that also the reconstructed Forsmark temperature curve has significant uncertainties. The comparison with proxy data seems, however, to indicate that the reconstructed Forsmark temperature curve is in broad agreement with the (few available) proxy data and furthermore that it does not overestimate temperatures for the compared last glacial cycle stadials and interstadials. The general picture from the comparison with Fennoscandian proxy data is that the reconstructed temperature curve gives roughly correct or slightly too low temperatures by a few degrees.

Based on how the air temperature curve has been constructed, on the comparison against Fennoscandian last glacial cycle stadial and interstadial proxy data, and on remaining uncertainties associated with the temperature curve that have not been quantified above, it is here pessimistically estimated that the uncertainty in the reconstructed Forsmark region temperature curve (Figure A1-3) is not larger than 6°C for the periods with largest uncertainties. Furthermore, an uncertainty of up to c. 4–5°C is estimated for the major part of the curve, and for some parts of the curve, such as for the Holocene and the Eemian, smaller than 4°C.

In SR-Site, the uncertainties in the reconstructed temperature curve for the Forsmark region mainly affect the permafrost modelling, see /Hartikainen et al. 2010/ and Section 3.4.4 and 5.5.3 and /Vidstrand et al. 2010/. In the permafrost simulations performed for Forsmark, see /Hartikainen et al. 2010/, Section 3.4.4 and 5.5.3, the uncertainties in the air temperature curve are covered by a range of sensitivity tests specifically on the air temperature curve and on surface conditions (for the calculation of ground surface temperatures). In some of the sensitivity tests, the entire air temperature curve reconstructed for the last glacial cycle (Figure A1-3) was lowered (and raised) by 6°C, in accordance with the estimated maximum uncertainty. This was also done in combination with uncertainties in other parameters of importance for the development of permafrost, see /Hartikainen et al. 2010/ and Section 3.4.4. Other sensitivity tests on the air temperature curve for permafrost simulations covered a temperature range significantly wider than the estimated uncertainty described in this section, up to a 16°C lowering of the air temperature curve in Figure A1-3, see /Hartikainen et al. 2010/ and Section 3.4.4.

Uncertainties in the original GRIP temperature curve have a direct effect only on the ice sheet modelling (Section 3.1.4), but the uncertainty is here to a large extent taken care of by the ice sheet modelling process (in which the ice sheet configurations during stadials periods, when the error is largest, were calibrated against known ice-marginal positions).

The *temporal* uncertainty in the reconstructed temperature curve, discussed above, is covered by the additional climate cases (Chapter 5), where e.g. permafrost might develop earlier than in the *reference glacial cycle* (based on the Weichselian reconstruction that includes the reconstructed temperature curve).

Appendix 2

Ice sheet profiles

A2.1 Background

In various SR-Site studies, e.g. on groundwater flow and THM processes, ice sheet profiles are useful as input for investigating how these processes are affected by glacial conditions. This section gives background and data for selection of two ice surface profiles to be used in the SR-Site safety assessment. Two different types of ice sheet profiles are discussed; ice profiles derived mainly from theoretical considerations, and ice profiles derived from more complex numerical ice sheet modelling.

The steepness of an ice sheet surface is determined by the combination and interplay of several factors such as basal shear stresses, englacial ice temperatures, temperatures at the ice sheet bed, the basal hydrological conditions and the presence or absence of deformable sediments at the bed. As a general rule of thumb, a retreating ice sheet has a less steep profile than an advancing ice sheet, and so does an ice sheet ending in the sea compared with a terrestrial ice sheet. Warm basal conditions, with presence of basal water, and presence of deformable bed sediments also results in less steep ice than cold-based conditions. The steepness of the ice sheet surface is important for the ice flow and for the water routing and water flow at the base of the ice. In addition, it is also of high importance for e.g. the flow of groundwater in the bedrock and for the stress situation in the Earth's crust.

A2.2 Theoretical ice sheet profiles

The easiest way of describing an ice sheet profile is by assuming that ice is a perfectly-plastic material. One can further assume that this ice sheet is circular and situated on a flat and horizontal bed, and that the ice sheet is in steady-state, i.e. that no change in ice configuration occurs over time. In this case the ice sheet surface profile constitutes a simple parabola e.g. /Paterson 1994/, and is calculated by:

$$h^2 = \frac{2\tau_0}{\rho g}(L - x) \qquad \text{Equation A2-1}$$

where h is the ice thickness at distance x from the centre, L is the radius of the ice sheet, τ_0 is the basal shear stress, ρ is the ice density and g is the acceleration of gravity. With L = 400 km, ρ = 0.9 kg/dm^3, g = 9.81 m/s^2 and τ_0 set to 50 and 100 kPa, the resulting parabolas are seen in Figure A2-1. A basal shear stress of 100 kPa is more valid for small valley glaciers while 50 kPa (with large variation) is more representative for ice sheet conditions.

In order to have a more realistic description, Equation A2-2 introduces a flow of the ice /Paterson 1994/. The same assumptions are made as above, except for a removal of the perfect-plasticity assumption, and the introduction of an assumption of basal frozen conditions.

$$(h/H)^{2+2/n} + (x/L)^{1+1/n} = 1 \qquad \text{Equation A2-2}$$

Here H is the ice thickness at the centre of the ice sheet and n is a flow parameter (the strain-rate exponent) in Glen's flow law of ice, often set to 3, e.g. /Paterson 1994/. The resulting profile when L is set to 400 km and 900 km, H = 3,000 m and n=3 is seen also in Figure A2-1.

Equation A2-2 results in a steeper profile (for the corresponding profile length) than the parabolas described by Equation A2-1, and presumably it is more in line with real ice sheet profiles /Paterson 1994/. For the further use of theoretical ice profiles, the steeper theoretical profiles of Equation A2-2 are chosen. Furthermore, steeper profiles also give larger impacts in studies of groundwater flow and crustal stresses under glacial conditions, and thus is a more pessimistic choice from the safety assessment point of view.

The theoretical profiles (Equation A2-1 and A2-2) are compared with an ice sheet profile from the western part of the Greenland ice sheet in Figure A2-2, see also /Jaquet et al. 2010/. Note that in this figure the ice sheet surface topography for the theoretical profiles is reflecting the full relief of the bed topography, which is not the case in the real world. The less steep theoretical profile is similar to the Greenland profile, whereas the steeper theoretical profile is steeper than the Greenland ice sheet profile.

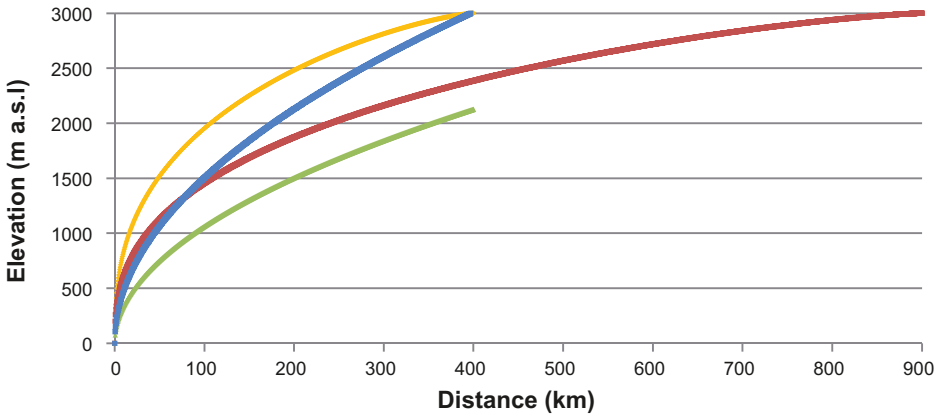

Figure A2-1. *Theoretical steady-state ice sheet profiles according to /Paterson 1994/. Parabolas produced by Equation A2-1 are shown in green (400 km long profile with a basal shear stress of 50 kPa) and blue (400 km long profile with a basal shear stress of 100 kPa). The steeper profiles produced by Equation A2-2 are shown in yellow (400 km long profile) and red (900 km long profile). The latter two profiles are considered to be more realistic representations of steady-state ice sheet profiles /Paterson 1994/.*

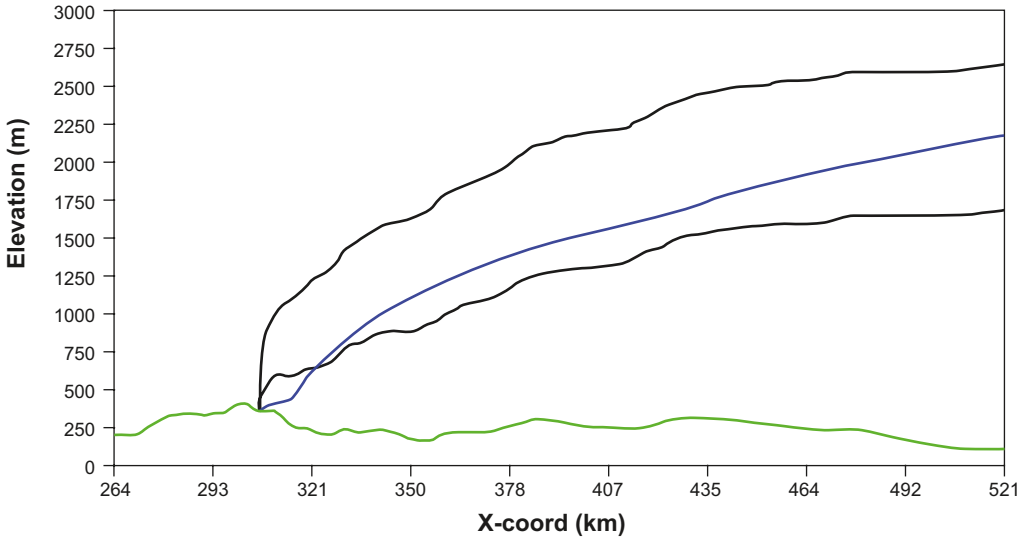

Figure A2-2. *Comparison between the theoretical ice profiles (Equation A2-1 with τ_0 set to 50 kPa upper black line and Equation A2-2 lower black line) with an ice sheet profile from the Greenland ice sheet (blue). The bed is shown in green. The theoretical profiles are, unrealistically, displayed as reflecting the full relief of the bed topography, which has resulted in too much relief in the ice surface. From /Jaquet et al. 2010/.*

A2.3 Ice profiles from numerical ice sheet simulations

For SR-Site, ice profiles were extracted from the time-transient reconstruction of the Weichselian ice sheet simulated by the University of Maine Ice Sheet Model (UMISM), see Section 3.1.4. In the following text, this model simulation is denoted the *reference glacial cycle ice sheet simulation*. The location of the transect from which the profiles were extracted is seen in Figure A2-3. Several ice sheet profiles from the last stadial of the reconstructed Weichselian ice sheet (e.g. from MIS 2 that included the Last Glacial Maximum (see Section 4.2), are seen in Figure A2-4. Figure A2-4a shows profiles from the advancing phase and Figure A2-4b from the retreating phase of the simulated MIS 2 ice sheet.

In the Weichselian ice sheet simulation, the ice sheet advances over the Forsmark region from NW-NNW while during the deglaciation it generally retreats in a more northerly direction. All profiles in Figure A2-4 were extracted along transect 1 (Figure A2-3). The orientation of transect 1 was selected in order to capture the steepest surface gradients during ice advance (i.e. generally oriented

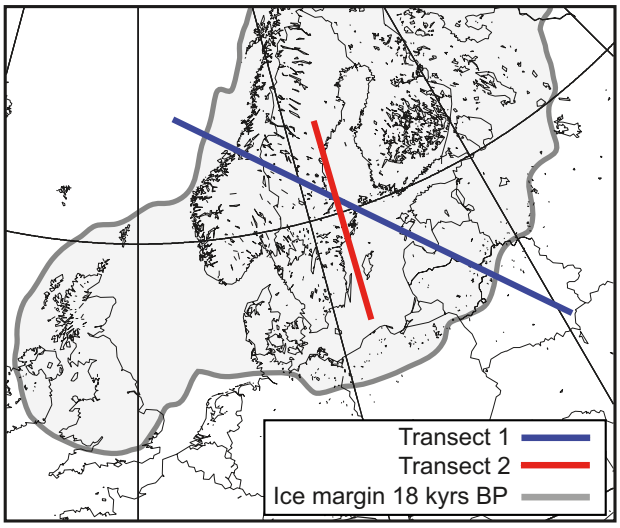

Figure A2-3. *Locations of ice sheet profiles. Transect 1: transect for all profiles seen in Figure A2-4 a and b. Transect 2: location of retreat profile extracted for 14.3 kyrs BP seen in Figure A2-7.*

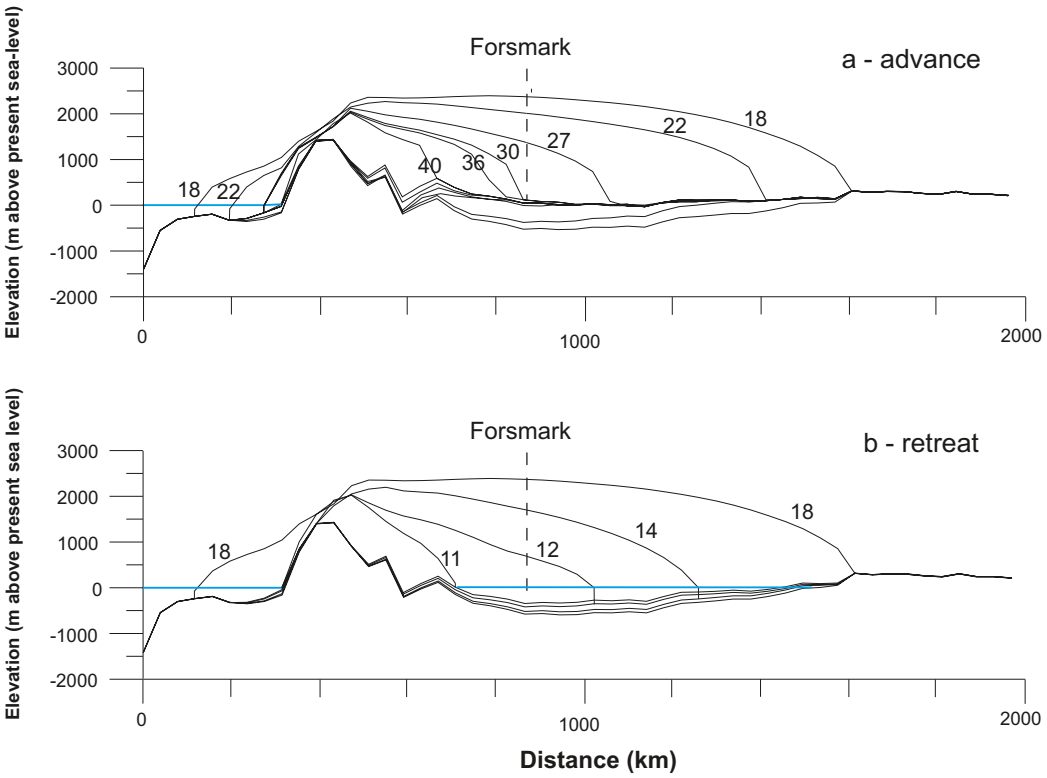

Figure A2-4. *Examples of ice sheet profiles from the Weichselian ice sheet simulation during the MIS 2 advance and retreat. Profiles are extracted from transect 1 (Figure A2-3). Numbers indicate time (kyrs BP). It should be noted that the y-scale has a vertical exaggeration of 100x and that sea-level change associated with ice sheet growth is not shown. In the frontal-most part of the profile, the 10 km spatial resolution of the ice sheet model can be seen as a sharp knick in the ice surface. Present-day sea-level is shown in blue. The LGM sheet configuration, along this specific profile, occurs at around 18 kyrs BP.*

along the flow lines of the advancing ice, perpendicular to the advancing ice margin). Consequently, profiles extracted along the same transect but for the retreat phase, which occurred in a somewhat other direction, are somewhat underestimating the steepness of the ice sheet surface.

In addition to the profiles selected along transect 1 (Figure A2-3), a c. 900 km long retreat profile was selected along transect 2. This profile was extracted for the time 14,300 kyrs BP. All profiles selected from the ice sheet advance phase are discussed in Section A2.4.1, while all profiles from the retreat phase are discussed in Section A2.4.3.

Ice surface gradients

Figure A2-5 shows the ice surface gradients that occur above the Forsmark site in the *reference glacial cycle* ice sheet model run. There are two phases of ice sheet coverage in this model simulation, during MIS 4 and MIS 2, and hence two periods with gradients in Figure A2-5. Steep gradients occur during the short periods when the ice front passes that area, while low gradients prevail during the long periods of time when the ice front is located far from the repository. For the second and main ice covered period, the mean value of low gradients is around 0.06 degrees (or 0.98 m/km), corresponding to about one third of the present-day regional topographic gradient at Forsmark (3 m/km) /Vidstrand et al. 2010/. The resulting steepest hydraulic gradient in the *reference glacial cycle* is about 0.8 degrees (0.014 m/m) over the first 10 km of the modelled ice sheet profile.

A2.4 Comparison of ice profiles from numerical simulations with the theoretical profile

In all comparisons below, it should be remembered that at a given time, the ice configuration of a realistically modelled ice sheet, such as the one used here, is quite complex; the ice surface is irregular on both small and large spatial scales, and thus far from being a circular and regularly shaped dome as in the theoretical examples. This is due to variations in the dynamics and flux of the ice as a response to e.g. varying mass balance at the surface and variations in bed topography. Such complex ice configurations are seen also on the present day Greenland and Antarctic ice sheets. Consequently, at a given time, ice surface profiles derived from one part of the simulated ice sheet may differ from profiles extracted from another part. When selecting profiles from the Weichselian ice sheet simulation, the aim has been to select profiles both relevant for a broad understanding of how the ice sheet looks and behaves and profiles specifically relevant for the Forsmark site.

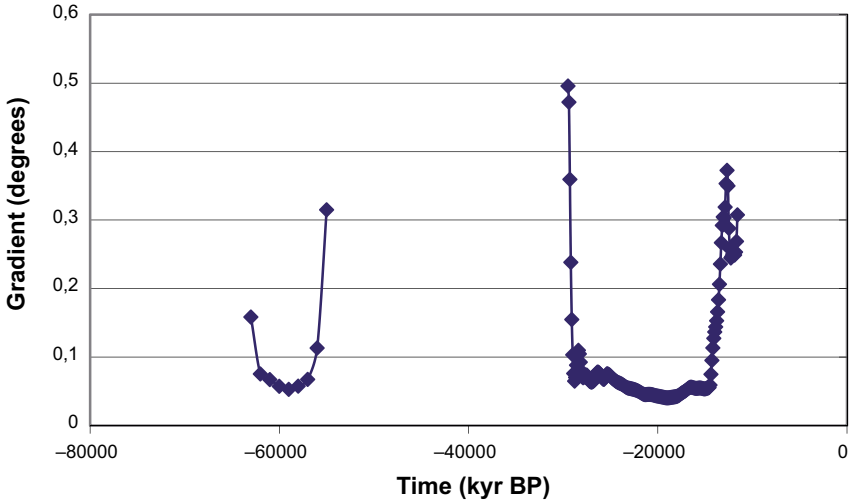

Figure A2-5. *Modelled ice surface gradients above the Forsmark site for the reference glacial cycle. Note that the steepest part of the ice sheet is not included in the figure and is estimated tohave an inclination of 0.8° (0.014 m/m). Steep gradients occur when the ice front passes the site, whereas low gradients prevail when the ice margin is situated far from the site.*

A2.4.1 Simulated advancing profiles compared with the theoretical steady-state profile

In the Weichselian ice sheet simulation, the main phase of ice sheet coverage at Forsmark takes place during the MIS 2 stadial (Section 4.4), with the ice sheet margin reaching Forsmark at around 30 kyrs BP (Section 4.5.1 and Figure A2-4a).

In Figure A2-6, all extracted profiles from the ice sheet *advance* phase (Figure A2-4a) are stacked and compared with the theoretical profiles of Equation A2-2 (Figure A2-1). It is seen that none of the simulated advancing profiles are steeper than the two theoretical steady-state profiles.

It is also seen that the steepest advancing profile, at 30 kyrs BP, is close to being as steep as one of the theoretical profiles described by Equation A2-2. The simulated 30 kyr BP profile is the ice sheet profile when the ice margin is located in the Forsmark area (Figure A2-6).

Having the seemingly contradiction that the steady-state profiles are not steeper than the advancing profiles, is in this case not surprising. Such differences are expected since the profiles are produced in completely different ways. All profiles derived from the numerical ice sheet model incorporate a number of parameters with considerably more realistic representations than how they are treated in the theoretical profile calculation. The ice sheet model includes for instance realistic bed topography instead of a flat horizontal bed, a description of ice sheet thermodynamics, where ice flow and ice temperatures are allowed to interact, and also a better representation of basal conditions (Section 3.1.4). Even if the ice sheet model is far from being a full and complete representation of the natural system, it is significantly better than the theoretical equations. Consequently, the simulated less steep profiles are here considered more realistic for the advancing phases than the steeper theoretical profiles.

There are no large variations in the steepness of the advancing profiles extracted from the ice sheet simulation (Figure A2-6). The steepest simulated advancing profile (from 30 kyrs BP) is close to being as steep as the least steep theoretical profile. Although the simulated profiles are here considered more realistic than the theoretical profiles, the above results show that if one uses the theoretical profiles of Equation A2-2, the ice sheet steepness is not underestimated if compared with the simulated advancing profiles. Therefore, the theoretical profiles of Equation A2-2 may be used as a good and pessimistic (from a safety assessment point of view) mathematical representation of an *advancing* ice sheet over Forsmark (Figure A2-6).

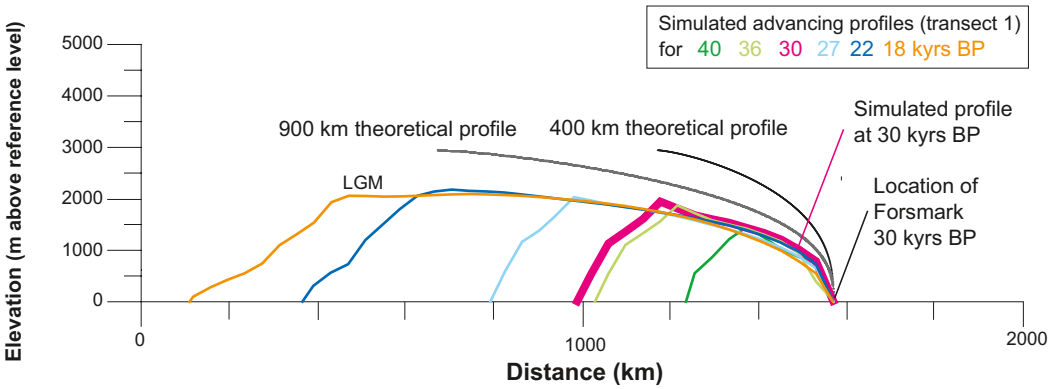

Figure A2-6. *Comparison of ice surface topography from simulated advancing Weichselian ice profiles (from Figure A2-4a) and two theoretical steady-state profiles of Equation A2-2 (from Figure A2-1) /Paterson 1994/. In order to make the comparison meaningful, the fronts of all simulated profiles have been normalized to start at the same position and elevation (0 m) as the theoretical profile. Note that the simulated profiles would be somewhat "steeper" if they were to show ice thickness instead of surface topography (since the bedrock in the ice sheet simulation gets depressed, Figure A2-4), i.e. if they were normalized also to have a flat bed, such as the theoretical profiles. However, for e.g. groundwater flow simulations, it is the gradient of the upper ice surface that is of interest for the water flux, and accordingly that is what is shown also for the simulated profiles. However, this results in differences between the theoretical and simulated profiles appearing larger. The frontal parts of all simulated advancing profiles are less steep than the theoretical steady-state profiles.*

In line with this, the theoretical profiles of Equation A2-2 are used in several other, but not all, safety assessment studies where the effect of a simple mathematical ice profile advancing over Forsmark is studied, for instance in groundwater flow studies /Vidstrand et al. 2010/ and THM studies of hydraulic jacking /Lönnqvist and Hökmark 2010/.

A2.4.2 Simulated LGM profile compared with the steady-state profile

The LGM profile at 18 kyrs BP represents the profile closest to steady-state in the Weichselian ice sheet simulation. In Figure A2-6 it is seen that both theoretical steady-state profiles are steeper than the simulated LGM profile. Given the expected differences due to the different approaches taken to produce the profiles, see above, there is also one additional reason why the simulated LGM profile is less steep than the theoretical steady-state profile. It is likely that the modelled Weichselian ice sheet never reached steady-state conditions during the LGM. This was most probably the case also for the real Weichselian ice sheet. In nature, ice sheets are constantly trying to adapt to the ever changing climate conditions, and the ice sheet probably did not have time to build a maximum-thick, steep ice at LGM.

A2.4.3 Simulated retreating profiles compared with theoretical steady-state profile

In Figure A2-7, the extracted profiles from the *retreat* phase of ice sheet model simulation (from Figure A2-4b), together with the retreat profile extracted from year 14.3 kyrs BP (Figure A2-3), are stacked and compared with the theoretical profiles of Equation A2-2.

The profile extracted along transect 2 for 14.3 kyrs BP has an ice margin that ends in the Baltic Sea, and so do the 14 and 12 kyr BP profiles along transect 1. When comparing the profiles in Figure A2-7, only the grounded parts of all profiles are seen and compared, i.e. the parts of the profiles that are located upstream the grounding-line.

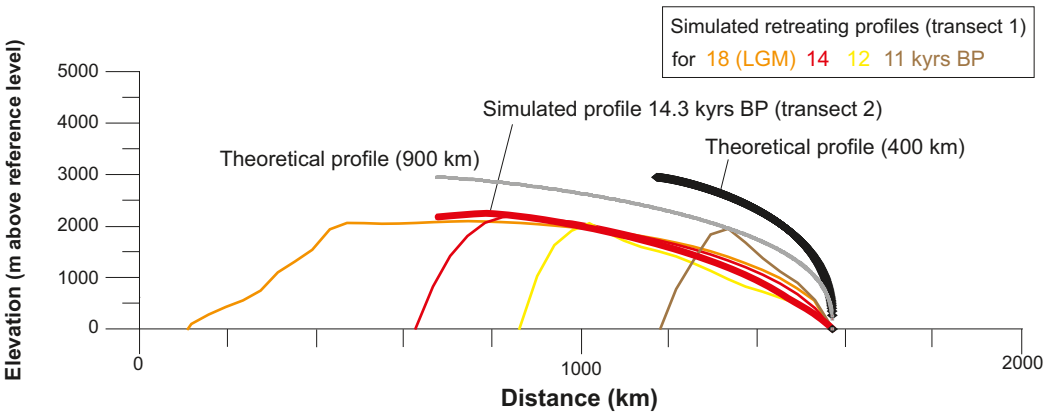

Figure A2-7. *Comparison of ice surface topography between simulated retreating reference glacial cycle ice profiles (from Figure A2-4b and the profile extracted from transect 2 for 14.3 kyrs BP) and the theoretical steady-state profiles of Equation A2-2 (from Figure A1-1). In order to make the comparison meaningful, the fronts of all simulated profiles have been normalized to start at the same position and elevation (0 m) as the theoretical profiles. Note that the simulated profiles would be somewhat "steeper" if they were to show ice thickness instead of surface topography (since the bedrock in the ice sheet simulation gets depressed, Figure A2-4), i.e. if they were normalized also to have a flat bed, such as the theoretical profiles. However, for e.g. groundwater flow simulations, it is the gradient of the upper ice surface that is of interest for the water flux, and accordingly that is what is shown also for the simulated profiles. However, this results in the differences between the theoretical and simulated profiles appearing larger. The frontal parts of all retreating profiles are considerably less steep than the theoretical steady-state profiles. Profiles selected for other SR-Site studies are shown as bold lines.*

In line with theory, it can be seen when comparing Figures A2-6 and A2-7 that the simulated profiles generally are steeper during the ice sheet advance than for the retreat. In Figure A2-7 it is also seen that the retreating profiles are, as expected, considerably less steep than the theoretical steady-state profiles. The steepest of the retreat profiles is from 11 kyrs BP. At this time the ice has a relatively steep profile caused by the steep bed topography in the mountainous region from where the profile is located (see Figure A2-4b). These topographic conditions of the ice sheet bed are not at all representative for the Forsmark area, and this profile is therefore not discussed further.

Comparing the steepness of the frontal parts of the profiles along transect 1, it can be seen that the steepest profile is the 18 kyrs BP (LGM) profile, followed by the 14, and 12 kyrs BP profiles (Figure A2-7), i.e. the ice sheet is getting less and less steep during the deglaciation over the lowland. It can also be noted that the 14.3 kyr BP profile from transect 2 has a steepness that is very similar to profile 14 kyrs of transect 1 (Figure A2-7), even though the profiles have different orientations. It is clearly seen that, for the Weichselian ice sheet simulation, profiles describing the retreat phase should be considerably less steep than the theoretical profiles.

Average hydraulic gradients from the selected theoretical ice sheet profile for various distances from the ice sheet margin are found in Table A2-1. The maximum hydraulic gradient associated with the steep frontal part of the theoretical profile is up to c. 1.5 m/m.

A2.4.4 Selection of profiles to use in SR-Site

Since the theoretical profiles of Equation A2-2 are considered to be more realistic than profiles from Equation A2-1, and because it is steeper than the steepest of the simulated advancing ice profiles (Figure A2-6), the steepest theoretical profile is selected to represent an advancing ice sheet over Forsmark for the SR-Site *reference glacial cycle*.

The frontal near parts of the profile extracted for 14.3 kyrs BP (transect 2) is the least steep retreat profile from the Weichselian ice sheet simulation (Figure A2-7). This profile is selected to represent a retreating ice sheet over Forsmark for the SR-Site *reference glacial cycle*.

The two selected profiles are shown by the bold lines in Figure A2-7. These two profiles constitute, in their frontal parts, the steepest and the least steep profiles of all profiles analyzed, and they are considered to cover a broad enough span of possible profiles to be employed in other SR-Site studies, such as modelling of groundwater flow under glacial conditions /Vidstrand et al. 2010/ and THM studies /Lönnqvist and Hökmark 2010/.

A2.5 Conclusions

1. The steepest theoretical profile (Equation A2- 2, Figure A2-7) /Paterson 1994/ is selected to represent an advancing ice sheet over Forsmark in the SR-Site *reference glacial cycle*. This profile is denoted "*the theoretical reference glacial cycle profile"*.
2. The least steep simulated profile from 14.3 kyrs BP (Figure A2-7) is selected to represent a retreating ice sheet over Forsmark in the SR-Site *reference glacial cycle*. This profile is denoted "*the simulated reference glacial cycle profile*".

The profiles can of course be used in other ways than suggested above, e.g. for sensitivity studies on ice sheet steepness.

Table A2-1. Hydraulic gradients (m/m) from the selected theoretical ice sheet profile (Equation A2-2) averaged over various distances from the ice sheet margin.

Distance from ice margin (m)	Hydraulic gradient (m/m)	Hydraulic gradient (degrees)
100	1.49	56
200	0.96	44
400	0.62	32
1,000	0.35	19
2,000	0.23	13
4,000	0.15	8.5

Appendix 3

Combination of buffer erosion and freezing

A3.1 Background

Based on the results on freezing depths analysed in the *reference glacial cycle* (Section 4.5.3) and the *severe permafrost case* (Section 5.5.3), freezing of water were excluded at repository depth for the first future glacial cycle in the buffer freezing scenario /SKB 2011/. For subsequent glacial cycles in the 1 Myr long safety assessment period, repository heat has declined. If making the most pessimistic combination of uncertainties in the input data to the permafrost simulations, there is a small risk of freezing of water at repository depth for these glacial cycles, while there is still ample margin to freezing of the bentonite buffer and deposition tunnel back-fill material, see the scenario on buffer freezing in /SKB 2011/. Because of this risk of freezing of water at repository depth, even if the risk is extraordinarily small, and for illustrative purposes, a combined case of buffer erosion and freezing at repository depth is here presented. If groundwater were to freeze in cavities formed by buffer erosion, the associated volume expansion would induce an additional pressure that possibly could affect the copper canister.

Two studies were made in order to illustrate the pressure effects of this hypothetical combined buffer erosion and freezing case. The first study (study A) investigated resulting freezing-point temperatures and freezing-induced pressures in buffer erosion cavities by considering various assumptions on compressibilities of remaining buffer, erosion cavity geometry, and surrounding ambient pressure (in this case surrounding groundwater pressure plus clay swelling pressure). It was also assumed that the cavity was filled with ordinary compressible water, free from solutes and impurities. The second study (study B) considered the chemical potential of water in bentonite in order to investigate equilibrium pressures in systems with various proportions of ice and bentonite and the resulting freezing temperatures and pressures. Effects of erosion cavity geometries were not included.

A3.2 Study A

A simple model was used to estimate the freezing point and pressure increase in a ring-shaped erosion cavity surrounding the canister (Figure A3-1). The full study was reported in /SKB 2006a, Section 4.4.1/. The compressibility of remaining clay was estimated from the swelling pressure of bentonite. It was also assumed that the erosion cavity was completely filled with ordinary compressible water, free from solutes and impurities. The effect of including these compressibilities is that they allow the freezing-induced expansion to occur at considerably higher temperatures than if the surroundings were incompressible. The compressibility of ice was also included, whereas the canister and the rock were assumed to be incompressible. Moreover, mean freezing temperatures for the erosion cavity as well as mean pressures for the erosion cavity and bentonite were assumed. For further details, see /SKB 2006a, Section 4.4.1/.

The surrounding groundwater pressure may vary between the ambient hydrostatic pressure, for completely unfrozen conditions, to a value up to the maximum freezing pressure for partially or fully frozen groundwater conditions. However, for a certain freezing temperature and for ambient pressures lower than the maximum freezing pressure, the pressure increase from freezing is affected by the ambient pressure, including the swelling pressure, in such a way that the resulting total pressure is constant, see below.

Calculations of freezing temperatures and associated pressure increases were made for ambient pressures between 4 and 100 MPa /SKB 2006a, Section 4.4.1/. As an example, the results of the calculations for an ambient pressure of 10 MPa are shown in Figure A3-2. Examples of pressure increase and total pressure after freezing for various ambient pressures are presented in Table A3-1. For further results see /SKB 2006a, Section 4.4.1/.

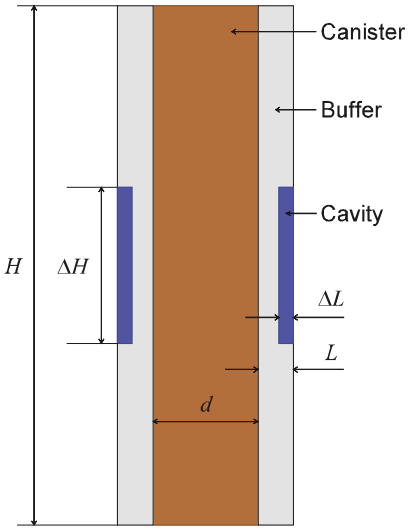

Figure A3-1. *Geometry for calculations of freezing temperatures and freezing-induced pressures in buffer erosion cavities.*

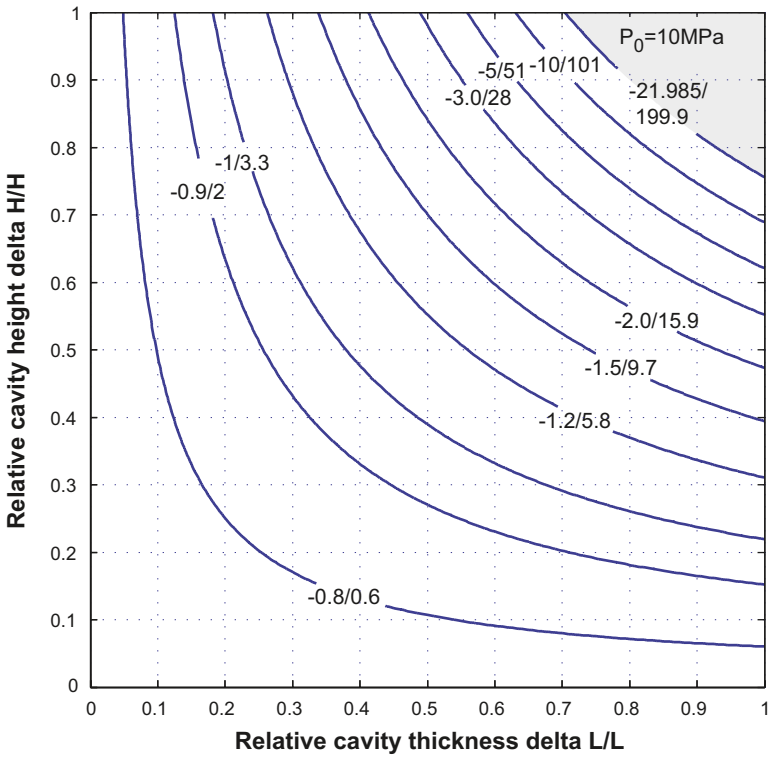

Figure A3-2. *Freezing point temperature (°C) and associated maximum pressure increase (MPa) in the erosion cavity, as a function of relative cavity thickness and height, at an ambient pressure of 10 MPa. In the figure, the first number is the freezing temperature and the second number is resulting pressure (i.e. temp/ pressure). The shaded area represents a region with very low temperatures, below approximately −22° C.*

Table A3-1. Examples of pressure increase and total pressure after freezing in an erosion cavity for various ambient pressures at a freezing temperature of −2°C. Note that the total pressure after freezing is independent of erosion cavity geometry and size.

Ambient pressure (sum of groundwater pressure and clay swelling pressure) (MPa)	Pressure increase from freezing in erosion cavity (MPa)	Total pressure (maximum freezing pressure) (MPa)
4	22	26
5	21	26
10	16	26
20	6	26
26	0	26
50	0 (no freezing occurs)	50

The results can be summarised as follows:

1. Freezing of water in an erosion cavity at a given freezing temperature can increase the pressure from the ambient pressure to the maximum freezing pressure, i.e. the maximum pressure at which freezing can occur at that temperature. For a freezing temperature of −2°C for instance, the *maximum* freezing pressure is ~26 MPa. For a freezing temperature of −2°C, the total pressure after freezing in the erosion cavity thus is between the ambient pressure and 26 MPa, depending on the size of the erosion cavity.
2. The *maximum* freezing pressure for a certain freezing temperature is independent of the geometry and size of the erosion cavity.
3. The pressure increase from freezing depends on the freezing temperature, the ambient pressure and the size or geometry of the erosion cavity. For certain combinations of freezing temperature and ambient pressure, complete freezing takes place and the resulting pressure increase grows with the size of the cavity. This occurs up to a certain point, at which the sum of the ambient pressure and the pressure increase equals the maximum freezing pressure. After that point, the freezing pressure is at its maximum and complete freezing can no longer take place.
4. If the ambient pressure exceeds the maximum freezing pressure of 26 MPa, no freezing can occur at a temperature of −2°C, see also Table A3-1.

A3.3 Study B

In order to assess the possible maximum pressure if an eroded KBS-3 buffer were to freeze, the equilibrium pressure between ice and bentonite was first considered. By considering this equilibrium pressure, and the expected deformation when ice is formed in a restricted volume, the maximum freezing pressure was estimated.

A3.3.1 Pressure of ice and bentonite in equilibrium

The chemical potential of water in bentonite is generally lower than in liquid bulk water at the same pressure and temperature. In order to reach equilibrium in a system with a confined clay sample contacted with an external reservoir of liquid water, a pressure difference between the clay and the external reservoir is therefore sustained. This pressure difference is usually referred to as the swelling pressure.

It is important to note that the occurrence of swelling pressure requires the external water reservoir to be mechanically separated from the clay, as is the case in a KBS-3 deposition hole where water is supplied by fractures in the surrounding rock or through the rock matrix itself. Liquid bulk water and bentonite at the same pressure cannot exist simultaneously in equilibrium (unless the clay density is very low).

The chemical potential of ice, on the other hand, can be lower, higher, or equal to that of bentonite water at the same pressure and temperature depending on the specific values of these variables as well as on the amount of water in the clay. In particular, this means that ice and bentonite can co-exist in equilibrium at the same pressure. The equilibrium pressure in a system containing both bentonite and ice can be derived by considering the following expression for the chemical potential of water in the bentonite /Birgersson et al. 2008/

$$\mu_{clay} = \mu_0 - s_{liq} \cdot T + v_{liq} \cdot P - v_{liq} \cdot P_s^0(w_u)$$ Equation A3-1

where μ_0 is the potential of a non-pressurized bulk water reference state at 0°C, T denotes temperature in °C, P denotes pressure, $P_s^0(w_u)$ is the measured swelling pressure at water to solid mass ratio w_u at 0°C, and s_{liq} and v_{liq} are the partial molar entropy and volume of liquid bulk water, respectively. Note that all chemical potentials used here refer to water in different phases. The partial molar quantities of the water in the clay is here approximated by the corresponding liquid bulk water properties and are further assumed independent of temperature and pressure. Note that $P_s^0(w_u)$ is not a physical pressure in the current state of the clay (the physical pressure is P), but rather a quantity describing the water retention properties of the specific clay under consideration. This function resembles an exponential expression at low enough water to solid mass ratios for typical bentonite materials, see e.g. /Kahr et al. 1990/.

$$P_s^0(w_u) \approx Ae^{-B \cdot w_u}$$ Equation A3-2

Using the data in /Karnland et al. 2006/ and /Karnland et al. 2009/, the least square fitted parameters for MX-80 bentonite in the range 0.5–12 MPa are A ≈ 382 MPa and B ≈ 13.9. The chemical potential in the ice can be expressed in a similar way as for the bentonite water

$$\mu_{ice} = \mu_0 - s_{ice} \cdot T + v_{ice} \cdot P$$ Equation A3-3

Note that this expression lacks the water retention term and that the partial molar properties are associated with ice (naturally). The equilibrium pressure is deduced by putting the two above expressions for the chemical potential of water equal,

$$P = \frac{\Delta s \cdot T + v_{liq} \cdot P_s^0(w_u)}{\Delta v}$$ Equation A3-4

where $\Delta s = s_{liq} - s_{ice}$ and $\Delta v = v_{liq} - v_{ice}$.

Notice that Δv is a negative quantity since ice has a lower density than liquid bulk water. Note further that the equilibrium pressure becomes negative for a given value of w_u if the temperature is high enough (although negative), indicating that ice and bentonite do not co-exist in equilibrium under such conditions. Consequently, the temperature where the equilibrium pressure is zero also defines the freezing point of the bentonite under consideration

$$T_c(w_u) = -\frac{v_{liq} \cdot P_s^0(w_u)}{\Delta s}$$ Equation A3-5

This expression for the freezing point is in agreement with earlier derivations /Birgersson et al. 2010/. Equation 5-4 can be re-expressed using $T_c(w_u)$ as

$$P = \frac{\Delta s \cdot (T - T_c(w_u))}{\Delta v}$$ Equation A3-6

which can be viewed as a generalized Clausius–Clapeyron relation where the presence of clay influences the phase boundary between ice and liquid water by a shift of the temperature scale.

A3.3.2 Pressure increase due to ice formation in a restricted volume

When a confined and water-saturated bentonite sample freezes (e.g. a KBS-3 buffer), some of the water will leave the bentonite (the montmorillonite interlayers) to form a separate ice phase (small ice crystals) /Svensson and Hansen 2010/. Because ice has lower density than liquid (clay) water, a pressure increase is expected under such a transformation. The pressure increase can be quantified by first considering the volume change when a certain amount of water, Δm, is transferred from clay to ice under non-pressurized conditions in an initially ice-free bentonite sample of water to solid mass ratio w_{tot}

$$\Delta V = \left(\frac{1}{\rho_{ice}} - \frac{1}{\rho_w}\right) \cdot \Delta m = \left(\frac{\rho_w}{\rho_{ice}} - 1\right) \cdot \frac{\Delta m}{\rho_w} = \xi \cdot \frac{m_s}{\rho_w}(w_{tot} - w_u)$$ Equation A3-7

Here ρ_{ice} and ρ_w denotes the density of ice and liquid bulk water, respectively, $\xi \equiv \rho_w/\rho_{ice} - 1$, m_s is the mass of dry clay and w_u denotes the amount of water in the bentonite after the transition (i.e. the amount of unfrozen water). If the total system (bentonite + ice) is to be kept a constant volume, a pressure causing the deformation $-\Delta V$ must be applied. Assuming isotropic stress state (hydrostatic pressure), bulk modulus β, and using Equation A3-7, the pressure after the transition is given by

$$P = -\beta\frac{-\Delta V}{V_w} = \beta\xi\frac{m_s}{V_w\cdot\rho_w}\left(w_{tot}-w_u\right) = \beta\xi\left(1-\frac{w_u}{w_{tot}}\right) \qquad \text{Equation A3-8}$$

where the first equality utilizes the definition of bulk modulus and V_w denotes the total water volume (liquid + ice). The presence of the total water volume rather than total volume in Equation A3-8 is equivalent to assuming that the dry clay particles are uncompressible.

A3.3.3 Estimated pressure of confined bentonite below 0°C

It can be shown /Birgersson et al. 2010/ that the swelling pressure decreases approximately linearly with temperature in the range between the freezing point of the external water reservoir (here assumed to be 0°C) and the freezing point of the bentonite. Furthermore, at the freezing point of the bentonite, the swelling pressure is zero. If the temperature of a confined bentonite sample is lowered below the freezing point, the pressure will start to increase due to the volume expansion of the water transformed from liquid state to ice. The equilibrium pressure at a given temperature below T_c can be deduced by first calculating the amount of unfrozen water by combining Equations A3-2 , A3-4 and A3-8 (assuming that the system has the total water to solid mass ratio w_{tot})

$$\frac{\Delta s\cdot T - v_{liq}\cdot A\cdot e^{-B\cdot w_u}}{\Delta v} = \beta\xi\left(1-\frac{w_u}{w_{tot}}\right) \qquad \text{Equation A3-9}$$

Once the unfrozen amount of water is calculated, the equilibrium pressure is given by either of Equations A3-4 or A3-8. All parameters in Equation A3-9 except for the bulk modulus β are firmly determined by either fundamental properties of bulk water or by accurate swelling pressure measurements. The parameter set when applied to MX-80 bentonite is listed in Table A3-2.

The specific value to be used of the bulk modulus, on the other hand, is not as clear. The compressibility of the full system will depend on the separate bulk moduli of clay, water and ice as well as the relative fraction of these phases. Hence, it is to be expected that β is a function of both w_u and w_{tot}. A way to treat this complication is to solve Equation A3-9 for two limiting values of β in order to achieve a pressure interval for the actual equilibrium pressure. Here the limiting values of β is chosen as that of pure ice (8,800 MPa) and that of liquid bulk water (2,200 MPa), and are assumed independent of temperature and pressure.

A solution to Equation A3-9 for MX-80 bentonite (Table A3-3) is illustrated in Figure A3-3. This example assumes $w_{tot} = 0.366$, which corresponds to a swelling pressure at 0°C of ca 2.5 MPa, and a freezing point of –2°C. In the diagram the ice/clay equilibrium line at –3°C (Equation A3-4) is displayed. When lowering the temperature from –2 to –3°C, water is expelled from the clay and pressure increases according to the compression curves (Equation A3-8, with two different values of the bulk modulus). The actual pressure of the system is given by the intersection between the compression and the ice/clay equilibrium curve. Hence, in the case of a bulk modulus of ice, the unfrozen water content is ca 0.360 and pressure is ca 13 MPa. If the bulk modulus instead is that of liquid bulk water, the unfrozen water content is ca 0.351 and the pressure is ca 8 MPa. Hence when lowering the temperature from –2°C to –3°C, this particular sample increases its pressure from 0 to 8–13 MPa.

Table A3-2. Values of parameters used in Equation A3-9. The partial molar entropies and volumes are approximated by bulk values (ice and liquid water) at 0°C. The swelling pressure parameters (Equation A3-2) are fitted to data for MX-80 bentonite /Karnland et al. 2006, Karnland et al. 2009/.

Δs (J/mol/°C)	v_{ice} (cm³/mol)	v_{liq} (cm³/mol)	A (MPa)	B (–)	$\Delta v = v_{liq} - v_{ice}$ (cm³/mol)	$\xi = v_{ice}/v_{liq} - 1$ (–)
22.0	19.65	18.03	382.1	13.86	1.62	0.09

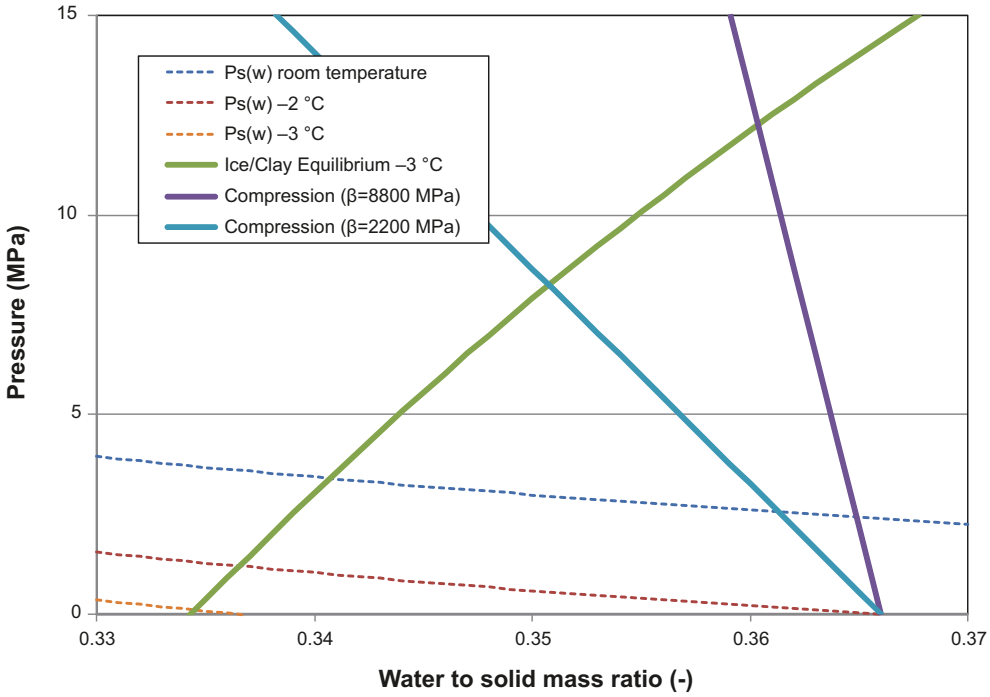

Figure A3-3. *Illustration of the obtained equilibrium pressure when ice forms in a confined MX-80 sample. Equilibrium pressure is reached where the compression line intersects the Ice/clay equilibrium line. Included in the figure is also the swelling pressure curve for different temperatures /Birgersson et al. 2010/.*

A3.3.4 The combination of erosion and freezing in a KBS-3 buffer

The nominal buffer density is 2.0 g/cm^3, corresponding to a water to solid mass ratio of ~0.27. The freezing point of the undisturbed buffer thus equals –7°C according to Equation A3-5. It is however evident from Equation A3-2 that swelling pressure, and thereby the freezing point, is a strong function of water content in this density region. This means that the buffer freezing point is expected to increase substantially if bentonite is lost from the deposition hole due to erosion. A freezing point of –2°C, for example, corresponds to a water to solid mass ratio of 0.366, or a density of 1.87 g/cm^3. This, in turn, corresponds to a mass loss of ca 13% or ca $2.7 \cdot 10^3$ kg if the buffer density can be assumed homogeneous (initial mass: $2.0 \cdot 10^4$ kg).

Table A3-3 shows the expected pressure intervals and unfrozen water contents at different temperatures for different values of buffer freezing points (i.e. different densities). Included in Table A3-3 is also the case where all clay has eroded. The equilibrium pressures for this case are given by the ordinary Clausius-Claperyon equation for phase equilibrium between liquid water and ice (Equation A3-6 with $T_c = 0$) and are independent of the value of the bulk modulus.

Table A3-3. The limiting pressures and unfrozen water contents at different temperatures for MX-80 bentonite of different freezing points (i.e. different densities). The listed eroded mass assumes a homogeneously distributed buffer with initial mass $2.0 \cdot 10^4$ kg.

T_c	w_{tot}	ρ_b	Eroded mass	at –1°C		at –2°C		at –3°C		at –4°C		at –5°C	
				P	w_u	P	w_u	P	w_u	P	w_u	P	w_u
°C	–	g/cm^3	kg	MPa	–	MPa	–	MPa		MPa		MPa	
0	–	1.00	$2.0 \cdot 10^4$	14	–	27	–	41	–	54	–	68	–
–1	0.416	1.82	$3.8 \cdot 10^3$	0	0.416	10–13	0.396–0.409	18–25	0.377–0.403	26–38	0.361–0.396	33–49	0.346–0.390
–2	0.366	1.87	$2.7 \cdot 10^3$	Unfrozen	0.366	0	0.366	8–13	0.351–0.360	15–24	0.338–0.355	22–35	0.326–0.350
–3	0.337	1.91	$1.9 \cdot 10^3$	Unfrozen	0.337	Unfrozen	0.337	0	0.337	7–12	0.324–0.332	14–23	0.314–0.327
–4	0.316	1.94	$1.4 \cdot 10^3$	Unfrozen	0.316	Unfrozen	0.316	Unfrozen	0.316	0	0.316	7–12	0.305–0.311

Table A3-3 lists the expected pressures in a frozen deposition hole whose buffer is eroded in such a way that the remaining clay is homogeneously distributed, which is the equilibrium state. However, since erosion occurs at the rock-buffer interface, substantial internal redistribution of the buffer mass is required to reach this state. Therefore, it cannot be excluded that the buffer density to a certain degree is inhomogeneous when it freezes, e.g. because of long equilibration times, or because of internal "friction". This means that freezing could occur above the freezing points listed in Table A3-3, as these correspond to buffer mean density. Consider for instance a homogeneous buffer of (mean) density 1.87 g/cm^3. This system would not experience any pressure increase at –2°C (which is the freezing point for this particular density). If instead the mass was distributed so that a certain fraction of the buffer had a density of 1.82 g/cm^3 (and a density higher than 1.87 g/cm^3 in the rest), a pressure increase would be experienced at –2° because the freezing point of the low density part is –1°C. The pressure increase, however, is smaller than for the case of a homogeneous buffer at density 1.82 g/cm^3 because the entire buffer is involved in the deformation. Hence, the values in Table A3-3 also put an upper limit for the pressure increase in inhomogeneous buffers if the density instead refers to minimum density.

It should be noted that the more heterogeneous the density distribution is the more unlikely the state, because larger and larger forces will act to redistribute the mass (Equation A3-2). But even for the highly unrealistic density distribution of a bulk water cavity (ρ_b = 1.0 g/cm^3) in conjunction with unaffected clay (ρ_b = 2.0 g/cm^3), the pressure increase will never exceed that for the case of a completely eroded deposition hole. Note further that the pressure increases experienced in heterogeneously distributed buffers are transient states; when freezing occur (in the part of the buffer with lowest density), the stress state changes radically and mass redistribution is expected, leading to a more homogeneous state of the clay and lower pressures.

The above considerations have not taken into account the additional hydrostatic pressure present under unfrozen conditions in a KBS-3 repository. However, the effect of any additional load (affecting both clay and reservoir) would, on one hand, lower the freezing point according to the conventional Clausius-Clapeyron relation (ca 0.074°C/MPa), but on the other hand the pressure would be non-zero at the freezing point (equal to the additional load). Similarly, if the groundwater (and thus the clay) contains a certain amount of salt, the freezing point of the external reservoir would lower accordingly and also the ice/clay equilibrium would adjust in such a way that the clay would contain more water for a given temperature and pressure. Consequently, neither the effect of a hydraulic head, nor the effect of salt in the water, will contribute to increase the values listed in Table A3-3.

A3.4 Discussion and conclusions

The lowest temperature at repository depth when considering the results of maximum freezing depths in the *reference glacial cycle* and the *severe permafrost case* (Table 5-11), and including the most pessimistic combination of all uncertainties relevant for the respective case, is approximately −0.5°C. In line with this the −2°C isotherm does not reach repository depth in the reference evolution, nor in the *severe permafrost case*. Nevertheless, as a pessimistic basis for a discussion on the theoretical consequences of the combined buffer erosion and freezing case, a lowest temperature of −2°C is assumed at repository depth. This corresponds to a lowering of the entire temperature curve reconstructed for the last glacial cycle of more than 10°C (Figure 5-33) which is considered unrealistic also when including the significant uncertainties associated with the temperature curve (Appendix 1).

The results from study A show that for a temperature of −2°C, the pressure increase from freezing of pure groundwater in buffer erosion cavities results in a maximum cavity pressure of 26 MPa (Table A3-1). Freezing at higher temperatures would yield lower freezing-induced pressures (Figure A3-2), while other ambient pressures would not result in a total pressure higher than 26 MPa. This pressure is in line with the maximum pressure obtained from study B for an ambient temperature of −2°C. Here the pressure in the cavity is 27 MPa for a case with a completely eroded buffer (Table A3-3), corresponding to a buffer loss of 20,000 kg. Cases with a less eroded buffer (i.e. a partially eroded buffer with a higher buffer density and lower freezing point, Table A3-3), yields lower erosion cavity pressures. For example, a buffer loss of 1,400 kg, which is close to the value of 1,200 kg of buffer loss that is used for the assumption of getting advective conditions in the buffer /SKB 2011/, results in unfrozen conditions if the temperature is −2°C (Table A3-3). For this case, the temperature needs to be as low as −5°C in order to freeze the buffer cavity, with a resulting maximum cavity pressure of 12 MPa.

A maximum pressure of 26–27 MPa in the erosion cavity is considerably lower than the maximum total pressure deduced for the SR-Site scenario on isostatic load where the maximum thick ice sheet from Section 5.4 is combined with clay swelling pressure and hydrostatic pressure due to the repository depth, resulting in a total pressure of around 50 MPa /SKB 2011/. Since this isostatic load scenario does not result in canister failure /SKB 2011/, the same is here concluded for the hypothetical case combining buffer erosion and freezing.

If the pressure from a maximum large ice sheet (30 MPa) (Section 5.4) were to be directly and unrealistically combined with the maximum pressure resulting from freezing in buffer erosion cavities (27 MPa), the resulting pressure would be 57 MPa. However, this case is not relevant since for ambient pressures greater than 26 MPa, a repository depth bedrock temperature of −2°C would not be low enough to freeze water in erosion cavities. In addition, during phases of ice sheet overriding, pre-existing permafrost degrades due to the insulation effect of the ice sheet, e.g. (Section 4.5.3), which means that deep permafrost is not compatible with large ice sheet thicknesses.

All in all, the following conclusions can be made:

- Based on the results on maximum permafrost and freezing depths in the *reference glacial cycle* (Section 4.5.3) and in the *severe permafrost case* (Section 5.5.3), freezing of water at repository depth was excluded for the first future glacial cycle in the buffer freezing scenario /SKB 2011/.
- Calculations made show that the maximum freezing-induced pressure in buffer erosion cavities would be 26–27 MPa for a pessimistically chosen ambient temperature of −2°C. This case corresponds to a total loss of buffer in the deposition hole. This pressure is considerably lower than the critical pressure for canister collapse as discussed in the scenario treating canister collapse due to isostatic load /SKB 2011/.
- The amount of buffer loss affects the freezing point of the remaining buffer and the resulting cavity pressures. A case with buffer loss approximately corresponding to the buffer loss assumed for getting advective conditions in the buffer does not result in frozen conditions in the erosion cavity if the ambient temperature is −2°C. In this case, the temperature needs to be −5°C in order to get freezing, with a resulting cavity pressure of up to 12 MPa as result.

A freezing-induced pressure in buffer erosion cavities and large pressures from ice sheet load do not occur simultaneously